THE BALTIC SEA REGION IN TRANSITION

EDITED BY: Marcus Reckermann, Markus Meier and Martin Stendel

PUBLISHED IN: Frontiers in Earth Science and Frontiers in Environmental Science

frontiers Research Topics

ISSN 1664-8714
ISBN 978-2-88966-192-3
DOI 10.3389/978-2-88966-192-3

About Frontiers

Frontiers is more than just an open-access publisher of scholarly articles: it is a pioneering approach to the world of academia, radically improving the way scholarly research is managed. The grand vision of Frontiers is a world where all people have an equal opportunity to seek, share and generate knowledge. Frontiers provides immediate and permanent online open access to all its publications, but this alone is not enough to realize our grand goals.

Frontiers Journal Series

The Frontiers Journal Series is a multi-tier and interdisciplinary set of open-access, online journals, promising a paradigm shift from the current review, selection and dissemination processes in academic publishing. All Frontiers journals are driven by researchers for researchers; therefore, they constitute a service to the scholarly community. At the same time, the Frontiers Journal Series operates on a revolutionary invention, the tiered publishing system, initially addressing specific communities of scholars, and gradually climbing up to broader public understanding, thus serving the interests of the lay society, too.

Dedication to Quality

Each Frontiers article is a landmark of the highest quality, thanks to genuinely collaborative interactions between authors and review editors, who include some of the world's best academicians. Research must be certified by peers before entering a stream of knowledge that may eventually reach the public - and shape society; therefore, Frontiers only applies the most rigorous and unbiased reviews.
Frontiers revolutionizes research publishing by freely delivering the most outstanding research, evaluated with no bias from both the academic and social point of view. By applying the most advanced information technologies, Frontiers is catapulting scholarly publishing into a new generation.

What are Frontiers Research Topics?

Frontiers Research Topics are very popular trademarks of the Frontiers Journals Series: they are collections of at least ten articles, all centered on a particular subject. With their unique mix of varied contributions from Original Research to Review Articles, Frontiers Research Topics unify the most influential researchers, the latest key findings and historical advances in a hot research area! Find out more on how to host your own Frontiers Research Topic or contribute to one as an author by contacting the Frontiers Editorial Office: frontiersin.org/about/contact

THE BALTIC SEA REGION IN TRANSITION

Topic Editors:
Marcus Reckermann, Helmholtz Centre for Materials and Coastal Research (HZG), Germany
Markus Meier, Leibniz Institute for Baltic Sea Research (LG), Germany
Martin Stendel, Danish Meteorological Institute (DMI), Denmark

Citation: Reckermann, M., Meier, M., Stendel, M., eds. (2021). The Baltic Sea Region in Transition. Lausanne: Frontiers Media SA. doi: 10.3389/978-2-88966-192-3

Table of Contents

frontiers in Earth Science

EDITORIAL
published: 01 October 2020
doi: 10.3389/feart.2020.589252

Editorial: The Baltic Sea Region in Transition

Marcus Reckermann[1]*, *H.E. Markus Meier*[2] *and Martin Stendel*[3]

[1] International Baltic Earth Secretariat, Helmholtz Centre for Materials and Coastal Research (HZG), Geesthacht, Germany, [2] Leibniz Institute for Baltic Sea Research Warnemünde, Rostock, Germany, [3] Danish Meteorological Institute (DMI), Copenhagen, Denmark

Keywords: Baltic Sea, Baltic Earth, Earth system, climate change, coastal research

Editorial on the Research Topic

The Baltic Sea Region in Transition

The Baltic Sea is a semi-enclosed sea in Northern Europe, draining about 20% of Europe in its catchment area, where about 85 Million people live; most of them in the southern part. The region and the Baltic Sea itself have been subject of interdisciplinary Earth system research for many decades, and especially so since the barriers between the eastern and western researchers fell in the early 1990. Baltic Earth and its precursor program BALTEX have fostered the collaboration of Earth system research across the countries and scientific disciplines for almost 30 years, also as part of the global GEWEX(Global Energy and Water Exchanges) program of WCRP, the World Climate Research Program of WMO, the World Meteorological Organization.

This Frontiers Research Topic in Frontiers is based on contributions from the 2nd Baltic Earth Conference in Helsingør, June 11–15, 2018. Like the previous Baltic Earth and BALTEX conferences (nine in total), it covered the themes of Baltic Earth, in particular highlighting the Baltic Earth Grand Challenges as defined by the Baltic Earth Science Plan 2017. The grand topic of the conference "The Baltic Sea region in transition" refers both to processes in the transition area between the North Sea and the Baltic Sea, but more so to temporal transition processes (e.g., regional climate change) in the energy, water and matter cycles of the Baltic Sea, its coasts, the atmosphere, land surface and socio-economic system of its catchment basin. At this conference, the Grand Challenges and research topics of the science plan were discussed within the following sessions:

- Salinity dynamics
- Land-Sea-Atmosphere biogeochemical feedbacks
- Natural hazards and high impact events
- Sea level dynamics, coastal morphology and erosion
- Regional variability of water and energy exchanges
- Multiple drivers of regional Earth system changes
- Regional climate system modeling

The 19 contributions in this Frontiers Research Topic are part of the 126 which were presented orally or as posters at the conference in Denmark (all available as extended abstracts), spanning the spectrum of Baltic Earth research, from observed and modeled processes in the atmosphere, the sea and on land, as well as transition processes between these compartments. Innovative methods and management issues were also discussed. In the following, we briefly introduce the papers of this Research Topic.

Quite a number of papers treated oceanographic issues. Salinity distribution is crucial for the vertical stratification of the water column, and to a large extent controls the distribution of organisms, from bacteria to fish. Liblik and Lips have analyzed 35 years of Baltic Sea

OPEN ACCESS

Edited and reviewed by:
Hayley Jane Fowler, Newcastle University, United Kingdom

***Correspondence:**
Marcus Reckermann
marcus.reckermann@hzg.de

Specialty section:
This article was submitted to Interdisciplinary Climate Studies, a section of the journal Frontiers in Earth Science

Received: *30 July 2020*
Accepted: *08 September 2020*
Published: *01 October 2020*

Citation:
Reckermann M, Meier HEM and Stendel M (2020) Editorial: The Baltic Sea Region in Transition. Front. Earth Sci. 8:589252. doi: 10.3389/feart.2020.589252

observational data and conclude that stratification, which is basically dependent on the distribution of salinity and temperature in the water column, and which is peculiar in the Baltic Sea, has increased over this period. While there was a clear warming trend in the water column (about twice as much as in the upper Atlantic), they found different salinity trends in different depth layers, causing an overall increase in stratification but no significant trend in mean salinity of the Baltic Sea.

The generation and distribution of internal waves in the Baltic Sea, which plays a role also in stratification and mixing, is investigated by Kurkin et al. Using a circulation model, they analyze the main properties of long-period subinertial baroclinic motions in the Baltic Sea, focusing on periods in the range of 2–12 days. Results suggest that the relevant field of motions in the Baltic Sea is highly inhomogeneous and strongly asymmetric.

A way to overcome the limitation of very few real sampling (data) points at sea, is to combine measured with modeled data. Elken et al. present a statistical method to reconstruct temperature and salinity data from measurements and models. For Sea Surface Temperature, their Empirical Orthogonal Functions method perform better than a similar technique (Optimal Interpolation), which is slightly better for Sea Surface Salinity. The authors claim that their Empirical Orthogonal Functions has certain advantages when real observations are very sparse.

The measurement of real field data to give insight into the distribution and velocity of water bodies in the Baltic Sea necessary to validate models. Paka et al. describe a new method for vertical profiling the water column, especially in the difficult narrow bottom layer. Using this new profiling method, some remarkable temperature and current velocities were measured in the deep water.

In the northern Baltic Sea, sea ice is a common feature in winter. Sea ice cover has a strong impact on the wave climate of adjacent sea areas, and consequently, on operational wave forecasting. Using wave models, Tuomi et al. compared two data sources and two methods to calculate significant wave heights. The results can help to optimize operational wave forecasts in the northern Baltic Sea in winter.

Good measurements of methane fluxes are crucial for climate models, as methane is a much more potent greenhouse gas than CO_2, albeit present in much lower concentrations. Gutiérrez-Loza et al. present a method to measure air–sea methane fluxes. They demonstrate that high-resolution micro-meteorological techniques can increase the understanding of the temporal variability and forcing processes of these fluxes, and thus improve the capability of climate models to incorporate them.

Rapid methodological innovations and developments are currently ongoing in Baltic Sea Operational Oceanography. In this review paper, She et al. introduce two large research networks in the Baltic Sea, which both work complimentary on scientific questions: BOOS (Baltic Sea Operational Oceanographic System) and Baltic Earth (formerly BALTEX). Both are different in their scientific scope but have the potential to significantly improve Baltic Sea oceanographic research in terms of operational measurements and model applicability and quality.

Sea level change and variability in the Baltic Sea is a quite complicated issue, due to the geological and meteorological situation of the Baltic Sea. There are not many sea level projections for the Baltic Sea. Madsen et al. (a) have calculated sea level trends and variabilities from statistical reconstructions (i.e., statistical treatments of monthly tide gauge measurements and re-analyses) and compared this with satellite altimetry. Generally, the results for the trends are comparable to global estimates.

Together with other collaborators, Madsen also performed an investigation on stakeholder needs concerning sea level change in Denmark (Madsen et al. (b)). Aim of the study is to map user needs of coastal municipalities, which are responsible for coastal protection. The study indicates the need for good storm surge warnings, extreme sea levels and wave heights. Common scenarios are needed to help the collaboration between municipalities.

Using different statistical methods, Medvedev et al. investigated the strong variability of Baltic Sea sea levels over different periods. The study demonstrates the strong influence of zonal wind variations, i.e., regional meteorological conditions, on the low-frequency sea level variability of the Baltic Sea.

Hydrology describes the transfer of water between the ocean, the atmosphere and the land surface including rivers and lakes. It is a crucial element in the global climate system, and is has been studied thoroughly in the Baltic Sea region. Coupled regional models are used to incorporate the water cycle into regional and global climate models, but to a rather unsatisfying degree. Hagemann et al. have further developed a hydrological model system to a very high temporal and spatial resolution, which can closely simulate the terrestrial hydrological cycle (discharge) in the climate model. However, human modifications to the water cycle (river regulations, dams) are not accounted for, making it difficult to model the discharge in many heavily regulated Scandinavian subbasins.

Two contributions deal with the hydrological conditions in the Russian sub-catchment of the river Dvina/Daugava. Terskii et al. provide a new assessment of the water cycle components in the catchment, using open source data and a hydrological model. The developed modeling approach can be used to assess water resources, climate change impacts and water quality issues.

In the same sub-catchment of the Russian part of the Dvina River, Danilovich et al. analyze past changes in climate and steam flow and projected future changes, using historical runoff data and different models using two representative concentration pathways scenarios. A positive monthly trend for stream flow for the past was found for December to April, but not for the rest of the year. For the future until the end of the century, a clear warming and stronger precipitation is projected, and runoff during the low-flow period in winter is expected to increase considerably.

Two papers investigate the impact of atmospheric circulation on temperature and droughts in the Baltic and Black Sea regions. Parts of the Baltic region, e.g., Estonia, have received stronger warming than the global average. Lakson et al. investigated the impact of atmospheric circulation on this exceptional warming, and they conclude that a higher frequency of certain circulation

types is probably not responsible for the warming, but rather a warming within circulation types.

The frequency of droughts and dry winds in the recent past was studied by Semenova et al. in the steppe region of southern Ukraine, in the catchment of the Black Sea. They found that during the two last decades, the Black Sea steppe province was characterized by a significant increasing frequency of droughts and dry winds, which is considered a problem for this agriculturally important region.

Regional climate models need to be validated with real measured observational data, which are quite heterogeneous in space and time. In order to serve as a validation reference, the input data for these data sets have to be homogenized with respect to quality as well as spatial and temporal dimensions. Hinrichs et al. have developed a new, comprehensive observation-based data product of both atmospheric and hydrographic parameters for the North Sea and Baltic Sea, for the period 1950–2015. The dataset is freely available on the institutional website.

Regional climate models can be coupled with biogeochemical and ecosystem models to estimate the impact of climate change on ecosystems and help with suitable management decisions. Uncertainties are intrinsic factors in regional and the driving global climate models, and more so in ecosystem models. Saraiva et al. have analyzed uncertainties in a coupled physical-biogeochemical Baltic Sea model (simulating nutrient loads, biogeochemical fluxes and oxygen conditions), forced by a regional climate model and driven by global climate models. The components have their own uncertainties, and it was found that the uncertainties related to the nutrient load scenarios are larger than those of the climate models and greenhouse gas scenarios. Substantial uncertainties of future projections for the Baltic Sea are caused by the driving global climate models, but it was nevertheless concluded that nutrient abatement measures implemented (the so-called Baltic Sea Action Plan) would significantly improve the ecosystem state.

Eutrophication, i.e., the surplus nutrition in an ecosystem, is subject of the last two papers presented here. Changes in nutrient concentrations over 20 years and their relation to coastal freshwater sources at the German Baltic Sea coast was analyzed by Kuss et al., by using a novel approach to correlate nutrient concentrations with salinity measurements. The authors show that nutrient concentrations in the freshwater have mostly decreased over the analyzed period.

Finally, Ivarsson et al. present a history of eutrophication for some sites on the Swedish east coast, based on sediment samples. They estimate the onset of anthropogenic eutrophication in the area to between 1800 and 1900 CE, depending on the sampling site. They did not find evidence that the extensive oxygen depletion during the Medieval Climate Anomaly was caused by human activities.

We believe that this compilation of research papers represents a good overview over the currently ongoing Earth system research activities in the Baltic Sea region, providing new insights for the scientific community.

AUTHOR CONTRIBUTIONS

All authors listed have made a substantial, direct and intellectual contribution to the work, and approved it for publication.

ACKNOWLEDGMENTS

We thank all authors for their valuable contribution to this Research Topic, and to all participants of the 2nd Baltic Earth Conference in Helsingor, Denmark.

Conflict of Interest: The authors declare that the research was conducted in the absence of any commercial or financial relationships that could be construed as a potential conflict of interest.

frontiers in Earth Science

ORIGINAL RESEARCH
published: 09 January 2019
doi: 10.3389/feart.2018.00244

Uncertainties in Projections of the Baltic Sea Ecosystem Driven by an Ensemble of Global Climate Models

Sofia Saraiva[1,2], *H. E. Markus Meier*[1,3]*, *Helén Andersson*[1], *Anders Höglund*[1], *Christian Dieterich*[1], *Matthias Gröger*[1], *Robinson Hordoir*[1,4,5] *and Kari Eilola*[1]

[1] Swedish Meteorological and Hydrological Institute, Norrköping, Sweden, [2] MARETEC, Instituto Superior Técnico, University of Lisbon, Lisbon, Portugal, [3] Department of Physical Oceanography and Instrumentation, Leibniz Institute for Baltic Sea Research Warnemünde, Rostock, Germany, [4] Institute of Marine Research, Bergen, Norway, [5] Bjerknes Centre for Climate Research, Bergen, Norway

Many coastal seas worldwide are affected by human impacts such as eutrophication causing, *inter alia*, oxygen depletion, and extensive areas of hypoxia. Depending on the region, global warming may reinforce these environmental changes by reducing air-sea oxygen fluxes, intensifying internal nutrient cycling, and increasing river-borne nutrient loads. The development of appropriate management plans to effectively protect the marine environment requires projections of future marine ecosystem states. However, projections with regional climate models commonly suffer from shortcomings in the driving global General Circulation Models (GCMs). The differing sensitivities of GCMs to increased greenhouse gas concentrations affect regional projections considerably. In this study, we focused on one of the most threatened coastal seas, the Baltic Sea, and estimated uncertainties in projections due to climate model deficiencies and due to unknown future greenhouse gas concentration, nutrient load and sea level rise scenarios. To address the latter, simulations of the period 1975–2098 were performed using the initial conditions from an earlier reconstruction with the same Baltic Sea model (starting in 1850). To estimate the impacts of climate model uncertainties, dynamical downscaling experiments with four driving global models were carried out for two greenhouse gas concentration scenarios and for three nutrient load scenarios, covering the plausible range between low and high loads. The results suggest that changes in nutrient supply, in particular phosphorus, control the long-term (centennial) response of eutrophication, biogeochemical fluxes and oxygen conditions in the deep water. The analysis of simulated primary production, nitrogen fixation, and hypoxic areas shows that uncertainties caused by the various nutrient load scenarios are greater than the uncertainties due to climate model uncertainties and future greenhouse gas concentrations. In all scenario simulations, a proposed nutrient load abatement strategy, i.e., the Baltic Sea Action Plan, will lead to a significant improvement in the overall environmental state. However, the projections cannot provide detailed information on the timing and the reductions of future hypoxic areas, due to uncertainties in salinity projections caused by uncertainties in projections of the regional water cycle and of the mean sea level outside the model domain.

Keywords: Baltic Sea, nutrients, eutrophication, climate change, future projections, uncertainties, ensemble simulations

OPEN ACCESS

Edited by:
Tomas Halenka,
Charles University, Czechia

Reviewed by:
Matthias Prange,
University of Bremen, Germany
Jofre Carnicer,
University of Barcelona, Spain

***Correspondence:**
H. E. Markus Meier
markus.meier@io-warnemuende.de

Specialty section:
This article was submitted to Interdisciplinary Climate Studies, a section of the journal Frontiers in Earth Science

Received: *11 October 2018*
Accepted: *17 December 2018*
Published: *09 January 2019*

Citation:
Saraiva S, Meier HEM, Andersson H, Höglund A, Dieterich C, Gröger M, Hordoir R and Eilola K (2019) Uncertainties in Projections of the Baltic Sea Ecosystem Driven by an Ensemble of Global Climate Models. Front. Earth Sci. 6:244. doi: 10.3389/feart.2018.00244

INTRODUCTION

Regional projections of future climate based on dynamical downscaling of global model results using regional climate models (RCMs) suffer from considerable uncertainties caused by (1) shortcomings of global and regional climate models, (2) unknown future greenhouse gas concentrations, (3) natural variability, and (4) experimental design (e.g., Hawkins and Sutton, 2009; Kjellström et al., 2011; Déqué et al., 2012; Mathis et al., 2018). Global climate models are based on General Circulation Models (GCMs) or even Earth System Models (ESMs) and are useful tools to address climate variability on the global scale (acronyms are explained in **Table 1**). However, they have still significant shortcomings on regional scales, *inter alia*, because their horizontal grids are too coarse to resolve details of the orography and the land-sea mask, which might be important to the regional climate (Stocker et al., 2013). To overcome the limitations of global climate models for regional climate studies, limited-area RCMs with high resolution were developed for the region of interest, driven by data from GCMs or ESMs at the lateral boundaries of the model domain (e.g., Giorgi and Mearns, 1991). With such an experimental setup, scenario simulations were carried out, with the aim to study the impact of climate change and to develop climate adaptation strategies for selected regions (e.g., Räisänen et al., 2004).

As mentioned above, these regional projections have limitations. For instance, Christensen et al. (2010) and Jacob et al. (2014) studied the uncertainties in regional atmospheric projections, whereas systematic analyses of uncertainties in regional ocean projections have not been performed yet. For marine ecosystems, another source of uncertainty has to be considered (in addition to the sources mentioned above). As the socioeconomic development in the catchment area of the coastal sea is unknown, future nutrient loads from land and atmospheric depositions of nitrogen and phosphorus are speculative, contributing to the uncertainties of the projections of the marine ecosystems (e.g., Meier et al., 2011a).

In this study, we focus on the Baltic Sea (**Figure 1**), which is a semi-enclosed coastal sea with a large catchment area located in northern Europe (Sjöberg, 1992). The Baltic Sea region is divided into two sub-regions. Extensive forests, low population density, mostly rocky coasts and subarctic winter climate characterize the north. On the other hand, the south is characterized by agricultural land, high population density, mostly sandy coasts, and a moderate winter climate. Approximately 90 million people live in the catchment area of the Baltic Sea, creating a considerable impact on the marine environment (Ahtiainen and Öhman, 2014). Reinforced river-borne nutrient loads from agriculture and sewage treatment plants since the 1940/50s caused the world largest anthropogenic-induced hypoxic bottoms (Conley et al., 2009; Conley, 2012; Gustafsson et al., 2012; Carstensen et al., 2014; Meier et al., 2018). In addition to environmental pressures, the Baltic Sea is affected by global warming more than other coastal seas, perhaps because of its proximity to the Arctic, hydrodynamic features and land-locked location (BACC II Author Team, 2015). During 1982-2006, the Baltic Sea has warmed up more than any other large marine ecosystem (Belkin, 2009).

Since 2000, future projections of the Baltic Sea have been carried out for supporting the design of appropriate management plans to more effectively protect the marine environment. The first projections were made with pure hydrodynamic models (Omstedt et al., 2000; Meier, 2002a, 2006; Döscher and Meier, 2004; Meier et al., 2004) and, later, with coupled physical-biogeochemical models (Meier et al., 2011c). However, these first studies did not address enough on the uncertainties related to future projections.

To estimate uncertainties, mini-ensembles of continuous simulations from the present to the future climate driven by two GCMs and two greenhouse gas emission scenarios were produced (Neumann, 2010; Friedland et al., 2012; Meier et al., 2012a; Ryabchenko et al., 2016). In addition, three different Baltic Sea ecosystem models were used to estimate the uncertainties caused by deficiencies in the representation of marine ecosystem processes (e.g., Meier et al., 2011a, 2012b,c). Omstedt et al. (2012) even used three GCMs and three greenhouse gas emission scenarios, although they applied a regional atmospheric model instead of a regional coupled atmosphere-ocean model for the dynamical downscaling. By using a regional atmosphere model, the projected sea surface temperatures (SSTs) were based on the SSTs from GCMs that do not take the regional details of the Baltic Sea region into account, causing considerable deficiencies in projections (e.g., Meier et al., 2011b). Hence, uncertainties of Baltic Sea projections originating from climate model uncertainties have not been thoroughly assessed. An exception is the study by Meier et al. (2006), who studied the spread of a multi-model ensemble consisting of 16 scenario simulations based on seven regional models, five global models and two greenhouse gas emission scenarios. However, Meier et al. (2006) focused only on salinity thus, not addressing the changes in the biogeochemical cycles. They also neglected changes in variability on time scales longer than 1 year. In all other dynamical downscaling studies of the Baltic Sea, only one or two GCMs were used.

In this study, we focus on uncertainties in Baltic Sea water quality projections caused by uncertainties due to climate model deficiencies and due to unknown greenhouse gas concentration, nutrient load and sea level rise scenarios. According to Hawkins and Sutton (2009), who have found that the uncertainties due to natural variability at the end of the 21st century are small, we have neglected this source of uncertainty. Climate model uncertainties are defined as the spread (variance) in regional projections for the Baltic Sea ecosystem caused by GCM deficiencies inherited to the applied RCM and regional ocean model via the dynamical downscaling approach. These climate model uncertainties are compared with estimated uncertainties due to unknown greenhouse gas concentration, nutrient load, and sea level rise scenarios. For our aim, we investigate variances of an ensemble of scenario simulations and of selected sub-sets of the entire ensemble.

The highly non-linear dynamics of the Baltic Sea ecosystem are controlled by nutrient loads from land and from the atmosphere, water temperature, salinity, light conditions, mixed

TABLE 1 | List of acronyms.

Acronym	Explanation	Comment	References
GCM	General Circulation Model	Model applied for global climate simulations	e.g., Meehl et al., 2004
ESM	Earth System Model	Model applied for global climate simulations including the carbon cycle	e.g., Heavens et al., 2013
RCP	Representative Concentration Pathway	Greenhouse gas concentration scenario	Moss et al., 2010
SSP	Shared Socio-economic Pathways	Narratives of socio-economic changes, here downscaled to the Baltic Sea region	O'Neill et al., 2014
IPCC	Intergovernmental Panel of Climate Change	Assessment of past and future climates	http://www.ipcc.ch
RCO-SCOBI	Rossby Center Ocean model–Swedish Coastal and Ocean Biogeochemical model	Coupled physical-biogeochemical ocean circulation model for the Baltic Sea	Meier et al., 2003; Eilola et al., 2009
RCA4-NEMO	Rossby Center Atmosphere model version 4—Nucleus for European Modeling of the Ocean	Coupled atmosphere-ocean model applied for the Baltic Sea and North Sea	Kupiainen et al., 2014; Wang et al., 2015; Madec, 2016
EURO-CORDEX	Coordinated Downscaling Experiment for Europe	Coordinated experiments on a defined domain	http://www.euro-cordex.net
MPI-ESM-LR	Max Planck Institute Earth System Model—Low Resolution	ESM, Model A	https://www.mpimet.mpg.de; Block and Mauritsen, 2013; Stevens et al., 2013
EC-EARTH	European Countries Earth System Model	ESM, Model B	https://www.knmi.nl; Hazeleger et al., 2012
CM5A-MR	Institut Pierre Simon Laplace Climate Model –Medium Resolution	ESM, Model C	http://icmc.ipsl.fr; Marti et al., 2010; Hourdin et al., 2013
HadGEM2-ES	Hadley Center Global Environment Model version 2—Earth System	ESM, Model D	http://www.metoffice.gov.uk; Jones et al., 2011
SMHI	Swedish Meteorological and Hydrological Institute	Swedish center for weather forecasts and climate scenarios	http://www.smhi.se
ERA40	40-year reanalysis of the European Center for Medium Range Weather Forecast	Reanalysis data used as atmospheric forcing for the ocean model	Uppala et al., 2005
EURO4M	European Reanalysis and Observations for Monitoring project	Reanalysis data used as atmospheric forcing for the ocean model	http://www.euro4m.eu; Dahlgren et al., 2016
E-HYPE	Hydrological Predictions for the Environment applied for Europe	process-based multi-basin model for the land surface	http://hypeweb.smhi.se; Donnelly et al., 2013, 2017; Hundecha et al., 2016
BED	Baltic Environmental Database	Marine observational data from the Baltic Sea monitoring programs	http://nest.su.se/bed
BSAP	Baltic Sea Action Plan	Nutrient load abatement strategy for the Baltic Sea	HELCOM, 2013

layer depth, sea-ice conditions (only in the northern Baltic Sea), saltwater water inflows (only in the Baltic proper and the Gulf of Finland, see **Figure 1**) and resuspension (e.g., Wulff et al., 2001). Hence, all uncertainties in scenario simulations of air temperature, precipitation, wind speed, cloudiness, atmospheric circulation patterns and river runoff will have an impact on projected biogeochemical cycles (BACC II Author Team, 2015). For example, higher water temperatures may increase the production and remineralization of organic material (i.e., may intensify the internal nutrient cycling) and reduce air-sea fluxes of oxygen (Meier et al., 2011a). Further, increased river runoff may reinforce river-borne nutrient loads (Stålnacke et al., 1999; Meier et al., 2012b) and a shallower mixed layer depth may alter phytoplankton blooms (Hieronymus et al., 2018). In the northern Baltic Sea, the shrinking sea-ice cover will lead to an earlier onset and termination of the spring bloom due to improved light conditions (Eilola et al., 2013). The frequency of saltwater inflows may slightly increase due to changes in the large-scale atmospheric circulation patterns (Schimanke et al., 2014). Global mean sea level rise may enhance the salt transport into the Baltic Sea causing increased stratification, reduced deep water ventilation, and expanding hypoxia in the Baltic proper (Meier et al., 2017). As the Baltic Sea is shallow with a mean depth of 52 m only, nutrient exchanges between sediment and water column and resuspension of organic matter are important processes for the biogeochemical cycling (Almroth-Rosell et al., 2011). Eilola et al. (2012) suggested that in future climate the exchange between shallow and deep waters might be intensified

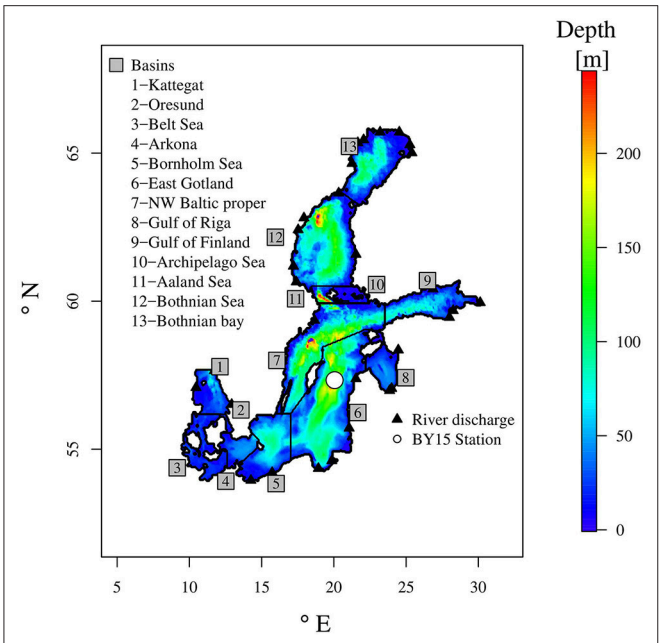

FIGURE 1 | The Baltic Sea: bathymetry, river discharges, and sub-basins as defined in this study. The Baltic proper comprises Arkona, Bornholm, East Gotland and Northwest Gotland basins. In addition, the location of the monitoring station at Gotland Deep (BY15) is shown (white circle).

and that the internal removal of phosphorus might be weaker. In areas with reduced sea-ice cover, the winter mixing may increase, and the oxygen conditions in lower layers may improve (Eilola et al., 2013). An increase of wave-induced resuspension may cause an increase of nutrient transportation from the productive coastal zone into the deeper areas (Eilola et al., 2013).

The paper is organized as follows. In the next section "Data and Methods," the regional climate ocean model, the regional coupled atmosphere-ocean model, driving GCMs, greenhouse gas concentration and nutrient load scenarios, and the experimental setup are introduced. In the section "Results," the results of future projections for temperature, salinity, selected biogeochemical fluxes (primary production and nitrogen fixation) and hypoxic areas are presented. Finally, uncertainties of the projections and the suspected shortcomings of the study are discussed and some conclusions of the study are drawn.

DATA AND METHODS

A series of scenario simulations with a coupled physical-biogeochemical Baltic Sea model (see next section) was performed. The Baltic Sea model was driven by regionalized GCM data using the dynamical downscaling approach (see section on Regional Climate Data Sets). In this approach, the atmospheric forcing data were calculated using a RCM with GCM data at the lateral boundaries. The resulting atmospheric surface fields of 10 m wind, 2 m air temperature, 2 m specific humidity, precipitation, total cloudiness, and sea level pressure were then applied to force the Baltic Sea model and a hydrological/land surface model for the Baltic Sea catchment area. The output variables of the latter model are river runoff and nutrient loads to the Baltic Sea model. As the nutrient loads depend on not only precipitation and air temperature at the land surface, but also on land use, agricultural practices and sewage water treatment, all scenario simulations were performed under different socio-economic scenarios covering a plausible range between low and high loads (see section on Nutrient Load Scenarios). **Figure 2** presents a conceptual diagram of the dynamical downscaling approach used in this study. As the global mean sea level rise is not considered in the scenario simulations, two additional sensitivity experiments were performed to estimate the impact of a higher sea level at the lateral boundary of the Baltic Sea model (see section on Experimental Setup).

Baltic Sea Model

In this study, a three-dimensional ocean circulation model is used in climate simulations for the period 1975–2098. RCO-SCOBI consists of the physical Rossby Center Ocean (RCO) (Meier et al., 1999, 2003; Meier, 2007) and the Swedish Coastal and Ocean Biogeochemical (SCOBI) models (Eilola et al., 2009; Almroth-Rosell et al., 2011). The model domain covers the Baltic Sea area with an open boundary in the northern Kattegat (**Figure 1**). For most of the variables (temperature, salinity, nutrients, and detritus), temporally immutable, climatological profiles are assumed in case of inflow conditions across the boundary. In case of outflow, a modified Orlanski radiation condition is used (Meier et al., 2003). Sea level heights at the boundary are computed from sea level pressure gradients over the North Sea derived from the different RCM simulations (see Meier et al., 2012a). Hence, the experimental setup allows any changes in salt water inflows between the Kattegat and the Baltic Sea. The horizontal and vertical resolutions are 3.7 km and 3 m (corresponding to 83 depth levels), respectively. Bulk formulae for wind stress, heat and freshwater fluxes and the radiation model are described by Meier et al. (1999).

In the water column, the biogeochemical model SCOBI describes the dynamics of nitrate, ammonium, phosphate, three phytoplankton groups (diatoms, flagellates and others, and cyanobacteria), zooplankton, detritus, oxygen, and hydrogen sulfide as negative oxygen equivalents (1 mL H_2S L^{-1} = -2 mL O_2 L^{-1}). In the present version, the nitrogen and phosphorus detritus were separated according to Savchuk (2002). The sediment contains nutrients in the form of benthic nitrogen and benthic phosphorus. A simplified wave model is used to estimate the resuspension of organic matter (Almroth-Rosell et al., 2011). RCO-SCOBI has previously been evaluated and applied in numerous long-term climate studies, e.g., by Meier et al. (2003), Meier (2007), Meier et al. (2011a), Meier et al. (2012a), Eilola et al. (2009), Eilola et al. (2011), Almroth-Rosell et al. (2011), Schimanke and Meier (2016), Saraiva et al. (2018a).

Regional Climate Data Sets

The Baltic Sea model was forced by atmospheric surface fields from the coupled Rossby Center Atmosphere Version 4 and Nucleus for European Modeling of the Ocean models (RCA4-NEMO). The RCA4-NEMO model covers the EURO-CORDEX

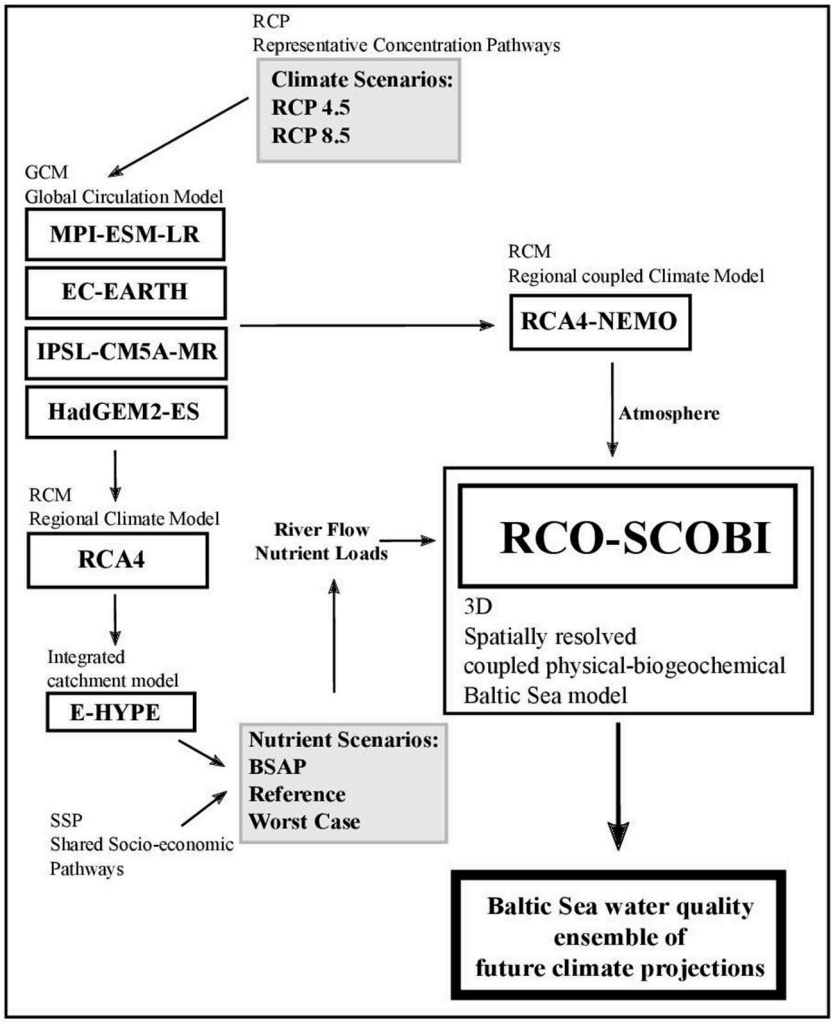

FIGURE 2 | Conceptual diagram of the modeling approach used in the study.

domain (Coordinated Downscaling Experiment for Europe, http://www.euro-cordex.net/) (Jacob et al., 2014) and is driven by lateral boundary data from scenario simulations of four GCMs. RCA4-NEMO is a regional coupled atmosphere-ocean climate model with an interactively coupled Baltic Sea and North Sea (Dieterich et al., 2013; Gröger et al., 2015; Wang et al., 2015), which allows a more realistic climate representation (Dieterich et al., submitted manuscript).

The set of GCMs used in this study includes: MPI-ESM-LR (https://www.mpimet.mpg.de; Block and Mauritsen, 2013; Stevens et al., 2013), EC-EARTH (https://www.knmi.nl; Hazeleger et al., 2012), IPSL-CM5A-MR (http://icmc.ipsl.fr/; Marti et al., 2010; Hourdin et al., 2013) and HadGEM2-ES (http://www.metoffice.gov.uk; Jones et al., 2011), called Model A, B, C, and D, respectively. This set is in agreement with the results obtained by Wilcke and Bärring (2016) for the climate systems of the North Sea and Baltic Sea regions, who tested the use of hierarchical clustering methods to select an optimum subset of models to estimate uncertainties inherent in an ensemble with a minimum number of simulations. The Rossby Center of the Swedish Meteorological and Hydrological Institute (SMHI) provided the lateral boundary data for RCA4-NEMO from each of these GCMs to calculate the atmospheric boundary conditions used by the RCO-SCOBI model.

Meier et al. (2011b) identified that strong winds in the regionalized atmospheric forcing resulting from RCA3 were underestimated compared to observations although ERA40 reanalysis data (Uppala et al., 2005) were used at the lateral boundaries. Hence, Meier et al. (2011b) applied an empirical correction of the strong winds based on gustiness. The modified wind speed at 10 m height was calculated from the maximum of the simulated wind gusts divided by 1.6 and the wind speed at 10 m height.

In this study, a similar deficiency was identified for RCA4 with EURO4M at the lateral boundaries, which is a more recent reanalysis (http://www.euro4m.eu/). As gustiness is not

available for the current regionalized forcing from RCA4, a different correction method was implemented. The statistical wind distribution in RCA4 over sea agrees well with observations up to 10 m s^{-1} but the winds above 10 m s^{-1} are underestimated (not shown). Therefore, a correction was made by multiplying the portion of the wind amplitude exceeding 10 m s^{-1} by 1.6 without altering the direction.

The river runoff and nutrient loads are based on results from the hydrological model E-HYPE (Hydrological Predictions for the Environment, http://hypeweb.smhi.se), which is a process-based multi-basin model applied for Europe (Donnelly et al., 2013, 2017; Hundecha et al., 2016). To minimize uncertainties caused by the hydrological model bias (results not shown), the runoff from each river was corrected for the historical and future periods so that the total annual flow to the Baltic Sea estimated by the model matches the observations during the historical period 1971-2005.

In this study, only results from Representative Concentration Pathways (RCPs) 4.5 and 8.5 (Moss et al., 2010) were analyzed. RCPs are greenhouse gas concentration trajectories adopted by the Intergovernmental Panel of Climate Change (IPCC) for its fifth Assessment Report (AR5) in 2013 (Stocker et al., 2013). The RCPs are named after the radiative forcing values in the year 2100 relative to pre-industrial values, i.e., +4.5 and +8.5 W m^{-2}, respectively. RCP 2.6 at the lower end of the IPCC concentration scenarios, corresponding to the goal of a global temperature rise limited to $<2°C$, was not studied. Hence, in our ensemble the range of warming in the Baltic Sea region is smaller than that of the full range of global scenario simulations.

Figures 3, **4** show the results of the seasonal cycles of regionalized 2 m air temperature over the central Baltic Sea and the total river runoff in present and future climates, respectively. During the historical period (1976–2005), annual and monthly biases of both variables were within the range of the variability of the observations, i.e., within the range of plus or minus one standard deviation from the monthly mean. In the future climate (2069–2098), air temperatures over the central Baltic Sea will increase more in winter than in summer, and river runoff from the entire catchment area will increase during winter but decrease during summer. In terms of the annual mean averaged over the Baltic Sea, river runoff will increase in future climate compared to historical climate. Due to the air temperature increase, a decrease in future sea-ice extent is expected, as shown in previous projections (e.g., Meier, 2002a,b; Meier et al., 2004, 2011b). A similar response as in Eilola et al. (2013) is found in the present study (see the introduction) but not investigated further.

Nutrient Load Scenarios

Climate projections for the Baltic Sea are carried out under the three nutrient load scenarios described below, spanning a range of plausible future socio-economic conditions from the most optimistic to the worst scenario. During the historical period (1976–2005), the observed nutrient loads from the Baltic Environmental Database (BED) are used (http://nest.su.se/bed/).

- Baltic Sea Action Plan (BSAP) scenario (HELCOM, 2013). In this scenario, nutrient loads from rivers and atmospheric deposition in the different sub-basins will linearly decrease after 2012 from the current values (average 2010–2012) as estimated by Svendsen et al. (2015) to the maximum allowable input defined by the BSAP until 2020. After 2020, nutrient loads will remain constant until 2098.
- Reference scenario. In this scenario, E-HYPE projections for future nutrient loads (2006–2098) under the two different greenhouse gas concentration scenarios (RCP 4.5 and RCP 8.5) are used, assuming no socio-economic changes compared to the historical period (1976–2005). Hence, e.g., land and fertilizer usage, soil properties and sewage water treatment in each sub-basin are assumed to be unchanged over time. Atmospheric deposition is also assumed to be constant in time. Only the impacts of the changing climate on air temperature and precipitation over the Baltic Sea catchment area are considered.
- Worst Case scenario. In this scenario, a socio-economic impact factor, corresponding to the worst case, is multiplied to the future nutrient loads calculated with E-HYPE under the RCP 4.5 and RCP 8.5 scenarios (2006–2098). The socio-economic impact factor summarizes the impact from Shared Socio-economic Pathways (SSPs) (O'Neill et al., 2014) on current nutrient loads and atmospheric deposition, based on the downscaling of the global trends of socio-economic drivers to the Baltic Sea region (Zandersen et al., in press). Following the assumptions of the global SSPs, changes in nitrogen and phosphorus loads were calculated from the regional assumptions, e.g., on population growth, changes in agricultural practices such as land and fertilizer use and expansion of sewage water treatment plants. To represent the worst conditions, the impact factor from the so-called SSP5 was selected, representing the changes caused by a "fossil-fuelled development" scenario.

In all three scenarios, nutrient loads into the Baltic Sea will decrease in the future following the historical efforts toward nutrient load reductions starting in the 1980s (**Figure 5**). However, in the Worst Case scenario the loads are close to the average observed loads during 1976–2005. Monthly and long-term changes in the Reference and Worst Case scenarios follow river runoff changes caused by changing climate. Only the BSAP scenario assumes that climate change does not counteract nutrient load abatement strategies. Hence, the latter is an optimistic scenario.

Experimental Setup

The combinations of future climate scenarios (RCP 4.5 and RCP 8.5; for Model C only RCP 4.5 is available) calculated with the four GCMs and three socio-economic scenarios (BSAP, Reference and Worst Case) result in an ensemble of 21 scenario simulations (**Table 2**). All simulations for the historical period 1975–2005 driven by the four GCMs start from the same initial conditions in March 1975, which were obtained from a long hindcast simulation starting in 1850. The latter simulation was driven by reconstructed atmospheric, hydrological, and nutrient loads estimated from available historical observations (Meier et al., 2012c, 2018).

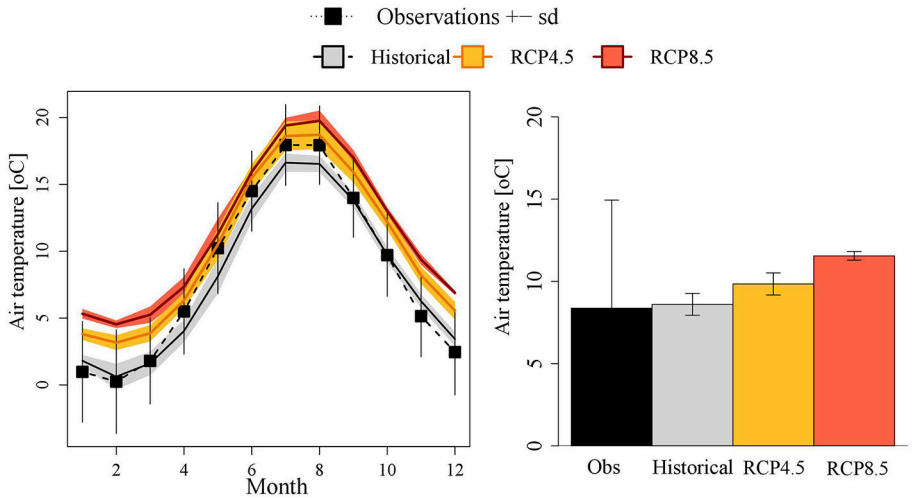

FIGURE 3 | Ensemble mean, monthly air temperature in 2 m height (in °*C*) at Gotland Deep (BY15) calculated from four regional climate simulations: historical period (1976–2005) (solid black line) and future period (2069-2098) according to RCP 4.5 and RCP 8.5 scenarios (solid orange and red lines, respectively). The colored shaded areas denote the range between minus and plus one standard deviation among the ensemble members. In addition, observations and their standard deviations are shown (black squares and vertical thin bars).

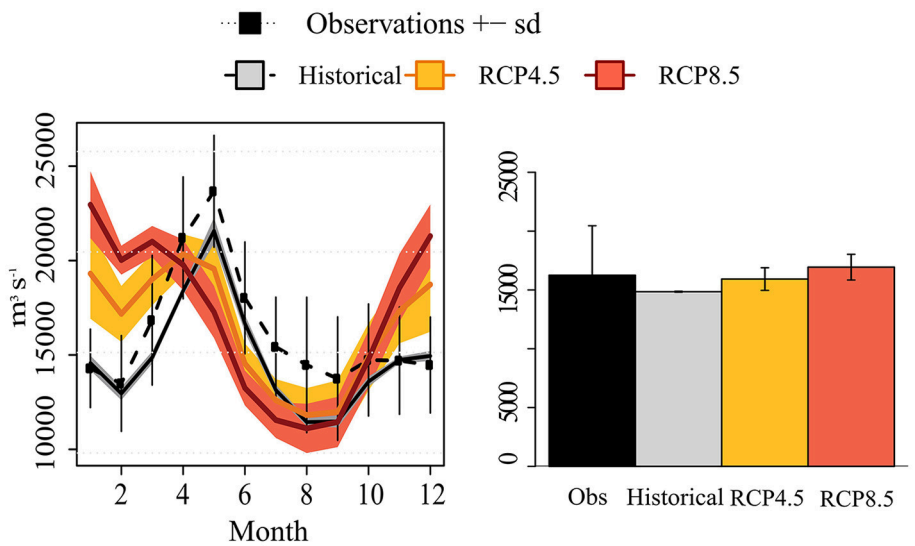

FIGURE 4 | Ensemble mean, monthly (left), and annual (right) runoff (in $m^3\ s^{-1}$) for the Baltic Sea calculated from four hydrological model simulations: historical period (1976–2005) (solid black line in the left panel and gray bar in the right panel) and future period (2069–2098) according to RCP 4.5 (orange) and RCP 8.5 (red) scenarios, respectively. The colored shaded areas in the left panel denote the range between minus and plus one standard deviation among the ensemble members. In addition, observations and their standard deviations are shown (dashed black line with squares and vertical thin bars in the left panel and black bar in the right panel).

In addition, two sensitivity experiments for Model A under RCP 8.5 (BSAP and Worst Case) with a 1 m higher sea level during 2006–2098 were performed. In these two experiments the thickness of the uppermost layer was increased by 1 m following Meier et al. (2017) (i.e., a 4 m surface layer instead of 3 m). Hence, during the start of the sensitivity experiment the difference between the depth of the pycnocline and the depth of the sills in the entrance area of the Baltic Sea (**Figure 1**) did not change compared to the scenario simulation with unchanged mean sea level.

The impacts of climate and nutrient load changes on the marine ecosystem were quantified by comparing various future scenarios (2069–2098) with the historical period of the GCM driven climate simulations (1976–2005). We focus our analysis on the changes and uncertainties of water temperature and salinity as well as on environmentally important indicators, such as nitrogen fixation, primary production and hypoxic areas. For

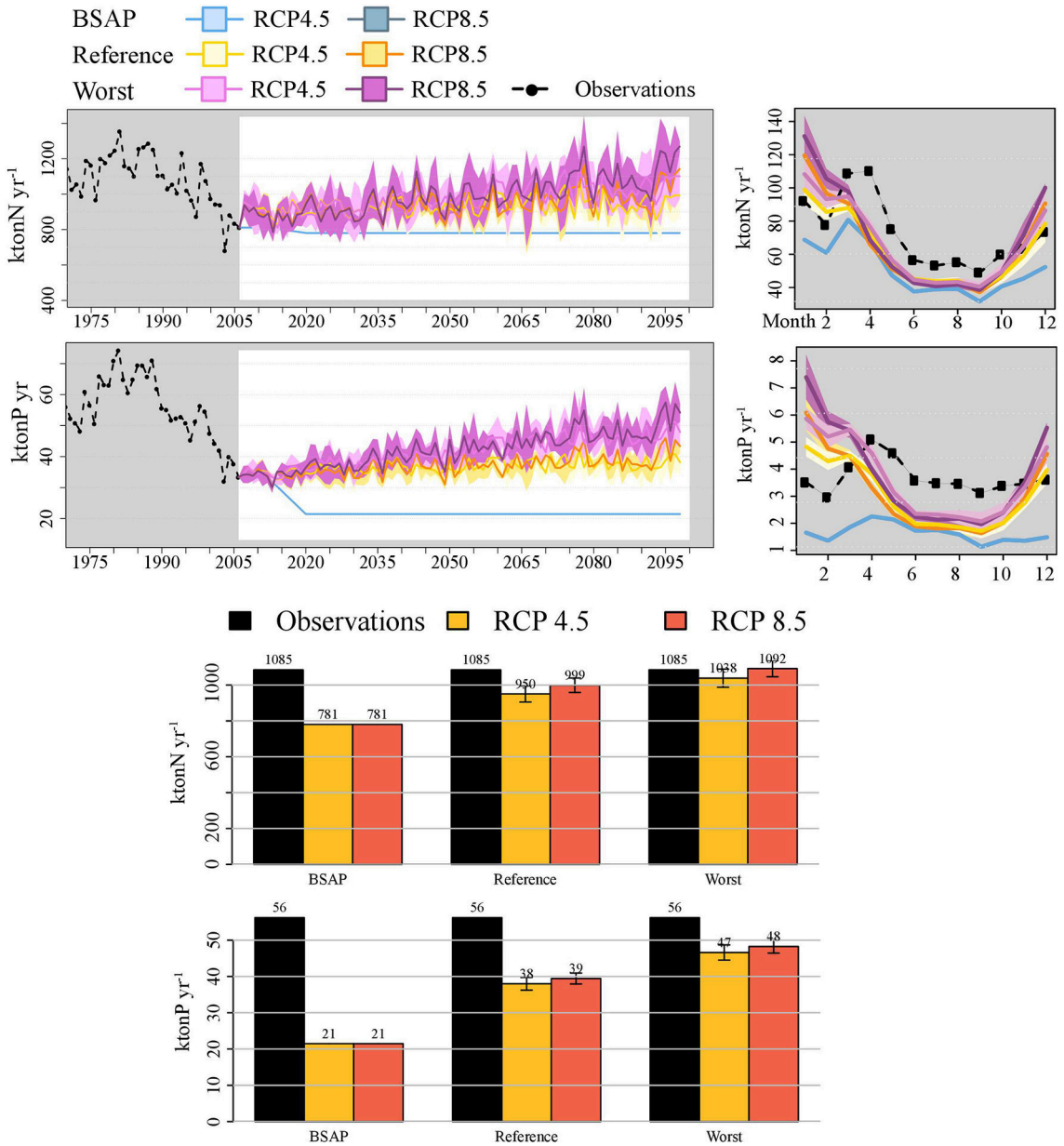

FIGURE 5 | Observed and projected ensemble mean of the total bioavailable nutrient loads (nitrogen and phosphorus) to the Baltic Sea between 1970 and 2098 (upper, left panels), mean seasonal cycle (upper, right panels) and annual mean loads (lower). Shown is the sum of loads from rivers, point sources and atmosphere. Results were calculated from four hydrological model simulations during the historical (1976–2005) and future (2069–2098) periods according to the RCP 4.5 and RCP 8.5 scenarios combined with three nutrient loads scenarios (BSAP, Reference, and Worst Case). The colored shaded areas denote the standard deviations among the ensemble members. Observations are shown as black dashed lines with squares.

more evaluation results of the model simulations during the historical period, the reader is referred to an accompanying paper (Saraiva et al., 2018a) and to the supplementary material (**Figure S1**).

To quantify the uncertainties (spread) in the projected changes we follow the approach by Ruosteenoja et al. (2016). For the evaluation of uncertainty in the 30 years mean changes between the future (2069–2098) and historical (1976–2005) climates, we calculate and compare the variances of changes caused by each of the different factors: GCMs (σ_1^2), RCPs (σ_2^2), nutrient loads (σ_3^2), and global mean sea level rise (σ_4^2).

$$\sigma_1^2 := \frac{1}{\sum_{l=1}^{L}\sum_{k=1}^{K}\sum_{m=1}^{M}(N_{m,k,l}-1)}\sum_{l=1}^{L}\sum_{k=1}^{K}\sum_{m=1}^{M}\sum_{n=1}^{N_{m,k,l}}\left(y_{n,m,k,l}-\overline{y_{m,k,l}}\right)^2$$

and

$$\sigma_2^2 := \frac{1}{\sum_{n=1}^{N}\sum_{l=1}^{L}\sum_{k=1}^{K}(M_{k,l,n}-1)}\sum_{n=1}^{N}\sum_{l=1}^{L}\sum_{k=1}^{K}\sum_{m=1}^{M_{k,l,n}}\left(y_{m,k,l,n}-\overline{y_{k,l,n}}\right)^2$$

etc.,

with the mean value for all four indices n, m, k and l

$$\overline{y_{m,k,l}} := \frac{1}{N_{m,k,l}}\sum_{n=1}^{N_{m,k,l}} y_{n,m,k,l}$$

and

$$\overline{y_{k,l,n}} := \frac{1}{M_{k,l,n}}\sum_{m=1}^{M_{k,l,n}} y_{n,m,k,l}$$

etc.. $N = 4$, m = 2, $K = 3$, and $L = 2$ are the total numbers of global models, greenhouse gas concentration scenarios, nutrient load scenarios and sea level rise sensitivity experiments (no change and + 1 m), respectively. $N_{\mathrm{m,k,l}} \leq 4$ is the number of global models for the greenhouse gas concentration scenario m, the nutrient load scenario k and the sea level rise experiment l, and so on. Global mean sea level sensitivity experiments exist only for Model A together with either BSAP or Worst Case. Further, for Model C the RCP 8.5 scenario is not available. Hence, the number of terms in the equations above are smaller than the product $N\ x\ M\ x\ K\ x\ L$. $M_{\mathrm{k,l,n}}$ is defined correspondingly. In case of σ_1^2, the variances caused by global models are summed for all combinations of RCPs, nutrient loads and sea level rise experiments. Finally, all variances of changes in primary production, nitrogen fixation and hypoxic area are normalized by the corresponding variance based upon the changes in all 23 simulations i.e., we calculated fractions of the total variances.

RESULTS OF FUTURE PROJECTIONS

Temperature and Salinity

According to our ensemble, water temperature will increase with time as a direct consequence of the increase in air temperature projected by the GCMs (**Figure 6**). The ensemble mean of the Baltic Sea volume averaged temperature change (and its standard deviation) between future (2069–2098) and historical (1976–2005) conditions amounts to $1.6 \pm 0.5^{\circ}C$ in RCP 4.5 and to $2.7 \pm 0.4^{\circ}C$ in RCP 8.5. The largest changes in SST follow the spatial pattern detected in previous projections (Meier et al., 2012a), with pronounced warming during the summers in the northern Baltic Sea (see **Figure S3**).

Due to the projected increased river runoff, the volume averaged salinity decreases in all scenario simulations at the end of the century (**Figure 6**). However, the differences between GCMs are substantial (**Figure 10**). The largest salinity decline of about $-1.5\,\mathrm{g\ kg^{-1}}$ in future relative to the historical period is found in the regionalization of Model C (IPSL-CM5A-MR). In contrast, Model B (EC-EARTH) shows first a slight increase in salinity until approximately 2030. During the second half of the 21st century salinity decreases, and the differences between RCP 4.5 and RCP 8.5 are smaller than the results given by other models. Thus, the range of salinity changes is large and, consequently, uncertainties in salinity projections are substantial and greater than those in the temperature projections (see section on Impact of Global Mean Sea Level Rise below). For Model C, the greenhouse gas concentration scenario RCP 8.5 was not simulated because a river runoff projection from E-HYPE was not available. Hence, the two ensembles of salinity projections shown in **Figure 6** should not be used to compare uncertainties in RCP 4.5 and RCP 8.5 projections.

Although the absolute values of the changes in temperature and salinity vary between the two greenhouse gas concentration scenarios, the shape of the average vertical profile does not change significantly (see **Figure S2**).

TABLE 2 | List of experiments (for details see text).

RCP/nutrient load scenario	BSAP	Reference	Worst Case
RCP 4.5	Model A-D	Model A-D	Model A-D
RCP 8.5	Model A, B, D	Model A, B, D	Model A, B, D
RCP 8.5	Model A + 1 m		Model A + 1 m

Biogeochemical Variables

Both changing nutrient loads and changing physical conditions have impacts on biogeochemical processes and nutrient cycling in the water column and sediments. In case of the Reference scenario, the model projects that the ensemble mean of the annual nutrient concentrations averaged for the entire Baltic Sea will change (between 1976–2005 and 2069–2098) under the RCP 4.5 scenario with about −62% for ammonium, +10% for nitrate and −24% for phosphate (**Figure 7**, middle panel). Decreased phosphate concentrations result in decreased primary production (−13%) and nitrogen fixation (−20%). As during the spring bloom nitrate is not completely consumed (due to lacking phosphate), nitrate concentration increases (+10%) relative to the average of the historical period. Average oxygen concentration is projected to slightly decrease by about −1%, probably because of the increasing water temperature. Following the decrease in phosphate and primary production, hypoxic area is 9% smaller than during the historical period.

In BSAP, the even larger reduction in nutrient loads results in a considerable reduction in primary production (−44%), nitrogen fixation (−96%), and hypoxic area (−32%) under the RCP 4.5 scenario (**Figure 7**, upper panel) whereas in the Worst Case primary production (+2%), nitrogen fixation (+22%) and hypoxic area (−3%) remain either unchanged or increase under the same greenhouse gas concentration scenario (**Figure 7**, lower panel). Hence, changes in nutrient supply, in particular phosphorus, control the long-term response of eutrophication, biogeochemical fluxes and oxygen conditions in the deep water.

Under the warmer RCP 8.5 scenario, the response of the biogeochemical cycles to changes in nutrient loads (BSAP,

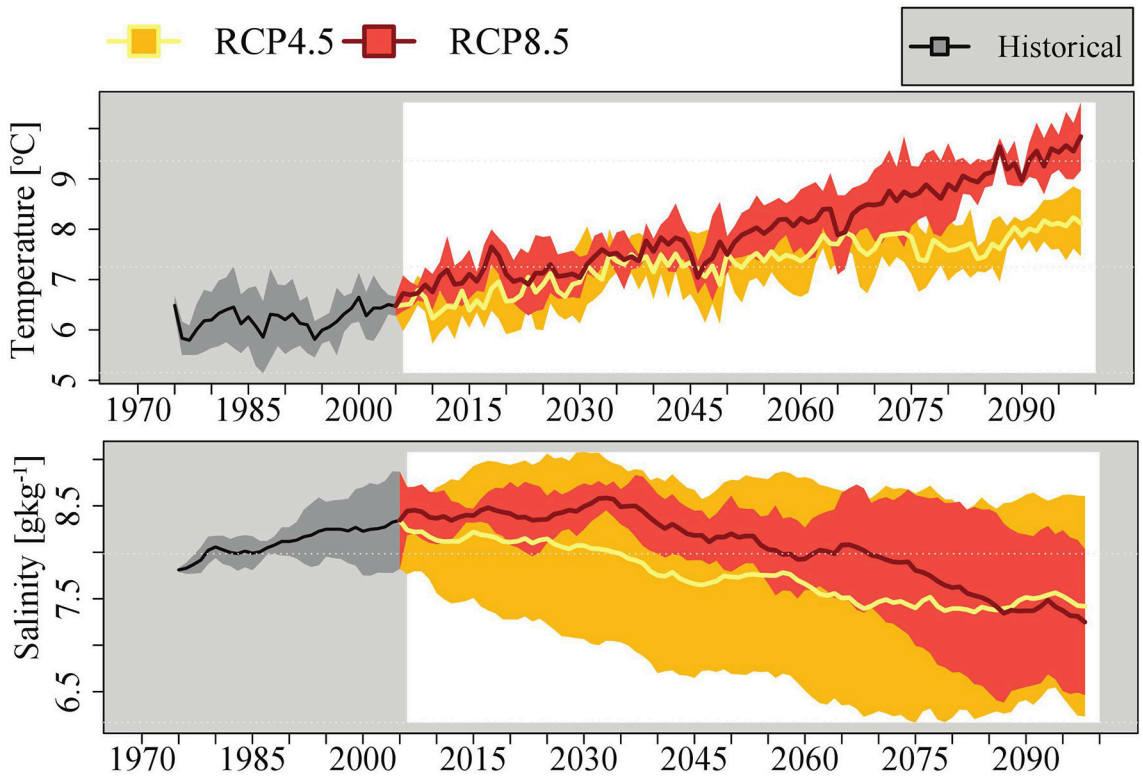

FIGURE 6 | Ensemble mean volume averaged temperature (in $^{\circ}C$) and salinity (in g kg^{-1}) as a function of time for 1975–2098 in the two climate scenarios, RCP 4.5 (orange) and RCP 8.5 (red). The colored shaded areas denote the standard deviations among the ensemble members.

Reference, Worst Case) is similar compared to RCP 4.5 (**Figure 7**). The projected changes in temperature, salinity and other variables result in larger eutrophication, productivity and oxygen depletion. However, the impact of changing climate is more pronounced in case of high nutrient loads like the Worst Case scenario than in case of low nutrient loads like the BSAP scenario. This conclusion follows from the finding that under the BSAP the differences between the projections driven by RCP 4.5 and RCP 8.5 are smaller than for the corresponding differences under the Worst Case. Hence, the response of biogeochemical cycles to warming climate under various nutrient load scenarios is non-linear. This result found in our ensemble study becomes particularly noticeable by analyzing summer bottom oxygen and hydrogen sulfide concentrations (**Figure 8**). For BSAP, the differences in summer bottom oxygen concentrations at the end of the century between RCP 4.5 and RCP 8.5 scenarios are small. Hydrogen sulfide does not occur even in the deepest parts of the Baltic Sea. However, in the Worst Case scenario large areas suffer from hydrogen sulfide with considerably larger concentrations in RCP 8.5 compared to RCP 4.5.

Under the BSAP, projected hypoxic area in the RCP 4.5 and RCP 8.5 scenario simulations is about −32 and −37% of present day, respectively (**Figure 7**). Hypoxic area is successively larger with increasing nutrient loads and increasing warming. In the combination of the Worst Case and RCP 8.5 scenarios, about 80% of the Baltic proper will have, on average, anoxic bottom conditions during summer. However, even in the latter scenario simulation, hypoxic area is still slightly smaller or about the same as under present conditions (**Figures 7**, **9**).

Independent of the climate scenario, RCP 4.5 or RCP 8.5, primary production and nitrogen fixation increase in future climate under the Worst Case scenario and decrease under the BSAP (**Figure 7**). Again, whether the response of the biogeochemical fluxes will be affected by changing climate depends on the nutrient loads. For instance, under the Worst Case scenario nitrogen fixation will increase by 22 and 56% in RCP 4.5 and RCP 8.5, respectively, whereas under the BSAP nitrogen fixation will approximately vanish in both cases.

In **Figure 9**, the temporal evolutions of primary production, nitrogen fixation and hypoxic area are shown. The standard deviation among the four ensemble members is large. However, at the end of the century the results for the Worst Case (or even for the Reference scenario) and the BSAP are clearly distinguishable.

Impact of Global Mean Sea Level Rise

In this section, we compare the results of the scenario simulations with those of the two sensitivity experiments with a 1 m higher mean sea level (Model A under the RCP 8.5 and BSAP or Worst Case scenarios plus 1 m). At the end of the century, the volume averaged salinity in the experiment with 1 m higher mean sea level (Model A under the RCP 8.5 scenario plus 1 m)

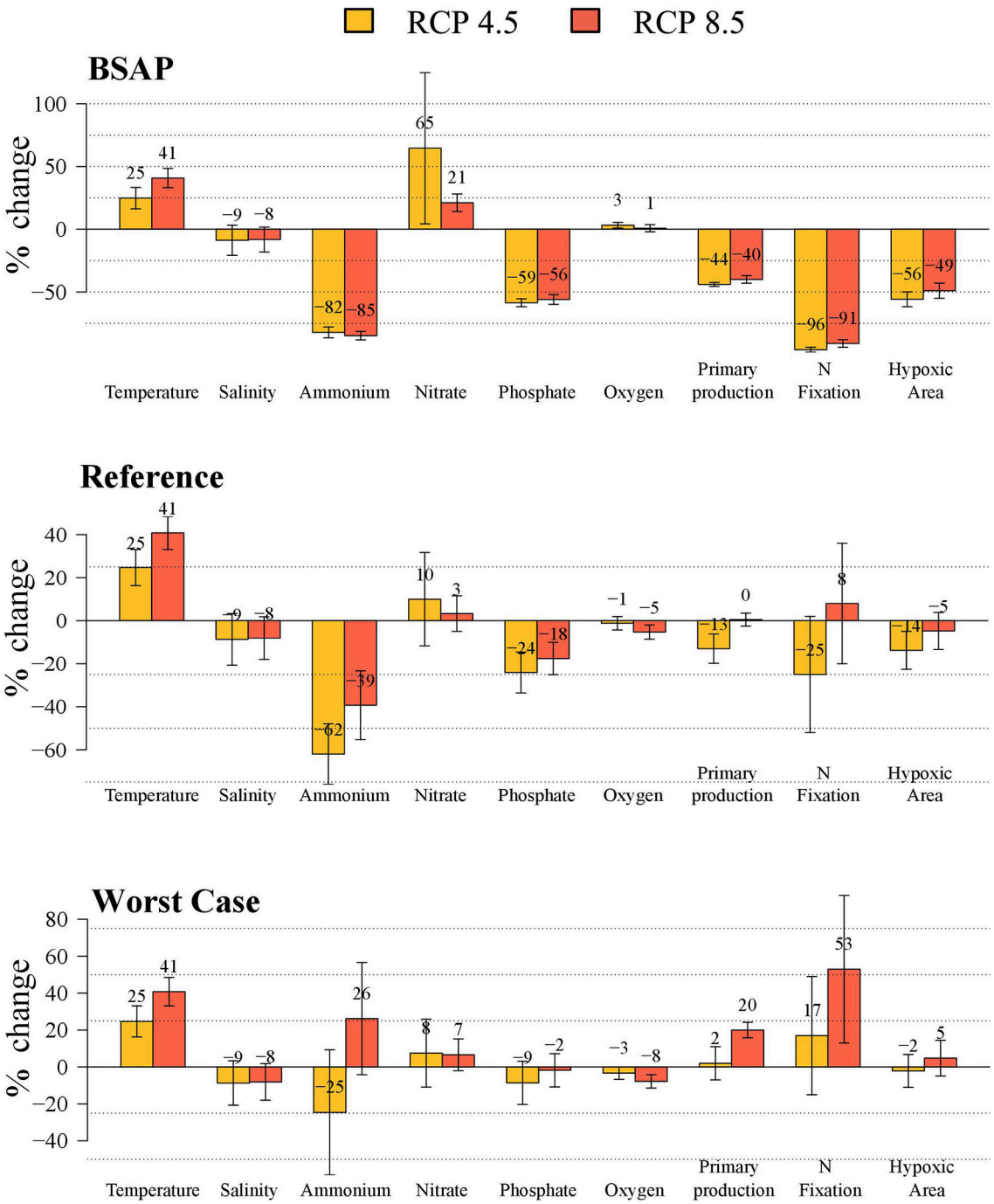

FIGURE 7 | Relative ensemble mean volume averaged, 30 years mean changes between the future (2069–2098) and historical (1976–2005) periods in temperature, salinity, nutrient and oxygen concentrations, primary production, nitrogen fixation and hypoxic areas in the entire Baltic Sea under the different climate and nutrient load scenarios: BSAP (upper panel), Reference (middle panel) and Worst Case (bottom panel). The relative temperature changes are based on temperatures in °*C*. In addition, the standard deviations of changes among the ensemble members are shown.

is approximately 1.5 g kg^{-1} higher than in the corresponding scenario simulation without changing the mean sea level (Model A under the RCP 8.5) (**Figure 10**). The higher mean sea level causes increases in both frequency and magnitude of saltwater inflows due to the greater water depth in the Danish straits causing an increase in the salt flux between Kattegat and Arkona Basin (cf. Meier et al., 2017). Hence, at the end of the simulation period salinity in the Baltic Sea is higher and the vertical

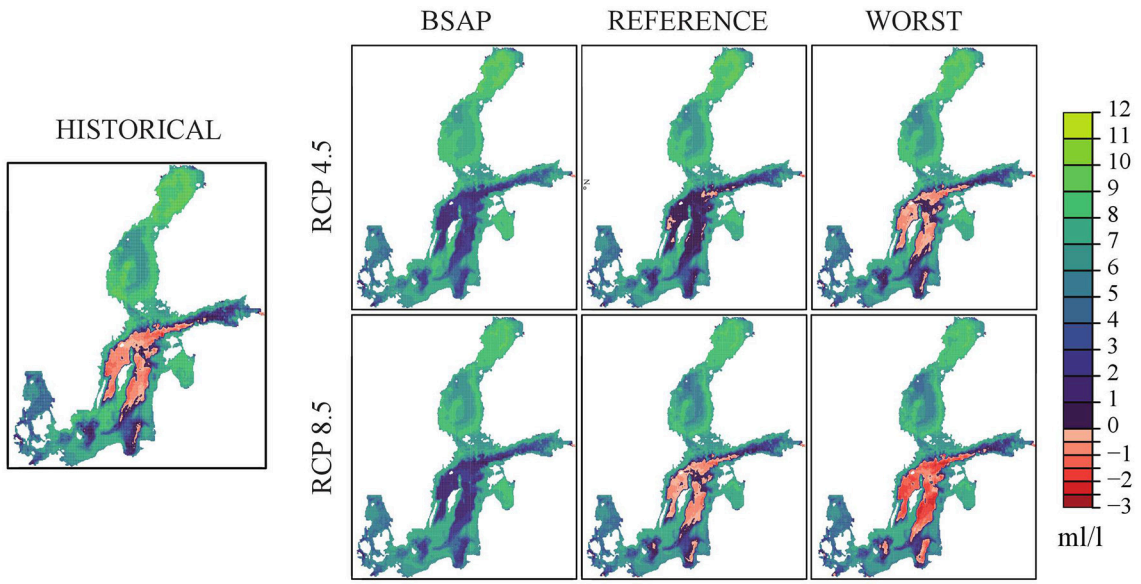

FIGURE 8 | Historical (1976–2005) and projected future (2069–2098) ensemble mean summer bottom oxygen concentrations (in mL L^{-1}) in three nutrient load (BSAP, Reference and Worst Case) and two greenhouse gas concentration scenarios (RCP 4.5 and 8.5). Hydrogen sulfide concentrations are represented by negative oxygen concentrations (1 mL H_2S L^{-1} = −2 mL O_2 L^{-1}).

stratification is larger compared to the corresponding scenario simulation without mean sea level rise. For comparison, in our ensemble the ranges of projected salinities at the end of the century under both RCP 4.5 and RCP 8.5 scenarios amount to approximately 2 g kg^{-1} (**Figure 6**). As wind fields do not change significantly (not shown), these ranges are mainly explained by differences in the projected river runoff.

As a consequence of a higher mean sea level, oxygen concentrations of salt water inflows are higher causing an improved ventilation of the deep water. However, since stratification is getting stronger, the vertical flux of oxygen from the surface to the bottom is reduced in bottom areas along the slopes of the deeper sub-basins, that are not directly affected by salt water inflows and that drop below the rising halocline. The latter process causes larger areas of hypoxia. The differences in the projected hypoxic areas at the end of the century between simulations with 1 m higher mean sea level and without changing mean sea level are less than 10% indicating a modest sensitivity to mean sea level change (**Figure 11**). Hence, the results suggest that the differing future nutrient loads will dominate the uncertainties in the hypoxic area projections if the range of nutrient loads is defined by the Worst Case and BSAP scenarios (cf. **Figure 7**). In addition, the uncertainty caused by the global models is considerable and significantly larger than the uncertainty due to greenhouse gas concentration scenarios (either RCP 4.5 or RCP 8.5).

DISCUSSION

In this study, an ensemble of 21 scenario simulations driven by four different GCMs and two sensitivity experiments on sea level rise was performed, by combining different future climate scenarios and nutrient load projections for the 21st century.

Compared to earlier Baltic Sea studies, the new features of this study are:

- simulations for the period 1850–2098 including a spin-up with reconstructed forcing for 1850–1975;
- consistent simulations without bias correction except for the wind speed and mean runoff;
- dynamical downscaling of four GCMs with the aim of estimating the impact of climate model uncertainties on the Baltic Sea properties;
- revised, more plausible nutrient load scenarios taking the latest observations into account;
- two greenhouse gas concentration scenarios corresponding to RCP 4.5 and RCP 8.5;
- improved version of the coupled physical-biogeochemical model of the Baltic Sea (Eilola et al., 2009); and
- improved versions of the global models from the Coupled Model Intercomparison Project 5 (CMIP5) of the IPCC (Stocker et al., 2013).

The sensitivity experiments are not scenario simulations following Stocker et al. (2013) because the 1 m higher mean sea level was applied as being constant in time during 2006–2098. The reason for this experimental setup is that the Baltic Sea model RCO has a linearized free sea surface following Killworth et al. (1991) that does not permit long-term changes in the mean sea surface height (Meier et al., 1999). Hence, our experiments overestimate the effect of the increasing global mean sea level and, thus, overestimate the increasing salinity in the Baltic Sea (**Figures 10**, **11**). In our sensitivity experiments, a 1 m higher

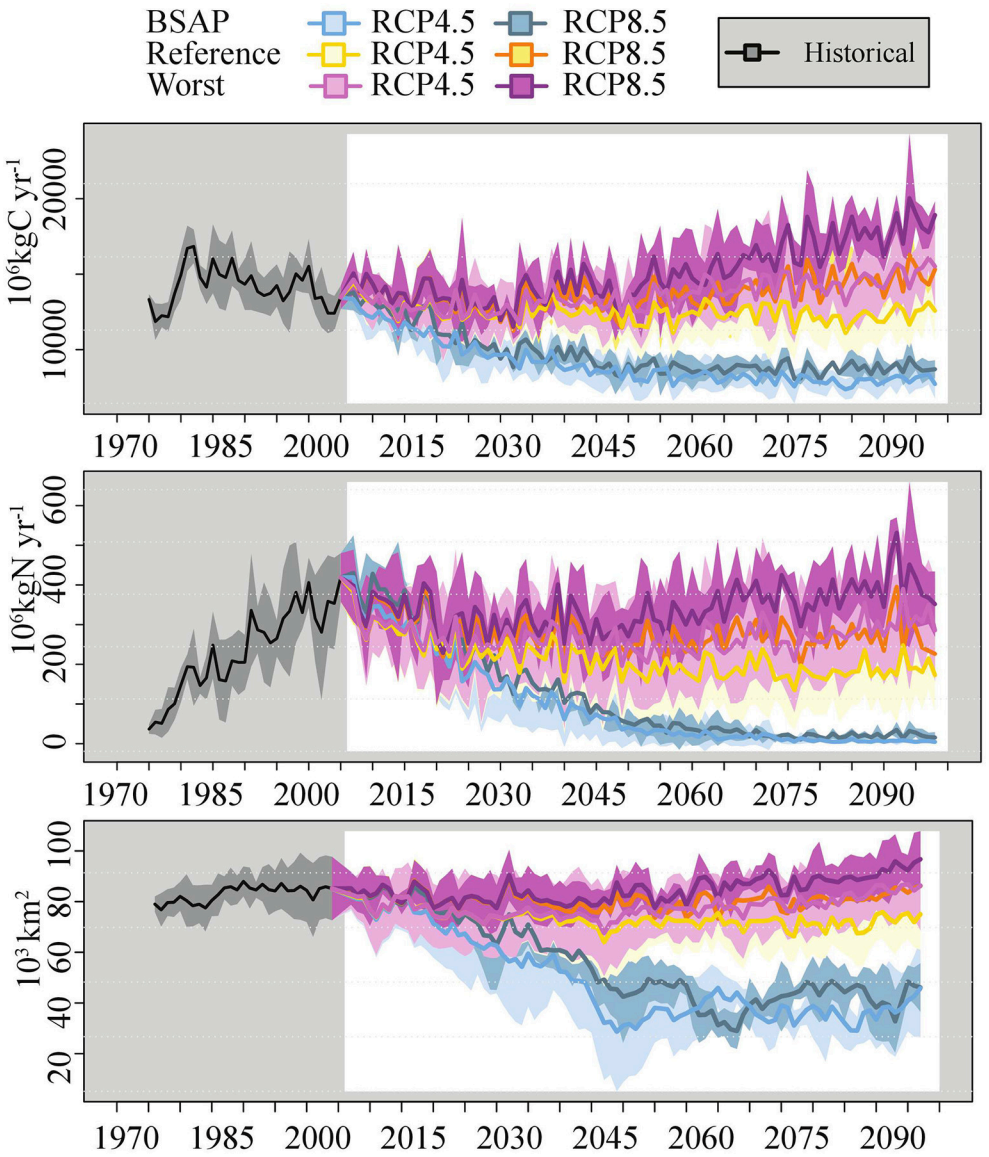

FIGURE 9 | Temporal evolution of ensemble mean volume averaged primary production (in 10^6 *kg C year*$^{-1}$, upper panel) and nitrogen fixation (in 10^6 *kg N year*$^{-1}$, middle panel), and hypoxic area (in 10^3 km^2, lower panel) in the entire Baltic Sea during 1975–2098 and their standard deviations (ensemble spread) among ensemble members. For all combinations of the two greenhouse gas concentration scenarios (RCP 4.5 and 8.5) and the three nutrient load scenarios (BSAP, Reference and Worst Case) the ensemble mean and spread were calculated from four regionalized global climate simulations.

mean sea level was chosen because this value is close to the high-end scenario simulation results at the end of the 21st century (Stocker et al., 2013). As projections of global mean sea level rise are rather uncertain (Stocker et al., 2013), the aim of our sensitivity experiments is only to illustrate a possible maximum effect of increasing global mean sea level that has been neglected in all previous scenario simulations of the Baltic Sea (Meier et al., 2017).

The projected ensemble mean change in salinity under the RCP 4.5 scenario amounts to −0.7 g kg^{-1} compared with that of the historical period, with a considerable ensemble spread among the different GCMs. Under the RCP 8.5 scenario, the ensemble mean change of the three GCMs amounts to −0.6 g kg^{-1}. However, since the ensemble excludes the model that shows the greatest projected salinity change under the RCP 4.5 scenario (Model C), we assume that under RCP 8.5 the change of the ensemble mean will also be greater if Model C is included (**Figure 10**). Hence, our ensemble is too small and the uncertainties, *inter alia*, in the salinity projections might be underestimated.

Substantial uncertainties in future projections for the Baltic Sea are caused by the driving climate models, e.g., those for

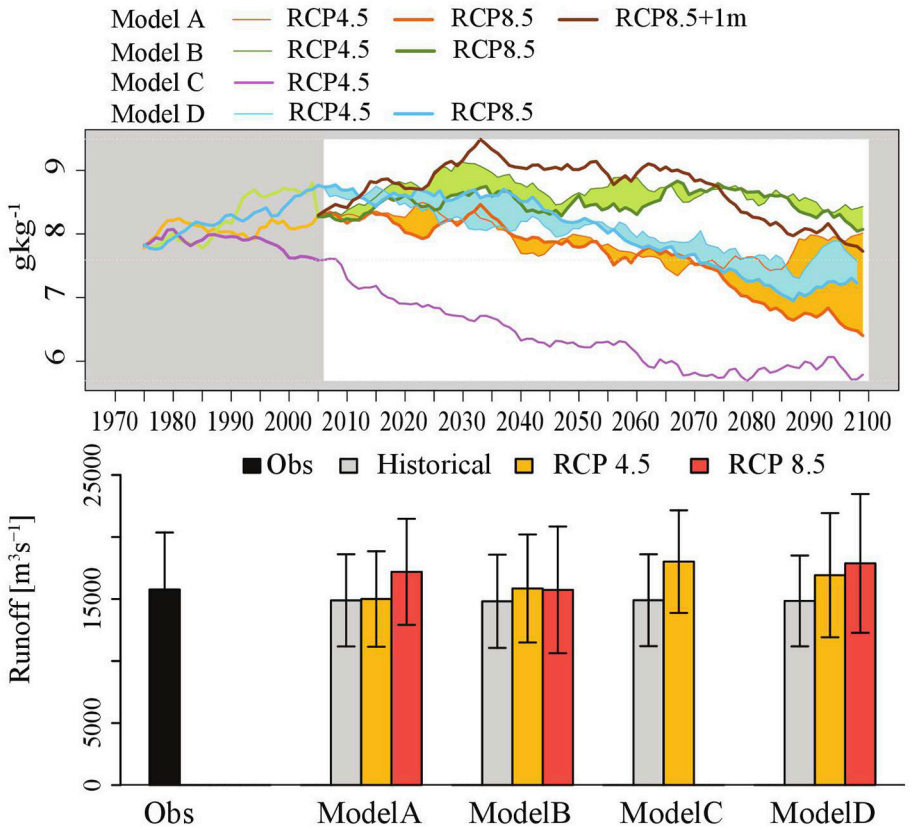

FIGURE 10 | Upper panel: Temporal evolution of volume averaged salinity (in g kg^{-1}) in the entire Baltic Sea during 1975–2098 in various climate scenarios (RCP 4.5 and 8.5) using four global climate models: MPI-ESM-LR (Model A); EC-EARTH (Model B); IPSL-CM5A-MR (Model C); HadGEM2-ES (Model D). Note, a scenario simulation driven by Model C and RCP 8.5 does not exist. A sensitivity experiment forced by Model A under the RCP 8.5 scenario assuming a 1 m higher mean sea level is also shown. Lower panel: Annual mean river runoff (in m^3 s^{-1}) in the scenario simulations and observations (1976–2005).

salinity due to uncertainties in projected river runoff and global mean sea level rise (**Figure 10**), cf. Meier et al. (2017). In RCP 4.5 and RCP 8.5, the projected river runoff varies between 1 and 21% and between 6 and 20%, respectively, explaining the considerable uncertainties in the projected salinity (Meier and Kauker, 2003b; their Figure 7), which are much greater than the natural variability (Meier and Kauker, 2003a). Uncertainties in salinity and stratification affect biogeochemical fluxes and hypoxic areas (Eilola et al., 2011). For instance, the vertical flux of oxygen between the well-oxygenated surface layer and the deep water is controlled by vertical stratification (Väli et al., 2013). Hence, deficiencies in climate models have considerable impacts on the water balance of the Baltic Sea that cannot be neglected in regional projections (Meier et al., 2011a). However, in our multi-model ensemble study the resulting uncertainties in biogeochemical fluxes, such as primary production and nitrogen fixation, and hypoxic areas are still significantly smaller than the differences caused by the different nutrient load scenarios, i.e., Worst Case and BSAP (**Table 3**). In addition, the uncertainties caused by unknown greenhouse gas concentration (RCP 4.5 and RCP 8.5) and global mean sea level rise scenarios are also smaller than the differences between nutrient load scenarios. Thus, we found an overwhelming impact of the various nutrient load scenarios on the changing biogeochemical cycles in the Baltic Sea. For (1) primary production and (2) nitrogen fixation and hypoxic area, the second largest uncertainties are based on the choice of the greenhouse gas concentration scenario (RCP 4.5 or RCP 8.5) and climate model uncertainties (calculated from four GCMs), respectively (**Table 3**). As one of the main uncertainties in the salinity projections is caused by the differing river runoff projections between the driving GCMs (**Table 3**, **Figure 10**), we conclude that projections of nitrogen fixation and hypoxic area suffer from shortcomings in the simulated water cycles. For changes in primary production, the magnitude of the temperature increase also plays an important role. In addition, our sensitivity experiment indicates that the uncertainty in salinity changes due to global mean sea level rise has an important impact on nitrogen fixation and hypoxic area as well. The latter result is in agreement with Meier et al. (2017).

In this study, only results from greenhouse gas concentration scenarios RCP 4.5 and RCP 8.5 were analyzed. RCP 2.6, at the lower end of the IPCC greenhouse gas concentration scenarios, corresponding to the goal of a global temperature rise limited to $<2^{\circ}C$, was not studied. Hence, in our ensemble the range of

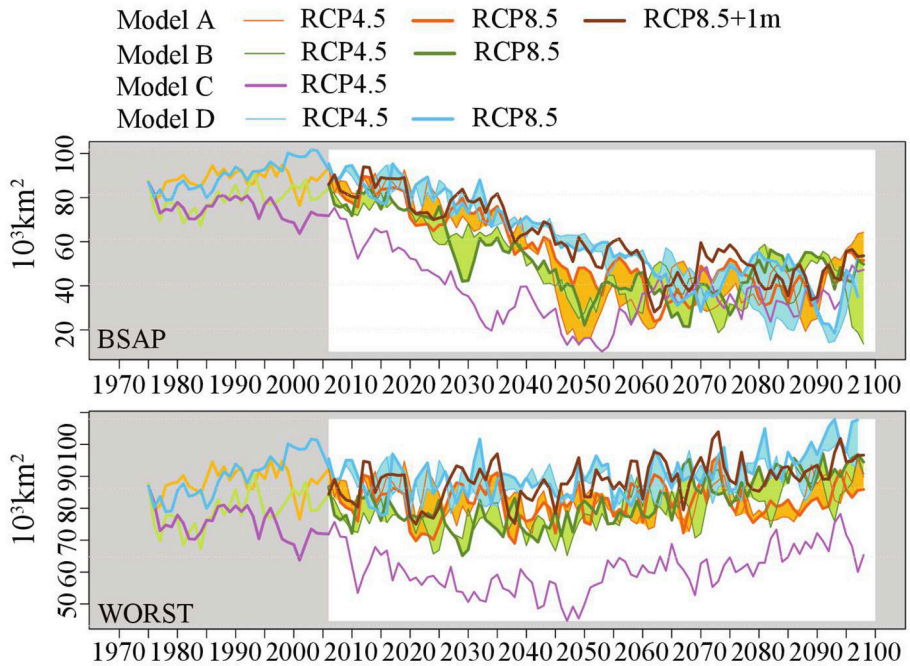

FIGURE 11 | As the upper panel in **Figure 10** but for hypoxic area under the BSAP and Worst Case scenarios.

TABLE 3 | Uncertainties expressed as standard deviations in temperature and salinity and variances of 30 years mean changes between the future (2069–2098) and historical (1976–2005) climates in primary production, nitrogen fixation and hypoxic area caused by GCMs, RCPs, nutrient loads, and global mean sea level rise (only model A, BSAP, and Worst Case, see **Table 2**).

Parameter/Uncertainty	GCMs	RCPs	Nutrient loads	Sea level rise
Temperature (in °C)	0.5	0.8	0	0
Salinity (in g kg^{-1})	0.9	0.4	0	1.1
Primary production (in %)	6	12	67	2
Nitrogen fixation (in %)	16	5	67	9
Hypoxic area (in %)	12	3	74	6

Variances of changes in the primary production, nitrogen fixation and hypoxic area are normalized by the corresponding variances based on the changes in all 23 simulations.

warming in the Baltic Sea region is smaller than that of the full range of global scenario simulations.

Further, we have not investigated the uncertainties caused by the shortcomings in the RCMs of the Baltic Sea. Eilola et al. (2011) compared three different coupled physical-biogeochemical models for the Baltic Sea under the present climate conditions. They concluded that the models reproduce much of the biogeochemical cycling in the Baltic proper in hindcast simulations during 1970–2005. However, uncertainties caused by the assumptions about the bioavailable fractions of nutrient loads from land and parameterizations of the key biogeochemical processes were considerable. The same models were also used in an ensemble of scenario simulations for 1961–2099 (Meier et al., 2011a, 2012b,c; Neumann et al., 2012). Within the latter studies, substantially differing nutrient load scenarios and driving GCMs were applied, making a direct comparison with our results impossible. As only two driving GCMs were used and as the impact of global mean sea level rise was neglected, the previously published ensemble spread in salinity was smaller than that found in our study. Uncertainties in the projections of the hypoxic area were about as large as those presented in the ensemble of scenario simulations of this study. Hence, future projections of the Baltic Sea ecosystem require multi-model ensembles of regional and global climate models to allow a suitable estimate of uncertainties.

The assumption that the ensemble spread due to natural variability at the end of the 21st century is small compared to the other uncertainties might be wrong on the regional scale. In a forthcoming study, the sources of uncertainty will be studied in more detail.

CONCLUSIONS

From the model results of this study, we draw the following conclusions:

(1) Implementation of the BSAP will lead to a significantly improved ecosystem state of the Baltic Sea irrespective of the driving GCM because changing climate will not counteract nutrient load reductions.
(2) The main driver of eutrophication is external nutrient loads. Climate change (mainly warming and global mean sea level rise) may amplify eutrophication. The response of biogeochemical fluxes, such as primary production and nitrogen fixation, and deep water oxygen conditions to

changing climate depend on the nutrient load scenario. In the case of high (low) nutrient loads, the impact of the changing climate would be considerable (negligible). However, the impacts of the changing climate within the range of the considered greenhouse gas concentration scenarios (RCP 4.5 and RCP 8.5) on biogeochemical cycles will be smaller than the impacts of the considered nutrient load changes (BSAP, Reference, Worst Case).

(3) Substantial uncertainties of future projections for the Baltic Sea are caused by the driving GCMs. For instance, salinity projections differ considerably due to the uncertainties in the projected river runoff and global mean sea level rise. Hence, for future projections an ensemble of various driving GCMs is necessary. This study also shows that dynamical downscaling is a useful tool because local drivers of marine biogeochemical cycling, such as nutrient load changes, are still more important than the estimated uncertainties caused by deficiencies of the climate models. Despite the large uncertainties caused by climate models, we were able to draw a conclusion concerning the impact of the BSAP in future climates (see Conclusion no. 1).

DATA AVAILABILITY STATEMENT

Observations from the Baltic Environmental Database (BED) are publicly available from http://nest.su.se/bed. Model codes and data used for the analysis of this study are available from the authors upon request.

AUTHOR CONTRIBUTIONS

For the BalticAPP proposal, concept and design of the study was developed by HM. SS performed the scenario simulations with the help of HM, AH, CD, MG, RH, HA, and KE. SS visualized and analyzed the model results. HM and SS wrote the text of the manuscript. All co-authors helped with comments, contributed to the manuscript revision, read and approved the submitted version.

FUNDING

The research presented in this study is part of the Baltic Earth program (Earth System Science for the Baltic Sea region, see http://www.baltic.earth) and was funded by the BONUS BalticAPP (Well-being from the Baltic Sea—applications combining natural science and economics) project which has received funding from BONUS, the joint Baltic Sea research and development programme (Art 185), funded jointly from the European Union's Seventh Programme for research, technological development and demonstration and from the Swedish Research Council for Environment, Agricultural Sciences and Spatial Planning (FORMAS, grant no. 942-2015-23). Support by FORMAS within the project Cyanobacteria life cycles and nitrogen fixation in historical reconstructions and future climate scenarios (1850-2100) of the Baltic Sea (grant no. 214-2013-1449) and by the CERES project, which has received funding from the European Union's Horizon 2020 research and innovation programme under grant agreement no. 678193, is acknowledged. In addition, SS would like to acknowledge the support by Fundação para a Ciência e a Tecnologia, Portugal (SFRH/BPD/120279/2016) in the later phase of this project.

ACKNOWLEDGMENTS

The observational data used for the weighting, analysis of nutrient content and lateral boundary conditions are open access and were extracted from the Baltic Environmental Database (BED, http://nest.su.se/bed) at Stockholm University and all data providing institutes (listed at http://nest.su.se/bed/ACKNOWLE.shtml) are kindly acknowledged. BED contains observations, *inter alia*, from the national, long-term environmental monitoring programs such as the Swedish Ocean Archive (SHARK, http://sharkweb.smhi.se) operated by the Swedish Meteorological and Hydrological Institute (SMHI) or the German Baltic Sea monitoring data archive (http://iowmeta.io-warnemuende.de) operated by the Leibniz Institute for Baltic Sea Research Warnemünde (IOW). The paper is based upon an earlier manuscript by Saraiva et al. (2018b).

SUPPLEMENTARY MATERIAL

The Supplementary Material for this article can be found online at: https://www.frontiersin.org/articles/10.3389/feart.2018.00244/full#supplementary-material

REFERENCES

Ahtiainen, H., and Öhman, H. C. (2014). *Ecosystem Services in the Baltic Sea: Valuation of Marine and Coastal Ecosystem Services in the Baltic Sea, vol. 563 of Report TemaNord*. Copenhagen: Nordic Council of Ministers.

Almroth-Rosell, E., Eilola, K., Hordoir, R., Meier, H. E. M., and Hall, P. O. J. (2011). Transport of fresh and resuspended particulate organic material in the Baltic Sea – a model study. *J. Mar. Syst.* 87, 1–12. doi: 10.1016/j.jmarsys.2011.02.005

BACC II Author Team (2015). *Second Assessment of Climate Change for the Baltic Sea Basin*. Cham: Regional Climate Studies, Springer. doi: 10.1007/978-3-319-16006-1

Belkin, I. M. (2009). Rapid warming of large marine ecosystems. *Prog. Oceanogr.* 81, 207–213. doi: 10.1016/j.pocean.2009.04.011

Block, K., and Mauritsen, T. (2013). Forcing and feedback in the MPI-ESM-LR coupled model under abruptly quadrupled CO_2. *J. Adv. Model. Earth Syst.* 5, 676–691. doi: 10.1002/jame.20041

Carstensen, J., Andersen, J. H., Gustafsson, B. G., and Conley, D. J. (2014). Deoxygenation of the Baltic Sea during the last century. *Proc. Natl. Acad. Sci. U. S. A.* 111, 5628–5633. doi: 10.1073/pnas.1323156111

Christensen, J. H., Kjellström, E., Giorgi, F., Lenderink, G., and Rummukainen, M. (2010). Weight assignment in regional climate models. *Clim. Res.* 44, 179–194. doi: 10.3354/cr00916

Conley, D. J. (2012). Ecology: save the Baltic Sea. *Nature* 486, 463–464. doi: 10.1038/486463a

Conley, D. J., Björck, S., Bonsdorff, E., Carstensen, J., Destouni, G., Gustafsson, B. G., et al. (2009). Hypoxia-related processes in the Baltic Sea. *Environ. Sci. Technol.* 43, 3412–3420. doi: 10.1021/es802762a

Dahlgren, P., Landelius, T., Kallberg, P., and Gollvik, S. (2016). A high-resolution regional reanalysis for Europe. Part 1: three- dimensional reanalysis with the regional HIgh-Resolution Limited-Area Model (HIRLAM). *Quart. J. R. Meteorol. Soc.* 142, 698(A), 2119–2131. doi: 10.1002/qj.2807

Déqué, M., Somot, S., Sanchez-Gomez, E., Goodess, C., Jacob, D., Lenderink, G., et al. (2012). The spread amongst ENSEMBLES regional scenarios: regional climate models, driving general circulation models and interannual variability. *Clim. Dyn.* 38, 951–964. doi: 10.1007/s00382-011-1053-x

Dieterich, C., Schimanke, S., Wang, S., Väli, G., Liu, Y., Hordoir, R., et al. (2013). *Evaluation of the SMHI Coupled Atmosphere-Ice-Ocean Model RCA4-NEMO*. vol. 47 of Report Oceanography, SMHI, Norrköping, Sweden

Donnelly, C., Arheimer, B., Capell, R., Dahné, J., and Strömqvist, J. (2013). "Regional overview of nutrient load in Europe – challenges when using a large-scale model approach, E-HYPE,"in *Proceedings of H04, IAHS-IAPSO-IASPEI Assembly*. Gothenburg, Sweden, IHS *Publ.* 361, 49–58.

Donnelly, C., Greuell, W., Andersson, J., Gerten, D., Pisacane, G., Roudier, P., et al. (2017). Impacts of climate change on European hydrology at 1.5, 2 and 3 degrees mean global warming above preindustrial level. *Climatic Change* 143, 13–26. doi: 10.1007/s10584-017-1971-7.

Döscher, R., and Meier, H. E. M. (2004). Simulated sea surface temperature and heat fluxes in different climates of the Baltic Sea. *Ambio* 33, 242–248. doi: 10.1579/0044-7447-33.4.242

Eilola, K., Almroth-Rosell, E., Dieterich, C., Fransner, F., Höglund, A., and Meier, H. E. M. (2012). Modeling nutrient transports and exchanges of nutrients between shallow regions and the open Baltic Sea in present and future climate. *Ambio* 41, 586–599. doi: 10.1007/s13280-012-0317-y

Eilola, K., Gustafsson, B. G., Kuznetsov, I., Meier, H. E. M., Neumann, T., and Savchuk, O. P. (2011). Evaluation of biogeochemical cycles in an ensemble of three state-of-the-art numerical models of the Baltic Sea. *J. Mar. Syst.* 88, 267–284. doi: 10.1016/j.jmarsys.2011.05.004

Eilola, K., Mårtensson, S., and Meier, H. E. M. (2013). Modeling the impact of reduced sea ice cover in future climate on the Baltic Sea biogeochemistry. *Geophys. Res. Lett.* 40, 149–154. doi: 10.1029/2012GL054375

Eilola, K., Meier, H. E. M., and Almroth, E. (2009). On the dynamics of oxygen, phosphorus and cyanobacteria in the Baltic Sea; A model study. *J. Mar. Syst.* 75, 163–184. doi: 10.1016/j.jmarsys.2008.08.009.

Friedland, R., Neumann, T., and Schernewski, G. (2012). Climate change and the Baltic Sea action plan: model simulations on the future of the western Baltic Sea. *J. Mar. Syst.* 105, 175–186. doi: 10.1016/j.jmarsys.2012.08.002

Giorgi, F., and Mearns, L. O. (1991). Approaches to the simulation of regional climate change: a review. *Rev. Geophys.* 29, 191–216.

Gröger, M., Dieterich, C., Meier, H. E. M., and Schimanke, S. (2015). Thermal air–sea coupling in hindcast simulations for the North Sea and Baltic Sea on the NW European shelf. *Tellus A Dyn. Meteorol. Oceanogr.* 67:26911. doi: 10.3402/tellusa.v67.26911

Gustafsson, B. G., Schenk, F., Blenckner, T., Eilola, K., Meier, H. E. M., Müller-Karulis, B., et al. (2012). Reconstructing the development of Baltic Sea eutrophication 1850–2006. *Ambio* 41, 534–548. doi: 10.1007/s13280-012-0318-x

Hawkins, E., and Sutton, R. (2009). The potential to narrow uncertainty in regional climate predictions. *Bull. Am. Meteorol. Soc.* 90, 1095–1108. doi: 10.1175/2009BAMS2607.1

Hazeleger, W., Wang, X., Severijns, C., Stefănescu, S., Bintanja, R., Sterl, A., et al. (2012). EC-Earth V2. 2: description and validation of a new seamless earth system prediction model. *Clim. Dyn.* 39, 2611–2629. doi: 10.1007/s00382-011-1228-5

Heavens, N. G., Ward, D. S., and Natalie, M. M. (2013). Studying and projecting climate change with earth system models. *Nat. Educ. Know.* 4:4

HELCOM (2013). "Copenhagen ministerial declaration," in *HELCOM Ministerial Meeting, Copenhagen, Denmark.*

Hieronymus, J., Eilola, K., Hieronymus, M., Meier, H. E. M., Saraiva, S., and Karlson, B. (2018). Causes of simulated long-term changes in phytoplankton biomass in the Baltic proper: a wavelet analysis. *Biogeosciences* 15, 5113–5129. doi: 10.5194/bg-15-5113-2018

Hourdin, F., Foujols, M.-A., Codron, F., Guemas, V., Dufresne, J.-L., Bony, S., et al. (2013). Impact of the LMDZ atmospheric grid configuration on the climate and sensitivity of the IPSL-CM5A coupled model. *Clim. Dyn.* 40, 2167–2192. doi: 10.1007/s00382-012-1411-3

Hundecha, Y., Arheimer, B., Donnelly, C., and Pechlivanidis, I. (2016). A regional parameter estimation scheme for a pan-European multi-basin model. *J. Hydrol. Region. Stud.* 6, 90–111. doi: 10.1016/j.ejrh.2016.04.002.

Jacob, D., Petersen, J., Eggert, B., Alias, A., Christensen, O. B., Bouwer, L. M., et al. (2014). EURO-CORDEX: new high-resolution climate change projections for European impact research. *Reg. Environ. Change* 14, 563–578. doi: 10.1007/s10113-013-0499-2.

Jones, C. D., Hughes, J. K., Bellouin, N., Hardiman, S. C., Jones, G. S., Knight, J., et al. (2011). The HadGEM2-ES implementation of CMIP5 centennial simulations. *Geosci. Model Dev.* 4, 543–570. doi: 10.5194/gmd-4-543-2011

Killworth, P. D., Webb, D. J., Stainforth, D., and Paterson, S. M. (1991). The development of a free-surface Bryan–Cox–Semtner ocean model. *J. Phys. Oceanogr.* 21, 1333–1348.

Kjellström, E., Nikulin, G., Hansson, U. L. F., Strandberg, G., and Ullerstig, A. (2011). 21st century changes in the European climate: uncertainties derived from an ensemble of regional climate model simulations. *Tellus A Dyn. Meteorol. Oceanog.* 63, 24–40. doi: 10.1111/j.1600-0870.2010.00475.x

Kupiainen, M., Jansson, C., Samuelsson, P., Jones, C.,Willén, U., Wang, S., et al. (2014). *Rossby Centre Regional Atmospheric Model, RCA4, Rossby Center News Letter*. SMHI, Norrköping, Sweden. Available online at : http://www.smhi.se/en/Research/Research-departments/climate-research-rossby-centre2-552/1.16562 (Accessed August 14, 2018)

Madec, G. (2016). *NEMO ocean engine. version 3.6 stable. Note du Pôle de modélisation. Institut Pierre-Simon Laplace (IPSL)-LOCEAN*. Paris: The NEMO team . Available online at : https://www.nemo-ocean.eu/wp-content/uploads/NEMO_book.pdf (Accessed August 17, 2018)

Marti, O., Braconnot, P., Dufresne, J.-L., Bellier, J., Benshila, R., Bony, S., et al. (2010). Key features of the IPSL ocean atmosphere model and its sensitivity to atmospheric resolution. *Clim. Dyn.* 34, 1–26. doi: 10.1007/s00382-009-0640-6

Mathis, M., Elizalde, A., and Mikolajewicz, U. (2018). Which complexity of regional climate system models is essential for downscaling anthropogenic climate change in the Northwest European Shelf? *Clim. Dyn.* 50, 2637–2659. doi: 10.1007/s00382-017-3761-3

Meehl, G. A., Washington, W. M., Ammann, C. M., Arblaster, J. M., Wigley, T. M. L., and Tebaldi, C. (2004). Combinations of natural and anthropogenic forcings in twentieth-century climate. *J. Clim.* 17, 3721–3727. doi: 10.1175/1520-0442

Meier, H. E., Kjellström, E., and Graham, L. P. (2006). Estimating uncertainties of projected Baltic Sea salinity in the late 21st century. *Geophys. Res. Lett.* 33:488. doi: 10.1029/2006GL026488

Meier, H. E. M. (2002a). Regional ocean climate simulations with a 3D ice-ocean model for the Baltic Sea. Part 1: model experiments and results for temperature and salinity. *Clim. Dyn.* 19, 237–253. doi: 10.1007/s00382-001-0224-6

Meier, H. E. M. (2002b). Regional ocean climate simulations with a 3D ice-ocean model for the Baltic Sea. Part 2: Results for sea ice. *Clim. Dyn.* 19, 255–266. doi: 10.1007/s00382-001-0225-5

Meier, H. E. M. (2006). Baltic Sea climate in the late twenty-first century: a dynamical downscaling approach using two global models and two emission scenarios. *Clim. Dyn.* 27, 39–68. doi: 10.1007/s00382-006-0124-x.

Meier, H. E. M. (2007). Modeling the pathways and ages of inflowing salt- and freshwater in the Baltic Sea. *Estuar. Coast. Shelf Sci.* 74, 610–627. doi: 10.1016/j.ecss.2007.05.019

Meier, H. E. M., Andersson, H. C., Arheimer, B., Blenckner, T., Chubarenko, B., Donnelly, C., et al. (2012c). Comparing reconstructed past variations and future projections of the Baltic Sea ecosystem – first results from multi-model ensemble simulations. *Environ. Res. Lett.* 7:034005. doi: 10.1088/1748-9326/7/3/034005

Meier, H. E. M., Andersson, H. C., Eilola, K., Gustafsson, B. G., Kuznetsov, I., Müller-Karulis, B., et al. (2011a). Hypoxia in future climates: a model ensemble study for the Baltic Sea. *Geophys. Res. Lett.* 38:L24608. doi: 10.1029/2011GL049929

Meier, H. E. M., Döscher, R., Coward, A. C., Nycander, J., and Döös, K. (1999). *RCO - Rossby Centre Regional Ocean Climate Model: Model Description (version*

1.0) and First Results From the Hindcast Period 1992/93. Reports Oceanography No.26, SMHI, Norrköping.

Meier, H. E. M., Döscher, R., and Faxén, T. (2003). A multiprocessor coupled ice-ocean model for the Baltic Sea: application to salt inflow. *J. Geophys. Res. Oceans* 108:3273. doi: 10.1029/2000JC000521

Meier, H. E. M., Döscher, R., and Halkka, A. (2004). Simulated distributions of Baltic Sea-ice in warming climate and consequences for the winter habitat of the Baltic ringed seal. *Ambio* 33, 249–256. doi: 10.1579/0044-7447-33.4.249

Meier, H. E. M., Eilola, K., and Almroth, E. (2011c). Climate-related changes in marine ecosystems simulated with a three-dimensional coupled biogeochemical-physical model of the Baltic Sea. *Clim. Res.* 48, 31–55. doi: 10.3354/cr00968

Meier, H. E. M., Eilola, K., Almroth-Rosell, E., Schimanke, S., Kniebusch, M., Höglund, A., et al. (2018). Disentangling the impact of nutrient load and climate changes on Baltic Sea hypoxia and eutrophication since 1850. *Clim. Dyn.* 1–22. doi: 10.1007/s00382-018-4296-y

Meier, H. E. M., Höglund, A., Döscher, R., Andersson, H., Löptien, U., and Kjellström, E. (2011b). Quality assessment of atmospheric surface fields over the Baltic Sea of an ensemble of regional climate model simulations with respect to ocean dynamics. *Oceanologia* 53, 193–227. doi: 10.5697/oc.53-1-TI.193

Meier, H. E. M., Höglund, A., Eilola, K., and Almroth-Rosell, E. (2017). Impact of accelerated future GMSL rise on hypoxia in the Baltic Sea. *Clim. Dyn.* 49:163–172. doi: 10.1007/s00382-016-3333-y

Meier, H. E. M., Hordoir, R., Andersson, H., Dieterich, C., Eilola, K., Gustafsson, B. G., et al. (2012a). Modeling the combined impact of changing climate and changing nutrient loads on the Baltic Sea environment in an ensemble of transient simulations for 1961-2099. *Clim. Dyn.* 39, 2421–2441. doi: 10.1007/s00382-012-1339-7

Meier, H. E. M., and Kauker, F. (2003a). Modeling decadal variability of the Baltic Sea: 2. Role of freshwater inflow and large-scale atmospheric circulation for salinity. *J. Geophys. Res. Oceans* 108. doi: 10.1029/2003JC001799

Meier, H. E. M., and Kauker, F. (2003b). Sensitivity of the Baltic Sea salinity to the freshwater supply. *Clim. Res.* 24, 231–242. doi: 10.3354/cr024231.

Meier, H. E. M., Müller-Karulis, B., Andersson, H. C., Dieterich, C., Eilola, K., Gustafsson, B. G., et al. (2012b). Impact of climate change on ecological quality indicators and biogeochemical fluxes in the Baltic Sea: a multi-model ensemble study. *Ambio* 41, 558–573. doi: 10.1007/s13280-012-0320-3

Moss, R. H., Edmonds, J. A., Hibbard, K. A., Manning, M. R., Rose, S. K., Van Vuuren, D. P., et al. (2010). The next generation of scenarios for climate change research and assessment. *Nature* 463, 747–756. doi: 10.1038/nature08823

Neumann, T. (2010). Climate-change effects on the Baltic Sea ecosystem: a model study. *J. Mar. Syst.* 81, 213–224. doi: 10.1016/j.jmarsys.2009.12.001

Neumann, T., Eilola, K., Gustafsson, B., Müller-Karulis, B., Kuznetsov, I., Meier, H. E. M., et al. (2012). Extremes of temperature, oxygen and blooms in the Baltic Sea in a changing climate. *Ambio* 41, 574–585. doi: 10.1007/s13280-012-0321-2.

Omstedt, A., Edman, M., Claremar, B., Frodin, P., Gustafsson, E., Humborg, C., et al. (2012). Future changes in the Baltic Sea acid–base (pH) and oxygen balances. *Tellus B Chem. Phys. Meteorol.* 64:19586. doi: 10.3402/tellusb.v64i0.19586

Omstedt, A., Gustafsson, B., Rodhe, J., and Walin, G. (2000). Use of Baltic Sea modelling to investigate the water cycle and the heat balance in GCM and regional climate models. *Clim. Res.* 15, 95–108. doi: 10.3354/cr015095

O'Neill, B. C., Kriegler, E., Riahi, K., Ebi, K. L., Hallegatte, S., Carter, T. R., et al. (2014). A new scenario framework for climate change research: the concept of shared socioeconomic pathways. *Climatic Change* 122, 387–400. doi: 10.1007/s10584-013-0905-2

Räisänen, J., Hansson, U., Ullerstig, A., Döscher, R., Graham, L. P., Jones, C., et al. (2004). European climate in the late twenty-first century: regional simulations with two driving global models and two forcing scenarios. *Clim. Dyn.* 22, 13–31. doi: 10.1007/s00382-003-0365-x

Ruosteenoja, K., Jylhä, K., and Kämäräinen, M. (2016). Climate projections for Finland under the RCP forcing scenarios. *Geophysica* 51, 17–50.

Ryabchenko, V., Karlin, L., Isaev, A., Vankevich, R., Eremina, T., Molchanov, M., et al. (2016). Model estimates of the eutrophication of the Baltic Sea in the contemporary and future climate. *Oceanology* 56, 36–45. doi: 10.1134/S0001437016010161

Saraiva, S., Meier, H. E. M., Andersson, H., Höglund, A., Dieterich, C., Hordoir, R., et al. (2018a). Baltic Sea ecosystem response to various nutrient load scenarios in present and future climates. *Clim. Dyn.* 1–19. doi: 10.1007/s00382-018-4330-0

Saraiva, S., Meier, H. E. M., Andersson, H., Höglund, A., Dieterich, C., Hordoir, R., et al. (2018b). Uncertainties in projections of the Baltic Sea ecosystem driven by an ensemble of global climate models. *Earth Syst. Dynam. Discuss.* 1–30. doi: 10.5194/esd-2018-16

Savchuk, O. P. (2002). Nutrient biogeochemical cycles in the Gulf of Riga: scaling up field studies with a mathematical model. *J. Mar. Syst.* 32, 253–280. doi: 10.1016/S0924-7963(02)00039-8

Schimanke, S., Dieterich, C., and Meier, H. E. M. (2014). An algorithm based on sea-level pressure fluctuations to identify major Baltic inflow events. *Tellus A Dyn. Meteorol. Oceanograp.* 66:23452. doi: 10.3402/tellusa.v66.23452

Schimanke, S., and Meier, H. E. M. (2016). Decadal-to-centennial variability of salinity in the Baltic Sea. *J. Climate* 29, 7173–7188. doi: 10.1175/JCLI-D-15-0443.1

Sjöberg, B. (1992). *Sea and Coast – National Atlas of Sweden, SMHI*. Stockholm: Swedish Meteorological and Hydrological Institute (SMHI).

Stålnacke, P., Grimvall, A., Sundblad, K., and Tonderski, A. (1999). Estimation of riverine loads of nitrogen and phosphorus to the Baltic Sea, 1970–1993. *Environ. Monitor. Assess.* 58, 173–200. doi: 10.1023/A:1006073015871

Stevens, B., Giorgetta, M., Esch, M., Mauritsen, T., Crueger, T., Rast, S., et al. (2013). Atmospheric component of the MPI-M Earth System Model: ECHAM6. *J. Adv. Model. Earth Syst.* 5, 146–172. doi: 10.1002/jame.20015

Stocker, T., Qin, D., Plattner, G.-K., Alexander, L., Allen, S., Bindoff, N., et al. (2013). "Technical summary", in *Climate Change 2013: the Physical Science Basis. Contribution of Working Group I to the Fifth Assessment Report of the Intergovernmental Panel on Climate Change*, eds. T. Stocker, G. K. Qin, M. Plattner, S.K. Tignor, J. Allen, A. Boschung, et al. (Cambridge: Cambridge University Press)

Svendsen, L. M., Pyhälä, M., Gustafsson, B., Sonesten, L., and Knuuttila, S. (2015). *Inputs of Nitrogen and Phosphorus to the Baltic Sea. HELCOM Core Indicator Report*. Helsinki Commission, Helsinki, Finland.

Uppala, S. M., Kållberg, P. W., Simmons, A. J., Andrae, U., Bechtold, V. D. C., Fiorino, M., et al. (2005). The ERA40 reanalysis. *Q. J. R. Meteorol. Soc.* 131, 2961–3012. doi: 10.1256/qj.04.176

Väli, G., Meier, H. E. M., and Elken, J. (2013). Simulated halocline variability in the Baltic Sea and its impact on hypoxia during 1961-2007. *J. Geophys. Res.* 118, 6982–7000. doi: 10.1002/2013JC009192

Wang, S., Dieterich, C., Döscher, R., Höglund, A., Hordoir, R., Meier, H. E. M., et al. (2015). Development and evaluation of a new regional coupled atmosphere–ocean model in the North Sea and Baltic Sea. *Tellus A Dyn. Meteorol. Oceanograp.* 67:24284. doi: 10.3402/tellusa.v67.24284

Wilcke, R. A. I., and Bärring, L. (2016). Selecting regional climate scenarios for impact modelling studies. *Environ. Modell. Software* 78, 191–201. doi: 10.1016/j.envsoft.2016.01.002

Wulff, F., Rahm, L., and Larsson, P. (2001). *A Systems Analysis of the Baltic Sea. Ecological Studies,* vol.148. Berlin; Heidelberg: Springer-Verlag. doi: 10.1007/978-3-662-04453-7

Zandersen, M., Hyytiainen, K., Meier, H. E. M., Tomzcak, M., Bauer, B., Haapasaari, P., et al. (in press). Extending shared socioeconomic pathways for the Baltic Sea region for use in studying regional environmental problems. *Region. Environ. Change*

Conflict of Interest Statement: The authors declare that the research was conducted in the absence of any commercial or financial relationships that could be construed as a potential conflict of interest.

frontiers in Earth Science

BRIEF RESEARCH REPORT
published: 18 April 2019
doi: 10.3389/feart.2019.00081

Sea Level Change: Mapping Danish Municipality Needs for Climate Information

Kristine S. Madsen, Jens Murawski, Marina Blokhina and Jian Su*

Danish Meteorological Institute, Copenhagen, Denmark

Climate change will affect the coastline of the Baltic Sea through changes in sea level, storm surges and waves. In Denmark, a large part of the responsibility for climate adaptation lies with the local municipalities. The purpose of this study was to map the user needs for coastal climate change information of five municipalities in the Danish south western Baltic Sea and the Danish Coastal Authority in a cost-efficient way and to transform the mapping into local climate indicators. An interview template was customized to form the basis for telephone interviews of key stakeholders and systematic gathering of the results. The interest for the interviews was high, and response from the interviewed persons on the use of the template was very positive. During the interviews, it was clear that the municipalities have access to extensive information on the population and infrastructure, as well as detailed geographical information. The main interests were in very high quality storm surge warnings and present day and future extreme sea level and wave heights. This should be based on modeling of past storm surges and future changes, taking observations, and historical records into account. There was a big need for more detailed information than presently available, and for common scenarios, which will help the collaboration between municipalities. Within this study, the user requirements were used to define targeted climate indicators. Within the C3S CODEC project, the indicators will be provided for the municipalities, based on a downscaling of European scale storm surge, and wave simulations to local scale.

Keywords: climate change, sea level change, user needs, user driven, Copernicus C3S

OPEN ACCESS

Edited by:
Marcus Reckermann, Helmholtz Centre for Materials and Coastal Research (HZG), Germany

Reviewed by:
Alex Oriel Godoy, Universidad del Desarrollo, Chile
Roger Brian Street, University of Oxford, United Kingdom

****Correspondence:***
Kristine S. Madsen
kma@dmi.dk

Specialty section:
This article was submitted to Interdisciplinary Climate Studies, a section of the journal Frontiers in Earth Science

Received: *04 December 2018*
Accepted: *03 April 2019*
Published: *18 April 2019*

Citation:
Madsen KS, Murawski J, Blokhina M and Su J (2019) Sea Level Change: Mapping Danish Municipality Needs for Climate Information. Front. Earth Sci. 7:81. doi: 10.3389/feart.2019.00081

INTRODUCTION

Climate change will affect the coastline of the Baltic Sea through changes in sea level, storm surges and waves, affecting, among others, the risk of flooding, and level of erosion (Olesen et al., 2014; Bacc II Author Team, 2015). The south western part of the Baltic Sea pose a special risk area, as the coastline is relatively well sheltered from frequently occurring sea level variability such as tides and high waves, and e.g., the harbor in Køge has not experienced storm surges above 1.52 m the last 63 years (Ditlevsen et al., 2018). At the same time, the region is known to have experienced some very extreme storm surges in historic time, most explicitly in 1872 (Colding, 1881). Thus, the coastline is relatively sensitive to general sea level rise. The southern shoreline of Copenhagen, the capital of Denmark, lies in this region. It is thus an area with an obvious coastal hazard emphasized

by coastal climate change and high societal and economic importance (Hallegatte et al., 2011) and has been selected as flood prone according to the EU flood directive (Andersen et al., 2018).

The need for climate information in various sectors in Europe is well established (Soares et al., 2018). Previous studies have shown that there is a need both for climate change information and information on decision making under large uncertainties (Turnpenny et al., 2004), not the least for the coastal region, where many aspects of society, including socio-economic and environmental issues, have to be taken into account (Tribbia and Moser, 2008). It has long been recognized that focusing only on the science, at the expense of user engagement, implies a risk of "simply providing too much of the wrong type of information" (McNie, 2007, p. 17). The information must be recognized as salient, credible, and legitimate to the users (Cash et al., 2002), and to ensure this, Vaughan et al. (2016) call for feedback and engagement between providers, purveyors and users of climate change services.

Several of the above studies have involved large user investigations involving online surveys and in depth interviews. Our motivation for this study was to test a relatively efficient and low cost method for early user interaction and mapping of user needs to design dedicated coastal climate indicators for the region, as the first step of a use case on Baltic Sea coastal climate change in the Copernicus Climate Change Service (C3S) CODEC project.

The section on Materials and Methods focuses on the use of an interview template designed for general user investigations for the C3S user need mapping, and use of interviews with few, but carefully selected responders. The results section describes the user response, including the early involvement and how the method fed into the C3S service, and allowed derivation of relevant and feasible climate change indicators.

MATERIALS AND METHODS

Study Area and Selected Municipalities

In Denmark, a large part of the responsibility for climate adaptation lies with the local municipalities.

The five municipalities Copenhagen, Dragør, Hvidovre, Ishøj, and Køge were selected for the study, to represent the variation of geographical conditions in the region, as well as various levels of focus on climate adaptation (see next paragraph). The selection was made based on our previous knowledge of, and engagement with, the municipalities. Further, the Danish Coastal Authority was included in the survey, as it has a central role in advising the municipalities on issues regarding flooding, and climate change. In total, six interviews were made.

All municipalities have coastline toward the Køge Bay region – the south coast of Copenhagen – in the south western Baltic Sea (**Figure 1**). The central Copenhagen Municipality represents the Copenhagen historical, governmental and cultural capital center and dense urban population, while the other municipalities are suburban, and also encompass rural areas and areas of natural and recreational interest. The Municipality of Copenhagen represents significantly more people than the other municipalities. It has an advanced program on climate change adaptation and is planning flood gate protection together with its closest neighbor municipalities. The other municipalities represent different awareness levels on the need for climate change adaptation. The municipalities all have access to extensive information on the population and infrastructure, as well as detailed geographical information, for their local area.

Interview Template

The interview template was originally developed for use within the SECTEUR project and for the C3S contract D422Lot2.TEC. Within this study, the wording of selected questions were tailored to focus on coastal climate change. The interview template (see **Supplementary Material**) consisted of a range of questions, space to write answers, and references to corresponding elements of the C3S User Requirement Database. That is, there was an almost one-to-one link between the template and the database elements.

The template contained an introductory part, focusing on identifying the interviewed person(s), their organization and professional role, and overall need for coastal climate information. The central part of the template consisted of identifying new essential climate variables and climate change indicators needed by the municipalities, by specifying key needs for climate information, needs for combination with socio-economic information or other data sources, and a range of meta-information, including data source, spatial-temporal resolution, quality and uncertainty information needs, and data format requirements. Also, there was room to discuss the needs for visualization and data processing tools. The interview template was rounded off with a talk on how new data will be used by the municipalities, the possibility to identify if more people in the organization or externally were relevant for the interview, and whether the interviewed person would like to be involved in the further process.

Interview Procedure

All interviewees were briefly introduced to the project and the interviews over e-mail, followed up with contact by phone. All invited municipalities were willing to participate in the interviews, and the interviews were conducted with representatives from the municipalities and the Coastal Authority over phone or through face to face meetings. They were limited to last 1 h. Before the interview, the interview template was sent to the interviewees for orientation, and to allow preparation of responses in the organization, but they were instructed not to fill it. During the interview, the template was followed with some flexibility, allowing focus on the areas of greatest importance to the individual interviewee, thus allowing a detailed interview of the needs for design of new climate indicators. Notes were taken during the interview, and based on this, the template was filled out by the research team. Finally, the filled template was sent to the interviewee for corrections and approval.

This study was carried out in accordance with the recommendations of the DMI Ethics Committee of the Danish Meteorological Institute, and the protocol was approved by the committee. All subjects gave written informed consent to participate.

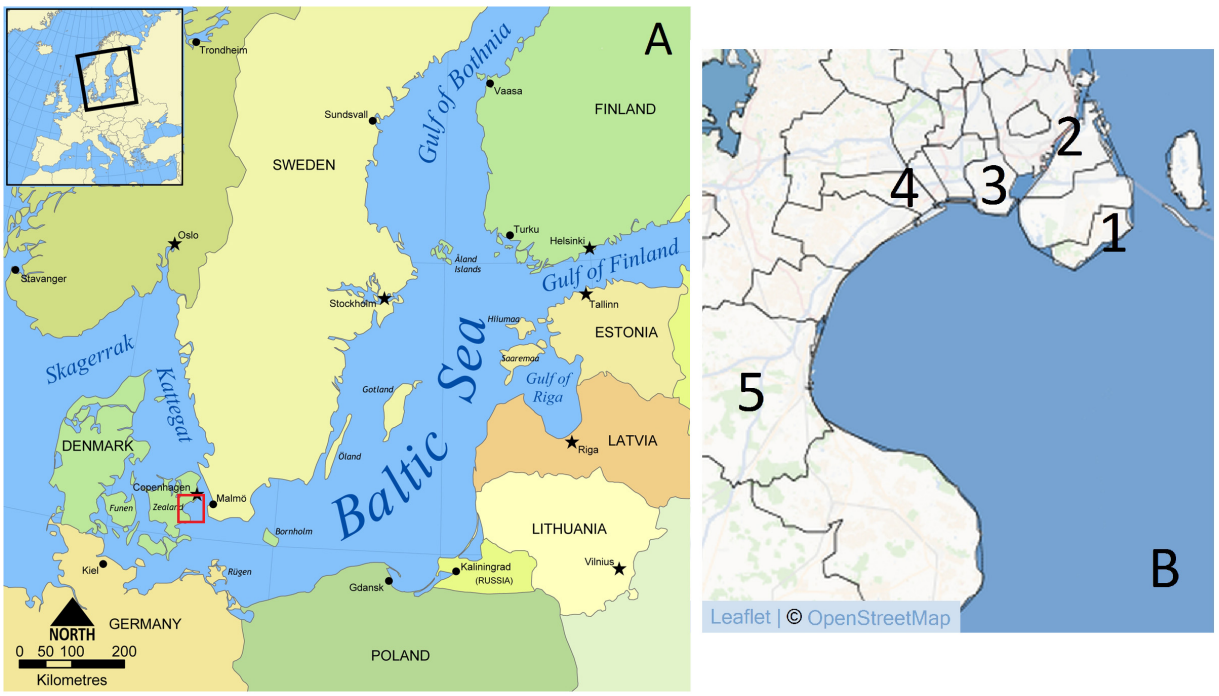

FIGURE 1 | (A) Overview map of the Baltic Sea region, with Køge bay marked with a red square. **(B)** Zoom to Køge Bay and the five municipalities of Dragør (1), Copenhagen (2), Hvidovre (3), Ishøj (4), and Køge (5).

RESULTS

Summary of Interview Findings

The main interest of the interviewees was very high quality storm surge warnings and projections of possible present day and future extreme sea level and wave heights for the detailed coastline (**Figure 2**). This should be based on modeling of past storm surges and future changes, taking observations, and historical records into account. The information was primarily required to prepare decision making in the municipalities, e.g., for preparation of information material to local politicians. There was a big need for more detailed information than presently available, and for authoritative (nationally selected or recommended) scenarios, which would help the collaboration between municipalities.

Secondary requirements included information on mean sea level changes for a range of planning purposes. This should be with a known reference level, preferably the Danish national DVR90 system, and should be complimented with information on land rise. For the planning of new flood gates and other infrastructure sensitive to exceedance of a specific sea level height, there was a request for a "gate index," indicating the frequency and duration of events where the sea level exceeds a given height. Also, there was a need for an indicator of changes in ocean currents relating to the distribution of seaweed deposition, and thus recreation and tourism.

The municipalities generally related to present day situations when discussing future climate change, and thus it will clearly make communication of climate change information, e.g., a future storm surge height indicator, easier, if it can be presented in the same terms as used for present day storm surge warnings and statistics.

The information should represent the region of Køge Bay including the Danish and Swedish coast. The time scales in focus varied between the municipalities, from mid-century (2050) to end century, and 150 years ahead (**Figure 2**). Regarding data formats, all municipalities are advanced users of GIS software and would like to integrate the climate information into their present systems, where many other layers of information are available.

The municipalities expect state of the art quality data, and were generally aware of the need for uncertainty information. They were ready to handle uncertainties in the form of standard deviations, percentiles, or upper- and lower bounds. The knowledge of ensembles was limited. Further, they would like information on underlying assumptions and datasets that goes into the calculations to be available, to assure a transparent dataflow.

The primary needs were to have data to improve long term planning in relation to climate adaptation, especially by giving neighboring municipalities common information as a basis for decision making; and to have the best possible foundation for emergency preparedness. The needs for visualization and data processing facilities were limited, as the municipalities in general preferred to do this within their own GIS systems.

To ease the planning process and integration with other products, there was a general request to have updates of the information on regular intervals, to give a predictable data flow to the decision making process. The preferred frequency for updates varied between 6 months and a few years, with most requests for

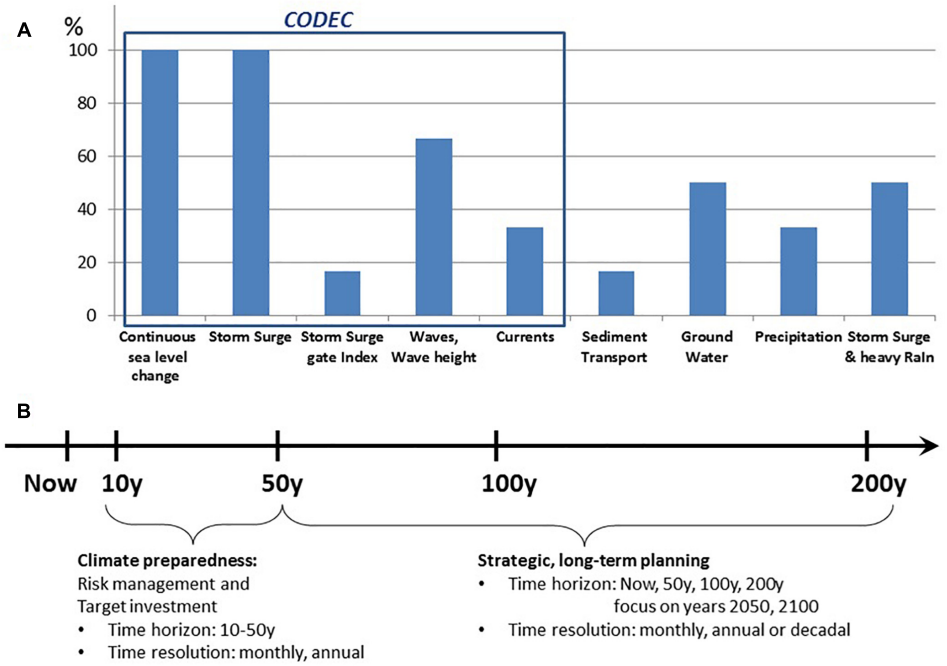

FIGURE 2 | (A) User interest in percentage of number of interviewed users. The interest areas are targeting: mean and extreme sea level for climate preparedness and planning; precipitation and coinciding storm surge and heavy rain events; as well as waves and currents for climate assessments of ocean variability and sediment transport in Køge Bay. The planned southern Copenhagen storm surge gate is in focus for one user, who has a large interest in a gate index indicating the number of high water events that will require a closing of the gates. The frame indicates topics selected to be translated into climate change indicators within the C3S_422_Lot2_Deltares CODEC contract; the selection was made based on a combination of the user requirements, the feasibility of deriving the indicators and the coastal frame of the project. **(B)** Illustration of the two main time scales in focus for the interviewees: user applications for climate preparedness and risk assessment (10–50 years), as well as long term strategic planning (50–200 years). The interviewed users require relatively low time resolution of the statistical products: monthly, annual or even decadal, but they require very high spatial resolution of about 1 km on regional scale (200 km × 200 km) and roughly 100 m on local, coastal scale.

annual updates. Only indicators with significant changes or new information should be updated.

All interviewed persons were willing to take part in the further development of the service, potentially getting involved in the project as a user-representative. They were generally happy to be involved early in the process, and eager to follow the development. They also indicated that the interview template covered the topic well, and the procedure with an interview of fixed duration was an efficient way for them to give input.

Derived Dedicated Coastal Climate Indicators for the Region

Based on the interviews, the following indicators were selected.

- Mean Sea level change indicator: Mean sea level change of selected reference periods, with, and without local land rise.
- Storm surge indicator: Storm surge height and duration changes.
- Gate index: Number of threshold exceedances per year and duration.
- Sea State (Waves) indicator: Changes in wave height in a future climate, both for average conditions and high-sea level events, that is, the wave setup during storm surges.
- Ocean current indicator: Strength of average currents during normal and stormy conditions.

The indicators will be derived from regional hydrodynamic and wave model simulations of the future climate.

DISCUSSION

The present study represents a cost efficient approach to early user interaction, completed with six carefully selected interviews of 1 h duration each. Yet, very detailed information on user needs were obtained, in a format that could relatively easily be translated into coastal climate change indicators, as well as fed back to the C3S User Requirement Database. Compared to larger user investigations, the main risk of the approach is to miss important user information from municipalities not invited for interviews. Thus, a well-defined target group and relatively high degree of pre-hand knowledge to select representative interviewees is required. Also, the degree of awareness of the topic was quite high among the interviewees. Without this, one would risk to get very little feedback. With these precautions in mind, the interviews have allowed identification of climate change indicators early in the contract, allowing understanding of how the information is relevant to, and why it is requested by the end user.

ETHICS STATEMENT

This study was carried out in accordance with the recommendations of the DMI Ethics Committee of the Danish Meteorological Institute, and the protocol was approved by the committee. All subjects gave written informed consent to participate.

AUTHOR CONTRIBUTIONS

KM and JM contributed to conception and design of the study and performed the interviews. MB and JS performed the calculations required for derivation of indicators. KM wrote the first draft of the manuscript. All authors contributed to manuscript revision, read, and approved the submitted version.

FUNDING

The research leading to these results has received funding from the C3S_422_Lot2_Deltares contract on coastal climate change (CODEC), for the Copernicus Climate Change Service.

ACKNOWLEDGMENTS

The research leading to these results has received funding from the C3S contract C3S_422 Lot2 Deltares-European Services to derive consistent European dataset for tide, storm surge, and wave conditions Climate Impact Indicators for the evaluation of climate change impacts on coastal areas in Europe (CODEC). The contract includes data for full European coastline, to be added to C3S data store, and five use cases, including the presented.

We kindly acknowledge the Copernicus C3S project SECTEUR (Sector Engagement for the Copernicus Climate Change Service: Translating European User Requirements, C3S_52_Lot2) and the Copernicus C3S contract D422_Lot 2, together with ECMWF, for provision of the original interview template. C3S_52_Lot2 was implemented by the Institute for Environmental Analytics, University of Reading, United Kingdom, contact Dr. Maria Noguer.

The Copernicus Climate Change Service (C3S) is funded by the European Union and aims to:

- Become an authoritative source of climate information for Europe.
- Build upon national investments and complement national climate service providers.
- Support the market for climate services in Europe.
- Provide free public access to climate change information.

SUPPLEMENTARY MATERIAL

The Supplementary Material for this article can be found online at: https://www.frontiersin.org/articles/10.3389/feart.2019.00081/full#supplementary-material

REFERENCES

Andersen, K. J., Piontkowitz, T., Jebens, M., Thomsen, M., and Henriksen, L. S. (2018). *Revurdering og Ajourføring af Risikoområder for Oversvømmelse fra hav og Vandløb*. Oversvømmelsesdirektivet, Anden planperiode. Lemvig: Kystdirektoratet, Miljø- og Fødevareministeriet.

Bacc II Author Team (2015). *Second Assessment of Climate Change for the Baltic Sea Basin*. Heidelberg: Springer International Publishing, doi: 10.1007/978-3-319-16006-1

Cash, D., Clark, W. C., Alcock, F., Dickson, N. M., Eckley, N., and Jäger, J. (2002). *Salience, Credibility, Legitimacy and Boundaries: Linking Research, Assessment and Decision Making. KSG Working Papers Series RWP*02-046. Cambridge, MA: Harvard University.

Colding, L. A. (1881). *Nogle Undersøgelser over Stormen over Nord- og Mellem-Europa af 12te – 14de November 1872 og over den derved fremkaldte Vandflod i Østersøen. Vidensk. Selsk. Skr.* 6. Copenhagen: Bianco Lunos Kgl. Hof-Bogtrykkeri.

Ditlevsen, C., Ramos, M. M., Sørensen, C., Ciocan, U. R., and Piontkowitz, T. (2018). *Højvandsstatistikker 2017*. Lemvig: Kystdirektoratet, Miljø- og Fødevareministeriet.

Hallegatte, S., Ranger, N., Mestre, O., Dumas, P., Corfee-Morlot, J., Herweijer, C., et al. (2011). Assessing climate change impacts, sea level rise and storm surge risk in port cities: a case study on Copenhagen. *Clim. Change* 104, 113–137. doi: 10.1007/s10584-010-9978-3

McNie, E. C. (2007). Reconciling the supply of scientific information with user demands: an analysis of the problem and review of the literature. *Environ. Sci. Policy* 10, 17–38. doi: 10.1016/j.envsci.2006.10.004

Olesen, M., Madsen, K. S., Ludwigsen, C. A., Boberg, F., Christensen, T., Cappelen, J., et al. (2014). Fremtidige Klimaforandringer i Danmark. DMI Climate Report 14-06. Copenhagen: Danish Meteorological Institute. doi: 10.1016/j.envsci.2006.10.004

Soares, M. B., Alexander, M., and Dessai, S. (2018). Sectoral use of climate information in Europe: a synoptic overview. *Clim. Serv.* 9, 5–20. doi: 10.1016/j.cliser.2017.06.001

Tribbia, J., and Moser, S. C. (2008). More than information: what coastal managers need to plan for climate change. *Environ. Sci. Policy* 11, 315–328. doi: 10.1016/j.envsci.2008.01.003

Turnpenny, J., Haxeltine, A., and O'Riordan, T. (2004). A scoping study of user needs for integrated assessment of climate change in the UK context: part 1 of the development of an interactive integrated assessment process. *Integr. Assess.* 4, 283–300. doi: 10.1080/13895170590514309

Vaughan, C., Buja, L., Kruczkiewicz, A., and Goddard, L. (2016). Identifying research priorities to advance climate services. *Clim. Serv.* 4, 65–74. doi: 10.1016/j.cliser.2016.11.004

Conflict of Interest Statement: The authors declare that the research was conducted in the absence of any commercial or financial relationships that could be construed as a potential conflict of interest.

frontiers in Earth Science

ORIGINAL RESEARCH
published: 03 May 2019
doi: 10.3389/feart.2019.00093

Measurement of Air-Sea Methane Fluxes in the Baltic Sea Using the Eddy Covariance Method

Lucía Gutiérrez-Loza[1]*, *Marcus B. Wallin*[1], *Erik Sahlée*[1], *Erik Nilsson*[1], *Hermann W. Bange*[2], *Annette Kock*[2] *and Anna Rutgersson*[1]

[1] *Department of Earth Sciences, Uppsala University, Uppsala, Sweden,* [2] *Chemical Oceanography Research Unit, Marine Biogeochemistry Research Division, GEOMAR Helmholtz Centre for Ocean Research Kiel, Kiel, Germany*

Methane (CH_4) is the second-most important greenhouse gas in the atmosphere having a significant effect on global climate. The ocean—particularly the coastal regions—have been recognized to be a net source of CH_4, however, the constraints on temporal and spatial resolution of CH_4 measurements have been the limiting factor to estimate the total oceanic contributions. In this study, the viability of micrometeorological methods for the analysis of CH_4 fluxes in the marine environment was evaluated. We present 1 year of semi-continuous eddy covariance measurements of CH_4 atmospheric dry mole fractions and air–sea CH_4 flux densities at the Östergarnsholm station at the east coast of the Gotland Island in the central Baltic Sea. The mean annual CH_4 flux density was positive, indicating that the region off Gotland is a net source of CH_4 to the atmosphere with monthly mean flux densities ranging between -0.1 and 36 nmol $m^{-2}s^{-1}$. Both the air–water concentration gradient and the wind speed were found to be crucial parameters controlling the flux. The results were in good agreement with other measurements in the Baltic Sea reported in the MEMENTO database. Our results suggest that the eddy covariance technique is a useful tool for studying CH_4 fluxes and improving the understanding of air-sea gas exchange processes with high-temporal resolution. Potentially, the high resolution of micrometeorological data can increase the understanding of the temporal variability and forcing processes of CH_4 flux.

Keywords: air-sea gas exchange, Baltic Sea, eddy covariance, CH_4 fluxes, micrometeorological methods

OPEN ACCESS

Edited by:
Markus Meier,
Leibniz Institute for Baltic Sea Research (LG), Germany

Reviewed by:
Volker Bruchert,
Stockholm University, Sweden
Tom Jilbert,
University of Helsinki, Finland

***Correspondence:**
Lucía Gutiérrez-Loza
lucia.gutierrez_loza@geo.uu.se

Specialty section:
This article was submitted to Interdisciplinary Climate Studies, a section of the journal Frontiers in Earth Science

Received: *11 January 2019*
Accepted: *15 April 2019*
Published: *03 May 2019*

Citation:
Gutiérrez-Loza L, Wallin MB, Sahlée E, Nilsson E, Bange HW, Kock A and Rutgersson A (2019) Measurement of Air-Sea Methane Fluxes in the Baltic Sea Using the Eddy Covariance Method. Front. Earth Sci. 7:93. doi: 10.3389/feart.2019.00093

1. INTRODUCTION

Methane (CH_4) is an atmospheric trace gas considered to be the second-most important greenhouse gas after carbon dioxide (CO_2). The estimated warming potential per molecule of CH_4 is 28 times greater than CO_2 over a 100-years horizon, and 72 times greater over a 20-years horizon (IPCC, 2013). The global average atmospheric concentration of CH_4 has more than doubled since the pre-industrial era, reaching values of over 1,800 ppb (WDCGG, 2015). CH_4 is emitted to the atmosphere by natural and anthropogenic sources, however, the rapid increase in the atmospheric CH_4 concentrations has been attributed to anthropogenic activities. Great uncertainties on the temporal and spatial variability of the individual sources of CH_4 still exist.

The ocean is a net source of CH_4 to the atmosphere. Considering biogenic, geological and hydrate sources, the global oceanic emissions have been estimated at 14 Tg yr^{-1} (range 5-25) value that represent about 1–3% of the total global sources of atmospheric CH_4 (Saunois et al., 2016).

Out of the total oceanic contribution, the shelf areas and estuaries account for up to 75%, being the major oceanic source (Bange et al., 1994). However, these estimates are still uncertain due to the limited availability of CH_4 data in the marine environment. The constrains on temporal and spatial resolution of CH_4 measurements have been the limiting factor to account for the diversity on the production and consumption mechanisms of CH_4, hindering our understanding of the oceanic contributions at regional scales, thus, the capacity to constrain the global emission estimates.

The Baltic Sea is a semi-enclosed basin at relatively high latitudes (Meier et al., 2014), it presents great spatial and temporal variability of surface CH_4 concentrations in open sea and in shallow coastal regions. Seasonal variations of water temperature, wind speed, and availability of organic matter have been identified to regulate CH_4 emissions to the atmosphere (Bange, 2006; Bange et al., 2010; Gülzow et al., 2013). A detailed description of the CH_4 budget at a basin scale in the Baltic Sea is still missing, and the lack of constrained air–sea exchange values is one of the major uncertainties.

Air–sea CH_4 fluxes (FCH_4) derived from bulk parameterizations and large-scale models based on surface water measurements have led to great uncertainties in the estimates of CH_4 global oceanic emissions (e.g., Bange et al., 1994; Rhee et al., 2009). Micrometeorological techniques, in contrast, allow direct estimations of turbulent fluxes at a high temporal resolution. The use of these techniques can significantly contribute to long-term monitoring of CH_4 emissions in marine environments to constrain the regional and global estimates. The improvement in the temporal resolution offered by the micrometeorological techniques can be specially important in coastal systems, where rapid terrestrial inputs due to hydrological events, upwelling events, and changes in the biogeochemical properties induce a high temporal variability of the forcing processes modulating FCH_4.

Micrometeorological techniques, such as eddy covariance (EC), have been widely used for estimation of momentum, energy, and mass fluxes in terrestrial (Baldocchi et al., 2001, and references therein), coastal (Crawford et al., 1993; Rutgersson and Smedman, 2010; Gutiérrez-Loza et al., 2018), and oceanic environments (McGillis et al., 2001; Miller et al., 2010). In marine applications, the EC method is commonly used for CO_2 and water vapor flux calculations. However, significantly less attention has been paid on FCH_4 with only a few studies existing about CH_4 measurements from EC (Yang et al., 2016a,b, 2019). Other micrometeorological techniques have been used—even to a lesser extent—for FCH_4 calculations. De Wilde and Duyzer (1995) reported the first FCH_4 estimates from micrometeorological measurements in the marine environment using the gradient method (Fowler and Duyzer, 1989). To our knowledge there are no available records of long-term FCH_4 from eddy covariance measurements or other micrometeorological techniques in the Baltic Sea.

In this study, we used 1 year of EC measurements of CH_4 at Östergarnholm site in the Baltic Sea with the following aims: (1) investigate the viability and quality of EC measurements when studying air–sea FCH_4 from a land-based station in a marine environment, (2) estimate the annual FCH_4 and the seasonal variations in the region, and (3) explore the controlling mechanisms on air–sea CH_4 exchange.

2. METHODOLOGY

2.1. Site Description

The Östergarnsholm station (57°27′N, 18°59′E) is located on a small and flat island 4 km off the eastern coast of Gotland in the Baltic Sea (**Figure 1**). The station has a 30-m land-based meteorological tower located on the southern tip of the island where the ground rises only 1–2 m above the sea surface. The station has being running semi-continuously since 1995 with the aim of monitoring and studying the marine atmospheric boundary layer and to assess the air-sea interaction processes (e.g., Smedman et al., 1999; Högström et al., 2008; Rutgersson et al., 2008; Sahlée et al., 2008; Rutgersson and Smedman, 2010). The station is part of the Integrated Carbon Observation System (ICOS) infrastructure.

The measurements at Östergarnsholm site represent open sea or coastal conditions depending on the wind direction (Rutgersson et al., 2008). For wind directions between $80^\circ < WD < 220^\circ$ the measurements from the tower are considered to be representative of open sea conditions as the wave field is undisturbed by the bathymetry and the atmospheric turbulence is not affected by coastal features (Högström et al., 2008; Rutgersson and Smedman, 2010). Processes characteristic of coastal environments are recognized for wind directions between $50^\circ < WD < 80^\circ$ and $220^\circ < WD < 295^\circ$ when the physical, biogeochemical, and hydrographical properties may be affected by the shore. In contrast, the northerly sector is strongly influenced by land, therefore data from $295^\circ < WD < 50^\circ$ are not representative for sea conditions and should not be used for air–sea interaction studies. Additionally, wind from $355^\circ < WD < 5^\circ$ is affected by the structure of the tower and should not be used for any analysis (Rutgersson et al., 2008). For this study, open sea and coastal conditions were included in the analysis ($50^\circ < WD < 295^\circ$) (see **Figure 1b**).

2.2. Instrumentation and Measurements

The tower was instrumented with high-frequency (20 Hz) sensors for EC measurements of FCH_4 at 9 m above the tower base. From September 2017 to September 2018, atmospheric CH_4 dry mole fractions were measured using a LI-7700 open-path gas analyzer (LI-COR, Inc., Lincoln, NE, USA). Simultaneously, the three wind-speed components were measured with a CSAT3 sonic anemometer (Campbell Scientific, Inc., Logan, UT, USA). The LI-7700 was factory calibrated just before the installation. According to the manufacturer, the factory calibration is carried out making a series of automated measurements with seven traceable reference gas concentrations under controlled conditions using an environmental chamber. The reference tanks are NIST (National Institute of Standards and Technology) certified standard gas mixtures with mole fractions of CH_4 ranging from 1 to 40 ppm (±1% accuracy). The calibration was conducted under temperature conditions of -25, 25, and 40°C in

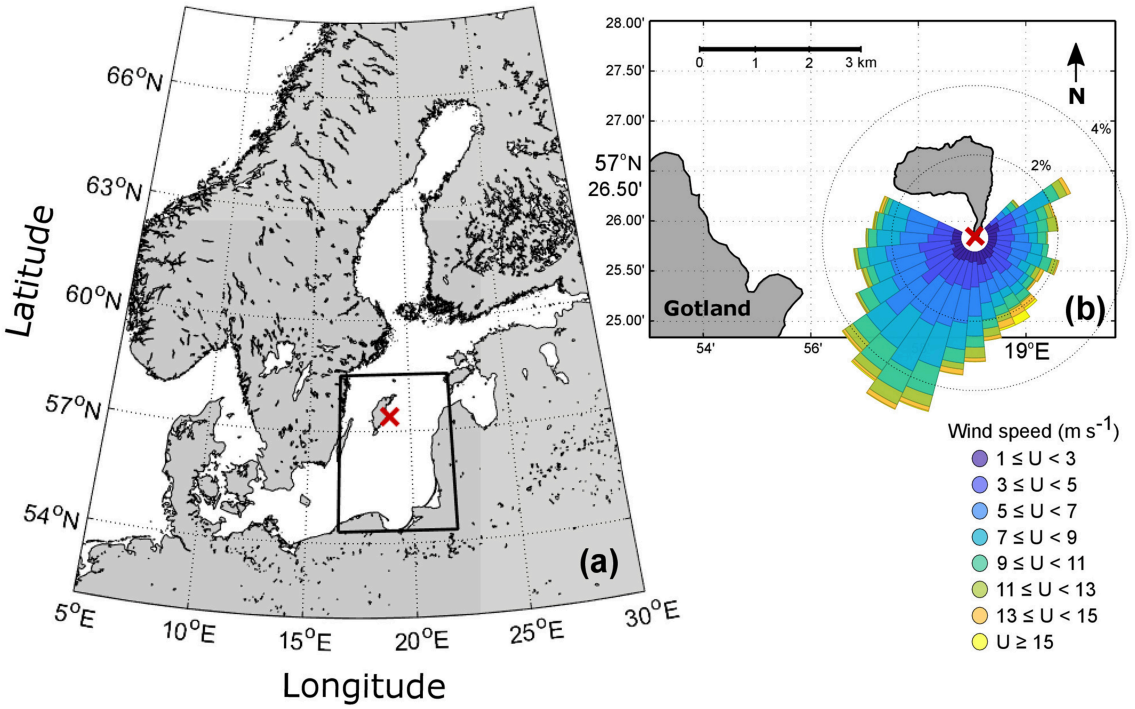

FIGURE 1 | (a) Map of the Baltic Sea. The red mark in the central Baltic Sea indicates the location of the Östergarnsholm station; the Gotland Basin is the area within the black rectangle. **(b)** Location of Östergarnsholm island situated ca 4 km off from the Gotland island. The red mark indicates the location of the tower; the colors are the wind rose representing the distribution of wind speed and wind direction at the Östergarnsholm station.

order to establish accurate relationships between the absorptance and the actual concentration.

The EC system (**Figure 2**) was oriented facing South, the sonic anemometer was placed on the tip of the boom and the gas analyzer LI-7700 was 0.8 m behind the sonic anemometer. The set-up of the instruments was such to minimize the air-flow disturbances, with the larger instrument (LI-7700) closer to the tower. A detailed description of the LI-7700, its functioning and calibration is given by McDermitt et al. (2011); see Sahlée et al. (2014) for the analysis of the instrument performance.

In addition to the tower measurements, water-side samplings were performed in the vicinities of the Östergarnsholm island to measure CH_4 in the seawater. Discrete samplings were carried out during the summers of 2016 and 2017. The samples were taken from a boat at three different depths (1, 10, and 18 m) using a 3 L Ruttner collector, transferred to a 60 ml gas-tight vial using a tubing and sealed with butyl rubber septa (Apodan) and aluminum caps. The samples were poisoned with 1 ml of saturated aqueous solution of mercury chloride ($HgCl_2$) immediately after sampling to prevent any biological activity prior to analysis. The samples were stored upside down in a dark place at 4°C until the analysis. All samples were analyzed in GEOMAR's trace gas laboratory within a few months after collection, the analysis was carried out following the static equilibration method of Bange et al. (2010). During the analysis, each individual sample was injected with 10 mL of He (99.999%), vibrated for 30 s and left to equilibrate for at least 2 h. A 9 mL subsample from the headspace was taken from each sample using a gas-tight syringe and manually injected into a gas chromatographic (GC) system (Hewlett Packard 5890 Series II) by using a 2 mL sample loop. The GC was equipped with a packed column (molsieve 5Å), He (99.999%) was used as a carrier gas

FIGURE 2 | Photograph of the eddy covariance system set-up at level 1 (9 m) at Östergarnsholm station.

with a flow rate of 30 mL min^{-1} and a temperature of 60°C. CH_4 was detected using a flame ionization detector (FID).

A surface water CH_4 mapping campaign was performed for 2 days in late June 2018 during stable weather conditions (clear days and low winds < 3 m s^{-1}). A boat was equipped with an Ultra-portable Greenhouse Gas Analyzer (UGGA, Los Gatos Research, San Jose, CA, USA) connected to a pump-based equilibrator system. Prior to the campaign, the UGGA was calibrated using standard gases (2 ppm and 50 ppm). During boat travel (2 kn), seawater was pumped at a constant rate through a polypropylene filter and led to a silicon membrane-based equilibrator (PermSelect, Ann Arbor, USA). Seawater flows outside the silicon hollow fibers in the equilibrator, while gas penetrates the fibers toward the gas analyzer. See Paranaíba et al. (2018) for further details about the equilibrator system. The continuous water-side CH_4 concentration data was measured at 1 Hz (precision of <2 ppb according to the manufacturer) and averaged over 15-s periods. Together with the geographic coordinates from a GPS, the data was stored on a CR1000 Campbell data logger (Campbell Scientific, Inc., Logan, UT, USA). With an estimated response time of 5 min, each data point represents a moving average integrated over ca 300 m according to the boat speed. The measurements were performed within the footprint of the tower covering all relevant wind sectors. The flux footprint area calculations—as reported by Högström et al. (2008)—indicates that for very stable conditions 60% of the fluxes are originated between 1.7 and 22 km from the tower base, and for very unstable conditions 60% of the fluxes originate between 75 and 300 m from the tower.

Water-side CH_4 values were reported in molar fraction (ppb) in order to directly compare atmospheric and oceanic measurements (see section 3.1.2 and **Figure 7**). Molar fractions can be further converted to concentration values—as commonly used—in nmol L^{-1} or nmol kg^{-1} using the solubility equation given by Wiesenburg and Guinasso (1979).

2.3. MEMENTO Database

The MarinE MethanE and NiTrous Oxide Database (MEMENTO, https://memento.geomar.de/home) collects dissolved and corresponding atmospheric CH_4 data from *in situ* measurements since 1986 (**Table 1**). We used these data to compare with the annual cycle observed from the EC results and with the water-side samples in the Baltic Sea. For this comparison, we selected data from the MEMENTO database collected within the Gotland Basin in the Baltic Sea (see **Table 1**). The Gotland Basin region was considered here from 54°N, 16.5°E to 58.5°N, 22°E. We defined a "coastal" sub-dataset which included the reported values from measurement sites with water depths lower than 25 m.

TABLE 1 | Datasets included in the MEMENTO database with data from the Baltic Sea.

Dataset	Campaign name	Date	PI (institution)	References
DS-80†	HELCOM 92-02	Feb 1992	Hermann W. Bange (GEOMAR)	Bange et al., 1994
DS-79†	HELCOM 92-05	May 1992	Hermann W. Bange (GEOMAR)	Bange et al., 1994
DS-117	Kiel Harbor Study	1992–1993	Rolf Schmaljohann (GEOMAR)	Schmaljohann, 1996
DS-61	GOAP 0694	Jun-Jul 1994	Hermann W. Bange (GEOMAR)	Bange et al., 1998
DS-62	GOAP 0996	Sep-Oct 1996	Hermann W. Bange (GEOMAR)	Bange et al., 1998
DS-63	GOAP 1296	Dec 1996	Hermann W. Bange (GEOMAR)	Bange et al., 1998
DS-64	GOAP 0397	Mar 1997	Hermann W. Bange (GEOMAR)	Bange et al., 1998
DS-65	GOAP 0497	Apr 1997	Hermann W. Bange (GEOMAR)	Bange et al., 1998
DS-78†	MSM 08/03	Jun-Jul 2008	Oliver Schmale (IOW)	Schmale et al., 2010
DS-225†	P392- BALTIC GAS	Dec 2009	Gregor Rehder, Michael Glockzin (IOW)	Gülzow et al., 2014
DS-218†	ICOS-D Baltic VOS Finnmade	Feb-Dec 2010	Gregor Rehder, Michael Glockzin (IOW)	Gülzow et al., 2011
DS-207†	AL 458	May 2015	Annette Kock, Hermann W. Bange (GEOMAR)	Unpublished

† *Datasets including data from the Gotland Basin.*

2.4. The Eddy Covariance Method

Air–sea FCH_4 were estimated using the EC method (Baldocchi et al., 1988; Aubinet et al., 2012). The general equation for the flux calculation is given by

$$F = \overline{\rho_a}\,\overline{w'c'}, \tag{1}$$

where ρ_a is the density of dry air, w is the vertical component of the wind speed, and c is the gas dry mole fraction. The overbar represents the temporal average and the turbulent fluctuations, indicated by the primes, are estimated from the high-frequency (20 Hz) time series of each variable through a Reynold's decomposition:

$$x = \overline{x} + x', \tag{2}$$

where x is the measured signal, $\overline{x}$ represents the time-mean value, and x' represents the fluctuating part.

EC is a straight-forward method to determine gas fluxes. The method avoids the use of empirical constants, as the bulk methods do, it does not rely on assumptions regarding the behavior of the gas or its properties and, it does not require approximations of the atmospheric boundary layer structure (Wanninkhof et al., 2009). However, in order to fulfill the method's assumptions, a strict quality control must be applied to the data (e.g., Foken, 2008).

2.5. Data Treatment and Quality Control

We used time series of wind speed and CH_4 atmospheric dry mole fraction data obtained at the Östergarnsholm site between September 2017 and September 2018. The high-frequency raw

measurements were used to calculate half-hourly values of FCH_4 using the EC method (Equation 1). Prior to the flux calculations, several selection criteria were applied to ensure high quality data representative of air–sea CH_4 exchange within the footprint.

The raw high-frequency wind components were first transformed to earth-system coordinates and the angles were corrected using a double rotation method to avoid any effects caused by the tilting of the sonic anemometer. Wind speed and wind directions were computed from the corrected wind components.

The LI-7700 gas analyzer automatically identifies CH_4 data with a -9999 flag when the sensor is not working properly. These records were removed prior to the calculations. Afterwards, a non-linear median filter algorithm was applied to the 20-Hz data over 30-min periods to eliminate outliers from the high-frequency time series (see Brock, 1986; Starkenburg et al., 2016). Half-hour periods with more than 1% (360 data points) of outliers were discarded (Foken, 2008). The turbulent fluctuations of each variable were calculated from of the de-trended time series using a Reynold's decomposition (Equation 2) over 30-min periods. A linear fit was considered for the de-trending procedure. The turbulent fluctuations were used to calculate the variance and covariance, as well as, other statistical moments used during the flux calculations and statistical analysis. Half-hour averages of each variable were then computed.

We set thresholds on some statistical parameters to ensure the homogeneity of the data and to avoid outliers. Data was excluded from the analysis when the standard deviation of the 30-min time series of CH_4 dry mole fraction exceeded 35 ppb (Baldocchi et al., 2012) and when its 4th-order moment was higher than 100 ppb^4. The skewness and kurtosis were set to range from -2 to 2 and from 1 to 8, respectively. Values outside these ranges were filtered out (Vickers and Mahrt, 1997).

The relative signal strength (RSSI) of the LI-7700 gas analyzer is closely related to the state of the optical mirrors. The mirrors are sensitive to water drops, dust, and—particularly in marine environments—they are sensitive to salt. Therefore, data was discarded when the RSSI was below 10%, this threshold value has been previously used by Podgrajsek et al. (2016). The instrument has a cleaning system for the lower mirror which was set to automatically turn on for 20 s every second-hour when RSSI $< 50\%$. The automatic cleaning was complemented with manual cleaning every 1–2 months. During both, automatic and manual cleaning, the RSSI values drop due to the presence of liquid on the mirrors, thus, data was automatically excluded during those periods by the minimum RSSI criterion.

Following Baldocchi et al. (2012), data was removed when the half-hour average values of atmospheric CH_4 dry mole fraction were smaller than the background atmospheric values, here considered as 1,800 ppb.

Only wind directions representing coastal and open sea environments were considered in the flux analysis, therefore only half-hour data corresponding to wind coming from $50^\circ < WD < 295^\circ$ was used. Other wind directions (northerly winds) were considered to be influenced by land or disturbed by the tower. Data with wind speeds lower than 1 m s^{-1} was also excluded from the analysis.

Density corrections (Webb et al., 1980) were applied during the FCH_4 calculations to account for the effect of the temperature and water vapor fluctuations. Additional corrections were included to account for the spectroscopic effects caused by water vapor, pressure, and temperature on the spectroscopic properties of the absorption line (McDermitt et al., 2011). The minimum detection limit for the computed fluxes was considered to be ± 4 nmol $m^{-2}s^{-1}$, thus, FCH_4 with magnitude smaller than that threshold value were filtered out (Detto et al., 2011; Baldocchi et al., 2012).

The data that fulfilled all quality control criteria were used for further analysis. The high-quality dataset analyzed in this study consists of 4,136 half-hour CH_4 dry mole fraction values and 1,660 half-hour FCH_4 values over the period of 1 year from October 2017 to October 2018. The data correspond to 23.7% and 9.5% of the study period (17,456 half-hours), respectively. The data covers 54% of the 366 days when considering CH_4 dry mole fractions, and 45% for FCH_4, including days with at least one half-hour measurement.

3. RESULTS

3.1. The Annual Cycle

The annual cycle of FCH_4 and other characteristic parameters were analyzed from measurements at Östergarnsholm station from October 1st, 2017 to September 30th, 2018 (**Figure 3**). During the period of this study, the wind speed did not show a clear seasonal pattern, however, higher wind-speed events were observed during autumn and winter causing relatively higher monthly means between September and March (ranging from 6.6 to 8.2 m s^{-1}) than those observed during summer (4.2 to 6.1 m s^{-1}). The maximum 30-min wind speed reached 19.5 m s^{-1} while the maximum daily average was 16.7 m s^{-1}, both during the same high-wind speed event on January 2018. The annual mean wind speed was 6.7 m s^{-1}.

Air and water temperature presented a seasonal cycle with lower values during the winter months (DJFM) and higher temperatures during summer (JJAS). The air temperature monthly means ranged between 0.6°C and 5.4°C during winter, being February the coldest month. During summer, the monthly mean air temperatures ranged between 16.2°C and 22.7°C, being July the warmest month of the year. The water temperature showed a very similar behavior with a minimum monthly mean of 1.3°C in March and a maximum value of 19.3°C in July. The minimum air and water temperatures were -7.5°C and 0.4°C, respectively, and were both observed during late winter. The maximum air and water temperatures reached values of 27.2°C and 23.9°C, respectively. The mean annual air temperature was 10.2°C, while the mean annual water temperature was 9.4°C.

Higher values of the atmospheric CH_4 dry mole fraction were observed during winter compared to the values observed during the rest of the year. The maximum monthly mean was 2,217.7 ppb observed during December and a second maximum of 2,201.8 ppb occurred during March. Lower monthly values

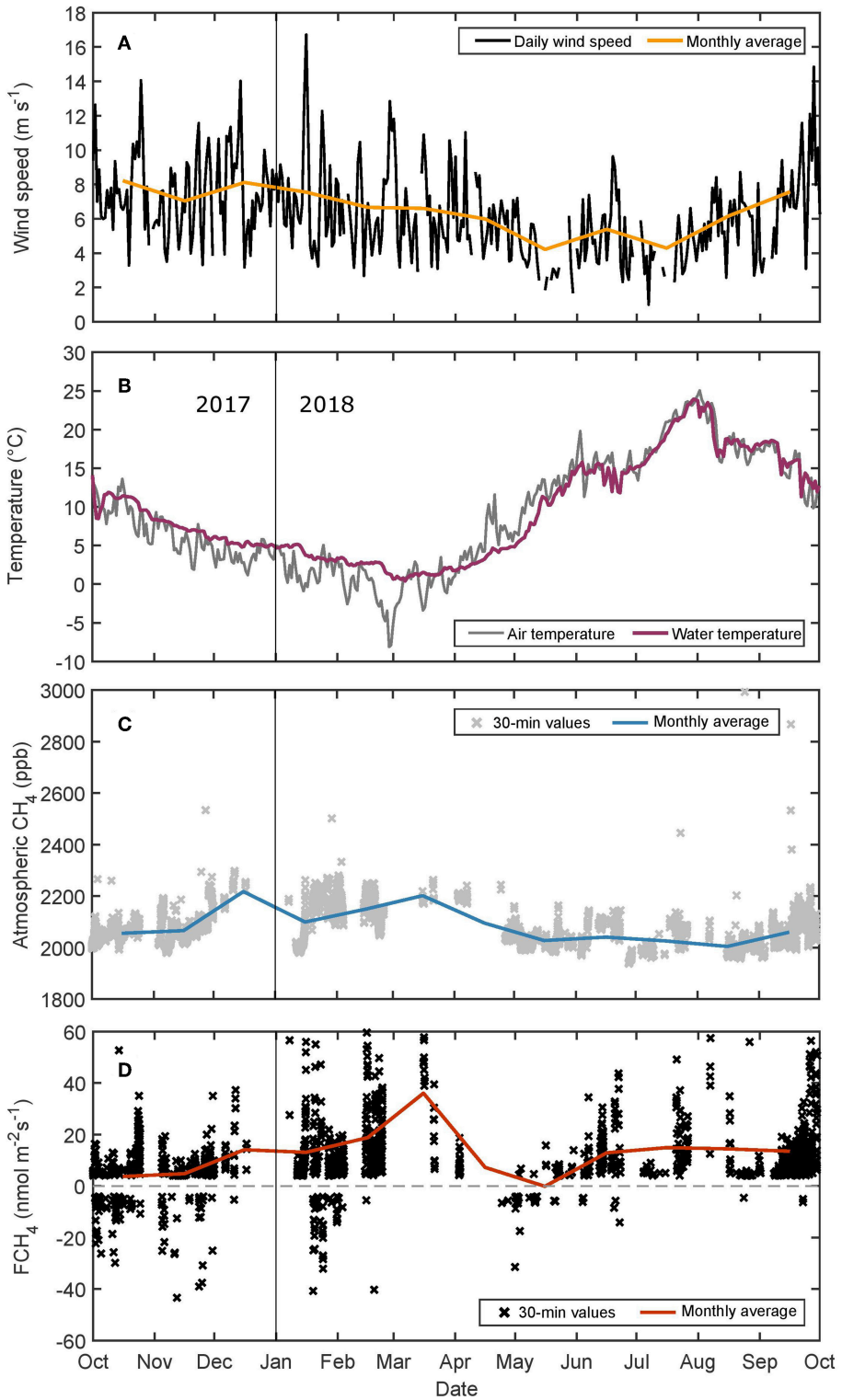

FIGURE 3 | Annual cycle of **(A)** wind speed, **(B)** daily averages of air and water temperature, **(C)** 30-min and monthly averages of atmospheric CH_4 dry mole fraction, and **(D)** 30-min and monthly averages of air–sea FCH_4.

(∼ 2,000 ppb) were found from April to November (**Figure 3C**). For FCH_4, positive monthly means were observed throughout the year with values of 3.7-36.1 nmol $m^{-2}s^{-1}$ (excluding May) indicating that the region was a net source of CH_4. May was the only month with a negative monthly mean value of -0.1 nmol $m^{-2}s^{-1}$. A maximum monthly mean of 36.0 nmol $m^{-2}s^{-1}$ was observed during March. Additionally to this maximum value, high FCH_4 were observed both during winter and summer with similar monthly values ranging from 13.1 to 18.8 nmol $m^{-2}s^{-1}$ and 12.9 to 14.9 nmol $m^{-2}s^{-1}$, respectively. Minimum FCH_4 were observed during the transition months between summer and winter seasons, with near-zero fluxes during May and October-November. The scatter of the individual 30-min values was large ranging from -76 to 251.6 nmol $m^{-2}s^{-1}$, with most of the negative values (163 out of 202 data points) observed during late autumn and winter.

3.1.1. Methane Concentrations: A Comparison With the MEMENTO Database

A comparison between the two datasets (Östergarnsholm data and MEMENTO) was carried out with the aim of understanding and validating the seasonal behavior observed from the EC measurements at Östergarnsholm. Monthly mean atmospheric CH_4 dry mole fraction observed from the EC measurements at Östergarnsholm during 2017-2018 ranged between 2,004.6 and 2,217.7 ppb, while the values previously reported in the MEMENTO database for the Gotland Basin region ranged from 1,860 to 1,905 ppb (**Figure 4**). Atmospheric values from the Gotland Basin included monthly averages over almost 30 years, excepting January for which no data was reported during those years. The long-term average showed a more clear seasonality, but it masked shorter-term changes and the higher variability observed in the 1-year record from Östergarnsholm. For both records, however, lower monthly CH_4 dry mole fractions were observed during summer (JJAS) with minimum values during August, 2,004.6 and 1,861.0 ppb, for Östergarnsholm and the Gotland Basin, respectively. Maximum values during November-April were observed also for both records.

Similar to what was observed for the atmospheric concentrations, the CH_4 mole fractions in the seawater measured in the vicinities of the Östergarnsholm site were higher than the average values observed in the Gotland Basin (**Figure 5**). The mean value of the seawater CH_4 mole fraction from the 2-day mapping campaign in late June 2018 was 3,897.1 ppb, and the mean value from the discrete samplings in summer 2016 and 2017 was 8,794.1 ppb. On the contrary, the annual mean value reported for the Gotland Basin was 2,676.3 ppb, with higher values from late June to October, reaching a maximum monthly mean of 3,360.5 ppb in October. The mean values from the coastal regions—as defined above as "coastal" sub-dataset—reported in the MEMENTO database did not show either such high values as those reported within this study. Even so, individual values reaching magnitudes up to 15,000 ppb were reported (**Figure 5**), showing that under certain conditions, mostly during summer, high values of CH_4 in the seawater can occur in the region. During winter, lower values were observed from the MEMENTO data, the minimum value was found during May with monthly mean of 1,923.7 ppb. No data was reported during January.

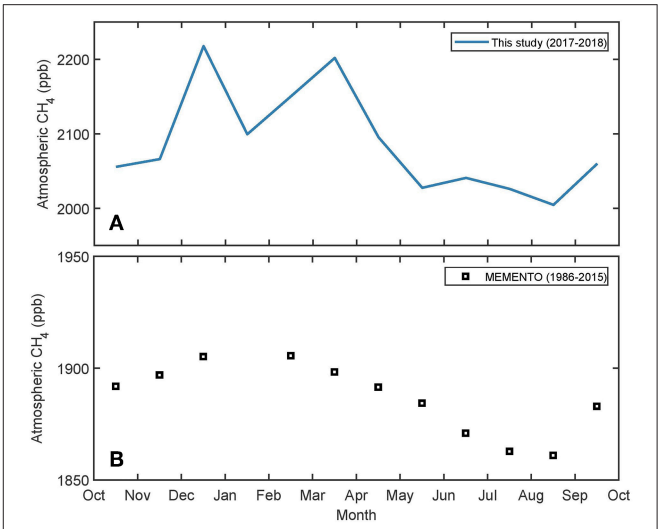

FIGURE 4 | Monthly means of atmospheric CH_4 dry mole fraction from **(A)** Östergarnsholm station during 2017–2018 (this study), and **(B)** MEMENTO database in the Gotland Basin obtained between 1986 and 2015.

A broader comparison using data from the whole Baltic Sea (**Table 1**) also supports that the magnitude of the seawater CH_4 mole fractions in the vicinities of the tower was much higher than values previously reported for the Baltic Sea (**Figure 6**). However, the measurements from the mapping campaign were in good agreement with values reported for the coastal regions. High-concentration events were observed for both the Baltic Sea and the coastal Baltic Sea datasets with values as high as 20,000 ppb.

3.1.2. Seasonality of the Air-Sea Concentration Gradient

A clear seasonal pattern was observed in the air–sea concentration gradient of CH_4 (ΔC) from atmospheric and water-side CH_4 mole fractions in the Gotland Basin (**Figure 7A**). The gradient was, to a great extent, caused by changes in the water-side mole fractions while atmospheric CH_4 remained fairly constant. The increase in the seawater mole fractions led to higher positive ΔC that reached values higher than 1,000 ppb during summer and early autumn. The maximum values were found in September and October when the ΔC values were higher than 1,460 ppb. The FCH_4 values observed from Östergarnsholm data during the summer months were consistent with the behavior of ΔC, showing an increase during these months (**Figure 7B**). In the same way, the minimum ΔC of 39.4 ppb during May was in agreement with the minimum FCH_4 when a near-zero flux was observed. During the winter months ΔC was small, even so, we observed high FCH_4, suggesting that other processes might have modulated the air–sea fluxes by enhancing the efficiency of the transport through the surface.

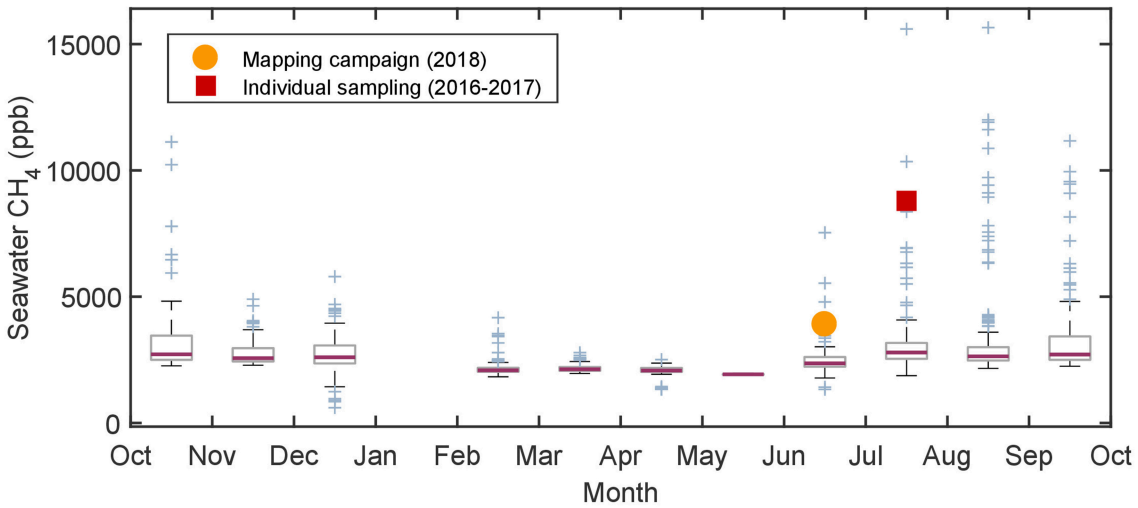

FIGURE 5 | Boxplots representing the annual cycle of seawater CH_4 mole fractions in the Gotland Basin from the MEMENTO database. The yellow dot is the average value from the mapping campaign, and the red square is the mean value from the individual samplings. In the boxplots, the median value is represented by the purple line, the 25th and 75th percentiles indicated by the gray boxes, and outliers are marked as blue crosses.

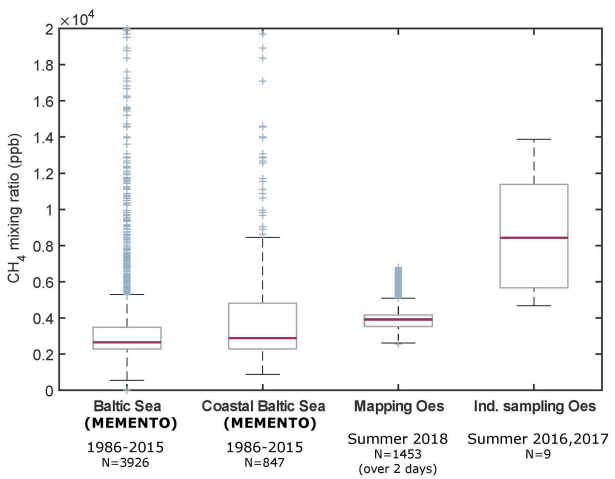

FIGURE 6 | Boxplots of CH_4 mole fraction in the seawater. From left to right, the first two boxes represent data from MEMENTO database, the first one considers all data available for the Baltic Sea and the second one only data corresponding to regions with depth < 25 m, here defined as coastal Baltic Sea. The last two boxes represent data from the vicinities of Östergarnsholm site, where "Mapping Oes" shows results from the mapping campaign and "Ind. sampling Oes" the results of the individual sampling. "N" is the number of data points. The representation of the boxplots is the same as in **Figure 5**.

3.2. Wind Dependency

Slightly soluble gases tend to be more easily transported across the air–sea interface under highly turbulent conditions (bubble-mediated transport). Based on the mean values (blue dots in **Figure 8**) such correlation between FCH_4 and the wind speed (U) was not noticeable. For high-wind speed values ($U > 14$ m s^{-1}) a tendency of FCH_4 to increase with wind speed was observed. However, these values had been identified to belong to a single high-wind speed event (see section 3.2.1) and further evidence is required to validate the relationship between FCH_4 under high-wind speeds.

When comparing FCH_4 as a function of the wind speed, several parameters affecting the flux were included in the comparison. A more fair comparison would be to represent the transfer velocity (k) as a function of U since FCH_4 is not only influenced by the U but also by ΔC. Unfortunately, we were not able to calculate k in this study due to the lack of continuous measurements of CH_4 mole fractions in the seawater.

3.2.1. High-Wind Speed Event

A high-wind speed event occurred in January 2018, the case is here highlighted as it revealed a strong wind speed dependence for FCH_4. This event is particularly interesting for further analysis since it occurred during winter when ΔC is assumed to be small, therefore, is unlikely the main driver of FCH_4.

During the high-wind speed event, a constant increase of the wind speed occurred over a 48-h period (**Figure 9A**). The initial wind speed at the beginning of the event was 5.1 m s^{-1} and steadily increased until it reached its maximum at 19.4 m s^{-1} almost 48 h later. The wind direction during the event was from south-east, with mean wind direction of 154°. South-east wind directions represent open sea conditions as defined by Rutgersson et al. (2008). We observed an increase of FCH_4 several hours after the event began (**Figure 9B**). During the high-wind speed event, FCH_4 increased exponentially from an initial value of 4.0 nmol m^{-2} s^{-1} to a maximum value of 187.1 nmol m^{-2} s^{-1}. Additional to the increase in FCH_4, an increment on the atmospheric CH_4 dry mole fraction was observed from an initial value of 2,006.1 ppb to a maximum value of 2,438.2 ppb.

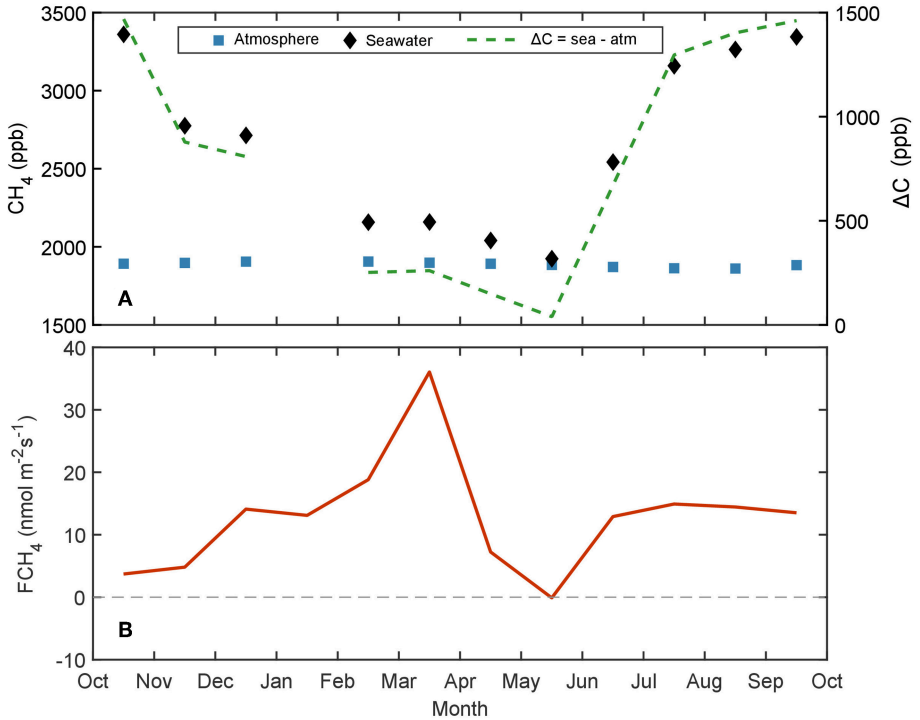

FIGURE 7 | (A) Annual cycle of seawater and atmospheric CH_4 mole fractions (principal y-axis) and mole fraction gradient ($\Delta C = C_{seawater} - C_{atmosphere}$) (secondary y-axis); data corresponding to the Gotland Basin from MEMENTO database (1986-2015). **(B)** Annual cycle of air–sea CH_4 flux (FCH_4) calculated from EC.

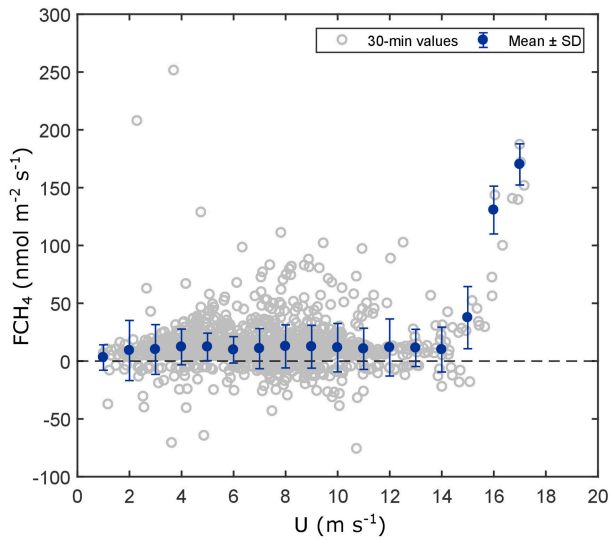

FIGURE 8 | Half-hourly FCH_4 values plotted as a function of the wind speed, U.

4. DISCUSSION

The annual cycle of atmospheric CH_4 dry mole fraction observed at Östergarnsholm station showed a good agreement with the seasonal variability of the Gotland Basin from previously reported data, lower atmospheric CH_4 values were observed during summer and higher values during winter time. The seasonal variability observed in both datasets might be explained by the increased consumption rate of CH_4 in the atmosphere due to OH radicals during summer (Khalil and Rasmussen, 1983). The magnitude of the monthly means observed during 2017-2018 at Östergarnsholm were significantly higher than the values presented for the Gotland Basin (**Figure 4**). To our knowledge there is no other continuous atmospheric CH_4 measurements in the region to compare with, however, the values from the Östergarnsholm station seem to be consistent with the global trends that indicate an increase of about 200 ppb in the global atmospheric CH_4 concentration since 1985 (Figure 1 in Saunois et al., 2016). Additionally, higher air–sea FCH_4 enhanced by coastal processes might also contribute to the observed atmospheric values. Higher variability is observed in the monthly means from the EC measurements of atmospheric CH_4. The variability is attributed to local processes which were not perceptible from the long-term averages in the Gotland Basin form the MEMENTO data. Even so, more data is still necessary to validate the measurements presented here and to explain the high variability on the atmospheric CH_4 mole fraction.

The CH_4 mole fractions in the seawater nearby the Östergarnsholm site were higher than both the mean and median values from measurements reported in the MEMENTO database for the Gotland Basin (**Figure 5**). However, similar values have been observed in the region during summer time. These results are consistent with the seasonal temperature cycle which enhances the CH_4 production rate under warmer water

conditions (Bange et al., 1998). Additionally, Gülzow et al. (2013) showed that upwelling events during the summer have a significant effect on surface CH_4 on the Gotland area by bringing CH_4-rich water masses from deeper layer to the surface.

The water-side measurements at Östergarnsholm were in good agreement with values reported for the coastal Baltic Sea regions (**Figure 6**), suggesting that coastal characteristics such as shallow waters, high biological activity, and upwelling events might have led to higher concentration values in the vicinities of the tower. High water-side CH_4 mole fractions have been previously reported for physical- and biogeochemically active areas such as coastal regions (Rhee et al., 2009; Borges et al., 2016) and lakes (Podgrajsek et al., 2014). Borges et al. (2016) attributed the high CH_4 concentrations observed in a near-shore region in the North Sea—and the consequent fluxes—to the shallow water-depth and the well-mixed water column. Gülzow et al. (2013) concluded that for other shallow areas in the Baltic Sea (i.e., Mecklenburg Bight and Arkona Basin) the methane oversaturation conditions follow the water temperature trend, with increasing concentrations during summer time. This fact is particularly relevant as 2018 presented significantly higher water temperatures than average years.

The monthly means of FCH_4 from EC measurements at Östergarnsholm site indicated that the region was a net source of CH_4 throughout the year. The role of the Baltic Sea as a source of CH_4 has been mentioned in previous studies, however, the reported values present a great degree of variability in time and space. On one hand, Bange et al. (1994) reported values ranging from 0.11 to 0.17 nmol $m^{-2}s^{-1}$ during a winter (February) and from 1.17 to 13.9 nmol $m^{-2}s^{-1}$ for the summer (July/August), indicating larger flux during summer than during winter. On the other hand, Gülzow et al. (2013) showed that the seasonality of FCH_4 depends on the characteristics of each region of the Baltic Sea. The fluxes calculated by Gülzow et al. (2013) are significantly smaller than those presented by Bange et al. (1994); for the same months they found values of 0.151-0.08 nmol $m^{-2}s^{-1}$ (February) and 0.01-0.076 nmol $m^{-2}s^{-1}$ (July/August) for the Arkona Sea, Bornholm Sea, and Gotland Sea. The highest monthly mean value reported by Gülzow et al. (2013) was 1.145 nmol $m^{-2}s^{-1}$ in the Gulf of Finland during February. In both cases, the fluxes were calculated based on bulk parameterizations.

The FCH_4 monthly means presented in this study ranged from -0.1 to 36.1 nmol $m^{-2}s^{-1}$ from EC measurements. These values are—in general—higher than those previously reported for the Baltic Sea. In a similar way, De Wilde and Duyzer (1995) reported FCH_4 values from the ASGASEX experiment up to 6 times higher using micrometeorological techniques than those calculated using Wanninkhof (1992) relationship. The authors mentioned that in order to explain those discrepancies between the two methods, more measurements are required using both methods simultaneously.

Despite the positive mean fluxes throughout the year and the general agreement of the Baltic Sea as a net source of CH_4, some negative FCH_4 values were observed from the 30-min data during late autumn and winter (**Figure 3D**). These values might have been caused by a temporary undersaturation of the water-side CH_4 with respect of the atmospheric values. Gülzow et al. (2013) calculated saturation values of 96% and 94% during winter in 2010 and 2011, respectively, in the Gotland Basin. The undersaturation was only reported for the Goltand Basin region during December-April and might be caused by the enhanced solubility of CH_4 due to low water temperatures. Thus, this behavior is not noticeable from the mole fraction time series (**Figure 3C**), however, it might cause frequent changes in the direction of the net FCH_4 in the region. In addition to the possibility of a temporary undersaturation state, highly turbulent conditions due to increased wind speeds during winter time may cause higher variability on the gas exchange across the interface, the direction of FCH_4 is then determined by the air-sea gradient. High temporal resolution measurements, such as those presented here, are necessary to detect this variability.

In the Gotland Basin, ΔC is mostly modulated by variations of CH_4 mole fraction in the seawater, while the atmospheric values remain relatively constant in comparison to the seawater values. From the MEMENTO data, it was noticeable that higher ΔC values are present during summer (**Figure 7**) due to the large increase in the seawater mole fractions observed in the warmer months. Similarly, Gülzow et al. (2013) observed a continuous increase of CH_4 saturation in all basins of the Baltic Sea from April to July due to the rise in water temperatures. The MEMENTO data is useful for describing the average seasonal behavior, however, sub-annual variability of ΔC for the particular period of this study is hardly represented. In order to understand the relationship between ΔC and the fluxes across the air-sea interface, simultaneous measurements of atmospheric and seawater concentrations are required, along with flux data.

In this study, FCH_4 values observed during the summer months (JJAS) were consistent with the increase of ΔC as observed from the MEMENTO data, suggesting that the main driver of the exchange is the air–water concentration difference. In this case, the effect of the strong stratification and shallow mixed layer depth in the Gotland Basin (Gülzow et al., 2013) during the summer due to the warming of the surface layers is not sufficient to hinder FCH_4, at least in this particular region. In contrast, high FCH_4 observed during winter were not explained solely by ΔC that showed small values from October to May. During winter, strong wind-speed events and higher mean wind speed values were observed. Regardless of the relatively small gradient, highly-turbulent conditions might have led to the enhancement of the transport processes causing an increase in positive FCH_4.

Air–sea gas exchange is not only dependent on ΔC, it is also modulated by environmental forcing factors that define the efficiency of the transport (Wanninkhof et al., 2009). Wind speed is considered to be one of the main parameters used to describe the efficiency of the gas exchange across the air–sea interface (Liss and Merlivat, 1986; Wanninkhof, 1992). Thus, a high correlation between FCH_4 and U was expected, however, no correlation was observed between the calculated FCH_4 and U (**Figure 8**). We considered that using k would be a more straightforward comparison. Gülzow et al. (2013)

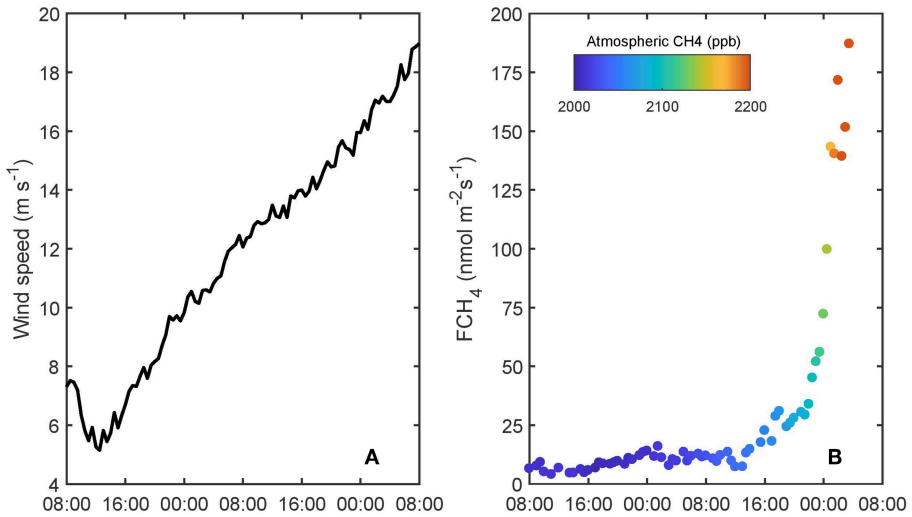

FIGURE 9 | (A) Wind speed, and **(B)** air–sea FCH_4 over a 48-h period during a high-wind speed event in January 14–16, 2018. The starting date is January 14 at 8:00 UTC, and the ending time is January 16 at 8:00 UTC.

presented values of k for different regions of the Baltic Sea calculated according to Wanninkhof et al. (2009) as a function of the wind speed. They showed that for all regions (including the Gotland Basin) the highest transfer coefficients occurred from September to January. These results are consistent with the increased wind speeds observed in this study during the winter months, and can be an indication of the high FCH_4 values observed during this period might be driven by wind-induced turbulence.

The analysis of a high-wind speed event showed that under certain conditions the wind speed might be a crucial parameter in the gas transport across the air-sea interface causing an increase in FCH_4. In the Baltic Sea, CH_4 is primarily produced in the sediments and then transported through the water column, therefore, the physical characteristics on the water-side (i.e., stratification, tides, mixed layer depth, etc.) are of great importance for the distribution of CH_4. However, high-wind speed events—such as the one analyzed here—can cause enough mixing to ventilate the water column enhancing the transport of CH_4 to the atmosphere, resulting in larger positive FCH_4. The delay on the increasing behavior of FCH_4 and CH_4 dry mole fraction during the high-wind speed event, suggests the existence of a threshold value below which the wind does not generate enough mixing. Alternatively, this behavior might be an indication of the need for a sufficiently-long time over which the wind develops the mixing in the ocean surface. Bell et al. (2017) showed that the effect of the bubble-mediated transport at intermediate-high wind speeds becomes significant after a threshold value that depends on the wave-breaking characteristics. The threshold value was found to be dependent on the characteristics of the gas. Analysis of the effect of bubble-mediated transport on FCH_4 is still missing. High-wind speed events are difficult to capture both by water and atmospheric measurements since they are sporadic and the strong weather conditions might limit the possibility of sampling.

Based on the results presented in this study, we show that high frequency measurements of CH_4 are a useful tool for direct flux estimations in the marine environment if the technical limitations are overcome. This technique can supply information about the net transport of the gas across the air-sea interface without using parameterizations. However, strict quality control criteria are required to ensure the good quality of the data and the fulfillment of the EC requirements. Long-term CH_4 data from Östergarnsholm station could be used along with other monitoring infrastructures to establish the methane budgets in the Baltic Sea.

5. CONCLUSIONS

Air-sea FCH_4 calculated in this study using the EC method are, to our best knowledge, the first continuous measurements of FCH_4 in the Baltic Sea. We present 1 year of direct FCH_4 using EC measurements from the land-based station at Östergarnsholm site. The annual cycle of FCH_4 seems to be controlled by the seasonality of ΔC, which at the same time is mostly modulated by the seawater concentrations. Further analysis of the impact of ΔC on FCH_4 based on simultaneous measurements is still required. Additionally, the wind seems to play an important role on the CH_4 gas exchange under high wind speed conditions.

The results presented here support previous analyses suggesting that the coastal regions are highly active areas that can contribute to a great extent to the oceanic CH_4 emissions. Small availability of CH_4 data in the marine environment is the main restriction to better understand of the processes involved on air-sea CH_4 exchange. Therefore, we suggest the use of EC measurements for the estimation and monitoring of FCH_4 in the

marine environment. EC measurements can contribute to the analysis of the mechanisms controlling the air-sea gas exchange, to establish regional carbon and methane budgets in the Baltic Sea, and to improve parameterizations of the gas transfer velocity in the region.

AUTHOR CONTRIBUTIONS

LG-L and MW participated in the installation and continuous maintenance of the instruments. AR conceived the idea and initial planning of the study. LG-L analyzed the data. EN developed part of the data treatment procedure and quality control. AR, ES, and MW participated in the interpretation of the results and contributed with the outline of the manuscript. LG-L wrote the article. HB and AK provided the MEMENTO data and contributed with the analysis and discussion of water-side data. All the co-authors participated in the discussion of results and revision of the article.

FUNDING

The BONUS INTEGRAL project receives funding from BONUS (Art 185), funded jointly by the EU, the Swedish Research Council Formas, the Academy of Finland, the Estonian Research Council, the Polish National Centre for Research and Development, and the German Federal Ministry of Education and Research. The ICOS station Östergarnsholm is funded by the Swedish Research Council (grants 2012-03902 and 2013-02044) and Uppsala University.

ACKNOWLEDGMENTS

The authors would like to thank the two reviewers for their constructive comments and suggestions that contributed to improving this manuscript.

This work forms part of the BONUS INTEGRAL project.

REFERENCES

Aubinet, M., Vesala, T., and Papale, D. (2012). *Eddy Covariance: A Practical Guide to Measurement and Data Analysis*. London; New York, NY; Dordrecht; Heidelberg: Springer.

Baldocchi, D., Falge, E., Gu, L., Olson, R., Hollinger, D., Running, S., et al. (2001). FLUXNET: a new tool to study the temporal and spatial variability of ecosystem-scale carbon dioxide, water vapor, and energy flux densities. *Bull. Amer. Meteorol. Soc.* 82, 2415–2434. doi: 10.1175/1520-0477(2001)082<2415:FANTTS>2.3.CO;2

Baldocchi, D. D., Detto, M., Sonnentag, O., Verfaillie, J., Teh, Y. A., Silver, W., et al. (2012). The challenges of measuring methane fluxes and concentrations over a peatland pasture. *Agricult. For. Meteorol.* 153, 177–187. doi: 10.1016/j.agrformet.2011.04.013

Baldocchi, D. D., Hincks, B. B., and Meyers, T. P. (1988). Measuring biosphere-atmosphere exchanges of biologically related gases with micrometeorological methods. *Ecology* 69, 1331–1340. doi: 10.2307/1941631

Bange, H. W. (2006). Nitrous oxide and methane in European coastal waters. *Estuar. Coast. Shelf Sci.* 70, 361–374. doi: 10.1016/j.ecss.2006.05.042

Bange, H. W., Bartell, U. H., Rapsomanikis, S., and Andreae, M. O. (1994). Methane in the Baltic and North Seas and a reassessment of the marine emissions of methane. *Glob. Biogeochem. Cycles* 8, 465–480. doi: 10.1029/94GB02181

Bange, H. W., Bergmann, K., Hansen, H. P., Kock, A., Koppe, R., Malien, F., et al. (2010). Dissolved methane during hypoxic events at the Boknis Eck time series station (Eckernförde Bay, SW Baltic Sea). *Biogeosciences* 7, 1279–1284. doi: 10.5194/bg-7-1279-2010

Bange, H. W., Dahlke, S., Ramesh, R., Meyer-Reil, L.-A., Rapsomanikis, S., and Andreae, M. O. (1998). Seasonal study of methane and nitrous oxide in the coastal waters of the southern Baltic Sea. *Estuar. Coast. Shelf Sci.* 47, 807–817. doi: 10.1006/ecss.1998.0397

Bell, T. G., Landwehr, S., Miller, S. D., Bruyn, W. J. D., Callaghan, A. H., Scanlon, B., et al. (2017). Estimation of bubble-mediated air–sea gas exchange from concurrent DMS and CO_2 transfer velocities at intermediate–high wind speeds. *Atmospher. Chem. Phys.* 17, 9019–9033. doi: 10.5194/acp-17-9019-2017

Borges, A. V., Champenois, W., Gypens, N., Delille, B., and Harlay, J. (2016). Massive marine methane emissions from near-shore shallow coastal areas. *Sci. Rep.* 6:27908. doi: 10.1038/srep27908(2016)

Brock, F. V. (1986). A nonlinear filter to remove impulse noise from meteorological data. *J. Atmospher. Ocean. Technol.* 3, 51–58. doi: 10.1175/1520-0426(1986)003<0051:ANFTRI>2.0.CO;2

Crawford, T. L., McMillen, R. T., Meyers, T. P., and Hicks, B. B. (1993). Spatial and temporal variability of heat, water vapor, carbon dioxide, and momentum air–sea exchange in a coastal environment. *J. Geophys. Res.* 98, 12869–12880. doi: 10.1029/93JD00628

De Wilde, H. P. J., and Duyzer, J. (1995). "Methane emissions off the Dutch coast: air-sea concentration differences versus atmospheric gradients," in *Third International Symposium on Air-Water Gas Transfer* (Heidelberg), 763–773.

Detto, M., Verfaillie, J., Anderson, F., Xu, L., and Baldocchi, D. (2011). Comparing laser-based open-and closed-path gas analyzers to measure methane fluxes using the eddy covariance method. *Agricult. For. Meteorol.* 151, 1312–1324. doi: 10.1016/j.agrformet.2011.05.014

Foken, T. (2008). *Micrometeorology*. Berlin; Heidelberg: Springer-Verlag.

Fowler, D., and Duyzer, J. H. (1989). "Micrometeorological techniques for the measurement of trace gas exchange," in *Exchange of Trace Gases between Terrestrial Ecosystems and the Atmosphere, Dahlem Workshop Report, Life Science Research Reports 47*, eds M. O. Andreae and D. S. Schimel (Berlin: Wiley Interscience), 189–208.

Gülzow, W., Gräwe, U., Kedzior, S., Schmale, O., and Rehder, G. (2014). Seasonal variation of methane in the water column of Arkona and Bornholm Basin, western Baltic Sea. *J. Mar. Syst.* 139, 332–347. doi: 10.1016/j.jmarsys.2014.07.013

Gülzow, W., Rehder, G., Schneider von Deimling, J., Seifert, S., and Tóth, Z. (2013). One year of continuous measurements constraining methane emissions from the Baltic Sea to the atmosphere using a ship of opportunity. *Biogeosciences* 10, 81–99. doi: 10.5194/bg-10-81-2013

Gülzow, W., Rehder, G., Schneider, B., von Deimling, J. S., and Sadkowiak, B. (2011). A new method for continuous measurement of methane and carbon dioxide in surface waters using off-axis integrated cavity output spectroscopy (ICOS): an example from the Baltic Sea. *Limnol. Oceanogr.* 9, 176–184. doi: 10.4319/lom.2011.9.176

Gutiérrez-Loza, L., Ocampo-Torres, F. J., and García-Nava, H. (2018). The effect of breaking waves on CO_2 air–sea fluxes in the coastal zone. *Boundary Layer Meteorol.* 168, 343–360. doi: 10.1007/s10546-018-0342-x

Högström, U., Sahlée, E., Drennan, W. M., Kahma, K. K., Smedman, A.-S., Johansson, C., et al. (2008). Momentum fluxes and wind gradients in the marine boundary layer: a multi platform study. *Boreal Environ. Res.* 13, 475–502.

IPCC (2013). *Climate change 2013: The Physical Science Basis. Contribution of Working Group I to the Fifth Assessment Report of the Intergovernmental Panel on Climate Change*. Cambridge: Cambridge University Press.

Khalil, M. A. K., and Rasmussen, R. A. (1983). Sources, sinks, and seasonal cycles of atmospheric methane. *J. Geophys. Res.* 88, 5131–5144. doi: 10.1029/JC088iC09p05131

Liss, P. S., and Merlivat, L. (1986). "Air–sea gas exchange rates: introduction and synthesis," in *The Role of Air–Sea Exchange in Geochemical Cycling* (Dordrecht: Springer), 113–127.

McDermitt, D., Burba, G., Xu, L., Anderson, T., Komissarov, A., Riensche, B., et al. (2011). A new low-power, open-path instrument for measuring methane flux by eddy covariance. *Appl. Phys. B* 102, 391–405. doi: 10.1007/s00340-010-4307-0

McGillis, W. R., Edson, J. B., Hare, J. E., and Fairall, C. W. (2001). Direct covariance air-sea CO_2 fluxes. *J. Geophys. Res.* 106, 16729–16745. doi: 10.1029/2000JC000506

Meier, H. E. M., Rutgersson, A., and Reckermann, M. (2014). An earth system science program for the Baltic Sea region. *Eos Trans. Amer. Geophys. Union* 95, 109–110. doi: 10.1002/2014EO130001

Miller, S. D., Marandino, C., and Saltzman, E. S. (2010). Ship-based measurement of air–sea CO_2 exchange by eddy covariance. *J. Geophys. Res.* 115, 1–14. doi: 10.1029/2009JD012193

Paranaíba, J. R., Barros, N., Mendonça, R., Linkhorst, A., Isidorova, A., Roland, F., et al. (2018). Spatially resolved measurements of CO_2 and CH_4 concentration and gas-exchange velocity highly influence carbon-emission estimates of reservoirs. *Environ. Sci. Technol.* 52, 607–615. doi: 10.1021/acs.est.7b05138

Podgrajsek, E., Sahlée, E., Bastviken, D., Natchimuthu, S., Kljun, N., Chmiel, H. E., et al. (2016). Methane fluxes from a small boreal lake measured with the eddy covariance method. *Limnol. Oceanogr.* 61, S41–S50. doi: 10.1002/lno.10245

Podgrajsek, E., Sahlée, E., and Rutgersson, A. (2014). Diurnal cycle of lake methane flux. *J. Geophys. Res.* 119, 236–248. doi: 10.1002/2013JG002327

Rhee, T. S., Kettle, A. J., and Andreae, M. O. (2009). Methane and nitrous oxide emissions from the ocean: a reassessment using basin-wide observations in the Atlantic. *J. Geophys. Res.* 114, 1–20. doi: 10.1029/2008JD011662

Rutgersson, A., Norman, M., Schneider, B., Pettersson, H., and Sahlée, E. (2008). The annual cycle of carbon dioxide and parameters influencing the air–sea carbon exchange in the Baltic Proper. *J. Mar. Syst.* 74, 381–394. doi: 10.1016/j.jmarsys.2008.02.005

Rutgersson, A., and Smedman, A.-S. (2010). Enhanced air–sea CO_2 transfer due to water-side convection. *J. Mar. Syst.* 80, 125–134. doi: 10.1016/j.jmarsys.2009.11.004

Sahlée, E., Rutgersson, A., Podgrajsek, E., and Bergström, H. (2014). Influence from surrounding land on the turbulence measurements above a lake. *Boundary layer Meteorol.* 150, 235–258. doi: 10.1007/s10546-013-9868-0

Sahlée, E., Smedman, A. S., Högström, U., and Rutgersson, A. (2008). Reevaluation of the bulk exchange coefficient for humidity at sea during unstable and neutral conditions. *J. Phys. Oceanogr.* 38, 257–272. doi: 10.1175/2007JPO3754.1

Saunois, M., Bousquet, P., Poulter, B., Peregon, A., Ciais, P., Canadell, J. G., et al. (2016). The global methane budget 2000-2012. *Earth Syst. Sci. Data* 8:697. doi: 10.5194/essd-8-697-2016

Schmale, O., Von Deimling, J. S., Gülzow, W., Nausch, G., Waniek, J. J., and Rehder, G. (2010). Distribution of methane in the water column of the Baltic Sea. *Geophys. Res. Lett.* 37, 1–5. doi: 10.1029/2010GL043115

Schmaljohann, R. (1996). Methane dynamics in the sediment and water column of Kiel Harbour (Baltic Sea). *Mar. Ecol. Prog. Ser.* 131, 263–273. doi: 10.3354/meps131263

Smedman, A. S., Högström, U., Bergström, H., Rutgersson, A., Kahma, K. K., and Pettersson, H. (1999). A case study of air–sea interaction during swell conditions. *J. Geophys. Res.* 104, 25833–25851. doi: 10.1029/1999JC900213

Starkenburg, D., Metzger, S., Fochesatto, G. J., Alfieri, J. G., Gens, R., Prakash, A., et al. (2016). Assessment of despiking methods for turbulence data in micrometeorology. *J. Atmospher. Ocean. Technol.* 33, 2001–2013. doi: 10.1175/JTECH-D-15-0154.1

Vickers, D., and Mahrt, L. (1997). Quality control and flux sampling problems for tower and aircraft data. *J. Atmospher. Ocean. Technol.* 14, 512–526. doi: 10.1175/1520-0426(1997)014<0512:QCAFSP>2.0.CO;2

Wanninkhof, R. (1992). Relationship between gas exchange and wind speed over the ocean. *J. Geophys. Res.* 97, 7373–7381. doi: 10.1029/92JC00188

Wanninkhof, R., Asher, W. E., Ho, D. T., Sweeney, C., and McGillis, W. R. (2009). Advances in quantifying air-sea gas exchange and environmental forcing. *Ann. Rev. Mar. Sci.* 1, 213–244. doi: 10.1146/annurev.marine.010908.163742

WDCGG. (2015). *Data Summary No. 39*. Volume IV-Greenhouse Gases and Other Atmospheric Gases. Japan Meteorological Agency, World Meteorological Organization.

Webb, E. K., Pearman, G. I., and Leuning, R. (1980). Correction of flux measurements for density effects due to heat and water vapour transfer. *Q. J. R. Meteorol. Soc.* 106, 85–100. doi: 10.1002/qj.49710644707

Wiesenburg, D. A., and Guinasso, N. L. (1979). Equilibrium solubilities of methane, carbon monoxide, and hydrogen in water and sea water. *J. Chem. Eng. Data* 24, 356–360. doi: 10.1021/je60083a006

Yang, M., Bell, T. G., Brown, I. J., Fishwick, J. R., Kitidis, V., Nightingale, P. D., et al. (2019). Insights from year-long measurements of air-water CH_4 and CO_2 exchange in a coastal environment. *Biogeosciences* 16, 961–978. doi: 10.5194/bg-16-961-2019

Yang, M., Bell, T. G., Hopkins, F. E., Kitidis, V., Cazenave, P. W., Nightingale, P. D., et al. (2016a). Air–sea fluxes of CO_2 and CH_4 from the Penlee Point Atmospheric Observatory on the south-west coast of the UK. *Atmospher. Chem. Phys.* 16, 5745–5761. doi: 10.5194/acp-16-5745-2016

Yang, M., Prytherch, J., Kozlova, E., Yelland, M. J., Parenkat Mony, D., and Bell, T. G. (2016b). Comparison of two closed-path cavity-based spectrometers for measuring air–water CO_2 and CH_4 fluxes by eddy covariance. *Atmospher. Meas. Techniq.* 9, 5509–5522. doi: 10.5194/amt-9-5509-2016

Conflict of Interest Statement: The authors declare that the research was conducted in the absence of any commercial or financial relationships that could be construed as a potential conflict of interest.

frontiers in Earth Science

ORIGINAL RESEARCH
published: 28 May 2019
doi: 10.3389/feart.2019.00111

Innovative Closely Spaced Profiling and Current Velocity Measurements in the Southern Baltic Sea in 2016–2018 With Special Reference to the Bottom Layer

Vadim T. Paka[1], Victor M. Zhurbas[2], Maria N. Golenko[1], Andrey O. Korzh[1], Alexey A. Kondrashov[1] and Sergey A. Shchuka[3]*

[1] Laboratory of Geoecology, Shirshov Institute of Oceanology, Russian Academy of Sciences, Moscow, Russia, [2] Laboratory of Marine Turbulence, Shirshov Institute of Oceanology, Russian Academy of Sciences, Moscow, Russia, [3] Laboratory of Marine Currents, Shirshov Institute of Oceanology, Russian Academy of Sciences, Moscow, Russia

OPEN ACCESS

Edited by:
Markus Meier, Leibniz Institute for Baltic Sea Research (LG), Germany

Reviewed by:
Laura Tuomi, Finnish Meteorological Institute, Finland
Tarmo Kõuts, Tallinn University of Technology, Estonia
Daniel Rak, Institute of Oceanology (PAN), Poland

***Correspondence:**
Vadim T. Paka
vpaka@mail.ru

Specialty section:
This article was submitted to Interdisciplinary Climate Studies, a section of the journal Frontiers in Earth Science

Received: *04 December 2018*
Accepted: *29 April 2019*
Published: *28 May 2019*

Citation:
Paka VT, Zhurbas VM, Golenko MN, Korzh AO, Kondrashov AA and Shchuka SA (2019) Innovative Closely Spaced Profiling and Current Velocity Measurements in the Southern Baltic Sea in 2016–2018 With Special Reference to the Bottom Layer. Front. Earth Sci. 7:111. doi: 10.3389/feart.2019.00111

A solution to the problem of determination of spatial variability of oceanographic fields, which contained a fine structure resolution higher than what was possible previously using towed scanning probes, was presented for the Baltic Sea. Another concurrently solved problem consisted in obtaining data on the structure of waters in the bottom layer, which was difficult to implement by way of application of previous methods. Instead of scanning along inclined paths, a new measurement technique allows for a quasi-free probe drop with a constant sink rate and which reaches the bottom at each dive cycle along the route of the ship, independent of the pitch of the ship and optimal for the applied probe. The new measurement technique is simpler and more efficient than the previous one. In addition, the problem of measuring the velocity of both very weak and strong currents in a thin bottom layer, including stagnant zones, slopes, sills, and underwater channels, was suggested to be solved using clusters consisting of a sufficiently large number of autonomous Tilt Current Meters (TCM) of original design. The innovation benefits are illustrated by the results of a monitoring campaign that was carried out in the southern Baltic Sea in 2016–2018. Among the new findings is the highest ever recorded temperature, 14.3°C, in the halocline of the Bornholm Basin, measured after a baroclinic inflow event in early Autumn 2018, and an extraordinarily large current velocity of saltwater flow of more than 0.5 m/s, recorded by a TCM within a 1 m thick bottom layer at the eastern slope of the Hoburg Channel during a period when the northwesterly wind had intensified to a severe gale.

Keywords: measurements, profiling, Baltic Sea, inflows, bottom layer

INTRODUCTION

The Baltic Sea is under the influence of a large number of hazardous substances of technogenic nature, polluting its waters, bottom sediments, and biota. A number of substances obviously have a negative impact and are therefore objects of environmental monitoring coordinated by HELCOM. However, unexploded chemical weapons (CW) with chemical warfare agents (CWA),

which were dangerous to leave on the coast and therefore dumped into the sea in the post-war years, turned out to be outside the framework of general environmental monitoring (Sanderson et al., 2010; Bełdowski et al., 2018b). This problem, albeit belatedly, nevertheless became the object of a special and still ongoing monitoring project (DAIMON Project, 2019). Experts were faced with the appearance of CWAs in the marine environment for the first time and had to start studying their behavior (release, decomposition, propagation) and effects on biota. There is no complete clarity on these issues yet and the research continues, but since the main sources of this type of pollution are well known, the task of minimizing the threat in one way or another has been set up. It is considered that the destruction of CW shells and the release of CWA have already begun. The released CWAs degrade due to hydrolysis and oxidation and are also spread over long distances from the dumpsites. However, the occurrence of concurrent adverse side effects that require prior evaluation is unavoidable. Therefore, to solve the problem, more complete information is required about the marine environment and, first of all, about the bottom layer, where all relevant transformations and movements occur. The CWAs that have survived to the present are highly stable in seawater; therefore, after the release, being sorbed by particles of fine easily suspendable silty mud, they can be relocated elsewhere and undergo chemical transformations along the way. From all this it follows that the special monitoring cannot be reduced to observations at a limited number of regular monitoring stations. Taking into account the fact that the two largest CW dumpsites are located in the center of the Bornholm Basin and in the southern part of the Gotland Basin, i.e., on the path of inflow currents, it can be concluded that, as part of a special monitoring to assess the cumulative impact on dumped CW and to estimate the distribution area of polluted resuspended silt, it is necessary to carry out measurements along the entire path of spreading of primary and transformed inflow waters.

Methods of special monitoring of physical processes in the Baltic Sea are developed and successfully used in field studies (Bełdowski et al., 2018a). The main attention is paid to obtaining data on the mesoscale structure of waters on transects, located along the route of inflow currents and in the bottom currents. The accumulated methodological experience of carrying out such measurements is used. Measurements on transects, carried out using towed undulating profilers, are well mastered (Piechura and Beszczyńska-Möller, 2004; Golenko et al., 2008; Rak, 2016). They provide very valuable information, but there is not enough data to describe the bottom conditions, since the undulating fish carrying a probe does not always reach the bottom. At the same time, reliable standard measurements at drift stations show that in some places, in particular where the halocline is at a small altitude above the bottom, the bottom stratification is especially sharp, and the stratification parameters at the bottom and a few meters above the bottom can differ greatly in magnitude. Special measures are required to increase the reliability of data on the bottom layer. The same applies to the bottom current measurements. Down-looking acoustic profilers do not provide information about the near-bottom motion because the signal from the bottom layer interferes with the sea bed reflection. Even up-looking bottom-mounted profilers do not solve the problem since the device with an anchor and acoustic release is elevated up to 1–2 m above the bottom. The only type of the velocity gauge that meets our requirements is an instrument designed for boundary layer measurements, for instance, NORTEK VECTOR velocimeter[1], though its high price might limit more extensive use. Therefore, we must to look for alternative solutions, and in this regard attention should be paid to the TCMs (Hansen et al., 2017), which are specially designed for bottom current measurements with rather moderate requirements to their metrological characteristics but have the advantage of relative simplicity and low cost. However, these devices also require an improvement.

Considering the problems outlined above, the objectives of this study were formulated as follows: (a) to develop and implement in practice of the field work in the Baltic Sea, a new profiling technique capable of allowing a quasi-free probe drop along the route of a ship with a constant sink rate, independent of the pitch of the ship, which is optimal for the applied probe and which reaches the bottom at each dive cycle, (b) to develop and implement in practice a new technique to measure the velocity of currents in a thin near-bottom layer consisting of a sufficiently large number of autonomous TCMs of original design, and (c) to illustrate the innovation benefits on the results of a monitoring campaign that was carried out in the southern Baltic Sea in 2016–2018.

MATERIALS AND METHODS

Measurements on Extended Transects

The measurements on transects were carried out along a track passing from the Arkona Deep to the Gdansk Deep through the Bornholm Strait, the Bornholm Deep, and the Słupsk Furrow repeatedly used during the last 20 years for CTD tow-yo profiling (Rak and Wieczorek, 2012). There is also a repeated measurement track in the Russian EEZ passing from the Gdansk Deep to the Hoburg Channel (the entrance to the Gotland Deep, see **Figure 1**).

The field work on the transects in the 2016–2018 cruises was carried out taking into account the new requirements arising from the tasks of special monitoring. Before 2018, in order to obtain reliable information about the bottom parameters at all points of the extended transect, instead of towed scanning fish carrying the probe we had to return to measurements with the vessel on drift. Because of the ship's stops every 2 miles, the mean speed of passage of the transect decreased twice relative to the towing speed with scanning. The modified measurement technique that we used in 2016 and 2017 was presented previously (Bełdowski et al., 2018a).

The probe Idronaut OS316+ was used in quasi-free fall mode. According to the manufacturer's recommendations, the fall rate was 1 m/s and the probe reached the bottom and was kept on the seabed before recovery for at least 20 s, which made it possible to eliminate the inertial error of the estimates of the bottom

[1]https://www.nortekgroup.com/ (accessed March 15, 2019).

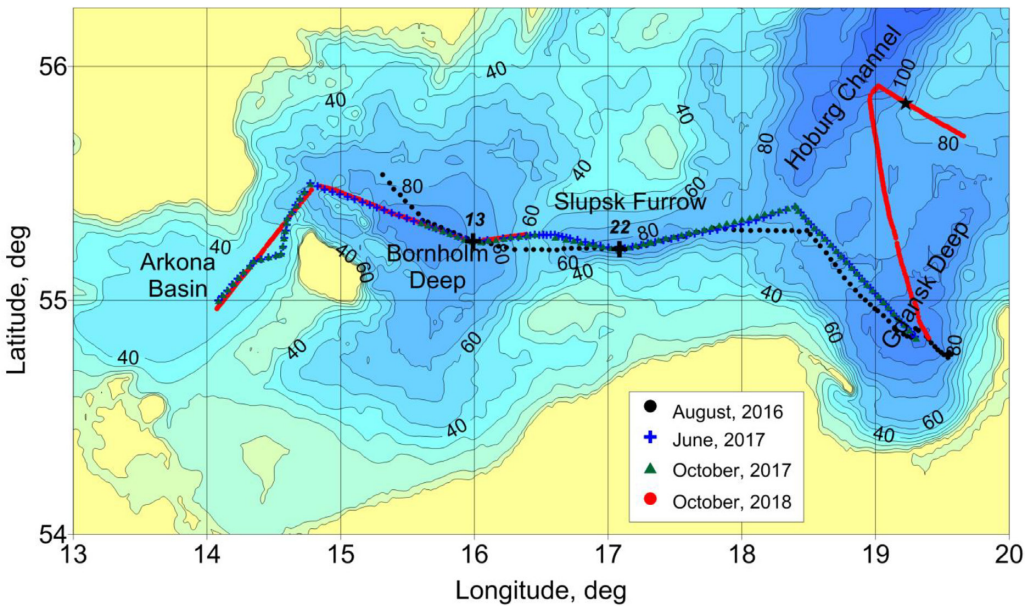

FIGURE 1 | Location of the transects (color lines), the TCM deployment site (black star), and the IOW main monitoring stations, TF0213 and TF0222 (black crosses labeled as 13 and 22, respectively).

parameters. Doing so, the most inert sensor—a polarographic oxygen sensor with the time constant of $\tau = 3$ s—provided the correct result at the end of the stand. The proposed method of correction is explained in **Figure 2**, which shows one of the measurements by the OS316 + probe, performed in an area with a large gradient in the bottom layer. A fragment of a record of temperature T, salinity S, density σ_θ, and oxygen saturation O_2 signals as functions of time is presented. The black vertical line

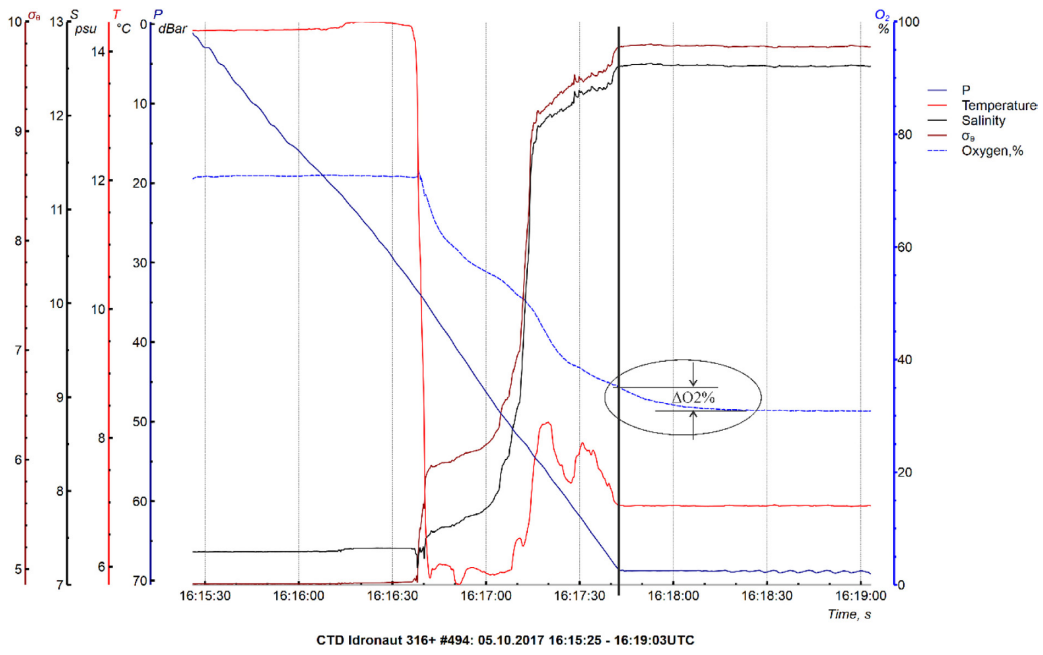

FIGURE 2 | A record of temperature T (°C), salinity S (psu), density σ_θ and oxygen saturation O_2 (%) signals as functions of time during measurements at a drift station. The probe was kept on the ground for 1 min before recovery as can be seen from the pressure signal. The black vertical line marks the moment of reaching the bottom and the start of holding the probe at the bottom. The space between the horizontal lines placed in the ellipse shows the change ΔO_2 (%) in the oxygen saturation signal due to the oxygen sensor inertia. Note that the rest of the parameters, T and S, remained unchanged at this time.

marks the moment of reaching the bottom. It can be seen that during the stay of the probe on the bottom, the signals T, S, and σ_θ practically did not change, whereas the O_2 signal regularly and expectedly changed, asymptotically approaching the value that differs from the initial one by 5% of saturation. Such a large error seems to be unacceptable, especially in the areas of steady hypoxia or oncoming hypoxia.

Further, we managed to carry out the final modernization of the method of profiling from the moving ship and increased its speed to the initial value of 4–6 knots. According to the new method, a probe with a tether loosely coiled on the deck was released from the stern and began to sink down vertically, not perceiving the movement of the vessel. At the moment of termination of the free fall, the tether was tensioned, and the probe quickly rose to the surface. At this position, the recovery began. For recovery, a mechanism, which is a modified version of longline haulers designed for fishery, was used[2]. It coils the tether on the deck instead of winding on the winch, and due to this allows repeating the next cast without delay due to preliminary preparation. Our mechanism provides a pulling force of about 50 kG, sufficient for recovery of the probe at a speed of about 1 m/s. For operation in this mode, the probe is placed between the load weighing about 5 kg and the float with a lifting force of about 2 kg, with the tether being fixed between the load and the probe, as shown in **Figure 3**. The load is chosen in such a way that the steady speed of fall is 1 m/s. When the bottom is reached, the probe, held by the float at a predetermined small distance from the bottom (40 cm), stops for a short time in the vertical position with the sensors directed downward (see **Figure 3a**). At the time of termination of the release, the tether is fixed on the deck, the outboard part is tensioned, and the onboard part is inserted in a hauler. Then, a recovery is implemented, ending when the probe approaches the stern. The bundle configuration during recovery is shown in **Figure 3b**. Unlike the towed probe, which rapidly moves with the travel speed at small distances from the bottom and with a high risk of scraping the bottom, the free-falling probe does not move in the horizontal direction from the moment of the beginning of free fall until the tether is fixed on the deck. Only when the probe takes off and is at a safe distance from the bottom does it perform horizontal movement. The loss of the probe with this sensing method is possible only due to the break of the tether, which is loaded with no more than 10% of the allowable tension.

[2]http://www.charlieengineering.com/portfolio-items/fishing-line-rope-hauler-winch/ (accessed March 15, 2019).

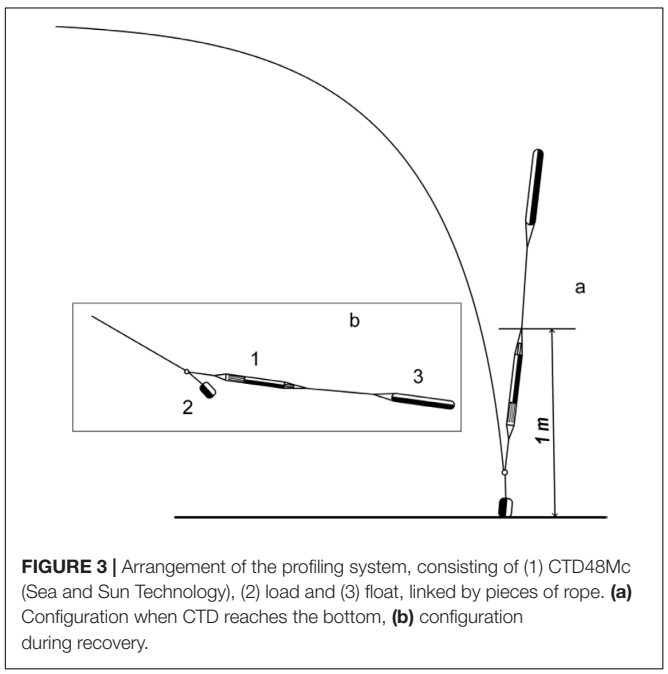

FIGURE 3 | Arrangement of the profiling system, consisting of (1) CTD48Mc (Sea and Sun Technology), (2) load and (3) float, linked by pieces of rope. **(a)** Configuration when CTD reaches the bottom, **(b)** configuration during recovery.

The use of the new profiling technique does not obviate the need to correct the dynamic error of the inertial oxygen sensor. On the contrary, the problem is exacerbated because even short-term retention of the probe at the bottom, during which the rapid tether payout continues, results in a loss of time for the slow recovery of the released tether. The solution for this problem can only be a reduction of the inertia of the adopted oxygen sensor. In our last cruise we used the CTD48Mc probe from Sea & Sun Technology, equipped with a fast-response (∼1 s) optical sensor of dissolved oxygen saturation along with a standard set of CTD sensors with a sampling rate of about 10. Within this response time value remains an unintended pause, occurring after the command "stop" is executed on the winch, which lasts for at least 3–5 s. Therefore, working with CTD48Mc, we did not resort to a special delay, and the analysis of continuous records of signals confirmed the absence of an explicit dynamic error. The memory capacity of the probe was sufficient for several hours of continuous work.

The measurements using the new technique were carried out in various regions of the southern and central Baltic in the depth range from 45 to 120 m on a speed of about 5 knots with a frequency of about 8 cycles per hour, which corresponds to a spatial resolution of about 1 km. Approximately the same horizontal resolution is provided by towed scanning probes, but concerning the vertical resolution of the fine structure and reliability of the data in the bottom layer, obtained during contact with the bottom, the new method has an obvious advantage. It can also be noted that the developed measurement method does not require either powerful winches or cranes. Due to this, the method can be implemented on small vessels, which makes it promising for multiple uses.

Microstructure Measurements in the Bottom Layer

For additional measurements in the most interesting areas at the inflow pathway, a microstructure quasi-free (tethered) probe of our own design, "Baklan," was used (Paka et al., 2010, Paka et al., 2013). The profiler was equipped with precision conductivity and temperature sensors manufactured at our special request by Idronaut S.r.l., a fast-response temperature sensor (type FP07) and an airfoil shear probe (type PNS06 from ISW). The sensors were sampled at 480 Hz with 16 bit resolution. Measurements in weakly turbulent regions showed that "Baklan" had a noise level of the order $\varepsilon \approx 10^{-9}$ W/kg, which is sufficiently small to resolve dissipation rates in the turbulent boundary and shear

layers. Sensors are protected from damage when they reach the bottom. This measure allows for probing at a very close distance from the bottom (∼10 cm).

Soundings are conducted at drift stations from the weatherboard or from the aft deck with the engine running if due to the weather conditions the vessel cannot be in free drift and is forced to move slowly upwind by bow trusters and a variable pitch propeller. The commonly practiced measurement technique, with the tether loosely slacked away from the deck after sinking the probe, is impossible under heavy drift since the tether lined up on the sea surface violates the vertical orientation of the probe, which is unacceptable for normal functioning of shear probes. Working from the aft deck when the vessel moves upwind is fraught with the risk of losing the probe, since strong wind gusts can force the vessel backward and the tether can get under the working propeller. When the vessel goes only forward, but not sufficiently slowly, then the same problem arises as during operation with a strong drift: the tether pulled out behind the vessel roll with the probe on its side and the turbulence sensor signal becomes noisy. To investigate the turbulence in any weather conditions, still allowing the vessel to work at sea, the construction of "Baklan" provides protection from the tether's tension. Unlike other microstructure sounds (MSSs), "Baklan" stores a necessary length of the tether inside its body. During the fall, the tether freely leaves the magazine at the tail end of the probe and does not affect the movement. A capron cord has almost zero buoyancy in water; therefore, when the cord is pulled out, the mass of the sinking body does not change. The magazine holds up to 500 m of a thin (4 mm) cord, which makes it possible to use the probe anywhere in the Baltic Sea even in cases when the vessel moves away from the sensing point, with a speed exceeding the speed of the falling probe (60 cm/s) when using other probes is impossible or difficult.

Measurements of Current in the Bottom Layer

To study the spatiotemporal variability of currents in a thin bottom layer, autonomous instruments are necessary, which can be located at a minimum distance from the bottom in a sufficiently large number of points. Universal current meters, in particular acoustic profilers, are of little use for this purpose, because of the fundamental impossibility of measuring near the surface, which reflects an acoustic signal, and because the cost of multiple use is too high. Our choice fell on TCMs, the principle of operation that is based on measuring the inclination of the pendulum under the condition of equal forces of hydrodynamic pressure and buoyancy. We have developed our own device design, shown in **Figure 4**.

The device can be manufactured in two versions—with positive or negative buoyancy. The second version is more complicated than the first one, but its sensitivity has a wider range and it can be used to measure strong currents, for example those occurring in the coastal zone. **Figure 4** shows a TCM with positive buoyancy, designed to measure weak and moderately strong currents in the open sea, for which we were preparing. The body of the device has a cylindrical shape. The main disadvantage of the cylindrical shape is the formation of Kármán vortices during a cross-flow and, as a result, the occurrence of auto-oscillations, but this refers to a smooth cylinder. A hard cylindrical perforated shroud is flown around without the formation of coherent vortices and does not oscillate. We utilized this property.

FIGURE 4 | A photograph of the TCM. Its shape is formed by a cylindrical perforated plastic pipe. Inside there are an instrument and buoyancy modules, and the entire floating package is attached to a lead plate by a piece of chain.

The shroud is made of a thin-walled plastic pipe with a diameter of 110 mm, a length of 1 m, and is evenly perforated with a perforation factor of about 50%, as can be seen in **Figure 4**. The dimensions of the shroud are chosen taking into account the dimensions of the instrument module and the thickness of the layer under study. A watertight module with electronics is placed in the lower part of the shroud at a minimum distance from the pivot point so that the accelerometer that measures the angle of inclination weakly reacts to linear accelerations due to rapid transient responses. In the same module, there are an electronic compass, which determines the direction of

tilt of the cylinder, an electronic clock and other elements that ensure continuous autonomous operation of the device with the possibility of programming the ratio of recording time and pause.

A precision watch was provided with the monthly accuracy of 10 s, which in the first approximation can be considered sufficient to perform synchronous measurements in a large number of points (in perspective). The buoyancy of the instrument module is close to neutral. To increase the buoyancy, a cylindrical float is placed in the upper part of the shroud (see **Figure 4**). By shifting it along the shroud, it is possible to change the moment of the buoyancy force, adjusting the sensitivity of the device. Sensitivity can be increased as long as acceptable stability of the signal corresponding to zero flow velocity is maintained. Studying the behavior of the device in standing water, it was determined that the lower threshold of measured speeds can be considered 2 cm/s with a relative accuracy of 25%. The full range of measured speeds at a setting for maximum sensitivity is 2–30 cm/s, with a maximum speed measurement error of about 3%. With a coarser adjustment of the sensitivity, the measuring range remains the same. Therefore, the increase of the maximum measured speed up to 1 m/s and more comes on the expense of the accuracy of measuring of weak currents.

We managed to achieve satisfactory quality of our products and calibrated them in the towing tank just before the last cruise. Field tests of new equipment were carried out in an area located on the eastern slope of the Hoburg Channel, along which saltwater flows into the Gotland Deep. Saltwater can come to the Hoburg Channel either directly from the Słupsk Furrow or in a roundabout way through the Gulf of Gdansk, and the choice of the route is probably controlled by the wind field over the water area. On a fragment of the bathymetric map (Gelumbauskaite et al., 1999) presented in **Figure 5**, the arrow shows a small gully along which saltwater can move from the Gulf of Gdansk in the direction of the arrow. In particular, this site was chosen for testing of TCMs. A group of 10 instruments were tested, and they were identically configured to measure currents with speeds of up to 60 cm/s (the float was placed in the upper part of the shroud, as can be seen in **Figure 4**). All instruments were deployed as a compact group so that they would be at equal conditions and show similar results. The tests were successful. All ten 5-day records turned out to be similar in terms of both slow and fast changes in flow. Based on this, we can use the data to describe the characteristics of the bottom current in the selected area (see section "Near-Bottom Currents").

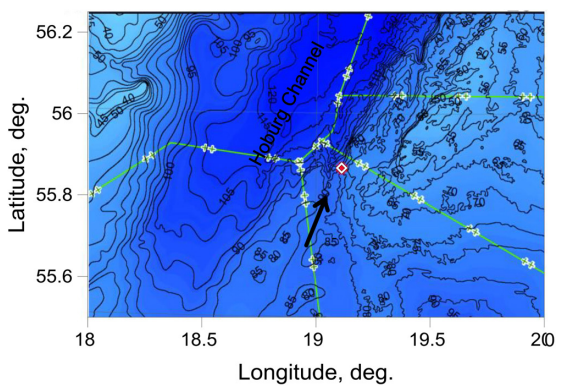

FIGURE 5 | Bottom relief and position of TCMs' group (diamond) at the test area. Lines mark boundaries of Exclusive Economic Zones of the Baltic States. Arrow points to the gully.

RESULTS

Results of Measurements on the Extended Transects

The transects demonstrate the water structure from the surface to the bottom, but changes in the surface's mixed and cold intermediate layers (CIL) are not a matter for analysis within the frame of our task. Each of these layers was formed in the process of the heat and momentum exchange with the atmosphere and is practically insensitive to the inflows, so they are not of particular interest for analyzing changes of water structure below the permanent halocline. The only parameter that depends on the intensity of the saltwater inflows is the depth and topography of the lower boundary of the CIL, since it corresponds to the upper boundary of the halocline. The halocline depth in the Bornholm Deep relative to the Słupsk Sill depth characterizes the ability of saltwater to spread eastward in the form of near-bottom gravity current.

Except for the periods of sufficiently powerful inflows that are able to ventilate the deepest layer of the Bornholm and Gdansk basins, the saltwater layer in the southern Baltic Sea can be divided into two parts: the upper, variable part corresponding to the interleaving zone of moderate and weak inflows, and the lower, conservative part containing water with maximum salinity and density where the moderate and weak inflows do not penetrate. If the period of lack of sufficiently powerful inflows lasts for a long time, then stagnation develops in the lower layer. Additionally, there are rare events of the most powerful inflows called the Major Baltic Inflows (MBIs) that can ventilate, apart from the Bornholm and Gdansk deeps, the deepest Baltic basins such as the Gotland Deep [see, e.g., Matthäus and Franck (1992)]. The last MBI took place in December 2014. The recent analysis of MBI statistics showed that until today, climate change has no obvious impact on the MBI-related oxygen supply to the central Baltic Sea, and the increased eutrophication during the last century is most probably responsible for temporal and spatial spreading of suboxic and anoxic conditions in the deep layer of the Baltic Sea (Mohrholz, 2018).

The first survey (**Figure 6**) was carried out at a time when the surplus of saltwater in the Bornholm Basin due to MBI 14 overflowed the Słupsk Sill, as a result of which the halocline depth in the Bornholm Basin decreased to the depth of the Słupsk Sill; the same happened beyond the Słupsk Sill in the Słupsk Furrow, where the halocline depth decreased to that at the exit from the Słupsk Furrow. In the Gdansk Deep, the halocline level was observed even deeper. In the Bornholm and Gdansk Deeps, the oxygen content dropped to almost zero. At the same time, in the Słupsk Furrow, through which the oxic water passes from the intermediate layers of the Bornholm Basin, the oxygen saturation

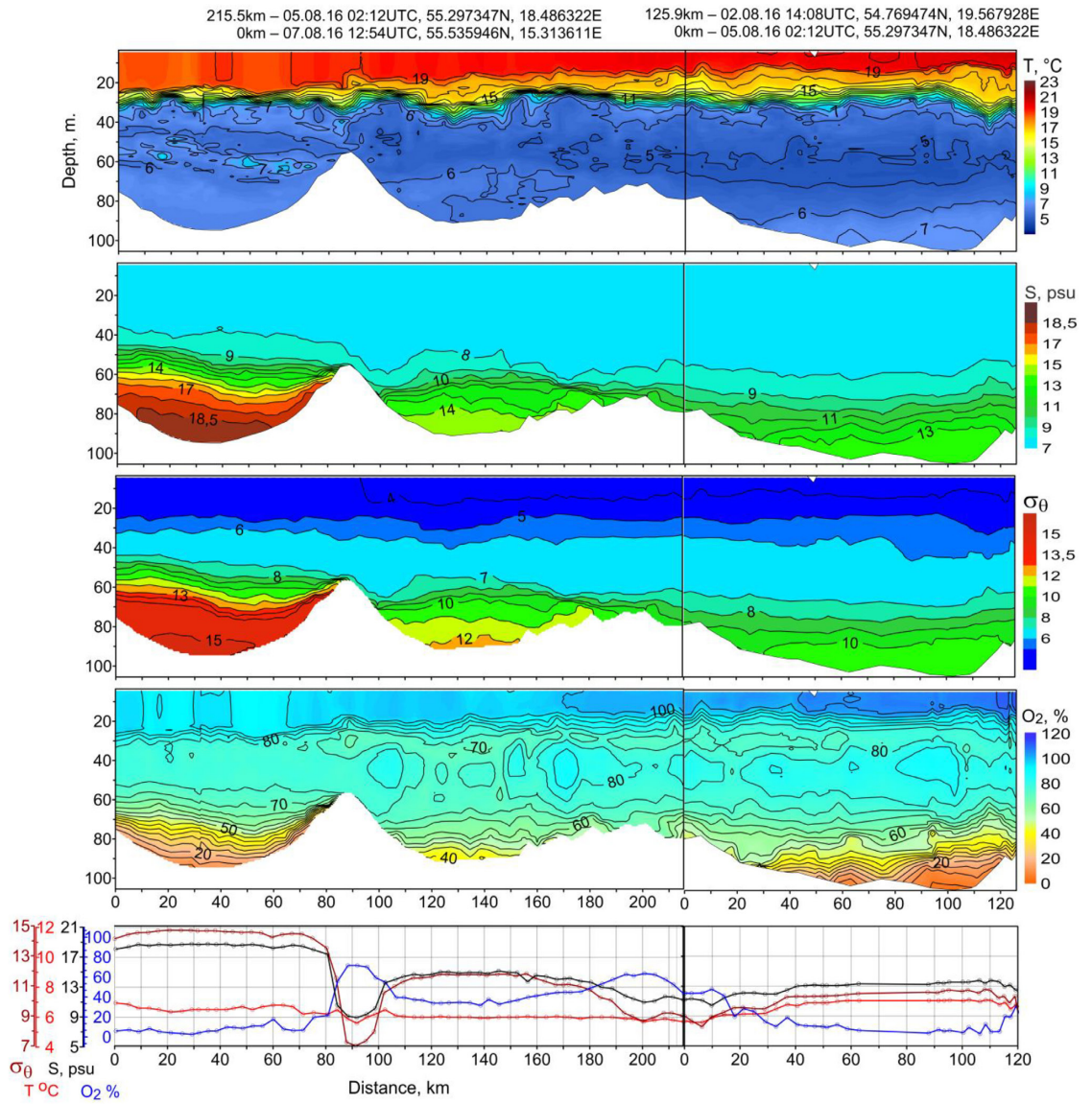

FIGURE 6 | Distributions of temperature T (°C), salinity S (psu), density σ_θ, and oxygen saturation O_2 (%) in the southern Baltic for the 1st survey (August 2016); bottom panels demonstrate graphs of the same parameters in the bottom layer.

was 30%, but, as we see, this water did not reach the bottom of the Gdansk Deep. There were no signs of active intra-basin dynamics in any of the basins. At the Słupsk Sill, the salinity contours of more than 9 psu had a gap, which can be considered as an indication of the absence of a significant saltwater overflow. However, water with salinity of about 14 psu was very close to the top of the Sill, which indicates a high probability of resumption of saltwater overflow, both as a result of a new, even weak, inflow into the Bornholm Basin, or as a result of fluctuations of the halocline level in the vicinity of the Słupsk Sill due to some dynamical reasons.

The second survey (**Figure 7**), carried out 10 months after the first one, showed a significant reduction in the volume of the saltiest/densest water, with a salinity of above 17 psu in the bottom layer of the Bornholm Deep and a simultaneous decrease of the maximum salinity and density, but in the upper saltwater layer the volume of less saline water (<17 psu) increased so much that the halocline level appeared to be elevated several meters above the Słupsk Sill depth. The conclusion is that during the preceding 10 months, there was no inflow of water capable of reaching the bottom, but there were likely some weak or moderate inflows which formed the interleaving and led to a rise of the halocline depth. The difference in halocline levels on both sides of the Słupsk Sill, determined conventionally by the isohaline of 9 psu, was 15 m, which indicates the formation of a gravity current above the eastern slope of the sill. This overflowing water was well oxygenated (60% of saturation), and in the Słupsk Furrow the saturation never decreased below 20%.

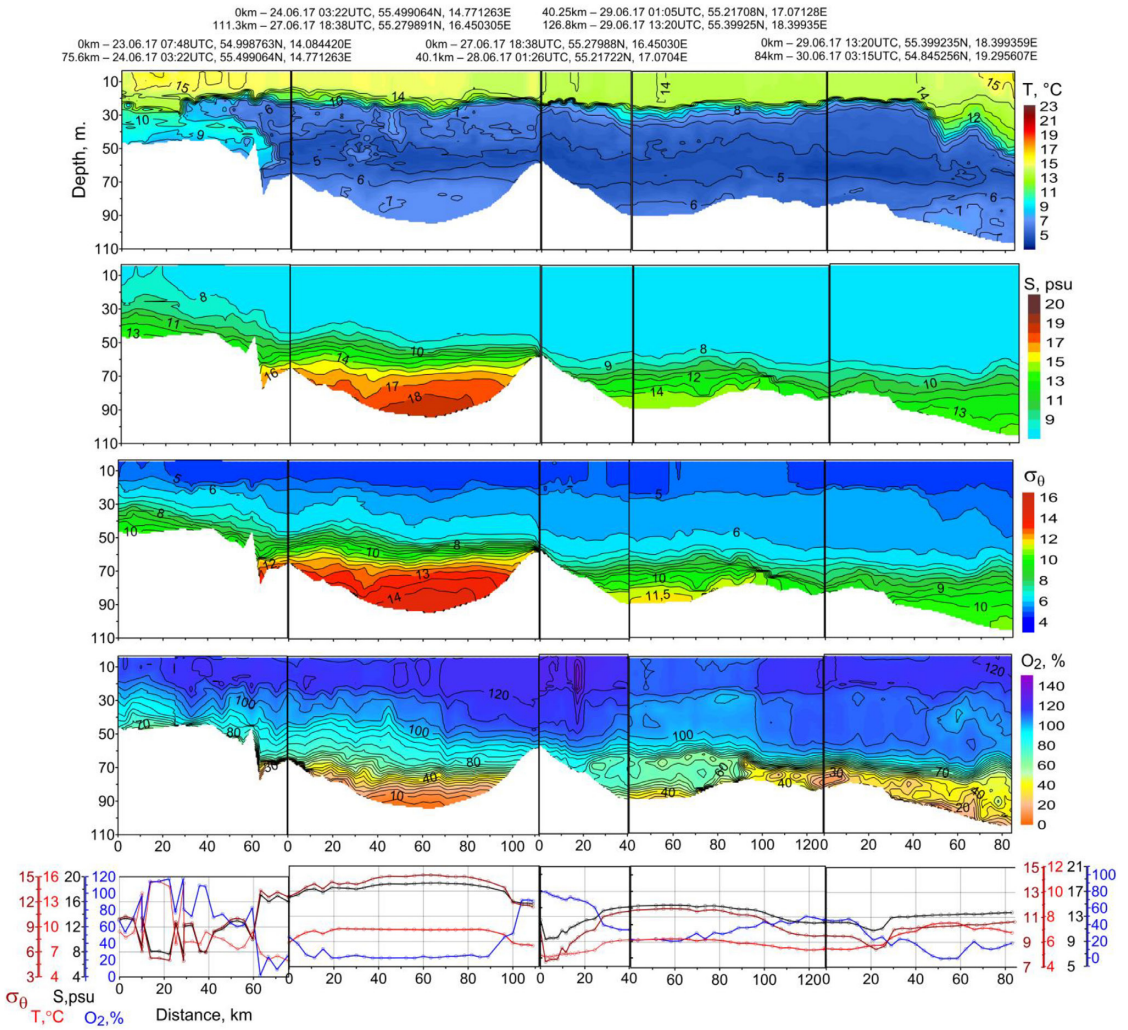

FIGURE 7 | Distributions of temperature T (°C), salinity S (psu), density σ_θ, and oxygen saturation O_2 (%) in the southern Baltic for the 2nd survey (June–July 2017); bottom panels demonstrate graphs of the same parameters in the bottom layer.

But the activity of water exchange through the Słupsk Sill did not affect the stagnation in the Bornholm bottom layer, where the anoxic zone at the bottom occupied 80 km along the line of the transect between the isobaths 72 and 83 m. As for the Gdansk Deep, the oxygen content there even slightly increased. Apparently, the bottom layer here was partially ventilated by oxic water flowing through the Słupsk Furrow.

The third survey (**Figure 8**) was made 4 months after the second. In this short time, the topography of the halocline near the Słupsk Sill was radically changed. The isohaline of 9 psu denoting the upper border of the halocline was found at a depth of 50 m, or 7 m above the Słupsk Sill depth, but the high level of the halocline was also observed just beyond the sill, which is not typical for this area and impedes the formation of a gravity current beyond the Słupsk Sill. One may suppose that the saltwater overflow stopped due to a surge of saline water toward the Sill from the middle of the Słupsk Furrow, which was most likely a consequence of the synoptic processes in the Southern Baltic (Krauss and Brügge, 1991). As for the maximum salinity in the bottom layer of the Bornholm Deep, Słupsk Furrow, and Gdansk Deep, it continued decreasing, as can be seen from the data presented in **Table 1**.

The fourth survey (**Figure 9**), carried out 1 year after the third one, showed radical changes of the water structure in the Arkona and Bornholm Basins. Nothing like that happened in the Gdansk Deep. In the Słupsk Furrow and on the Słupsk Sill, measurements were not taken due to the lack of permission to work in Polish waters. Evidently, an inflow occurred, manifested in the renewal of the bottom waters in the Bornholm Deep. Together with the salty, dense and warm water, a large amount of oxygen was supplied (see **Table 1**). Judging by the horizontal heterogeneity of the density field, the inflow water has not yet found its stable position in the deep. This is evidenced by the signs of spreading of relatively warm, maximum saline/dense and sufficiently oxic water from the core, located in the central part of the deep with a slight shift to the east with the upper

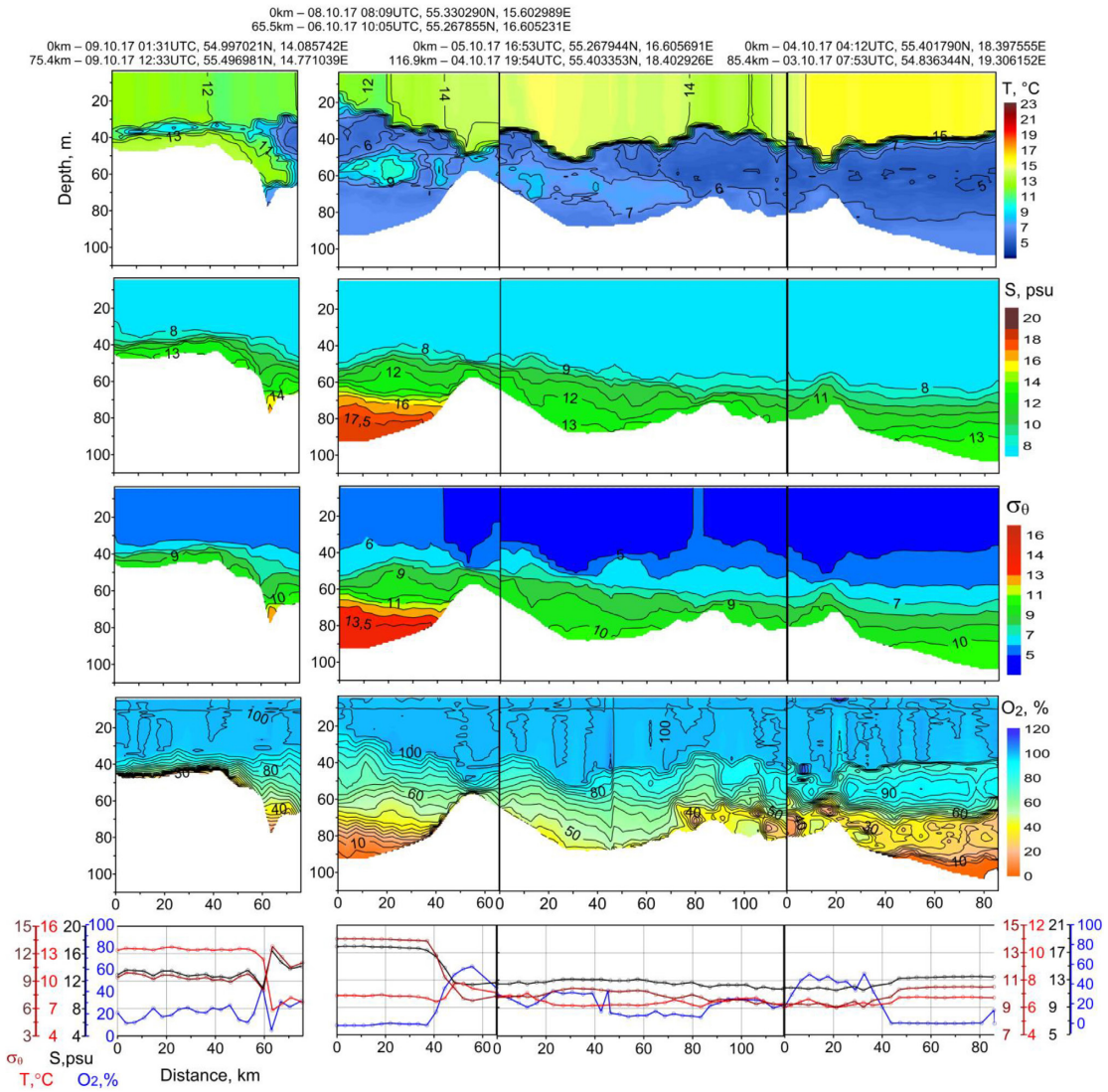

FIGURE 8 | Distributions of temperature T (°C), salinity S (psu), density σ_θ, and oxygen saturation O_2 (%) in the southern Baltic for the 3rd survey (October 2017); bottom panels demonstrate graphs of the same parameters in the bottom layer.

TABLE 1 | Maximum bottom temperature, salinity and minimum dissolved oxygen (DO) saturation at the transects through the southern Baltic basins.

	Aug. 2016			June–July 2017			Oct. 2017			Oct. 2018		
	T, °C	S, psu	DO, %	T, °C	S, psu	DO, %	T, °C	S, psu	DO, %	T, °C	S, psu	DO, %
Ark.B.	–	–	–	9,5	13,2	58,9	13,8	13,6	11,5	15,4	19,1	47,1
Born.D.	7,0	18,8	2,5	7,0	18,3	−0,1	7,0	18,0	0,3	14,3	19,0	−1,6
Sl.Furr.	6,1	15,2	31,5	5,4	14,8	21,5	7,1	13,2	11,4	–	–	–
Gd.D.	7,1	13,8	2,2	7,5	13,6	−1,0	6,8	13,5	−0,1	6,7	11,7	−1,4

boundary conventionally determined by the 18 psu contour, at a depth of 80 m. In the process of spreading, a layer stretching to the west at a distance of about 20 km was formed so thin that it could only be detected by the new method of measuring the bottom parameters. In the western part of the deep in the near-slope region, another large new water pool was observed with $T = 13°C$ and $S = 18$ psu, the upper boundary of which was situated even higher—at a depth of 68 m. From this water body, a thin layer of salty/dense water—even richer in oxygen than in the central intrusion—spread to the east descending to greater depths. In addition, large intrusions with a slightly lower salinity of 14.5–15.5 psu reached a depth of 55–60 m, corresponding

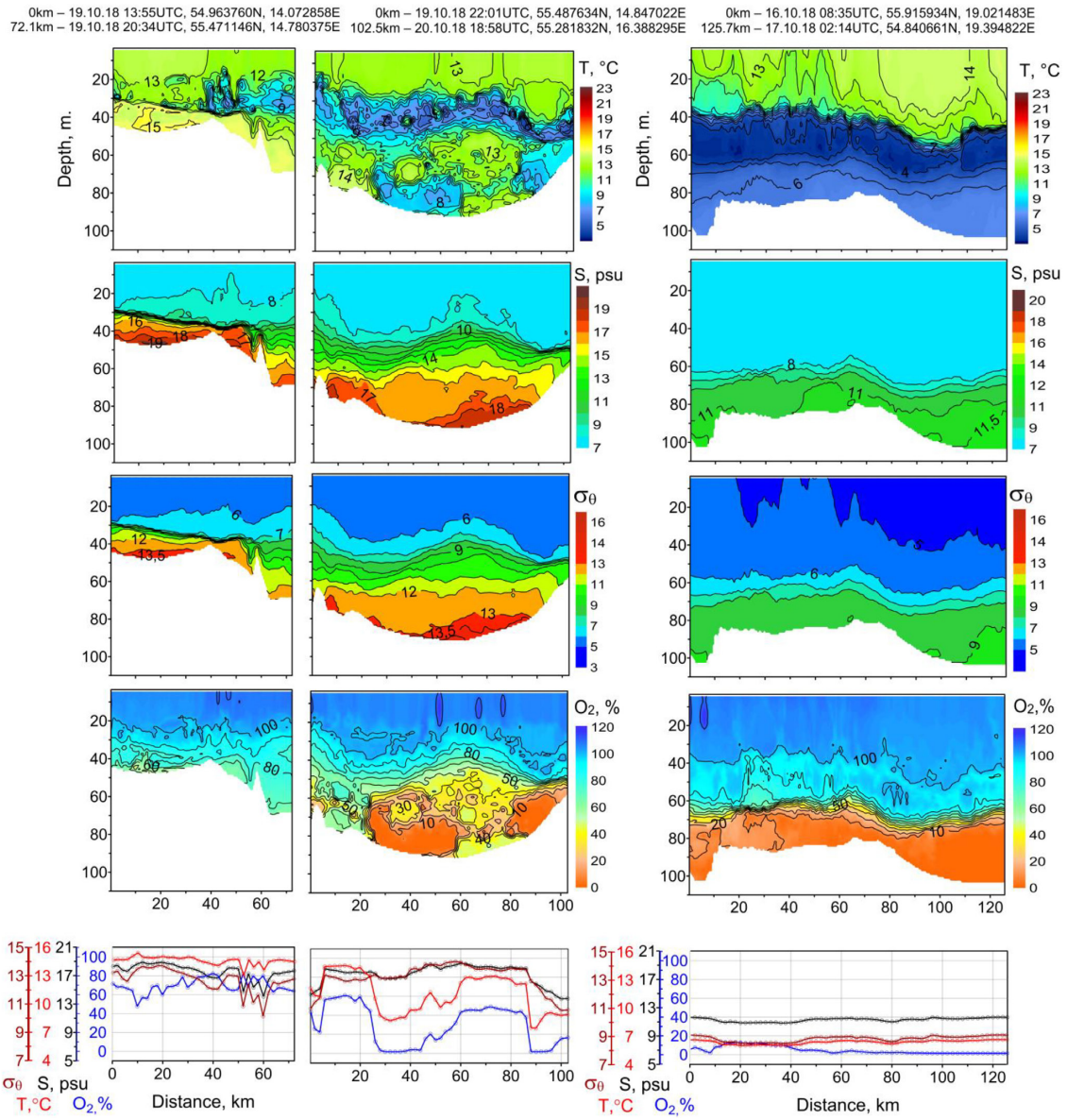

FIGURE 9 | Distributions of temperature T (°C), salinity S (psu), density σ_θ, and oxygen saturation O_2 (%) in the southern Baltic for the 4th survey (October 2018); bottom panels demonstrate graphs of the same parameters in the bottom layer.

to the depth of the Słupsk Sill. These intrusions, as well as the bottom ones, also have a temperature of about 13°C, which is higher than the temperature of the surrounding water by 3°C, undoubtedly indicating its recent arrival from the Arkona Basin, where the entire water column, with the exception of a thin layer at the halocline border, has a temperature of about 12.5–13.5°N.

Warm water intrusions in the bottom and intermediate layers below the permanent halocline in the Bornholm Deep (**Figure 9**) indicate a strong baroclinic inflow event that took place in autumn 2018 (Volker Mohrholz, personal communication). Note that in the past, the highest ever recorded temperature of 13.9°C in the halocline of the Bornholm Basin was measured in October 2002 after an exceptionally warm summer inflow event (Mohrholz et al., 2006). In October 2018, this temperature record was exceeded by 0.4°C: the maximum temperature in the Bornholm Deep halocline rose to 14.3°C.

The maximum values of salinity and minimum values of dissolved oxygen (DO) saturation at the bottom in the Bornholm Deep and Słupsk Furrow recorded at the extended transects (**Table 1**) are close to the IOW monitoring data obtained using the standard method at stations TF0213 and TF0222 (see **Figure 1**), respectively[3]. Some discrepancies can be explained by the fact that our data were selected from the transects, while the IOW data were obtained at single locations, and the main

[3]https://www.io-warnemuende.de/cruise-reports.html

monitoring station in the Bornholm Deep (TF0213) was located not at the maximum depth of the basin (approximately 95 m) but at a depth of 88 m, where the bottom layer parameters could not reach their limits. Note that some of the minimum values of DO measured on the extended transects in the bottom layer of the Bornholm and Gdansk deeps are negative (see **Table 1**). We consider the negative DO values as an indicator of the presence of hydrogen sulfide, not as an error of calibrating the oxygen sensor. Our conclusion is qualitative, because we did not make a special calibration of the sensor with the purpose of quantitative determination of hydrogen sulfide content.

To provide more adequate comparison of our data with the IOW monitoring measurements of the oceanographic parameters at the bottom at stations TF0213 and TF0222, we chose values of temperature, salinity, and oxygen recorded at the same depth and as close as possible to the location and time allowed by the transects available (**Table 2**). Note that **Table 2** does not contain the comparison for the October 2018 transect performed after the early Autumn 2018 baroclinic inflow event because the corresponding data of the November 2018 IOW monitoring cruise are not yet available at https://www.io-warnemuende.de/cruise-reports.html. According to **Table 2**, the oceanographic parameters measured in the near-bottom layer by the standard method in the IOW monitoring cruises correspond well to the IO RAS data obtained at the extended transects performed using the innovative measurement technique: the mean/standard deviation of the difference between the IO RAS and IOW data are −0.16/0.53°C, −0.17/0.38 psu, and −0.28/6.18% for temperature, salinity, and oxygen saturation, respectively. Since the time discrepancy between the IOW and IO RAS measurements was as large as 2 months, such a small discrepancy in the measured oceanographic parameters seems quite acceptable.

Results of Microstructure Measurements

During the campaign, the microstructure measurements were carried out mostly in cases when in the water structure there were signs of a strong gravity current with a developed turbulence. On CTD transects, segments of high probability of turbulent motion in the bottom layer were distinguished as thin layers with increased salinity, located above the sloping bottom. It is just the way the gravitational current manifests in the thermohaline structure. A targeted search for turbulent bottom currents was performed over the Słupsk Sill, where this property was predicted (Piechura et al., 1997) and found by direct measurements, as reported by Mohrholz and Heene (2018) at the 2nd Baltic Earth Conference in Helsingor, 2018. Favorable conditions were observed in July–August 2017. In the next survey in October 2017 at the same site, there were no signs of a gravity current in the bottom layer, but we decided to investigate this situation anyway. This allowed us to evaluate and compare turbulence for a situation, different from the strong eastward overflow, when nevertheless a weaker flow occurs, and its interaction with the obstacle can generate nonstationary turbulence with poorly studied properties.

Examples of microstructure measurements performed in July and October 2017 are presented in **Figures 10**, **11**. All data including the pressure signal are drawn as time functions, and the time is replaced by number counts. To show a background water structure, the microstructure plots are accompanied by the temperature, salinity and density plots. A dashed line marks the end of the probe's motion when it reaches the seabed, and at this moment the pressure signal becomes constant, while any changes of other signals do not carry any information.

The vertical microstructure is closely related to the background stratification, and the upper quasi homogeneous layer can be distinguished. Within the upper mixed layer, which is under the direct influence of wind and surface waves, turbulence decreases with depth from a maximum value of $\varepsilon \sim 10^{-4}$–$\varepsilon \sim 10^{-8}$ W/kg, approaching the thermocline at a close but definite distance with a value of $\varepsilon \sim 10^{-7}$ W/kg (**Figure 10A**). The vessel's weather station during the experiment recorded a wind of 10–15 m/s from W-NW; its stress was not enough to perform the mixing to the depth of the main thermocline, which was apparently formed with a stronger wind. The distribution of turbulence with depth within the mixed layer is uneven. It is

TABLE 2 | Comparison of the bottom oceanographic parameters at the IOW monitoring stations TF0213 and TF0222 with the corresponding data extracted from the IO RAS extended transects.

	Station TF0213				Station TF0222			
	Depth, m	T, °C	S, psu	DO, %	Depth, m	T, °C	S, psu	DO, %
May (IOW), August (IO RAS) 2016								
IO RAS	88	6.56	18.54	9.9	90	6.03	14.98	33.6
IOW	88	6.24	18.84	21	88	5.96	15.2	34
May (IOW), June (IO RAS) 2017								
IO RAS	88	6.95	18.04	1.3	89	6.12	14.53	33.15
IOW	87	6.92	18.21	4	88	6.43	15.22	41
November (IOW), October (IO RAS) 2017								
IO RAS	87	6.92	17.76	0.35	88	7.32	12.37	42.4
IOW	88.2	6.83	17.28	1.6	90.0	8.47	12.46	36

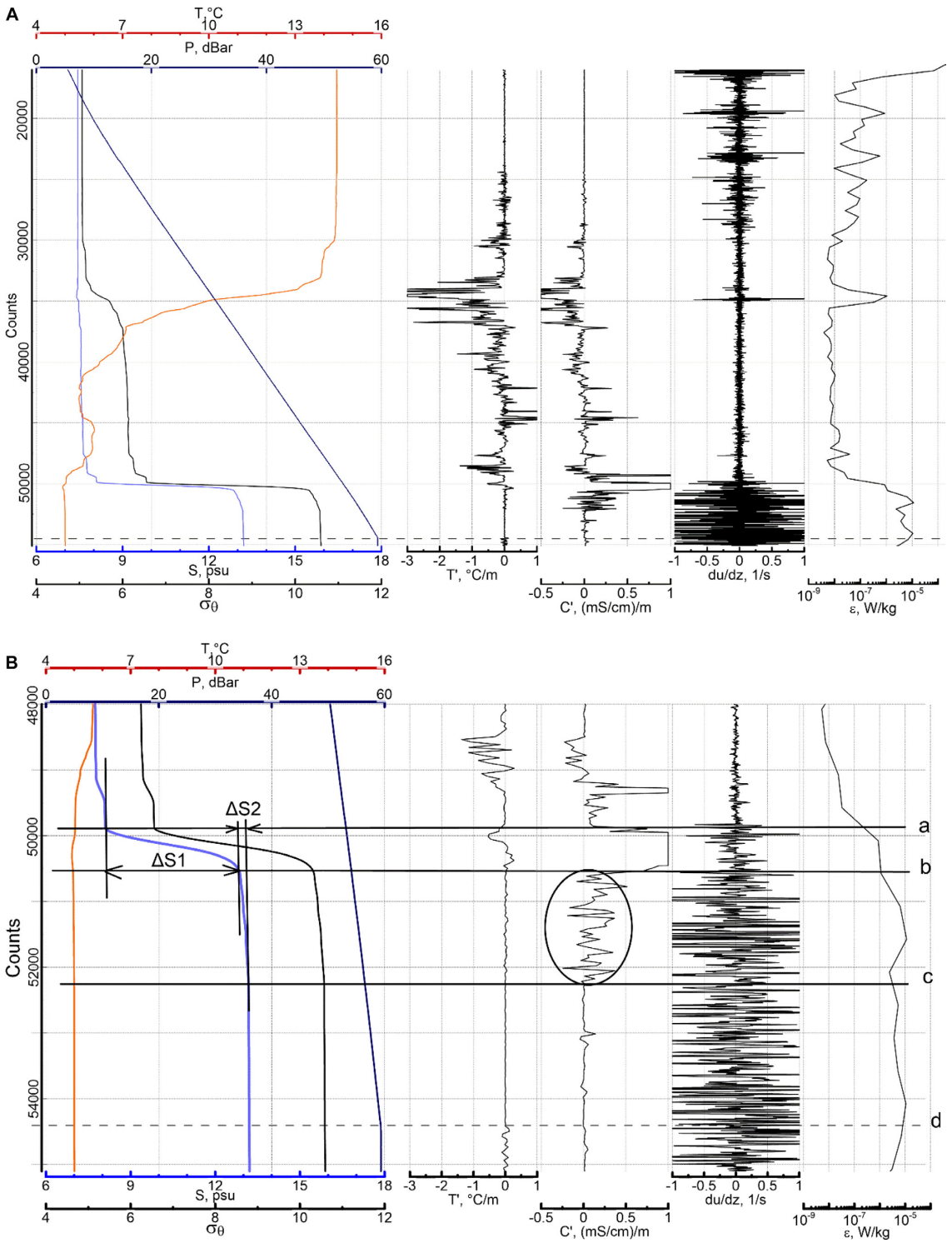

FIGURE 10 | (A) Example of turbulent bottom layer on the Słupsk Sill, the profile was registered on 02.07.2017, 19:40 at the following position: 55° 13.167′N, 16° 33.423′E. A westerly wind of 5–15 m/s prevailed. On the left panel: temperature T, °C; salinity S, psu; density σ_θ, pressure P, dBar. On the next panels from left to right: microstructure of temperature T′, °C/m and conductivity C′, (mSim/cm)/m; shear velocity fluctuations du/dz, 1/s; dissipation rate ε, W/kg. Dashed line marks the moment when the probe reaches the seabed and the pressure signal becomes constant. **(B)** Zoomed fragment of the profile shown in **(A)** presenting the fine- and micro- structures of the salt/dense bottom layer. Horizontal solid lines show upper bounds of (a) high gradient sheet, (b) moderate gradient sublayer (entrainment layer), (c) homogeneous sublayer; dashed line (d) marks the end of profiling. Ellipse marks a segment of developed conductivity microstructure. Crossing of the salinity plot with vertical lines show where salinity increments $\Delta S1 = 4.68$ psu and $\Delta S2 = 0.29$ psu were evaluated.

possible to allocate two sublayers, analyzing the microstructure not only for the shear velocity du/dz, but also for temperature T′ and conductivity C′, the last is a function of temperature fluctuations because the salinity gradient is weak. The surface sublayer is characterized by maximum dissipation rate and by completely smooth scalar fields. In the next sublayer, there are a noticeable scalar microstructure and decrease of dissipation rate. It can be noted that this feature corresponds to the erosion of a thermocline under the influence of turbulent entrainment.

The layer situated between the seasonal thermocline and the permanent halocline is characterized by a well-developed microstructure of scalar fields. The core of this layer is the cold intermediate layer (CIL) with a temperature of 5.5°C at depths of 40–45 m. Being in permanent interaction with overlaying and underlying layers, CIL is subjected to continuous erosion, reducing its thickness. The distribution of density in the upper part of the intermediate layer is determined by temperature, while in the bottom part is determined by salinity. The density gradient is not as great as in the main halocline and, hence, it is not a big hindrance to stirring. As a result of such stirring, a scalar microstructure is formed, the intensity of which depends on the temperature and salinity gradients in the presence of a weak shear of the velocity originated by the independent motion of the upper and bottom layers. However, the level of turbulence here is small ($\varepsilon \approx 10^{-8}$ W/kg). Short sharp impulse on the plots of shear signal du/dz and dissipation rate ε at the depth of the thermocline is undoubtedly an artifact, the result of collision with the extraneous object.

Similarity of the microstructure of the temperature and conductivity fields is disturbed only near the halocline, which indicates that from this depth the determining factor becomes the distribution of salinity.

The bottom layer is easily distinguished by increased salinity and density. In July 2017, there was a 6 m thick bottom layer with a salinity/density increasing from 8.16 psu/6.55 σ_θ at the top of the layer to 13.16 psu/10.57 σ_θ at the bottom, with the temperature only slightly changed. The distribution of all parameters within the saltwater layer is not as homogeneous as what might have been expected due to the fact that the dissipation rate here reaches $\varepsilon = 10^{-5}$ W/kg. To show some peculiar properties of the turbulent bottom layer, let us consider its zoom in **Figure 10B**. There are three horizontal solid lines which mark the following: (a) an upper boundary of high gradient sheet that is 0.9 m thick and with a salinity increment of $\Delta S1 = 4.68$ psu; (b) a moderate gradient sublayer, or an entrainment layer that is 2.5 m thick—the salinity increment here is $\Delta S2 = 0.29$ psu; (c) a homogeneous sublayer that is 2.8 m thick with zero salinity increment. Dashed line (d) marks the end of profiling. The mentioned sheet and sublayers have different microstructure. Within the highest gradient sheet, the microstructure is not expected. The entrainment sublayer must have the microstructure due to entrained water of lesser salinity, and it is clearly seen in the conductivity signal. Temperature pulsations are insignificant, as the temperature in the bottom layer changes in narrow limits.

In October 2017 the bottom layer with increased salinity (up to 11.4 psu) and density (up to 9.0 σ_θ) also existed, but its properties changed as is clearly seen in **Figure 11**. There was no sharp interface. Within the bottom boundary layer, the previously mentioned homogeneity of the fields T, S, and σ_θ disappeared, while the microstructure of scalar fields appeared. This occurred due to the increasing of the density gradient and weakening of the turbulence; the dissipation rate decreased to the value of 10^{-8} W/kg, which was typical for the main part of the water column below the upper mixed layer.

Thus, we obtained quantitative data characterizing microstructure properties for two situations which could be considered as typical for the Słupsk Sill when the period of time passed from an MBI exceeds 1 year. The first situations correspond to the moderate activity of salt water overflow, when the elevation of the halocline in the Bornholm Deep with respect to the Słupsk Sill exists but is not very high, while the halocline in the Słupsk Furrow is situated deeper than the depth of the sill (see **Figure 7**). The second situation corresponds to interruption of the continuous overflow, when the difference of halocline depths at the west and east edges of the Słupsk Sill disappears (**Figure 8**). This occurs due to some kind of synoptic reasons, which are not extraordinary, which is why we consider this situation as also typical for the Słupsk Sill area.

Data of microstructure measurements performed in July 2017 revealed a high turbulence dissipation spot immediately beyond the sill in the near-bottom layer filled with eastward spreading saltwater (**Figure 10A**). Assuming a steady balance between the eastward advection of saltwater and the turbulent entrainment of fresher water from the above-lying layer, an approach was developed to quantitatively estimate the role of a topographic obstacle like the Słupsk Sill in mixing/transformation of saltwater based on direct measurements of dissipation rate of turbulence kinetic energy [see Zhurbas et al. (in press) for details].

Near-Bottom Currents

In the October 2018 cruise, the TCMs were planned to deploy in the Słupsk Sill overflow, known as a mixing hot spot of eastward spreading saline water, where an enhanced level of turbulence dissipation was repeatedly observed (Mohrholz and Heene, 2018; Zhurbas et al., in press). Unfortunately, the permission to work on the Słupsk Sill in October 2018 was not obtained from Polish authorities, so we had to search for "a proxy" for the mixing hot spot in the Russian economic zone. To do that, we addressed the results of modeling the bottom friction velocity u_* in the Baltic Sea (Zhurbas et al., 2018). The modeling showed that along the inflow water pathway in the Baltic Sea, there are several local sites where $P(u_* > 0.005 \text{ m/s})$, i.e., the probability to meet enhanced value of the bottom friction velocity $u_* > 0.005$ m/s for the modeling period 2010–2016, exceeded 0.5:$P(u_* > 0.005 \text{ m/s}) > 0.5$. These local sites that can be supposedly treated as the mixing hot spots of eastward/northward spreading saline waters, were located in the Bornholm Strait, the Słupsk Sill and the Słupsk Furrow outlet (a sill at the eastern end of the Słupsk Furrow), as well as at the eastern slope of the Hoburg Channel in a coordinate box (19.00-19.23°E, 55.73°-55.96°N) partially located in the Russian economic zone [see **Figure 11** of Zhurbas et al.

(2018)]. Therefore, we decided to deploy the TCMs within the latter coordinate box (see black asterisk in the map of **Figure 1**).

The current velocity 5-day long time series measured by the TSMs (see **Figure 12**) displays a number of striking features that can be formulated in the form of the following questions.

1. Why was the near-bottom current exceptionally unidirectional while its magnitude varied considerably within a range of 0.15–0.56 m/s?
2. Why did the direction of the current remain unchanged when the wind direction and force change?

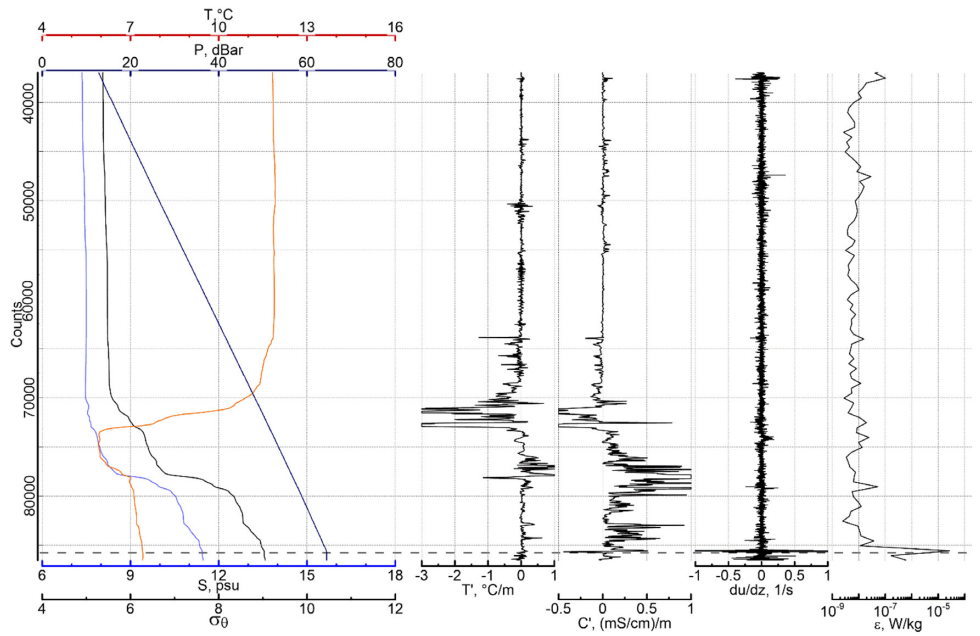

FIGURE 11 | Examples of non-turbulent bottom layer on the Słupsk Sill, the profile was registered on 18.10.2017, 14:03 at a position 55° 17.999′N, 16° 31.350′E. A westerly wind of 5–10 m/s prevailed. The presented variables are the same as in **Figure 10A**.

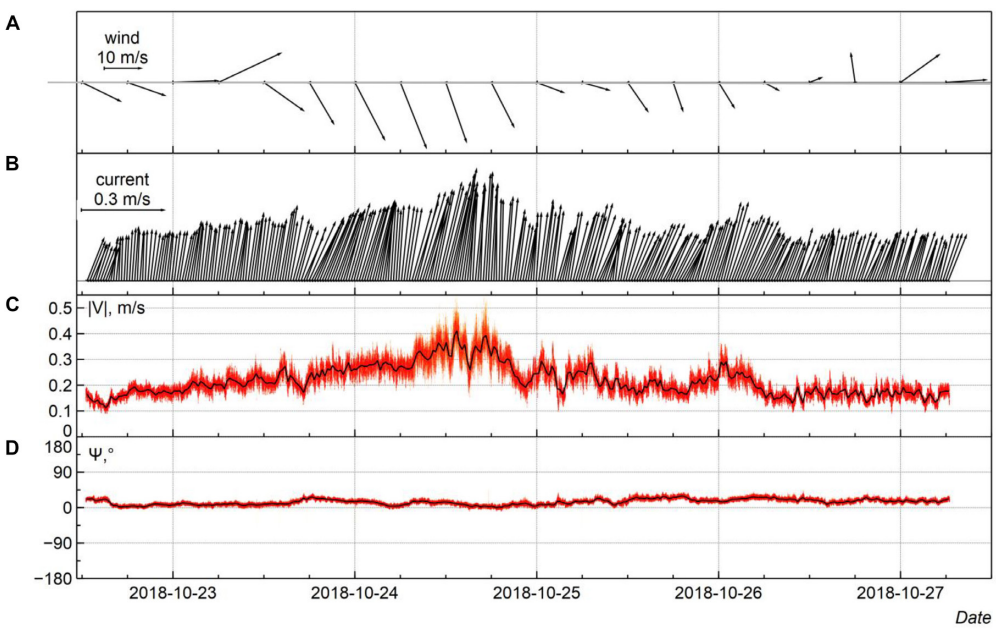

FIGURE 12 | The bottom current measured by TCM was installed on the eastern slope of the Hoburg Channel (see **Figure 5**) for the period 22–27.10.2018. **(A)** wind vectors with a 6 h interval for the point (19°E, 56°N) from the ECMWF database (www.ecmwf.int), **(B)** current velocity vectors, **(C)** current velocity magnitude |V| (red line is the instant current, black line is the 20 min running average value), **(D)** current direction Ψ relative to North and positive clockwise.

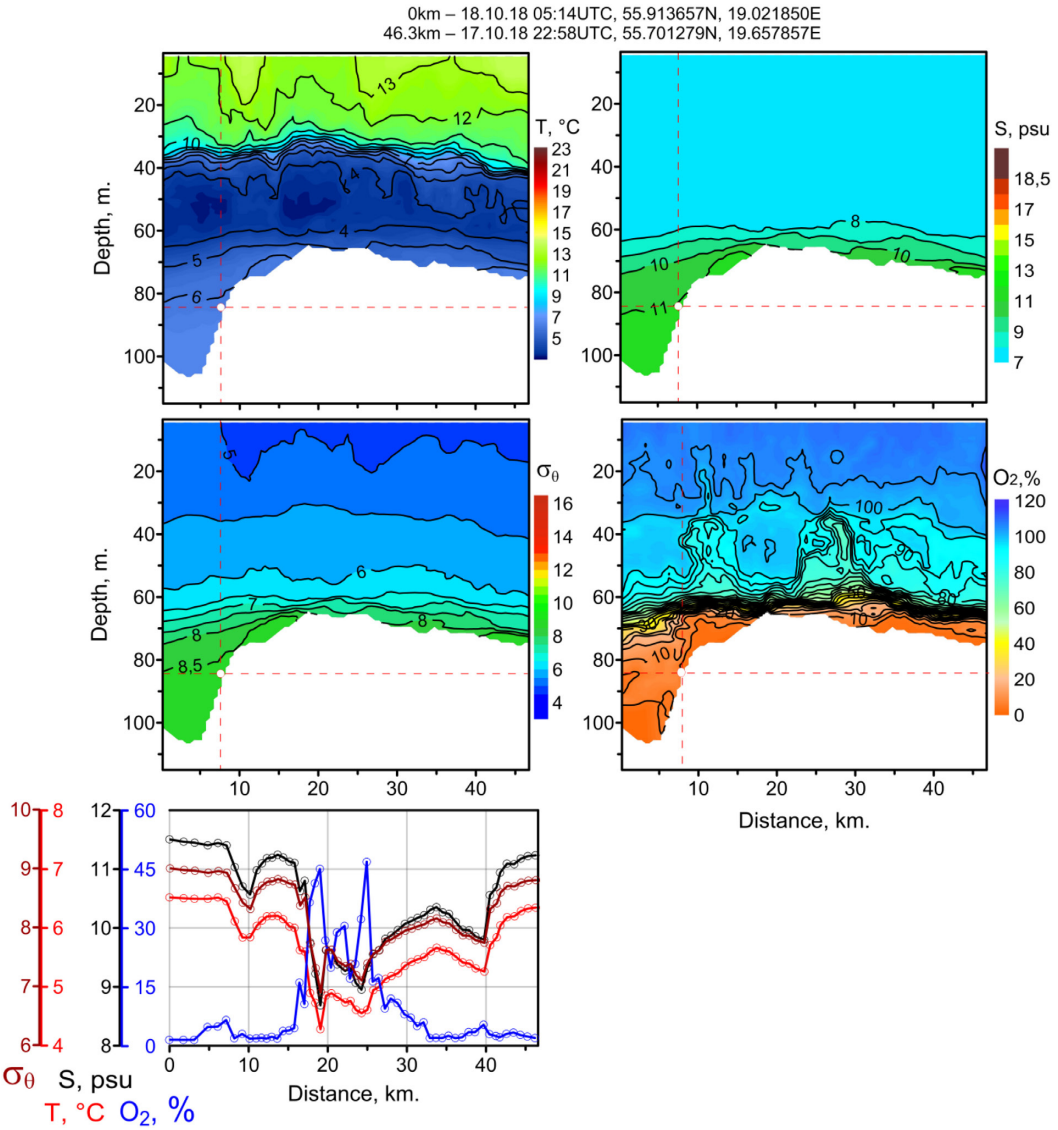

FIGURE 13 | Distributions of temperature T (°C), salinity S (psu), density σ_θ, and oxygen saturation O_2 (%) in a transect across the eastern rim of the Hoburg Channel passing through the TCMs deployment site. Position of the TCMs on the transect is marked by a small white bullet intersected by dashed lines. Bottom panels demonstrate graphs of the same parameters in the bottom layer.

3. Why was the flow not affected by inertial oscillations?
4. Why did the velocity of the NE near-bottom current increase largely (from 0.2 to 0.5 m/s) with the strengthening of the NW wind to severe gale?
5. What makes the TCM location exceptional, so that at the distance of only 0.5 m from the bottom, the flow velocity can reach values greater than 0.5 m/s?

A closely spaced CTD transect passing though the TCMs site (**Figure 13**) showed that TCMs were placed at the bottom in the midpoint of the eastern rim of the Hoburg Channel at a depth of 85 m, where the bottom tilt reaches a maximum value of $\gamma = 0.0074$ and the buoyancy frequency is as high as $N = 0.017\ s^{-1}$. The flow near the sloping bottom in stratified media is expected to be directed along the intersection of isopycnal surfaces with the inclined seabed surface. Therefore, if the isopycnal surfaces are horizontal, the near-bottom flow will be exactly aligned to the sea depth contours (isobaths). In fact, the isopycnal surfaces are not exactly horizontal, and, therefore, the near-bottom currents are only approximately aligned to the depth contours. Looking at the bathymetric map in **Figure 1** (or at the close-up in **Figure 5**) and the time series of the near-bottom current vector in **Figure 12**, one can see that the near-bottom flow was aligned to the sea depth contours, which does explain approximate constancy of the flow direction.

Looking at the potential density vs. distance and depth on the transect across the eastern rim of the Hoburg Channel (**Figure 13**), one can observe that the isopycnals in the saltwater

(halocline) layer are sloping down in the western direction, implying northward geostrophic transport in the near-bottom gravity current which is in accordance with the time series of the measured near-bottom current vector shown in **Figure 12**. Note that for geostrophic considerations in the near-bottom gravity currents, the reference level of zero geostrophic velocity should be adopted above the gravity current layer.

The inertial motion of a fluid particle with horizontal component of velocity U in a rotating media with the Coriolis parameter f implies anticyclonic (clockwise in the Northern Hemisphere) rotation of the particle with the period $2\pi/f$, so the diameter of the particle's trajectory is $D = 2U/f$. If the particle is at a height h above the inclined bottom with the slope γ, the inertial circular motion with diameter D will be possible only if $h/\gamma > D$ or $h > h_i = 2\gamma U/f$, where h_i is the height of bottom layer in which the inertial oscillations are hampered by the presence of the bottom slope. Having $\gamma = 0.0074$, $f = 1.21 \times 10^{-4}$ s^{-1} (for latitude 56°N), and $U = 0.2$–0.5 m/s we get $h_i = 24.4$–61.0 m. The time series of current velocity presented in **Figure 12** is free of inertial oscillations because it was measured at a distance of 0.5 m from the bottom, which is much smaller than h_i.

It can be seen from the bathymetric map (**Figure 1**) that in the vicinity of the TCM deployment point, the 70 m depth contour, which approximately depicts the lateral boundary of the saltwater reservoir in the lower layer of the Baltic Proper, turns sharply to the east, making the reservoir much wider. For this reason, the TCMs happened to be deployed in the "bottle neck" on the pathway of northward spreading saltwater. When the NW wind has grown to severe gale, the low-salinity water in the upper layer rushed to the southwest owing to the Ekman transport, causing an intensification of the oppositely directed northeast flow of the saltwater in the lower layer through the Hoburg Channel. The situation is quite similar to that of the Słupsk Furrow, where the northerly and easterly winds drive the westward transport in the upper layer and intensify the eastward transport of the saltwater in the lower layer of the Furrow, while the westerly and southerly winds result in weakening and even blocking the eastward transport of the saltwater through the Furrow (Krauss and Brügge, 1991; Zhurbas et al., 2012).

Keeping in mind that the flow velocity at $h = 0.5$ m above the bottom reached as large a value as $U = 0.5$ m/s, it seems interesting to estimate the corresponding value of the bottom friction velocity u_* and also the rate of dissipation of kinetic energy of turbulence ε based on the celebrated formulas of von Kármán's "law of the wall" [e.g., Paka et al. (2013)]:

$$u_*^2 = C_\mathrm{d} U^2,\ C_\mathrm{d} = \frac{K^2}{[\ln(h/z_0)]^2},\ \varepsilon = \frac{u_*^3}{Kh},$$

where C_d is the drag coefficient, $K = 0.4$ is the von Kármán's constant, and z_0 is the roughness parameter. The roughness parameter value adjusted in (Zhurbas et al., 2018) to fit the simulated and observed time series of bottom salinity, in particular the arrival time of the 2014–2015 MBI to BY15 (i.e., to the Gotland Deep), was $z_0 = 0.002$ m. Substituting $U = 0.5$ m/s at $h = 0.5$ m to the above formulas, we get $u_* = 0.036$ m/s, $\varepsilon = 2.3 \times 10^{-4}$ W/kg. Such large values of bottom friction velocity and dissipation undoubtedly indicate a high level of turbulence in the gravity current of northward spreading saline water in the Hoburg Channel.

SUMMARY AND CONCLUSION

By participating in experimental studies of the physical processes and environmental conditions in the Baltic Sea and analyzing published materials based on the results of the general environmental monitoring, the authors concluded that the volume and completeness of the information received do not meet the requirements of the scientific community.

First, this refers to high-resolution data on mixing, ventilation and circulation of deep waters, which, if obtained, are not regular. To increase the volume and quality of such data, it is necessary to carry out additional special monitoring that meets these requirements.

According to the presented materials, we managed to solve a number of innovative tasks necessary for the organization of a special monitoring exercise in accordance with the decisions of high-level international organizations and programs, establishing and financing projects on the protection of the Baltic Sea environment (European Commission, HELCOM, Interreg Baltic Sea Region, The NATO Science for Peace and Security, et al.).

In particular:

- A new technology of field works on hydrographic transects is developed that assumes the use of standard multiparameter probes, and the repeated casts are performed from the stern of the moving vessel. The probe drops vertically, its loose tether does not spoil the uniform sink but provides fast recovery using a rather simple longline hauler. This technique is not inferior to the previous "Tow-Yo CTD" method in technical efficiency, but surpasses it in terms of the volume and quality of information, including the characteristics of a fine structure in the water column and especially in the bottom layer, requiring neither powerful winches nor specially equipped research vessels. The main requirement to the vessel is not its size but its seaworthiness. In the near future, the new method of work on the vessel could allow carrying out special monitoring of the Baltic Sea and other seas, optimal by the criterion of data price-quality.
- A possibility to carry out regular measurements of microstructure without significant restrictions on weather conditions is shown. The proposed method of working with a quasi-free falling probe equipped with a magazine to store the required amount of tether can allow measurements in any areas of the Baltic Sea at any drift speed of the vessel, as well as at slow speeds moving forward against strong winds and sea swells. Field tests carried out in the area of the Słupsk Sill showed that the advanced system allows for the determination of the basic characteristics of the microstructure and the background thermohaline stratification but requires additional currents measurements. We hope to find a solution to this task in the near future.

- A possibility to fill the gap of data on the bottom currents is shown using an improved TCM model, the serial production of which can be provided by any manufacturer of oceanographic equipment, given the serially produced main metrological components to measure the tilt and orientation of the current meter—the 3D accelerometer and electronic compass—are already commercially available.

Comparison with the reference data obtained in the IOW monitoring cruises showed that the innovative technology of field work on hydrographic transects, consuming less ship time and fuel, is nevertheless able to provide measurements of oceanographic parameters in the near-bottom layer of the quality comparable with the quality obtained at the standard drift stations.

Among the interesting findings received thanks to the innovative measurement technology are the highest ever recorded temperature of 14.3°C in the halocline of the Bornholm Basin, measured after a baroclinic inflow event of early Autumn 2018, and the high rate of dissipation of turbulence kinetic energy in the near-bottom layer filled with eastward-flowing saltwater beyond the Słupsk Sill. But from our point of view, the most interesting result was obtained using the TCM.

Our search for the site for TCM deployment was based on the results of modeling of the bottom stress velocity in the Baltic Sea (Zhurbas et al., 2018); we sought to find a location with high probability to meet large bottom stress and, therefore, large velocity of near-bottom currents. Our attention was caught by a plot on the eastern rim of the Hoburg Channel which was in accordance to the simulations (Zhurbas et al., 2018) whereby the probability to meet $u_* > 0.005$ m/s exceeded 0.5, and the plot was located within the Russian Economic Zone. Our expectations were not misplaced: the TSM deployed there for a relatively short period of 5 days did record a current velocity of more than 0.5 m/s within a 1 m above the bottom depth of 85 m, which corresponds to large values of bottom friction velocity and a dissipation rate of $u_* = 0.036$ m/s, $\varepsilon = 2.3 \times 10^{-4}$ W/kg. Such a large value of the bottom friction velocity and dissipation rate undoubtedly indicated a high level of turbulence in the gravity current of northward-spreading saline water in the Hoburg Channel.

The close inspection of the bathymetry map showed that, figuratively speaking, the TCM happened to be deployed in the "bottleneck" on the pathway of the northward-spreading saltwater. For this reason, we plan to use this location as an easily accessible polygon for future field studies of near-bottom gravity flows and related turbulence using the innovative technologies described above.

AUTHOR CONTRIBUTIONS

VP provided measurements, data analysis, and interpreted field data. VZ and MG carried out data analysis and interpreted field data. AOK and AAK set up the equipment, provided measurements, and processed data. SS provided measurements.

FUNDING

Measurements and analysis of hydrodynamic parameters were performed within the framework of the IO RAS state assignment (Theme No. 0149-2019-0013); production of inclinometers was supported by the Russian Foundation for Basic Research (Grant No. 17-05-41196); the improvement of the sounding technique, the development of the design of inclinometers, as well as the analysis of the variability of currents depending on local geographic factors were supported by the Russian Foundation for Basic Research (Grant No. 18-05-80031); analysis of the data obtained by the microstructure probe was supported by the Russian Foundation for Basic Research (Grant No. 19-05-00962); the report on the results of measurements on transects and by inclinometers at an international conference was supported by the EU INTERREG Baltic Sea Region Program 2014–2020, Project DAIMON (Decision Aid for Marine Munition).

REFERENCES

Bełdowski, J., Jakacki, J., Grabowski, M., Lang, T., Weber, K., Kotwicki, L., et al. (2018a). "Best Practices in Monitoring," in *NATO Science for Peace and Security Series C: Environmental Security*, eds J. Bełdowski, R. Been, and E. Turmus (Dordrecht: Springer).

Bełdowski, J., Long, T., and Söderström, M. (2018b). "Introduction," in *Towards the Monitoring of Dumped Munitions Threat (MODUM). NATO Science for Peace and Security Series C: Environmental Security*, eds J. Bełdowski, R. Been, and E. Turmus (Dordrecht: Springer).

DAIMON Project (2019). *Decision Aid for Marine Munitions*. Available at: https://projects.interreg-baltic.eu/projects/daimon-22.html (accessed March 15, 2019).

Gelumbauskaite, L. Z., Grigelis, A., Cato, I., Repecka, M., and Kjellin, B. (1999). *Bottom Topography and Sediment Maps of the Central Baltic Sea LGT Series of Marine Geological Maps No. 1, SGU Series of Geological Maps BA No. 54, Scale 1:500000*. Vilnius: Lithuanian-Swedish project GEOBALT.

Golenko, N., Paka, V., Golenko, M., and Korzh, A. (2008). Meso-scale water structure in the southern Baltic in the summer of 2006. *J. Mar. Syst.* 74, S13–S19. doi: 10.1016/j.jmarsys.2008.01.015

Hansen, A. B., Carstensen, S., Christensen, D. F., and Aagaard, T. (2017). Performance of a tilt current meter in the surf zone. *Coast. Dyn.* 218, 944–954.

Krauss, W., and Brügge, B. (1991). Wind produced water exchange between the deep basins of the Baltic Sea. *J. Phys. Oceanogr.* 21, 373–384.

Matthäus, W., and Franck, H. (1992). Characteristics of major Baltic inflows - a statistical analysis. *Cont. Shelf Res.* 12, 1375–1400.

Mohrholz, V. (2018). Major Baltic inflows statistics – revised. *Front. Mar. Sci.* 5:384. doi: 10.3389/fmars.2018.00384

Mohrholz, V., Dutz, J., and Kraus, G. (2006). The impact of exceptionally warm summer inflow events on the environmental conditions in the Bornholm Basin. *J. Mar. Syst.* 60, 285–301.

Mohrholz, V., and Heene, T. (2018). *The Słupsk Sill Overflow – Mixing Hot Spot of the Eastward Spreading Saline Water*. Available at: https://www.baltic.earth/events/helsingor2018/material/2ndBalticEarthConferenceProceedings_IBESP_No13_lowres.pdf (accessed May 13, 2019).

Paka, V., Zhurbas, V., Rudels, B., Quadfasel, D., Korzh, A., and Delisi, D. (2013). Microstructure measurements and estimates of entrainment in the Denmark Strait overflow plume. *Ocean Sci.* 9, 1003–1014. doi: 10.5194/os-9-1003-2013

Paka, V. T., Rudels, B., Quadfasel, D., and Zhurbas, V. M. (2010). Measurements of turbulence in the zone of strong bottom currents in the Strait of Denmark. *Dokl. Earth Sci.* 432, 613–617.

Piechura, J., and Beszczyńska-Möller, A. (2004). Inflow waters in the deep regions of the southern Baltic Sea — transport and transformations. *Oceanologia* 46, 113–141.

Piechura, J., Walczowski, W., and Beszczynska-Möller, A. (1997). On the structure and dynamics of the water in the Słupsk Furrow. *Oceanologia* 39, 35–54.

Rak, D. (2016). The inflow in the Baltic proper as recorded in January–February 2015. *Oceanologia* 58, 241–247.

Rak, D., and Wieczorek, P. (2012). Variability of temperature and salinity over the last decade in selected regions of the southern Baltic Sea. *Oceanologia* 54, 339–354.

Sanderson, H., Fauser, P., Thomsen, M., Vanninen, P., Soderstrom, M., Savin, Y., et al. (2010). Environmental hazards of sea-dumped chemical weapons. *Environ. Sci. Technol.* 44, 4389–4394. doi: 10.1021/es90 3472a

Zhurbas, V., Elken, J., Paka, V., Piechura, J., Väli, G., Chubarenko, I., et al. (2012). Structure of unsteady overflow in the Słupsk Furrow of the Baltic Sea. *J. Geophys. Res. Oceans* 117:C04027. doi: 10.1029/2011JC00 7284

Zhurbas, V., Väli, G., Golenko, M., and Paka, V. (2018). Variability of bottom friction velocity along the inflow water pathway in the Baltic Sea. *J. Mar. Syst.* 184, 50–58.

Zhurbas, V. M., Paka, V. T., Golenko, M. N., and Korzh, A. O. (in press). Transformation of eastward spreading saline water at the Słupk Sill of the Baltic Sea: an estimate based on microstructure measurements. *Fundamentalaya i Prikladnaya Gidrofizika* 12.

Conflict of Interest Statement: The authors declare that the research was conducted in the absence of any commercial or financial relationships that could be construed as a potential conflict of interest.

frontiers in Earth Science

ORIGINAL RESEARCH
published: 12 June 2019
doi: 10.3389/feart.2019.00131

The Impact of Atmospheric Circulation on Air Temperature Rise in Estonia

*Merily Lakson[1], Piia Post[2] and Mait Sepp[1]**

[1] Department of Geography, University of Tartu, Tartu, Estonia, [2] Institute of Physics, University of Tartu, Tartu, Estonia

In comparison to the global average, the climate in the Baltic Sea region, including in Estonia, has warmed particularly fast. From synoptic climatology's point of view, a question can be posed: is this warming caused by changes in the frequency of particular circulation types or has warmer weather started accompanying these types? The main aim of the present study is to analyze the relationship between the increase of air temperature and changes in atmospheric circulation during the period of 1966–2015. Changes in the frequency of circulation types belonging to 12 classifications from the COST733 data set and changes in accompanying air temperature were analyzed. The circulation types were divided into "warm" and "cold" for a given season according to daily temperature anomalies in three Estonian meteorological stations. On the basis of the similar air flow direction, circulation types from different classifications were selected for inter-comparison. Linear trend analysis showed that there were only a few statistically significant ($p < 0.05$) changes in the frequency of circulation types. The major changes occurred in spring – the frequency of eastern and northeastern flow types decreased, and the frequency of types related to northwestern flow increased. However, the positive temperature anomalies increased for practically all circulation types. Particularly strong warming has taken place in winter "cold" types. In conclusion, the increase of Estonian air temperature during the analyzed period is more likely associated with the changes of temperature within circulation types than of their frequency.

Keywords: air temperature rise, atmospheric circulation, circulation types, Estonia, COST733

OPEN ACCESS

Edited by:
Markus Meier,
Leibniz Institute for Baltic Sea Research (LG), Germany

Reviewed by:
Anna Rutgersson,
Uppsala University, Sweden
Dimitrios Melas,
Aristotle University of Thessaloniki, Greece

***Correspondence:**
Mait Sepp
mait.sepp@ut.ee

Specialty section:
This article was submitted to Interdisciplinary Climate Studies, a section of the journal Frontiers in Earth Science

Received: *04 December 2018*
Accepted: *13 May 2019*
Published: *12 June 2019*

Citation:
Lakson M, Post P and Sepp M (2019) The Impact of Atmospheric Circulation on Air Temperature Rise in Estonia. Front. Earth Sci. 7:131. doi: 10.3389/feart.2019.00131

INTRODUCTION

Climate change, especially global warming is one of the major challenges of our time. The average global air temperature of the last decades is already about 0.8°C above the 20th century average of 13.9°C (IPCC, 2014; NOAA, 2018). However, the air temperature in the Baltic Sea basin is warming even more rapidly. In the Northern part of the Baltic Sea basin (north of 60°N) the annual mean temperature anomalies from 1871 to 2011 were 0.11°C per decade and in the Southern part (south of 60°N) 0.08°C per decade (BACC Author Team, 2015). Studies on Estonia have shown that the air temperature in Estonia has risen about 2°C during the last half century (Jaagus, 2006; Jaagus et al., 2014).

Estonia lies in the transition zone between maritime and continental climate on the eastern coast of the Baltic Sea (**Figure 1**). As the Baltic Sea and Estonia are situated in relatively high latitudes, atmospheric circulation is one of the principal factors that determines the climate variability here (Keevallik, 2003; Jaagus, 2006). The Baltic Sea region is mainly controlled by the North Atlantic Oscillation (NAO) and the impact of the NAO is most pronounced during the cold half-year from November to March (Hurrell, 1995; Hurrell et al., 2003; Keevallik, 2003; Kyselý and Huth, 2006; BACC Author Team, 2015). There are numerous studies linking changes in NAO indexes with changes in climate variables in Estonia (e.g., Keevallik, 2003; Jaagus, 2006; Jaagus et al., 2008; Jaagus and Suursaar, 2013). In general, rainy, and mild winters in Estonia, as well as decrease of the Baltic Sea ice (Jevrejeva et al., 2004) or increased storminess (Jaagus et al., 2008; Jaagus and Suursaar, 2013), can be explained by the domination of the positive phase of the NAO index. However, those connections are not persistent in time and space (Jevrejeva et al., 2004; Lehmann et al., 2017; Sepp et al., 2018) and contain some contradictions. For example, it is known that the NAO index shows long-term variability, but from the mid-1960s to the mid-1990s it was in a generally positive phase (Hurrell, 1995; Hurrell et al., 2003). After the mid-1990s, there was a trend toward more negative NAO index values (Hurrell et al., 2003; Kyselý and Huth, 2006), meaning that mild winters should have been replaced by severe winters. But this has not happened.

Various studies (Jaagus, 2006; Hoy et al., 2013; Cahynová and Huth, 2016) suggest that the changes in air temperature over the last decades have been due to the changes in atmospheric circulation. From synoptic climatology's point of view, air temperature rise may either be caused by increased frequency of particular "warm" circulation patterns or they started to bring warmer air masses. As mentioned in the previous section, many studies (e.g., Sepp and Jaagus, 2002; Jaagus, 2006; Hoy et al., 2013; Cahynová and Huth, 2016) indicate that warming in winter is mainly caused because the frequency of westerly circulation types that bring warm air from the ocean during winter have increased.

On the other hand, the internal variability of circulation types – for example, whether the types themselves have warmed up – has been rarely studied. Results from Beck et al. (2007) and Cahynová and Huth (2016) indicate that the long-term variations in climate and seasonal temperature trends can only partly be explained by the changing frequency of circulation types. They suggest that both frequency-related and within-type changes play a certain role in the observed climatic trends. However, Cahynová and Huth (2016) also emphasized that the observed climatic trends are rather caused by changing climate within circulation types in spring, summer and autumn.

The main objective of the present study is to analyze the relationships between the air temperature rise and changes in atmospheric circulation in Estonia during the period of 1966–2015. The questions we pose are (1) whether the air temperature change in Estonia is related to changes in the frequency of circulation types, and (2) has the air temperature relative to circulation types changed. In addition, we try to explain the reasons under the trends that have emerged in our study.

DATA AND METHODS

Air Temperature Data

We used temperatures from three meteorological stations – Vilsandi, Türi, and Jõhvi (**Figure 1**). Vilsandi is a coastal station representing the maritime climate region of Estonia, while Türi and Jõhvi are inland stations; the latter one represents a slightly more continental climate (Jaagus and Truu, 2004). Due to the non-homogeneity and missing data issues in earlier time series of these three meteorological stations, our data set consisted of daily average air temperature from the period of 1966–2015 obtained from the Estonian Weather Service.

Circulation Classifications

The variety of methods and algorithms used to classify daily circulation patterns is large (Yarnal, 1993; Huth et al., 2008). COST Action 733 "Harmonization and Applications of Weather Type Classifications for European Regions" gathered and analyzed a set of 33 methods or algorithms that have been used to classify daily circulation patterns (Philipp et al., 2016; Tveito et al., 2016). This comprehensive set consists of well-known manual classifications, where the expertise of meteorologists has been applied up to methods that are used in data mining and machine learning. A lack of inherent structure in the daily fields of classified variables is the reason why there is no clear statistical ground to prefer any of these known methods (Philipp et al., 2016). Huth et al. (2016) conclude that different classification methods tend to perform differently, depending on number of classes, season, climate variable, size of the domain and the region. This means that for a certain purpose a variety of methods should be assessed to obtain unbiased and generalizable results.

We selected seven circulation classification methods which performed best with temperature in small domains (Huth et al., 2016) from this COST733 data set (see **Table 1**). These classifications belong to the following methodological groups: threshold-based classifications, principal component analysis-based and optimization methods. Threshold-based classifications rely on the concept of subjectively pre-defined types, which are assigned automatically by using threshold values for certain indices. Most often the indices characterize the strength of large-scale air flow meridional and zonal components and vorticity. Principal component analysis-based classifications are grounded in empirical orthogonal functions of various matrixes, either in S- or T-mode [KRZ uses S-mode, i.e., grid points correspond to rows of the data matrix and time realizations (days) to its columns]. The idea of optimization methods is to arrange the whole set of objects under study (the objects here are days with different circulation patterns) into groups (circulation types) in such a way that a certain function is optimized. In most circulation classifications based on optimization methods, the purpose of this optimization is to minimize the within-type variability measured as the overall sum of the Euclidean distances between the member objects of a type and the average of the type (centroid). Here are represented k-means clustering algorithm (CKM, CAP) as well as hierarchical clustering (HLC) (Philipp et al., 2016; Tveito et al., 2016).

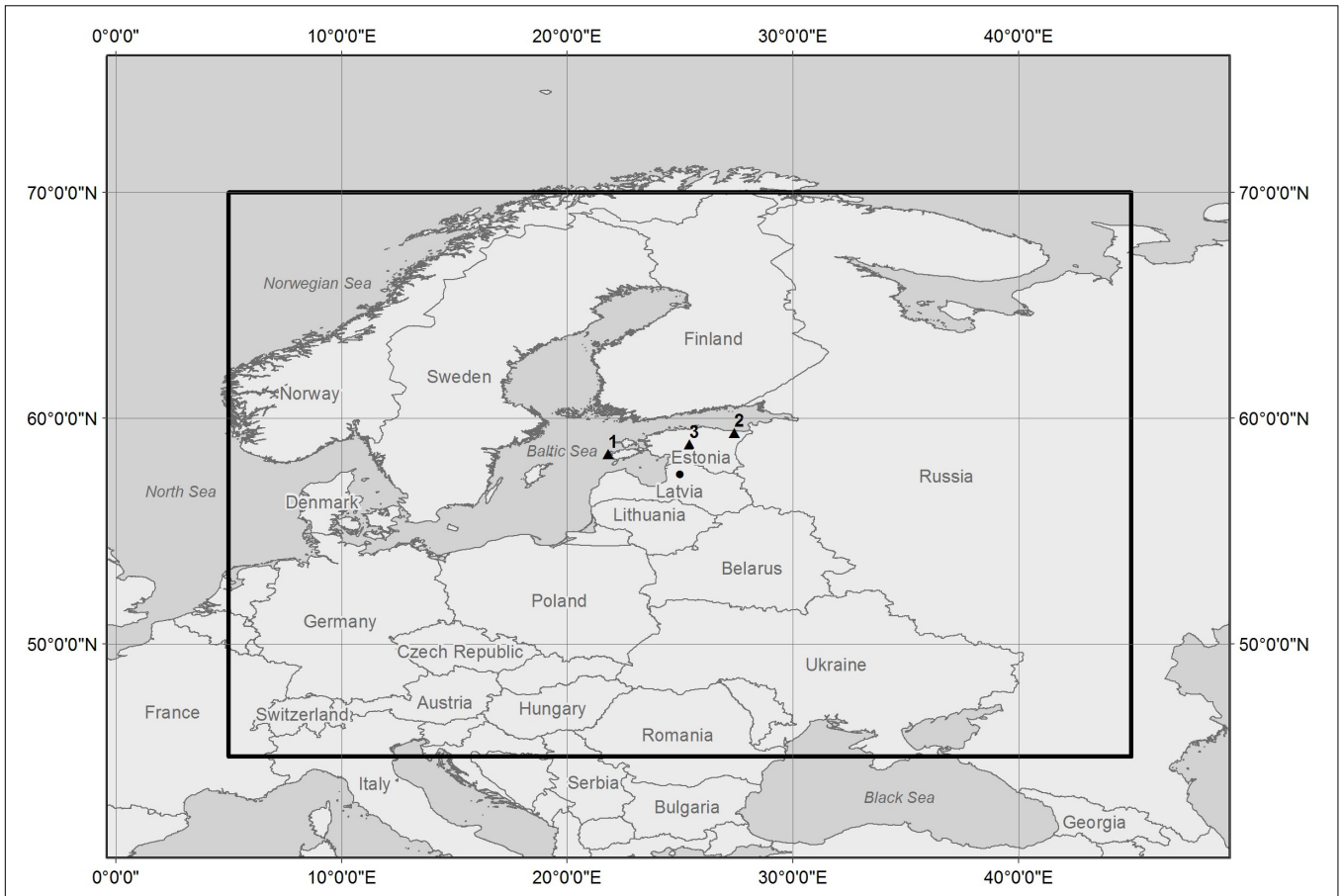

FIGURE 1 | Study area. Dark line: the border of the domain. Black dot: the center of the domain. Triangles: positions of meteorological stations (1, Vilsandi; 2, Jõhvi; 3, Türi).

TABLE 1 | Classification methods applied in the present study, the list includes abbreviations used within this paper, commonly used names of the methods, the key references of methods and the methodological group.

Abbrev.	Classification name	Implemented methods	Key references	Classification group
JCT	Jenkinson–Collison classification	Automatized scheme for Lamb weather types	Jenkinson and Collison, 1977	Threshold-based
GWT	Grosswetter-types	Correlation based, with raw or normalized vorticity coefficients	Beck, 2000; Beck et al., 2007	Threshold-based
LIT	Litynski	Thresholds on a single circulation field	Litynski, 1969	Threshold-based
KRZ	Kruizinga P27	Principal component analysis-scheme, S-mode	Kruizinga, 1979	Principal component analysis based
CKM	k-means (differing start partitions)	Simple k-means algorithm with most different start partitions, skipping small clusters < 5% population	Enke and Spekat, 1997	Optimization algorithm
CAP	k-means (Ward's start partition)	11-day low pass filtrated data, S-mode PCA, ward-clustering, k-means	Yarnal, 1993	Optimization algorithm
HCL	Complete Linkage	Hierarchical cluster analysis one of seven different algorithms	Murtagh, 1985	Optimization algorithm

For further details, (see Philipp et al., 2016; Tveito et al., 2016).

Daily fields of mean sea level pressure fields from NCEP/NCAR reanalysis (Kalnay et al., 1996) are classified into circulation types for the period 1948–2015. As we need to use a rather large sample of methods that are applied in the same way to the same data set, then we used a cost733class software (Philipp et al., 2016). Cost733class is an open source software package that has been developed especially for creating, comparing and evaluating classifications in various versions (Philipp et al., 2016). All methods from the COST733 data set have been programmed there as subroutines in order to apply

it to the same input data. This software enables people to use their own data files, to vary the number of types, to classify the whole year or only by season, etc. If the same parameters are used for all the methods, then the differences among classification results may be ascribed to the classification algorithm itself and not to the different ways they are used (Philipp et al., 2016). We used the nine type versions of classifications only. However, several classifications have two versions, either with 8 and 10 (GWT) or 9 and 10 types (CKM, CAP, HCL), thus altogether 12 classifications (**Table 1**) were compared here.

The calculations produced catalogs of classifications, where each day is specified by one certain circulation type from every classification. As we used only Estonian air temperature point measurements, and the types characterize circulation best in the center of the domain, we calculated classifications for the domain 5° E – 45° E and 45°N – 70° N, centered in 25° E and 57.5° N (**Figure 1**). Our domain size is remarkably smaller than the area that is characteristic for the NAO type of atmospheric teleconnections, which are known not to influence local weather in summer. However, we can assume that circulation types, created specifically for a small domain, reflect local specificities as well.

The maps of GWT10 circulation types for our domain are shown in **Figure 2**. Presented are eight main directional types

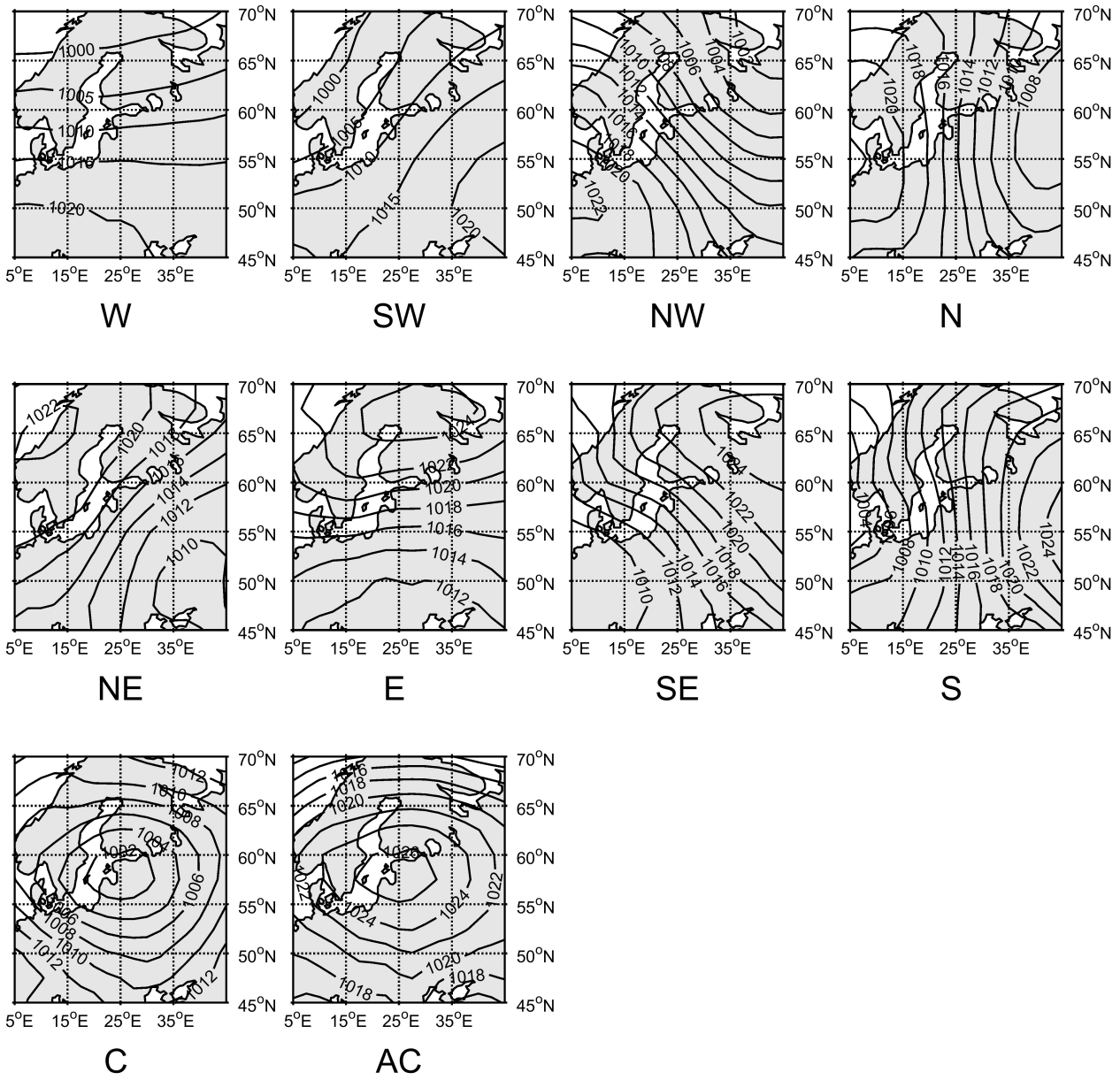

FIGURE 2 | Mean sea level pressure values for GWT10 weather types estimated from daily values for 1948–2015. Directional types W, SW, NW, N, NE, E, SE, S, and C – cyclonic and AC – anticyclonic type.

plus the cyclonic (C) and anticyclonic types (AC). The size of the domain suits the synoptic scale: the positions of one cyclone and anticyclone determine the geostrophic air flow over the domain. The circulation types are derived by calculating correlations with prototype fields of zonal flow, meridional flow and cyclone in the center of the domain (Beck et al., 2007). Types are easily interpretable and the days belong to the same types regardless of whether a different period is used for classification.

Methods

All the analysis is carried out using the common seasons – spring (MAM), summer (JJA), autumn (SON), and winter (DJF). December belongs to the preceding year and because of that, the winter time series is shorter by 1 year (1967–2015). Annual averages were not used here as the same circulation type can cause warm weather in summer and extreme cold in winter.

As a first step we defined "warm" and "cold" circulation types – i.e., types that are accompanied by either positive (warm) or negative (cold) air temperature anomalies during the given season. For that we calculated the daily long-term average temperatures for the period of 1966–2015; the 29 of February was left out. As the daily average air temperature varies highly between years (especially in winter), some random extreme values can significantly bias circulation types' long-term average temperatures. Thus, we approximated annual air temperature by cosine function (**Figure 3**). The Excel function "Solver" was used to find the optimal parameters for the function.

Thus, the temperature anomaly is a deviation from the idealized air temperature curve. As a next step we sorted out daily temperature anomalies for each given circulation type. If the long-term average temperature anomaly for a season was positive, the circulation type was considered as "warm" – if negative, then "cold."

We wanted to intercompare the circulation types from various classifications from the side of airflow direction that is considered, in our minds, to represent either cold or warm advection. We calculated a catalog of circulation types that in most cases are somewhat anonymous, i.e., the name of the type is just a number. The task of circulation classifications is to describe the highly variable atmospheric circulation by dividing the daily airflow patterns into a quite small number of characteristic classes/types. In this study we used classifications with nine types. It is reasonable to assume that if these kinds of discrete states really exist, then all classifications should contain types with similar flow patterns according to the positions of low- and high-pressure areas. In order to understand which types represent similar circulation conditions we, at first, visually intercompared mean sea level maps of all circulation types from all classifications. We classified the circulation types according to the similarity of air flow directions and used GWT10 types as the reference due to the straightforward interpretation of its ten circulation types (Cahynová and Huth, 2016).

As the numbers of types in classifications were the same and the majority of patterns in different classifications were visually very similar, an overlap analysis was conducted. The main aim of this analysis was to understand whether the types of similar airflow from different classifications occur at the same day. We compared GWT10 types with other classifications' similar circulation types and counted in how many days similar types co-occurred.

Linear trend analysis ($p < 0.05$) was used to describe changes in time series of circulation types and air temperature in the period of 1966–2015 as well as in the sub-periods 1966–1991 and 1992–2015. In addition, we analyzed trends for 30-year sub-periods to show how sensitive the sign and magnitude of the trend are depending on the starting and ending point.

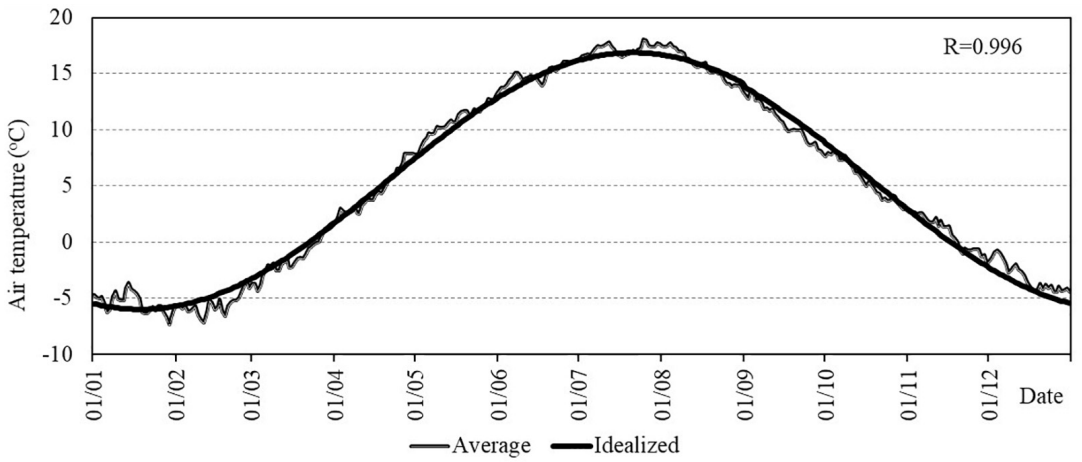

FIGURE 3 | The modeled (idealized) daily average temperature of Türi station for the period 1966–2015 and the daily long-term average temperature of the same period. The correlation coefficient R was found between the model and the average temperature for each calendar day averaged over all years. Türi idealized temperature X was calculated using the following equation:

$$X = -11.429 \cdot cos\,(0.017098 \cdot t + (-2.40077)), \quad (1)$$

where t is the day of year.

RESULTS AND DISCUSSION

Although the Türi, Vilsandi, and Jõhvi meteorological stations represent different microclimatic regions of Estonia, no substantial differences occurred in the results of these three stations. Thus, here we demonstrate only the results of Türi station as it represents the majority of air temperature variations on the Estonian mainland.

The overlap analyses showed somewhat controversial results. On one hand the patterns of circulation types of different classifications are visually very similar with each other and well compatible with the corresponding patterns of the GWT10 types. Still, some classifications do not contain certain patterns and some patterns are not comparable with GWT10 patterns. The percentage of co-occurrence of similar circulation type with a corresponding GWT10 type is also relatively low (**Table 2**). These results suggest that although the averaged maps of circulation types may look similar, the sets consist of actually quite variable circulation conditions. This supports the understanding (Philipp et al., 2016; Tveito et al., 2016) of why so many different methods are needed to classify circulation patterns, and there is not just one best classification that exists. Philipp et al. (2016) found that even the same group classification methods show often low similarity. This is also the reason why the following results are presented in a generalized mode, and analysis of any exact circulation type is avoided if possible.

Defining "warm" and "cold" types gave rather expected results (**Table 3**). Air temperature anomalies showed clearly the advection of relatively cold or warm air masses. Thus, Northern types (N) are accompanied by negative temperature anomalies in every season and South-Western types (SW) are "warm" types all year around. Western types (W) represent the advection of maritime air masses from the North Atlantic that are relatively warm in winter but cold in summer. In general, Eastern types (E, NE, and SE) can be associated with the advection of continental air masses being extra cold in winter and extra warm in summer. In the case of the AC, a high pressure area is located in the middle of the domain, taking along radiative cooling in winter and warming in summer.

TABLE 2 | Visually similar circulation types and percentage of co-occurrence. First column: names of classifications.

GWT10	W	SW	NW	N	NE	E	SE	S	C	AC
JCT10	1/44	8/45	2/46	**3/54**	4/42	5/37	6/49	**7/55**	**9/71**	**10/82**
HCL10	2/32	5/18	8/23	**10/72**	–	**9/91**	4/37	1/35	**3/67**	–
HCL09	2/32	5/18	8/23	**3/89**	–	**9/91**	4/37	1/35	–	–
CKM10	6/21	4/31	8/38	–	**1/53**	**3/60**	–	7/43	–	5/29
CKM09	4/24	2/30	1/41	–	**3/78**	–	–	**7/51**	–	**5/51**
CAP10	2/29	5/26	8/46	**10/91**	–	**9/92**	**4/66**	6/37	**3/61**	**1/52**
CAP09	2/28	5/26	8/47	**3/93**	–	**9/94**	**4/68**	6/36	–	**1/61**
LIT09	7/39	6/45	8/47	1/47	**2/75**	**3/66**	**4/72**	5/36	–	9/26
GWT08	**1/100**	**2/100**	**3/100**	**4/100**	**5/100**	**6/100**	**7/100**	**8/100**	–	–
KRZ08	–	1/45	3/37	**7/54**	**8/52**	–	5/50	–	–	–
KRZ09	2/37	**1/59**	3/47	–	**9/71**	**8/80**	**7/86**	**4/59**	–	5/28

For details, (see Philipp et al., 2016). Header of columns show the air flow directions by the nomenclature of GWT10 types: W is west, SW is southwest, etc., C is cyclonic, AC is anticyclonic type. First number in cells represents the name of the type, second is the percentage of co-occurrence of the type with corresponding GWT10 type. In bold: percentages higher than 50.

TABLE 3 | "Warm" and "cold" types.

Type	DJF	*SD*	MAM	*SD*	JJA	*SD*	SON	*SD*
N	−1.9	*0.8*	−1.9	*0.3*	−0.9	*0.2*	−2.6	*0.3*
NE	−4.5	*0.9*	−1.7	*0.7*	**0.3**	*0.5*	−2.6	*0.4*
E	−5.8	*0.8*	−0.6	*0.3*	**1.7**	*0.3*	−2.3	*0.3*
SE	−4.2	*0.5*	**1**	*0.8*	**2.7**	*0.7*	−1.2	*0.4*
S	−0.9	*0.8*	**1.4**	*0.3*	**1.5**	*0.5*	**0.5**	*0.4*
SW	**2.3**	*1.6*	**1.2**	*0.5*	**0.7**	*0.5*	**1.7**	*0.8*
W	**3.6**	*0.5*	**0.6**	*0.2*	−0.6	*0.3*	**1.2**	*0.4*
NW	**1.8**	*1.1*	−0.3	*0.5*	−1.4	*0.6*	−0.8	*0.5*
AC	−2.9	*1.1*	−0.1	*0.4*	**1.3**	*0.8*	−1.4	*0.7*
C	−1	*1.3*	−0.6	*0.7*	−0.4	*0.5*	−1.1	*0.5*

Average air temperature anomalies (in °C) of all types in winter (DJF), spring (MAM), summer (JJA), and autumn (SON), and standard deviation (SD, in °C), based on data of Türi station. Positive anomalies ("warm" types) are in bold.

Values of air temperature anomalies shown in **Table 3** are averages of long-term mean anomalies of all classifications. The relatively high standard deviation suggests again that similar types represent slightly different circulation conditions and may cause somewhat different weather. For example, CKM10 type SW is accompanied by a temperature anomaly of −0.6°C and the same SW type of CAP10, CAP09, and LIT09 by +3.8°C in winter. However, in general, there are only a few types whose "cold" or "warm" status would differ from the one presented in **Table 3**.

As several circulation types showed opposite air temperature anomalies in winter and summer, we analyzed trends in frequency and air temperature anomalies by seasons.

Winter

Based on the literature, the most drastic climate changes in Estonia have occurred in winter. For example, the long-term average air temperature has increased by 4°C in January during the last half century (Jaagus, 2006; Jaagus et al., 2017). All those changes have been reported both in Estonia (Tomingas, 2002; Jaagus, 2006; Jaagus et al., 2008) and in Europe (Kyselý and Huth, 2006; Cahynová and Huth, 2010, 2016; Küttel et al., 2011; Hoy et al., 2013; Kučerová et al., 2017) to be concurrent with the increase in the frequency and magnitude of western circulation. The increase in the frequency of the Western type has been explained by the NAO positive phase after the 1960s (Hurrell, 1995; Jaagus, 2006). Jaagus et al. (2008) found that the Western type became more frequent in winter at the expense of the cold eastern type. However, our analysis showed no such tendencies. Statistically significant changes in the frequencies of circulation types occurred only in a few classifications during the period of 1967–2015. Virtually no changes occurred in Western types (SW, W, NW, **Table 4**).

When looking at the temperature anomalies associated with circulation types at Türi station, the majority of analyzed time

TABLE 4 | Long-term average (1966–2015) frequency of circulation types (in days) and changes by trend line in days per the period in winter [DJF (A)] and long-term average air temperature anomalies (in °C) at Türi station associated with particular circulation types and changes by trend line in °C in winter [DJF (B)].

DJF (A)	W	SW	NW	N	NE	E	SE	S	C	AC
GWT10	28/2	18/1	11/0	4/1	2/1	3/0	5/2	9/−4	4/−1	8/−3
JCT10	14/5	14/5	9/−1	5/1	3/0	3/0	6/−2	**11/−6**	12/−1	14/−4
HCL10	29/2	9/4	5/2	8/0	–	10/1	5/−2	20/−6	4/0	–
HCL09	29/2	9/4	5/2	12/0	–	10/1	5/−2	20/−6	–	–
CKM10	26/8	10/2	21/−3	–	7/0	7/2	–	**10/−5**	–	11/−3
CKM09	29/6	10/2	21/−2	–	7/2	–	–	**10/−5**	–	14/−3
CAP10	23/4	13/6	9/−1	6/1	–	6/0	8/−1	11/−2	6/−3	10/−4
CAP09	23/4	13/5	12/−3	6/1	–	6/1	9/0	11/−3	–	**9/−5**
LIT09	10/3	10/4	12/1	10/−1	9/1	10/−3	11/−4	10/−1	–	9/−3
GWT08	29/2	21/0	13/0	4/2	3/1	4/0	7/2	10/−5	–	–
KRZ08	–	31/2	29/0	5/1	6/0	–	18/−3	–	–	–
KRZ09	11/0	19/−7	26/1	–	**4/3**	6/−2	10/0	**10/−7**	–	5/−1
DJF (B)	**W**	**SW**	**NW**	**N**	**NE**	**E**	**SE**	**S**	**C**	**AC**
GWT10	**3.3/3.3**	**1.5/3.8**	1.2/2.1	**−2.1/6.2**	**−6.3/3.5**	−6.7/3.2	−4.4/−0.5	−1.7/−0.3	**0/4.4**	−4.5/−0.4
JCT10	**4.6/3.3**	**3/3.6**	3.1/1.8	**−0.7/4**	**−4.2/3.4**	−6.6/2.3	−4.6/−1.8	−1.4/1.9	**0.7/2.9**	−3.2/0.1
HCL10	**3.3/2.8**	3.7/1.8	2.3/−1	**−2/3.3**	–	−6/1.5	−4/−1.7	−0.9/1.8	**−2.4/4.1**	–
HCL09	**3.3/2.7**	3.7/1.8	2.3/−1	**−2.1/3.4**	–	−6/1.5	−4/−1.7	−0.9/1.8	–	–
CKM10	4.2/2.3	−0.6/1.4	**1/2.4**	–	−4/3	−4.5/−0.3	–	−0.9/2.2	–	−3.5/0
CKM09	**4/2.7**	−0.5/1.4	**0.1/2.4**	–	−4.5/1.9	–	–	−1.2/1.6	–	−3.7/−0.4
CAP10	**3.7/3.2**	3.8/1.6	1.5/−0.1	**−2.8/4.5**	–	−6.3/0.8	−4.5/−2.1	0.1/0.9	**−2.2/5.1**	−2.3/0.6
CAP09	**3.5/3**	3.8/1.7	0.8/−0.7	**−2.7/5.3**	–	−6.2/1.3	−4.1/−1.8	0.1/0.9	–	**−3.3/3.7**
LIT09	4/1.9	3.8/2	4.1/1.8	**−0.2/3.8**	**−3.8/3.6**	−4.2/1.4	−2.9/0.5	**0.6/2.6**	–	**−0.7/3.2**
GWT08	**3/3.4**	**1.1/3.5**	0.8/2.3	**−2.3/4.9**	−5.6/2.6	−6.1/2	−4.7/−1.9	−2/0.8	–	–
KRZ08	–	**1.7/3.5**	**2.6/2.4**	**−2.3/5**	**−4.2/5.3**	–	−4/−1	–	–	–
KRZ09	**3/3.4**	**2.4/2.6**	2.2/2	–	−3.5/1.7	**−5.3/3.2**	−4.4/−3.1	−1.5/1.4	–	**−2.1/4.6**

Statistically significant changes ($p < 0.05$) are in bold.

series show drastic increasing trends (**Table 4**). It is important to note that "cold" types have warmed up relatively more than "warm" ones, especially N and NE types. In general, those two types represent the advection of Arctic air masses. Some negative trends occurred in types of NW group.

Spring

As the winters become warmer and shorter, the springs start earlier and are warmer in Estonia (Keevallik, 2003; Ahas and Aasa, 2006; Jaagus, 2006; Schwartz et al., 2006; Jaagus et al., 2017). Our analysis showed that most of the statistically significant changes in the frequency of circulation types occurred in spring. Based on trends, we can observe certain shifts in atmospheric circulation: the occurrence of E and SE types have decreased while the frequency of extra cold N and cold NW types have increased (**Table 5**). This suggests that springs must have become cooler. However, the trends in the air temperature time series indicate exactly the opposite (**Table 5**). Basically, all circulation types have become significantly warmer during the period 1966–2015.

Summer

No significant changes in Estonian summer climate have been reported. The exception is the cooling tendency in June (Jaagus, 2006). Also, there were only a few statistically significant changes during 1966–2015 in our analysis. In general, we can talk only of some decrease (by ca 6 days) of NE type frequency and increasing tendencies of SE and S types' frequencies (by 3–4 days). Those mentioned above are all warm types. The average temperature anomaly that accompanies the SE, S, and NE types is +2.7°C, +1.5°C, and +0.3°C, respectively.

Changes in air temperature indicate that almost all "warm" types have become cooler (except NE) and "cold" types warmer (except C) by about 1.5°C.

Autumn

Similar to summer, signals of climate change in autumn are reported to be somewhat vague (Jaagus, 2006). Our analysis also revealed just a few statistically significant changes in the frequency of types. Only the frequency of NW types has decreased by up to 6 days. However, almost all circulation types show positive trends in air temperature anomalies. In general, most intensive warming is characteristic for "warm" autumn types (S, SW, and W) which have become warmer by 1.7–2.9°C.

Plausible Reasons

The results of our trend analysis are somewhat contradictory. On one hand, the general lack of trends in time series of

TABLE 5 | Long-term average (1966–2015) frequency of circulation types (in days) and changes by trend line in days in spring [MAM (A)] and long-term average air temperature anomalies associated with circulation types at Türi station and changes by trend line in °C in spring [MAM (B)].

MAM (A)	W	SW	NW	N	NE	E	SE	S	C	AC
GWT10	17/3	14/−2	**9/7**	**5/3**	6/−1	**10/−6**	8/−3	9/−2	5/0	10/1
JCT10	9/1	10/−3	**8/6**	7/2	6/−1	**6/−3**	6/−2	9/−3	11/−1	20/4
HCL10	14/5	2/−1	**3/3**	**12/5**	–	23/−6	**5/−3**	24/−3	10/1	–
HCL09	14/5	2/−1	3/3	**22/6**	–	**23/−6**	**5/−3**	24/−3	–	–
CKM10	9/−1	12/0	**17/10**	–	18/1	**18/−8**	–	12/0	–	6/−2
CKM09	11/1	13/−2	**22/12**	–	**23/−7**	–	–	14/−1	–	9/−3
CAP10	12/1	4/−2	**5/5**	**11/7**	–	**18/−7**	9/−5	7/−2	14/1	12/1
CAP09	13/2	4/−2	**8/6**	**12/7**	–	**18/−7**	10/−4	7/−3	–	19/2
LIT09	9/2	11/0	**11/8**	10/3	9/0	**11/−5**	**11/−8**	11/−1	–	**10/8**
GWT08	18/3	17/−3	**11/9**	**6/3**	8/−1	**11/−6**	10/−3	10/−2	–	–
KRZ08	–	20/−5	**18/9**	11/2	13/3	–	**30/−16**	–	–	–
KRZ09	9/−1	9/−2	**17/10**	–	**10/4**	14/−3	**14/−7**	11/−2	–	10/1
MAM (B)	**W**	**SW**	**NW**	**N**	**NE**	**E**	**SE**	**S**	**C**	**AC**
GWT10	**0.5/1.9**	1.5/1.3	**−1/2.3**	**−2/1.8**	**−2.2/2.4**	**−0.8/2.8**	**1.4/2.2**	**1.7/2**	**−1.1/2**	**−0.2/2.6**
JCT10	**0.8/1.9**	**1.1/2.1**	**−0.4/1.5**	**−1.7/2.4**	**−2.2/3**	**−0.5/3.3**	1.6/0.3	1.7/1.8	**−0.4/2.1**	**−0.1/1.5**
HCL10	**0.6/1.8**	1.9/0	0.4/1.3	**−1.8/1.8**	–	**−0.2/2.9**	1.3/2.2	**1/1.7**	**−1.3/2.1**	–
HCL09	**0.6/1.8**	1.9/0	0.4/1.3	**−1.6/1.7**	–	**−0.2/2.9**	1.3/2.2	**1/1.7**	–	–
CKM10	**1/1.5**	**0.4/1.9**	**−0.4/1.3**	–	**−1.2/2.3**	0/1.6	–	1.6/1	–	−0.7/2.6
CKM09	**0.8/1.6**	0.3/1.8	**−0.8/1.3**	–	**−0.5/2.0**	–	–	1.6/1.1	–	**−0.3/3.5**
CAP10	**0.6/3.2**	1.9/0	**−0.3/1.8**	**−2.2/1.7**	–	**−1/2.3**	**1.4/2.5**	1.5/1.1	**0.4/1.9**	0.4/1.7
CAP09	**0.4/2.9**	1.8/0.1	−0.1/1.1	**−2.3/1.6**	–	**−0.9/2.6**	−1.4/2.1	1.3/0.6	–	**0.6/1.8**
LIT09	**0.4/1.9**	**1.5/1.9**	**0.1/1.7**	**−1.5/2**	**−2.3/2.4**	**−0.9/2.7**	1.2/1.8	1.7/1.2	–	**−0.3/1.8**
GWT08	**0.4/2**	**0.9/1.5**	**−1/2.1**	**−1.8/1.8**	**−2.1/2.3**	**−0.7/3**	**1.2/2.4**	**1.3/1.8**	–	–
KRZ08	–	**0.8/1.5**	**0/1.5**	**−2.1/1.5**	**−1.1/2.4**	–	**0.8/2.5**	–	–	–
KRZ09	**0.4/2.3**	**1.3/1.7**	**−0.3/1.6**	–	**−2.3/2.6**	**−0.6/2.4**	**1.3/2.7**	**1.3/1.8**	–	**−0.4/2.3**

Statistically significant changes ($p < 0.05$) are in bold.

circulation types of COST733 classifications is concurrent with similar findings from Cahynová and Huth (2010, 2016) and Kučerová et al. (2017). At the same time, the lack of trends, especially in Western types in winter and the abundance of changes in spring, somewhat contradict the results of Kučerová et al. (2017) and many other works (e.g., Tomingas, 2002; Kyselý and Huth, 2006; Jaagus et al., 2008; Cahynová and Huth, 2010, 2016; Küttel et al., 2011; Keevallik, 2011; Hoy et al., 2013). Differences in the winter are so fundamental that they cannot be explained by differences in domain location or in the input database. For example, Kučerová et al. (2017) used air pressure data from ERA40 (Uppala et al., 2005) and domain 05 by COST733 Action (8°E – 34°E; 53°N – 68N), although the usage of different databases can cause substantial differences in classifications (Stryhal and Huth, 2017).

The search for the root cause of differences would be a separate topic for research and goes beyond the scope of the present paper. However, some conclusions can already be drawn by looking at trends in the frequency of types for the sub-periods 1966–1991 and 1992–2015. There are altogether only five statistically significant trends in the frequency of circulation types in the winters of 1967–2015 (**Table 4**), but 29 in the period of 1967–1991 and 52 in the period of 1992–2015. The most drastic changes occurred in the SE and especially in S types in the first half period. The frequency of those types decreased by up to 14 days (classifications HCL09, KRZ09, and HCL10). At the same time, the frequency of W types increased by up to 15 days (CAP09). In the second sub-period, however, the trends are opposite – i.e., the occurrence of E, SE, and S types have drastically increased (up to 19 days; KRZ08 E type) and the frequency of W, NW, and N types have steeply decreased (up to 21 days, W type of HCL09, and HCL10). All in all, the opposite tendencies of sub-periods tend to cancel trends of whole period (**Figures 4**, **5**). The trends in the W type from the CAP09 classification calculated for 30-year running periods show clearly a strong rise up to the year 2000, while the trends from the 1980s are negative (**Figure 5**). A similar mismatch is between periods in other seasons. For example, the decrease of E and SE types in spring are mostly caused by negative trends in 1966–1991. However, the drastic increase of NW types (**Table 5**) is noticeable only in the period 1992–2015.

To some extent, the mentioned changes can be addressed as a sign of strengthening and an eastward shift of the NAO, and a north-eastward shift of storm tracks, reported in recent years (Jung et al., 2003; Pokorná and Huth, 2015; Kučerová et al., 2017). However, the issue of NAO interconnections with regional circulation patterns as well as with temperature is a

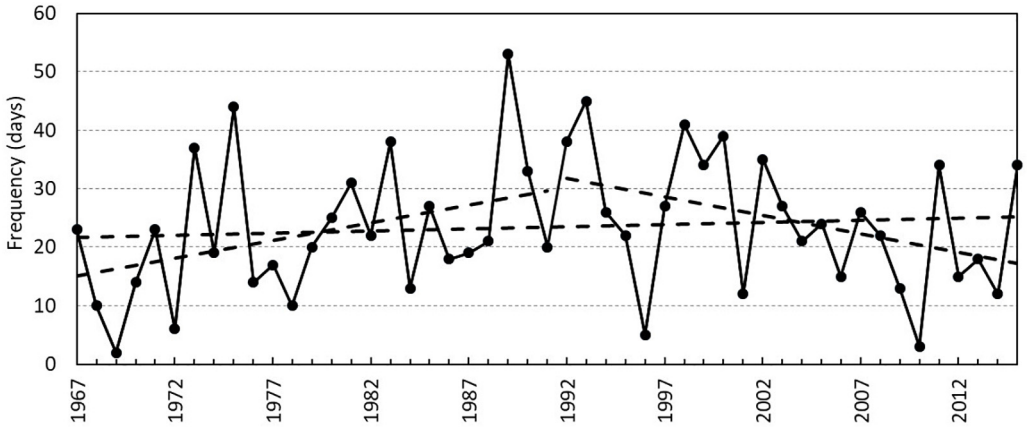

FIGURE 4 | Frequency (in days) of CAP09 classification circulation type W and change by trend line in days in winter (1967–2015). Long trend line is for the whole period 1967–2015. Two shorter ones are for 1967–1991 and 1992–2015. Both short trend lines are statistically significant ($p < 0.05$), the long one is not.

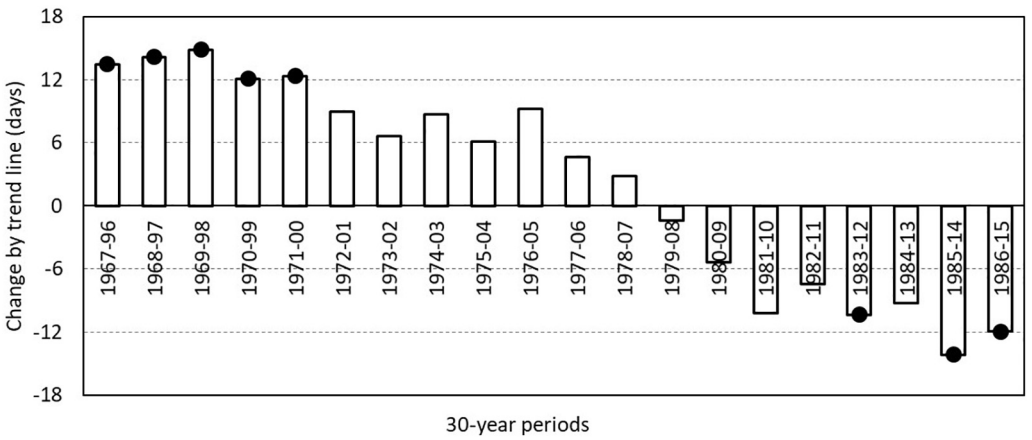

FIGURE 5 | Running trends of frequency (in days) of CAP09 classification circulation type W for 30-year periods. Statistically significant ($p < 0.05$) trends are marked with black dots.

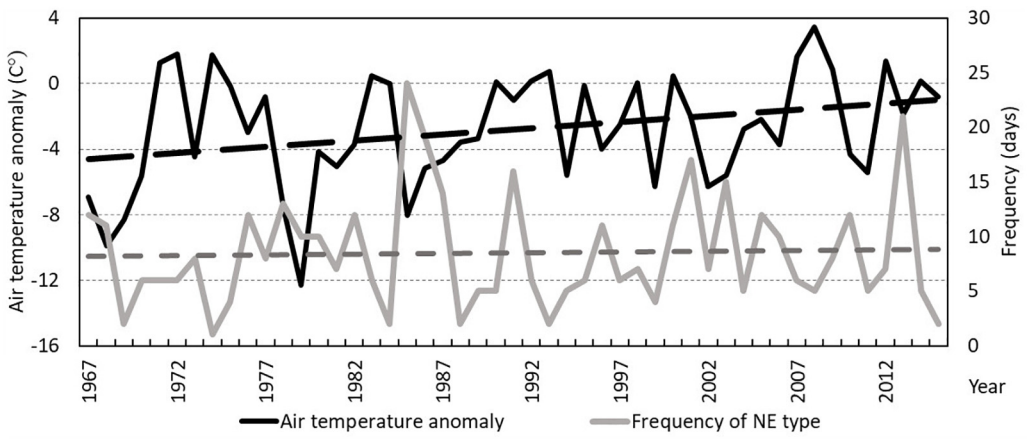

FIGURE 6 | Frequency of LIT09 classification circulation type NE and change by trend line in days in winter (1967–2015). And long-term average air temperature anomaly associated with circulation types at Türi station and changes by trend line in °C in winter.

complex subject that needs to be studied in more depth. One of the reasons for incomplete understanding is the non-stationarity of the NAO spatial pattern and the temporal correlations (Lehmann et al., 2011, 2017).

The increase in air temperature anomalies has been virtually univocal. Nevertheless, we may say that the warming in Estonia is only partly explainable by the changes in the frequency of circulation types. The other possibility is that the types themselves have become warmer either due to the changes in larger territory, meaning that the air advected here is already warmer, or due to the changes in other properties like cloudiness or humidity, which modify the energy budget and the heating takes place locally. It is a rather critical issue for synoptic climatology as the variation within types is rarely studied, because circulation types themselves are usually considered to be constant (Yarnal, 1993).

As mentioned, most drastic changes occurred in case of coldest types representing advection of Arctic air masses (N and NE) in winter and spring. Although still "cold" by long-term average anomalies, some Northern types can nowadays already be considered as "warm" (**Figure 6**). These positive temperature anomalies are found in years when this "cold" type has lower than average frequency, giving hints that lower persistence may mean warmer "cold" types.

This kind of change may reflect, at least in some extent, the drastic warming and changes in the atmospheric circulation over the Arctic Basin, reported by numerous authors (e.g., Serreze et al., 2000; Bekryaev et al., 2010; Vihma, 2014; Walsh, 2014; Screen et al., 2018). At the same time, Küttel et al. (2011) argued that 70% of the variation in winter temperature in Europe can be explained by changes within types. But if, for example, the NE type has become warm in winter (**Figure 6**), it refers either to changes in the source domains of temperature advection or changes in pattern of the type. On the one hand it means that the territorial distribution of temperature in winter has changed in the larger European region. The airflow from this direction is now warm in this time of year. On the other hand, it can refer to the changes of positions of low- and high-pressure systems, defining the circulation type. Spatial fluctuation of those systems by several hundred kilometers does not necessarily redefine a type but can cause redirection of advection (Yarnal, 1993).

CONCLUSION

In order to examine how the rise in Estonian air temperature is associated with the changes in atmospheric circulation, circulation types from different classification methods were used. All the classifications vary to a degree and have their own specifics, so to understand if apparently similar types represent similar circulation conditions an overlap analysis was carried out. Analysis shows that north, northeast and eastern types are in the best overlapping, which in turn indicates that they describe atmospheric circulation situations, when a high-pressure system sets for several days. Western types are in the worst overlapping, from which we can conclude that each classification describes a slightly different circulation situation. This, however, means that the classifications are difficult to compare, and a relatively large number of different classifications must be used to obtain robust results.

Trends in circulation types' frequency were studied by seasons and only few statistically significant trends can be observed during the whole period of 1966–2015. Most of the statistically significant changes in the frequency of circulation types occurred in spring. It contradicts with earlier studies, which have found an increase in the frequency and intensity of Western circulation types in winter and have explained with it the general tendency of winter warming in the Baltic Sea region. While analyzing the sub-periods 1967–1991 and 1992–2015 separately, we get trends with different directions. The frequency of Western types has increased rapidly (ca 12 days by trend line) in the period of 1967–1991, but since 1992, the frequency has decreased (−14 days). Altogether no statistically significant changes were given during 1967–2015 in winter.

We analyzed the changes in the mean air temperature of Jõhvi, Vilsandi, and Türi stations in 1966–2015. The average annual temperature rise in the three stations is in the range of 2–2.2°C. According to the trend line, the air temperature has risen most in winter, about 2.8°C. In spring, summer and autumn, the temperature rise is in the range of 1.5–1.9°C. However, it must be noticed that most drastic air temperature rise (up to 6°C by trend line) has occurred in the case of "cold" types (N and NE) in winter.

The general conclusion is that the warming in Estonia is only partly explained by the changes in the frequency of circulation types. Basically, the change in temperature is caused by the changes in the types itself. This, however, contradicts to the axiom of synoptic climatology and suggests the possibility that circulation types are not really constant.

AUTHOR CONTRIBUTIONS

ML was responsible for collecting and analyzing the data, trend analyses, and preparing the manuscript. PP was responsible for calculations of circulation types and completing the manuscript. MS was responsible for the idea and methodology of the study.

FUNDING

This study was supported by the projects IUT2-16 and IUT20-11 of the Estonian Ministry of Education and Research, and the Estonian Research Council grant PUT1439.

ACKNOWLEDGMENTS

We thank Evelyn Uuemaa for assistance. The software COST733class for calculating circulation types was worked out during COST action 733 "Harmonization and Applications of Weather Types Classifications for European Regions" and we are grateful to its creators.

REFERENCES

Ahas, R., and Aasa, A. (2006). The effects of climate change on the phenology of selected Estonian plant, bird and fish populations. *Int. J. Biometeorol.* 51, 17–26. doi: 10.1007/s00484-006-0041-z

BACC Author Team. (2015). *Second Assessment of Climate Change for the Baltic Sea Basin*. New York, NY: Springer.

Beck, C. (2000). Zirkulationsdynamische variabilität im bereich nordatlantik-europa seit 1780. *Würzburger Geographische Arbeiten* 95:350

Beck, C., Jacobeit, J., and Jones, P. D. (2007). Frequency and within-type variations of large-scale circulation types and their effects on low-frequency climate variability in Central Europe since 1780. *Int. J. Climatol.* 27, 473–491. doi: 10.1002/joc.1410

Bekryaev, R. V., Polyakov, I. V., and Alexeev, V. A. (2010). Role of polar amplification in long-term surface air temperature variations and modern arctic warming. *J. Climate* 23, 3888–3906. doi: 10.1175/2010JCLI3297.1

Cahynová, M., and Huth, R. (2010). Circulation vs. climatic change over the czech republic: a comprehensive study based on the COST733 database of atmospheric circulation classifications. *Phys. Chem. Earth* 35, 422–428. doi: 10.1016/j.pce.2009.11.002

Cahynová, M., and Huth, R. (2016). Atmospheric circulation influence on climatic trends in Europe: an analysis of circulation type classifications from the COST733 catalogue. *Int. J. Climatol.* 36, 2743–2760. doi: 10.1002/joc.4003

Enke, W., and Spekat, A. (1997). Downscaling climate model outputs into local and regional weather elements by classification and regression. *Clim. Res.* 8, 195–207. doi: 10.3354/cr008195

Hoy, A., Sepp, M., and Matschullat, J. (2013). Large-scale atmospheric circulation forms and their impact on air temperature in Europe and northern Asia. *Theor. Appl. Climatol.* 113, 643–658. doi: 10.1007/s00704-012-0813-9

Hurrell, J. W. (1995). Decadal trends in North Atlantic Oscillation: regional temperature and precipitation. *Science* 269, 676–679. doi: 10.1126/science.269.5224.676

Hurrell, J. W., Kushnir, Y., Ottersen, G., and Visbeck, M. (2003). An overview of the North Atlantic oscillation. the North Atlantic oscillation. climatic significance and environmental impact. *AGU Geophy. Monogr.* 134, 1–35. doi: 10.1029/GM134

Huth, R., Beck, C., and Kuèerová, M. (2016). Synoptic-climatological evaluation of the classifications of atmospheric circulation patterns over Europe. *Int. J. Climatol.* 36, 2710–2726. doi: 10.1002/joc.4546

Huth, R., Beck, C., Philipp, A., Demuzere, M., Ustrnul, Z., Cahynová, M., et al. (2008). Classifications of atmospheric circulation patterns: recent advances and applications. *Ann. N. Y. Acad. Sci.* 1146, 105–152. doi: 10.1196/annals.1446.019

IPCC (2014). "Climate change 2014," in *Synthesis Report. Contribution of Working Groups I, II and III to the Fifth Assessment Report of the Intergovernmental Panel on Climate Change*, eds Core Writing Team, R. K. Pachauri, and L. A. Meyer (Geneva: IPCC).

Jaagus, J. (2006). Climatic changes in estonia during the second half of the 20th century in relationship with changes in large-scale atmospheric circulation. *Theor. Appl. Climatol.* 83, 77–88. doi: 10.1007/s00704-005-0161-0

Jaagus, J., Briede, A., Rimkus, E., and Remm, K. (2014). Variability and trends in daily minimum and maximum temperatures and in the diurnal temperature range in Lithuania. Latvia and Estonia in 1951–2010. *Theor. Appl. Climatol.* 118, 57–68. doi: 10.1007/s00704-013-1041-7

Jaagus, J., Post, P., and Tomingas, O. (2008). Changes in storminess on the western coast of Estonia in relation to large-scale atmospheric circulation. *Clim. Res.* 36, 29–40. doi: 10.3354/cr00725

Jaagus, J., Sepp, M., Tamm, T., Järvet, A., and Mõisja, K. (2017). Trends and regime shifts in climatic conditions and river runoff in Estonia during 1951–2015. *Earth Syst. Dynam.* 8, 963–976. doi: 10.5194/esd-8-963-2017

Jaagus, J., and Suursaar, Ü. (2013). Long–term storminess and sea level variations on the Estonian coast of the Baltic Sea in relation to large-scale atmospheric circulation. *Estonian J. Earth Sci.* 62, 73–92. doi: 10.3176/earth.2013.07

Jaagus, J., and Truu, J. (2004). "Climatic regionalisation of Estonia based on multivariate exploratory techniques," in *Estonia. Geographical Studies*, eds K. Tiia and P. Jaan-Mati (Tallinn: Estonian Academy Publishers), 41–55.

Jenkinson, A. F., and Collison, F. P. (1977). *An Initial Climatology of Gales Over the North Sea*. Technical report Synoptic Climatology Branch Memorandum 62. Bracknell: Meteorological Office

Jevrejeva, S., Drabkin, V. V., Kostjukov, J., Lebedev, A. A., Leppäranta, M., Mirnov, Y. U., et al. (2004). Baltic Sea ice seasons in the twentieth century. *Clim. Res.* 25, 217–227. doi: 10.3354/cr025217

Jung, T., Hilmer, M., Ruprecht, E., Kleppek, S., Gulev, S. K., and Zolina, O. (2003). Characteristics of the recent eastward shift of interannual NAO variability. *J. Clim.* 16, 3371–3382.

Kalnay, E., Kanamitsu, M., Kistler, R., Collins, W., Deaven, D., Gandin, L., et al. (1996). The NCEP/NCAR 40-year reanalysis project. *Bull. Amer. Meteorol. Soc.* 77, 437–472.

Keevallik, S. (2003). Changes in spring weather conditions and atmospheric circulation in Estonia (1955–95). *Int. J. Climatol.* 23, 263–270. doi: 10.1002/joc.875

Keevallik, S. (2011). Shifts in meteorological regime of late winter and early spring in Estonia during recent decades. *Theor. Appl. Climatol.* 105, 209–215. doi: 10.1007/s00704-010-0356-x

Kruizinga, S. (1979). "Objective classification of daily 500 mbar patterns," in *Proceedings of the: Preprints Sixth Conference on Probability and Statistics in Atmospheric Sciences*, (Boston, MA: American Meteorological Society), 126–129.

Kučerová, M., Beck, C., Philipp, A., and Huth, R. (2017). Trends in frequency and persistence of atmospheric circulation types over Europe derived from multiple classifications. *Int. J. Climatol.* 37, 2502–2521. doi: 10.1002/joc.4861

Küttel, M., Luterbacher, J., and Wanner, H. (2011). Multidecadal changes in winter circulation-climate relationship in Europe: frequency variations, within-type modifications, and long-term trends. *Clim. Dyn.* 36, 957–972. doi: 10.1007/s00382-009-0737-y

Kyselý, J., and Huth, R. (2006). Changes in atmospheric circulation over Europe detected by objective and subjective methods. *Theor. Appl. Climatol.* 85, 19–36. doi: 10.1007/s00704-005-0164-x

Lehmann, A., Getzlaff, K., and Harlaß, J. (2011). Detailed assessment of climate variability in the Baltic Sea area for the period 1958 to 2009. *Clim. Res.* 46, 185–196. doi: 10.3354/cr00876

Lehmann, A., Höflich, K., Post, P., and Myrberg, K. (2017). Pathways of deep cyclones associated with large volume changes (LVCs) and major baltic inflows (MBIs). *J. Mar. Syst.* 167, 11–18. doi: 10.1016/j.jmarsys.2016.10.014

Litynski, J. (1969). A numerical classification of circulation patterns and weather types in Poland. *Prace Panstwowego Instytutu Hydrologiczno-Meteorologicznego* 97, 3–15.

Murtagh, F. (1985). *Multidimensional Clustering Algorithms. Vol. 4 of COMPSTAT Lectures*. Würzburg: Physica-Verlag.

NOAA. (2018). Global Climate Report - Annual 2017. Available at: https://www.ncdc.noaa.gov/sotc/global/201713 (accessed 4 December, 2018)

Philipp, A., Beck, C., Huth, R., and Jacobeit, J. (2016). Development and comparison of circulation type classifications using COST733 dataset and software. *Int. J. Climatol.* 36, 2673–2691. doi: 10.1002/joc.3920

Pokorná, L., and Huth, R. (2015). Climate impacts of the NAO are sensitive to how the NAO is defined. *Theor. Appl. Climatol.* 119, 639–652.

Schwartz, M. D., Ahas, R., and Aasa, A. (2006). Onset of spring starting earlier across the Northern Hemisphere. *Glob. Change Biol.* 12, 343–351.

Screen, J. A., Bracegirdle, T. J., and Simmonds, I. (2018). Polar Climate change as manifest in atmospheric circulation. *Curr. Clim. Change* 4:383. doi: 10.1007/s40641-018-0111-4

Sepp, M., and Jaagus, J. (2002). Frequency of circulation patterns and air temperature variations in Europe. *Boreal Environ. Res.* 7, 273–279.

Sepp, M., Post, P., Mändla, K., and Aunap, R. (2018). On cyclones entering the Baltic Sea region. *Boreal Environ. Res.* 23, 1–14.

Serreze, M. C., Walsh, J. E., Chapin, F. S., Osterkamp, T., Dyurgerov, M., Romanovsky, V., et al. (2000). Observational evidence of recent change in the northern high-latitude environment. *Clim. Change* 46:159. doi: 10.1023/A:1005504031923

Stryhal, J., and Huth, R. (2017). Classifications of winter Euro-Atlantic circulation patterns: an intercomparison of five atmospheric reanalyses. *J. Clim.* 30, 7847–7861. doi: 10.1175/JCLI-D-17-0059.1

Tomingas, O. (2002). Relationship between atmospheric circulation indices and climate variability in Estonia. *Boreal Environ. Res.* 7, 463–469.

Tveito, O. E., Huth, R., Philipp, A., Post, P., Pasqui, M., Esteban, P., et al. (2016). *COST Action 733 Harmonization and Application of Weather Type Classifications for European Regions*. Final Scientific Report. Augsburg, University of Augsburg.

Uppala, S. M., Kållberg, P. W., Simmons, A. J., Andrae, U., Da Costa Bechtold, V., Fiorino, M., et al. (2005). The ERA-40 re-analysis. *Q. J. R. Meteorol. Soc.* 131, 2961–3012. doi: 10.1256/qj.04.176

Vihma, T. (2014). Effects of Arctic sea ice decline on weather and climate: a review. *Surv. Geophy.* 35, 1175–1214. doi: 10.1007/s10712-014-9284-9280

Walsh, J. E. (2014). Intensified warming of the Arctic: causes and impacts on middle latitudes. *Global Planet. Change* 117, 52–63. doi: 10.1016/j.gloplacha.2014.03.003

Yarnal, B. (1993). *Synoptic Climatology in Environmental Analysis. A Primer*. London: Belhaven Press.

Conflict of Interest Statement: The authors declare that the research was conducted in the absence of any commercial or financial relationships that could be construed as a potential conflict of interest.

frontiers in Environmental Science

ORIGINAL RESEARCH
published: 12 June 2019
doi: 10.3389/fenvs.2019.00088

Baltic Sea Coastal Eutrophication in a Thousand Year Perspective

Lena Norbäck Ivarsson[1], Thomas Andrén[1], Matthias Moros[2], Thorbjørn Joest Andersen[3], Mikael Lönn[1,4] and Elinor Andrén[1]*

[1] School of Natural Sciences, Technology and Environmental Studies, Södertörn University, Huddinge, Sweden, [2] Leibniz Institute for Baltic Sea Research Warnemünde, Rostock, Germany, [3] Department of Geosciences and Natural Resource Management, University of Copenhagen, Copenhagen, Denmark, [4] Department of Electrical Engineering, Mathematics, and Science, Faculty of Engineering and Sustainable Development, University of Gävle, Gävle, Sweden

Sediment cores from three sites along the east-coast of Sweden, north-western Baltic Proper, have been studied with respect to lithologies, geochemistry, and diatom assemblages to trace and date early human impact with emphasis on nutrient discharge. The three sites Bråviken, Himmerfjärden, and Ådfjärden, have been impacted to various degree during the last millennia by multiple stressors like excessive nutrient discharge and hazardous substances, leading to coastal hypoxia, eutrophication, and pollution. These stressors are mainly caused by drivers in the drainage area as increased human population, changed land use, and point sources as industries and a sewage treatment plant. Even though their detailed history differs, the results show similar general patterns for all three sites. We find no evidence in our data from the coastal zone supporting the hypothesis that the extensive areal distribution of hypoxia in the open Baltic Sea during the Medieval Climate Anomaly was caused by human impact. Timing of the onset of man-made eutrophication, as identified from $\delta^{15}N$ and changes in diatom composition, differs between the three sites, reflecting the site specific geography and local environmental histories of these areas. The onset of eutrophication dates to ∼1800 CE in Bråviken and Himmerfjärden areas, and to ∼1900 CE in the less urban area of Ådfjärden. We conclude that the recorded environmental changes during the last centuries are unique in a thousand year perspective.

Keywords: diatom stratigraphy, stable nitrogen isotopes, hypoxia, Medieval Climate Anomaly, NW Baltic proper, nutrient discharge

OPEN ACCESS

Edited by:
Marcus Reckermann, Helmholtz Centre for Materials and Coastal Research (HZG), Germany

Reviewed by:
Selvaraj Kandasamy, Xiamen University, China
Oscar E. Romero, University of Bremen, Germany

****Correspondence:***
Lena Norbäck Ivarsson
lena.norback.ivarsson@sh.se

Specialty section:
This article was submitted to Interdisciplinary Climate Studies, a section of the journal Frontiers in Environmental Science

Received: *18 December 2018*
Accepted: *27 May 2019*
Published: *12 June 2019*

Citation:
Norbäck Ivarsson L, Andrén T, Moros M, Andersen TJ, Lönn M and Andrén E (2019) Baltic Sea Coastal Eutrophication in a Thousand Year Perspective. Front. Environ. Sci. 7:88. doi: 10.3389/fenvs.2019.00088

INTRODUCTION

The Baltic Sea is a brackish water basin with a large and densely populated catchment area. Strong salinity gradients, both vertically and horizontally, set the preconditions for all life in this sea. Since the Baltic Sea is semi-enclosed and has a water residence time of about 30–40 years it is especially sensitive to stressors like chemical pollution, nutrient discharge, and overfishing (Snoeijs and Andrén, 2017). The ca 85 million people living in the drainage area are causing a severe pressure on the ecosystem resulting in environmental deterioration and one of the most polluted seas in the world (Leppäranta and Myrberg, 2009). Increased anthropogenic nutrient loads during the twentieth century have led to eutrophication of the Baltic Sea manifested in e.g., altered species composition, more intense cyanobacterial blooms, decreased secchi-depth, and increased sea bottom hypoxia in the open parts of the Baltic Sea (Elmgren, 2001; Gustafsson et al., 2012). Since the 1950s, hypoxia has also increased in the Baltic Sea coastal zones (Persson and Jonsson, 2000; Conley et al., 2011).

Some of the recorded changes resulting from present eutrophication are not new phenomena for the Baltic Sea. Pigment analyses in sediments have shown cyanobacteria blooms to be natural features of the open Baltic Sea for the last ca 8000 years (Bianchi et al., 2000). A compilation of laminated sediment sequences used as proxy for hypoxia show evidence for three time periods with extensive areal distribution of hypoxia in the open Baltic Sea; 8000–4000 years before present (BP), 2000–800 years BP, and from 1800 CE to present (Zillén et al., 2008).

The hypoxic event 2000–800 years BP coincide with a climatic event named the Medieval Climate Anomaly, MCA, including the Roman Warm Period, and has been suggested to be caused by an increase in human population and large scale changes in land use in the drainage area at this time (Zillén and Conley, 2010). Around the turn of the last millennium a series of technological innovations, including the iron plow, promoted an expansion of agricultural land (Myrdal, 1999). The favorable climate conditions during the MCA, with temperatures similar to those of today, also enabled a demographic expansion (Myrdal and Morell, 2011; Ljungqvist et al., 2012). It has also been suggested (Kabel et al., 2012) that the warmer climate during this time caused intensified cyanobacterial blooms and stronger stratification resulting in hypoxia. The following oxygenation of the bottom waters in the open Baltic Sea has been explained both by the onset of the Little Ice Age, LIA, (Kabel et al., 2012), and by the drastic decrease in population due to the plague (Zillén and Conley, 2010). Throughout the present paper, when we refer to the climatic events Medieval Climate Anomaly and Little Ice Age, we use the definitions by Mann et al. (2009), which means the MCA = 950–1250 Common Era (CE), and the LIA = 1400–1700 CE.

There is a need to improve our understanding of the natural variability of the Baltic Sea and its response to climate, as well as human induced forcing. Paleoecology can fill the gap when long term data is lacking, and provide us with a scientific base on past environmental conditions (Willis and Birks, 2006; Renberg et al., 2009; Saunders and Taffs, 2009). Whilst the open Baltic Sea has been extensively studied with respect to Holocene natural climate variability and environmental change (e.g., Andrén et al., 2000a,b; Bianchi et al., 2000), this is not the case in the coastal zone, where studies on long-term trends in hypoxia and its causes have not been performed (Conley et al., 2011). Land use changes will most likely influence the coastal zone before possible effects are registered in the open Baltic Sea, and these areas should consequently be more carefully studied. There are several studies from the Baltic Sea coastal zones focusing on changes in eutrophication and nutrient reconstructions the last century, for example in the Oder estuary (Andrén, 1999), the Roskilde fjord in Denmark (Clarke et al., 2006) and from the Gulf of Finland (Weckström, 2006). Recently, Ning et al. (2018) reported from a coastal site at the Swedish east-coast that the onset of eutrophication can be traced back to the nineteenth century, identifying intensified land use as the main driver. A multiproxy study from the Archipelago Sea, northern Baltic Proper, indicates an onset of eutrophication at ca 1900 CE (Jokinen et al., 2018).

A long-term perspective concerning how environmental changes affect the marine system will provide us with a deeper knowledge of possible future scenarios, highly important for the management of the Baltic Sea (Kotilainen et al., 2014). In this paper we present a multiproxy study using diatom stratigraphies and geochemistry data from three carefully selected coastal sites in the northwestern Baltic Proper. The aim of the study is to investigate and date long-term environmental changes in these coastal regions. Our results will be discussed both in a local and a regional perspective and we aim to put the present severe environmental situation in the Baltic Sea, in terms of nutrient loads and external forcing, in a thousand year perspective.

STUDY SITES

The three sites chosen for this study are located along the Swedish east-coast, north-western Baltic Proper (**Figure 1**, **Table 1**). This area has been, and still is, affected by the last glaciation, resulting in an isostatic rebound of ca 3–4 mm/year (Harff and Meyer, 2011). None of the cored sites have thresholds shallow enough for the isostatic rebound to have affected the water circulation in the basins during the time covered by this study. The seafloor at all three sites consists of glacial and postglacial clays, with large areas of gaseous sediments (Swedish Geological Survey, 2018).

Bråviken

Bråviken (N58°38.828′, E16°23.630′) is a long, ca 50 km, and narrow bay of 130 km^2, with a threshold depth of 16 m. There are several small streams that drains into Bråviken, but by far the largest input comes from the river Motala ström. The mean discharge between years 1991–2018 was 93 m^3/s (Swedish Metrological Hydrological Institute, 2018). In the inner, southern part of Bråviken, the city of Norrköping is located, for which Bråviken is recipient. Salinity in bottom waters of Bråviken is ca 6–6.5. Surface waters salinity fluctuates a lot, fresher during winter months (ca 1–3) and more saline during summer and autumn months (ca 4–5). The drainage area is large and covers 15,480 km^2, most of which consists of cultivated glacial and postglacial clays (Swedish Geological Survey, 2018). The northern shore of Bråviken consists of a fault, which also constitutes the rim of the drainage area. The shoreline on this side is steep and the vegetation is dominated by coniferous forest. The water depth along the northern shore is ca 30 m, with a maximum depth of 36 m. The southern side of Bråviken is flat and shallow (<5 m) and the adjacent land is used for agriculture. In these shallow parts the seafloor vegetation is dominated by green algae, mostly *Cladophora* and *Ulva* spp., and seaweed such as *Potamogeton perfoliatus*, *Zostera marina*, *Zannichellia palustris*, *Stuckenia pectinate*, and *Myriophyllum spicatum*. The deeper parts are dominated by the thalloid red algae *Hildenbrandia* and an extensive distribution of barnacle, *Amphibalanus improvisus*. Epiphytic filamentous brown algae like *Ectocarpus* and *Pylaiella* spp. are common in Bråviken, both in shallow and deeper parts (Swedish Metrological Hydrological Institute, 2018).

According to the Swedish Maritime Administration, 2800 commercial ships passes through Bråviken, to the harbor in Norrköping, every year. To enable this there has been extensive dredging of the seafloor and dumping of sediments about 8 km from our sampling site. We consider 8 km to be enough of

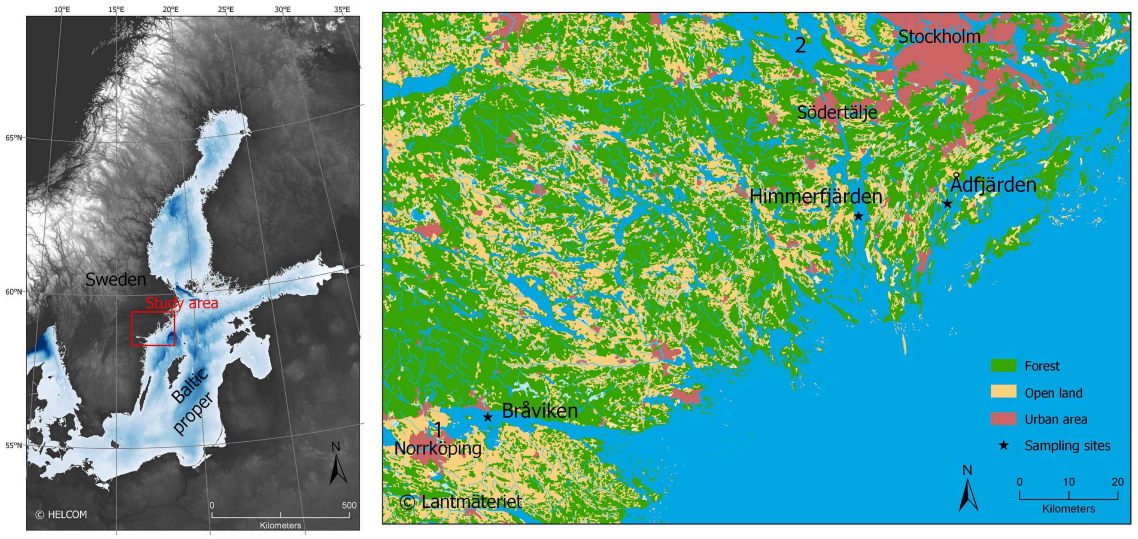

FIGURE 1 | Maps showing the location of the three investigated sites Bråviken, Himmerfjärden, and Ådfjärden in the Baltic Sea. Number 1 is Motala ström and number 2 is Lake Mälaren.

TABLE 1 | Retrieved sediment cores from Bråviken, Himmerfjärden, and Ådfjärden.

Site	Core label	Date	Equipment	Water depth (m)	Core length (m)	Lat	Long
Bråviken	GC1212	June 2012	Gravity corer	23.9	0.70	N58°38.834′	E16°23.636′
Bråviken	PC1205	June 2012	Piston corer	24	4.5	N58°38.832′	E16°23.664′
Himmerfjärden	GC1219	June 2012	Gravity corer	45	0.77	N58°59.629′	E17°43.291′
Himmerfjärden	PC1208	June 2012	Piston corer	44.1	5	N58°59.616′	E17°43.295′
Ådfjärden	UPP6A	June 2014	Piston corer	28	ca 3	N59°00.573′	E18°02.282′
Ådfjärden	UPP6C	June 2014	Gravity corer	28	0.67	N59°00.570′	E18°02.279′
Ådfjärden	UPP6D	June 2014	Gravity corer	28	0.72	N59°00.570′	E18°02.289′

a buffer zone not to disturb our cored site. Norrköping has a long history of industries, starting with iron and weapon manufactories in the seventeenth century. During the eighteenth century the metal industry was declining due to the peace, while the textile and paper industries were on the rise (Gejvall-Seger, 1978). These two industries dominated the area during the nineteenth century, with several paper mills located in Norrköping and its surroundings (Sjunnesson and Wahlberg, 2003). Norrköping has continued to be an important industrial city during the twentieth century. Today, the ecological status of the outer part of Bråviken is moderate, while the inner parts are considered having poor ecological status (Vatteninformation Sverige, 2018), and hence heavily affected by eutrophication.

Himmerfjärden

Himmerfjärden (N58°59.616′, E17°43.295′) is an estuary of ca 30 km^2, located ca 40 km south of Stockholm. The bathymetry of Himmerfjärden is steep since the estuary is the result of a tectonically induced fault in the bedrock. Threshold depth at the inlet is ca 15 m, and the maximum and mean water depths are 45 and 17 m, respectively. Salinity is ca 6–7 in the surface, with slightly more saline bottom waters. In 2011, macrophyte cover was investigated at several sites in Himmerfjärden (Swedish Metrological Hydrological Institute, 2018). At 2 meters depth *Cladophora* spp. were dominating, and below 3 meters filamentous brown algae (*Ectocarpus*/*Pylaiella* spp.), attached to *Fucus vesiculus* were covering the seafloor.

The third largest lake in Sweden, Lake Mälaren, has its main outlet in Stockholm, but is also drained through a lock in Södertälje, into the Himmerfjärden estuary (Elmgren and Larsson, 1997). The lock opened in 1819, and was rebuild in 1924 (Nordström, 1968). Prior to the opening of the lock, Lake Mälaren was isolated from the Baltic Sea since around 1200 CE (Douglas Price et al., 2018). The drainage area for Himmerfjärden is 1,286 km^2, of which ca 20% is arable land (Elmgren and Larsson, 1997). Södertälje is the major urban area, located upstream from Himmerfjärden estuary. During the nineteenth century several industries were established in Södertälje and they expanded and became more numerous in the early twentieth century. This enabled population growth in Södertälje and the vicinities, especially during the 1940s (Nordström, 1968). Today Södertälje has a population of ca 70,000 residents. According to the Swedish Maritime Administration, 2700 commercial ships and 9000 leisure boats passes through Himmerfjärden, in and out of Lake Mälaren, every year.

In 1974 the sewage treatment plant, Himmerfjärdsverket, opened with ca 90,000 people connected, using the Himmerfjärden estuary as recipient. Since the opening, there has been several full-scale experiments with nutrient discharge in the bay, and the water quality in Himmerfjärden has been closely studied in the environmental monitoring of the recipient, with respect to e.g., nutrient levels, redox conditions of bottom waters, and phytoplankton biomass (Elmgren and Larsson, 1997; Savage et al., 2002). Today the sewage treatment plant serves ca 314,000 people and most of the wastewater from the southern suburbs of Stockholm end up here (Winnfors, 2009). Himmerfjärden is at present affected by eutrophication and is classified as having moderate ecological status (Vatteninformation Sverige, 2018).

Ådfjärden

Ådfjärden (N59°00.573′, E18°02.282′) is located in the southern part of Stockholm archipelago, ca 30 km south of Stockholm. This water basin has an area of ca 5 km^2, a maximum water depth of 30 m, and thresholds in the north and south are 12 and 19 m, respectively. Salinity in the basin is ca 6, with more freshwater surface waters during winter and spring months. The national environmental monitoring program has no site in Ådfjärden, and therefore there is almost no such data available for this site. Epibenthos was investigated once in 2011 on the eastern side of Ådfjärden. At 7 meters depth Blue mussels, *Mytilus edulis*, and the red algae *Coccotylus truncatus* were dominating the seafloor (Swedish Metrological Hydrological Institute, 2018).

Ådfjärden is surrounded by mainland and islands, which are characterized by a thin soil cover and bare bedrock. The vegetation is typical for the archipelago with sparse, mixed forests and some, not extensive, agricultural land. There are no urban areas within the drainage area nor fairway through Ådfjärden, which means it is relatively unaffected by boat traffic. This site is sheltered with about 10 km of archipelago separating it from the open Baltic Sea. Also Ådfjärden is classified as having moderate ecological status and is thus affected by eutrophication (Vatteninformation Sverige, 2018).

MATERIALS AND METHODS

Sediment Coring and Handling

The geographic locations of the sites were selected based on the bathymetry of the basins i.e., the deepest part of a basin is assumed to have recorded the most expanded and complete sediment sequence. All sites cored were positioned by the ships (R/V Skagerak and M/S Fyrbyggaren) GPS position system (**Table 1**). The long cores from each site (PC1205, PC1208, and UPP6A) were retrieved by a 3 or 5-meters long piston corer (PC) using 20 to 30 kg of lead weights and a freefall of 0.5 meter. PVC liners with an inner diameter 4.6 cm were used. After retrieval the cores were cut into 1 m (respective 1.25 m) long sections, sealed with end caps, marked and stored cold for later analyses in the laboratory.

To also recover the topmost soft and unconsolidated sediments the long piston cores were supplemented using a short, 1 m long, gravity corer (GC) with an inner diameter of 8 cm (GC1212, GC1219, UPP6C, and UPP6D, **Table 1**). The GC's were sliced into 1 cm slices, marked and stored in plastic Ziploc bags. For Ådfjärden, a second short core (UPP6D) was collected and pushed out on deck, where it was documented by photography. The number of laminas were estimated by counting of the laminas visual to the naked eye.

All sediment core sections were stored in the cold room before opening. In the laboratory, the piston core liner sections were opened by cutting them lengthwise. One half of the core was placed into a core tray for visual inspection and documentation, both as written core description and by photography. This core section was then put back into the cold room and stored as a reference half. The other half of each core section was used for sub-sampling for radiocarbon dating, diatom stratigraphy, and geochemistry.

Dating, Core Correlation, and Age-Depth Modeling

Sediment samples were sieved using a mesh size of 250 μm for datable macrofossils. Found macrofossils were examined under a stereo microscope when needed, determined to species, or genus level when possible and dried in an oven at 40°C before dating. A total of 13 macrofossil samples, both terrestrial and marine, have been dated by radiocarbon accelerator mass spectrometry (AMS) at the Radiocarbon Dating Laboratory, Lund University, Sweden and at Beta Analytical, USA. The results are summarized in **Table 2**. Sample LuS11138 from Bråviken was excluded from the age-depth modeling as it was impossible to calibrate due to its young age.

The age-depth modelings were performed using the age-modeling software CLAM version 2.2 (Blaauw, 2010) by the means of applying a smooth spline curve between dated levels with 10,000 iterations. The marine samples were calibrated using a custom-built calibration curve with a ΔR of -135 ± 40 to compensate for the regional offset from the Marine13 calibration dataset (Reimer et al., 2013). The chosen ΔR is a mean based on the values for ΔR for clams, both suspension and deposit feeders, in three study sites relatively close to Bråviken, Himmerfjärden, and Ådfjärden as reported in the Marine Reservoir Correction Database (http://calib.org/marine/), Map No 1710, 1717, and 1718 (Lougheed et al., 2013). In the case of Bråviken and Himmerfjärden with both marine and terrestrial macrofossils in the dataset, radiocarbon ages derived from terrestrial macrofossils were calibrated separately using CLAM and the IntCal13 calibration dataset (Reimer et al., 2013) and entered as calendar years at the age-depth modeling. Ådfjärden contained only terrestrial macrofossils and was therefore age-depth modeled using the IntCal13 calibration dataset.

Gamma Dating Center, Institute of Geography, University of Copenhagen has analyzed the short gravity cores for the activity of ^{210}Pb and ^{137}Cs via gamma spectrometry. The measurements were carried out on Canberra ultralow-background Ge-well-detector. ^{137}Cs measurements of cores UPP6A, PC1205, and PC1208 were carried out at the Leibniz Institute for Baltic Sea Research Warnemünde (IOW) using Canberra detectors (GCW4021-7500SL-RDC-6-ULB).

TABLE 2 | Dating results.

Site	Core	Lab ID	Depth bsf (cm)	Corrected depth bsf (cm)	Material dated	^{14}C age (years BP)	Error	Calibrated age (years BP)	Min (years BP)	Max (years BP)
Bråviken	PC1205	LuS11138	63–64	77–78	Clam (*Macoma baltica*)	355	40	126	−5	256
Bråviken	PC1205	LuS11139	150–152	164–166	Fragments of leafs	300	35	405	290	520
Bråviken	PC1205	LuS11588	248–250	262–264	Fragments of algae	1180	45	833	735	930
Bråviken	PC1205	LuS11589	329	343	Plant remnant (probably Poaceae sp.)	1455	40	1351	1240	1462
Bråviken	PC1205	LuS11141	360–362	374–376	Fragments of algae	1825	70	1498	1315	1681
Himmerfjärden	PC1208	Beta418048	139	165	Clam (*Macoma baltica*)	220	30	59	−5	123
Himmerfjärden	PC1208	Beta418049	218	244	Clam (*Macoma baltica*)	560	30	361	282	440
Himmerfjärden	PC1208	Beta418050	320	346	Shell fragments	1620	30	1273	1190	1355
Himmerfjärden	PC1208	Beta418051	447	473	Plant remnant, seeds	3000	30	2865	2773	2957
Ådfjärden	UPP6A	LuS11132	90–91	124–125	Seeds (*Betula* sp.)	950	55	850	745	955
Ådfjärden	UPP6A	LuS11133	110–112	144–146	Fragments of leafs	1155	35	1078	981	1175
Ådfjärden	UPP6A	LuS11135	160–162	194–196	Plant remnant	1715	35	1630	1,554	1,705
Ådfjärden	UPP6A	LuS11137	280–282	314–316	Plant remnant	2440	70	2534	2354	2714

Dated material have when possible been identified to genus or species level.

Constant Rate of Supply (CRS) method was applied for the upper parts of the cores using the modified method by Appleby (2001). Apart from the ^{137}Cs signal deriving from the Chernobyl accident in 1986 CE we have also included the increase in ^{137}Cs-curve attributed to the nuclear weapons testing dated to ca 1960 CE in the age determination. The lower parts of the cores were dated by a linear regression assuming constant sediment accumulation.

For mercury measurements at the IOW we used a DMA-80 analyzer from MLS Company. Data were calibrated against CRM (BCR) 142R certified reference material and SRM 2709 soil standard using 5 concentration steps covering a range from 5 to 500 ng Hg. Sample weights were between 20 and 100 mg. For further analytical details and details regarding quality assurance see Leipe et al. (2013).

Correlations and estimations of offsets between long and short cores are based on matching of the mercury (Hg) and the ^{137}Cs profiles in both the short gravity cores and the long piston cores (**Figure 2**). To further strengthen this correlation we used two ^{137}Cs markers, 1960 CE and 1986 CE, as fix-points in addition to the Hg-curve, an approach successfully applied to offshore Baltic Sea sediments (Moros et al., 2017). It was then possible to construct a complete splice sediment sequence for each site. Based on this splice sequence the ages from the ^{210}Pb dating were added to the age dataset and entered into CLAM as calendar years and thus been included in the age-depth models. Using these ^{210}Pb ages it has been possible to determine the sediment accumulation rate in the upper part of the sediment sequence which is too young for the radiocarbon dating method, and to achieve similar sedimentation rates in the overlapping intervals. These correlations show that between 14 and 34 centimeters of the very soft water saturated sediments were "lost" in the top of the long piston cores. All ages discussed in the following refer to calibrated ages in years CE.

Geochemical Analyses

For the analyses of organic carbon (C_{org}), nitrogen (N) and stable isotopes $\delta^{13}C$ and $\delta^{15}N$ all samples were run twice to detect carbonates in the sediment. However, no carbonates were detected in any of the samples. A quantity of 7–8 mg of freeze-dried, grinded, and homogenized sediment were put in tin and silver capsules. The tin capsules were immediately sealed. In the silver capsules, ca 100 µl of 2M HCl was added to remove carbonates, and the samples were dried overnight at 60°C. The silver capsules were then sealed the next day. The samples were analyzed in a Finnigan DeltaV advantage mass spectrometer connected to a CarloErba NC2500 elemental analyzer through a ConfloIV open split interface. The carbon and nitrogen isotope measurements were normalized to the Vienna PeeDee Belemnite and atmospheric N according to (‰) = [(Rsample - Rstandard) / Rstandard] × 1,000. Accuracy of the C_{org} and N measurements was 0.01%, and the precision was +/−0.09 and +/−0.02% for C_{org} and N, respectively. Precision of the stable isotopes $\delta^{13}C$ and $\delta^{15}N$ measurements was +/−0.15‰, and the accuracy was 0.04 and 0.05‰ for $\delta^{13}C$ and $\delta^{15}N$, respectively. The same methods as well as similar instruments and pretreatment of samples have previously been used for Baltic Sea sediments (e.g., Voss et al., 2000; Jokinen et al., 2018; Ning et al., 2018). A total of 50 subsamples were analyzed from Bråviken, 55 subsamples from Himmerfjärden and 35 subsamples from Ådfjärden.

The $\delta^{13}C$ values were corrected for the depletion in atmospheric $\delta^{13}C$ since 1840 CE due to fossil-fuel burning, the so called "Suess effect" (Keeling, 1979). We used the equation from Verburg (2007) to calculate the modeled $\delta^{13}C_{atm}$ for a given year, which was then subtracted from the modeled $\delta^{13}C_{atm}$ for the year 1840 CE. This time-dependent depletion of $\delta^{13}C_{atm}$ was then added to the measured $\delta^{13}C_{org}$ of our samples. The geochemical analyses were carried out at the Stable Isotope Lab, Department of Geological Sciences at Stockholm University.

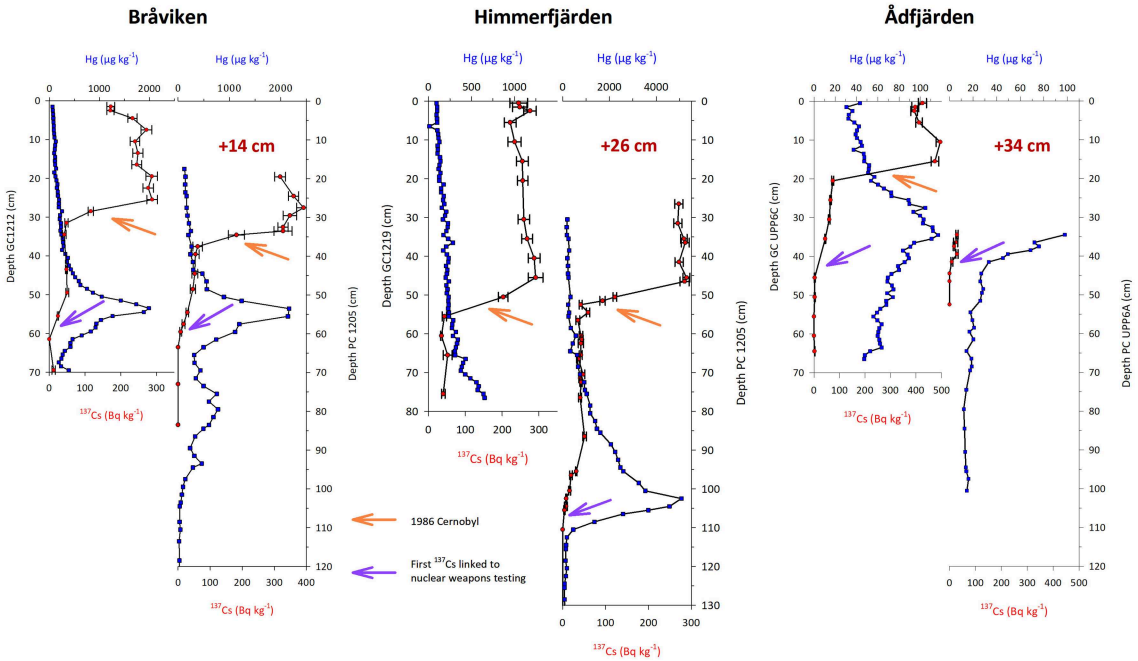

FIGURE 2 | Correlation between the short gravity cores (GC) and the long piston cores (PC) from the sites Bråviken, Himmerfjärden, and Ådfjärden. Marker levels used as fixpoint for the correlations, ^{137}Cs increase linked to the nuclear weapons testing at c. 1960 and the 1986 Cernobyl accident, indicated by purple and orange arrows, respectively. Offset between the gravity cores and the piston cores indicated in red text.

Diatom Analysis

For each subsample, a quantity of ca 0.1 g freeze-dried sediment was prepared according to standard procedures (Battarbee, 1986). After the last rinse 1 ml of a microsphere stock solution with a concentration of 5.5603×10^6 microspheres/ml was added. Diatoms were analyzed under light microscope using differential interference contrast and magnification × 1,000 with oil immersion. Counting of diatom valves was carried out according to the method described by Schrader and Gersonde (1978). A minimum of 300 diatom valves were counted at each level. Floras used for identification include Cleve-Euler (1951–1955), Krammer and Lange-Bertalot (1986–1991), Snoeijs (1993–1998), and Witkowski et al. (2000). Concentration of diatom valves was calculated according to the method described by Battarbee (1986). A total of 33 subsamples were prepared and analyzed from Bråviken, 24 subsamples from Himmerfjärden and 33 subsamples from Ådfjärden.

Due to a large amount of broken valves, *Epithemia adnata*, *Epithemia sorex*, and *Epithemia turgida* were merged into *Epithemia* aggregate. This will not affect the interpretation, since all these *Epithemia* species have similar ecology in terms of life form (epiphytic) and salinity tolerance (brackish to brackish-freshwater) (Snoeijs, 1993–1998). *Diatoma moniliformis* and *Diatoma tenuis* are both common in coastal waters of the Baltic Sea. *Diatoma moniliformis* is an epiphyte, while *Diatoma tenuis* constitutes a large part of the coastal plankton (Snoeijs and Potapova, 1998). Our samples showed a gradual transition between these two species and it was in many cases not possible to assign the valves either as *Diatoma moniliformis* or *Diatoma tenuis*. These taxa are also known to hybridize (Snoeijs and Potapova, 1998), and many of the valves in our samples were possible hybrids. We have chosen to present them as *Diatoma* aggregate. Based on data from the environmental monitoring we know that *Diatoma tenuis* is found in the plankton of Bråviken, and we have therefore chosen to interpret this species complex as pelagic. This interpretation also fits well with the other results since the increase in *Diatoma* aggregate is simultaneous to increases in other pelagic taxa. Vegetative cells of *Skeletonema* and *Chaetoceros* spp. were counted when possible but left out from the base sum of diatom relative abundance because of mass blooms in some levels and fluctuating preservation due to their very thin frustules.

The diatom results were assembled and cluster analyses were performed using the software Tilia and CONISS (Grimm, 1987). To detect trends and compositional changes in the diatom dataset over time, a Detrended Correspondence Analysis (DCA) was performed on the relative abundance data for each core for taxa with more than 3% in a single sample, using the rioja package (Juggins, 2015) in R 3.5.1 (R Core Team, 2018). Species richness was calculated using rarefaction analysis in the vegan package (Birks and Line, 1992; Oksanen et al., 2015).

RESULTS

Age-Depth Modeling

It has been possible to construct calendar years age-depth models based on the splice sediment sequences and by merging the ^{14}C and the ^{210}Pb ages together in the calibration dataset

(**Figure 3**). No apparent hiatuses have been detected and the splice records can therefore be considered having recorded a continuous sedimentation throughout their respective time span. The highest sedimentation rate, 15–20 mm/year, is recorded in the upper part of the core from site Himmerfjärden but also Bråviken displays a high (ca 10 mm/year) sediment accumulation rate in the upper part. The recorded sediment accumulation rate at site Ådfjärden is lower, 6 mm/year. Downcore, from ca 50–100 cm, the sediment accumulation rates decrease significantly and varies between 1 and 3 mm at all sites.

Lithology

The lithologies of the sediment cores from Bråviken, Himmerfjärden, and Ådfjärden are illustrated in **Figure 4**. Bråviken (PC1205) consists of mud, laminated the upper ca 80 cm below sea floor (bsf), and homogeneous down to ca 210 cm bsf. The rest of the core is laminated to sulfide banded/stained. Himmerfjärden (PC1208) consists of distinctly laminated mud in the upper ca 120 cm, the laminae thickness varies between a few mm to 2 cm. The following meter is weakly/diffusely laminated (laminas on mm-scale). From ca 220 cm bsf the sediment is homogeneous with increased amount of silt downcore. Ådfjärden (UPP6A) consists of mud, distinctly to weakly laminated the upper ca 80 cm bsf, and very weakly to diffusely laminated further downcore. The 72 cm long parallel gravity core sampled in Ådfjärden (UPP6D) was laminated throughout, and the laminas were visually counted to 120 ± 10.

Geochemical Analyses

The results from the geochemical analyses (C_{org}, N, C/N ratio, and stable isotopes $\delta^{13}C$ and $\delta^{15}N$) are plotted vs. depth cm bsf in **Figure 4**. C_{org} varies between 1 and 3% in all cores. Bråviken shows stable values of ca 2% throughout the core. Himmerfjärden displays values of 1–2% in the bottom part of the core, and higher values of ca 3% from 350 cm bsf. Ådfjärden shows values of 3.5%, with lower values of ca 2.5% from ca 150 cm bsf. As for nitrogen, Bråviken shows stable values of 0.2% throughout the core. Himmerfjärden displays values of ca 0.1% in the bottom part of the core, and higher values of ca 0.3–0.4% from 350 cm bsf. Ådfjärden shows values of ca 0.5 %, with lower values of ca 0.4% from ca 150 cm bsf. C/N ratios in all cores ranges between ca 7 and 11, with decreasing values toward the top in Bråviken and Ådfjärden, from ca 9–10 to 7–8. Stable isotope $\delta^{13}C$ shows relatively stable values in Bråviken of ca −24‰, with slightly lower values of ca −25‰ from ca 150 cm bsf. In Himmerfjärden there is an increasing trend throughout the core, from values of ca −24 to −22‰ in the top. Ådfjärden shows values of ca −22‰, and from ca 130 cm bsf lower values of ca −23‰. Stable isotope $\delta^{15}N$ shows the same pattern in all three cores with values of ca 3‰ in the bottom part of the core, and then an increasing trend toward the top. In Bråviken, the increasing trend starts at ca 150 cm bsf with values of 6 to 7‰ toward the top. In Himmerfjärden, the increasing trend is visible from ca 200 cm bsf with values of ca 6‰ in the top. In Ådfjärden this increasing trend starts at 50 cm bsf and continues to values of ca 4‰.

The Diatom Records

In total 177 taxa were identified in Bråviken, 116 in Himmerfjärden and 160 in Ådfjärden (**Supplementary Tables 1–3**). The time resolution for diatom samples varies between sites and with depths in the stratigraphies, from <10 years to 100–200 years (244 years is the maximum time between two samples). The taxa occurring with a relative abundance of at least 5% in one level are divided into benthic and pelagic taxa and plotted in order of first appearance in **Figures 5–7**. Based on the cluster analyses and visual inspection of the taxa in the diagrams, each stratigraphy is divided into two local diatom assemblage zones (Brå 1-2, Him 1-2, and Åd 1-2). Site by site these zones are described below.

Bråviken

This site is dominated by benthic taxa up to about 120 cm bsf (∼ 1800 CE), where the diatom composition changes to being dominated by pelagic taxa (**Figure 5**). The concentration of diatom valves show an increasing trend throughout the stratigraphy.

Brå 1, 367–115 cm bsf, ∼500–1830 CE: This part of the stratigraphy is dominated by benthic taxa, for example *Rhoicosphenia curvata*, *Epithemia* aggregate, *Opephora mutabilis*, and *Amphora pediculus*. The pelagic taxa are dominated by *Aulacoseira* species; *A. ambigua* (which shows a decreasing trend), *A. islandica* and *A. subarctica*. *Pauliella taeniata* is present in this zone with two peaks at 360 and 270 cm bsf, followed by a decline. Other pelagic taxa present in this zone include for example *Thalassiosira levanderi*, *Cyclotella choctawhatcheeana*, and *Melosira arctica*.

Brå 2, 115-0 cm bsf, ∼1830–2012 CE: This zone shows a dramatic decrease in benthic taxa, simultaneously to an increase in pelagic taxa, consisting mostly of *Diatoma* aggregate. This species complex shows a maximum of 60% at ca 70 cm bsf. Benthic taxa that decrease throughout this zone includes for example *R. curvata* and *Epithemia* aggregate. In the upper ca 70 cm bsf small pelagic taxa such as *Thalassiosira proshkinae*, *Stephanodiscus medius*, *Stephanodiscus parvus*, and *Stephanodiscus minutulus* are increasing. Also, *P. taeniata* increases to relative abundances similar to those before the decrease in zone Brå 1. *A. subarctica* show higher relative abundances toward the top of the stratigraphy.

Himmerfjärden

This site is dominated by pelagic taxa, with the exceptions in three levels at 170–210 cm bsf (∼1520–1730 CE) (**Figure 6**). The concentration of diatom valves shows an increasing trend upwards throughout the stratigraphy.

Him 1A, 359–227 cm bsf, ∼400–1570 CE: *P. taeniata* dominates this zone with relative abundances of ca 20–50%. *C. choctawhatcheeana* is present with relative abundances of ca 15–20%. *T. levanderi* shows an increasing trend followed by a decrease in this zone. *T. proshkinae* is also present in this zone with relative abundances of ca 2–5%. Benthic taxa present in this zone is for example *Epithemia* aggregate, *R. curvata*, *Cocconeis placentula*, *A. pediculus*, and *Planothidium delicatulum*.

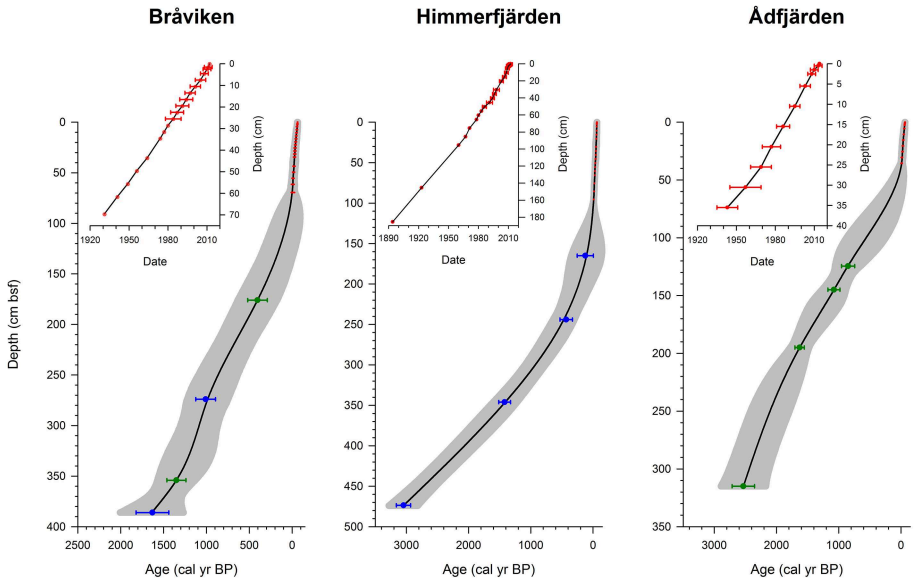

FIGURE 3 | Age-depth plots based on ^{210}Pb (upper panel) and ^{14}C (lower panel). The age-depth ^{14}C curves are spline smoothed and the gray shaded area indicates the uncertainty (1 sigma) in the modeling. Samples marked in green are terrestrial macrofossils calibrated with IntCal13 and samples marked in blue are marine macrofossils calibrated with Marine13.

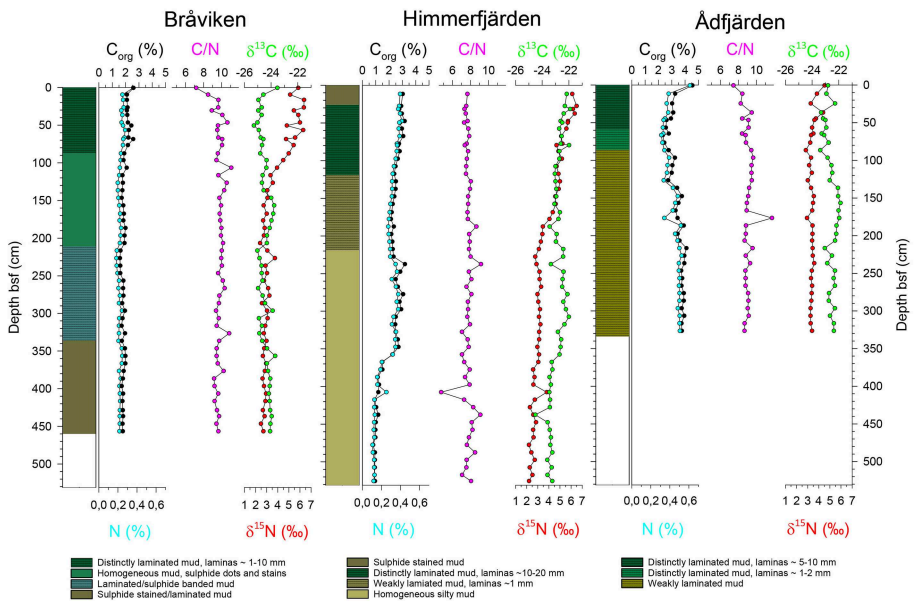

FIGURE 4 | Lithologies and geochemical profiles for Bråviken, Himerfjärden, and Ådfjärden. Geochemistry parameters are organic carbon (C_{org}), nitrogen (N), organic carbon/nitrogen (C/N) ratio, and stable isotopes of δ^{13}C and δ^{15}N.

Him 1B, 227–110 cm bsf, ∼1570–1950 CE: At the bottom of this zone many benthic species show a maximum in their relative abundance, for example *Epithemia* aggregate, *R. curvata*, *C. placentula*, *A. pediculus*, and *P. delicatulum*. From the peak of benthic taxa at ca 220 cm bsf, these taxa show a continuous decrease throughout this zone, simultaneous with an increase in pelagic taxa. The pelagic assemblage is dominated by the same taxa as in Him 1A but with slightly higher relative abundances of *M. arctica*, and *Diatoma* aggregate.

Him 1C, 110–53 cm bsf, ∼1950–1984 CE: The decrease in benthic taxa continues in this zone, while pelagic taxa such as *T. levanderi*, *T. proshkinae* and *Diatoma* aggregate increases. The ice associated species *M. arctica* has its maximum occurrence in this zone.

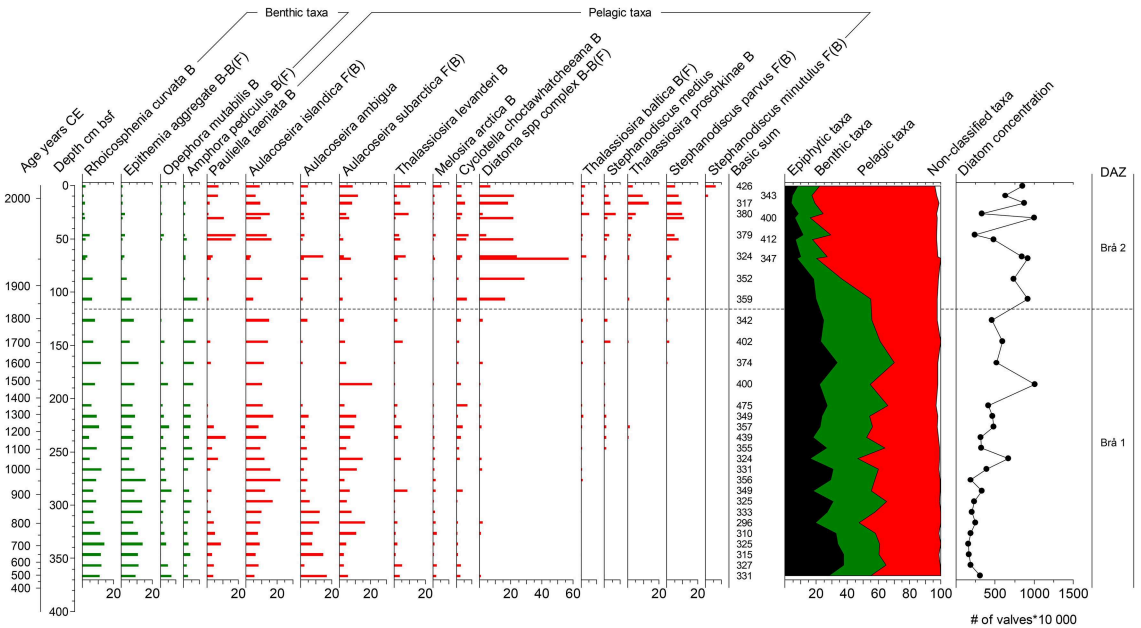

FIGURE 5 | Diatom diagram for the site Bråviken. Taxa are grouped into benthic and pelagic taxa and plotted in order of first appearance. The linear scale is a depth scale and the secondary scale is an age scale in calendar years CE. The summary diagram shows all taxa grouped by life-form. The epiphytes constitutes a part of the benthic community. Diatom concentration are given in # of valves *100,000 per gram dry weight sediment. Salinity distribution (F = Freshwater; B = Brackish; BF = Brackish-freshwater; BM = Brackish-marine) from Snoeijs (1993–1998).

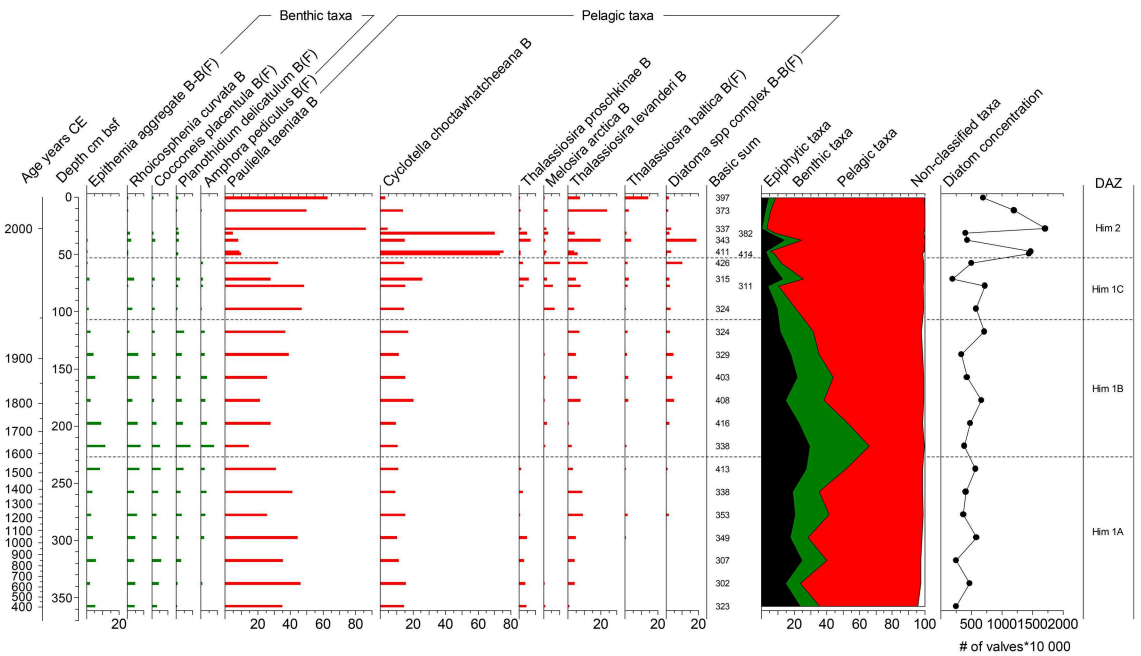

FIGURE 6 | Diatom diagram for the site Himmerfjärden. For details see legend to **Figure 5**.

Him 2, 53–0 cm bsf, ∼1984–2012 CE: The topmost part of the Himmerfjärden stratigraphy is characterized by a drastic increase in *C. choctawhatcheeana*. The relative abundance of *P. taeniata* co-varies with *C. choctawhatceeana*, and also shows maximum values in this zone. *Thalassiosira baltica, T. levanderi*, and *T. proschkinae* are present and show their maximum relative

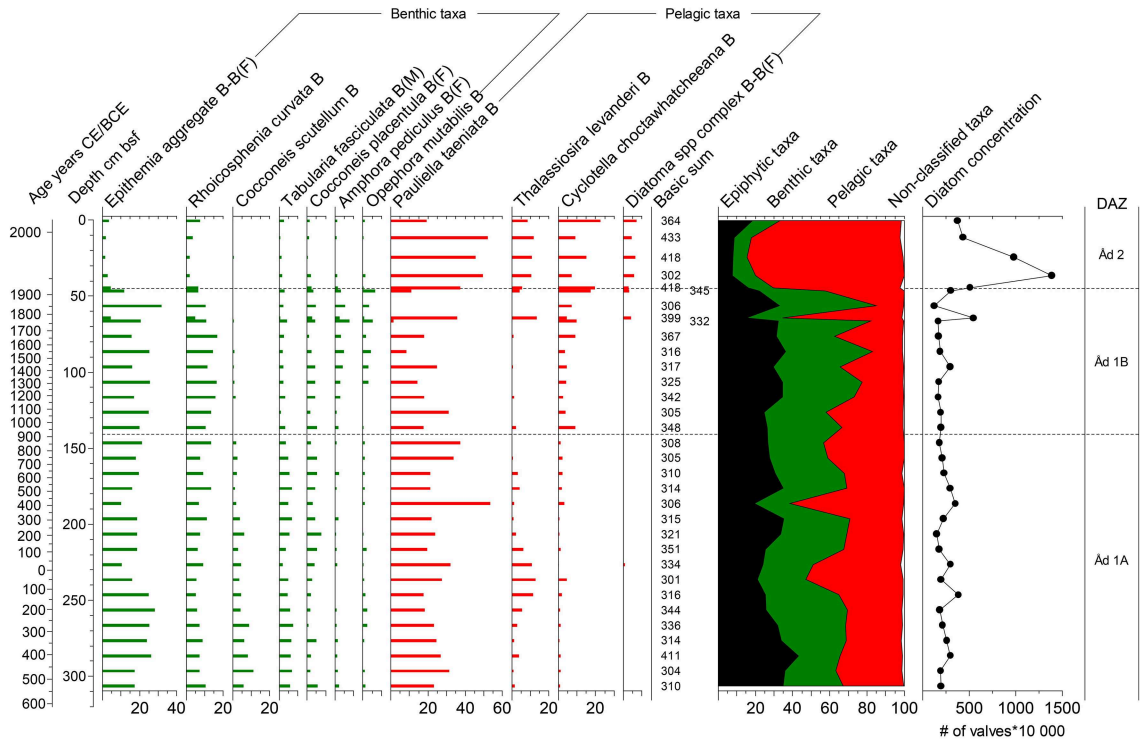

FIGURE 7 | Diatom diagram for the site Ådfjärden. For details see legend to **Figure 5.**

abundances in Him 2, as well as *Diatoma* aggregate. All benthic taxa are decreasing and/or disappearing in this zone.

Ådfjärden

This site is dominated by benthic taxa up to Åd 2, which is then instead dominated by pelagic taxa (**Figure 7**). The concentration of diatom valves shows relatively stable values up to Åd 2, where the concentration dramatically increases.

Åd 1A, 310–140 cm bsf, ∼530 BCE −800 CE: This zone is dominated by benthic taxa, for example *Epithemia* aggregate, *R. curvata*, *Cocconeis scutellum*, *C. placentula*, and *Tabularia fasciculata*. *P. taeniata* is present with relative abundances of ca 20–40%. *T. levanderi* shows an increase followed by a decrease from ca 230 cm bsf. *C. choctawhatcheeana* is present in this zone with relative abundances of ca 0–5%.

Åd 1B, 140-45 cm bsf, ∼800–1920 CE: In this zone *A. pediculus* and *O. mutabilis* show their maximum occurrence. Simultaneously *C. scutellum* and *T. fasciculata* have decreased compared to zone Åd 1A. Toward the top of this zone several pelagic taxa are increasing, e.g., *T. levanderi*, *C. choctawhatcheeana*, and *Diatoma* aggregate. *C. choctawhatcheeana* also shows a minor increase already at the bottom of this zone.

Åd 2, 45–0 cm bsf, ∼1920–2014 CE: The topmost part of the Ådfjärden stratigraphy is characterized by a drastic decrease in benthic taxa, e.g., *Epithemia* aggregate and *R. curvata*. Up to this level, benthic taxa have been dominating with percentages of ca 50–70%. This now drops to values of ca 20–30%. The pelagic taxa dominating this zone are *P. taeniata*, *T. levanderi*, and *C. choctawhatcheeana*. This shift in the diatom assemblage is simultaneous with the increase in concentration of diatom valves in the sediment.

DISCUSSION

Geochemical Proxies and Lithologies

In the Baltic Sea stable nitrogen isotope ($\delta^{15}N$) values at the sediment surface are generally higher in coastal areas (5–13‰) than in the open Baltic Sea (3–5‰) (Voss et al., 2000, 2005). The cause for the elevated values in coastal areas is suggested to be anthropogenic nitrogen delivered by rivers and diffuse runoff (Voss et al., 2005). Our results show that all three sites have low values of ca 2–3‰ until a point from which they start to increase toward present day (**Figures 4**, **8**). In Bråviken and Himmerfjärden an early slight increase is recorded already from ca 1700 CE and 1600 CE, respectively. A more pronounced increase starts ca 1800 CE at these two sites and continues to values of ca 6‰ toward present day. In Ådfjärden an increase in sedimentary $\delta^{15}N$ is visible from ca 1900 CE. However, at this site the values never exceed 5‰, which suggests that this site is to a lesser degree impacted by anthropogenic nitrogen. Savage et al. (2010) have studied the drivers of eutrophication in an embayment in the northern part of Himmerfjärden. Their core dates back to ca 1800 CE, and records elevated $\delta^{15}N$ values from early nineteenth century. The early changes in our record from Himmerfjärden with respect to $\delta^{15}N$ are not captured in

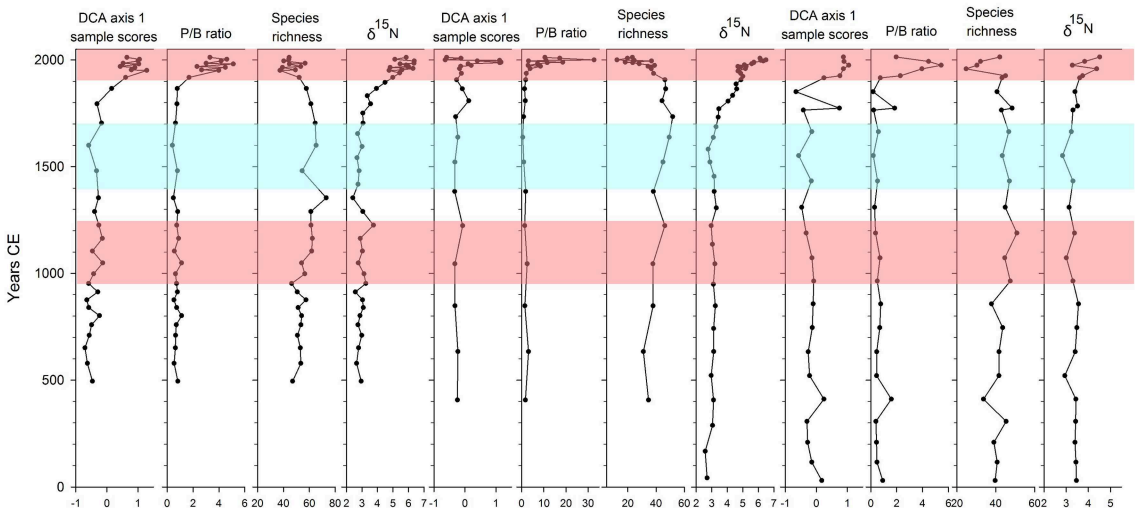

FIGURE 8 | Summary figure showing axis 1 sample scores from a Detrended Correspondence Analysis (DCA), the pelagic/benthic (P/B) ratio, diatom species richness, and changes in the nitrogen stable isotope $\delta^{15}N$. DCA axis 1 summarizes trends and compositional changes in the diatom dataset over time. Medieval Climate Anomaly and Modern Warm Period are marked in red, and Little Ice Age in blue. These time periods are defined as by Mann et al. (2009) and Harland et al. (2013).

their study, since the values from 1800 CE are interpreted as background levels.

Due to the differences in carbon sources for phytoplankton and land plants, they produce organic matter with different stable carbon isotope ($\delta^{13}C$) values. Marine phytoplankton produce organic matter with $\delta^{13}C$ values of −18 to −22‰, while land plants show values of −25 to −28 ‰ (Kandasamy and Nagender Nath, 2016 and references therein). The $\delta^{13}C$ values from Bråviken, Himmerfjärden, and Ådfjärden (**Figure 4**) lie between these two intervals with values of ca −22 to −25‰, indicating that the origin of the organic material derives both from terrestrial plants and marine phytoplankton. In Himmerfjärden there is a decrease in $\delta^{13}C$ toward the top, suggesting increased primary production at this site. However, in a coastal and brackish system where the primary producers are a mixture of marine and freshwater algae, the interpretation of $\delta^{13}C$ becomes more complicated. According to Lamb et al. (2006) $\delta^{13}C$ values of land plants and freshwater algae overlaps, land plants displaying values of −21 to −32‰, and freshwater algae −26 to −30‰. The C/N ratio can then aid in interpreting the sources of organic matter. Since terrestrial plants consists to a high degree of nitrogen-poor cellulose and lignin, the C/N ratios are usually >12. In algae the C/N ratios are <10. The C/N ratios from Bråviken, Himmerfjärden, and Ådfjärden are all in the range of 6–10, suggesting that the origin of organic material in these sediments mostly derives from algae, i.e., is produced in the basin (Lamb et al., 2006). Bråviken and Ådfjärden display a decrease in C/N ratio in the topmost part of the cores, which could indicate even less input from land, or, more likely, higher primary production in these coastal waters. However, Lamb et al. (2006) also points out that even with the help of C/N ratio, it can be difficult to distinguish the sources of organic material in coastal areas with high algal production.

Laminated sediments have proven to be a useful proxy for hypoxia in the open Baltic Sea (Zillén et al., 2008 and references therein). Absence of major benthic fauna and bioturbation under hypoxic conditions facilitates the preservation of laminas. However, the lithologies of the cores from Bråviken, Himmerfjärden, and Ådfjärden are not as easy to interpret as the ones from the open Baltic Sea. Lithologies are shown in **Figure 4**, but these are in some measure uncertain in the identification of hypoxic intervals because of presence of diffusely laminated sediments and sulfide banding. Presumably these results can for example be explained by seasonal hypoxia and the dynamic nature of the coastal zone, with redox conditions shifting from oxic to hypoxic and *vice versa*. Recolonization events of benthic fauna would lead to bioturbation of laminated sequences, leaving them weakly laminated.

Changes in the Diatom Assemblages

The diatom records in this study dates back to ca 400 CE in Bråviken and Himmerfjärden, and to 500 BCE in Ådfjärden. We consider these records to reflect pristine conditions of the sites. In Bråviken and Ådfjärden the diatom assemblages are dominated by benthic taxa, with a high share of epiphytes (diatoms living attached to algae or submerged plants). These are for example *Epithemia* spp., *Rhoicosphenia curvata*, *Cocconeis* spp., *Amphora pediculus* and *Opephora mutabilis*. Also in Himmerfjärden these taxa are present, although in this record, pelagic taxa are dominating, except for in three levels, corresponding to ca 1520–1730 CE.

At a certain point in time, all three diatom records start to display major changes. These trends and compositional changes over time are summarized in the DCA axis 1 (**Figure 8**). The changes in life-form of the diatom taxa is reflected in the Pelagic/Benthic (P/B) ratio where an increasing trend in the P/B ratio reflects a decrease in benthic and epiphytic taxa, and a simultaneous increase in pelagic taxa.

The increasing trend in the P/B ratios starts ca 1900 CE in Bråviken and Ådfjärden, and ca 1950 CE in Himmerfjärden and is likely caused by a deterioration in water transparency, leading to a loss in benthic habitats, in particular macrophytes. This interpretation is further supported by the decreases in epiphytic taxa as illustrated in **Figures 5–7**. Similar patterns with increased P/B ratios have been shown in several studies from the Baltic Sea drainage area (Clarke et al., 2006; Ellegaard et al., 2006; Weckström, 2006; Andrén et al., 2016; Ning et al., 2018), and have been linked to agricultural expansion, industrialization and urbanization. In addition, several of these studies report a simultaneous decrease in species richness, also evident in our study (**Figure 8**).

The change in P/B ratios is also a result of an increase in the relative abundance of small centric diatom taxa which has been recognized in several paleoecological studies from the Baltic Sea as a response to eutrophic conditions (e.g., Andrén, 1999; Weckström, 2006; Tuovinen et al., 2010). In a dataset of 49 shallow embayments from the Gulf of Finland Weckström and Juggins (2006) showed how these taxa clearly increase in abundance with elevated nutrient levels (>600 $\mu g \cdot L^{-1}$ for total dissolved nitrogen and >60 $\mu g \cdot L^{-1}$ for total phosphorous). In the records from Bråviken, Himmerfjärden, and Ådfjärden, we register a pattern with increased relative abundances of small centric diatom taxa toward present day. These taxa include e.g., *Stephanodiscus parvus*, *Thalassiosira proschkinae*, *Thalassiosira levanderi*, and *Cyclotella choctawhatcheeana*, and this is interpreted as a result of eutrophication at these sites.

Small *Stephanodiscus* species (in particular *S. parvus*) are freshwater species, typical of nutrient-rich lakes (Bradshaw and Anderson, 2001; Renberg et al., 2001; Bradshaw et al., 2005). *S. parvus* and *S. medius* have been recorded in high abundances in the eutrophic and brackish Curonian Lagoon in the southeast Baltic Proper (Snoeijs, 1993–1998). *S. medius*, *S. minutulus*, and *S. parvus* have increased since the end of the nineteenth century in Bråviken, indicating enhanced eutrophic conditions.

The small pelagic taxon *Cyclotella choctawhatcheeana* is present in all three sites and is increasing toward present day in Himmerfjärden and Ådfjärden. This species blooms during warm summer months and has been shown to be an indicator of eutrophic conditions in the Baltic Sea (Andrén et al., 1999; Weckström et al., 2004) and in Chesapeake Bay, USA (Cooper, 1995). In Himmerfjärden *C. choctawhatcheeana* shows stable relative abundances of ca 15–20% until the 1970s−1980s when this species increases to relative abundances of almost 80% at some levels. This is attributed to the opening of the sewage treatment plant in the 1970s. Also *Thalassiosira proschkinae* has been found to indicate eutrophication in Chesapeake Bay (Cooper, 1995), and in a training set from the Gulf of Finland this species has been shown to respond to high phosphorus levels (Weckström and Juggins, 2006). *T. proschkinae* is present in Himmerfjärden from about 400 to 1500 CE when it disappears and reappear ca 1960 CE. This species is also present in Bråviken, showing an increase toward the end of the twentieth century.

Thalassiosira levanderi has been reported to dominate the spring bloom together with *Pauliella taeniata* and *Chaetoceros* spp. after winters with extended sea ice and late ice-out conditions in Himmerfjärden (Hajdu et al., 1997). However, *T. levanderi* is hard to interpret since it also seems to respond to elevated nutrient conditions (Hajdu et al., 1997). It has also been suggested that this species is more common after winters with weak or no ice cover (Tuovinen et al., 2010). *T. levanderi* is present at all our three study sites, with higher relative abundances toward the present day. This pattern has also been reported from a sediment core from the Bornholm basin (Andrén et al., 2000b). In Ådfjärden this species was more common during two intervals, ca year 0 CE, and toward present day. Since both ice extent and nutrient conditions play a role for the distribution of this species these two events might not represent comparable environmental conditions. However, these time intervals correspond to Roman Warm Period and Modern Warm Period (Wang et al., 2012; Harland et al., 2013), and our results indicate that this species benefits from conditions that prevail during warmer periods, e.g., with respect to salinity, stronger stratification, or nutrient availability.

Pauliella taeniata is very common in the plankton of the Baltic Sea (Snoeijs, 1993–1998). This species has also been shown to live in and on sea ice (Hajdu et al., 1997). With the exception of Himmerfjärden, this species shows an increasing trend toward the present day. The same general pattern has been reported from Gotland basin (Andrén et al., 2000a). *P. taeniata* shows its lowest relative abundances ca 1250–1950 CE in Bråviken, ca 1650 CE and from 2000 CE in Himmerfjärden, and ca 1850 CE in Ådfjärden. Nothing in our data indicates that *P. taeniata* reflects ice conditions, but this species probably responds to some other environmental variables such as nutrient availability, stratification or upwelling.

Aulacoseira islandica, *Aulacoseira subarctica,* and *Aulacoseira ambigua* are freshwater species that are common in Bråviken throughout the stratigraphy. *Aulacoseira* spp. form colonies, the frustules are heavily silicified and have a fast sinking rate (Lotter et al., 2010). Due to this, *Aulacoseira* spp. are favored by nutrient upwelling and turbulent waters (Wang et al., 2008). It has been recorded from lakes in regions with pronounced warming during the last century that heavily silicified *Aulacoseira* spp. decrease in abundance (Rühland et al., 2008). However, it has also been reported from a lake in the southern part of Kamchatka peninsula that *A. subarctica* did not do well in years with ice cover. This species need wind induced mixing and thrives during years when thermal stratification was delayed by cold and windy weather (Lepskaya et al., 2010). In Bråviken the recorded pattern indicates higher relative abundances of *Aulacoseira* spp. during the last 50 years and the MCA than during the LIA. This could be attributed to changes in the extension and duration of sea ice, but also to decreased river discharges during the LIA (Schimanke and Meier, 2016). Low levels of river discharges affect the salinity, but would also reduce the availability of silica in the Baltic Sea, which could have a negative effect on the heavily silicified *Aulacoseira* spp.

Baltic Sea Environmental Deterioration in a Long-Term Perspective

It has been suggested that the extensive areal distribution of hypoxia in the open Baltic Sea during the MCA, and the following re-oxygenation event was caused by fluctuations in land use, as a result of demography changes in the drainage area (Zillén and Conley, 2010). The results from Bråviken, Himmerfjärden, and Ådfjärden indicate that conditions in the coastal zone were not severely altered during the MCA (**Figure 8**). Since land use changes likely will influence the coastal zone first, before possible effects are registered in the open Baltic Sea, our results indicate that the changes in redox conditions in the open Baltic Sea during the MCA and the LIA were not caused by human activities on land. Land use changes during the last millennium might have affected the coastal ecosystems slightly. However, as the coastal areas were not heavily affected, it is unlikely that changes in demography and land use would have had major effects on development and persistence of hypoxia in the open Baltic Sea. This interpretation is further supported by results from Jokinen et al. (2018) and Ning et al. (2018). The extensive areal distribution of hypoxia in the open Baltic Sea during the MCA was more likely caused by the warmer climate. A warmer climate enhances stratification, which sustains hypoxia and anoxia in deep waters (Kabel et al., 2012).

In Bråviken the first signs of eutrophication are recorded ca 1800 CE. This is reflected in the increase in $\delta^{15}N$ and in changes in the diatom assemblages, as illustrated by DCA axis 1 (**Figure 8**). Eutrophication of Bråviken could have been a direct result of the paper and textile industries and their discharges, intensified agriculture in the large drainage area, or an interaction of both causes. In Himmerfjärden the earliest sign of eutrophication is the increase in $\delta^{15}N$, starting ca 1800 CE. The eutrophication signals in Himmerfjärden get more pronounced from ca 1900 CE, with the decrease in diatom species richness, and from ca 1950 CE the increase in P/B ratio is recorded (**Figure 8**). This corresponds to the expansion of Södertälje and the industries in this area, during the 1940s. The opening of the sewage water treatment plant in 1974 is distinct in the diatom stratigraphy from Himmerfjärden, as reflected in DCA axis 1. In Ådfjärden the eutrophication signals are recorded from ca 1900 CE. This site is the most remote and "pristine" of the three sites in this study, with no urban area or extensive agriculture in its vicinity.

In a sediment record from the Swedish east coast dating back to 900 CE Ning et al. (2018) interpreted more eutrophic conditions from ca 1850 CE using the stable nitrogen isotope record. The diatom data in this study shows an increase in the P/B ratio starting ca 1900 CE. A study from the Archipelago Sea traced hypoxia and eutrophication in a record covering more than 1500 years (Jokinen et al., 2018). They report elevated $\delta^{15}N$ values from ca 1900 CE. Both these studies show similar trends as those we have recorded in Bråviken, Himmerfjärden and Ådfjärden, although Bråviken, and Himmerfjärden show signs of eutrophication even earlier, around 1800 CE. Our results highlight the importance of a longer time perspective than the environmental monitoring can provide. Additional methods are needed in order to determine reference conditions and our studies of sediment cores have shown that this type of archives have great potential to fill the current knowledge gaps.

CONCLUSIONS

- We find no evidence in our data supporting that the extensive distribution of hypoxia in the open Baltic Sea during the Medieval Climate Anomaly was caused by human activities on land.
- The onset of eutrophication, as identified from stable nitrogen isotopes and changes in diatom composition, dates to ca 1800 CE in Bråviken and Himmerfjärden, and to ca 1900 CE in Ådfjärden.
- The ecosystem deterioration that have occurred in our three investigated coastal sites during the last two centuries and that have escalated during the twentieth century is unique in a thousand year perspective.
- The onset of these ecosystem changes is site dependent and reflects the local history and geography of the drainage areas.
- Our study highlights the importance of a long time perspective in the management of the Baltic Sea.

AUTHOR CONTRIBUTIONS

LN, TA, and EA designed the study and performed the field work. LN did lab work, prepared the samples for geochemistry analyses and did the diatom analysis and wrote the manuscript for most parts. EA and TA aided in interpreting and discussing the results. TA produced the age models and wrote the parts on this in the manuscript. ML performed and supervised statistical analyses. MM provided Hg and ^{137}Cs for correlation of the cores. TJA performed ^{210}Pb-datings. All authors contributed to the writing of the manuscript.

FUNDING

This study was financially supported by a grant to EA provided by The Foundation for Baltic and East European Studies (1562/3.1.1/2013). EA and TA were further supported by Stockholm County Council. Östersjöstiftelsen is the Swedish name for The Foundation for Baltic and East European Studies.

ACKNOWLEDGMENTS

We thank the captain and crew of M/S *Fyrbyggaren*, as well as R/V *Skagerak*. Heike Siegmund, Department of Geological Sciences, Stockholm University is thanked for help with stable isotope and elemental analyses. We also thank the two reviewers for constructive and helpful comments on the manuscript.

SUPPLEMENTARY MATERIAL

The Supplementary Material for this article can be found online at: https://www.frontiersin.org/articles/10.3389/fenvs.2019.00088/full#supplementary-material

REFERENCES

Andrén, E. (1999). Changes in the composition of the diatom flora during the last century indicate increased eutrophication of the oder estuary, South-western Baltic Sea. *Estuar. Coast. Shelf Sci.* 48, 665–676. doi: 10.1006/ecss.1999.0480

Andrén, E., Andrén, T., and Kunzendorf, H. (2000a). Holocene history of the Baltic Sea as a background for assessing records of human impact in the sediments of the Gotland Basin. *Holocene* 10, 687–702. doi: 10.1191/09596830094944

Andrén, E., Andrén, T., and Sohlenius, G. (2000b). The Holocene history of the southwestern Baltic Sea as reflected in a sediment core from the Bornholm Basin. *Boreas* 29, 233–250. doi: 10.1080/030094800424259

Andrén, E., Shimmield, G., and Brand, T. (1999). Environmental changes of the last three centuries indicated by siliceous microfossil records from the southwestern Baltic Sea. *Holocene* 9, 25–38. doi: 10.1191/095968399676523977

Andrén, E., Telford, R. J., and Jonsson, P. (2016). Reconstructing the history of eutrophication and quantifying total nitrogen reference conditions in Bothnian Sea coastal waters. *Estuar. Coast. Shelf Sci.* 198, 320–328. doi: 10.1016/j.ecss.2016.07.015

Appleby, P. G. (2001). "Chronostratigraphic techniques in recent sediments," in *Tracking Environmental Change Using Lake Sediments*, *Vol 1: Basin Analysis, Coring and Chronological Techniques*, eds W. M Last and J. P.Smol (Dordrecht: Kluwer Academic Publishers), 171–204.

Battarbee, R. W. (1986). "Diatom analysis," in *Handbook of Holocene Palaeoecology and Palaeohydrology*, ed B. E. Berglund (Chichester: Johan Wiley & Sons Ltd.), 527–570.

Bianchi, T. S., Engelhaupt, E., Westman, P., Andrén, T., Rolff, C., and Elmgren, R. (2000). Cyanobacterial blooms in the Baltic Sea: natural or human-induced? *Limnol. Oceanogr.* 45, 716–726. doi: 10.4319/lo.2000.45.3.0716

Birks, H. J. B., and Line, J. M. (1992). The use of rarefaction analysis for estimating palynological richness from quaternary pollen-analytical data. *Holocene* 2, 1–10. doi: 10.1177/095968369200200101

Blaauw, M. (2010). Methods and code for 'classical' age-modelling of radiocarbon sequences. *Quat. Geochronol.* 5, 512–518. doi: 10.1016/j.quageo.2010.01.002

Bradshaw, E. G., and Anderson, N. J. (2001). Validation of a diatom–phosphorus calibration set for Sweden. *Freshw. Biol.* 46, 1035–1048. doi: 10.1046/j.1365-2427.2001.00732.x

Bradshaw, E. G., Rasmussen, P., Nielsen, H., and Anderson, N. J. (2005). Mid-to late-Holocene land-use change and lake development at Dallund Sø, Denmark: trends in lake primary production as reflected by algal and macrophyte remains. *Holocene* 15, 1130–1142. doi: 10.1191/0959683605hl885rp

Clarke, A. L., Weckström, K., Conley, D. J., Anderson, N. J., Adser, F., Andrén, E., et al. (2006). Long-term trends in eutrophication and nutrients in the coastal zone. *Limnol. Oceanogr.* 51, 385–397. doi: 10.4319/lo.2006.51.1_part_2.0385

Cleve-Euler, A. (1951–1955). "Die Diatomeen von Schweden und Finnland," in *Kungliga Vetenskapsakademiens Handlingar I-V*. (Stockholm: Almqvist & Wiksell), 4:e serien 2:1 (1951), 3:3 (1952), 4:1 (1953), 4:5 (1953), 5:4 (1955).

Conley, D. J., Carstensen, J., Aigars, J., Axe, P., Bonsdorff, E., Eremina, T., et al. (2011). Hypoxia is increasing in the coastal zone of the Baltic Sea. *Environ. Sci. Technol.* 45, 6777–6783. doi: 10.1021/es201212r

Cooper, S. R. (1995). Diatoms in sediment cores from the mesohaline chesapeake bay, U.s.a. *Diatom Res.* 10, 39–89 doi: 10.1080/0269249X.1995.9705329

Douglas Price, T., Arcini, C., Gustin, I., Drenzel, L., and Kalmring, S. (2018). Isotopes and human burials at Viking Age Birka and the Mälaren region, east central Sweden. *J. Anthropol. Archaeol.* 49, 19–38. doi: 10.1016/j.jaa.2017.10.002

Ellegaard, M., Clarke, A. L., Reuss, N., Drew, S., Weckström, K., Juggins, S., et al. (2006). Multi-proxy evidence of long-term changes in ecosystem structure in a Danish marine estuary, linked to increased nutrient loading. *Estuar. Coast. Shelf Sci.* 68, 567–578. doi: 10.1016/j.ecss.2006.03.013

Elmgren, R. (2001). Understanding human impact on the baltic ecosystem: changing views in recent decades. *AMBIO J. Hum. Environ.* 30, 222–231. doi: 10.1579/0044-7447-30.4.222

Elmgren, R., and Larsson, U. (1997). *Himmerfjärden: Förändringar i ett Näringsbelastat Kustekosystem i Östersjön*. Stockholm: Naturvårdsverket.

Gejvall-Seger, B. (1978). *Boken om Norrköping*. Stockholm: Natur och kultur.

Grimm, E. C. (1987). CONISS: a FORTRAN 77 program for stratigraphically constrained cluster analysis by the method of incremental sum of squares. *Comput. Geosci.* 13, 13–35. doi: 10.1016/0098-3004(87)90022-7

Gustafsson, B. G., Schenk, F., Blenckner, T., Eilola, K., Meier, H. E. M., Müller-Karulis, B., et al. (2012). Reconstructing the development of baltic Sea eutrophication 1850–2006. *AMBIO J. Hum. Environ.* 41, 534–548. doi: 10.1007/s13280-012-0318-x

Hajdu, S., Larsson, U., and Skärlund, K. (1997). "Växtplankton," in *Himmerfjärden: Förändringar i ett Näringsbelastat Kustekosystem i Östersjön*, eds R. Elmgren and U. Larsson (Stockholm: Naturvårdsverket), 63–79.

Harff, J., and Meyer, M. (2011). "Coastlines of the Baltic Sea – Zones of Competition Between Geological Processes and Changing Climate: Examples from the Southern Baltic.," in *The Baltic Sea Basin,* eds J. Harff, S. Björck, and P. Hoth (Berlin; Heidelberg: Springer-Verlag), 149–164. doi: 10.1007/978-3-642-17220-5_7

Harland, R., Polovodova Asteman, I., and Nordberg, K. (2013). A two-millennium dinoflagellate cyst record from Gullmar Fjord, a Swedish Skagerrak sill fjord. *Palaeogeogr. Palaeoclimatol. Palaeoecol.* 392, 247–260. doi: 10.1016/j.palaeo.2013.09.006

Jokinen, S. A., Virtasalo, J. J., Jilbert, T., Kaiser, J., Dellwig, O., Arz, H. W., et al. (2018). A 1500-year multiproxy record of coastal hypoxia from the northern Baltic Sea indicates unprecedented deoxygenation over the 20th century. *Biogeosciences* 15, 3975–4001. doi: 10.5194/bg-15-3975-2018

Juggins, S. (2015). *Rioja: Analysis of Quaternary Science Data*. Available online at: https://cran.r-project.org/web/packages/rioja/index.html (accessed November 7, 2015).

Kabel, K., Moros, M., Porsche, C., Neumann, T., Adolphi, F., Andersen, T. J., et al. (2012). Impact of climate change on the Baltic Sea ecosystem over the past 1,000 years. *Nat. Clim. Change* 2, 871–874. doi: 10.1038/nclimate1595

Kandasamy, S., and Nagender Nath, B. (2016). Perspectives on the terrestrial organic matter transport and burial along the land-deep sea continuum: caveats in our understanding of biogeochemical processes and future needs. *Front. Mar. Sci.* 3:259 doi: 10.3389/fmars.2016.00259

Keeling, C. D. (1979). The Suess effect: 13 carbon-14 carbon interrelations. *Environ. Int.* 2, 229–300. doi: 10.1016/0160-4120(79)90005-9

Kotilainen, A. T., Arppe, L., Dobosz, S., Jansen, E., Kabel, K., Karhu, J., et al. (2014). Echoes from the Past: a healthy baltic sea requires more effort. *AMBIO J. Hum. Environ.* 43, 60–68 doi: 10.1007/s13280-013-0477-4

Krammer, K., and Lange-Bertalot, H. (1986–1991). In: Ettl, H., Gärtner, J. G., Gerloff, J., Heynig, H. and Mollenhauer, D. eds. *Süsswasserflora von Mitteleuropa Bd 2.* Stuttgart: Fischer. T. 1, Naviculaceae (1986), T. 2, Bacillariaceae, Epithemiaceae, Surirellaceae (1988), T. 3, Centrales, Fragilariaceae, Eunotiaceae (1991) and T. 4, Achnanthaceae (1991).

Lamb, A. L., Wilson, G. P., and Leng, M. J. (2006). A review of coastal palaeoclimate and relative sea-level reconstructions using δ13C and C/N ratios in organic material. *Earth-Sci. Rev.* 75, 29–57. doi: 10.1016/j.earscirev.2005.10.003

Leipe, T., Moros, M., Kotilainen, A., Vallius, H., Kabel, K., Endler, M., et al. (2013). Mercury in Baltic Sea sediments - natural background and anthropogenic impact. *Chem. Erde-Geochem.* 73, 249–259. doi: 10.1016/j.chemer.2013.06.005

Leppäranta, M., and Myrberg, K. (2009). *Physical Oceanography of the Baltic Sea*. Berlin: Springer/Praxis Pub.

Lepskaya, E. V., Jewson, D. H., and Usoltseva, M. V. (2010). Aulacoseira subarctica in Kurilskoye Lake, Kamchatka: a deep, oligotrophic lake and important Pacific salmon nursery. *Diatom Res.* 25, 323–335. doi: 10.1080/0269249X.2010.9705853

Ljungqvist, F. C., Krusic, P. J., Brattström, G., and Sundqvist, H. S. (2012). Northern Hemisphere temperature patterns in the last 12 centuries. *Clim. Past* 8, 227–249. doi: 10.5194/cp-8-227-2012

Lotter, A. F., Pienitz, R., and Schmidt, R. (2010). "Diatoms as indicators of environmental change in subarctic and alpine regions," in *The Diatoms : Applications for the Environmental and Earth Sciences*, eds J. P. Smol and E. F. Stoermer (Cambridge: Cambridge University Press), 231–248. doi: 10.1017/CBO9780511763175.013

Lougheed, B. C., Filipsson, H. L., and Snowball, I. (2013). Large spatial variations in coastal ^{14}C reservoir age–a case study from the Baltic Sea. *Clim. Past* 9, 1015–1028. doi: 10.5194/cp-9-1015-2013

Mann, M. E., Zhang, Z., Rutherford, S., Bradley, R. S., Hughes, M. K., Shindell, D., et al. (2009). Global signatures and dynamical origins of the little ice age and medieval climate anomaly. *Science* 326, 1256–1260. doi: 10.1126/science.1177303

Moros, M., Andersen, T. J., Schulz-Bull, D., Häusler, K., Bunke, D., Snowball, I., et al. (2017). Towards an event stratigraphy for Baltic Sea sediments deposited since AD 1900: approaches and challenges. *Boreas* 46, 129–142. doi: 10.1111/bor.12193

Myrdal, J. (1999). *Det Svenska Jordbrukets Historia. [Bd 2], Jordbruket Under Feodalismen : 1000–1700*. Stockholm: Natur och kultur.

Myrdal, J., and Morell, M. (2011). *The Agrarian History of Sweden: From 4000 BC to AD 2000*. Lund: Nordic Academic Press.

Ning, W., Nielsen, A. B., Norbäck Ivarsson, L., Jilbert, T., Åkesson, C. M., Slomp, C. P., et al. (2018). Anthropogenic and climatic impacts on a coastal environment in the Baltic Sea over the last 1000 years. *Anthropocene* 21, 66–79. doi: 10.1016/j.ancene.2018.02.003

Nordström, A. (1968). *Södertälje Stads Historia.* D.1-2. Stockholm: Norstedt & Söner.

Oksanen, J., Blanchet, F. G., Kindt, R., Legendre, P., Minchin, P. R., O'Hara, R. B., et al. (2015). *Vegan: Community Ecology Package*. Available online at: https://cran.r-project.org/web/packages/vegan/index.html (accessed November 7, 2015).

Persson, J., and Jonsson, P. (2000). Historical development of laminated sediments – an approach to detect soft sediment ecosystem changes in the Baltic Sea. *Mar. Pollut. Bull.* 40, 122–134. doi: 10.1016/S.0025-326X.(99)00180-0

R Core Team (2018). *R: A Language and Environment for Statistical Computing*. R Foundation for Statistical Computing, Vienna, Austria. Available online at: https://www.R-project.org/.

Reimer, P. J., Bard, E., Bayliss, A., Beck, J. W., Blackwell, P. G., Bronk Ramsey, C., et al. (2013). *IntCal13 and Marine13 Radiocarbon Age Calibration Curves 0-50,000 Years Cal BP*. Available online at: http://researchcommons.waikato.ac.nz/handle/10289/8955 (accessed December 9, 2015). doi: 10.2458/azu_js_rc.55.16947

Renberg, I., Bigler, C., Bindler, R., Norberg, M., Rydberg, J., and Segerström, U. (2009). Environmental history: a piece in the puzzle for establishing plans for environmental management. *J. Environ. Manage.* 90, 2794–2800. doi: 10.1016/j.jenvman.2009.03.008

Renberg, I., Bindler, R., Bradshaw, E., Emteryd, O., and McGowan, S. (2001). Sediment evidence of early eutrophication and heavy metal pollution of lake mälaren, Central Sweden. *AMBIO J. Hum. Environ.* 30, 496–502. doi: 10.1579/0044-7447-30.8.496

Rühland, K., Paterson, A. M., and Smol, J. P. (2008). Hemispheric-scale patterns of climate-related shifts in planktonic diatoms from North American and European lakes. *Glob. Change Biol.* 14, 2740–2754. doi: 10.1111/j.1365-2486.2008.01670.x

Saunders, K. M., and Taffs, K. H. (2009). Palaeoecology: a tool to improve the management of Australian estuaries. *J. Environ. Manage.* 90, 2730–2736. doi: 10.1016/j.jenvman.2009.03.001

Savage, C., Elmgren, R., and Larsson, U. (2002). Effects of sewage-derived nutrients on an estuarine macrobenthic community. *Mar. Ecol. Prog. Ser.* 243, 67–82. doi: 10.3354/meps243067

Savage, C., Leavitt, P. R., and Elmgren, R. (2010). Effects of land use, urbanization, and climate variability on coastal eutrophication in the Baltic Sea. *Limnol. Oceanogr.* 55, 1033–1046. doi: 10.4319/lo.2010.55.3.1033

Schimanke, S., and Meier, H. M. (2016). Decadal-to-centennial variability of salinity in the Baltic Sea. *J. Clim.* 29, 7173–7188. doi: 10.1175/JCLI-D-15-0443.1

Schrader, H.-J., and Gersonde, R. (1978). "Diatoms and silico-flagellates," in *Utrecht Micropaleontological Bulletins 17, Micropaleontological Counting Methods and Techniques,* eds W. J. Zachariasse, W. R. Riedel, A. Sanfilippo, R. R. Schmidt, M. J. Brolsma, H. J. Schrader, et al. (Hoogeveen: Loonzetterij Abe), 127–176.

Sjunnesson, H., and Wahlberg, T. (2003). *Papper och Massa i Östergötland: från Handpappersbruk Till Processindustri*. Stockholm: Skogsindustrierna.

Snoeijs, P., et al. (1993–1998). *Intercalibration and distribution of diatom species in the Baltic Sea*. Vol. 1-5. Uppsala: Opulus press. Vol 1 (1993). Snoeijs, P. ed., Vol 2 (1994). Snoeijs, P., and Vilbaste, S. eds. Vol 3 (1995). Snoeijs, P., and Potapova, M. eds. Vol 4 (1996). Snoeijs, P., and Kasperovičiene, J. eds. Vol 5 (1998). Snoeijs, P., and Balashova, N. eds.

Snoeijs, P., and Andrén, E. (2017). "Why is the Baltic Sea so special to live in?" in *Biological Oceanography of the Baltic Sea,* eds P. Snoeijs-Leijonmalm, H. Schubert, and T. Radziejewska (Dordrecht: Springer), 23–84. doi: 10.1007/978-94-007-0668-2_2

Snoeijs, P., and Potapova, M. (1998). Ecotypes or endemic species?-a hypothesis on the evolution of Diatoma taxa (Bacillariophyta) in the northern Baltic Sea. *Nova Hedwig.* 67, 303–348.

Swedish Geological Survey (2018). Swedish Geological Survey. *Marine Geological Maps, Open Access Data* (2018). Available online at: http://apps.sgu.se/kartgenerator/maporder_sv.html (access September 18, 2018).

Swedish Metrological and Hydrological Institute (2018). *Swedish Metrological and Hydrological Institute (SMHI) Open Access Data* (2018). Available online at: https://www.smhi.se/klimatdata/oceanografi/havsmiljodata/marina-miljoovervakningsdata (access September 18, 2018).

Tuovinen, N., Weckström, K., and Virtasalo, J. J. (2010). Assessment of recent eutrophication and climate influence in the Archipelago Sea based on the subfossil diatom record. *J. Paleolimnol.* 44, 95–108. doi: 10.1007/s10933-009-9390-z

Vatteninformation Sverige (2018). *Vatteninformation Sverige, (VISS) Open Access Data* (2018). Available online at: http://viss.lansstyrelsen.se (accessed March 11, 2018).

Verburg, P. (2007). The need to correct for the Suess effect in the application of $\delta^{13}C$ in sediment of autotrophic Lake Tanganyika, as a productivity proxy in the Anthropocene. *J. Paleolimnol.* 37, 591–602. doi: 10.1007/s10933-006-9056-z

Voss, M., Emeis, K.-C., Hille, S., Neumann, T., and Dippner, J. W. (2005). Nitrogen cycle of the Baltic Sea from an isotopic perspective. *Glob. Biogeochem. Cycles* 19:GB3001. doi: 10.1029/2004GB002338

Voss, M., Larsen, B., Leivuori, M., and Vallius, H. (2000). Stable isotope signals of eutrophication in Baltic Sea sediments. *J. Mar. Syst.* 25, 287–298. doi: 10.1016/S0924-7963(00)00022-1

Wang, L., Lu, H., Liu, J., Gu, Z., Mingram, J., Chu, G., et al. (2008). Diatom-based inference of variations in the strength of Asian winter monsoon winds between 17,500 and 6000 calendar years BP. *J. Geophys. Res. Atmospheres* 113:D21101 doi: 10.1029/2008JD010145

Wang, T., Surge, D., and Mithen, S. (2012). Seasonal temperature variability of the Neoglacial (3300–2500BP) and Roman Warm Period (2500–1600BP) reconstructed from oxygen isotope ratios of limpet shells (*Patella vulgata*), Northwest Scotland. *Palaeogeogr. Palaeoclimatol. Palaeoecol.* 317–318, 104–113. doi: 10.1016/j.palaeo.2011.12.016

Weckström, K. (2006). Assessing recent eutrophication in coastal waters of the gulf of finland (Baltic Sea) using Subfossil Diatoms. *J. Paleolimnol.* 35, 571–592. doi: 10.1007/s10933-005-5264-1

Weckström, K., and Juggins, S. (2006). Coastal diatom–environment relationships from the gulf of finland, Baltic Sea1. *J. Phycol.* 42, 21–35. doi: 10.1111/j.1529-8817.2006.00166.x

Weckström, K., Juggins, S., and Korhola, A. (2004). Quantifying background nutrient concentrations in coastal waters: a case study from an urban embayment of the Baltic Sea. *AMBIO J. Hum. Environ.* 33, 324–327. doi: 10.1579/0044-7447-33.6.324

Willis, K. J., and Birks, H. J. B. (2006). What is natural? The need for a long-term perspective in biodiversity conservation. *Science* 314, 1261–1265. doi: 10.1126/science.1122667

Winnfors, E. (2009). *. . . Och Vid Himmerfjärden Ligger Syvab*. Örebro: Ohlson & Winnfors AB.

Witkowski, A., Lange-Bertalot, H., and Metzeltin, D. (2000). *Diatom Flora of Marine Coasts / Iconographia Diatomologica,* Vol. 7. Ruggell: Gantner.

Zillén, L., and Conley, D. J. (2010). Hypoxia and cyanobacteria blooms-are they really natural features of the late Holocene history of the Baltic Sea? *Biogeosciences* 7, 2567–2580. doi: 10.5194/bg-7-2567-2010

Zillén, L., Conley, D. J., Andrén, T., Andrén, E., and Björck, S. (2008). Past occurrences of hypoxia in the Baltic Sea and the role of climate variability, environmental change and human impact. *Earth-Sci. Rev.* 91, 77–92 doi: 10.1016/j.earscirev.2008.10.001

Conflict of Interest Statement: The authors declare that the research was conducted in the absence of any commercial or financial relationships that could be construed as a potential conflict of interest.

frontiers in Earth Science

ORIGINAL RESEARCH
published: 02 July 2019
doi: 10.3389/feart.2019.00174

Stratification Has Strengthened in the Baltic Sea – An Analysis of 35 Years of Observational Data

Taavi Liblik and Urmas Lips*

Department of Marine Systems, Tallinn University of Technology, Tallinn, Estonia

Stratification of the water column, consisting of the three layers (upper, intermediate, and deep layer) separated by the seasonal thermocline and the permanent halocline, respectively, is an important factor for the functioning of the brackish Baltic Sea. In the present work, changes in the vertical structure of temperature and salinity, as well as heat content, salt mass, and stratification conditions were estimated on the basis of *in situ* and remote sensing data in 1982–2016. The seasonal thermocline and the halocline have strengthened in most of the sea by a rate of 0.33–0.39 and 0.70–0.88 kg m^{-3}, respectively, during 35 years. The upper layer has warmed by 0.03–0.06°C $year^{-1}$ and sub-halocline deep layer 0.04–0.06°C $year^{-1}$ in most of the sea. The total warming trend in the whole Baltic has been 1.07°C for 35 years, being approximately twice higher compared to the upper 100 m in the Atlantic Ocean. Average upper layer warming of the sea from May to September has been 0.07–0.08°C $year^{-1}$ while in winter, trends were mostly statistically not significant. More rapid warming during summers has occurred in shallower, closed-end areas of gulfs if compared to the rest of the sea. Possible reasons for high warming there might be shallow depths and limited water exchange, stronger stratification, and/or higher turbidity. Sea surface temperature trends estimated by *in situ* and satellite data agree well. Trends of freshening (−0.005 to −0.014 g kg^{-1} $year^{-1}$) of the upper layer and increasing salinity (0.02 to 0.04 g kg^{-1} $year^{-1}$) in the sub-halocline deep layer were detected. Increased salinity in the deep layer is likely caused by the increased lateral import of saltier water from the North Sea. Changes in the upper layer salinity might not be related to the accumulated river runoff only, but decadal changes of vertical salt flux might also contribute. The vertically distinct changes cancel each other and no significant trend in the mean salinity of the Baltic Sea was detected. No remarkable changes have occurred in the cold intermediate layer. In conclusion, different dominating processes have caused distinct long-term trends in the three layers of the Baltic Sea.

Keywords: Baltic Sea, salinity, heat content, stratification, climate change

OPEN ACCESS

Edited by:
Markus Meier,
Leibniz Institute for Baltic Sea Research (LG), Germany

Reviewed by:
Peter Sigray,
KTH Royal Institute of Technology, Sweden
Frank Janssen,
Federal Maritime and Hydrographic Agency, Germany
Andreas Lehmann,
GEOMAR Helmholtz Center for Ocean Research Kiel, Germany

****Correspondence:***
Taavi Liblik
taavi.liblik@taltech.ee

Specialty section:
This article was submitted to Interdisciplinary Climate Studies, a section of the journal Frontiers in Earth Science

Received: *04 December 2018*
Accepted: *19 June 2019*
Published: *02 July 2019*

Citation:
Liblik T and Lips U (2019) Stratification Has Strengthened in the Baltic Sea – An Analysis of 35 Years of Observational Data. Front. Earth Sci. 7:174. doi: 10.3389/feart.2019.00174

INTRODUCTION

The Baltic Sea is a brackish, shallow sea with limited water exchange and enclosed character. The sea has strong seasonality and stratification. In winter, the water column is mixed down to the permanent halocline at depths of 40–80 m, while in summer, the seasonal thermocline and three-layer structure develop in the sea: warm and fresher upper layer (UL), saltier cold intermediate

layer (CIL), and saltiest and warmer deep layer (DL). Density gradients between the three layers have great importance for vertical fluxes and functioning of the sea in general (BACC Author Team, 2015). Unlike to open ocean, the contribution of vertical salinity gradient to the density stratification is as important as temperature in the Baltic Sea.

Changes in air-sea heat fluxes (Large et al., 2012) have led to an increase in the upper ocean heat content in recent decades (Gouretski, 2018). Due to the small volume of the sea, changes in atmospheric conditions impact the Baltic Sea quite rapidly. The mean warming trend in the sea surface temperature (SST) of 0.04–0.05°C year^{-1} has been detected in the Baltic Sea covering 1982–2012/13 (Stramska and Białogrodzka, 2015; Høyer and Karagali, 2016). There is an inter-annual variability in the SST (Bradtke et al., 2010), which quite well follows the changes in air temperature (Tronin, 2017). The warming signal has been confirmed by *in situ* observations in coastal stations (Dailidienė et al., 2011; Laakso et al., 2018). Available remotely sensed salinity product (Kao et al., 2018) is not capable of resolving dynamics in the Baltic Sea. A decline in the SSS has been detected in the Baltic (Girjatowicz and Świątek, 2016), which could have caused a shift of the threshold salinity for freshwater and marine species (Vuorinen et al., 2015). The Baltic Sea is very sensitive to wind forcing. Therefore, long-term trends of sea surface properties might also be caused by changes in the wind regime. Wind-induced processes, such as upwellings, movement of fronts and vertical mixing alter water properties considerably in the sea (Astok et al., 1999; Lips et al., 2009; Haavisto et al., 2018).

Cold intermediate layer forms in winter due to mixing by convection and wind stirring of the previous year intermediate water and the upper layer (Stepanova et al., 2015). Erosion of the halocline contributes to the formation of intermediate layer water mass as well during storm events due to wind stirring (Lass et al., 2003). Water column turn-overs caused by estuarine circulation reversals (Liblik et al., 2013; Elken et al., 2014) during winters also enhance diapycnal mixing through the halocline (Lips et al., 2017). Inter-annual changes of temperature of the CIL depend on the severity of winter and are well correlated with the NAO (Jones et al., 1997) and BSI (Lehmann et al., 2002) indexes (Mohrholz et al., 2006; Liblik and Lips, 2011).

Bottom waters of the Baltic Proper, the largest central basin of the Baltic Sea, are renewed by sporadic barotropic (Fischer and Matthäus, 1996) and baroclinic (Feistel et al., 2006) large inflows, so-called Major Baltic Inflows (MBI) from the North Sea. The strong MBIs have been quite rare, e.g., the major event in 2003 was followed by the strong inflow in December 2014 (Mohrholz et al., 2015). The inflow events can be followed in the deep layer properties as peaks in time-series. The variations have a higher amplitude in the south-western Baltic (Rak, 2016; Mohrholz, 2018) while in the north-eastern Baltic, the signal is more damped. However, the impact of MBIs is detectable all the way to the Gulf of Finland (Liblik et al., 2018). Temperature of the deep layer depends on source water properties of the MBIs that origin from the North Sea and on mixing with the ambient water in the Baltic. For instance, after the 2003 MBI arrived in the Gotland Deep, temperature was <4.5°C (Feistel et al., 2006), while after the 2014 December and concurrent MBIs, it was >7.5°C (Liblik et al., 2018). Positive temperature trend in the deep waters of the Baltic can be expected as warming of the SST was detected in the North Sea (Høyer and Karagali, 2016). Reduction of MBIs has been reported since the early 1980s (Fischer and Matthäus, 1996). However, recently, it was claimed that large volume changes did not decrease (Lehmann and Post, 2015) and that there is no long term trend in MBI occurrence (Mohrholz, 2018). Deep waters of the open Baltic do not penetrate the Gulf of Riga and the Gulf of Bothnia, which are separated by sills from the rest of the Baltic. Thus, the permanent halocline does not exist in those basins, and the direct impact of MBIs cannot be seen there (Hietala et al., 2007; Skudra and Lips, 2017).

A linear trend is the most straightforward statistical parameter to describe long-term changes in water characteristics. It misses the dynamical properties of the time-series, but on the other hand, it is a widely used standard method. Numerous studies have shown linear SST trends based on remote sensing data (Bradtke et al., 2010; Lehmann et al., 2011; BACC Author Team, 2015; Stramska and Białogrodzka, 2015; Høyer and Karagali, 2016) and coastal observations (Dailidienė et al., 2011; Laakso et al., 2018) in the Baltic Sea. Future predictions are often presented as differences to a reference period. For instance, a remarkable increase in temperature (2–3°C) and a decrease in salinity (1–2 g kg^{-1}) through the three layers are predicted in the deeper basins for 2069–2098 relative to the reference period 1978–2007 (BACC Author Team, 2015). The motivation of the present study comes from the fact that most of the available water column trend studies in the Baltic are dealing with the SST (BACC Author Team, 2015). In the present study, we estimated the temperature and salinity trends in the whole water column.

The main aim of the study was to analyze the changes in the SST of the Baltic Sea on the basis of remote sensing products and the changes in the water column properties in eight selected locations around the Baltic Sea on the basis of *in situ* data in 1982–2016. This period was chosen to have the study period covered by satellite-derived SST measurements. It allows us to combine remotely sensed and *in situ* measurements. There were four main objectives in this investigation: first, to estimate the SST trends based on remote sensing and *in situ* observations in selected open sea locations in the Baltic; secondly, to reveal the vertical structure of temperature, salinity and density trends; thirdly, to estimate the changes in heat and salt content of the sea, and fourthly, to describe the changes in stratification conditions.

MATERIALS AND METHODS

In situ data from eight areas (red polygons in **Figure 1**) around the Baltic Sea from years 1982–2016 were analyzed: the Gulf of Finland, the Bothnian Bay, the Bothnian Sea, the Northern Baltic Proper, the Eastern Gotland Basin, the Bornholm Basin, the Arkona Basin, and the Gulf of Riga. Monitoring data of Department of Marine Systems at TalTech and its predecessors were used: data acquired by research vessels in 1982–2016, autonomous vertical profilers (Lips et al., 2016) in 2009–2016 and bottom-mounted devices (Liblik et al., 2013) in

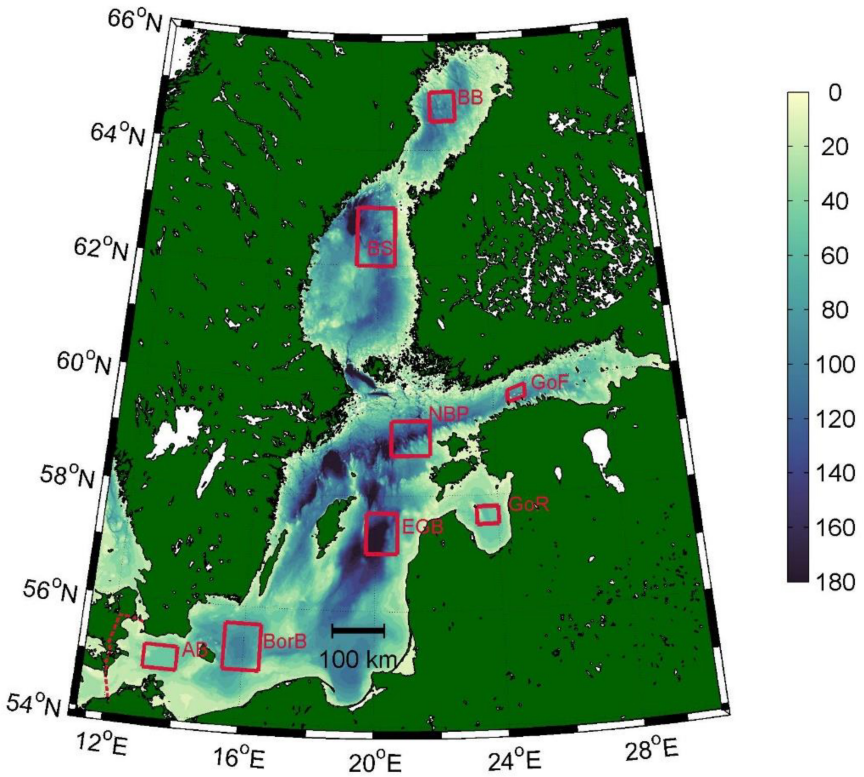

FIGURE 1 | Bathymetric map of the Baltic Sea with eight selected areas (red polygons) and the western edge of the study area (red dashed line). Color scale shows sea depths.

2010–2015. Likewise, available data from HELCOM (Helsinki Commission) database[1] and EU Copernicus Marine Service Information[2] product "Baltic *in situ* observations yearly delivery in delayed mode" were used. Measurements, quality assurance and data processing were in accordance with the HELCOM Monitoring Manual[3].

Two sources of remotely sensed SST were used: (1) EU Copernicus Marine Service Information[4] product "Baltic Sea – Sea surface temperature reprocessed" 1982–2011 and (2) GHRSST Level 4 G1SST Global Foundation Sea Surface Temperature Analysis[5] data 2012–2016. The GHRSST data were interpolated to the Copernicus data grid, which has a spatial resolution of 0.03°.

Satellite SST data were checked against *in situ* data in the upper 2 m layer. Data inside the eight polygons were used. Satellite-derived SST was linearly interpolated to a location of *in situ* measurements. Linear regression slope, correlation, absolute average error, and bias for the whole satellite data set and separately for the two products are shown in **Table 1**. Strong correlation between satellite data and *in situ* data was found. A smaller absolute average error was found for the Copernicus data. The Copernicus satellite data had a bias of −0.28°C and GHRSST data +0.11°C. In order to avoid a jump between the two datasets at 2011/2012, we shifted the GHRSST data by −0.39°C.

First, daily mean profiles with a vertical resolution of 10 m (centered to the depths of 5, 15, 25 m, etc.) were calculated in each area. Secondly, 10-day mean profiles were calculated, and from those, the mean seasonal cycle was determined. Next, the mean seasonal course was subtracted from daily profiles, and

TABLE 1 | Regression, correlation, absolute average error (°C), and bias (°C) between *in situ* measurements and satellite-derived SST (°C).

	All data	Copernicus reprocessed 1982–2011	GHRSST* 2012–2016
Regression slope	0.97	0.96	1.00
Correlation	0.98	0.98	0.97
Absolute average error (°C)	0.68	0.62	0.91
Bias (°C)	−0.28	−0.28	−0.28
Number of observations	13673	10799	2874

**GHRSST data were shifted by −0.39°C after the first comparison with in situ data.*

[1]http://ocean.ices.dk/helcom (accessed January 31, 2018).

[2]http://marine.copernicus.eu/ (accessed January 31, 2017).

[3]http://www.helcom.fi/action-areas/monitoring-and-assessment/manuals-and-guidelines/salinity-and-temperature/ (Manual for Marine Monitoring in the COMBINE Programme of HELCOM, 2017).

[4]http://marine.copernicus.eu/ (accessed October 1, 2018).

[5]https://podaac.jpl.nasa.gov/dataset/JPL_OUROCEAN-L4UHfnd-GLOB-G1SST (accessed October 1, 2018).

monthly mean profiles were calculated from deviations. Finally, yearly mean vertical profiles of deviations were calculated, and linear trends were determined using these annual averages. Same calculation steps were applied for each cell of the daily satellite SST data.

Hypsographic curves for the heat and salt content calculations were derived from the Baltic Sea Hydrographic Commission (2013) database. Temperature and salinity trends in eight areas were extrapolated in respective basins according to the hypsographic curves with a vertical step of 1 m. For instance, there is a salinity trend of +0.04 g kg^{-1} y^{-1} in the Eastern Gotland Basin at 80 m depth. We assumed that this +0.04 g kg^{-1} y^{-1} change took place in the whole basin at 80 m depth. Finally, the eight sub-basins were integrated to get the heat and salt content change profiles for the whole Baltic Sea. The western edge of the study area in the present work is shown in **Figure 1**.

Mean SST trends for the various classes of sea bottom depth, mean Secchi depth and mean salinity were calculated in the three areas: the Northern Bothnian Bay, the Eastern Gulf of Finland and the Bornholm/Arkona area (see locations in **Figure 3**). Mean Secchi depth data from March to October 2003–2012 (Stock, 2015) and mean surface salinity from April to October (Janssen et al., 1999) were used.

Trend values in the present paper were calculated as linear regressions, and trends were considered significant when the p-value was ≤ 0.05.

It has to be noted that the Gulf of Riga, the Bothnian Bay, and the Bothnian Sea had less *in situ* data available compared to other areas (see **Figure 2**) and that might be one reason, why trends there deviate from the rest of the basins.

RESULTS

Trends in Temperature, Salinity, Heat Content, and Salt Mass

There is a significant positive trend in annual SST all over the Baltic Sea (**Figure 3**). In 85.3% of the area, the trend is in the range between 0.03 and 0.06°C $year^{-1}$. A higher rate of warming (>0.06°C $year^{-1}$) has occurred in the shallower, closed-end areas of the gulfs, e.g., the northern part of the Bothnian Bay, the eastern part of the Gulf of Finland, the eastern part of the Gulf of Riga, and the Curonian lagoon. Shallower areas with active water exchange such as the Arkona Basin, the Irbe Strait or the Åland Sill area, have not experienced such fast warming. The average trend in the entire Baltic is stronger (>0.05°C $year^{-1}$) from May to October, and it is significant in most of the Baltic Sea in these months (78–95% of the area) (inlays in **Figure 3**). A slight positive temperature trend, although mostly not significant, can be found in winter as well.

Temperature trend profiles are presented in **Figure 4**. Diamond-markers in the figure represent satellite-based estimates of trends. Warming trends based on *in situ* measurements and remote sensing coincide well. Only in the areas, where fewer measurements are available, some discrepancies are evident: the *in situ* data estimated trend is higher than the remote sensing estimated trend in the Gulf of Riga and lower in the Bothnian area.

It is clear that the warming trend prevails in the water column of the Baltic Sea (**Figure 4**). The warming signal is not homogenous in the water column, but has a layered structure. Most of the areas (Gulf of Finland, Eastern Gotland Basin, Bornholm Basin, Northern Baltic Proper and Arkona Basin) have significant positive temperature trend with a rate of 0.04–0.05°C $year^{-1}$ in the upper layer. A slightly higher significant trend in the upper layer can be found in the Gulf of Riga (0.06°C $year^{-1}$) and a lower trend in the Bothnian Bay (0.03°C $year^{-1}$). An insignificant positive trend of 0.02°C $year^{-1}$ is revealed in the upper layer of the Bothnian Sea. The two locations in the central Baltic (Eastern Gotland Basin and Northern Baltic Proper) have significant warming trends in the two upper bins 5 and 15 m depth. The warming has been higher in the sub-surface layer of the Gulf of Finland at the 15–35 m depth. Such a vertical maximum of warming trend can be found in the Bothnian Sea, but in the depth range of 35–75 m.

There is a minimum in temperature trend profiles in the Gulf of Finland, Northern Baltic Proper, Eastern Gotland Basin, and Bornholm Basin at the depth around 50 m. A significant positive trend of 0.03°C $year^{-1}$ can be found in the Gulf of Finland while no trend exists or the trend is statistically insignificant in the intermediate layer of the rest of the three basins. There is a clear positive trend of 0.04–0.06°C $year^{-1}$ in the deeper layers of the four basins. Significant temperature trends were not found in the deep layers of the Bay of Bothnia, the Bothnian Sea and the Gulf of Riga. There is, however, a strong warming signal in the Gulf of Riga at the depth of 35 m. A closer look to data shows that it is caused by warmer mixed layer during the decay of stratification in autumn in recent years.

Most of the areas have had a significant negative surface salinity trend of −0.005 to −0.014 g kg^{-1} a year. Such a negative trend reaches down to 40–50 m depth. The negative salinity trend in the upper layer prevails in most of the areas in all seasons. A significant positive salinity trend of 0.02–0.04 g kg^{-1} a year was detected in the deep layers of the Bornholm Basin, the Eastern Gotland Basin, the Northern Baltic Proper, and the Gulf of Finland. A similar trend, but not statistically significant, has occurred in the Arkona Basin. A significant salinity trend was not detected in the deep layer of the rest of the three areas.

There is no seasonality in temperature and salinity trend in the deep layer in most of the areas. An exception is the deep layer of the Gulf of Finland, where the warming trend is stronger (0.06–0.08°C $year^{-1}$) from March to August and weaker (0.02–0.04°C $year^{-1}$) from September to February. A similar tendency appears in salinity trend in the deep layer of the Gulf of Finland. There is no significant trend from December to February (−0.02 to +0.01 g kg^{-1} $year^{-1}$) while in March to August, a significant positive salinity trend (0.03 to −0.06 g kg^{-1} $year^{-1}$) is evident.

Vertical profiles of the trends in the heat content and salt mass in the whole Baltic Sea are shown in **Figure 4**. The water column of the upper 50 m has contributed 65% of the total heat content change while the layer deeper than 100 m 12% of the change. The total heating trend in the Baltic has been 2.5×10^{18} J $year^{-1}$, reflecting the temperature trend of 0.031°C $year^{-1}$,

FIGURE 2 | Availability of the data in the eight selected locations. Black dots show the month/year when the data were available at least from the surface layer and green dots indicate the month/year when the data were available throughout the entire water column.

which corresponds to the temperature increase of 1.07°C from 1982 to 2016. The changes in salt mass are driven by a slight decrease in salinity in the upper layer that covers large areas and a stronger increase in salinity in the deeper layer, which has a smaller volume of water. The salt mass decrease in the upper 56 m has been 1.34×10^8 t year^{-1} and the increase below that depth 1.10×10^8 t year^{-1}. The total estimated decrease of salt mass in the Baltic has been -0.24×10^8 t year^{-1}, which corresponds to

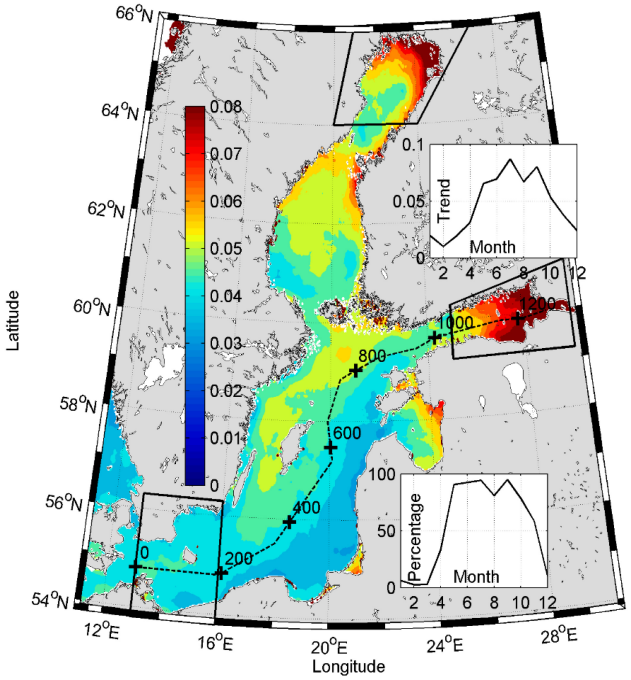

FIGURE 3 | Sea surface temperature trend in °C year^{-1} from 1982 to 2016. The upper inlay shows the mean seasonal temperature trend (°C year^{-1}) in the entire Baltic Sea. The lower inlay shows by months the percentage of the area, where positive temperature trends were significant ($p \leq 0.05$). The dashed line shows the transect, which is shown in **Figure 8A**. Numbers indicate the distance from the southwestern end of the transect Boxes show areas of Arkona/Bornholm, Northern Bothnian Bay, and Eastern Gulf of Finland. Data from these areas are used in **Figures 8B–D**.

salinity decrease of -1.1×10^{-3} g kg^{-1} year^{-1} or -0.040 g kg^{-1} during 35 years. Such a small trend is strongly overshadowed by variability in shorter time scales, and it is not significant. Thus, in conclusion, no trend in the mean salinity and salt mass for the entire Baltic Sea for the 35-year period was detected.

Changes in Stratification

Accompanied seawater density (**Figures 5A,B**) trends are associated with the changes in temperature and salinity. There is a negative density trend in the upper 50 m, which has the highest magnitude in the near-surface layer. The decreasing trend is very similar (-0.013 to -0.014 kg m^{-3} year^{-1}) in five basins: Arkona Basin, Bornholm Basin, Eastern Gotland Basin, Gulf of Riga, and Northern Baltic Proper. The decreasing trend in density has been stronger in summer in the five areas and was in the range from -0.017 to -0.023 kg m^{-3} year^{-1}. The trends were smaller in the Bothnian Bay and the Bothnian Sea being -0.010 kg m^{-3} year^{-1} (based on annual averages) and -0.010 and -0.011 kg m^{-3} year^{-1}, respectively, in summer, and the Gulf of Finland -0.007 and -0.003 kg m^{-3} year^{-1} based on annual and summer values. The decreasing trend in density in the Gulf of Finland has a higher magnitude (-0.013 to -0.015 kg m^{-3} year^{-1}) in the subsurface layer at the 15–35 m depth. The latter corresponds to the decreasing trend in salinity and increasing trend in temperature at this depth range in the gulf (**Figures 4A,B**). A significant density trend was detected in the basins where the halocline exists and an increasing trend in salinity in the deep layers (**Figures 4B,D**) has occurred: Bornholm Basin, Eastern Gotland Basin, Northern Baltic Proper and Gulf of Finland. The increase in salinity overshadows the effect of the increase in temperature on density in the deep layer. A density increase, mostly in the range of 0.020–0.030 kg m^{-3} year^{-1}, has occurred in the sub-halocline layers. No significant density trend was detected in the near-bottom layers of the Bothnian Sea, the Bothnian Bay and the Gulf of Riga. A remarkable seasonality in the deep layer density trend was found in the Gulf of Finland, where in winter, no significant trend exists, while in the rest of the year a significant trend was detected.

As a proxy of stratification strength, trends in density differences between the upper layer (UL, 5–15 m), the intermediate layer (CIL, 45–55 m) and the deep layer (DL, 65–85 m), are shown in **Figure 5C**. Stratification between the upper layer and intermediate layer has become stronger in all basins. The trend in the Gulf of Finland, the Gulf of Riga, the Eastern Gotland Basin and the Northern Baltic Proper has been in the range of 0.009–0.011 kg m^{-3} year^{-1}. A higher trend was found in the Arkona and Bornholm basins. This is, however, likely related to the fact that the halocline is located there shallower compared to the Central and Eastern Baltic. Weaker trends are revealed in the Bothnian Sea and the Bothnian Bay. The density difference between the intermediate layer and the deep layer has increased at a rate of 0.020–0.025 kg m^{-3} year^{-1} in the Bornholm Basin, the Eastern Gotland Basin, the Northern Baltic Proper, and the Gulf of Finland. This change is driven by lateral water exchange and a corresponding increase in deep layer salinity. Since haline stratification is very weak in the Bothnian Bay and the Bothnian Sea, such a trend there cannot be found.

DISCUSSION

Heat and Salt Content Changes

An increase in the total heat content of 2.5×10^{18} J year^{-1} (7×10^{12} J year^{-1} km^{-2}), which corresponds to the mean temperature increase of 1.07°C in 1982–2016, has occurred in the Baltic Sea. No significant change in the salt content of the sea during the same period has occurred. The pentadal time-series of mean salinity (**Figure 6B**) show a decrease from the 1980s to the mid-1990s, confirming the earlier observation-based estimate (Winsor et al., 2001) and model results (Meier and Kauker, 2003). Thus, even if there was no decline in the occurrence of smaller barotropic inflows since the 1980s (Mohrholz, 2018), a decrease in the mean salinity still occurred, likely due to the lack of strong MBIs since the early 1980s until the 1993 MBI. The pentadal averages of temperature in 2002–2016 had a higher mean temperature than those in 1982–1996, indicating a warming trend of the Baltic Sea (**Figure 6A**). Pentadal averages of temperature in the upper 100 m in the Atlantic Ocean (Levitus et al., 2012) had similar temporal development (**Figure 6A**), although warming has been more rapid in the Baltic Sea. If taking the mean depth of the Baltic Sea of 54 m

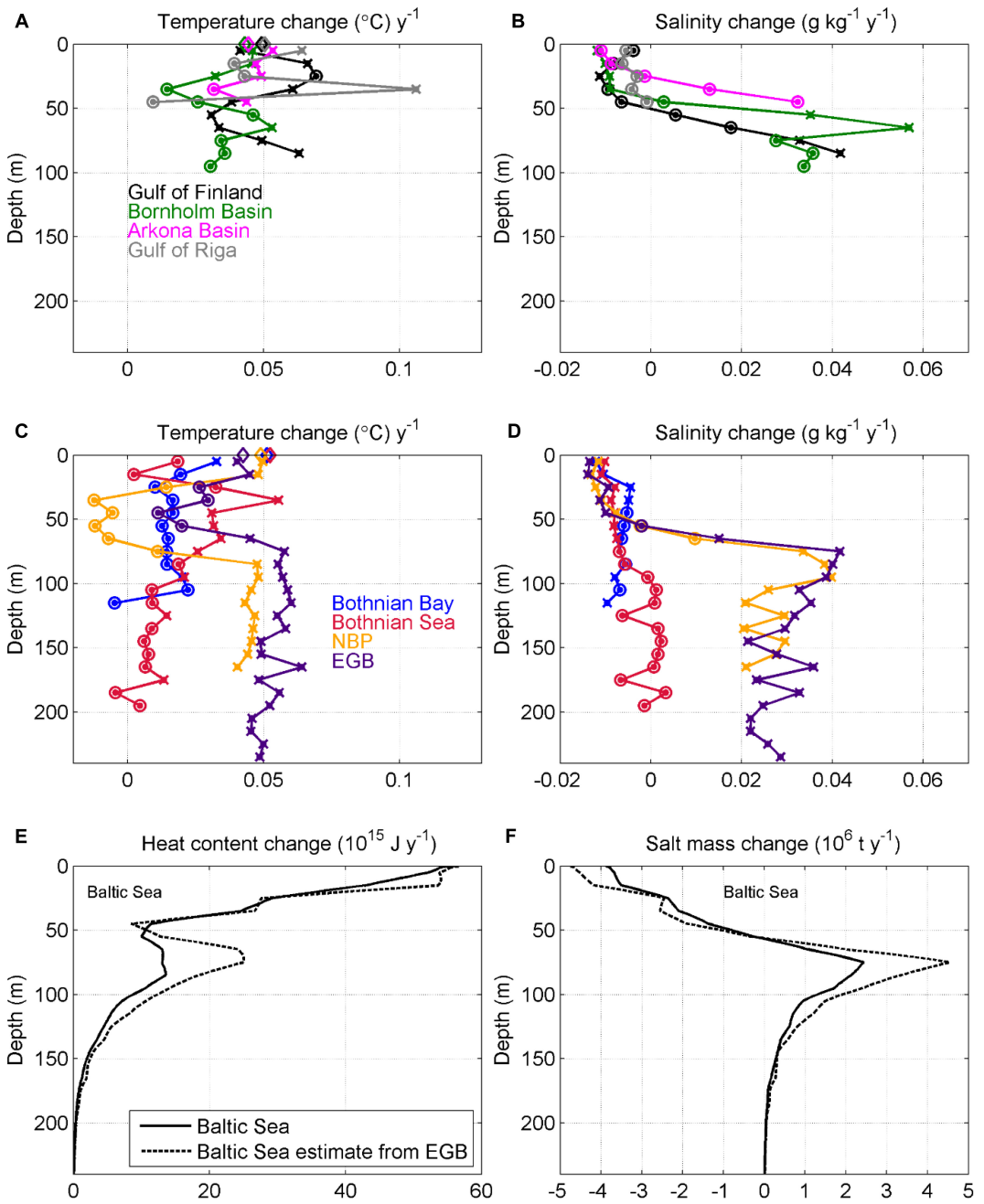

FIGURE 4 | Temperature **(A,C)**, salinity **(B,D)** trends in the sub-basins (Gulf of Finland, Bothnian Bay, Bothnian Sea, NBP – Northern Baltic Proper, EGB – Eastern Gotland Basin, Bornholm Basin, Arkona Basin, Gulf of Riga) and heat content **(E)**, salt mass **(F)** trends of the whole Baltic Sea from 1982 to 2016. Crosses in the upper panel indicate a statistically significant trend ($p \leq 0.05$) and circles not significant trend ($p > 0.05$). Diamonds in the upper part of **(A,C)** show satellite-based estimates of SST trend in the same areas. Solid lines in the lower panels show the heat content and salt mass estimates if temperature and salinity changes in all eight areas are taken into account. Dashed lines show the estimates if only changes in the Eastern Gotland Basin (EGB) area are taken into account and extrapolated over the entire Baltic Sea using the hypsographic curve.

(Leppäranta and Myrberg, 2009), the heat content change of the Baltic has been rather similar to the change in the upper 100 m in the Atlantic Ocean. In other words, a similar trend in heat content has caused a higher temperature rise in the Baltic in proportion to the mean depth. Thus, the Baltic Sea had roughly two times higher temperature increase rate, compared to the upper 100 m in the Atlantic Ocean. This important factor has to be taken into account when long-term changes of temperature-sensitive species are explained in the past or predicted for the future. Similar heat content rise in the Baltic

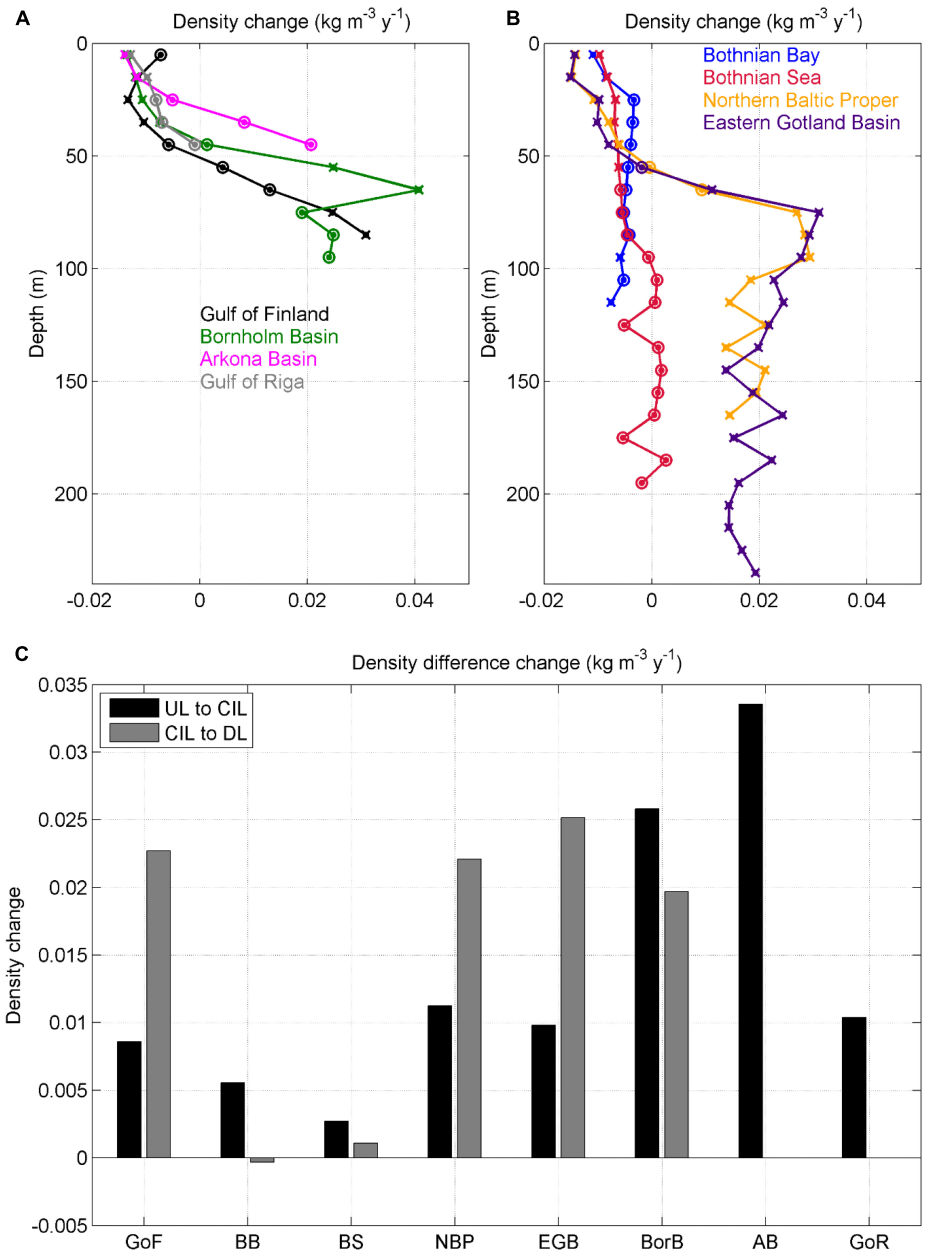

FIGURE 5 | Density trends **(A,B)**: trends of density differences **(C)** between the upper mixed layer and cold intermediate layer (UL to CIL, from 5–15 to 45–55 m), and between cold intermediate layer and sub-halocline deep layer (CIL to DL, from 45–55 to 65–85 m) in the sub-basins (GoF – Gulf of Finland, BB – Bothnian Bay, BS – Bothnian Sea, NBP – Northern Baltic Proper, EGB – Eastern Gotland Basin, BorB – Bornholm Basin, AB – Arkona Basin GoR – Gulf of Riga) of the Baltic Sea.

Sea and the upper layer of the Atlantic Ocean hints that there are large-scale (Kniebusch et al., 2019) rather than local reasons for the temperature trend in the Baltic.

Distinct Changes in the Three Layers and Pycnoclines

Temperature and salinity trends are not homogenous in the water column. There is a warming trend of 0.03–0.06°C year^{-1} in the upper layer and below the halocline in the deep layer. The negative salinity trend of −0.005 to −0.014 g kg^{-1} year^{-1} in the upper 40–50 m has simultaneously occurred with a positive trend of 0.02–0.04 g kg^{-1} year^{-1} below the halocline. The trends in the deep layer have not occurred in the basins, where the halocline does not exist – the Bothnian Sea, the Bothnian Bay, and the Gulf of Riga. In the rest of the areas, the three layers have had the following distinct changes: the upper layer has become warmer and fresher while the deep layer has become warmer and saltier. The smallest changes have occurred in the cold intermediate layer. These distinct changes are revealed not

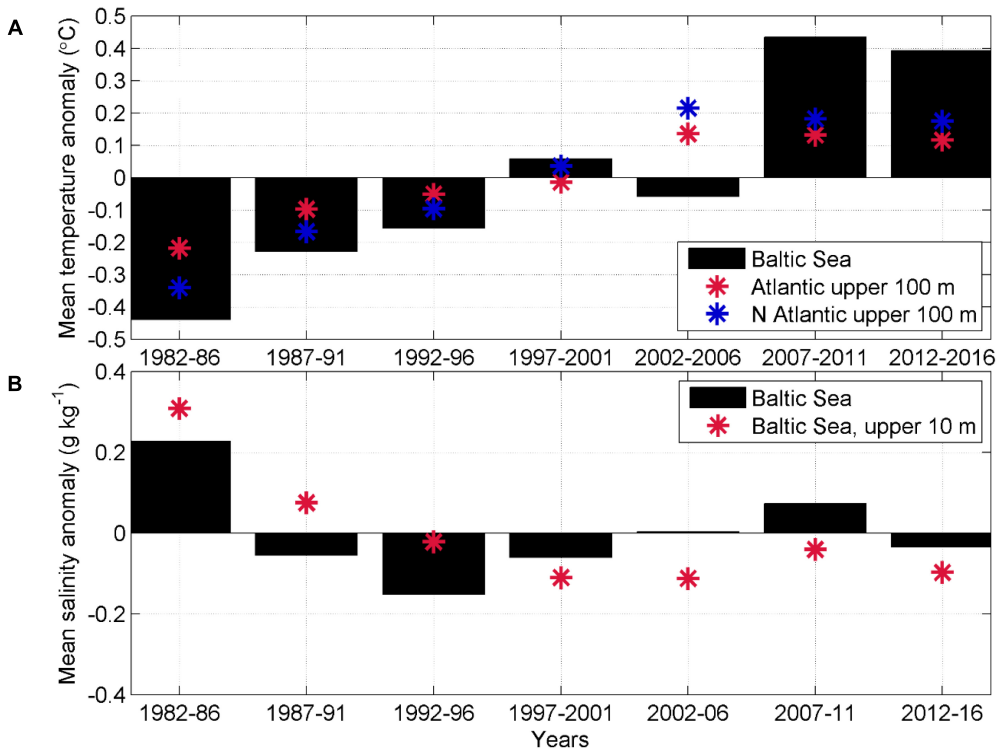

FIGURE 6 | Pentadal averages of temperature **(A)** and salinity **(B)** anomalies in the entire Baltic Sea in 1982–2016. Pentadal averages of temperature in the upper 100 m in the Atlantic Ocean and its part in the northern hemisphere are shown in the upper panel. Extended time-series of vertically integrated temperature change in the (Northern) Atlantic Ocean by Levitus et al. (2012) are presented.

only from the trends but also visually from the time-series of temperature and salinity anomalies (**Figure 7**). For instance, it is clear that in all three selected areas – the western (Bornholm Basin, **Figure 7B**), central (Eastern Gotland Basin, **Figure 7D**) and eastern (Gulf of Finland, **Figure 7F**) part of the Baltic Sea, there has been higher (lower) salinity in the beginning of the study period and lower (higher) salinity in the recent decade in the surface (deeper) layer. A nearly homogenous change in the entire water column has been reported (Zorita and Laine, 2000) and predicted (BACC Author Team, 2015) though.

The main reason for distinct changes is that different processes in various spatial and temporal scales dominate in the three layers. The upper layer is about half a year separated from the rest of the water column by the seasonal thermocline. It means, the changes in the heat flux through the sea surface and riverine/atmospheric freshwater flux impact only the upper 10–30 m thick layer during half a year. The cold intermediate layer instead is formed in the winter period. Even if the trend in the heat flux would be the same in winter and summer, the extra heat is distributed in the 60–70 m layer in winter in most of the Baltic. Therefore, the annual temperature change would be higher in the upper layer compared to the intermediate layer. Moreover, even if there is a change in temperature of the cold intermediate layer, it almost does not have any impact on stratification, since, at low temperatures, density changes caused by temperature changes are very small. There is no direct effect of changes in river runoff and winter mixing on the deep layer. Thus, the deep layer, which is controlled by abrupt inflows from the North Sea, and the upper layer, which is controlled by vertical salt flux and accumulated river runoff, show different long-term temporal courses. This can be observed from long-term records (Fonselius and Valderrama, 2003) – temperature and salinity in the surface layer do not follow the changes in the deep layer. Exceptions might be the areas where pycnoclines do not exist, e.g., the Gulf of Bothnia (Raateoja, 2013). Our results show that the thermohaline properties change in different directions and have different magnitudes in the three layers.

The Baltic Sea has become more stratified during the recent 35 years. The upper pycnocline is stronger due to the increase in temperature and decrease in salinity in the upper layer. The deeper pycnocline is stronger due to higher salinity in the deep layer. Warming of the deep layer contributes to the slight decrease in density, but this effect is overshadowed by the salinity increase. The increase in density difference between UL and CIL (between CIL and DL) in most of the Baltic Sea has been in a range of 0.009–0.011 (0.020–0.025) kg m^{-3} $year^{-1}$ or 0.32–0.39 (0.70–0.88) kg m^{-3} for 35 years. Only slight trends can be found in the Bothnian Sea and the Bothnian Bay. Trends in the deeper pycnocline did not have seasonality. An exception was the Gulf of Finland where an inter-annual trend to stronger pycnocline was found, but such a trend did not exist in winter. The likely reason is the increased frequency of westerly winds during

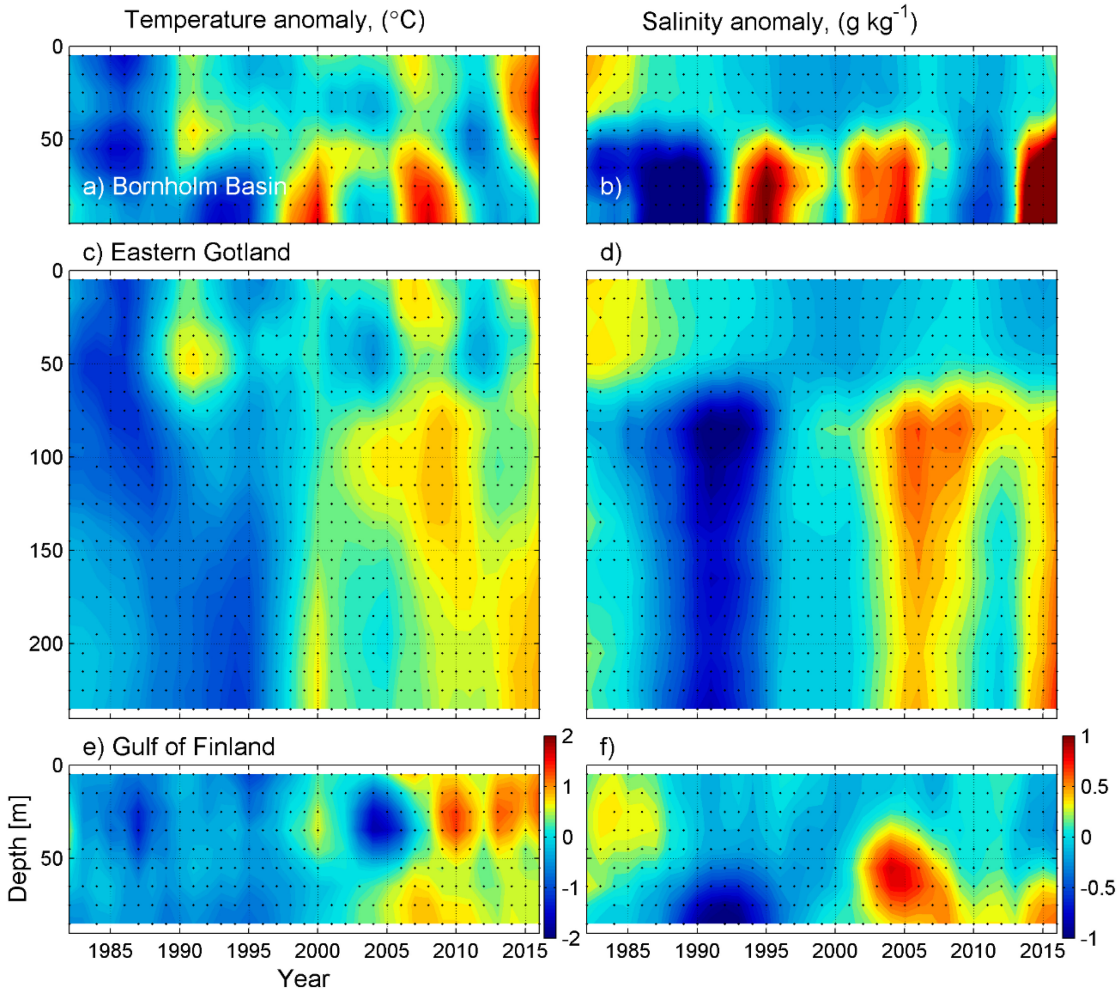

FIGURE 7 | Time-series of annual anomalies of temperature **(A,C,E)** and salinity **(B,D,F)** in the Bornholm Basin, the Eastern Gotland Basin, and the Gulf of Finland.

winters (Keevallik, 2011; Lehmann et al., 2011), which causes more frequent estuarine circulation reversals and consequent weakening of the halocline in the Gulf of Finland (Liblik et al., 2013; Elken et al., 2014; Lips et al., 2017).

In the present work, we concentrated on stratification strength, but the stratified period has extended as well. SST statistics (Kahru et al., 2016) suggest that the onset of stratification has occurred earlier, and the start of the decay of stratification later in recent years.

Sea Surface Temperature Trend

The average increase in the SST in the Baltic Sea for the period 1982–2016 was 0.05°C year^{-1}, which is very similar to earlier estimates: 0.05°C year^{-1} for the period 1982–2013 (Stramska and Białogrodzka, 2015) and 0.04°C year^{-1} for the period 1982–2012 (Høyer and Karagali, 2016). The increase of the SST in the Baltic Sea has been more rapid than the globally averaged SST rise, but in a similar order with other marginal seas around Europe: the North Sea (Høyer and Karagali, 2016), the Mediterranean Sea (Pastor et al., 2018), and the Black Sea (Shaltout and Omstedt, 2014). As noted by previous studies (Stramska and Białogrodzka, 2015; Høyer and Karagali, 2016; Tronin, 2017), warming is stronger in summer – the mean positive SST trend in the sea is between 0.07 and 0.08°C year^{-1} from May to September while in December – March statistically significant trend was not detected in most of the sea areas (**Figure 3**). This seasonal warming has extended favorable conditions for cyanobacteria blooms in the Baltic (Kahru et al., 2016). The spatial pattern of the SST trend shown in the present study is very similar to the trend in the study by Stramska and Białogrodzka (2015). Spatial distribution of trend slopes is much more patchy and likely much more impacted by inter-annual variability if shorter periods are used for SST trend calculation (BACC Author Team, 2015).

An interesting feature in the SST trend is stronger warming in shallow ends of the gulfs and areas with limited water exchange (**Figure 3**). In locations with more active water exchange, such intense warming cannot be seen. In **Figure 8A**, the seasonal course of temperature trend along the line from the Arkona Basin to the Eastern Gulf of Finland is shown (location of the line

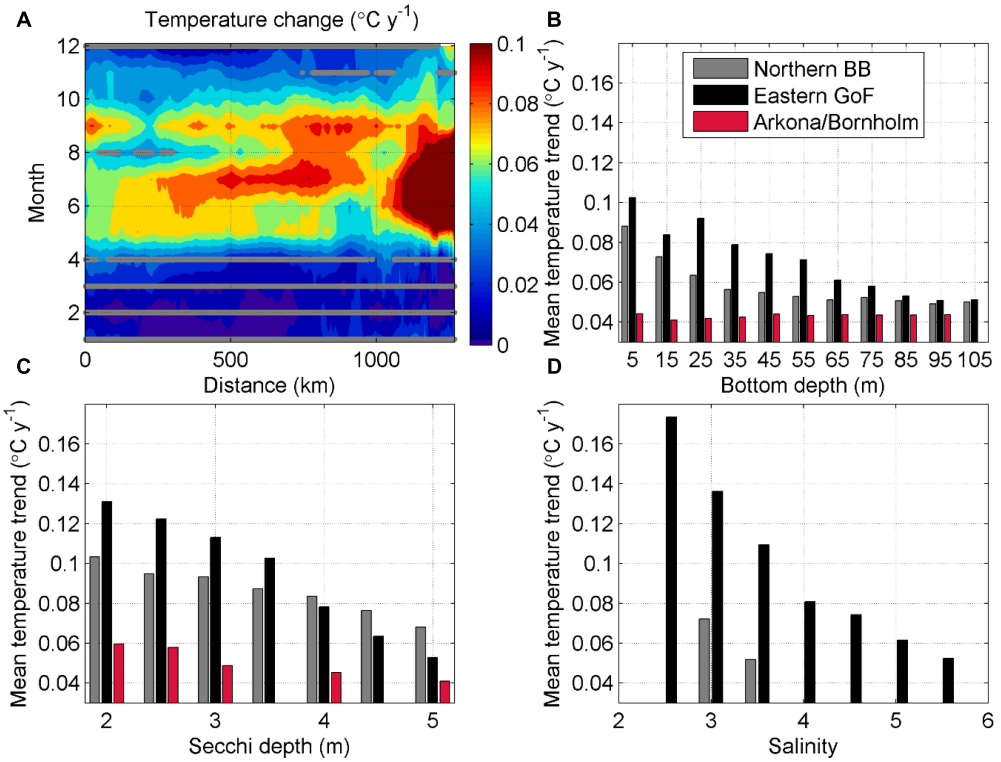

FIGURE 8 | (A) Seasonal course of SST trend (°C year^{-1}) along the line from Arkona basin to the Eastern Gulf of Finland (**Figure 3**). Gray lines/dots at subplot **(A)** show locations/months, where/when the trend was not significant ($p > 0.05$). Mean SST trend (°C year^{-1}) at different **(B)** sea bottom depths, **(C)** Secchi depth (m), and **(D)** upper layer salinities in the Eastern Gulf of Finland, Northern Bothnian Bay, and Arkona/Bornholm area. Mean Secchi depth data from March to October 2003–2012 (Stock, 2015) and mean surface salinity from April to October (Janssen et al., 1999) were used. Salinity in this figure is given on the Practical Salinity Scale.

is shown in **Figure 3**). It is clear that the higher SST increase (compared to the open Baltic, for instance) in the annual signal (**Figure 3**) in the eastern part of the Gulf of Finland is caused by a stronger trend in summer. Thus, the Eastern Gulf of Finland and other such areas have experienced more rapid warming, particularly in summer, compared to the rest of the Baltic Sea. The explanation of the stronger warming is not clear, but might be related to the bathymetry, stronger stratification or higher turbidity in these regions.

Extra heat in shallow areas is distributed in a thinner water column compared to deeper areas. To illustrate the effect, we have selected the following three areas (see boxes in **Figure 3**): Northern Bothnian Bay, Eastern Gulf of Finland and Arkona/Bornholm area, and calculated mean temperature trends for different bottom depth ranges inside those areas (**Figure 8B**). It shows that the temperature trend in shallower areas of the Eastern Gulf of Finland and the Northern Bothnian Bay has been higher than in deeper areas in the same regions. No such tendency can be found in the Arkona/Bornholm area. One can see (**Figure 3**) that the relationship between the higher temperature trend and shallower sea depth is valid (particularly in the Gulf of Finland) not only in very shallow areas but also in areas where sea bottom is well greater than the typical upper mixed layer depth. This might indicate that the warmed water formed in shallow areas has been transported toward central parts of the basins. Estuarine nature of mean circulation in both basins supports transport in the upper layer to deeper areas – to the west in the Gulf of Finland and the south in the Bothnian Bay (Andrejev et al., 2004; Myrberg and Andrejev, 2006).

The second possible explanation for the stronger warming in these areas, particularly for the Eastern Gulf of Finland, might be stronger haline stratification that coincides in summer with the seasonal thermocline (Vankevich et al., 2016). The mouth of the largest river in the Baltic Sea, the Neva River, is located at the eastern end of the Gulf of Finland. This riverine water causes stratification, which impedes vertical mixing, e.g., convection due to diurnal heat flux cannot reach that deep. Therefore, heat is kept in a relatively thin water column compared to the areas with less riverine water impact. Proxy of haline stratification and the impact of riverine water on the upper layer is the upper layer salinity. It is clear that the SST trend in the Gulf of Finland is well correlated with the upper layer salinity (**Figure 8D**). In case of easterly winds, this fresher and warmer thin layer can occasionally drift to the central Gulf of Finland and increase stratification there (Liblik and Lips, 2017; Suhhova et al., 2018). Another reason for enhanced stratification in these regions might be a lower activity of surface waves (Tuomi et al., 2010).

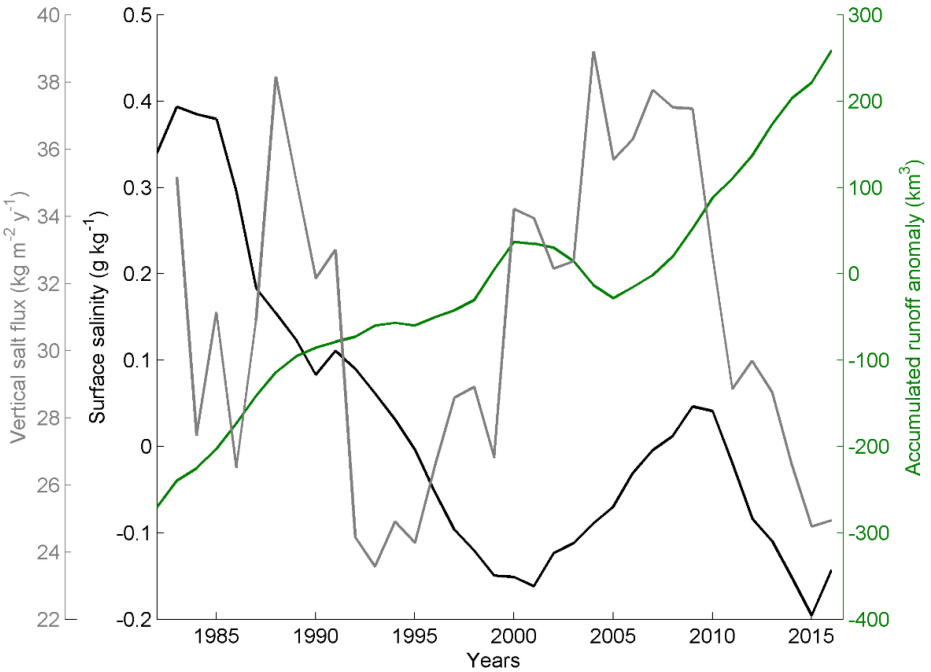

FIGURE 9 | Smoothed (by cut-off period 5 years) time-series of surface salinity anomalies in the Eastern Gotland Basin, accumulated river runoff anomalies, and vertical salt flux. River runoff data from Johansson (2018) were used.

The third possible explanation might be shallower attenuation of solar radiation of more turbid waters in the eastern Gulf of Finland (Ylöstalo et al., 2016) and consequent higher warming rate in the sea surface (Morel et al., 1994; Gildor and Naik, 2005; Lin et al., 2007). There is a clear correlation between the mean Secchi depth and SST trend (**Figure 8C**). Modeling experiment (Löptien and Meier, 2011) has shown that turbidity impacts the SST trends in the Baltic. Probably all three possible components (shallow depths and limited water exchange, stronger stratification, and higher turbidity) contribute to the higher warming rate of these areas. Further investigations of the components are out of the scope of the present work, but all three are worthy of studying in the future.

Upper Layer Salinity Trend

Freshening of the upper 50 m and an increase in salinity below that depth in the Baltic Sea has occurred during 1982–2016. The uppermost layer has become fresher at a rate of −0.005 to −0.014 g kg^{-1} year^{-1}. The trend is not continuous, but it is clear that the upper layer salinity has been lower in the recent decade compared to the first decade of the study period (**Figure 7**). A negative salinity trend, but with a smaller magnitude (between −0.003 and −0.008 g kg^{-1} year^{-1}) near the southern coast of the Baltic has been detected for the period 1950–2010 (Girjatowicz and Świątek, 2016). Possible causes for the decrease in the upper layer salinity are (1) reduced vertical salt fluxes from the deeper layers and/or (2) increased freshwater flux from atmosphere and land and its storage in the Baltic. It has been hinted that the upper layer salinity decrease since the beginning of the 1980s is related to the absence of MBIs (Reissmann et al., 2009) or has been mainly related to the accumulated river runoff (Winsor et al., 2001).

The reduced vertical salt flux might be caused by reduced vertical mixing or decreased salinity below the halocline. Latter is not the case, as salinity has increased in the deep layers of the Baltic (**Figures 4B,D**). Contributions of various processes to the vertical mixing and upward salt transport are not clear (Reissmann et al., 2009). Mean salinity in the Eastern Gotland Basin quite well describes the changes in the whole Baltic Sea (Winsor et al., 2001). We can confirm this by **Figure 4F** – the total salt mass change rate on the basis of the salinity changes and hypsographic curves in all basins is similar to the estimate where only the salinity changes in the Eastern Gotland Basin and the hypsographic curve of the whole Baltic Sea are taken into account. Moreover, the profiles of the heat content change calculated by the same two methods also fit well (**Figure 4E**). Discrepancies in the magnitude of the salinity and temperature increase can be found in the halocline, where the Eastern Gotland Basin-based estimate shows a higher increasing rate. This overestimation can be explained by the absence of the halocline in the Bothnian Sea and the Bothnian Bay, which is not taken into account by the Eastern Gotland Basin-based method. Nevertheless, multiyear salinity changes in the Eastern Gotland Basin can be used as a proxy of the mean salinity changes in the whole Baltic Sea.

Due to its central location and long distances from main fresh- and saltwater sources and coastal slopes, offshore areas of the Eastern Gotland Basin are not that strongly impacted by synoptic scale movements of fronts, upwelling events, etc.

Taking the mean residual current of 0.2 cm s^{-1} (Meier, 2007; Reissmann et al., 2009) and mean horizontal salinity gradient between the Northern Baltic Proper and the Eastern Gotland Basin above halocline 0.0013 g kg^{-1} km^{-1} (Janssen et al., 1999), freshening of the upper layer caused by the advection (residual current) would be 0.007 g kg^{-1} $month^{-1}$ or 0.04 g kg^{-1} during 6 months. The average seasonal increase of upper layer salinity in the Eastern Gotland Basin from August-September to February-March has been 0.52 g kg^{-1} in 1982–2016. Thus, the vertical mixing overshadows the effect of lateral freshwater flux on the upper layer salinity in a seasonal time-scale during autumn-winter. This can be well seen in the annual cycle of the upper layer salinity. Salinity increases in the upper layer of the Eastern Gotland Basin every autumn-winter. By taking the upper layer thickness of 60 m and the upper layer salinity change from summer to winter, we can estimate the upward salt flux (Reissmann et al., 2009). The mean vertical salt flux has been 31 kg m^{-2} $year^{-1}$ during 1982–2016 that is very close to the estimate by Reissmann et al. (2009). If the mean salinity decrease by lateral advection is taken into account, the mean estimated flux would be 34 kg m^{-2} $year^{-1}$. The flux does not show a trend suggesting that the negative salinity trend in the upper layer is not a consequence of changes in vertical salt transport.

Total runoff to the Baltic has been lower in the 1960s–1970s and higher since the 1980s (Johansson, 2018). Smoothed time-series (by 5-years cut-off period) of salinity in the Eastern Gotland Basin show a declining tendency from 1983 to 2001, an increase from 2002 to 2009 and a decline again until 2015 (**Figure 9**). Smoothed (by 5-years cut-off period) accumulated river runoff anomaly (anomalies from the average in 1950–2016) has a negative correlation with the upper layer salinity change in the Eastern Gotland Basin (**Figure 9**). A relationship between the mean salinity of the Baltic Sea (freshwater storage) and the accumulated runoff perturbations was shown by Winsor et al. (2001) and Väli et al. (2013). A decrease in accumulated river runoff anomaly (i.e., runoff was smaller than the average in 1950–2016) fits with the period of the salinity increase. However, the decrease in runoff was not as pronounced as the increase in the upper layer salinity in 2002–2009. One can see (**Figure 9**) that higher than average vertical salt flux occurred during that period. Further studies are needed to check if this discrepancy is related to the vertical salt flux or not. It also has to be noted that no statistically significant trends have been detected in annual river discharge in the Baltic Sea basin as a whole (BACC Author Team, 2015).

CONCLUSION

Stratification has strengthened in the Baltic Sea from 1982 to 2016. The trend in the annually averaged density gradient through the seasonal thermocline (halocline) in most of the Baltic Sea has been in the range of 0.009–0.011 (0.020–0.025) kg m^{-3} $year^{-1}$ or 0.33–0.39 (0.70–0.88) kg m^{-3} for 35 years. The strengthening trend of the halocline does not have a remarkable seasonality. An exception is the Gulf of Finland where no trend was found for the winter period likely due to the sensitivity of the gulf to increased frequency of westerly winds.

Distinct changes due to different dominating processes in various spatial and temporal scales in the three layers have occurred. The upper layer in most of the Baltic Sea is characterized by increasing temperature (0.03–0.06°C $year^{-1}$) and decreasing salinity (−0.005 to −0.014 g kg^{-1} $year^{-1}$). SST trends estimated based on *in situ* and remote sensing data agree well. The decrease in the upper layer salinity is likely caused by accumulated river runoff. However, in the second half of the study period, the time-series of accumulated river runoff and upper layer salinity do not agree well. We suggest that decadal changes in vertical salt transport might be the reason for this. Further studies are needed to confirm this hypothesis. Increased salinity in the deep layer is likely associated with increased lateral salt import from the North Sea. Areas, where the halocline exists have had temperature trend of 0.04–0.06°C $year^{-1}$ and salinity trend of 0.02 to 0.04 g kg^{-1} $year^{-1}$ in the deep layers. Only minor and mostly statistically not significant changes have occurred in the cold intermediate layer.

Upper layer warming is stronger from May to September (0.07–0.08°C $year^{-1}$ for the whole Baltic Sea). The mostly not significant trend in winter has been 0.01–0.02°C $year^{-1}$. Higher rate of warming (>0.06°C $year^{-1}$) has occurred in shallower, closed-end areas of gulfs, e.g., the northern part of the Bothnian Bay, the eastern part of the Gulf of Finland, and the eastern part of the Gulf of Riga. These areas have been warmed faster compared to the rest of the Baltic Sea during summers. The following three possible reasons could be responsible for high warming in these areas: shallow depths and limited water exchange, stronger stratification, and higher turbidity.

The warming trend in the whole Baltic has been 0.031°C $year^{-1}$ or 1.09°C from 1982 to 2016. The temperature increase has been, proportionally to the mean depth of the sea, approximately two times higher in the Baltic Sea compared to the upper 100 m in the Atlantic Ocean. Such a more rapid temperature increase has to be considered in the predictions of future changes. No significant trend in the mean salinity of the Baltic Sea was detected.

AUTHOR CONTRIBUTIONS

TL was responsible for compiling the data, data analyzes, and writing manuscript. UL contributed to writing of the manuscript.

FUNDING

This work was supported by Institutional Research Funding IUT (IUT19-6) of the Estonian Ministry of Education and Research.

ACKNOWLEDGMENTS

We would like to thank everybody who has contributed to performing the measurements and producing valuable data in the Baltic Sea.

REFERENCES

Andrejev, O., Myrberg, K., Alenius, P., and Lundberg, P. A. (2004). *Mean Circulation and Water Exchange in the Gulf of Finland-a Study Based on Three-Dimensional Modelling*. Available at: http://www.borenv.net/BER/pdfs/ber9/ber9-001.pdf (accessed November 22, 2018).

Astok, V., Otsmann, M., and Suursaar, Ü (1999). Biological, physical and geochemical features of enclosed and semi-enclosed marine systems. *Hydrobiologia* 393, 11–18. doi: 10.1007/978-94-017-0912-5_2

BACC Author Team (2015). *Second Asesment of Climate Change Impact for the Baltic Sea Basin. Book Series: Regional Climate Studies*. Berlin: Springer.

Baltic Sea Hydrographic Commission (2013). *Baltic Sea Bathymetry Database version 0.9.3*.

Bradtke, K., Agnieszka, H., and Urbański, J. A. (2010). Spatial and interannual variations of seasonal sea surface temperature patterns in the Baltic Sea Sea surface temperature seasonality global climate change Baltic Sea. *Oceanologia* 52, 345–362. doi: 10.5697/oc.52-3.345

Dailidienė, I., Baudler, H., Chubarenko, B., and Navrotskaya, S. (2011). Long term water level and surface temperature changes in the lagoons of the southern and eastern Baltic. *Oceanologia* 53, 293–308. doi: 10.5697/OC.53-1-TI.293

Elken, J., Raudsepp, U., Laanemets, J., Passenko, J., Maljutenko, I., Pärn, O., et al. (2014). Increased frequency of wintertime stratification collapse events in the Gulf of Finland since the 1990s. *J. Mar. Syst.* 129, 47–55. doi: 10.1016/j.jmarsys.2013.04.015

Feistel, R., Hagen, E., and Nausch, G. (2006). Unusual Baltic inflow activity in 2002–2003 and varying deep-water properties. *Oceanologia* 48, 21–35.

Fischer, H., and Matthäus, W. (1996). The importance of the Drogden Sill in the sound for major Baltic inflows. *J. Mar. Syst.* 9, 137–157. doi: 10.1016/S0924-7963(96)00046-2

Fonselius, S., and Valderrama, J. (2003). One hundred years of hydrographic measurements in the Baltic Sea. *J. Sea Res.* 49, 229–241. doi: 10.1016/S1385-1101(03)00035-2

Gildor, H., and Naik, N. H. (2005). Evaluating the effect of interannual variations of surface chlorophyll on upper ocean temperature. *J. Geophys. Res* 110:7012. doi: 10.1029/2004JC002779

Girjatowicz, J. P., and Świątek, M. (2016). Salinity variations of the surface water at the southern coast of the Baltic Sea in years 1950–2010. *Cont. Shelf Res.* 126, 110–118. doi: 10.1016/J.CSR.2016.08.005

Gouretski, V. (2018). World Ocean circulation experiment-argo global hydrographic climatology. *Ocean Sci.* 14, 1127–1146. doi: 10.5194/os-14-1127-2018

Haavisto, N., Tuomi, L., Roiha, P., Siiriä, S.-M., Alenius, P., and Purokoski, T. (2018). Argo floats as a novel part of the monitoring the hydrography of the Bothnian Sea. *Front. Mar. Sci.* 5:324. doi: 10.3389/fmars.2018.00324

Hietala, R., Lundberg, P., and Nilsson, J. A. U. (2007). A note on the deep-water inflow to the Bothnian Sea. *J. Mar. Syst.* 68, 255–264. doi: 10.1016/J.JMARSYS.2006.12.004

Høyer, J. L., and Karagali, I. (2016). Sea surface temperature climate data record for the North Sea and Baltic Sea. *J. Clim.* 29, 2529–2541. doi: 10.1175/JCLI-D-15-0663.1

Janssen, F., Schrum, C., and Backhaus, J. O. (1999). A climatological data set of temperature and salinity for the Baltic Sea and the North Sea. *Dtsch. Hydrogr. Zeitschrift* 51:5. doi: 10.1007/BF02933676

Johansson, J. (2018). *Total and Regional Runoff to the Baltic Sea - HELCOM. HELCOM Baltic Sea Environment Fact Sheets*. Available at: http://www.helcom.fi/baltic-sea-trends/environment-fact-sheets/hydrography/total-and-regional-runoff-to-the-baltic-sea/ (accessed November 15, 2018).

Jones, P. D., Jonsson, T., and Wheeler, D. (1997). Extension to the North Atlantic oscillation using early instrumental pressure observations from Gibraltar and south-west Iceland. *Int. J. Climatol.* 17, 1433–1450. doi: 10.1002/(SICI)1097-0088(19971115)17:13<1433::AID-JOC203<3.0.CO;2-P

Kahru, M., Elmgren, R., and Savchuk, O. P. (2016). Changing seasonality of the Baltic Sea. *Biogeosciences* 13, 1009–1018. doi: 10.5194/bg-13-1009-2016

Kao, H.-Y., Lagerloef, G., Lee, T., Melnichenko, O., Meissner, T., Hacker, P., et al. (2018). Assessment of aquarius sea surface salinity. *Remote Sens.* 10:1341. doi: 10.3390/rs10091341

Keevallik, S. (2011). Shifts in meteorological regime of the late winter and early spring in Estonia during recent decades. *Theor. Appl. Climatol.* 105, 209–215. doi: 10.1007/s00704-010-0356-x

Kniebusch, M., Meier, H. E. M., Neumann, T., and Börgel, F. (2019). Temperature variability of the Baltic Sea since 1850 and attribution to atmospheric forcing variables. *J. Geophys. Res. Ocean.* 2018:JC013948. doi: 10.1029/2018JC013948

Laakso, L., Mikkonen, S., Drebs, A., Karjalainen, A., Pirinen, P., and Alenius, P. (2018). 100 years of atmospheric and marine observations at the Finnish Utö Island in the Baltic Sea. *Ocean Sci.* 14, 617–632. doi: 10.5194/os-14-617-2018

Large, W. G., Yeager, S. G., Large, W. G., and Yeager, S. G. (2012). On the observed trends and changes in global sea surface temperature and air–sea heat fluxes (1984–2006). *J. Clim.* 25, 6123–6135. doi: 10.1175/JCLI-D-11-00148.1

Lass, H. U., Prandke, H., and Liljebladh, B. (2003). Dissipation in the Baltic proper during winter stratification. *J. Geophys. Res.* 108:3187. doi: 10.1029/2002JC001401

Lehmann, A., Getzlaff, K., and Harlaß, J. (2011). Detailed assessment of climate variability in the Baltic Sea area for the period 1958 to 2009. *Clim. Res.* 46, 185–196. doi: 10.3354/cr00876

Lehmann, A., Krauss, W., and Hinrichsen, H.-H. (2002). Effects of remote and local atmospheric forcing on circulation and upwelling in the Baltic Sea. *Tellus A Dyn. Meteorol. Oceanogr.* 54, 299–316. doi: 10.3402/tellusa.v54i3.12138

Lehmann, A., and Post, P. (2015). Variability of atmospheric circulation patterns associated with large volume changes of the Baltic Sea. *Adv. Sci. Res.* 12, 219–225. doi: 10.5194/asr-12-219-2015

Leppäranta, M., and Myrberg, K. (eds) (2009). "Topography and hydrography of the Baltic Sea," in *Physical Oceanography of the Baltic Sea* (Berlin: Springer), 41–88. doi: 10.1007/978-3-540-79703-6_3

Levitus, S., Antonov, J. I., Boyer, T. P., Baranova, O. K., Garcia, H. E., Locarnini, R. A., et al. (2012). World ocean heat content and thermosteric sea level change (0-2000 m), 1955-2010. *Geophys. Res. Lett.* 39:L10603. doi: 10.1029/2012GL051106

Liblik, T., Laanemets, J., Raudsepp, U., Elken, J., and Suhhova, I. (2013). Estuarine circulation reversals and related rapid changes in winter near-bottom oxygen conditions in the Gulf of Finland, Baltic Sea. *Ocean Sci.* 9, 917–930. doi: 10.5194/os-9-917-2013

Liblik, T., and Lips, U. (2011). Characteristics and variability of the vertical thermohaline structure in the Gulf of Finland in summer. *Boreal Environ. Res.* 16, 73–83.

Liblik, T., and Lips, U. (2017). Variability of pycnoclines in a three-layer, large estuary: the Gulf of Finland. *Boreal Environ. Res.* 22, 27–47.

Liblik, T., Naumann, M., Alenius, P., Hansson, M., Lips, U., Nausch, G., et al. (2018). Propagation of impact of the recent major baltic inflows from the Eastern Gotland Basin to the Gulf of Finland. *Front. Mar. Sci.* 5:222. doi: 10.3389/fmars.2018.00222

Lin, P., Liu, H., and Zhang, X. (2007). Sensitivity of the upper ocean temperature and circulation in the equatorial Pacific to solar radiation penetration due to phytoplankton. *Adv. Atmos. Sci.* 24, 765–780. doi: 10.1007/s00376-007-0765-7

Lips, I., Lips, U., and Liblik, T. (2009). Consequences of coastal upwelling events on physical and chemical patterns in the central Gulf of Finland (Baltic Sea). *Cont. Shelf Res.* 29, 1836–1847. doi: 10.1016/j.csr.2009.06.010

Lips, U., Kikas, V., Liblik, T., and Lips, I. (2016). Multi-sensor in situ observations to resolve the sub-mesoscale features in the stratified Gulf of Finland. *Baltic Sea Ocean Sci.* 12, 715–732. doi: 10.5194/os-12-715-2016

Lips, U., Laanemets, J., Lips, I., Liblik, T., Suhhova, I., and Suursaar, Ü (2017). Wind-driven residual circulation and related oxygen and nutrient dynamics in the Gulf of Finland (Baltic Sea) in winter. *Estuar. Coast. Shelf Sci.* 195, 4–15. doi: 10.1016/J.ECSS.2016.10.006

Löptien, U., and Meier, H. E. M. (2011). The influence of increasing water turbidity on the sea surface temperature in the Baltic Sea: a model sensitivity study. *J. Mar. Syst.* 88, 323–331. doi: 10.1016/J.JMARSYS.2011.06.001

Meier, H. E. (2007). Modeling the pathways and ages of inflowing salt- and freshwater in the Baltic Sea. *Estuar. Coast. Shelf Sci.* 74, 610–627. doi: 10.1016/J.ECSS.2007.05.019

Meier, H. E. M., and Kauker, F. (2003). Modeling decadal variability of the Baltic Sea: 2. Role of freshwater inflow and large-scale atmospheric circulation for salinity. *J. Geophys. Res.* 108:3368. doi: 10.1029/2003JC001799

Mohrholz, V. (2018). Major baltic inflow statistics – revised. *Front. Mar. Sci.* 5:384. doi: 10.3389/fmars.2018.00384

Mohrholz, V., Dutz, J., and Kraus, G. (2006). The impact of exceptionally warm summer inflow events on the environmental conditions in the Bornholm Basin. *J. Mar. Syst.* 60, 285–301. doi: 10.1016/j.jmarsys.2005.10.002

Mohrholz, V., Naumann, M., Nausch, G., Krüger, S., and Gräwe, U. (2015). Fresh oxygen for the Baltic Sea - an exceptional saline inflow after a decade of stagnation. *J. Mar. Syst.* 148, 152–166. doi: 10.1016/j.jmarsys.2015.03.005

Morel, A., Antoine, D., Morel, A., and Antoine, D. (1994). Heating rate within the upper ocean in relation to its bio–optical state. *J. Phys. Oceanogr.* 24, 1652–1665. doi: 10.1175/1520-04851994024<1652:HRWTUO<2.0.CO;2

Myrberg, K., and Andrejev, O. (2006). Modelling of the circulation, water exchange and water age properties of the Gulf of Bothnia mean circulation water age water exchange. *Oceanologia* 48, 55–74.

Pastor, F., Valiente, J. A., and Palau, J. L. (2018). Sea surface temperature in the Mediterranean: trends and spatial patterns (1982–2016). *Pure Appl. Geophys.* 175, 4017–4029. doi: 10.1007/s00024-017-1739-z

Raateoja, M. (2013). Deep-water oxygen conditions in the Bothnian sea. *Boreal Environ. Res.* 18, 235–249. doi: 10.1007/s13280-015-0675-3

Rak, D. (2016). The inflow in the Baltic proper as recorded in January–February 2015. *Oceanologia* 58, 241–247. doi: 10.1016/J.OCEANO.2016.04.001

Reissmann, J. H., Burchard, H., Feistel, R., Hagen, E., Lass, H. U., Mohrholz, V., et al. (2009). Vertical mixing in the Baltic Sea and consequences for eutrophication - a review. *Prog. Oceanogr.* 82, 47–80. doi: 10.1016/j.pocean.2007.10.004

Shaltout, M., and Omstedt, A. (2014). Recent sea surface temperature trends and future scenarios for the Mediterranean Sea. *Oceanologia* 56, 411–443. doi: 10.5697/OC.56-3.411

Skudra, M., and Lips, U. (2017). Characteristics and inter-annual changes in temperature, salinity and density distribution in the Gulf of Riga. *Oceanologia* 59, 37–48. doi: 10.1016/J.OCEANO.2016.07.001

Stepanova, N. B., Chubarenko, I. P., and Shchuka, S. A. (2015). Structure and evolution of the cold intermediate layer in the southeastern part of the Baltic Sea by the field measurement data of 2004–2008. *Oceanology* 55, 25–35. doi: 10.1134/S0001437015010154

Stock, A. (2015). Satellite mapping of Baltic Sea Secchi depth with multiple regression models. *Int. J. Appl. Earth Obs. Geoinf.* 40, 55–64. doi: 10.1016/j.jag.2015.04.002

Stramska, M., and Białogrodzka, J. (2015). Spatial and temporal variability of sea surface temperature in the Baltic Sea based on 32-years (1982–2013) of satellite data. *Oceanologia* 57, 223–235. doi: 10.1016/J.OCEANO.2015.04.004

Suhhova, I., Liblik, T., Lilover, M.-J., and Lips, U. (2018). A descriptive analysis of the linkage between the vertical stratification and current oscillations in the Gulf of Finland. *Boreal Environ. Res.* 23, 83–103.

Tronin, A. (2017). The satellite-measured sea surface temperature change in the Gulf of Finland. *Int. J. Remote Sens.* 38, 1541–1550. doi: 10.1080/01431161.2017.1286057

Tuomi, L., Kahma, K. K., and Pettersson, H. (2010). Wave hindcast statistics in the seasonally ice-covered Baltic sea. *Boreal Environ. Res.* 16, 451–472.

Väli, G., Meier, H. E. M., and Elken, J. (2013). Simulated halocline variability in the Baltic Sea and its impact on hypoxia during 1961-2007. *J. Geophys. Res. Ocean* 118, 6982–7000. doi: 10.1002/2013JC009192

Vankevich, R. E., Sofina, E. V., Eremina, T. E., Ryabchenko, V. A., Molchanov, M. S., and Isaev, A. V. (2016). Effects of lateral processes on the seasonal water stratification of the Gulf of Finland: 3-D NEMO-based model study. *Ocean Sci.* 12, 987–1001. doi: 10.5194/os-12-987-2016

Vuorinen, I., Hänninen, J., Rajasilta, M., Laine, P., Eklund, J., Montesino-Pouzols, F., et al. (2015). Scenario simulations of future salinity and ecological consequences in the Baltic Sea and adjacent North Sea areas–implications for environmental monitoring. *Ecol. Indic.* 50, 196–205. doi: 10.1016/J.ECOLIND.2014.10.019

Winsor, P., Rodhe, J., and Omstedt, A. (2001). Baltic Sea ocean climate: an analysis of 100 yr of hydrographic data with focus on the freshwater budget. *Clim. Res.* 18, 5–15. doi: 10.3354/cr018005

Ylöstalo, P., Seppälä, J., Kaitala, S., Maunula, P., and Simis, S. (2016). Loadings of dissolved organic matter and nutrients from the Neva River into the Gulf of Finland – biogeochemical composition and spatial distribution within the salinity gradient. *Mar. Chem.* 186, 58–71. doi: 10.1016/J.MARCHEM.2016.07.004

Zorita, E., and Laine, A. (2000). Dependence of salinity and oxygen concentrations in the Baltic Sea on large-scale atmospheric circulation. *Clim. Res.* 14, 25–41. doi: 10.3354/cr014025

Conflict of Interest Statement: The authors declare that the research was conducted in the absence of any commercial or financial relationships that could be construed as a potential conflict of interest.

frontiers in Earth Science

ORIGINAL RESEARCH
published: 02 July 2019
doi: 10.3389/feart.2019.00158

The Baltic and North Seas Climatology (BNSC)—A Comprehensive, Observation-Based Data Product of Atmospheric and Hydrographic Parameters

Iris Hinrichs[1], Annika Jahnke-Bornemann[1], Axel Andersson[2], Anette Ganske[3], Viktor Gouretski[1], Corinna Jensen[3], Birgit Klein[3], Jens Möller[3], Remon Sadikni[1] and Birger Tinz[2]*

[1] CEN, University of Hamburg, Hamburg, Germany, [2] German Meteorological Service, Deutscher Wetterdienst (DWD), Hamburg, Germany, [3] Federal Maritime and Hydrographic Agency, Hamburg, Germany

OPEN ACCESS

Edited by:
Markus Meier, Leibniz Institute for Baltic Sea Research (LG), Germany

Reviewed by:
Vladimir Alexeevich Ryabchenko, P. P. Shirshov Institute of Oceanology (RAS), Russia
Germo Väli, Tallinn University of Technology, Estonia

***Correspondence:**
Iris Hinrichs
iris.hinrichs@uni-hamburg.de

Specialty section:
This article was submitted to Interdisciplinary Climate Studies, a section of the journal Frontiers in Earth Science

Received: *19 December 2018*
Accepted: *05 June 2019*
Published: *02 July 2019*

Citation:
Hinrichs I, Jahnke-Bornemann A, Andersson A, Ganske A, Gouretski V, Jensen C, Klein B, Möller J, Sadikni R and Tinz B (2019) The Baltic and North Seas Climatology (BNSC)—A Comprehensive, Observation-Based Data Product of Atmospheric and Hydrographic Parameters. Front. Earth Sci. 7:158. doi: 10.3389/feart.2019.00158

The Baltic and North Seas Climatology (BNSC) presented here is a new climatology calculated solely from marine *in situ* observations. Created in cooperation between University of Hamburg (UHH), Federal Maritime and Hydrographic Agency [Bundesamt für Seeschifffahrt und Hydrographie (BSH)] and German Meteorological Service [Deutscher Wetterdienst (DWD)], the BNSC is an update of the KLIWAS ("**Kli**mawandel und **Was**serstraßen") climatology for the North Sea and is extended to the Baltic Sea. A thorough quality control, the reduction of the temporal sampling error and spatial and temporal averaging were applied to the observations, yielding time series of gridded fields of atmospheric and hydrographic parameters in the region of the Baltic, the North Sea and adjacent regions of the North Atlantic. The atmospheric subset of the BNSC consists of time series of monthly mean gridded fields of 2 m air and dew point temperature and air pressure at sea level for the period 1950–2015 on a horizontal 1° × 1° grid. Climatological fields are provided as well. The hydrographic part of the BNSC comprises the variables water temperature and salinity on 105 depth levels for the time interval 1873–2015. The grid boxes' edge length is 0.25° in both zonal and meridional direction. Monthly and annual mean fields are provided as well as decadal monthly mean fields. To create homogenous fields, the method of objective analysis was applied to the fields of decadal means. Furthermore, an extensive sensitivity study was carried out to assess the sensitivity of the data product to the amount of observational data. The BNSC introduced here is compared to several different data products: three reanalyses (ERA-Interim, ERA-40 and COSMO-REA6), the corresponding KLIWAS product and meteorological station data for the atmospheric part. The hydrographic subset is compared to the KLIWAS climatology, the BALTIC ATLAS and the Baltic Sea Physical Reanalysis Product. The BNSC data product allows studying of climate variability but also holds the chance to validate regional numerical climate simulations, which makes it a valuable reference data set. The BSNC is freely available via the website of University of Hamburg's Integrated Climate Data Center.

Keywords: North Sea, Baltic Sea, climatology, reanalysis, *in situ* data, quality control

INTRODUCTION

In comparison to other oceanic regions, the Baltic and the North Sea is very well-sampled with respect to both marine and meteorological observations. Different platforms (voluntary observing ships [VOS], buoys (drifting and stationary), research vessels, fire ships etc.) contribute to the wealth of *in situ* observations that help to assess the conditions of the ocean and the atmosphere and to analyze changes in those two important components of the climate system. Numerical modeling studies in climate science aim at reproducing complex and dynamic processes in order to predict future climate change. Regional climate models, however, depend on observational data as a reference and validation, as was stated in the goals of both the KLIWAS project (Kofalk et al., 2010) and the project "Network of Experts" (both founded by the German Ministry of Transport and Digital Infrastructure). The KLIWAS project (Climate Water Navigation: Impacts of Climate Change on Waterways and Navigation) looked for the effects of climate change on navigation on coastal waterways and on coastal protection infrastructure by running regional climate models. In this project, a gridded climatological reference data set over the North Sea was required to evaluate the quality of hindcast runs of these models. Since there were no sufficient climatologies for the North Sea region in the form of a long term data set, such a reference data set based on *in situ* observations was created for meteorological and hydrographic parameters on a compatible grid: the KLIWAS North Sea Climatology [KNSC (Bersch et al., 2013, 2016) (hydrographic part) and (Sadikni et al., 2013, 2018) (atmospheric part)]. In order to serve as a validation reference, the input data for these data sets had to be homogenized with respect to quality as well as spatial and temporal dimensions.

Similar data products exist for the North and Baltic Sea: The first to mention that includes atmosphere is Korevaar (1990), a climatology of the North Sea for the time period 1961–1980 based on observations from ships and lightvessels, that was best at that time. The atmospheric North Sea climatology for 1981–1990 by Michaelsen et al. (1998) could be seen not only as an update of the previous, but as well as a precursor of the KNSC, as it, too, was produced in a cooperation between the DWD and the University of Hamburg. Janssen et al. (1999) created a hydrographic climatology of monthly mean fields for both marginal seas based on observational data from 1900 to 1996; (Feistel et al., 2008) provide a time series of monthly mean fields of various marine and atmospheric parameters up to 2005 for the Baltic Sea. A similar data product, but solely focussed on hydrographic parameters, was produced by Núñez-Riboni and Akimova (2015). But in contrast to the BNSC data product presented in this paper, these products do not cover the entire North and Baltic Seas for meteorological and hydrographic parameters on a compatible grid.

Comparison between the atmospheric KNSC data product and the output of regional climate models was performed by Bülow et al. (2014). The hydrographic part of KNSC was used in an intercomparison study between various ocean models in Pätsch et al. (2017). A comprehensive assessment of the atmospheric KNSC and global reanalysis products was done by Schade et al. (2018). Here, the global reanalyses NCEP-1 (Kalnay et al., 1996), ERA-40 (Uppala et al., 2005), ERA-Interim (Dee et al., 2011), MERRA (Rienecker et al., 2011), and 20CRv2 (Compo et al., 2011) were used.

The idea of the data product presented here is to pursue the concept of a combined meteorological-hydrographical data product realized in the KLIWAS project by creating the KNSC data product, to update the climatologies for the ocean and the atmosphere with recent observational data and to extend the data product to the Baltic Sea.

The data and methods applied in this work are described in section Data and Methods. The sources of data of the atmospheric part of the BNSC (hereafter referred to as BNSCatm) and changes in the creation procedure of the BNSCatm data product with respect to the creation of KNSC are briefly described in section Atmospheric BNSC.

The data and methods applied for the calculation of the hydrographic BNSC data product (hereafter referred to as BNSChydr) are elaborately described in section Hydrographic BNSC.

In contrast to the KNSC data product, a sensitivity analysis is applied to the BNSC data products which assesses the sensitivity of the data product with respect to the chosen base of observational data. The description of this study can be found in section Hydrographic BNSC.

Additionally, both BNSC data products are compared to several other data products. A description of the data used and the methods applied is provided in section Comparison With Other Data Products.

The description of the data products themselves (BNSCatm and BNSChydr), the outcome of the sensitivity study and the comparison with the other data products is presented in section Results. It is followed by a summary and an outlook (section Summary and Outlook). The data availability and description of the data files and the provided variables are listed in section Data Availability and Description.

DATA AND METHODS

Overview

The BNSC data product bases on marine observational data in the longitudinal range of 15°W to 31°E. The lower limit of the latitudinal range is set to 47°N; the upper limit is 66°N for the Baltic and 65°N for the North Sea region. The data product consists of temporally averaged fields of the following atmospheric and hydrographic parameters:

- sea level air pressure (SLP)
- air temperature at 2 m height (AT)
- dew point temperature at 2 m height (DP)
- sea water temperature (T)
- sea water salinity (S)

The latter two are available as 3-D fields.
The box size of the horizontal grids is set to:

- $1^\circ \times 1^\circ$ for BNSCatm.
- $0.25^\circ \times 0.25^\circ$ for BNSChydr

The different temporal resolutions and periods are:

- for BNSCatm, monthly and climatological monthly for 1950–2015
- for BNSChydr, monthly, annual and decadal monthly for 1873–2015.

Atmospheric BNSC

Sources of Data

The atmospheric part of this climatology (BNSCatm) is produced with marine *in situ* observations originating from the Marine Data Center of the DWD, which maintains an extensive climatological archive of national and international weather data gathered by vessels and buoys (see https://www.dwd.de/EN/ourservices/marine_data_center/maritimesdatenzentrum.html, last access May 14th 2019). The data collection of this archive started in the middle of the nineteenth century and is ongoing. Most of these observations come from ships and buoys and are recorded using a variety of methods, including manual observations at specific times as well as automated transmission of measurements that were taken with a high frequency, which is described in more detail by Schade et al. (2013) and Sadikni et al. (2018). All data are checked using the DWD high quality control (HQC) procedure to ensure the maximum degree of reliability before they are added to the archive. These procedures do not only check the individual observation but also implement checks on a sequence of observations from a specific observation platform in order to identify data errors of location and their time series consistency, as is described by Sadikni et al. (2018) in their section 2.a. Even though parts of the data that are included in this archive are a subset of ICOADS, checking all data in the same way with the same method was the main argument to use it for this study. Only data with flags "C" (climatologically right), "D" (analysis consistent), "E" (temporally consistent), "F" (internally consistent), "G" (spatially consistent, or "H" (manually consistent) are used in this study. This leads to about 31 million quality-controlled sets of meteorological *in situ* observations in the BNSC region for the period January 1950 to December 2015. Due to a relatively small amount of available data in the years before 1950, the period starts later than for the hydrographical part. The data used here can be considered as atmospheric observations near sea level at meteorological standard heights, as is sea level for air pressure and 2 m for the air and dew point temperatures.

Data Processing

For the calculation of the climatology, it has to be taken into account, that the observational data are not equally distributed in space or time. Therefore, measures have been taken to homogenize the data. Since the creation of the atmospheric part of the KNSC and the atmospheric BNSC data product do not differ substantially, the reader is referred to the detailed description in Sadikni et al. (2018).

Only observations at standard observation times (0, 6, 12, and 18 UTC) are used, like it was done for the KNSC climatology in order to reduce possible sampling biases caused by the high frequency of observations by automated measurements. The selected quality controlled observations are checked for duplicates, which is an additional test compared to the precursor KNSC.

In the data, there are fewer observations for the dew point temperature than for the other two parameters. The number of observations was increased by calculating dew point temperature from air temperature and relative humidity, unless it was directly measured. This method adds several hundred values to dew point temperature data.

The further procedure is carried out in nearly the same way as described by Sadikni et al. (2018). In the first step, the data is sorted into grid boxes of one degree edge length for each month of each year, to obtain a time series of monthly means. The $1^\circ \times 1^\circ$ spatial resolution is coarser than that of the hydrographic part, but is chosen due to the low data density to get statistically meaningful results for each grid box.

The air and dew point temperature have distinct diurnal and annual cycles, and therefore a sampling error can occur due to an unbalanced temporal data distribution. Corrections for the hours of the day, and as well the day of a month were calculated to shift the values to the middle of the day and month, respectively. As this is done on a monthly basis, still the annual cycle is kept in the climatology. See Sadikni et al. (2018) for a detailed description of this process. In the first step, for the diurnal cycle correction terms, they were calculated for each month and grid cell as difference between the long-term mean and the 6 h means. A more complex approach was used in the second step for the annual cycle. For each month, the differences between the long-term monthly mean and the daily means were calculated and afterwards, the results for the month were fitted with a polynomial of second order. The difference between the result of the polynomial on a day and the long-term-mean of the month was used as correction term. These corrections were applied to the observations to reduce errors due to the diurnal and annual cycles.

Since the air pressure observations do not show a pronounced mean annual cycle, especially in the northern region, and no diurnal cycle, a different method is applied: The number of days within a month without pressure data must not exceed 14 consecutive days to ensure an even data distribution in time. This criterion differs from the previous version, described by Sadikni et al. (2018), in which data averages over 6 day windows were used, where 4 of 5 windows had to be covered with data, which means a maximum possible data gap of 16 days. In the KNSC, the averages of the 6 day windows were used for monthly mean values, resulting in temporally strongly smoothed results, and in small standard deviations, compared to reanalysis data for example. This is the reason for this new approach for temporal correction of air pressure data.

In the next step, it is ensured that, if possible, there is a sufficient number of values per grid box for averaging. For this purpose, a threshold for the number of observations per grid point is set for each parameter. This threshold is 20 observations for the temperatures and 500 observations for the pressure, which are the same values as in the KNSC (Sadikni et al., 2018). In the first step, if the number of observations in the grid box is below this threshold value, the observations of the eight surrounding

grid boxes are added to the average. If the number of observations is still smaller than the threshold, then, in the second step, the data of the next 16 environment boxes are added for the averaging. Thus, observations of up to 24 surrounding grid boxes can contribute to the result of the center grid box. The results of these calculations are time series of monthly mean fields of the parameters on the one-degree grid.

From these monthly mean fields, the BNSC climatology is calculated for the 30-year periods 1951–1980, 1961–1990, 1971–2000, and 1981–2010. For this, the mean values of the fields for each month of the respective period are computed. A grid box gets no value if it had no value in 1/6 of the time, which is 6 or more months. For the longtime climatology 1950–2015, due to the long time series of 66 years, the criterion is slightly less strict and needs a value in at least 4/5 of the time steps.

Hydrographic BNSC

Sources of Data

Observed temperature and salinity profiles from different data sources are the base of the BNSC data product. The sources of observational data are:

- **WOD** (World Ocean Data Center, Boyer et al., 2013)
- **DOD** (Deutsches Ozeanografisches Datenzentrum, Germany, www.bsh.de)
- **IOW** (Leibniz Institute for Baltic Sea Research Warnemünde, Germany,
- www.io-warnemuende.de)
- **ICES** (International Council for Exploration of the Sea, www.ices.dk)
- **IMGW-PIB** (The Institute of Meteorology and Water Management – National Research Institute, Poland, www.imgw.pl)
- **NIOZ** (Royal Netherlands Institute for Sea Research, www.nioz.nl)
- **BODC** (British Oceanographic Data Center, www.bodc.ac.uk)
- **SCANFISH** (SCANfish data, provided by BSH, www.bsh.de)
- **CTD_DK** (Danish National Marine Monitoring Data, Bioscience, Aarhus University - http://Mads.dmu.dk)
- **ARGO** (International ARGO-Project, www.ifremer.fr).

The authors do not claim the list of sources of data to be complete. By the time starting working on BNSChydr, the data sources listed above were the ones the authors were aware of. Considering the creation of marine climatologies a process, future versions may not only include future observational data but also data sources not included yet, as, for example, the Baltic Environmental Database (BED, http://nest.su.se/bed/), the Copernicus Marine Environment Monitoring Service, the SeaDataNet program and the database compiled within the international project "The Year of the Gulf of Finland 2014" (see "The Gulf of Finland assessment., 2016" in the reference list for more details).However, the expansion to more data sources has always to be considered with respect to the cost-value ratio: there is already a strong overlap between some of the above listed data sources. Janssen et al. (1999) also found a great intersection between the ICES/DOD data bases (which they chose for their data product) and other data sources. Thus, new data sources might contribute some observations not included yet but, at the same time, each new data source also adds workload to the data processing procedure which is explained in the following.

TABLE 1 | Number of remaining BNSChydr profiles after sorting of duplicates.

Source	Number of Profiles
WOD	765,395
DOD	221,383
IOW	9,614
ICES	146,874
IMGW-PIB	6,334
NIOZ	2,798
BODC	3,723
SCANFISH	9,798
CTD_DK	25,564
ARGO	2,992
$\sum$	1,194,475

Data Processing

The observational data are processed in several consecutive steps described in detail in the following.

Duplicate Profiles

Incorporation of several data sources in the research of observational data includes intersection of different sources of data, e.g., profiles contained in the WOD data base are also provided by ICES. Duplicate profiles, however, would bias the result of the BNSC. Therefore, it is necessary to exclude the duplicate profiles in the further data processing. The numbers of remaining profiles after identification of duplicates are listed in **Table 1**, sorted by the different data sources.

To get an overview of the distribution of the observations, a time series (1873–2015) of the frequency of observed profiles per year is displayed in **Figure 1A**. In the period between 1873 and 1882, there are only 1–6 profiles recorded in the whole area. In general, the number of observations is rather low until approximately 1950. The periods of the First and Second World War can clearly be recognized by depressions in the observational frequency. From 1950 on, the observation rate moderately rises to a maximum in the 1990s. For the year 1989, the number of profiles exceeds the value of 30,000 profiles and sticks out. Closer analysis revealed, that most of the profiles in this year can be found in only five $0.25^\circ \times 0.25^\circ$ boxes close to the German North and Baltic Sea coast.

Additionally, **Figure 1B** shows the distribution of the observed profiles in the 12 months of the year. It can clearly be seen that the observational frequency is higher in the summer than in the winter months. In **Figure 2**, this distribution is horizontally resolved; a distinctly higher data density can be seen in the months May-September than in the rest of the year. This is most obvious in the area of the Baltic and the central North Sea. A rather low number of observations characterizes the outer regions of the BNSC area. With respect to the data coverage as a function of depth (not shown) it can be stated, that the

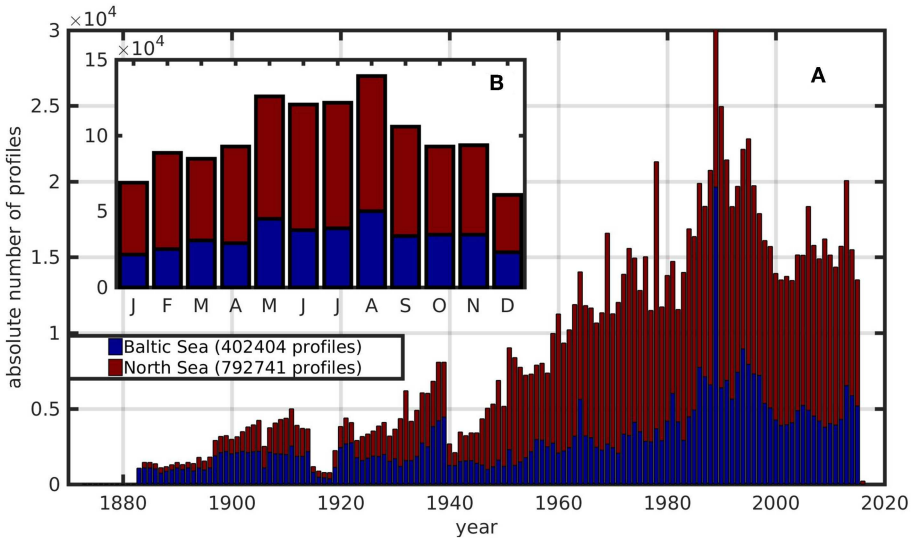

FIGURE 1 | Annual **(A)** and monthly **(B)** frequency of marine observational profiles for the BNSC area of the North and Baltic Sea (1873–2015).

data density is highest at the surface and that a low data density characterizes the deep areas of the BNSC region (i.e., especially the North Atlantic).

Quality Control

Erroneous observations have to be filtered out during the creation of the climatology. Here, we follow the data quality control strategy implemented for the automated quality control of the global hydrographic archive for the compilation of the WOCE-Argo global hydrographic climatology (Gouretski, 2018). The number of profiles in the BNSC region (after sorting out duplicates) accounts to more than 1 million and reveals that a check of all these observations with respect to their quality is only possible with an automatic procedure.

The quality control consists of eight different single checks described in the following.

1. Crude range check
   In general: Temperature and salinity in the North and Baltic Sea have a characteristic range. Temperature values below −2°C and above 25°C and salinity values above 38 PSU can certainly be regarded as erroneous for the regarded area. Those values are flagged by this check.
   Depth dependent: Additionally, this check is based on the frequency distributions of temperature and salinity as a function of depth, and based on this, defines characteristic value ranges for single depth levels. The purpose of this check is to reject crude outliers, which passed the overall range check for temperature and salinity.
2. Maximum observed depth
   Each instrument or station type has a characteristic maximum depth level to which observations are recorded. If this value is exceeded in a profile, all values are flagged. Information about the instrument or station type, if available, is stored in the meta data.
3. Constant value
   If a profile shows a certain number (N) of consecutive constant values in a defined depth interval, those values will be flagged. The number N depends on the instrument type.
4. Spikes
   Spikes are an unnatural change of the parameter value from one depth level to another and therefore have to be flagged. For this purpose, parameter-specific threshold values defining a spike are taken into account as well as the distance between the consecutive depth levels regarded for this check.
5. Vertical gradient
   Ranges for the vertical parameter gradient are defined. For this purpose, corresponding frequency distributions are created based on the observational data and ranges for the vertical gradient are defined at a set of levels. For neighboring depth levels with observed parameter values, a vertical gradient can be calculated. In case this lies outside the vertical gradient range for this depth level, both observations are flagged.
6. Number of extrema
   The procedure aims at checking the shape of the vertical profile. The number of local extrema (for T and S separately) is found for each observed profile. If the number of identified extrema is more than three, all observed values for this profile are flagged. The extrema are taken into account only if the difference between the parameter values at the neighbor minimum and maximum points exceed predefined tolerances. The tolerances for these differences do not depend on depth and are set to 0.5°C and 0.5 PSU for temperature and salinity.
7. Comparison with digital bathymetry
   For this check the digital bathymetry GEBCO2 (Weatherall et al., 2015) is used. If the digital bathymetry indicates solely "land" near the hydrographic station, it is assumed that the position of that hydrographic station is erroneous and all observed values of the profile are flagged. If the digital bathymetry indicates the presence of "sea" points in a certain

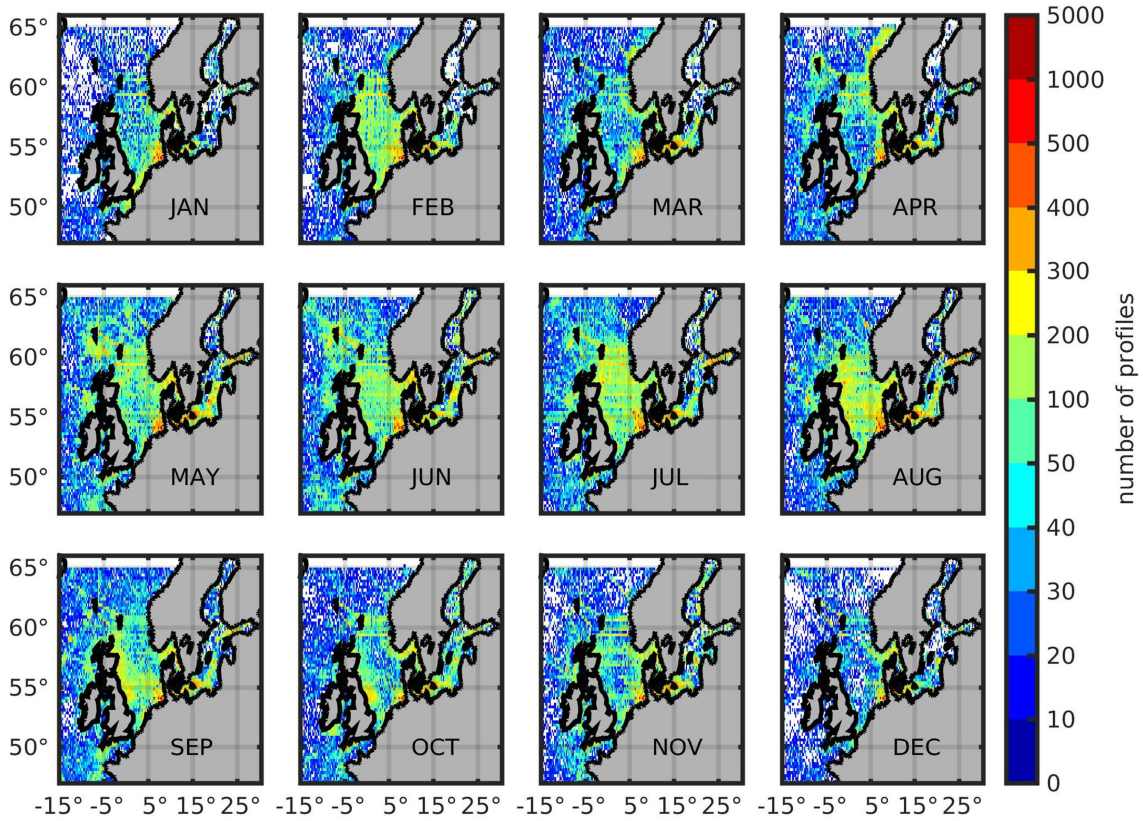

FIGURE 2 | Absolute monthly frequency of marine profiles, 1873–2015, box size 0.25° × 0.25°, $\sum = 1{,}194{,}475$ profiles.

vicinity of the profile position, the last depth level is compared to the maximum bottom depth among the "sea" points. In case the last observed depth level is deeper than the bottom depth (including a tolerance value), all observed values below the "digital bottom" are flagged.

8. Local climatology
   This check tests if the observed parameter values are in a local climatological range. The climatological median value is determined regionally based on the observations that are not flagged by any of the previous quality checks. The median value and the acceptable value range are derived from the frequency distribution of the parameter values. It has to be stressed that the skewness of the frequency distribution is taken into account when defining the parameter range, so that for example in regions of strong horizontal gradients (for example salinity in estuaries) not too many true high, respectively, low values are flagged, see Vandervieren and Hubert (2004). The local parameter range is defined as follows:

$$P_{\min} = Q1 - (Q3 - Q1) \cdot e^{-2 \cdot MC}$$
$$P_{\max} = Q3 + (Q3 - Q1) \cdot e^{-2 \cdot MC},$$

where $Q1$ and $Q3$ define the location of the first and third quartile, respectively, of the frequency distribution. Consequently, the difference $Q3 - Q1$ corresponds to the interquartile range. MC, the "medcouple"-value, is a measure for the skewness of the distribution. For more details on this, see Brys et al. (2003).

The quality control is performed separately, on the one hand, for the parameters salinity and temperature and on the other hand, since the North and Baltic Sea differ strongly in their hydrographic characteristics, for the two regions. The longitudinal segregation line is set at 55.8°N in the transition between Kattegat and Belt Sea and splits the entity of observational profiles into 792,741 for the North and 402,404 for the Baltic Sea.

Figure 3 shows the results of the quality control: the fraction of profiles flagged by the quality control is shown here in spatially horizontal resolution. The numerically summarized results of the quality control for the two regions and parameters are given in **Table 2**.

Interpolation on Standard Depth Levels and Horizontal Grid

The temperature and salinity observations, as provided by the different data sources, are on observed depth levels. To allow a further processing, a spatially vertical interpolation on common standard depth levels is necessary. The distribution of those depth levels is determined as follows: in the upper region of the North and Baltic Sea: to a depth of 50 m, the difference between the depth levels is chosen to be 5 m. Further down, the difference between the two consecutive levels increases steadily by 1 m.

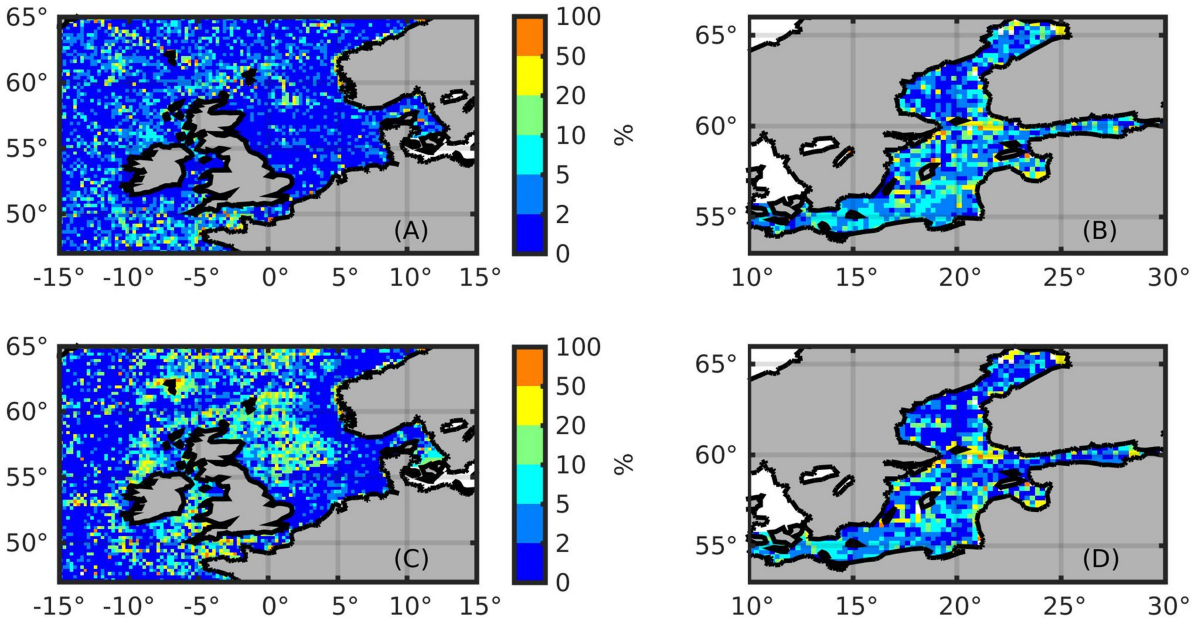

FIGURE 3 | Results of the quality control for water temperature [North Sea **(A)**, Baltic Sea **(B)**] and salinity [(North Sea) **(C)**, (Baltic Sea) **(D)**]: spatial distribution of percentage of flagged profiles, box size 0.25° × 0.25°.

TABLE 2 | Results of the quality control for the North and the Baltic Sea and the two parameters temperature and salinity: summary.

	North Sea	Baltic Sea
TEMPERATURE		
Number of profiles	792,741	402,404
Number of observed depth levels	37,929,677	6,872,538
% flagged depth levels	5.18	6.38
% profiles (min. one flagged depth level)	15.45	22.39
SALINITY		
Number of profiles	637,868	365,111
Number of observed depth levels	34,225,844	6,470,368
% flagged depth levels	6.86	6.45
% profiles (min. one flagged depth level)	21.20	27.20

Altogether, there are 105 different depth levels from 0 m to almost 5,000 m depth; the maximum distance (between the last and second last depth levels) accounts for 99 m.

The interpolation is performed following the procedure described by Reiniger and Ross (1968).

The applied horizontal grid has an edge length of 0.25° both in meridional and in zonal direction.

Correction of the Temporal Sampling Error

The observational data are available in temporal irregular distribution, see also inset in **Figure 1B**. Simple temporal averages of those observations are biased by periods with a high data density. Therefore, the irregular temporal distribution of the observations has to be taken into account and the observations must be adjusted accordingly before averaging. With respect to the annual mean, a single observation of parameter P, P_{obs}, can be described as the sum of three terms:

$$P_{obs} = P_{lt} + P_{interann} + P_{seas}$$

where P_{lt} denotes the long-term mean, $P_{interann}$ stands for the part corresponding to the interannual variability and finally, P_{seas} expresses the seasonally variable fraction. It is this last term in combination with the temporal irregular sampling of the observations that would lead to the above mentioned bias if a simple arithmetic mean was applied to the original observations in order to receive an annual mean. The solution for this problem is to eliminate the influence of the seasonal variability on the observations and subtract the last term P_{seas} from P_{obs}, This allows the calculation of unbiased annual averages independent on the temporal distribution and number of observations. The adjustment is performed on the basis of a depth dependent long-term mean annual cycle that is derived from the observational data for each grid box separately. The long-term mean annual cycle is expressed as a polynomial (11th order) that is fitted to the observations in a certain area including the respective grid box b. This daily resolved fit for temperature (T) and salinity (S) observations is given in the following two equations.

$$T^b_{fit}(d) = \sum_{i=1}^{12} p^T_i(b) d^{(12-i))},\ d = [1:365]$$

$$S^b_{fit}(d) = \sum_{i=1}^{12} p^S_i(b) d^{(12-i)},\ d = [1:365]$$

$p^T_i(b)$, $p^S_i(b)$: *polynomial coefficients for T and S for the corresponding fit in box b*

The annual cycle does not have to be considered on all depth levels, but only in the upper layers with a distinct seasonal signal. For the creation of the BNSC, an adjustment is performed down to a depth of 200 m. In preparation of creation of the time series of annual mean values (am), the procedure is applied as follows: daily anomalies of the long-term mean annual cycle with respect to the long-term annual mean are calculated based on the polynomial fit and are referred to as the adjustment terms; in the following shown exemplarily for temperature T:

$$adjT^b_{am}\left(d\right) = T^b_{fit}(d) - \frac{1}{365}\sum_{d=1}^{365} T^b_{fit}\left(d\right)$$

These adjustment terms form a set of 365 values. Each single observed value has a corresponding adjustment term, depending on the calendar day of the observation. The adjustment term is subtracted from the observed value.

In case of the monthly mean values, it is not the seasonal variability that could lead to a bias, but the intra monthly variability. Consequently, ly, the correction is applied to the observed values in preparation of creation of the time series of monthly mean values (mm) as follows: the long-term mean annual cycle is split into 12 sections, according to the months of a year. For each single section, a long-term monthly mean value is estimated and the corresponding daily anomalies are calculated, yielding for each month m an individual set of adjustment terms, exemplarily shown here for temperature T:

$$adjT^b_{mm}\left(d_m\right) = T^b_{fit}(d_m) - \frac{1}{31}\sum_{d_m=1}^{31} T^b_{fit}\left(d_m\right)$$

In contrast to the adjustment term for the creation of the annual mean, only the days corresponding to the respective month m are considered here, denoted by d_m. Then, the adjustment term corresponding to the calendar day of observation is subtracted from the observed value.

Creation of Mean Values

Temporal mean averages are composed calculating the arithmetic mean of the corrected observational data in each box. Monthly and annual mean values are calculated. It has to be stressed, that boxes lacking observations are left empty.

Horizontally Interpolated Fields

Based on the fields of box averages (monthly and annual mean values), horizontally interpolated fields are composed, aiming at closing the gaps between populated grid boxes. The applied procedure is the method of optimal interpolation (also known as optimal analysis). It was introduced by Gandin (1965) and since then has been widely used in different hydro-meteorological applications, for instance for the World Ocean Circulation Experiment Climatology (Gouretski and Koltermann, 2004). A vast literature exists about the usage of the optimal interpolation, but we leave this beyond the scope to this paper and only crudely outline the optimal interpolation method below.

In this method, for the arbitrary point (o) the interpolated parameter value F_o is represented as the sum of the parameter first guess value, G_o, and the weighted sum of the parameter deviations from the first guess at N observation locations (i):

$$F_o = G_o + \sum w_o \left\lfloor f\left(i\right) - G(i) \right\rfloor, \qquad i = 1, .., N$$

The optimal weights w_o are defined by the spatial correlation structure of the analyzed field. Generally, the optimal interpolation is preferred when the true correlation function can be accurately estimated; otherwise, other methods can provide comparable results. In many applications, the isotropic Gaussian (bell shaped) correlation function $C\left(r\right)$ is used with the e-folding correlation length scale:

$$C\left(r\right) = e^{\frac{-r^2}{R^2}},$$

where r denotes the horizontal spatial distance and R being the correlation length scale.

As noted by Sokolov and Rintoul (1999), the intrinsic correlation length scale for the optimal interpolation will be dictated more by the size of the data-void region than by the actual estimate.

The BNSC region is characterized by strong variations in data density with the central part (central North Sea and Skagerrak, Kattegat, Belt Sea) being much better sampled than the adjacent Atlantic regions and the Gulfs of the Baltic Sea. As a trade-off, we used the e-folding correlation scale of 166 km in all our calculations. The interpolated fields produced by the optimal interpolation procedure may be considered as the result of applying a filter to the data. The optimal interpolation produces a spatial average of the data where smoothing length scales are in dependent on the data configuration, with the small scale oscillations being filtered uniformly, resulting in interpolated fields with homogeneous statistics. In data-poor regions, the optimal interpolation relaxes to the first-guess field.

It needs to be taken into account that the interpolation errors are higher for the data poor time periods. Especially in the starting years of the BNSC time series, the spatial coverage is very low, however. The same refers to greater depths. In the following, the number of populated boxes on each depth level is analyzed and set into relation to the maximum number of possibly populated ("wet") boxes. The maximum coverage accounts to a little more than 14%; large areas in time and depth, however, show values of 5% and less. Based on this analysis and taking into account the frequency of observations as a function of time (see **Figure 1**), it was chosen to perform interpolation on all depth levels in monthly resolution for the period 1950–2015. Additionally, the spatial coverage can be improved when box-averaged fields for wider time-windows (e.g., several years) are used. For a time window of 10 years from 1955 on, the maximum value of horizontal coverage improves to more than 50% and large areas show more than 20% horizontal coverage. Still, the coverage in the deeper layers remains rather poor. A monthly resolution is applied to the standard depth levels of up to 101 m. For greater depths, the annual mean is applied.

To summarize:

- Before 1950, the spatial coverage is not sufficient to produce reasonable interpolated fields.
- The merging of box averages in a time window of 10 years yields a satisfying spatial coverage. For this reason, the interpolated fields are created based on decadal mean monthly and annual mean values of the box averages. The following decades are chosen for this:
- 1956–1965,
- 1966–1975,
- 1976–1985,
- 1986–1995,
- 1996–2005,
- 2006–2015.

The seasonal signal only reaches to a certain depth. For the BNSC, the standard depth level of 101 m marks the depth to which decadal monthly box averages are taken as a basis; for greater depths, the decadal annual mean is applied.

Sensitivity Analysis

The BNSC box averages, i.e., the core of the data product, is sensitive to the available observations. A lack of some observations might alter the data product as well as additional observations becoming available in future. To estimate the influence of the observational basis on the data product, a sensitivity analysis is performed.

The sensitivity analysis is applied to all parameters for the time periods 1950–2015 and 1960–2015 for the atmospheric and the hydrographic part, respectively.

The analysis works with fields of anomalies as deviations from fields of long-term mean values. Based on the box averages of the atmospheric and the hydrographic data product, long-term climatological monthly mean values are calculated by temporally averaging over the available box values in the complete respective period. As a reference for the sensitivity analysis, the anomaly fields are then calculated as the difference between the long-term mean fields and fields of box averages of the BNSC product. Additionally, anomaly fields are calculated that are not based on the entity but on only 90% of the BNSC observations. The reduction of observations is applied randomly and repeated 100 times. In the following, each 10%-reduction and the subsequent box averaging is referred to as a "run."

Furthermore, the BNSC region is divided into eight sub-regions:

- the Atlantic part of the BNSC is divided into a
- northern (north of 60°N),
- a southern (south of 53°N) and
- a middle part;
- the central North Sea,
- the Skagerrak/Kattegat area (east of 8°E and north of 56°N),
- the Belt Sea
- the central Baltic Sea (east of 13°E and south of 59°N, including the Gulf of Riga),
- and finally the two greater gulfs of the Baltic Sea (north of 59°N).

It has to be mentioned that the Skagerrak/Kattegat and the Belt Sea area are regarded separately only for the hydrographic parameters; for the atmospheric variables, those two regions are treated as one.

For each of the above mentioned runs, the anomaly fields are averaged horizontally in each of these eight (seven) sub-regions. The same is applied to the anomaly fields of the reference. This yields time series for each run, which form a kind of "hose" around the time series of the reference, with an upper and a lower envelope.

The distance of the envelopes from the reference, however, critically depends on the number of runs that are performed. To illustrate that the chosen number of 100 runs is sufficient, the envelope-reference distances are investigated with respect to their dependency on the number of runs. The envelope as a function of the number of runs (not shown) reveals that both the distance to the lower and the upper envelope increases considerably from one to about 10 runs but experiences a rather low augmentation after the number of runs exceeds 60. With even more runs, the distances converge to a maximum. The respective negative maximum for the lower envelope and the positive maximum for the upper envelope define the measure for the minimum number of required runs: it is the number of runs corresponding to a value of 95% of the maximum of the respective envelope. For all the three atmospheric parameters in all seven regions it shows, that the minimum number of required runs lies between 70 and 80.

For the hydrographic parameters, envelopes exist around the time series of reference anomalies on each depth level and also here a clear convergence of the envelope distances can be seen for all regions, both parameters and the two different temporal resolutions. This confirms that the number of 100 runs is sufficient.

Comparison With Other Data Products

The BNSCatm is compared to different data products. These include the KNSC, three different reanalyses and station data. In addition, the BNSCatm was compared with available temperature data from Schmager et al. (2008), and with 30-year means 1981–2010 from ICOADS.

KNSCatm, Re-analyses and Station Data

The BNSC is compared to the previous project, the KNSC (Sadikni et al., 2018) to identify changes in the new version. The KNSC has the same spatial and temporal resolutions as BNSC, and covers the period from 1950 to 2010.

The sea level pressure is compared to three different reanalysis products. The first two re-analyses are ERA40 and ERA-Interim, both from ECMWF, and are analyzed for the overlapping time period 1979–2001. ERA-40 (Uppala et al., 2005) has a 125 km spatial resolution and the original data was uploaded in 6 h values. ERA-Interim (Berrisford et al., 2011; Dee et al., 2011) is the following project, which analyzes data from 1979 on with constant updates to the present. It has a spatial resolution of 79 km and a temporal resolution of 6 h. The climatologies of the variables temperature and sea level pressure of BNSCatm are also compared to ERA-Interim over the time period from 1981

to 2010. Additionally, the BNSC is compared to the COSMO-REA6 reanalysis (Bollmeyer et al., 2015) from the DWD and the University of Bonn. COSMO-REA6 was calculated for the time period 1995 to 2015 and has a spatial resolution of 6 km and an hourly temporal resolution. For the comparison, only monthly means are used. Before comparing the field, it is always interpolated onto the coarser grid.

The compared station data are time series of sea level pressure of 10 different stations along the German coast. The data was provided by the DWD (www.dwd.de/cdc). For comparison, the nearest grid cell of the ERA-40 reanalysis, respectively, the BNSCatm, is used.

In most comparisons, the monthly means are calculated and then a difference time series is created. Afterwards, these difference time series are averaged over the whole time period, single month or seasons. For the comparison of climatologies 1981–2010, a climatology for the same period is calculated from ERA Interim and this is monthly subtracted from the BNSCatm climatology.

14 Areas From Climatology of the Baltic Sea and ICOADS

The BNSCatm was compared to available air and dew point temperature data in the Climatology of the Baltic Sea based on the ICOADS-Data Set (1951–2000) by Schmager et al. (2008). They provide monthly means of air and dew point temperature for 14 areas in the Baltic Sea. For the same areas and period, means were calculated for each month from the monthly means of air and dew point temperature of the BNSCatm.

The hydrographic subset of the BNSC is compared to three data products:

- the precursor of the BNSC, the KNSCv2 data set for the North Sea region (Bersch et al., 2016)
- the BALTIC ATLAS (Feistel et al., 2008) for the Baltic Sea region.

(the latter two are based on *in situ* observations).

- the BALTIC SEA PHYSICAL REANALYSIS PRODUCT (Axell and Liu, 2016).

All three data products together with the applied comparison methods are described in the following.

KNSCv2

The precursor of the data product presented here, the KLIWAS North Sea climatology (KNSCv2, Bersch et al., 2016) is used for comparison with time series of box-averages of the BNSC data product. The KNSCv2 product comes on altogether 179 depth levels on a horizontal grid with a box length of 0.5° (zonal) and 0.25° (meridional). It covers the period 1873–2013. For the comparison, the BNSC box averages in both annual and monthly resolution are used. Concerning the spatial resolution, BNSC is adapted to KNSCv2 by horizontally averaging the two BNSC boxes corresponding to one KNSCv2 box. BNSC values are linearly interpolated on KNSCv2 depth levels. In case of spatial and temporal correspondence, absolute differences are computed.

BALTIC ATLAS

The time series of monthly mean values for the Baltic Sea (BALTIC: Monthly Time Series 1900–2005, Feistel et al., 2008) is used for the comparison with the monthly BNSC box averages of temperature and salinity. The BALTIC grid has an edge length of 1° and regularly spaced (10 m) depth levels. For the comparison, the BNSC product is horizontally averaged over the 16 boxes that correspond to one BALTIC box. Additionally, the BNSC values are linearly interpolated on the BALTIC depth levels. Absolute differences are then computed for every spatial and temporal correspondence between BALTIC and BNSC in the period 1900–2005.

Baltic Sea Physical Reanalysis Product

The BALTIC SEA PHYSICAL REANALYSIS PRODUCT, hereafter referred to as BSRA, provides, among others, temperature and salinity fields in monthly resolution. The horizontal grid has an edge length of 5 km. BSRA has 50 irregularly spaced depth levels with a distance of 4 m in the upper and a maximum distances of 40 m in the lower part of the water column. The period covered by the BSRA product is 1989–2015.

For the comparison, the BSRA boxes corresponding to one BNSC box are spatially averaged and subsequently linearly interpolated to the BNSC depth levels. Absolute differences between the two data products are then computed.

The **BNSCatm** data products are available from https://icdc.cen.uni-hamburg.de/1/daten/atmosphere/bnsc-met/

and should be cited as

Jahnke-Bornemann, Annika; Sadikni, Remon (2018). Baltic and North Sea Climatology meteorological part (Version 2.0). World Data Center for Climate (WDCC) at DKRZ. https://doi.org/10.1594/WDCC/BNSClim_meteo_v2

The **BNSChydr** data products are available from

https://icdc.cen.uni-hamburg.de/1/daten/ocean/bnsc/

and should be cited as

Hinrichs, Iris; Gouretski, Viktor (2018). Baltic and North Sea Climatology hydrographic part (Version 1.0). World Data Center for Climate (WDCC) at DKRZ. https://doi.org/10.1594/WDCC/BNSClim_hydro_v1.0

Free download as well as visual exploration of the data product is possible here.

After first submission of this manuscript, an update of the BNSChydr product has taken place. The authors recommend to use the update, which can be found under the same above given link. Until no new DOI has been assigned, the above given citation remains. All analysis presented in this paper are based on BNSChydr v1.0.

The spatial dimensions of the BNSC data products are described in **Table 4**.

The BNSC data product itself is complemented by information about the distribution of sea and land in the BNSC region in order to be able to distinguish between the two spheres.

For BNSChydr and BNSCatm, there are two NetCDF-files available with the same dimensions as described in **Table 4**. They consist of a binary field, which determines whether a grid box corresponds to water (value = 1) or land (value = 0). The distinction between water and land was made based on the highly spatially resolved GEBCO bathymetry (Weatherall et al., 2015) by estimating the fraction of GEBCO water boxes in one BNSC box. The threshold value for distinction wass set to 0.9 for BNSChydr and to 0.6 for BNSCatm for this purpose. This means that more than 10% (40%) for BNSChydr (BNSCatm) water fraction determine the BNSC box to be water. In addition, the land sea fraction for each grid box is also provided.

Table 5 lists the file names of the BNSC data product and gives an overview about the nomenclature of the file names in the individual data products.

Finally, **Table 6** gives an overview and short explanation of the different variables stored in the .nc-files.

RESULTS

As all results for the BNSC can be found under https://icdc.cen.uni-hamburg.de/projekte/bnsc-project/, we only show some chosen examples of the results.

BNSCatm

General Results

The longtime climatology 1950–2015, from which the months January and July are shown in **Figure 4** for the three atmospheric parameters, exhibits an acceptable spatial coverage for all months, with poor data coverage just in the north of the North Sea, and the Gulf of Bothnia, as well as west of Ireland.

General climatological characteristics are well represented by the BNSC. The values in the air temperature and dew point temperature climatology range from −2 to19°C and −5 to 20°C, respectively. The results for January and July are shown in **Figures 4A,B** for mean air temperature and (D) and (E) for mean dew point temperature. As expected, the temperatures are higher in summer than in winter and have a tendency to decrease from south to north. The mean intra monthly standard deviations are smaller in summer than in winter and the values are in the range of 1 to 4 K for both parameters. Mean values of the intra monthly standard deviations over all months are shown for air temperature in **Figure 4C** and dew point in **Figure 4F**.

The values of the air pressure climatology range between 1000 and 1019 hPa and are higher in summer than in winter with a tendency to decrease from southeast to northwest. The results for mean air pressure in January and July are shown in **Figures 4G,H**. The standard deviation has higher values in winter than in summer and ranges between 6 and 16 hPa in the monthly data. It is smallest in the south of Great Britain and largest in the north west over the open water of the Atlantic Ocean. A mean of the standard deviations of the climatology product over all months is shown in **Figure 4I**.

The four 30-years climatologies (not shown) exhibit a temporal evolution of data distribution, where the largest data gaps exist in the 1951–1980 climatology for all parameters, and best spatial coverage has the climatology for the period 1961–1990. It can be suggested that the poorer data coverage in the early period is due to the setup of a monitoring network after the Second World War, whereas the gaps in later periods are due to changes in the measurement technologies, like replacements of old drifting buoys, less manual observations from ships, but an increasing number of automated observations. The dew point temperature has fewer observations than the other two parameters and therefore larger data gaps. The climatologies for all parameters show the expected behavior over the year.

Sensitivity Study

The sensitivity study yields regional fluctuation ranges caused by the random reduction of the basis of observations by 10%. As a result, the fluctuation ranges are listed in **Table 3** (first three rows for BNSCatm) for the regions defined in section Sensitivity analysis. The values shown here are based on monthly mean fields and are the temporal mean differences between the spatial mean of the reference run (full data collection) and the upper and the lower envelope. For all three atmospheric BNSC parameters, the central North Sea exhibits the lowest and the region of the Gulfs of Finland and Bothnia the highest fluctuation ranges (marked with bold font weight in the table). This is most probably a direct consequence of the sampling density, which is very high in the central North Sea and rather low in the two greater gulfs of the Baltic Sea, also due to seasonal ice coverage.

In most of the seven regions of the sensitivity study, the fluctuation ranges of all parameters exhibit a temporal evolution (not shown). Except for the region of the two gulfs and the central Baltic Sea, the fluctuation ranges are significantly higher in the period 1950–1960 than from 1960 onward for the BNSCatm data product: The fluctuation ranges of the earlier period are about two to seven times the ranges of the later period. This is probably also caused by the poor data base in the earlier periods.

The climatological mean fields of BNSCatm are also subjected to this analysis, but the results are not listed in **Table 3**. For the 30-year climatological monthly mean fields the fluctuation ranges are in general of similar magnitude as the values for the time series of the monthly mean field. Similar to the findings for the time series of the monthly mean fields, a difference in the fluctuation ranges can be seen between the first 30-year-window (1951–1980) and the other three time periods. Lessons to be learned from the sensitivity analysis are that the data set of BNSCatm is more stable in the period from 1960 onward and in the later 30-year climatologies than before 1960 and in the first climatology from 1951 to 1980.

Comparison With KNSC

For the purpose of comparison, monthly averages of the KNSC period from 1950 to 2010 are subtracted from those of the BNSC, resulting in a difference time series.

For the mean air pressure, the largest differences between BNSC and KNSC seem to occur in areas and at times that have fewer observations than the surroundings. The differences in the

TABLE 3 | Results of the sensitivity study: temporal mean differences between the spatial mean of the reference run (full data collection) and the upper (positive) and lower (negative) envelope formed by the spatial mean of the 100 runs with 90% randomly chosen observations.

		Central Baltic Sea			**Central North Sea**			**Skagerrak/Kattegat**			**Belt Sea**			**Gulfs**		
AT [K]	Monthly	+0.10/–0.11			**±0.04**			±0.11						**+0.27/−0.26**		
DP [K]	Monthly	+0.26/–0.25			**±0.09**			+0.20/–0.19						**+0.56/−0.52**		
SLP [hPa]	Monthly	+0.35/–0.33			**±0.16**			+0.34/–0.38						**±1.20**		
depth levels [m]		0	50	80	0	50	80	0	50	80	0	15	30	0	20	50
T [°C]	Annual	+0.07/–0.05	+0.06/–0.07	+0.04/–0.05	**±0.02**	**+0.02/−0.03**	**+0.02/−0.03**	+0.08/–0.07	+0.09/–0.11	+0.09/–0.10	**+0.11/−0.10**	**+0.13/−0.12**	**+0.30/−0.29**	+0.12/–0.09	+0.13/–0.11	+0.08/–0.09
	Monthly	±0.09	±0.13	±0.12	**±0.05**	**±0.06**	**±0.07**	±0.1	±0.16	+0.15/–0.16	**±0.15**	**±0.22**	**+0.24/−0.23**	±0.13	+0.19/–0.18	+0.17/–0.16
S [PSU]	Annual	+0.04/–0.03	+0.04/–0.05	+0.05/–0.04	**±0.02**	**±0.01**	**±0.01**	+0.16/–0.17	+0.04/–0.03	+0.04/–0.03	**+0.22/−0.23**	**+0.30/−0.33**	**+0.61/−0.58**	±0.02	±0.02	±0.02
	Monthly	±0.04	±0.11	±0.13	±0.08	±0.03	±0.03	±0.33	+0.08/–0.07	±0.05	**+0.41/−0.42**	**+0.61/−0.60**	**+0.60/−0.58**	±0.05	±0.05	±0.05

		Atlantic								
		North			**Middle**			**South**		
AT [K]	Monthly	+0.08/–0.07			±0.08			±0.05		
DP [K]	Monthly	+0.21/–0.20			+0.16/–0.14			+0.12/–0.11		
SLP [hPa]	Monthly	±0.39			+0.48/–0.50			±0.20		
depth levels [m]		0	90	563	0	90	563	0	90	563
T [°C]	Annual	+0.03/–0.02	±0.03	+0.12/–0.13	±0.03	±0.03	±0.08	±0.04	±0.04	+0.05/–0.04
	Monthly	±0.06	±0.05	+0.15/–0.16	**±0.06**	**±0.06**	**±0.06**	+0.09/–0.10	±0.08	±0.04
S [PSU]	Annual	**±0.02**	**±0.01**	**±0.01**	±0.03	±0.01	+0.02/–0.01	+0.03/–0.02	+0.02/–0.01	±0.00
	Monthly	+0.05/–0.05	±0.01	±0.01	±0.08	±0.02	±0.01	**±0.04**	**±0.01**	**±0.00**

Highest and lowest values are marked in bold font weight.

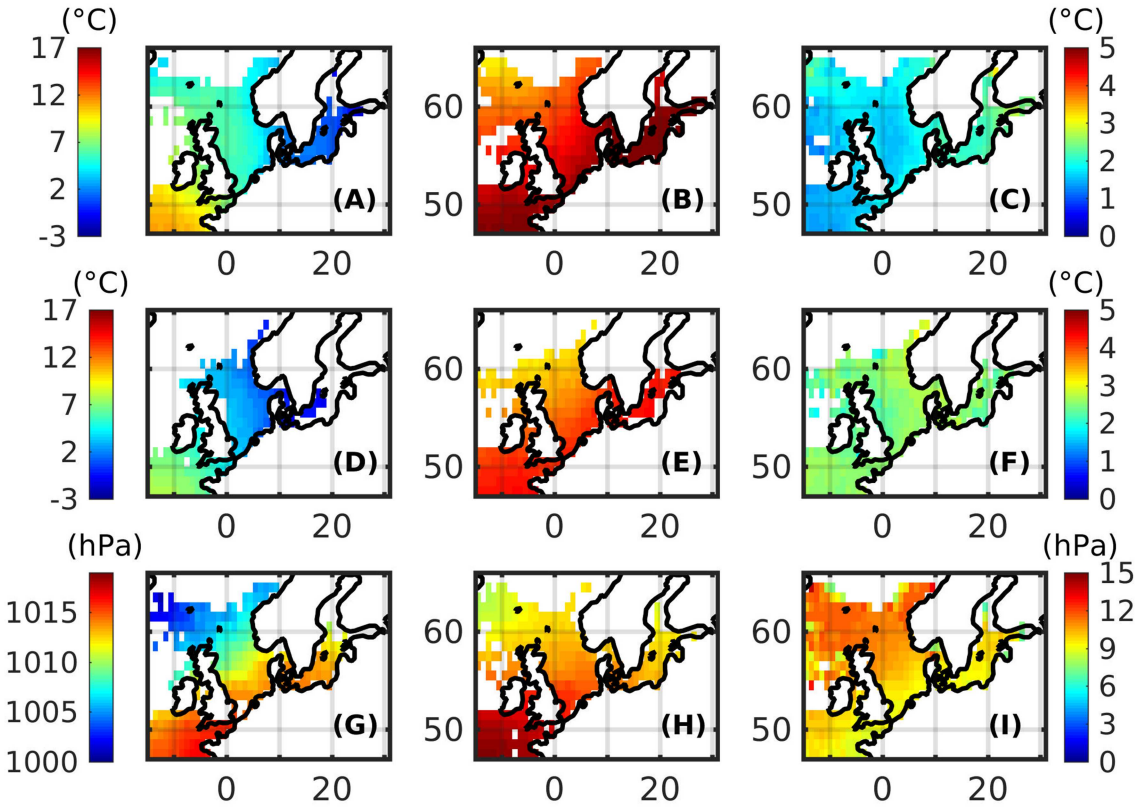

FIGURE 4 | BNSCatm Climatology for 1950 to 2015: means of the parameters 2 meter air temperature **(A,B)**, 2 m dew point temperature **(D,E)**, and sea level pressure **(G,H)** for the months January **(A,D,G)** and July **(B,E,H)** and the mean standard deviation of each parameter over the whole period **(C,F,I)**. Boxes with insufficient data coverage are white.

extended winter months from December to March are in the interval −1.5 to 2 hPa. In the summer months, the deviations are slightly smaller in the interval −0.5 to 0.7 hPa. Due to the changes in the procedure, that were described in Data processing, the differences between BNSC and KNSC are quite large and the BNSC standard deviation is larger in most grid boxes. These differences are smaller in the summer than in the winter months and in the range −1 hPa to 15 hPa.

The differences in air temperature climatology are very small and caused by the changes to the input data. The changes are of the order of a tenth of a degree for means as well as for standard deviations. Changes in the input data caused changes smaller than 1 K in the dew point temperature climatology as well, that are spatially and temporally statistically distributed.

Comparison With Reanalyses

The time series of the monthly mean values of the BNSCatm parameters 2 m air temperature and air pressure are compared with the corresponding parameters from the ERA-Interim reanalysis (Dee et al., 2011). For this purpose, in the first step, the ERA Interim data was transformed to the BNSC grid. Then climatologies for the period 1981–2010 of air pressure and air temperature are calculated from ERA-Interim data and compared with the corresponding climatology of the BNSCatm.

Figure 5 shows the results for the mean air pressure difference between BNSCatm and ERA-Interim climatologies for January (A) and July (B). The mean monthly differences are in the interval −2.2 hPa (November) to +2.7 hPa (February). In winter they are positive in most parts of the open sea, but negative close to most coastlines except for the Danish coast, the Skagerrak and Kattegat. This means that, especially during winter, the ERA-Interim reanalysis has higher pressure values near most of the coasts than the BNSCatm. A possible reason is that the BNSCatm only contains averaged data from observations above sea, whereas the reanalysis has grid boxes, where results above sea were mixed with land data that had higher pressure values. On the other hand, ERA-Interim has slightly lower pressure values over open water than BNSCatm and there are particularly large deviations in the north, where the number of observation data is lower. So it can be assumed that this is caused by sampling errors of the BNSCatm, especially as the largest differences tend to occur at the edges of the data field.

A similar comparison on a monthly basis for sea level pressure was done for ERA-40 (Uppala et al., 2005) and ERA-Interim for the time period from 1979 to 2001, as well as with COSMO-REA6 (Bollmeyer et al., 2015) for the time period from 1995 to 2015 (not shown). The comparison between sea-level pressure in BNSCatm, ERA-Interim and ERA-40 climatology showed mean

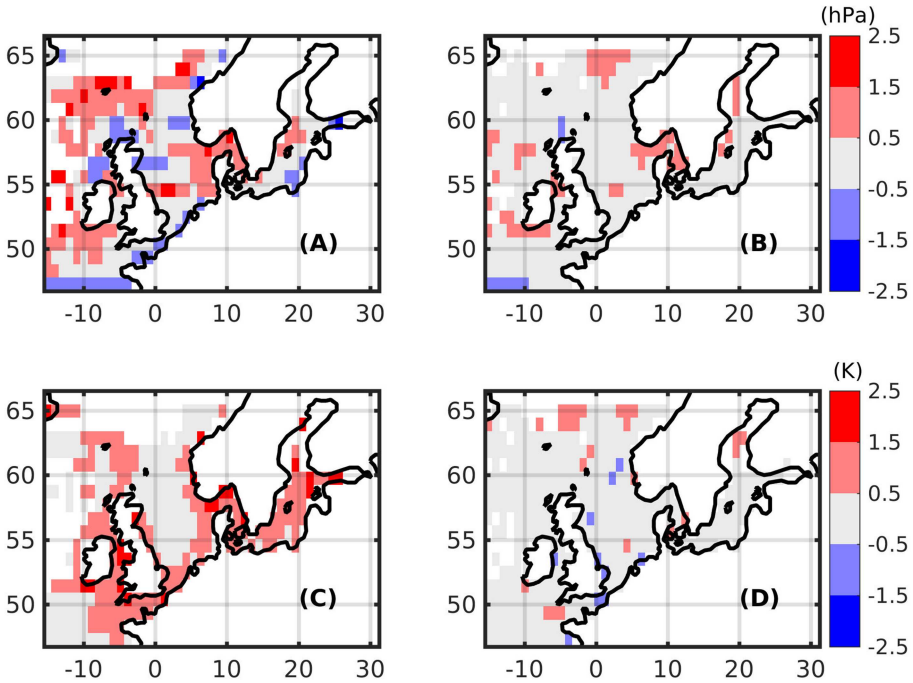

FIGURE 5 | Difference between BNSC and ERA Interim Climatology 1981–2010 for mean sea level pressure **(A,B)** and air temperature **(C,D)** for the months January **(A,C)** and July **(B,D)**.

monthly differences in the interval of −1.5 hPa and 1.5 hPa. The comparison with COSMOS-REA6 showed mean monthly differences in the interval of −1 hPa to 1 hPa overall mean difference. All reanalyses show similar patterns as described above, with negative values at the coast and slightly positive values at open water. The differences in winter are higher compared to differences in summer.

One possible explanation for the average lower pressures of the re-analyses over open water is the "fair weather bias," which means that ships avoid the bad weather conditions associated with low pressures, and therefore there are fewer measurements in these situations. These low pressure values are therefore missing in the mean values of the BNSCatm, but are included in the re-analyses. On the coasts, on the other hand, the re-analyses seems to have on average too high pressure values, which is probably again due to mixed land/sea grid boxes in the re-analyses.

The mean 2 m air temperature difference between the climatologies of BNSCatm and ERA Interim is shown in **Figure 5** for January (C) and July (D). The differences are between −2.1 K (May) and 8 K (December), but this occurs only at a single box at the Norwegian coast, most differences are below 2 K. The average air temperatures of the BNSCatm are higher during winter on the coasts and especially over the Baltic Sea than in the ERA-Interim data set. This is a well-known effect (Schade et al., 2013), as in ERA-Interim, during winter the cooler temperatures of the land points are mixed with the warmer ocean. During summer, this effect occurs in the opposite direction, but in this case the temperature differences between warm land and cold sea are smaller than in winter, since land is a worse heat storage. Again, the differences north of the UK are most likely related to a sampling error caused by the lower number of observations in this region, and most extreme values occur at the edges of the data field as well.

Comparison With Station Data

Data from coastal measurements are not included in the calculation of the BNSCatm, Therefore, these data can be used to investigate the differences between BNSCatm and reanalysis data at the coasts. The monthly mean of the measurements at a station and in the nearest grid cell in the BNSCatm and ERA-40 is compared for the overlapping time periods. **Figure 6** shows the station names (A) and the mean difference of monthly means of BNSCatm and ERA-40 to the measurements (B). In most cases, the mean values of both BNSCatm and ERA-40 are lower than the values of the measurements. At the North Sea coast, the differences between BNSCatm and measurements are smaller than those between the reanalysis and the measurements. At the Baltic Sea coast, the reanalysis is closer to the observations than the BNSC. Nevertheless, these differences of both products lie within the range of uncertainty, as they are also due to the fact that we compared means over an area to a point measurement and that the areas of the corresponding grid cells were completely over sea and not over the coast.

Comparison With Area Means and ICOADS

The 14 results for the different areas showed in general excellent conformity with each other, only small differences

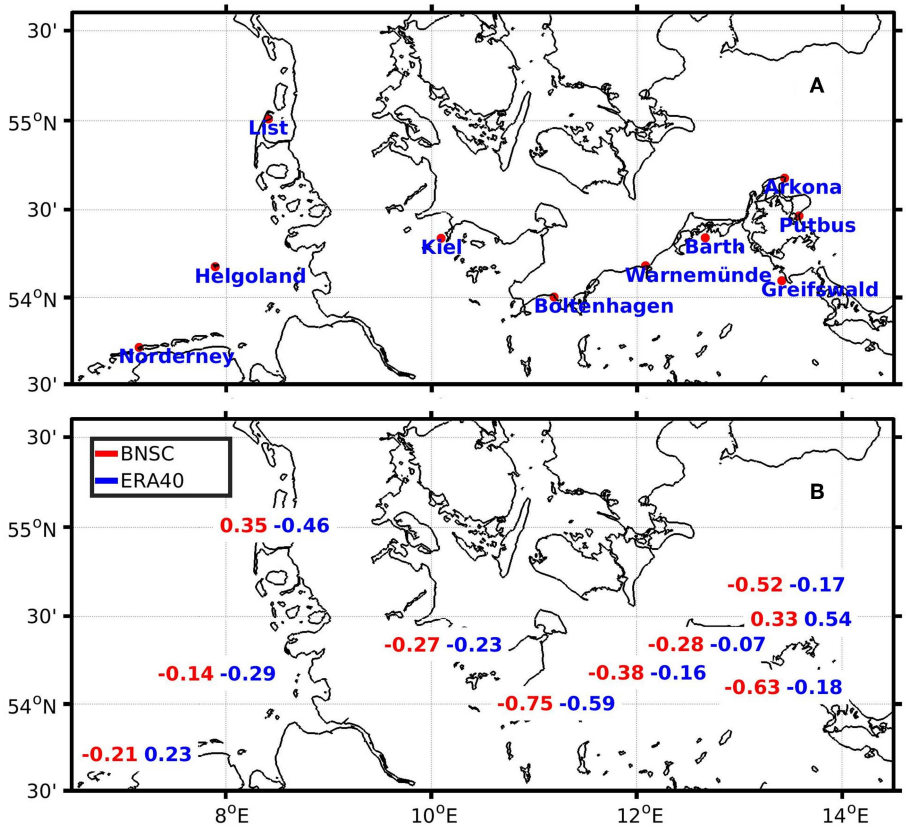

FIGURE 6 | (A) Station names, **(B)** Mean Difference of monthly mean sea level pressure [hPa] in measurements to closest grid cell in BNSCatm (red) and ERA-40 (blue).

of up to 2°C in winter for some areas in the North. One explanation is, as we know, that these are the months and areas with lowest data density. A direct comparison of the BNSCatm 30-year climatology 1981–2010 with the ICOADS 30-year mean 1981–2010 (available online at https://icoads.noaa.gov/data.icoads.html) confirms this assumption. In principle, the data sets show similar patterns and values for all atmospheric parameters and months. However, the ICOADS data set has a much coarser resolution on a 2 × 2 degree grid. The ICOADS product is a simple monthly mean of all available data, that includes everything without checking the quality and number of data per grid point. In the averaged 30-year data product, ICOADS exhibits obvious artifacts in areas of low data density that are not in the BNSCatm. Sadikni et al. (2018) found similar results when KNSC was compared to ICOADS. This shows the importance of careful quality checks and averaging methods that take several aspects like diurnal cycles and data density into account.

BNSChydr

The data products for the hydrographic part of the BNSC are available as time series of monthly and annual mean values on standard depth levels for the parameters temperature and salinity. There are three different kinds of data products

1. Time series of box averages (temporal mean values over all observations in a 0.25° × 0.25° grid boxes in 1 year, respectively 1 month)
2. Decadal box averages (based on 1)
3. Interpolated fields (based on 2).

In the following, those three data products are described in more detail.

Time Series of Box Averages

As described in section Creation of mean values, box averages of temperature and salinity are calculated for the BNSC region. This yields a time series of annual and monthly mean values for the period 1873–2015. Grid boxes that either do not contain any observation or solely observations that do not pass the quality control, are left empty. As an example, **Figure 7** shows the annual mean values at the surface for the year 2000. Additionally, the corresponding standard deviations and the number of observations contributing to the mean value are shown for temperature and salinity.

Concerning the distribution of populated boxes as a function of depth and time (not shown) it can be stated that deeper water layers (below approximately 1,000 m) show only very few populated boxes until the beginning of the 1950s, in salinity as

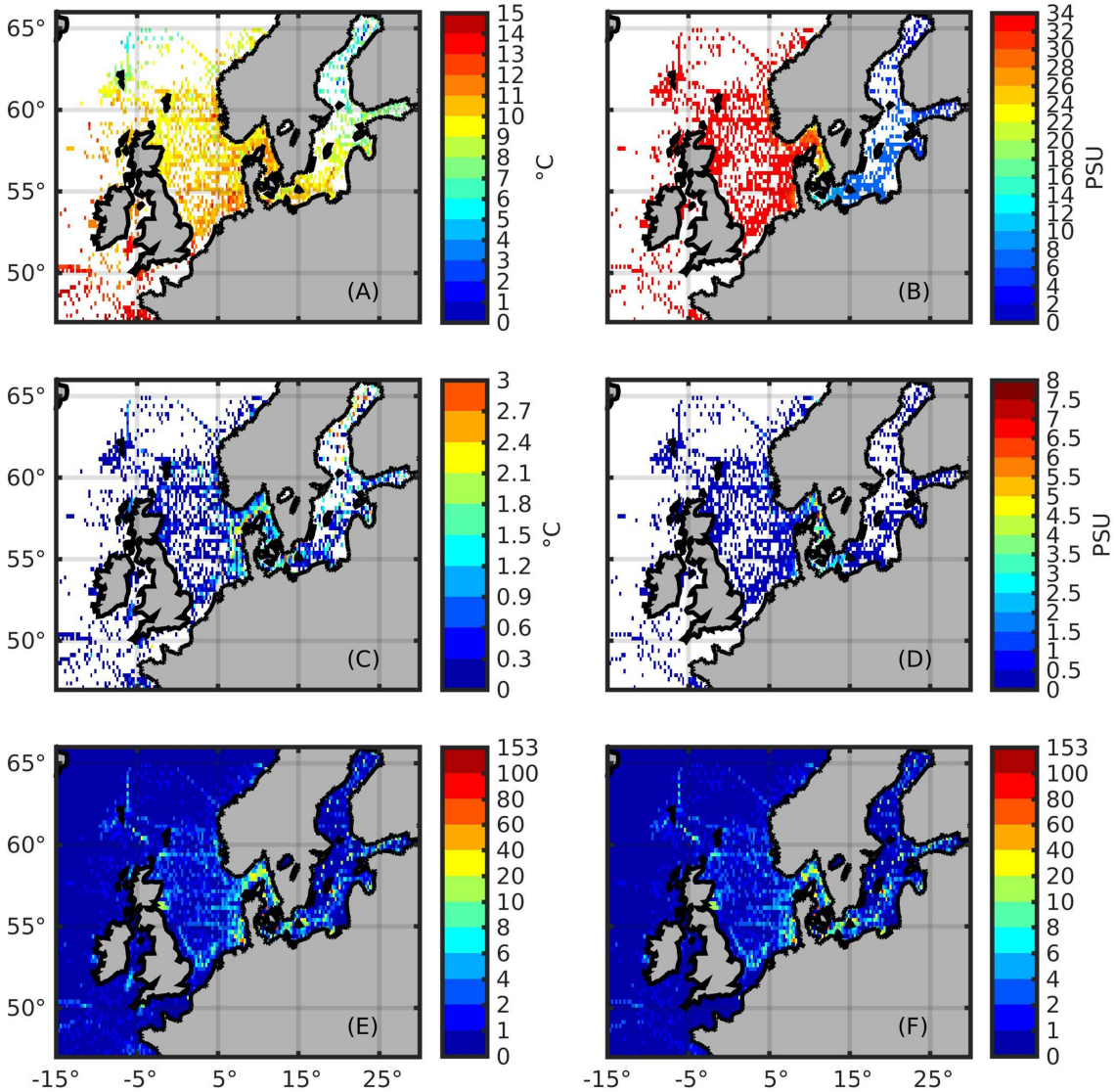

FIGURE 7 | Sea surface: annual mean values of both BNSChydr parameters [temperature: **(A)** and salinity: **(B)**] for the year 2000, together with the respective standard deviation **(C,D)** and the number of observations **(E,F)**.

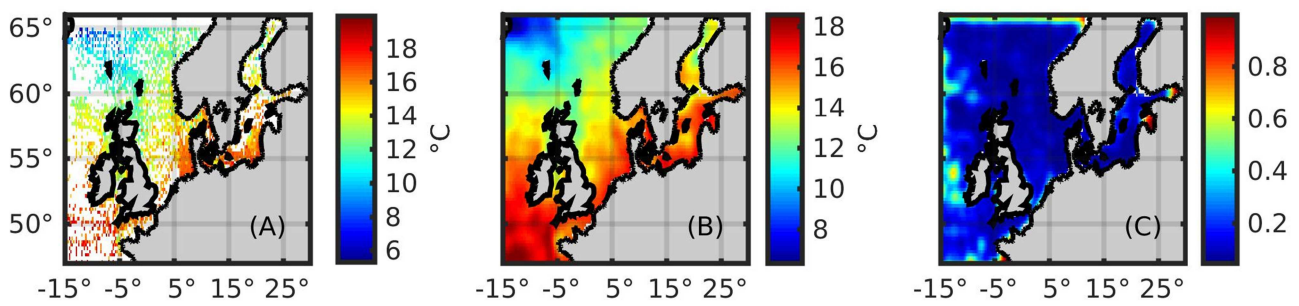

FIGURE 8 | TEMPERATURE, August 1976–1985, depth = 10 m, decadal monthly mean values as box averages **(A)**, interpolated field **(B)** (both in °C) and the corresponding relative interpolation error (**C**, dimensionless).

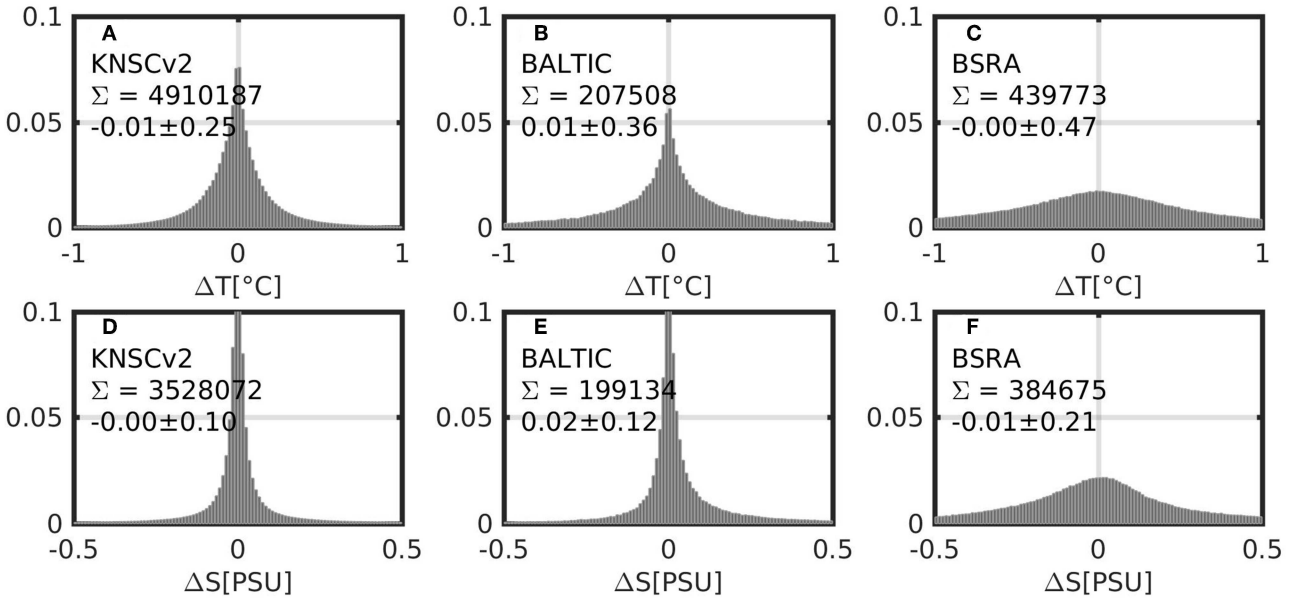

FIGURE 9 | Relative frequency distributions of absolute differences between the BNSC data product and KNSCv2 [temperature: **(A)** and salinity: **(D)**], the Baltic ATLAS [temperature: **(B)** and salinity: **(E)**] and BSRA [temperature: **(C)** and salinity: **(F)**]. Additional information are the number of collocated boxes (i.e., 4910187 in the case of KNSCv2) and the mean and standard deviation of the absolute differences.

TABLE 4 | Dimensions of the BNSChydr and BNSCatm data products.

Variable	Explanation
BNSChydr	
lat	Vector of latitude values defining the box center (47.125°N–65.875°N, edge length 0.25°, length of vector: 76)
lon	Vector of longitude values defining the box center (14.875°W–29.875°E, edge length 0.25°, length of vector: 180)
depth	Standard depth levels (0–4985 m, 5 m-distance up to 50 m depth, after that, continuous increase of distance by 1 m, 105 depth levels in total)
BNSCatm	
lat	Vector of latitude values defining the box center (47.5°N–65.5°N, edge length 1°, length of vector: 19)
lon	Vector of longitude values defining the box center (14.5°W–30.5°E, edge length 1°, length of vector: 46)

well as in temperature. After that, the data density increases (see also **Figure 1**) and also the deeper layers are populated.

Decadal Box Averages

For the decades determined in section Creation of mean values, a temporal mean over the box averages is created together with the corresponding standard deviation. Every populated box is considered for this. An example, the decadal temperature mean of August, is shown in **Figure 8A** at 10 m depth for the decade 1976–1985.

To be able to estimate the representativeness of the temporal mean for the respective decade, further statistics are made available together with the decadal monthly mean and the corresponding standard deviation. This is, on the one hand, the number of years that went into the decadal monthly mean with the maximum number consequently accounting to 10. On the other hand, information about the coverage of the time window of the decade is provided. For this purpose, an average and corresponding standard deviation are calculated of the years that contribute to the decadal mean. This defines the temporal center and spread of the decadal box average. A decadal monthly mean, for which all of the 10 years contribute, yields a mean value of, for example, 1990.5 (for the decade 1986–1995) and a standard deviation of 3.0.

Interpolated Fields

Based on the decadal box averages, as described in section Horizontally interpolated fields, the interpolated fields of the decadal monthly means are created. An example is displayed in **Figure 8B**. Besides other statistical parameters that are not explicitly shown here, a relative interpolation error is made available and is shown for the example in **Figure 8C**. For the definition of the interpolation error, see Gouretski and Koltermann (2004). The relative interpolation error differs between 0 and 1 and should always be considered together with the interpolated field. It can be used to mask field values. One example would be to use only interpolated values that correspond to a relative interpolation error of < 0.5.

Sensitivity Study

In contrast to the BNSCatm, the sensitivity study for BNSChydr was done on different depth horizons, thus yielding of up to 105 different fluctuation ranges, depending on the region in focus. For the display of the results, **Table 3** is restricted to three exemplary depth levels for each region for temperature

TABLE 5 | File names of BNSC data products.

Data product	File name
BNSChydr	
Time series of box averages	BNSC__[parameter]__UHAM_ICDC__v1__0.25deg__[yyyy].nc (annual, 143x2 files) BNSC__[parameter]__UHAM_ICDC__v1__0.25deg__[yyyymm].nc (monthly, 1716x2 files)
Decadal box averages	BNSC__[parameter]__UHAM_ICDC__v1__0.25deg__[yyyy1]__[yyyy2].nc (6x2 files)
Interpolated fields	BNSC__[parameter]__UHAM_ICDC__v1__0.25deg__OAN__[yyyy1]__[yyyy2].nc (6x2 files)
Land fraction	BNSC_land_area_fraction__UHAM_ICDC__v1.0__0.25deg.nc
Land-sea mask	BNSC_land_sea_mask__UHAM_ICDC__v1.0__0.25deg.nc
BNSCatm	
Monthly time series	BNSC_[parameter]___UHAM_ICDC__v2__1deg__[yyyymm].nc (792x3 files)
Climatological mean fields	BNSC_[parameter]___UHAM_ICDC__v2__1deg__climatology_[yyyy1]_[yyyy2].nc (5x3 files)
Land-sea-mask	BNSC_land_sea_mask__UHAM_ICDC__v2__1deg.nc

The variable parts of the file names are set in squared brackets and define the parameter ("temperature," "salinity," "Air_Pressure," "Air_Dewpoint_Temperature"or "Air_Temperature"), the date (e.g., "1995" instead of "[yyyy]" for the year 1995, or "199506" instead of "[yyyymm]" for June 1995) or the period (e.g., "1956" instead of "[yyyy1]" and "1965" instead of "[yyyy2]" for the decade 1956–1965).

and salinity, which were examined in two different temporal resolutions. In general, it can be stated that the fluctuation ranges for temperature and salinity are higher in monthly resolution. Regarding the different regions, the Belt Sea seems to be most sensitive to the observational database not only in salinity but also in temperature. The lowest fluctuation ranges, similar to the results of BNSCatm, are found in the central North Sea for temperature and annual mean salinity. The monthly mean salinity fields are least sensitive to the observational database in the southern region of the Atlantic part of the BNSC region.

Comparison With Other Data Products

The results of the comparison of the monthly mean BNSChydr fields with other data products are summarized in **Figure 9**. Shown here are the distributions of the relative frequency of the absolute differences between the BNSC and the three other data products, derived as described in section Comparison With Other Data Products. The results show that the mean value of the absolute differences is close to zero for all three comparisons, implying that the data products in general agree well. The spread of the distributions, however, is significantly different between the three data product comparisons: it is least in the comparison with KNSCv2 and highest in the comparison with BSRA.

Regarding salinity, the highest discrepancies between the data products can be found (not shown) in the transition area between the Baltic and the North Sea, the area of Skagerrak, Kattegat and Belt Sea. This area is characterized by high horizontal salinity gradients, which explains the large differences between the data products.

Except of singularities, no regional emphasis can be found in the comparison of the temperature fields of the data products. However, the differences exhibit a seasonal signal that is most pronounced in the subsurface waters. This implies that the reproduction of the seasonal cycle is different between the BNSC and the other three data products. Intercomparison of BSRA and KNSCv2, however, yields a similar result, which means that the differences in the seasonal cycle cannot be explained by the BNSC alone. Yet, this requires further investigation.

BNSChydr fields in annual resolution were compared only to the KNSCv2- annual fields and show good agreement. The absolute differences are symmetrically distributed around zero with a mean difference of 0.00 and a standard deviation of 0.34°C for temperature, respectively, 0.01 ± 0.10 PSU for salinity.

SUMMARY AND OUTLOOK

The main characteristics of the BNSC product are the following:

1. It comprises the entire North and Baltic Seas and includes fields of atmospheric and hydrographic parameters in different temporal resolutions on a compatible grid over a long common period (1950–2015).
2. The temporal sampling error was effectively reduced by appropriate correction methods.
3. There is one uniform quality control procedure for all *in situ* measurements of the ocean, and one for the atmosphere.

BNSCatm

A new atmospheric climatology of North and Baltic Sea on a one degree grid was created based on marine *in situ* observations. It contains monthly means of the parameters sea level pressure, 2 meter air temperature, and 2 meter dew point temperature for the period 1950–2015, a climatology for all 12 months of this

TABLE 6 | Overview, variables of the data product.

Variable	Explanation
BNSChydr (para = temperature, salinity)	
Monthly and annual box averages	
[para]_mean	Mean value
[para]_stddev	Standard deviation
[para]_noobs	Number of observations
Decadal box averages	
[para]_mean	Decadal monthly mean value
[para]_stddev	Decadal standard deviation
[para]_year_mean	Mean year, lies in range of calendar years of respective decade
[para]_year_stddev	Standard deviation corresponding to mean year
[para]_n_of_ys	Number of years that went into decadal mean
Interpolated fields	
[para]_oan	Decadal monthly mean (interpolated)
[para]_amd	Absolute median deviation (based on all neighboring boxes contributing to the optimal interpolation)
[para]_nobins	Number of neighboring boxes included for the optimal interpolation, maximum 8. _nobins = 0 means corresp. value of the first guess field is attributed to this box.
[para]_firstguess	"First guess"-value, corresponds to the long term mean of 1873–2015
[para]_relative_interpolation_error	Relative interpolation error, values between 0 and 1
[para]_mean_year	Mean year, does not necessarily lie in the range of calendar years of respective decade; depends on mean year of decadal box averages or, if those are not sufficient for the optimal interpolation, on the "first guess"-field
[para]_mean_distance	Mean distance of box center and the neighboring boxes considered for the optimal interpolation
BNSCatm (para = air_pressure, dewpoint, airtemp)	
Time series of monthly + climatological mean values mean values	
[para]	Mean
[para]_stddev	Standard deviation
[para]_noobs	Number of observations (for the climatologies : average number of observations)
climatological mean values	
[para]_boxcount	Number of neighboring boxes

time period, and monthly climatologies of the periods 1951–1980, 1961–1990, 1971–2000, and 1981–2010. The resulting data set contains mean values as well as standard deviations, and the mean number of observations per grid point.

The present version includes time and area of the KNSC climatology, on the same grid, but some small improvements were applied in the production that caused differences. The differences are largest in air pressure (between −1.5 to 2 hPa) and especially its standard deviation (about −1 to 15 hPa) as this is calculated with a different method. The values of mean air temperature and dew point temperature and associated standard deviations show only small changes of < 1 degree compared to the KNSC climatology.

The monthly comparison between BNSCatm and ERA-Interim climatologies for the period 1981–2010 showed for mean pressure differences in the interval −2.2 hPa to +2.7 hPa. The mean 2 m air temperature differences are between −2.1 K and 8 K at a single point at the Norwegian coast, and if that is ignored, the maximum difference is below 2 K. Most extreme values occur at the edges of the data field. A part of these differences can be explained by the so called "fair weather bias," which means that there are fewer measurements under severe weather conditions. This can cause a bias compared to the reanalysis results, which includes land stations and fills such gaps at sea with modeled data. But this inclusion of the land data leads in the analysis to mixed land/sea boxes that arise on the coasts and tend to have higher values than the BNSC.

The comparison between sea-level pressure in BNSCatm, ERA-Interim and ERA-40 climatology for 1979–2001 showed mean differences in the interval of −1.5 hPa and 1.5 hPa. Additionally the comparison with COSMOS-REA6 for 1995–2015 showed mean deviations between −1 hPa to 1 hPa. Highest absolute differences between the reanalysis and BNSCatm occur in winter and lowest in summer with better agreement over the open water and less good agreement close to the coast.

An intercomparison between BNSCatm, the ERA-40 reanalysis and observations based on station data was carried out. The mean deviations of both BNSCatm and ERA-40 from the observational data are within the range of uncertainty and show a regional pattern with the BNSC being closer to the observations at the North Sea coast and ERA-40 at the Baltic Sea coast.

Lessons to be learned from the sensitivity analysis are that the data set of BNSCatm is more stable in the period from 1960 onward and in the later 30-year climatologies than before 1960 and in the first climatology from 1951 to 1980.

Regular updates of the dataset and an extension of the data set for wind speed and direction are planned for the future.

BNSChydr

The BNSChydr data product presented here consists of gridded 3D-fields in different temporal resolutions (monthly, annual, decadal monthly) and different processing levels (box-averages and horizontally interpolated fields). A comprehensive description of the data used and the methods applied to create the data product are followed by the results of a sensitivity analysis, which estimates, on a regional basis, the sensitivity of the temporal mean fields to the basis of the observational data. The Belt Sea exhibits the highest fluctuation ranges in this respect, in both temperature and salinity, whereas the central North Sea is characterized by a low sensitivity in both parameters.

The comparison with other data products yields good agreement in general, yet further investigations, which are beyond the scope of this paper, are necessary.

In future, it is desirable to continue this work by implementing further and future observations. Based on the entity of quality-controlled observations of T und S, one can also think of creating more aggregated data products with respect to, for example, the ocean's heat content, and stratification or climate indices.

AUTHOR CONTRIBUTIONS

IH created the hydrographic part of the BNSC, carried out the sensitivity analysis of both the BNSCatm and the BNSChydr, compared the BNSChydr to other data sources, and wrote the corresponding parts of the manuscript. IH is the lead author of this manuscript. AJ-B has created the atmospheric part of the BNSC climatology data set, carried out the analysis of the results, the comparisons with ERA Interim and has therefore written the description of the methodology, and the analysis of the atmospheric part of the data set as well as the comparisons with ERA Interim. AA provided the input data set from DWD for the BNSCatm, participated in meetings for the planning and discussion of the analysis of the climatology, and corrected the manuscript. AG participated in meetings for the planning and discussion of the analysis of the climatology and corrected the manuscript. VG created the hydrographic part of the BNSC. CJ contributed to the analysis of the final product as well as comparison to other products and the writing of the manuscript. BK provided input data for BNSChydr, participated in meetings for the planning and discussion of the analysis of the BNSC data product. JM participated in meetings for the BNSC and corrected the manuscript. RS created most of the predecessor of the atmospheric part of the BNSC, i.e., the KLIWAS North Sea climatology, and revised this manuscript. BT participated in meetings for the planning and discussion of the analysis of the climatology and corrected the manuscript.

FUNDING

This work was partly funded by the Cluster of Excellence CliSAP (EXC177) Universität Hamburg, funded through the German Science Foundation (DFG). IH received funding for this work from BSH.

ACKNOWLEDGMENTS

The authors would like to thank the Maritime Data Center of the DWD for providing the atmospheric observational data. The hydrographic observational data were obtained from different data sources. Thanks, for providing marine *in situ* data, to the World Ocean Data Center (WOD), the Deutsches Ozeanografisches Datenzentrum, Germany (DOD), the Leibniz Institute for Baltic Sea Research Warnemünde, Germany (IOW), the International Council for Exploration of the Sea (ICES), the Institute of Meteorology and Water Management – National Research Institute, Poland (IMGW-PIB), the Royal Netherlands Institute for Sea Research (NIOZ), the British Oceanographic Data Centre (BODC), the University of Aarhus, and the International ARGO-Project (www.ifremer.fr). The authors would like to thank Kerstin Jochumsen, Sabine Hüttl-Kabus, Nils Schade, Hartmut Heinrich, (all BSH), Natacha Féry (DWD) and Manfred Bersch (UHH) for support and useful discussions concerning the work presented in this paper. Thanks to Detlef Stammer for the support of this work. This work would not have been possible without the wealth of scientific observations in the North and Baltic Sea region. To take measurements at sea and analyze the samples is often a stressful, yet important, work. The authors are grateful to all the scientists and technicians that were involved in sampling, analyzing and publishing the observational data via the data centers. The authors would like to thank the two reviewers for their valuable and detailed comments which helped to improve the manuscript.

REFERENCES

Axell, L., and Liu, Y. (2016). Application of 3-D ensemble variational data assimilation to a Baltic Sea reanalysis 1989–2013. *Tellus A Dynamic Meteorol. Oceanography* 68:24220. doi: 10.3402/tellusa.v68.24220

Berrisford, P., Dee, D., Poli, P., Brugge, R., Fielding, K., Fuentes, M., et al. (2011). *The ERA-Interim Archive Version 2.0, ERA Report Series 1*. Available online at: http://www.ecmwf.int/en/elibrary/8174-era-interim-archive-version-20

Bersch, M., Gouretski, V., Sadikni, R., and Hinrichs, I. (2013). *KLIWAS North Sea Climatology of Hydrographic Data (Version 1.0)*. World Data Center for Climate (WDCC) at DKRZ. doi: 10.1594/WDCC/KNSC_hyd_v1.0

Bersch, M., Hinrichs, I., Gouretski, V., and Sadikni, R. (2016). *Hydrographic climatology of the North Sea and surrounding regions – version 2.0, Center for Earth System Research and Sustainability (CEN), University of Hamburg*. Available online at: https://icdc.cen.uni-hamburg.de/daten/ocean/knsc-hydrographic.html

Bollmeyer, C., Keller, J. D., Ohlwein, C., Wahl, S., Crewell, S., Friederichs, P., et al. (2015). Towards a high-resolution regional reanalysis for the European CORDEX domain. *Q. J. Roy. Meteor. Soc.* 141, 1–15. doi: 10.1002/qj.2486

Boyer, T. P., Antonov, J. I., Baranova, O. K., Coleman, C., Garcia, H. E., Grodsky, A., et al. (2013). "World Ocean Database 2013," in *NOAA Atlas NESDIS 72, Technical Edn.*, eds S. Levitus and A. Mishonov (Silver Spring, MD), 209. doi: 10.7289/V5NZ85MT

Brys, G., Hubert, M., and Struyf, A. (2003). *A Comparison of Some New Measures of Skewness*, Heidelberg: Physica-Verlag HD.

Bülow, K., Dietrich, C., Elizalde, A., Gröger, M., Heinrich, H., Hüttl-Kabus, S., et al. (2014). *Comparison of Three Regional Coupled Ocean Atmosphere Models for the North Sea Under Today's and Future Climate Conditions (KLIWAS Schriftenreihe; KLIWAS-27/2014),* Koblenz: *Bundesanstalt für* Gewasserkunde.

Compo, G. P., Whitaker, J. S., Sardeshmukh, P. D., Matsui, N., Allan, R. J., Yin, X., et al. (2011). The Twentieth Century Reanalysis Project. *Q. J. Roy. Meteor. Soc.* 137, 1–28. doi: 10.1002/qj.776

Dee, D. P., Uppala, S. M., Simmons, A. J., Berrisford, P., Poli, P., Kobayashi, S., et al. (2011). The ERA-Interim reanalysis: configuration and performance of the data assimilation system. *Q. J. Roy. Meteor. Soc.* 137, 553–597. doi.org/10.1002/qj.828

Feistel, R., Feistel, S., Nausch, G., Szaron, J., Łysiak-Pastuszak, E., and Ærtebjerg, G. (2008). "*BALTIC: monthly time series 1900–2005*," in *State and Evolution of the Baltic Sea, 1952–2005*, eds R. Feistel, G. Nausch, and N. Wasmund (John Wiley & Sons, Inc.), 311–336. doi: 10.1002/9780470283134.ch11

Gandin, L. (1965). *Objective Analysis of Meteorological Fields (Leningrad: Gidromet), 1963*, [English Translation]. Jerusalem: Israel Program for Scientific Translation.

Gouretski, V. (2018). World ocean circulation experiment – argo global hydrographic climatology. *Ocean Sci.* 14, 1127–1146. doi: 10.5194/os-14-1127-2018

Gouretski, V. V., and Koltermann, K. P. (2004). "WOCE global hydrograhic climatology," in *Berichte des BSH, 35, Bundesamt für Seeschiffsfahrt und Hydrographie* (Hamburg), 52.

Janssen, F., Schrum, C., and Backhaus, J. O. (1999). A climatological data set of temperature and salinity for the Baltic Sea and the North Sea. *Deutsche Hydrografische Zeitschrif.* 51:5. doi: 10.1007/BF02933676

Kalnay, E., Kanamitsu, M., Kistler, R., Collins, W., Deaven, D., Gandin, L., et al. (1996). The NCEP/NCAR 40-Year reanalysis project. *Bull. Am. Meteorol. Soc.* 77, 437–472. doi: 10.1175/1520-0477(1996)077<0437:TNYRP>2.0.CO;2

Kofalk, S., Moser, H., Rudolf, B., Heinrich, H., and Heyer, H. (2010). "Facing the impacts on navigation and waterways by climate change: *The German Research Program KLIWAS*," *32nd PIANC International Navigation Congress 2010*, *Vol. 1*, PLI-ANC. 134–140.

Korevaar, C. G. (1990). *North Sea Climate, XII.* Springer: Netherlands. doi: 10.1007/978-94-867009-1982-2

Michaelsen, K., Krell, U., Reinhardt, V., Graßl, H., and Kaufeld, L. (1998). *Climate of the North Sea*. Deutscher Wetterdienst. Available online at: www.dwd.de

Núñez-Riboni, I., and Akimova, A. (2015). Monthly maps of optimally interpolated *in situ* hydrography in the North Sea from 1948 to 2013. *J. Marine Syst.* 151, 15–34. doi: 10.1016/j.jmarsys.2015.06.003

Pätsch, J., Burchard, H., Dieterich, C., Gräwe, U., Gröger, M., Mathis, M., et al. (2017). An evaluation of the North Sea circulation in global and regional models relevant for ecosystem simulations. *Ocean Model.* 116, 70–95. doi: 10.1016/j.ocemod.2017.06.005

Reiniger, R. F., and Ross, C. K. (1968). A method of interpolation with application to oceanographic data. *Deep Sea Res. Oceanograp. Abstr.* 15, 185–193. doi: 10.1016/0011-7471(68)90040-5

Rienecker, M. M., Suarez, M., Gelaro, J., Todling, R., Julio Bacmeister, R., Liu, E., et al. (2011). MERRA: NASA's Modern-era retrospective analysis for research and applications. *J. Climate* 24, 3624–3648. doi: 10.1175/JCLI-D-11-00015.1

Sadikni, R., Bersch, M., Jahnke-Bornemann, A., and Hinrichs, I. (2013). *KLIWAS North Sea Climatology of Meteorological Data (Version 1.0), World Data Center for Climate (WDCC) at DKRZ.* doi: 10.1594/WDCC/KNSC_met_v1.0

Sadikni, R., Schade, N. H., Andersson, A., Jahnke-Bornemann, A., Hinrichs, I., Gates, L., et al. (2018). The KLIWAS North sea climatology. part I: processing of the atmospheric data. *J. Atmos. Oceanic Technol.* 35, 111–126. doi: 10.1175/JTECH-D-17-0044.1

Schade, N. H., Heinrich, H., and Rosenhagen, G. (2013). Regional evaluation of ERA-40 reanalysis data with marine atmospheric observations in the North Sea Area. *Meteorol. Z.* 22, 675–684. doi: 10.1127/0941-2948/2013/0471

Schade, N. H., Sadikni, R., Jahnke-Bornemann, A., Hinrichs, I., Gates, L., Tinz, B., et al. (2018). The KLIWAS north sea climatology. part II: assessment against global reanalyses. *J. Atmos. Oceanic Technol.* 35 127–145. doi: 10.1175/JTECH-D-17-0045.1

Schmager, G., Fröhle, P., Schrader, D., Weisse, R., and Müller-Navarra, S. (2008). *Sea State, Tides, in State and Evolution of the Baltic Sea, 1952-2005: A Detailed 50-Year Survey of Meteorology and Climate, Physics, Chemistry, Biology, and Marine Environment.* John Wiley & Sons, Inc. doi: 10.1002/9780470283134.ch7

Sokolov, S., and Rintoul, S. R. (1999). Some remarks on interpolation of nonstationary oceanographic fields. *J. Atmos. Oceanic Technol.* 16, 1434–1449. doi: 10.1175/1520-0426(1999)016<1434:SROION>2.0.CO;2

The Gulf of Finland assessment. (2016). "The gulf of finland assessment," in *Reports of the Finnish Environment Institute 27/2016*, eds M. Raateoja and O. Setälä (Helsinki: Finnish Environment Institute).

Uppala, S. M., KÅllberg, P. W., Simmons, A. J., Andrae, U., Bechtold, V. D. C., Fiorino, M., et al. (2005). The ERA-40 re-analysis. *Q. J. Roy. Meteor. Soc.* 131, 2961–3012. doi: 10.1256/qj.04.176

Vandervieren, E., and Hubert, M. (2004). "An adjusted boxplot for skewed distributions," in *Proceedings in Computational Statistics 2004*, eds J. Antoch. 1933-1940 (Heidelberg: Springer-Verlag).

Weatherall, P., Marks, K. M., Jakobsson, M., Schmitt, T., Tani, S., Arndt, J. E., et al. (2015). A new digital bathymetric model of the world's oceans. *Earth Space Sci.* 2, 331–345. doi: 10.1002/2015EA000107

Conflict of Interest Statement: The authors declare that the research was conducted in the absence of any commercial or financial relationships that could be construed as a potential conflict of interest.

frontiers in Earth Science

ORIGINAL RESEARCH
published: 10 July 2019
doi: 10.3389/feart.2019.00166

Impact of Ice Data Quality and Treatment on Wave Hindcast Statistics in Seasonally Ice-Covered Seas

Laura Tuomi[1], Hedi Kanarik[1], Jan-Victor Björkqvist[1], Riikka Marjamaa[1,2], Jouni Vainio[3], Robinson Hordoir[4,5], Anders Höglund[6] and Kimmo K. Kahma[1]*

[1] Marine Research Unit, Finnish Meteorological Institute, Helsinki, Finland, [2] Eniram Ltd., Helsinki, Finland, [3] Weather and Safety Centre, Finnish Meteorological Institute, Helsinki, Finland, [4] Oceanography & Climate Research Group, Institute of Marine Research, Bergen, Norway, [5] Bjerknes Centre for Climate Research, Bergen, Norway, [6] Research Department, Swedish Meteorological and Hydrological Institute, Norrköping, Sweden

The seasonal ice cover has significant effect on the wave climate of the Baltic Sea. We used the third-generation wave model WAM to simulate the Baltic Sea wave field during four ice seasons (2009–2012). We used data from two different sources: daily ice charts compiled by FMI's Ice Service and modeled daily mean ice concentration from SMHI's NEMO-Nordic model. We utilized two different methods: a fixed threshold of 30% ice concentration, after which wave energy is set to zero, and a grid obstruction method up to 70% ice concentration, after which wave energy is set to zero. The simulations run using ice chart data had slightly better accuracy than the simulation using NEMO-Nordic ice data, when compared to altimeter measurements. The analysis of the monthly mean statistics of significant wave height (SWH) showed that the differences between the simulations were relatively small and mainly seen in the Bothnian Bay, the Quark, and the eastern Gulf of Finland. There were larger differences, up to 3.2 m, in the monthly maximum values of SWH. These resulted from individual high wind situations during which the ice edge in the ice chart and NEMO-Nordic was located differently. The two different methods to handle ice concentration resulted only in small differences in the SWH statistics, typically near the ice edge. However, in some individual cases the two methods resulted in quite large differences in the simulated SWH and the handling of ice concentrations as additional grid obstructions could be important, for example, in operational wave forecasting.

Keywords: wave modeling, seasonal ice cover, forecasting, statistics, Baltic Sea

OPEN ACCESS

Edited by:
Martin Stendel, Danish Meteorological Institute (DMI), Denmark

Reviewed by:
Tarmo Soomere, Tallinn University of Technology, Estonia
Xander Wang, University of Prince Edward Island, Canada

****Correspondence:***
Laura Tuomi
laura.tuomi@fmi.fi

Specialty section:
This article was submitted to Interdisciplinary Climate Studies, a section of the journal Frontiers in Earth Science

Received: *04 December 2018*
Accepted: *14 June 2019*
Published: *10 July 2019*

Citation:
Tuomi L, Kanarik H, Björkqvist J-V, Marjamaa R, Vainio J, Hordoir R, Höglund A and Kahma KK (2019) Impact of Ice Data Quality and Treatment on Wave Hindcast Statistics in Seasonally Ice-Covered Seas. Front. Earth Sci. 7:166. doi: 10.3389/feart.2019.00166

1. INTRODUCTION

The Baltic Sea experiences seasonal ice cover every year. Even in the mildest winters there is ice in the Bothnian Bay and in the eastern Gulf of Finland (sub-basins of the northern Baltic Sea are presented in **Figure 1**). The ice interacts with the surface waves in several ways. The short waves are rapidly attenuated by the ice field. Long waves can propagate further into the ice field and alter the distribution of sea ice as well as cause fragmentation (e.g. Squire et al., 1995; Squire, 2018). The fragmented ice cover is more exposed to the effects of wind, waves, and surface currents. During the ice winter, the wave growth in the open sea areas is also affected by the ice field. The fetch over

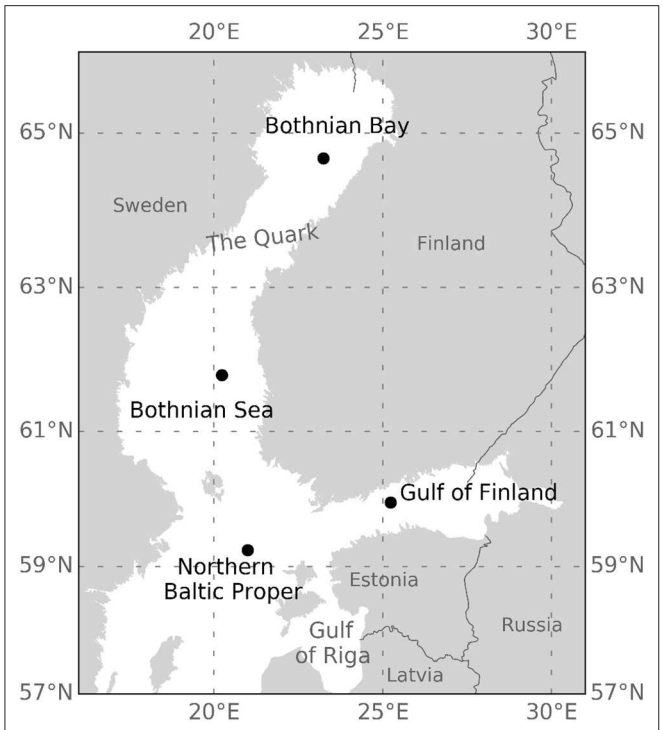

FIGURE 1 | Sub-basins of the northern Baltic Sea and locations of the FMI wave buoys (black dots).

which the waves grow, changes as the waves start to grow from the edge of the ice field instead of the shoreline. This has a significant effect on the wave climate, especially in the small enclosed or semi-enclosed basins such as the Baltic Sea (Tuomi et al., 2011).

Third-generation wave models, such as WAM, WAVEWATCH III®, and SWAN, are able to account for ice conditions. Therefore, many of the existing wave hindcast statistics have somehow accounted for ice conditions (e.g., Günther et al., 1998; Swail et al., 2006; Reistad et al., 2011; Tuomi et al., 2011; Björkqvist et al., 2018). A typical way to account for ice in wave models is to exclude grid points from the calculations if the ice concentration is greater than a certain threshold value, e.g., 30% (Tuomi et al., 2011). A more sophisticated method to account for ice conditions has been presented by e.g., Tolman (2003), who proposed that ice concentration is treated as an additional grid obstruction, which attenuates the propagation of wave energy between the grid points. Recently, Doble and Bidlot (2013) also presented a method to attenuate the modeled wave energy in order to achieve better wave forecasts in the marginal ice zone. Furthermore, sophisticated source terms are being developed in order to account for wave-ice interaction in wave models more accurately (e.g., Rogers and Orzech, 2013; Rogers and Zieger, 2014; Rogers et al., 2016).

There are several different sources for ice data. In the Baltic Sea, one good source is the ice charts produced by the national Ice Services. The ice charts are based on combined information from satellite analyses, ice observations from ships and coastal measurement sites, and expert analyses. These products have existed in digitized format for at least the past 10–20 years. When making hindcasts for longer historical periods, or when making climate scenarios, ice concentrations produced by 3D ocean-ice models are typically used. The accuracy of the present state-of-the-art models in presenting the Baltic Sea ice conditions has been shown to be relatively good, e.g., by Löptien et al. (2013) and Pemberton et al. (2017). There are also satellite-based products such as OSISAF (Tonboe et al., 2016), which provide ice concentration data for northern and southern latitudes. However, their resolution is still quite coarse considering the small size and complex shape of the Baltic Sea.

In addition to the different sources of ice data—and the various ways to handle them—there is another complication in compiling wave statistics for seasonally ice-covered seas: how to handle the time of year when a sea area is ice covered and the significant wave height equals zero. A common approach is to include only values from the time when the sea is ice free (e.g., MacLaren Plansearch Limited, 1991). This is the prevailing method when measured data is presented. On the other hand, when wave statistics are used to estimate wave energy resources, the wave height is set to zero when there is ice (e.g., Cornett, 2008). The lack of historical sea ice data may also hinder the use of ice conditions when compiling wave statistics from model data (Gorman et al., 2003). Also, ignoring ice conditions in model calculations and in the formulation of statistics is the simplest way to compile wave hindcast statistics in seasonally ice-covered seas.

Tuomi et al. (2011) and Tuomi (2014) have presented five different ways to compile wave statistics in seasonally ice-covered sea areas. The statistics types are as follows: (1) measurement statistics (type M), (2) ice-time-included statistics (type I), (3) ice-free time statistics (type F), (4) hypothetical no-ice statistics (type N), and (5) exceedance time statistics (type ET). They differ in how they deal with the time when there is ice or when the data is missing. None of them is perfect, and each type has a specific application for which it is more suitable than the other types.

In this study, we use two different methods to handle the ice conditions in the wave model WAM. The first method excludes grid points from the calculations if the ice concentration exceeds a certain threshold value. This method was chosen since it has been traditionally used in operational forecasting and in wave hindcast statistics presented for the Baltic Sea. The second method is based on the work by Tolman (2003). This approach has been utilized in the Baltic Sea to account for unresolved coastal archipelagos (Tuomi et al., 2014) and also lately in the development of the CMEMS BAL MFC wave forecast (Tuomi et al., 2018). We also use ice information from two different sources: the daily ice concentrations from the Finnish Meteorological Institute's (FMI) ice service and daily mean ice concentrations from the Swedish Meteorological and Hydrological Institute's (SMHI) NEMO-Nordic simulation. The effect of the different handling of ice is studied by running the wave model for four different ice winters. The wave hindcasts are validated against altimeter measurements. Monthly mean, maximum, and exceedance statistics are presented for the northern Baltic Sea and differences between the four hindcasts

in presenting the wave conditions and statistics are analyzed and discussed.

2. MODELING

We made simulations for four winters: 2009, 2010, 2011, and 2012. All simulations were run with the wave model WAM, using wind forcing from RCA4 down-scaled ERA-Interim. The simulations were run for January–April, which are the months that typically have an ice cover even in the mildest winters. We used two different methods to handle ice in the WAM model and two data sources for ice concentrations. The details of the modeling and forcing used are explained in the following Sections.

2.1. Wave Model WAM

We used the third-generation wave model WAM (WAMDI, 1988; Komen et al., 1994) to simulate the Baltic Sea wave field, which evolution is determined by calculating the wave energy spectrum. To this end, WAM solves the action balance equation, which in deep water without currents can be written for spherical coordinates as:

$$\frac{\partial F}{\partial t} + (\cos\phi)^{-1}\frac{\partial}{\partial \phi}(\dot{\phi}\cos\phi F) + \frac{\partial}{\partial \lambda}(\dot{\lambda}F) + \frac{\partial}{\partial \theta}(\dot{\theta}F) = S_{in} + S_{ds} + S_{nl}, \quad (1)$$

where $F(t, \phi, \lambda; \theta, \omega)$ is the spectral density, which is a function of the time t, the latitude ϕ and the longitude λ. The spectral density is also a function of the spectral variables describing the wave direction (θ) and the angular frequency (ω).

The velocities in the longitudinal and latitudinal directions are given by

$$\dot{\phi} = (c_g \cos\theta)R^{-1}, \quad (2)$$

$$\dot{\lambda} = (c_g \sin\theta)(R\cos\phi)^{-1}, \quad (3)$$

where c_g is the group velocity and R is the radius of the Earth. Finally, the change in wave direction in spectral space is given by

$$\dot{\theta} = c_g \sin\theta \tan\phi R^{-1}. \quad (4)$$

The left side of Equation (1) is solved numerically using a first-order upwind scheme.

The right side of Equation (1) lists the different sources and sinks that add, dissipate, or redistribute the energy in the wave spectrum. The deep-water source terms include the wind input (S_{in}, Janssen, 1991), the dissipation of waves due to whitecapping (S_{ds}, Komen et al., 1994), and the discrete interaction approximation (DIA) of the nonlinear four-wave interactions (S_{nl}, Hasselmann et al., 1985).

WAM has been developed to be used also in areas with finite depth (Monbaliu et al., 2000), and cycle 4.5.4, therefore also includes source terms to account for the bottom friction (Hasselmann et al., 1973) and the depth-induced wave breaking (Battjes and Janssen, 1978). In this study, all properties accounting for the finite depth were switched on.

We used a 1 nmi (c. 1.852 km) resolution grid for the Baltic Sea with additional grid obstructions for the coastal archipelagos in the northern Baltic Sea. The model wave spectra comprised of 36 directions and 35 frequencies (0.04177–1.06719 Hz). The same grid and model configuration is used in the CMEMS BAL MFC wave analysis and forecast system (marine.copernicus.eu, BALTICSEA_ANALYSIS_FORECAST_WAV_003_010), run by FMI (e.g., Tuomi et al., 2018).

2.2. Methods to Handle Ice in a Wave Model

A method to handle the seasonal ice cover has been present in FMI's operational wave model applications since 2001, when operational forecasts with a coupled atmosphere-wave model started (Järvenoja and Tuomi, 2002). At first, the ice conditions were handled by excluding grid points from the calculations if they had an ice concentration over 30%. Until 2009, this was done through a bathymetry modification by changing the ice-covered areas to land points. Since 2009, ice conditions have been handled by setting the energies in the wave spectrum to zero at points where the ice concentration exceeds the threshold value.

To further develop the methods to handle ice conditions in seasonally ice-covered seas, we used the method introduced by Tolman (2003) to treat unresolved ice in a wave model grid. We have previously implemented this method to account for the wave energy attenuation caused by unresolved islands in order to improve the quality of the WAM-model results in the coastal archipelagos of the northern Baltic Sea (Tuomi et al., 2014).

Tolman (2003) presented how the energy fluxes between the grid cells can be reduced according to subgrid-scale obstructions

$$F_i^{n+1} = F_i^n + \frac{\Delta t}{\Delta x}[\alpha_{i,-}G_{i,-} - \alpha_{i,+}G_{i,+}]^n, \quad (5)$$

where $\alpha_{i,-}$ and $\alpha_{i,+}$ are transparencies at cell boundaries and $G_{i,-}$ and $G_{i,+}$ are fluxes at the cell boundaries.

The transparencies at cell boundaries vary between 0 and 1, with 0 meaning a closed boundary and 1 a totally open boundary. The obstructions, land or ice, that are typically defined at the center of the grid boxes are converted to transparencies at cell boundaries according to

$$\alpha_{i,+} = 1 \quad (6)$$

$$\alpha_{i,-} = \frac{\alpha_{i-1}(1+\alpha_i)}{1+\alpha_{i-1}}, \quad (7)$$

where α_i is the obstruction at the cell center. The outflow transparency $\alpha_{i,+}$ is set to 1 by default.

We used a threshold value of 70% to determine the treatment of the ice in a grid cell. When the ice concentration in a grid point was smaller than 70%, the ice was treated as additional grid obstruction, which reduced the energy between grid points according to Equation (5). Grid points having an ice

TABLE 1 | WAM configurations.

Name	Ice source	Threshold	Obstructions
WAM_IC30	FMI ice charts	30%	No
WAM_IC70	FMI ice charts	70%	Yes
WAM_NI30	NEMO-Nordic	30%	No
WAM_NI70	NEMO-Nordic	70%	Yes

concentration of over 70% were excluded from the calculations. Different wave model configurations are described in **Table 1**.

The threshold values used for ice concentration in this study are based on the World Meteorological Organization (WMO) classification of ice compactness (WMO, 2015). In the classification, 30% is used as an upper limit for very open drift ice and 70% as a lower limit for close drift ice.

2.3. Forcing

2.3.1. Wind Forcing

We used downscaled ERA-Interim data (Dee et al., 2011) as a wind forcing for the wave model. The downscaling was done with the Swedish Meteorological and Hydrological Institute's regional climate model RCA4, using spectral nudging (Berg et al., 2013). The re-analysis is available for the years 1979–2013. The horizontal resolution of the forcing is 11 km, and the wind fields are available with 3-h intervals.

2.3.2. Gridded Ice Charts

FMI's Ice Service produces daily ice concentration maps, which are also available as a gridded product. The daily updated charts are compiled on the basis of satellite observations, available *in-situ* observation and expert analysis. For the period 2009–2012, the ice charts were available in gridded format with $0.02^\circ \times 0.01^\circ$ resolution, for longitude and latitude, respectively. The ice concentrations were interpolated to the WAM grid points using the nearest neighbor method.

2.3.3. NEMO-Nordic

Daily mean ice concentrations from the SMHI NEMO-Nordic (e.g., Hordoir et al., 2019) simulation were used as forcing for the wave model. The data was available in 2 nmi (c. 3.7 km) resolution for the Baltic Sea region and the NEMO-Nordic simulations were run using the same atmospheric forcing as the WAM model runs (see description in section 2.3.1). The ice concentrations were interpolated to the WAM grid points using the nearest neighbor method.

3. ICE WINTERS 2009–2012

The winters 2009–2012 were selected for this study, since they included different types of Baltic Sea ice winters, namely one mild, one severe, and two average winters (**Figure 2**). The severity classification of the Baltic Sea ice season is based on the maximum extent of the ice cover from the winters 1960/1961 to 2009/2010. The severity of the winter is determined by the area of total extent compared to the long-term mean. A winter with a maximum extent below 115,000 km^2 is classified as mild,

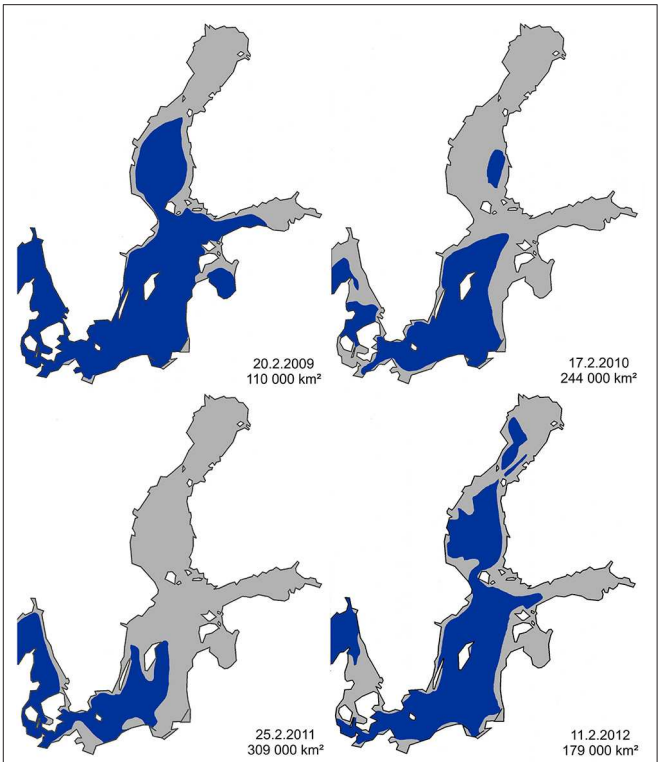

FIGURE 2 | Maximum ice extent in the Baltic Sea in 2009 **(Upper left)**, 2010 **(Upper right)**, 2011 **(Lower left)**, 2012 **(Lower right)**. Open water is shown with blue color and ice-covered areas with gray.

while severe winters have a maximum extent of over 230,000 km^2. The classification does not consider duration, ice concentration, thickness, or deformation degree.

The ice winter 2008/2009 was mild in the Baltic Sea, compared to the long-term average. There was a significant amount of sea ice only in the Bothnian Bay and the eastern part of the Gulf of Finland (**Figure 2**, upper left). In the Bothnian Bay, the freezing started after mid-November, which was 3 weeks later than the long-term average. Larger areas started to freeze in the beginning of January. The maximum ice extent occurred on February 20, which is 1 week earlier than an average winter. The Bothnian Sea and Gulf of Finland were mostly ice free by the April 19. By the end of May the Bothnian Bay was also free of ice, thus ending the ice season.

The ice winter of 2009/2010 was average when considering the maximum ice extent. However, the ice winter was over a month shorter than average in the northern parts of the Bothnian Bay. The ice season started in mid-December, and during January most of the Bothnian Bay was ice covered, along with coastal areas of the Bothnian Sea. The maximum ice extent was reached by February 17, almost 2 weeks earlier than on average (**Figure 2**, upper right). The Gulf of Finland and the Bothnian Sea were free of ice on April 19 and the Bothnian Bay on May 31.

Of the four winters in this study, the ice winter of 2010/2011 was the most severe. In the Bothnian Sea, the northern Baltic Proper, and the Gulf of Finland, the ice winter was between 2

and 6 weeks longer than the average. The maximum ice cover was reached on February 25 (**Figure 2**, lower left). By this time the Bothnian Bay, Bothnian Sea, Gulf of Finland, and Gulf of Riga, as well as the northern part of the Baltic Proper, were totally ice covered. At the end of February, southerly winds packed the ice toward the coast, thus reducing the ice-covered area while causing ice ridges and difficulties for the ship traffic. By May 14, the Gulf of Finland was completely ice-free, and 1 week later also the Bothnian Sea. The ice season ended on the May 24.

The ice winter of 2011/2012 was average based on the ice extent evaluation, but it started exceptionally late and also ended earlier than on average. In the Bothnian Bay the ice winter was from over 4 weeks to almost 6 weeks shorter than on average, and in the Bothnian Sea and the Gulf of Finland about 3 weeks shorter than on average. The northern Baltic Proper remained ice-free throughout the winter. The ice extent reached its maximum on February 11, 2 weeks earlier than on average (**Figure 2**, lower right). The Gulf of Finland was free of ice by the first week of May and the Bothnian Bay on May 19.

4. VALIDATION

The validation of the wave model results in, and close to, the ice-covered areas is difficult. The wave buoys are usually recovered well before the sea area freezes, and in the northern part of the Baltic Sea the measurement period is typically from May/early June until December/early January.

We used altimeter data to get some estimate of how the two different ice products and two different ways to handle ice conditions in the wave model affected the quality of the wave hindcasts. Data were extracted from the IFREMER Global altimeter SWH data set (Queffeulou and Croizè-Fillon, 2017). For the period in question there were data from five different satellites, namely ERS2, ENVISAT, JASON1, JASON2, and CRYOSAT. We used corrected SWH values, which for ERS2, ENVISAT, JASON1 and JASON2 are based on Queffeulou (2004); Queffeulou et al. (2011), and for CRYOSAT on Queffeulou (2013). In the dataset, the ice covered areas have been masked out based on the Polar Sea Ice concentration product by CERSAT (cersat.ifremer.fr). In the Baltic Sea, Kudryavtseva and Soomere (2016) have evaluated, that ice starts to affect the altimeter SWH

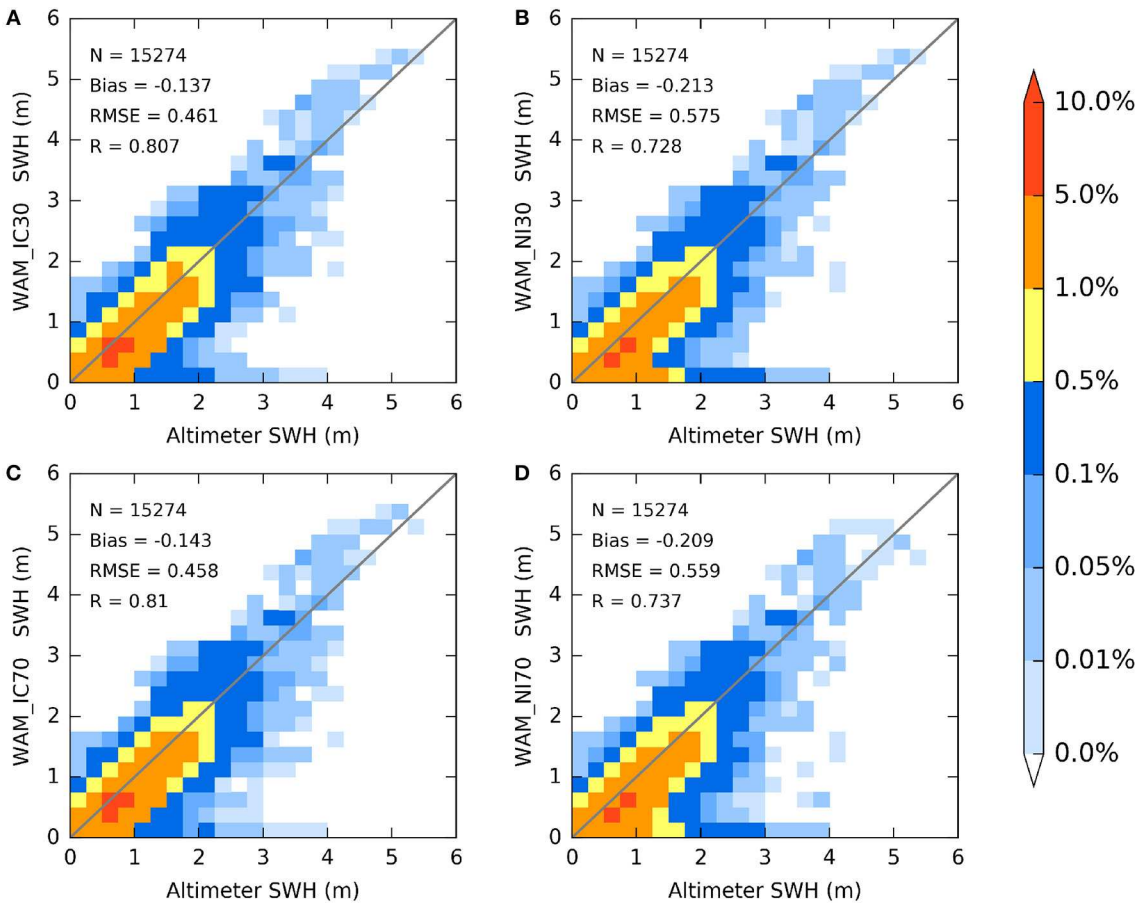

FIGURE 3 | Scatter plots where the SWH from four model setups are compared to the altimeter SWH. The colors indicate the concentration of the values. Explanations of model setups **(A)** WAM_IC30, **(B)** WAM_NI30, **(C)** WAM_IC70, and **(D)** WAM_NI70 are presented in **Table 1**. Number of comparison points (N), bias, root-mean-square error (RMSE) and Pearson correlation (R) are presented together with each setup.

already with a 10% concentration and that the effects are notable at concentrations of 30%. Therefore, using the ice data to mask out the altimeter SWH values from partially ice-covered areas is important.

The comparison of the simulated and altimeter SWH was performed only for the Gulf of Bothnia, i.e., the Bothnian Sea, the Quark, and the Bothnian Bay. This area also has ice during mild winters, as described in section 3, and has been shown to have good-quality altimeter data when compared with wave buoy measurements (e.g., Kudryavtseva and Soomere, 2016).

The accuracy of the simulations was relatively good (**Figure 3**) and comparable to earlier wave model studies presented for this area (e.g., Tuomi et al., 2011). Generally, the lower values of SWH were underestimated and higher values (over 3.5 m) were overestimated by the model. The underestimation of the lower values of SWH was larger when the ice concentrations were obtained from NEMO-Nordic than for the runs using ice concentrations from the FMI ice charts. As the ice charts are based on satellite and *in-situ* data, this was expected. However, the differences were relatively small, indicating that the NEMO-Nordic can reproduce the ice concentrations quite well in the northern Baltic Sea. There were also some discrepancies resulting from the different ways to handle ice conditions, but these were significantly

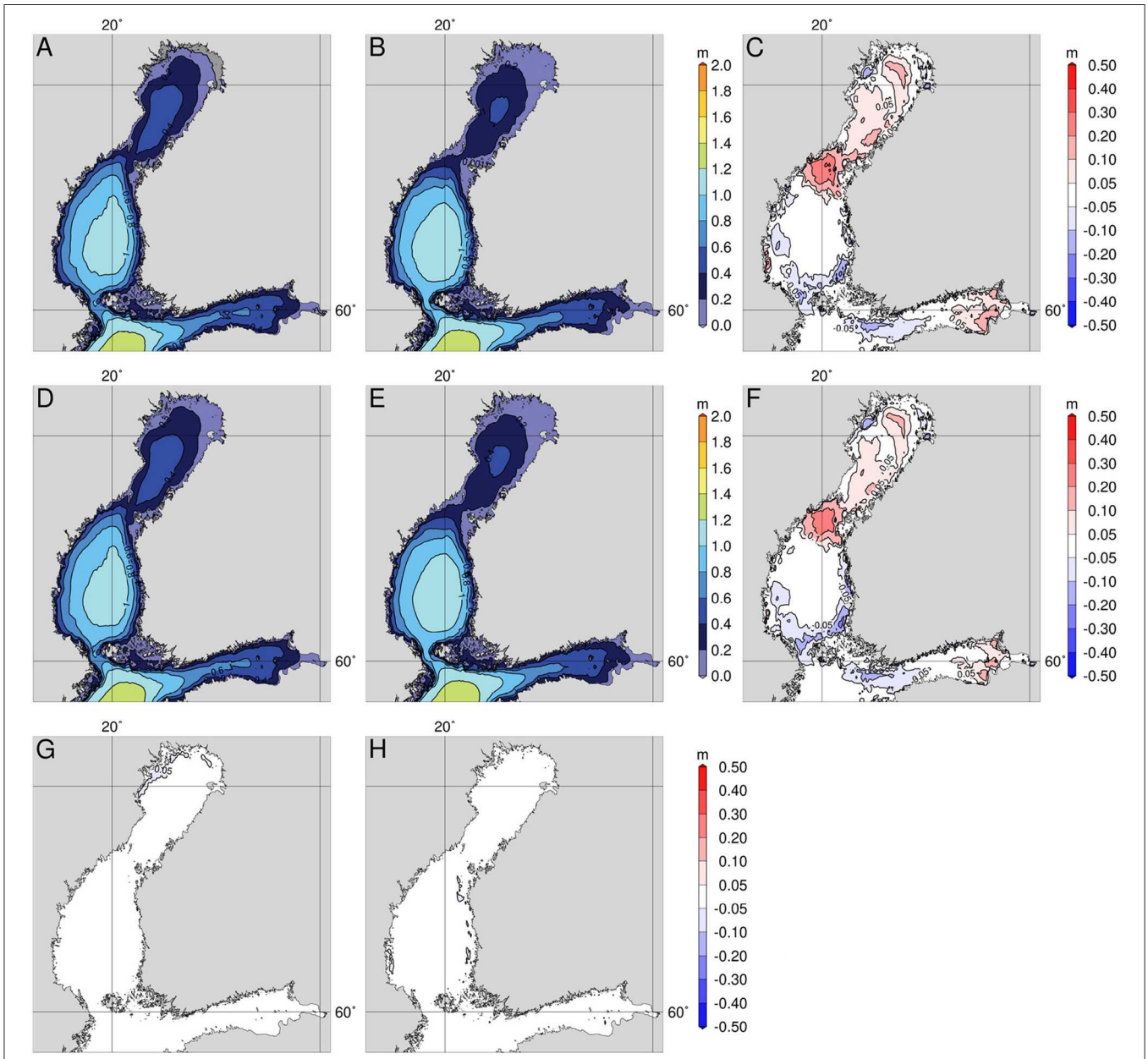

FIGURE 4 | Mean values of significant wave height in January 2009–2012. Ice-included-time statistics, type I. **(A)** WAM_IC30. **(B)** WAM_NI30. **(C)** WAM_IC30–WAM_NI30. **(D)** WAM_IC70. **(E)** WAM_NI70. **(F)** WAM_IC70–WAM_NI70. **(G)** WAM_IC30–WAM_IC70. **(H)** WAM_NI30–WAM_NI70.

smaller than those arising from using different sources of ice data.

The comparison also revealed a few occasions when the altimeter measured a non-zero SWH, even though both ice data sources showed the grid cell to contain ice. There are fewer of these cases in the runs that use data from FMI's ice charts than in those using data from NEMO, and the discrepancy can mostly be attributed to small differences in the location of the ice edge between the different products.

Due to the small size and shape of the Baltic Sea, the accuracy of the modeled significant wave height is quite sensitive to the accuracy and resolution of the forcing wind field. The wind forcing used in this study (cf. section 2.3.1) has quite a coarse resolution, 11 km, and is intended for running hindcasts or reanalysis. We used it to have a consistent simulation with the NEMO-Nordic, which was run using the same meteorological forcing. The wave model setup used in this study, is also used in the CMEMS BAL MFC wave analysis and forecast system. Those forecasts utilize the operational FMI-HARMONIE wind fields with about 2.5 km horizontal resolution, which naturally leads to considerably better accuracy in simulated SWH (Tuomi et al., 2018; Vähä-Piikkiö et al., 2019).

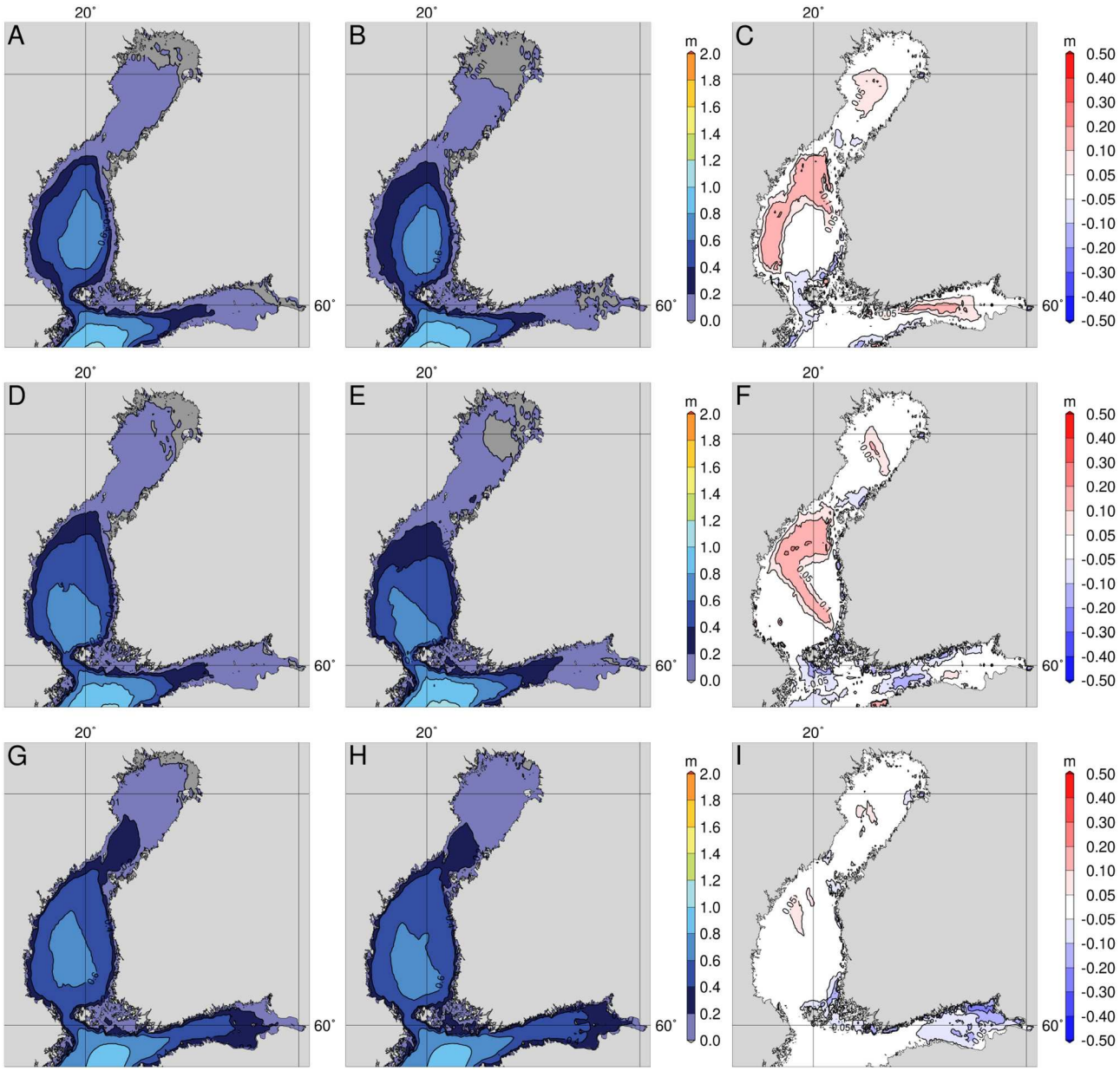

FIGURE 5 | Mean values of significant wave height in February **(A–B)**, March **(D–E)**, and April **(G–I)** 2009–2012 for WAM_IC30 **(A,D,G)** and WAM_NI30 **(B,E,H)** and the difference between them (**C,F,I**; WAM_IC30–WAM_NI30).

5. WAVE STATISTICS

The WAM simulations for Jan–Apr 2009–2012 were used to calculate the mean and maximum values of significant wave height. When presenting the statistics we use the ice-time-included statistics (type I, Tuomi et al., 2011), i.e., during the time when the sea area is ice-covered, the significant wave height is set to zero. These types of statistics give lower mean values in the seasonally ice-covered areas than the other statistics types. Considering the applications, for which type I statistics is a good choice, one example is the estimation of wave energy resources, as already discussed in Section 1. Recently, for example Nilsson et al. (2019), have used Type I statistics to evaluate the wave energy potential for the Baltic Sea. Type I statistics is also a good choice when evaluating the fatigue loads from waves on offshore structures, and similar phenomena of a cumulative nature in seasonally ice-covered seas, when the loads imposed by ice conditions are evaluated separately. Furthermore, type I statistics can be used when the wave-related requirements and economic risks for shipping are estimated for the lifetime of operations, which are carried out year-round.

5.1. Monthly Mean Values

The monthly mean values of SWH, calculated from the four wave model runs for 2009–2012, showed some differences (**Figures 4**, **5**). The largest differences, up to 0.3 m, were between the runs using the ice chart (WAM_IC) and NEMO (WAM_NI) data. The different methods to handle ice resulted in considerably smaller differences, typically smaller than 0.05 m (**Figures 4G,H**). Therefore, for Feb–Apr, we only present the mean values of the WAM_IC30 and WAM_NI30 runs (**Figure 5**). The differences in the monthly mean SWH values between WAM_IC and WAM_NI resulted from the differences in the ice extent and the location of the ice edge in two ice products. In the Bothnian Bay, the use of NEMO-Nordic ice concentrations resulted in a lower mean SWH in every month. The choice of ice product also affected the values in the Quark and the Bothnian Sea. However, in these areas, the higher mean SWH was sometimes obtained when using NEMO-Nordic ice concentrations.

The lower mean values of SWH when using the NEMO-Nordic ice concentration results from the overestimation of ice extent in the model reported e.g., by Pemberton et al. (2017). They also found that, on average, the ice cover increased faster and retreated earlier in NEMO-Nordic than in observations.

Of the individual years, the differences between WAM_IC and WAM_NI runs were largest in 2009 (not shown). During this year, the ice extent in NEMO-Nordic runs was considerably larger than in the FMI ice charts both in February and March. The ice winters of 2010 and 2011 had smaller differences, since almost the whole Gulf of Bothnian and Gulf of Finland was covered in ice

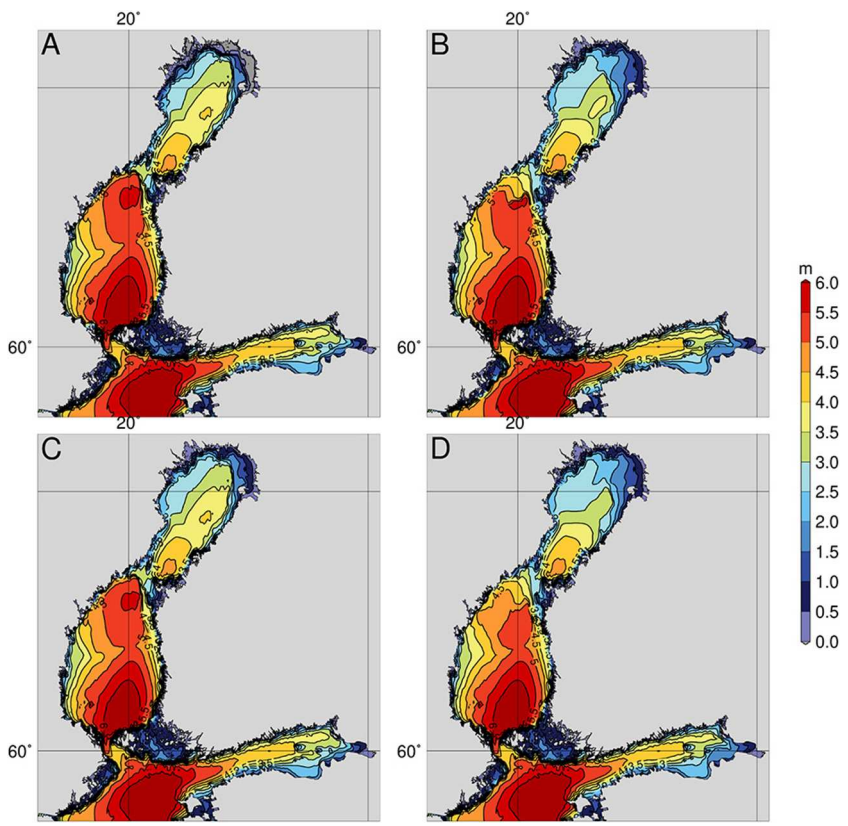

FIGURE 6 | Maximum values of significant wave height in January 2009–2012 for **(A)** WAM_IC30, **(B)** WAM_NI30, **(C)** WAM_IC70, and **(D)** WAM_NI70.

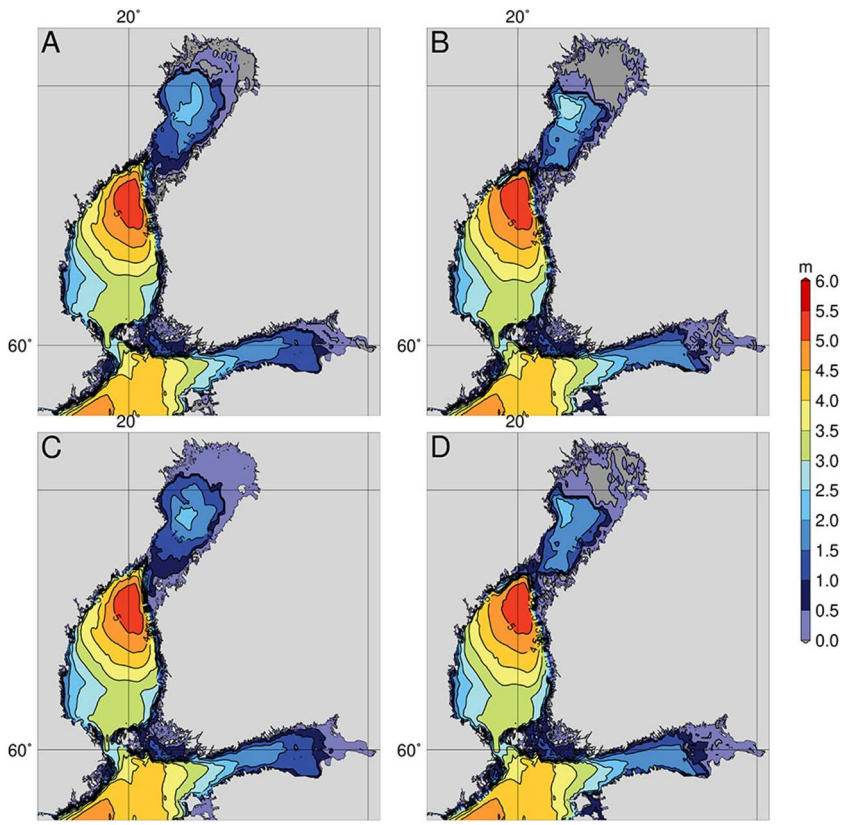

FIGURE 7 | Maximum values of significant wave height in February 2009–2012 for **(A)** WAM_IC30, **(B)** WAM_NI30, **(C)** WAM_IC70, and **(D)** WAM_NI70.

during these times (cf. **Figure 2**). In 2012, there were differences mainly in the Bothnian Bay and the eastern part of the Gulf of Finland.

5.2. Monthly Maximum Values

There were larger differences between the monthly maximum values than the monthly mean values (**Figures 6–9**). The two ways to handle the ice conditions lead to the largest differences in the Bothnian Bay and in the northern part of the Bothnian Sea. In March, there were also differences in the northern Baltic Proper (**Figure 8**) caused by the ice concentrations below 30% in the FMI ice charts, which were treated as only partly open water in the WAM_IC70 run. The method by Tolman (2003) reduces the propagation of wave energy in partially ice-covered areas (cf. section 2.2), which leads to lower values of significant wave height. However, there were also some areas in which the runs utilizing the Tolman (2003) method gave higher maximum values than the runs using the 30% threshold value: for example, in February, in the northernmost part of Bothnian Bay and in the easternmost part of the Gulf of Finland (**Figure 7**). This will be further discussed in section 6.

There were also significant differences in the monthly maximum values between WAM_IC and WAM_NI. The largest differences were again in the Bothnian Bay, the northern part of the Bothnian Sea, and in the easternmost part of the Gulf of Finland. The largest difference was 3.2 m in January in the northern part of the Bothnian Sea near the Quark. The maximum value of SWH simulated by WAM_IC30 and WAM_IC70 was 5–6 m, whereas by WAM_NI30 and WAM_NI70, it was 2.5–4.5 m (**Figure 6**).

The situation resulting in the largest differences in the maximum values is shown in more detail in **Figure 10**. Although NEMO-Nordic simulates the ice extent fairly well, there was slightly more ice in the northern part of the Bothnian Sea than in the FMI ice charts. Because of this, WAM_NI30 and WAM_NI70 simulated no waves in the area where WAM_IC30 and WAM_IC70 produced the maximum values. This resulted in an over 5 m difference in the SWH in the northern part of the Bothnian Sea. The difference in the January maximum values is naturally lower, since there are other high wind situations in which the sea area has also been free from ice in the WAM_NI30 and WAM_NI70.

Figure 10 also shows how the additional grid obstructions affect the simulation of the wave field. The WAM_IC70 and WAM_NI70 runs showed slightly smaller values of significant wave height in the southwestern Bothnian Sea, north of the area, which was ice covered in all runs, than the WAM_IC30 and WAM_NI30 runs. All simulations showed the close drift ice field (ice concentration over 70%), but only the method relying on grid obstructions captured the surrounding, very open, drift

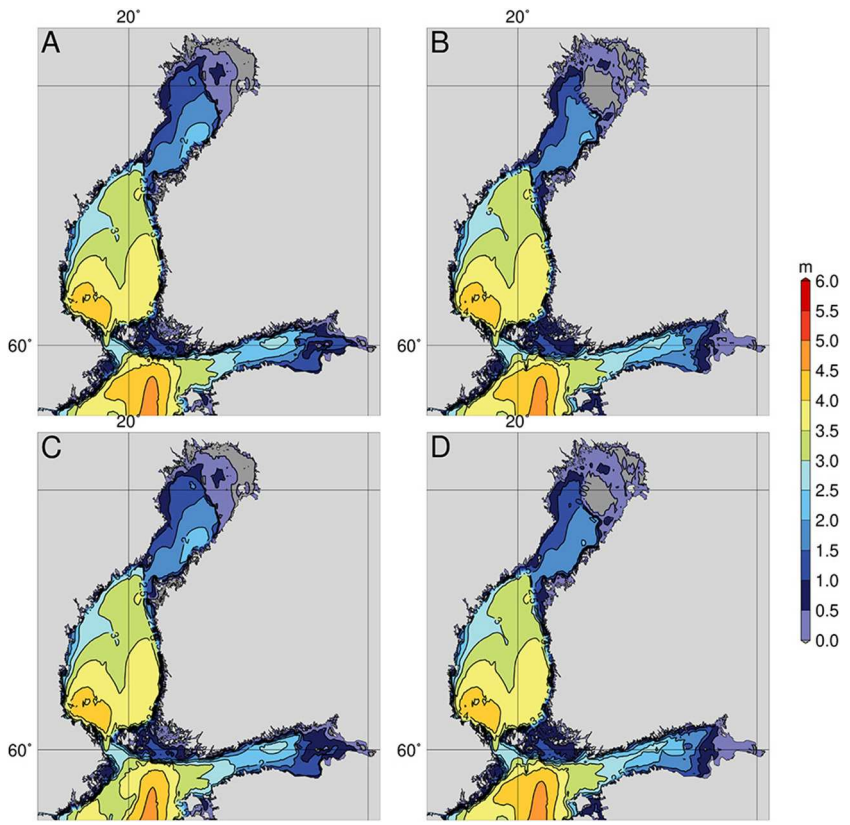

FIGURE 8 | Maximum values of significant wave height in March 2009–2012 for **(A)** WAM_IC30, **(B)** WAM_NI30, **(C)** WAM_IC70, and **(D)** WAM_NI70.

ice field (ice concentration less than 30%). The grid obstruction attenuates the wave energy in the grid cells that have partial ice cover according to the method presented in section 2.2. The effect of the additional grid obstruction is demonstrated even better between the WAM_NI30 and WAM_NI70 runs in the north-western part of the Bothnian Sea, where WAM_NI70 produces lower values of SWH than WAM_NI30, since it is also able to account for ice concentrations less than 30%.

5.3. Statistics at Wave Buoy Locations

We studied the monthly statistics in more detail at four locations. The locations were selected to be those of FMI's operational wave buoy locations in the Bothnian Bay, the Bothnian Sea, the northern Baltic Proper, and the Gulf of Finland (locations shown in **Figure 1**). These sites represent open sea conditions for each of the sub-basins in the northern Baltic Sea.

The monthly mean, maximum and exceedance values at these locations showed that the differences between the four wave model simulations were relatively small in the Bothnian Sea (**Figure 11**) and in the Northern Baltic Proper (not shown). In the Gulf of Finland, the different sources of ice information had only small effects on the mean, maximum, and exceedance values when the 30% threshold value for ice concentration was used (**Figure 11C**). However, there were larger differences between the WAM_IC70 and WAM_NI70 runs, which used the grid obstructions (**Figure 11F**).

In the Bothnian Bay, the differences between the simulations were larger than at the other locations (**Figures 11A,D**). The largest differences were in March, when WAM_IC30 and WAM_IC70 gave c. 1.8 m as the maximum value, whereas WAM_NI30 and WAM_NI70 gave 0 m. The maximum value from the WAM_IC30 and WAM_IC70 is from a high wind situation on March 16, 2012. The 2012 ice winter was average, but the length of the ice season was shorter than on average (cf. section 3). In mid-March the ice edge was close to the Bothnian Bay buoy location and retreated northward on 15–16th, which allowed higher waves to propagate into this location. In the simulations WAM_NI30 and WAM_NI70, the area is totally ice covered during March, leading to a maximum SWH of 0 m.

The histograms and cumulative probability distribution curves for the four buoy locations also show that the differences between WAM_IC30 and WAM_NI30 simulations are largest in the Bothnian Bay (**Figure 12**). In the Bothnian Sea and the northern Baltic Proper, the differences are small, almost nonexistent. The WAM_IC70 and WAM_NI70 differed only slightly from the WAM_IC30 and WAM_NI30, respectively and are, therefore, excluded from this analysis. The histograms also demonstrate that, in the Bothnian Bay and the Gulf of Finland, the ice season has the strongest effect on the wave climate. In the Bothnian Bay 83–88%, of the SWH values during Jan–Apr are in the range 0.00–0.25 m, while the corresponding percentages for the Gulf of Finland wave buoy location are 67–70%. In the

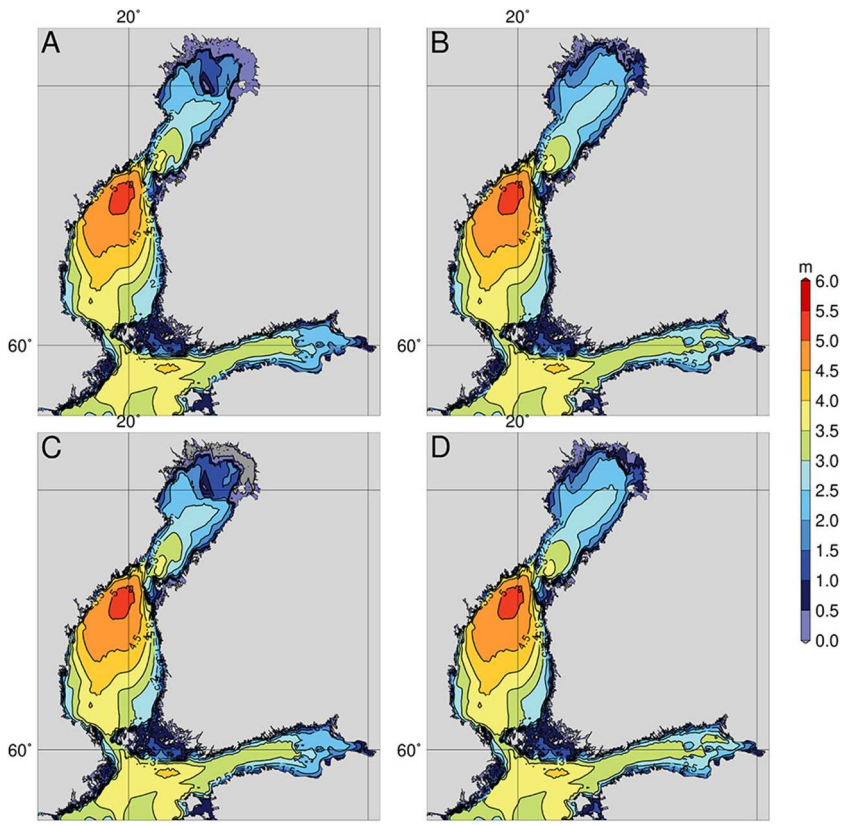

FIGURE 9 | Maximum values of significant wave height in April 2009–2012 for **(A)** WAM_IC30, **(B)** WAM_NI30, **(C)** WAM_IC70, and **(D)** WAM_NI70.

Bothnian Sea buoy location, only 34% and in the Northern Baltic Proper, c. 12%.

6. WAVE FORECASTING IN SEASONALLY ICE-COVERED SEAS

Even though the different approaches to account for ice in the wave model induced only relatively small differences in the hindcast statistics, the effects can be considerably larger in operational wave forecasting. When using the method adapted from Tolman (2003), the threshold for a point to be completely excluded from the calculations is set to a relatively high value, such as 70%. Smaller ice concentrations are accounted for by additional grid obstruction, which allows for the forecasting of waves in areas that have only a partial ice cover, such as open drift ice fields. The grid obstructions also, at least to some extent, account for how the drift ice attenuates the waves.

To demonstrate what consequences the various ways to account for the ice conditions can have on the modeled wave field, we examined a high wind and wave situation from March 2011 in more detail. This occasion was discussed in section 5.2, since it caused large differences in the monthly maximum values in the northern Baltic Proper. The two approaches to implement the FMI ice chart data in the wave model produced different simulated significant wave heights in both the Bothnian Sea and in the northern Baltic Proper on March 9, 2011 at 18 UTC (**Figure 13**, upper panel). In the Bothnian Sea there was drift ice with a 40–60% concentration, which means that the 30% threshold completely excluded these points from the calculations. Still, the significant wave height in these areas was 0.5–1 m when the 70% threshold and additional grid obstructions were used. Conversely, in the northern Baltic Proper north off the Gotland island, there was a drift ice field with a concentration of only 10–30%. With the 30% threshold value, these grid points were considered as completely open water, while the grid obstructions captured the effect of the drift ice on the growth and propagation of the waves, thus leading to considerably lower wave heights (**Figure 13**, upper panel).

As discussed earlier, the ice conditions shorten the fetch over which the waves grow, while also changing the fetch geometry. On Jan 11, 2009, there was a high wind situation in the Gulf of Bothnia inducing over 3 m significant wave heights both in the Bothnian Sea and in the Bothnian Bay (**Figure 13**, lower left panel). During this occasion, the NEMO-Nordic simulated ice in the Quark and in the eastern part of the Bothnian Bay, although no ice was present in the FMI ice charts. The NEMO-ice completely changed the fetch conditions in the Bothnian Bay, leading to lower significant wave heights (**Figure 13**, lower right panel). These types of differences in the ice concentrations can also have quite a significant impact on the exceedance values and maximum values of the significant wave height, as already shown

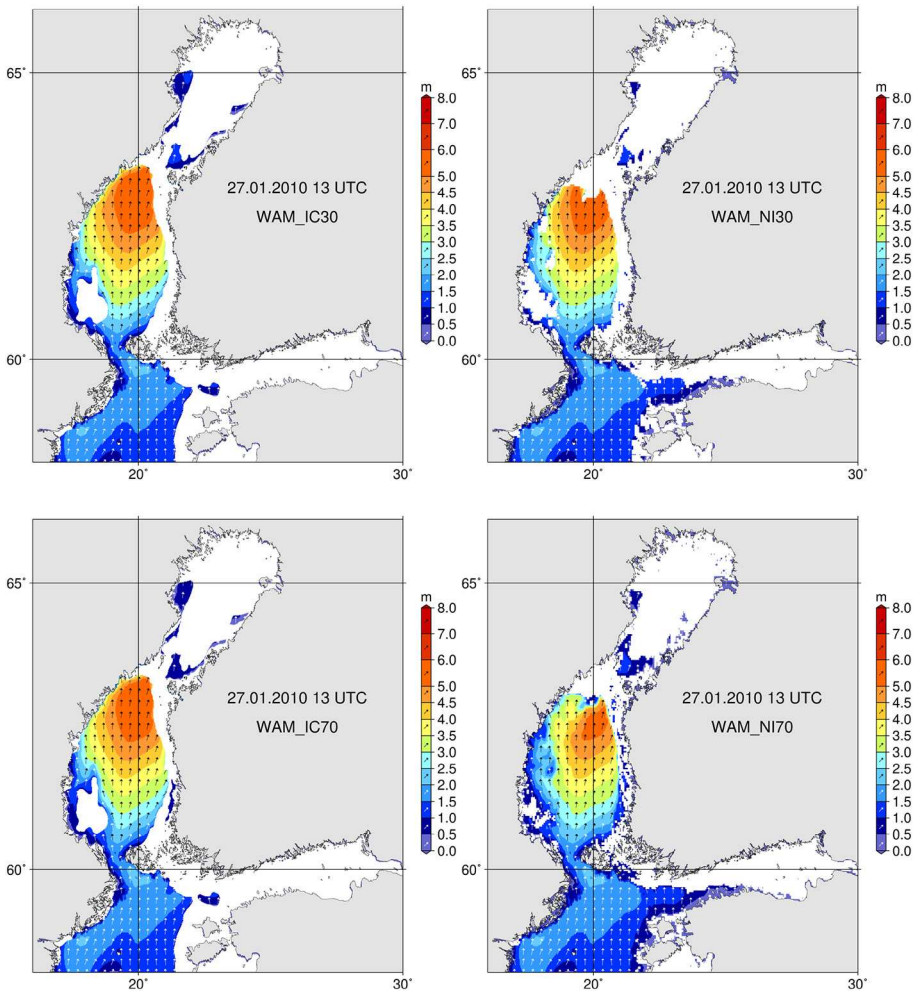

FIGURE 10 | Wave hindcast for 27.1.2010 13 UTC with WAM_IC30 **(Upper left)**, WAM_NI30 **(Upper right)**, WAM_IC70 **(Lower left)**, and WAM_NI70 **(Lower right)**.

in section 5.3. Nevertheless, the differences would most likely be minimized if a longer hindcast period was used.

7. DISCUSSION

We presented two different methods to handle ice conditions in wave model simulations and ran the wave model WAM using two different sources for ice concentrations, namely FMI ice charts and an SMHI NEMO-Nordic hindcast. The results showed that, in most of the areas, the choice of data source had a larger impact on the results than the choice of the method with which the ice concentrations were handled in the wave model. This is quite expected, since the two ways to handle ice only result in small differences in the wave field, typically near the ice edge.

We did not evaluate the accuracy of the ice concentrations used in this study. The ice concentrations simulated by NEMO-Nordic have been evaluated in Pemberton et al. (2017). They found, that, overall the NEMO-Nordic simulated ice concentrations with relatively good accuracy, but the ice extent was slightly overestimated in the Gulf of Bothnia, and the ice winter started and ended earlier compared to the observations. The FMI ice charts or ice charts produced by the other operational centers in the Baltic are the best available information of the Baltic Sea ice conditions, as they are based on satellite data, *in-situ* measurements, and expert evaluations. Also, the validation against altimeter data showed that the WAM runs, using FMI ice chart data, were more accurate than those forced with NEMO-Nordic ice concentrations. The differences in the monthly mean values, however, were relatively small and mostly related to the slightly larger ice extent in the NEMO-Nordic hindcasts compared to the FMI ice charts. This resulted in somewhat smaller values of mean SWH for model runs forced with NEMO ice, especially in the Bothnian Bay and in the Gulf of Finland. The monthly maximum values showed larger differences, up to 3.2 m in the northernmost part of the Bothnian Sea, and there were also significant differences in other areas. For example, the more detailed analysis of the wave statistics at the buoy locations showed that, in the Bothnian Bay, the four simulations lead to considerable differences in the maximum and 1% exceedance values. The analysis of the maximum values for

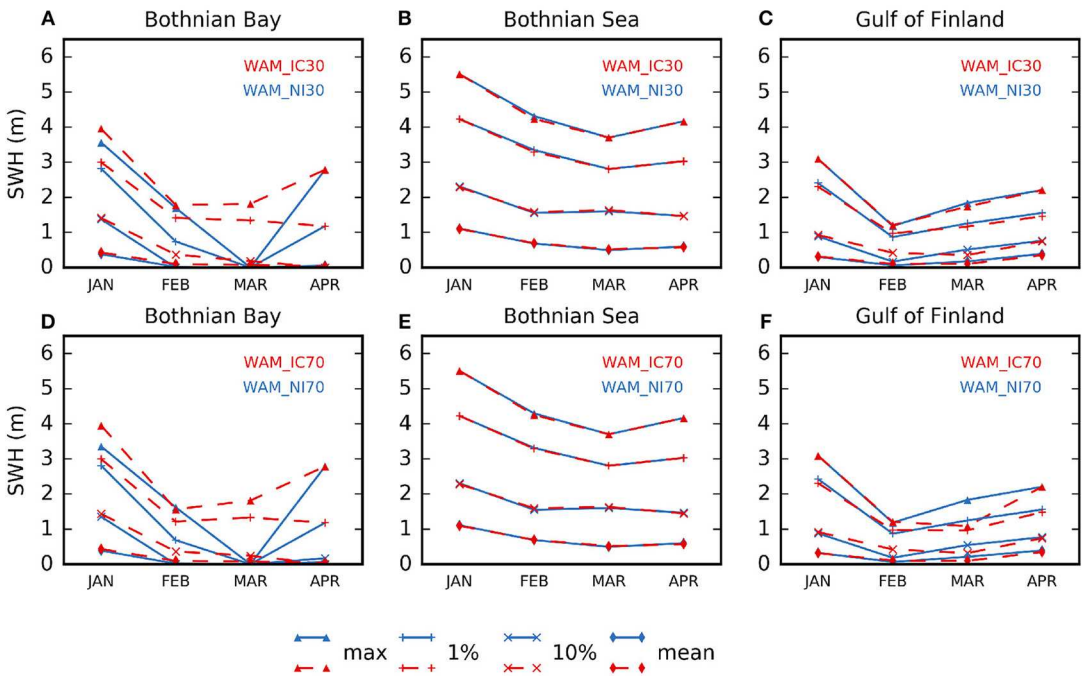

FIGURE 11 | Monthly mean and maximum values of SWH and 1% and 10% exceedance values at 3 locations in the Baltic Sea (locations shown in **Figure 1**). **(A,D)** show statistics at the Bothnian Bay buoy location, **(B,E)** at the Bothnian Sea buoy location and **(C,F)** at the Gulf of Finland buoy locations. See **Table 1** for further details about the model configurations.

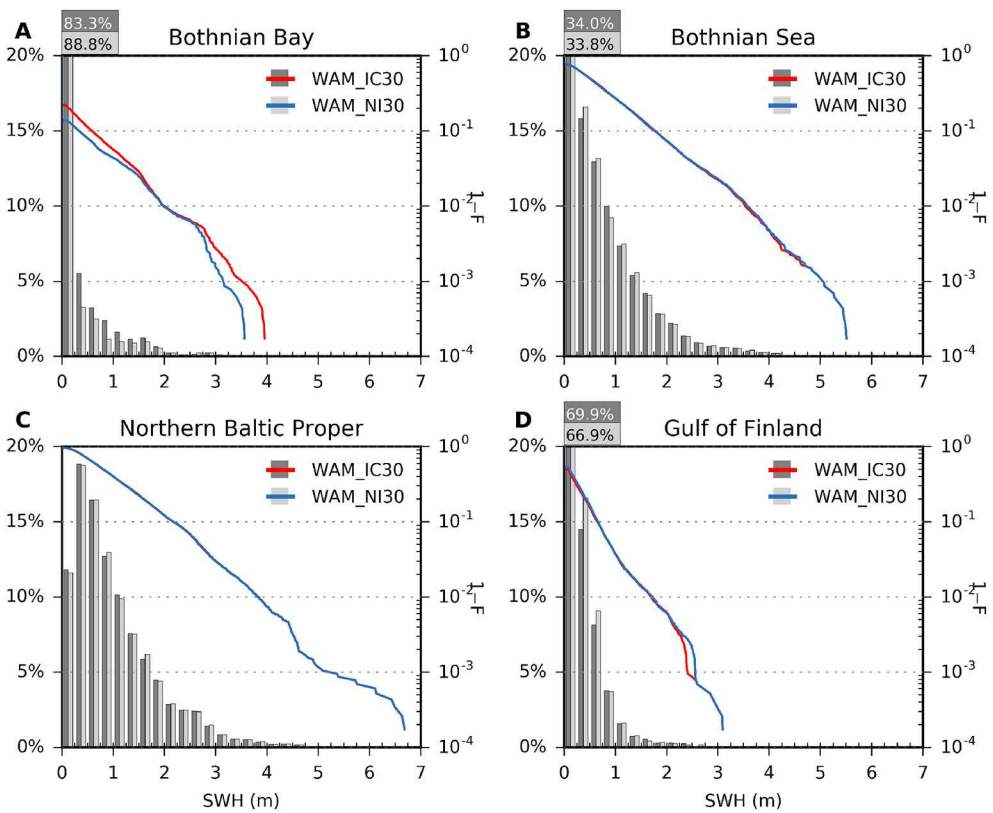

FIGURE 12 | Histograms and cumulative probability distributions of hindcast SWH at the four wave buoy locations **(A)** Bothian Bay, **(B)** Bothian Sea, **(C)** Northern Baltic Proper and **(D)** Gulf of Finland (locations shown in **Figure 1**). Values for configuration WAM_IC30 are presented with dark gray and red and for WAM_NI30 with light gray and blue. The percentage of the first bin (0–0.25 m) is presented in the upper-left corner of the plot with corresponding color.

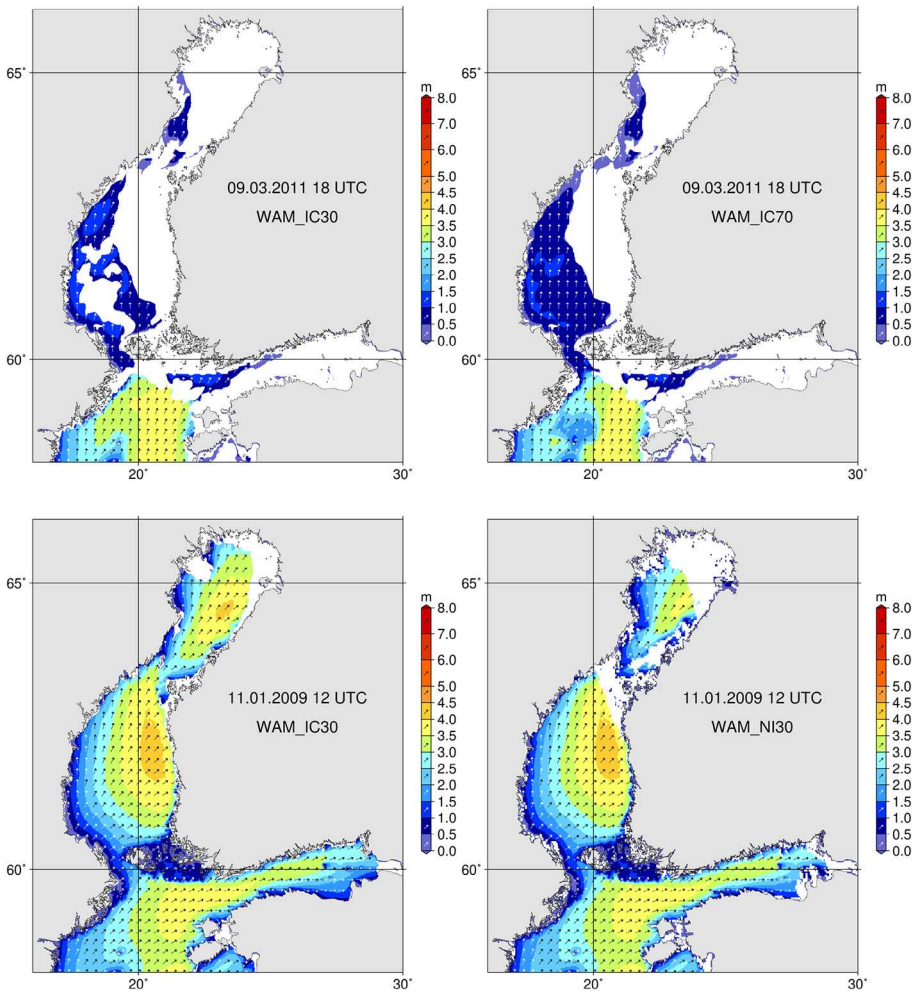

FIGURE 13 | Wave hindcast for 9.3.2011 18 UTC with WAM_IC30 **(Upper left)** and WAM_IC70 **(Upper right)** and for 11.1.2009 12 UTC with WAM_IC30 **(Lower left)** and WAM_NI30 **(Lower right)**.

the northern Baltic Sea indicated that similar differences between the WAM_IC and WAM_NI runs also exist in the Quark area and in the coastal areas of the Bothnian Sea.

Because the Baltic Sea is small, the changes in fetch are important for the generation of waves. The location of the ice edge, therefore, becomes an important factor in the high-wind and storm situations, as demonstrated in section 5.2 (**Figure 10**) and section 6 (**Figure 13**, lower panel). We also showed that, under such weather conditions the use of obstruction grids might become important, since they can capture the attenuating effect of possible drift ice fields that have a relatively low ice concentration. However, it is difficult to evaluate, the accuracy of the wave simulations near the ice edge or in the drift ice field, since there are no measurements to compare the results against. To further develop the wave modeling during the Baltic Sea ice winter, measurements with instruments that are able to measure waves in the ice field and near the ice edge are needed.

In this study, we only modeled the months that have significant ice cover in the Baltic Sea, namely Jan–Apr. Therefore, only the differences in the monthly statistics could be studied. Most of the earlier studies in the Baltic Sea handle either annual or seasonal statistics. We estimate that the differences in the annual wave statistics will be smaller than the ones presented here for the monthly statistics, since the ice season only covers less than 6 months of the year and outside ice season, the different methods results to exactly the same SWH. In seasonal statistics, the differences can be significant, for winter and spring seasons, at least in the Bothnian Bay and the Gulf of Finland. However, 4 years is a relatively short time to study maximum values, especially in monthly stratified statistics. The differences will most likely diminish when longer periods are used.

The temporal resolution of the ice data used in this study was 1 day. In operational forecasting, when the ice is taken from a 3D ocean-ice model, such as NEMO-LIM3, the ice fields could be updated hourly. This means that the changes in the ice conditions during the forecast run can be accounted for with higher temporal resolution, leading to better estimates of the

SWH, especially in high-wind and storm situations, when there can be quite rapid changes in the ice concentration.

The data and methods used in this study only included ice concentrations. Other parameters, such as ice thickness, can be important in the wave–ice interactions. For example, thin new ice is more easily broken and fragmented by waves than, for example, thick landfast ice. However, accounting for these types of interactions, a coupled wave–ice model is needed.

8. CONCLUSIONS

We made a wave hindcast study to illustrate how different methods to handle ice conditions in the wave model simulations and different sources for ice data affect the wave model results, wave hindcast statistics, and operational wave forecasts.

The comparison against altimeter data showed that the accuracy of the wave hindcasts during the ice season was better, when FMI ice charts were used as the source of ice concentrations compared to the runs where ice concentrations were taken from SMHI NEMO-Nordic simulations.

There were only small differences in the monthly mean values of SWH between the four runs. The differences were up to 0.3 m and were seen in the Bothnian Bay, the Quark, the northern part of the Bothnian Sea, and the eastern part of the Gulf of Finland. In the Bothnian Bay, the use of NEMO ice data lead to smaller mean values for all the months (Jan–Apr) studied in this paper. In other areas, the mean values produced by runs using NEMO ice data could also be higher than those using data from FMI ice charts. In the maximum values, the differences were larger, up to 3.2 m, since in individual high-wind or storm situations, the location of ice edge and the existence and location of drift ice fields becomes important. Also, in the exceedance values studied at the buoy locations, representing the open sea conditions in each of the northern Baltic Sea sub-basins, there were significant differences in the Bothnian Bay and in the Gulf of Finland. In the Bothnian Sea and Northern Baltic Proper buoy locations, the differences between the four hindcast runs were insignificant.

The ice charts were naturally found to be a better source for ice data in the Baltic Sea wave hindcasts than the NEMO-Nordic ice concentrations. However, the differences were quite small in the mean values and when running wave hindcasts for periods for which ice charts data are not available in digitized form, using data from 3D ocean–ice model leads to sufficient accuracy in most of the Baltic Sea sub-basins. Furthermore, ice concentration forecasts provided by a 3D ocean-ice model, might improve the wave forecasts accuracy in high wind situations, when there can be large changes in the ice field.

The use of the two different methods to handle ice concentrations in the wave model resulted only in small differences in the monthly statistics. However, in specific situations the two methods lead to significant differences in the hindcast wave field. Although, it was not possible to verify the accuracy of the wave hindcasts in areas and times these differences occurred, the possibility to provide wave forecast to partially ice-covered areas supports the use of handling ice as additional grid obstructions in operational wave forecasting.

AUTHOR CONTRIBUTIONS

LT had the original idea for this research work, and she performed the WAM simulations and most of the data analysis. HK was responsible for the model validation and formulating and analyzing the statistics at the buoy locations. HK and J-VB contributed to the analysis of the wave statistics. RH and AH performed the NEMO runs, from which the ice concentrations were used in the wave model simulations. RM developed the programs for analyzing the monthly mean and maximum statistics. JV analyzed the FMI ice chart data. KK enlightened the ways different types of statistics can be applied. LT and HK wrote the paper with help from all the co-authors.

FUNDING

This work has been supported by the Strategic Research Council at the Academy of Finland, project SmartSea (grant number 292 985) and E.U. Copernicus Marine Service Programme.

ACKNOWLEDGMENTS

We thank SMHI for making the wind forcing from SMHI-RCA4 down-scaled ERA Interim available to us. Altimeter SWH data was extracted from the merged altimeter dataset produced by IFREMER.

REFERENCES

Battjes, J. A., and Janssen, J. P. F. M. (1978). "Energy loss and set-up due to breaking of random waves," In *Proceedings of the 16th International Conference on Coastal Engineering* (New York, NY: American Society of Civil Engineers), 569–587.

Berg, P., Döscher, R., and Koenigk, T. (2013). Impacts of using spectral nudging on regional climate model RCA4 simulations of the Arctic. *Geosci. Model Dev.* 6, 849–859. doi: 10.5194/gmd-6-849-2013

Björkqvist, J.-V., Lukas, I., Alari, V., van Vledder, G. P., Hulst, S., Pettersson, H., et al. (2018). Comparing a 41-year model hindcast with decades of wave measurements from the Baltic Sea. *Ocean Eng.* 152, 57–71. doi: 10.1016/j.oceaneng.2018.01.048

Cornett, A. (2008). "A global wave energy resource assesment," in *Proceedings of the Eighteenth (2008) International Offshore and Polar Engineering Conference* (Vancouver, BC), 318–326.

Dee, D. P., Uppala, S. M., Simmons, A. J., Berrisford, P., Poli, P., Kobayashi, S., et al. (2011). The ERA-Interim reanalysis: configuration and performance of the data assimilation system. *Q. J. R. Meteorol. Soc.* 137, 553–597. doi: 10.1002/qj.828

Doble, M. J., and Bidlot, J.-R. (2013). Wave buoy measurements at the Antarctic sea ice edge compared with an enhanced ECMWF WAM:

Progress towards global waves-in-ice modelling. *Ocean Model.* 70, 166–173. doi: 10.1016/j.ocemod.2013.05.012

Gorman, R. M., Bryan, K. B., and Laing, A. K. (2003). Wave hindcast for the New Zeland region: deep-water wave climate. *N. Z. J. Mar. Freshw. Res.* 37, 589–612. doi: 10.1080/00288330.2003.9517191

Günther, H., Rosenthal, W., Stawarz, M., Carretero, J., Gomez, M., Lozano, I., et al. (1998). The wave climate of the Northeast Atlantic over the period 1955-1994: the WASA wave hindcast. *Glob. Atmos Ocean Syst.* 6, 121–163.

Hasselmann, K., Barnett, T. P., Bouws, E., Carlson, H., Cartwright, D. E., Enke, K., et al. (1973). Measurements of wind-wave growth and swell decay during the Joint North Sea Wave Project (JONSWAP). *Dtsch. Hydrogr. Zeitschrift* 12, 1–95.

Hasselmann, S., Hasselmann, K., Allender, J. H., and Barnett, T. P. (1985). Computations and parameterizations of the nonlinear energy transfer in a gravity-wave spectrum. Part II: Parameterizations of the nonlinear energy transfer for application in wave models. *J. Phys. Oceanogr.* 15, 1378–1391.

Hordoir, R., Axell, L., Höglund, A., Dieterich, C., Fransner, F., Gröger, M., et al. (2019). Nemo-Nordic 1.0: a NEMO-based ocean model for the Baltic and North seas-research and operational applications. *Geosci. Model. Dev.* 12, 363–386. doi: 10.5194/gmd-12-363-2019

Janssen P. A. E. M. (1991). Quasi-linear theory of wind-wave generation applied to wave forecasting. *J. Phys. Oceanogr.* 21, 1631–1642.

Järvenoja, S., and Tuomi, L. (2002). Coupled atmosphere-wave model for FMI and FIMR. *Hirlam Newslett.* 40, 9–22.

Komen, G. J., Cavaleri, L., Donelan, M., Hasselmann, K., Hasselmann, S., and Janssen, P. A. E. M. (1994). *Dynamics and Modelling of Ocean Waves*. Cambridge: Cambridge University Press.

Kudryavtseva, N. A., and Soomere, T. (2016). Validation of the multi-mission altimeter wave height data for the Baltic Sea region. *Estonian J. Earth Sci.* 65, 161–175. doi: 10.3176/earth.2016.13

Löptien, U., Mårtensson, S., Meier, H. E. M., and Höglund, A. (2013). Long-term characteristics of simulated ice deformation in the Baltic Sea (1962-2007). *J. Geophys. Res.* 118, 801–815. doi: 10.1002/jgrc.20089

MacLaren Plansearch Limited (1991). *Wind and Wave Climate Atlas Volume I, The East Coast of Canada*. Transport Canada Publication No. TP10820E.

Monbaliu, J., Padilla-Hernández, R., Hargreaves, J. C., Albiach, J. C. C., Luo, W., Sclavo, M., et al. (2000). The spectral wave model, WAM, adapted for applications with high spatial resolution. *Coast. Eng.* 41, 41–62. doi: 10.1016/S0378-3839(00)00026-0

Nilsson, E., Rutgersson, A., Dingwell, A., Björkqvist, J.-V., Pettersson, H., Axell, L., et al. (2019). Characterization of wave energy potential for the Baltic Sea with focus on the Swedish Exclusive Economic Zone. *Energies* 12:793. doi: 10.3390/en12050793

Pemberton, P., Löptien, U., Hordoir, R., Höglund, A., Schimanke, S., Axell, L., et al. (2017). Sea-ice evaluation of NEMO-Nordic 1.0: a NEMO–LIM3.6-based ocean–sea-ice model setup for the North Sea and Baltic Sea. *Geosci. Mod. Dev.* 10, 3105–3123. doi: 10.5194/gmd-10-3105-2017

Queffeulou, P. (2004). Long term validation of wave height measurements from altimeters. *Mar. Geodesy* 27, 495–510. doi: 10.1080/01490410490883478

Queffeulou, P. (2013). *Cryosat-2 IGDR SWH Assessment Update*. Technical Report.

Queffeulou, P., Ardhuin, F., and Lefèvre, J.-M. (2011). "Wave height measurements from altimeters: validation status and applications," in *OSTST Meeting, 19–21 October, 2011* (San Diego, CA).

Queffeulou, P., and Croizè-Fillon, D. (2017). *Global Altimeter SWH Data Set*. Technical report, Laboratoire d'Océanographie Physique et Spatiale, IFREMER, Plouzané.

Reistad, M., Breivik, Ø., Haakenstad, H., Aarnes, O. J., Furevik, B. R., and Bidlot, J.-R. (2011). A high-resolution hindcast of wind and waves for the North Sea, the Norwegian Sea, and the Barents Sea. *J. Geophys. Res.* 116:C05019. doi: 10.1029/2010JC006402

Rogers, W., and Orzech, M. D. (2013). *Implementation and Testing of Ice and mud Source Functions in Wavewatch III.*® NRL Memo. Rep. NRL/MR/7320-13-9462, Naval Research Laboratory, Washington, DC.

Rogers, W., and Zieger, S. (2014). "New wave-ice interaction physics in WAVEWATCH III®," in *Proceedings of 22nd IAHR International Symposium on Ice* (Singapore: International Association for Hydro-environment Engineering and Research (IAHR)).

Rogers, W. E., Thomson, J., Shen, H. H., Doble, M. J., Wadhams, P., and Cheng, S. (2016). Dissipation of wind waves by pancake and frazil ice in the autumn Beaufort Sea. *J. Geophys. Res.* 121, 7991–8007. doi: 10.1002/2016JC012251

Squire, V. A. (2018). A fresh look at how ocean waves and sea ice interact. *Philos. Trans. R. Soc. Lond. A Math. Phys. Eng. Sci.* 376:2129. doi: 10.1098/rsta.2017.0342

Squire, V. A., Dugan, J. P., Wadhams, P., Rottier, P. J., and Liu, A. K. (1995). Of ocean waves and sea ice. *Annu. Rev. Fluid Mech.* 27, 115–168. doi: 10.1146/annurev.fl.27.010195.000555

Swail, V., Cardone, V., Ferguson, M., Gummer, D., Harris, E., Orelup, E., et al. (2006). "The MSC50 wind and wave reanalysis," in *9th International Wind and Wave Workshop, September 25–29* (Victoria, BC).

Tolman, H. L. (2003). Treatment of unresolved islands and ice in wind wave models. *Ocean Model.* 5, 219–231. doi: 10.1016/S1463-5003(02)00040-9

Tonboe, R., Lavelle, J., Pfeiffer, R.-H., and Howe, E. (2016). *Product User Manual for OSI SAF Global Sea Ice Concentration*. Technical report. Product OSI-401-b, Version 1.4.

Tuomi, L. (2014). *On modelling waves and surface mixing in the Baltic Sea* (Ph.D. thesis). Finnish Meteorological Institute - Contributions, No. 104. Helsinki, Finland.

Tuomi, L., Kahma, K. K., and Pettersson, H. (2011). Wave hindcast statistics in the seasonally ice-covered Baltic Sea. *Boreal Environ. Res.* 16, 451–472.

Tuomi, L., Pettersson, H., Fortelius, C., Tikka, K., Björkqvist, J.-V., and Kahma, K. K. (2014). Wave modelling in archipelagos. *Coast. Eng.* 83, 205–220. doi: 10.1016/j.coastaleng.2013.10.011

Tuomi, L., Vähä-Piikkiö, O., Siili, T., and Alari, V. (2018). "CMEMS Baltic Monitoring and Forecasting Centre: high-resolution wave forecasts in the seasonally ice-covered Baltic Sea," in *Operational Oceanography serving Sustainable Marine Development. Proceedings of the Eight EuroGOOS International Conference. 3-5 October 2017, Bergen, Norway*, eds E. Buch, V. Fernàndez, D. Eparkhina, P. Gorringe, and G. Nolan (Brussels: EuroGOOS).

Vähä-Piikkiö, O., Tuomi, L., and Huess, V. (2019). *Quality Information Document (QUID) Baltic Sea Wave Analysis and Forecasting Product BALTICSEA_ANALYSIS_FORECAST_WAV_003_010: issue 2.0.* Technical report.

WAMDI (1988). The WAM model–a third generation ocean wave prediction model. *J. Phys. Oceanogr.* 18, 1775–1810.

WMO (2015). *WMO Sea-Ice Nomenclature, Volumes I, II and III.* Technical Report WMO-No.259. JCOMM Expert Team on Sea Ice.

Conflict of Interest Statement: RM was employed by the Finnish Meteorological Institute at the time of the study, but has since moved to Eniram Ltd. This has no impact on the research conducted.

The remaining authors declare that the research was conducted in the absence of any commercial or financial relationships that could be construed as a potential conflict of interest.

frontiers in Earth Science

ORIGINAL RESEARCH
published: 13 August 2019
doi: 10.3389/feart.2019.00204

The Past and Future Estimates of Climate and Streamflow Changes in the Western Dvina River Basin

Irina Danilovich[1], Sergey Zhuravlev[2,3]*, Lubov Kurochkina[2] and Pavel Groisman[4,5]*

[1] Institute for Nature Management, National Academy of Sciences of Belarus, Minsk, Belarus, [2] State Hydrological Institute, Saint Petersburg, Russia, [3] Saint Petersburg State University, Saint Petersburg, Russia, [4] National Centers for Environment Information, North Carolina State University, Asheville, NC, United States, [5] Hydrology Science and Services Corporation, Asheville, NC, United States

The study presents an assessment of the recent and projected changes of the middle and upper Western Dvina River runoff and regional climate during the 20th and 21st centuries. For this assessment, we used historical runoff data, the output of EURO-CORDEX consortium calculations for scenarios RCP4.5 and RCP8.5, and hydrological model "Hydrograph." Analysis of monthly runoff data for the 1945–2015 period revealed positive trends for each of the five months from December to April. These trends are statistically significant at the 0.05 level. No significant trends were found for other months. Significant negative trends were established for spring flood peak discharges (from −69 to −88 m^3 s^{-1} per 10 years). Usually, maximum discharges are observed during spring floods. Minimum discharges during winter low-water period were increased by 6 m^3 s^{-1} per 10 years. The annual runoff trend was statistically significant only at the Polotsk gauging station (9.5 m^3 s^{-1} per 10 years). To the end of the current century over the study region, estimates of projected meteorological parameters (air temperature and precipitation) show positive tendencies of air temperature (from 2.4°C to 4.7°C depending on scenario) and precipitation (up to 15 to 30 mm). Changes of seasonal and annual temperature and precipitation vary depending on the models and scenarios used. The strongest changes were noticed for the RCP8.5 scenario. The greatest changes within each scenario were revealed for the winter and spring seasons. It is projected that during the 2021–2100 period according to both RCP scenarios, annual discharges will not change in the upper part of the Western Dvina River Basin and increase by 10–12% in its lower part. The maximum spring flood discharges in both RCP scenarios are expected to decrease by 25%. The minimum runoff of winter low-flow period is expected to increase by up to 60 to 90% above the present long-term mean values.

Keywords: climate, streamflow, Western Dvina River, model, trend, change scenarios

OPEN ACCESS

Edited by:
Markus Meier,
Leibniz Institute for Baltic Sea Research (LG), Germany

Reviewed by:
Jukka Käyhkö,
University of Turku, Finland
Xander Wang,
University of Prince Edward Island, Canada

****Correspondence:***
Irina Danilovich
irina-danilovich@yandex.ru
Sergey Zhuravlev
hydromod@gmail.com

Specialty section:
This article was submitted to Interdisciplinary Climate Studies, a section of the journal Frontiers in Earth Science

Received: *14 January 2019*
Accepted: *25 July 2019*
Published: *13 August 2019*

Citation:
Danilovich I, Zhuravlev S, Kurochkina L and Groisman P (2019) The Past and Future Estimates of Climate and Streamflow Changes in the Western Dvina River Basin. Front. Earth Sci. 7:204. doi: 10.3389/feart.2019.00204

INTRODUCTION

The Baltic Sea Basin belongs to regions with a relatively high availability of water resources and possesses a dense hydrographic network. The transboundary location of the major rivers in the Baltic Sea Basin promotes intensive use of the international freshwater sources. Rivers and lakes are used for population and industry water supply, energy production, and shipping. Water resource

management requires careful revisions and regular assessments of hydrological regime changes as well as analyses and accounting for the controlling climate factors.

The present research work is a regional case study of climatic and hydrological changes within the eastern part of the Baltic Sea Basin during the recent decades and for the rest of the 21st century. The study object is the upstream part of the Western Dvina (or Zapadnaya Dvina, or Daugava) River Basin, which is located within the boundaries of two countries – Russia and Belarus. We investigated the temporal and spatial variations in hydroclimatic conditions across the Basin having two primary objectives:

(1) to assess annual, seasonal and monthly historical trends in hydrological variables affecting river flows using hydrological instrumental time series for the 1945–2015 time period; and
(2) to assess the projected decadal trends of the hydroclimatic variables in the Basin for the 2021–2100 period.

Several groups of authors have previously documented hydroclimatic changes in the Baltic Sea Basin and particularly in the Western Dvina River Basin. The detailed assessment of climatic change for northern Europe was provided by the BACC Author Team (2008, 2015). The Team studied the past, present, and projected future changes in atmospheric, hydrological and oceanographic conditions over the Baltic Sea Basin and assessed the observed and potential impacts of these changes on natural environment and socio-economic conditions. Hydrological studies within the BACC collaboration provided valuable information for the entire Sea Basin, as well as for individual countries.

The regional peculiarities of streamflow formation in the Baltic Sea Basin during the last decades according to Stahl et al. (2010) consist in positive trends with increasing streamflow in winter months in most catchments of the Basin, while in spring and summer months, strong negative trends were found (decreasing streamflow and shift toward drier conditions).

Regional pattern of changes was provided by Hisdal et al. (2010) and Wilson et al. (2010). They showed the trends toward increased annual, winter and spring streamflow over many rivers of the Sea Basin. The tendency for a decrease in annual discharge in the southern catchments was recognized by Gailiušis et al. (2011) and Hansson et al. (2011). Reihan et al. (2007) have reported a significant increase in winter river discharge and a tendency for decreasing spring floods for the east Baltic States (excluding Russia and Belarus). Kriauciuniene et al. (2012) found no significant change in runoff in 1991–2006 relative to the reference period. An increasing trend in annual mean discharge for the 1961–2000 period was found for Latvian rivers and the increasing trends were statistically significant for many rivers including Daugava (Kıaviņš and Rodinov, 2008; Kıaviņš et al., 2008). Trends in the annual maximum and minimum discharges for the major rivers Daugava, Lielupe, Venta, Gauja, and Salaca indicate a statistically significant decrease in maximum discharge.

Studies of streamflow fluctuations due to climate change within the northwest Russia (Frolova et al., 2017; Nasonova et al., 2018), and Belarus (Polishchuk and Chekan, 2009; Volchek and Gryadinova, 2010; Volchek and Shelest, 2012; Volchek and Parfomuk, 2013; Loginov et al., 2014; Lopukh and Partasenok, 2014) show no significant long-term trends in annual streamflow. Meanwhile, the intra-annual distribution of runoff has changed significantly during the last decades. In particular, runoff during winter low-flow periods increased significantly. This increase was connected with the growing repeatability of thaws, which led to frequent floods occurring during winter low-water period, while spring runoff and snowmelt floods were decreasing due to the exhausted water supply in snow prior to the spring season. However, the general pattern of described changes in water regime varies from year to year due to the increasing of frequency of extreme flow events and of their duration.

The majority of hydrological projections in the Baltic Sea Basin have been done at national levels. The decrease of annual and seasonal streamflow by 2–40% according to the Special Report on Emissions Scenarios (SRES) scenario A1B, A2 and B2 was projected for the rivers in Norway (Beldring et al., 2008), Finland (Veijalainen et al., 2010), Latvia (Apsīte et al., 2011), Lithuania (Kriaučiūnienė et al., 2008) and Poland (Szwed et al., 2010). The annual streamflow increase by 9–34% has been projected for Denmark (Thodsen et al., 2008; Jeppesen et al., 2009). Large uncertainties in the future hydrological regime were reported for Sweden (Yang et al., 2010; Olsson et al., 2011) and projected the streamflow changes within ± 30% (Arheimer and Lindström, 2015). Donnelly et al. (2017) reported the runoff increase in the northern Europe. Roudier et al. (2015) found the relatively strong decrease in flood magnitude in some parts of Finland, NW Russia and north of Sweden. According to Thober et al. (2018), the floods' intensity decreased by 5–12% in northern Europe. In the eastern part of the Baltic Sea Basin, the current changes in the hydrological regime observed within the Belorussian territory during the past decades (increase of winter and decrease of spring streamflow) are projected to continue for four major river basins of the country (Volchek et al., 2017). The estimates of projected runoff changes over the Russian Northwest show a considerable change of seasonal runoff dynamics for the Volga (Georgievskiy et al., 2018) and the Northern Dvina Basins (Krylenko et al., 2015).

The conducted researches showed the detailed assessment of historical and projected hydroclimatic regime changes in the Baltic Sea Basin. Nevertheless, large-scale studies often describe the general changes without regional details or are presented at the national level and are limited by administrative boundaries cutting the original water system. As a result, there were no regional assessments of possible change in hydrological regime for the entire Western Dvina River Basin. That is why the aim of our study is to estimate current and future changes in climatic and hydrological regimes of this transboundary river basin within at least two countries, to assess their directions and significance, and to analyze possible reasons caused these transformations.

The present study is a contribution to the Baltic Earth Science Plan within the topic "Regional variability of water and energy exchanges in the Baltic Sea region."

STUDY AREA

The Western Dvina River Basin is about 87900 km^2. The basin has common borders with the Lielupe river basins (Latvia), the Neman (Belarus and Lithuania) and the Dnieper (Russia, Belarus and Ukraine) in the south and the Volga River (Russia) in the east. The Western Dvina River Basin's length is the highest in the east-west direction with a basin's convexity turned to the south. Basin's length is about 700 km, width on average is 120 km. The largest part of the catchment is shared almost equally between Russia, Belarus and Latvia. The common length of the Western Dvina River is about 1020 km. The location of the study Basin is presented on the **Figure 1**.

There are many lakes within the Basin; the lake area percentage is about 3%. The wetland fraction riches 14%, 4% among them are presented by pure bogs and 10% are extra-wet forests, bushes and meadows. In general, about 50% of the Basin's area is occupied by forests, 4% by bogs, 3% by lakes, and 42% by agricultural lands.

DATA AND METHODS

Data Sources

In this study, we used meteorological and hydrological data of different origin. The first type of data was obtained from the hydrometeorological network of instrumental observations belonging to the State Hydrometeorological Services of Russia and Belarus. It was used to estimate recent changes in climate and runoff of the study region. The dataset consists of:

(1) meteorological data of 18 stations (**Figure 2** and **Table 1**): time series of monthly and annual precipitation and surface air temperature;
(2) hydrological data of 21 stations (**Figure 2**): time series of monthly and annual streamflow, minimum discharges during winter and summer low-water periods, and maximum discharges during spring high-water periods.

The hydrological time series were used to define trends and to analyze the spatial distribution of monthly, minimum and maximum streamflow changes within the studied region as well as for the calibration of the hydrological model described below.

The second type of data was derived from climate models, i.e., from the regional downscaled dataset delivered by EURO-CORDEX consortium. We used daily mean values of air temperature and precipitation and calculated monthly, seasonal, and annual means from 10 to 11 climate models for each characteristic and scenario. The ensemble median was used as generalizing characteristic of projected climatic conditions over the River Basin.

FIGURE 1 | Location of the study area.

FIGURE 2 | Stations in the Western Dvina River Basin with instrumental observations of meteorological and hydrological characteristics.

TABLE 1 | Meteorological stations in the Baltic Sea part of Russia and Belarus (numbers in the table correspond to numbers in **Figure 2**).

N	Stations within the Russian part	N	Stations within the Belarusian part
1	Velizh	10	Verhnedvinsk
2	Smolensk	11	Vitebsk
3	Toropets	12	Senno
4	Velikiye Luki	13	Ezerische
5	Bely	14	Dokshitsy
6	Ostashkov	15	Lepel
7	Rzhev	16	Lyntupy
8	Vyazma	17	Polotsk
9	Pushkinskie Gory	18	Sharkovschina

For its projections, the consortium uses the scenario of greenhouse gases concentrations of the RCP family (Representative Concentration Pathways) (Meinshausen et al., 2011) according to the report of the Intergovernmental Panel Climate Change. For the present study, we used two such scenarios of radiative forcing: RCP4.5 (which corresponds to the concentration of 650 ppm) and RCP8.5 (1370 ppm).

For the analysis of climate projections over the Western Dvina River Basin, we selected the 2021–2100 period. The historical period of 1970–2000 was used for comparison with the current climate and the calculation of deviations from meteorological means.

Land use data were derived from the National Atlases of Belarus (Zhmoydyak, 2009), topographic maps, and digital soil map (Sanchez et al., 2009).

Methodology

The assessment of current changes included the calculations of intra-annual distribution, time series of synchronic fluctuations over the study basin, trend analysis, and the study of spatial peculiarities of runoff formation over the region.

The calculation of the intra-annual distribution of runoff was conducted based on monthly discharges time series, which firstly were merged by seasons and thereafter the seasonal values, were used to calculate seasonal streamflow ratio (percentage) to the runoff annual mean values.

Data analysis was conducted on a monthly basis to identify month-to-month variation in the selected hydroclimatic variables and to determine trend consistency within multiple months. However, the results were discussed and spatially analyzed only on a seasonal basis. The winter season was defined as December through February, spring was from March to May, summer was June through September, and autumn from October to November.

The winter season across the study area covers mostly the snow accumulation period up to the spring river ice break-up. Spring includes the river break-up and flooding until the summer and autumn seasons when low-water flow is interrupted time to time by rapid rain-induced floods.

Extreme hydrological characteristics are defined as maximum and minimum discharges. The maximum discharges are sampled as highest values among the two-term daily time series during floods for each year. The maximum discharges are usually observed during the spring season and are associated with snowmelt floods. Minimum discharges defined as the lowest values from two-term daily time series of each year.

The minimum discharges (and in some cases minimum flow levels) were defined for cold and warm periods separately. The cold period lasts from November to April and the warm period lasts from May to October. The definitions of these periods are connected to the climatic conditions of the region and the passing of the air temperature through the 0°C isotherm in spring and autumn respectively.

The specific discharge (SD) from the basin was used to build the spatial distribution of streamflow. The SD is defined as the quantity of water which is derived for a drainage basin unit area in the given time interval. The SD unit is liter s^{-1} km^{-2}.

A Student's *t*-test was used to determine if there is a significant difference between the means of two groups of climatic or hydrological characteristics.

The trend analysis was carried out using the Mann-Kendall (MK) test (Mann, 1945; Kendall, 1975). The test statistically assesses an upward or the downward trend of variable over time. A monotonic upward (downward) trend means that the variable consistently increases (decreases) through time, but the trend may or may not be linear. The MK test was used to test the slope of the estimated linear regression line. The trend slopes were studied using the Sen's method by choosing the median of the slopes of all lines through the pairs of points (Sen, 1968).

Hydrological Modeling

Runoff modeling was carried out by applying the "Hydrograph" model. The model was developed at the Russian State Hydrological Institute (Vinogradov et al., 2011; Makarieva, 2018).

The model describes the streamflow formation processes in the river basins with different physic-geographical characteristics and uses climate and land-use information as an input data. The climatic input includes the time series of daily air temperature, water vapour pressure deficit (VPD), precipitation and its duration.

Meteorological data for the historical period were obtained from E-OBS archive (Haylock et al., 2008). We used typical intra-annual VPD distribution for wet and dry days, respectively. The output of the model is the continuous hydrograph of runoff in the closing gauge observation point for the defined period. **Figure 3** presents the runoff change assessment scheme.

Hydrological projections were made using daily air temperature and precipitation output from the EC-EARTH driving model and SMHI-RCA4 regional climate model. These climate models were selected because they showed the best coherence between observed (E-OBS) and the historical modeled time series of air temperature and precipitation. The air temperature and precipitation bias adjusted model output was used in the study. It was produced according to the Distribution-Based Scaling method (SMHI-DBS45; Yang et al., 2010) developed by EURO-CORDEX members. The calculations were made for RCP4.5 and RCP8.5 scenarios.

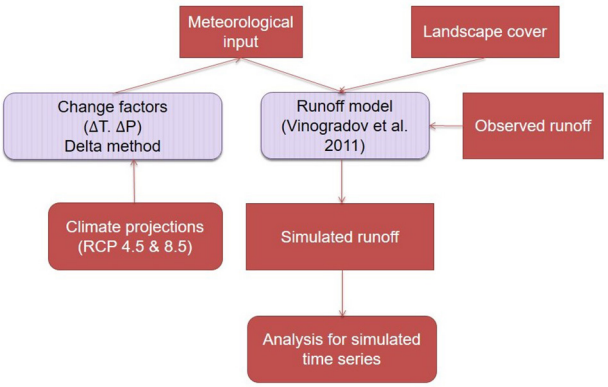

FIGURE 3 | Runoff change assessment scheme.

The Nash-Sutcliffe model efficiency coefficient (NSE; Nash and Sutcliffe, 1970) and PBIAS criterion (Gupta et al., 1999) were used for model suitability assessment and calculations of expected changes in the streamflow pattern. The PBIAS (percent bias) measures the average tendency of the simulated flows to be larger or smaller than their observed counterparts. The optimal PBIAS value is 0.0. Its positive values indicate a model bias toward the underestimation of the flow, while negative PBIAS values indicate a bias toward the overestimation of the flow. For the period of 1970–2015, we received the following NSE and PBIAS criteria for the Western Dvina River: 0.79 and 9.7% respectively. Modeling results can be considered as satisfactory (Moriasi et al., 2015). The results of historical simulating are presented in **Figure 4**.

RESULTS AND DISCUSSION

Climatic Conditions

The climate of the study basin strongly depends on the Atlantic Ocean. The air streams from the Atlantic Ocean bring wet and warm air to the region. As a result, the climate of the Western Dvina River Basin is characterized by mild climate, high humidity, and moderate air temperature. In general, it is possible to earmark three areas in the Western Dvina River Basin, which vary by physiographic factors: the upstream part from the river originating to Vitebsk, the middle part from Vitebsk to Daugavpils, and the near-estuary part. These three areas differ by their climatic conditions, which are formed by the level of the sea and continent interactions.

In the upstream part of the Basin that is located quite far from the influence of the Baltic Sea, the climate is continental. Frequently, this part of the Basin becomes under the influence of wet and cold arctic air masses. The middle part of the Basin in Belarus is located in a transitional zone. Here the weather can be controlled by the prevalence of continental air, the same way as in the upper part of the Basin. However, frequently the sea air masses may arrive here keeping in this part of the Basin

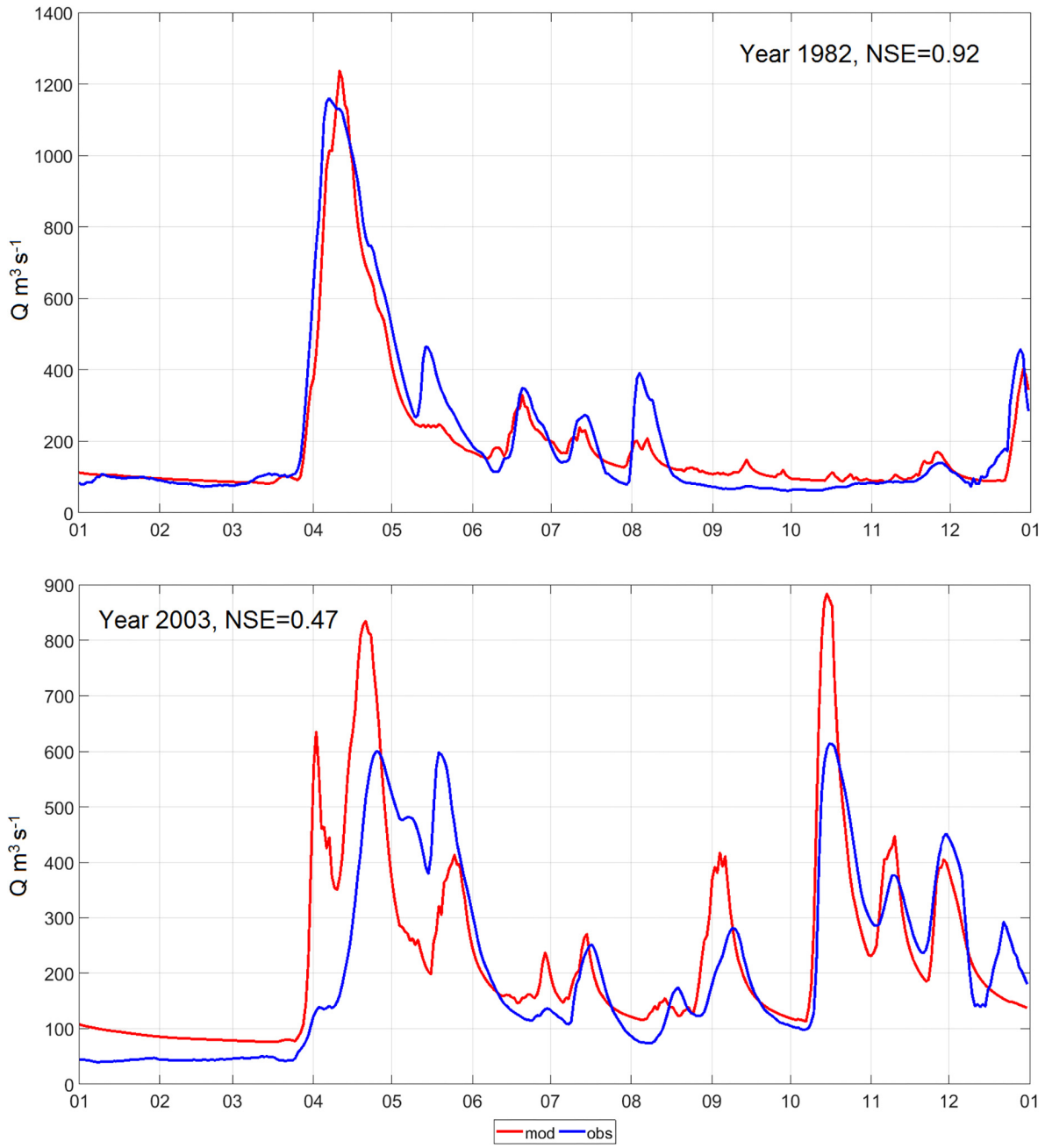

FIGURE 4 | The results of the historical simulating of streamflow on the Western Dvina River at the Vitebsk gauging station. The upper figure presents the best coherence of the observed and modeled streamflow in 1982, the bottom figure presents the worst simulated results for 2003.

mild maritime weather conditions, especially in the transitional periods of spring and autumn.

In the lower part of the Basin, which is the closest to the Baltic Sea, the climate is mild due to the domination of the Baltic Sea air masses that are quite warm in winters and relatively cold in summers.

The annual average temperature across the Basin fluctuates from 4.4°C in the south and west to 5.8°C in the east (**Figure 5**), with mean January temperatures varying from −5.3°C in the northeast to −4.8°C in the southwest, while mean July temperatures vary from 14°C in the northwest to 15°C in the southeast. The dynamics of the air temperature during the year is smoothed over the entire Basin with annual air temperature amplitudes being about 25°C. Absolute minimum of air temperatures may be about −30 to −40°C (in January); the absolute maximum temperatures can reach from + 31 up to + 37°C (in July to August). During the decades since 1989, the temperature in the region has grown with annual mean values

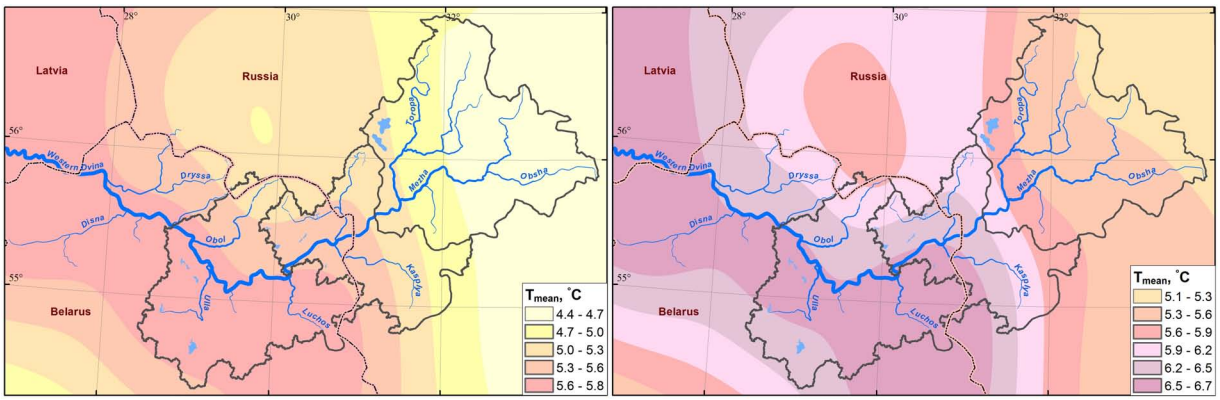

FIGURE 5 | The spatial distribution of the annual temperature mean values over the Western Dvina River Basin for two different periods: 1945 to 2015 **(left)** and 1989 to 2015 **(right)**.

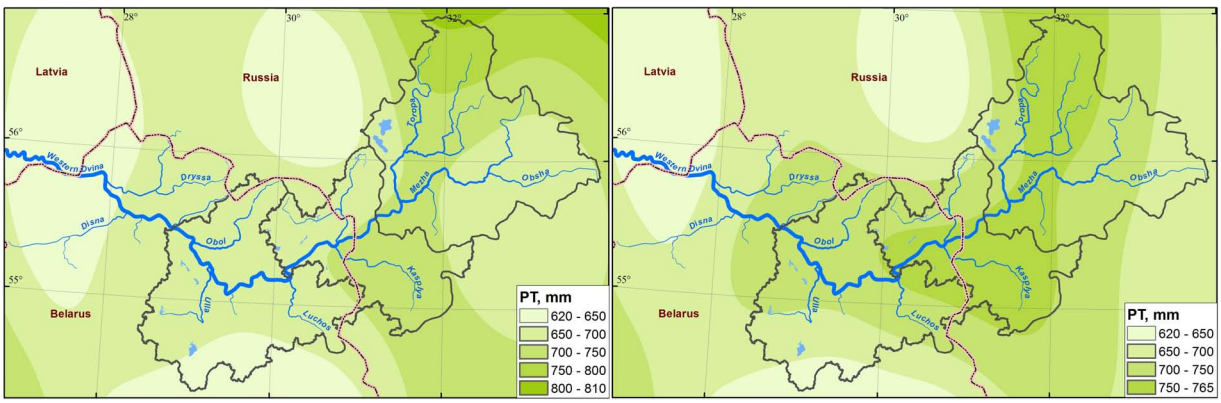

FIGURE 6 | The spatial distribution of annual precipitation totals over the Western Dvina River Basin for two different periods: 1945–2015 **(left)** and 1989–2015 **(right)**.

increased by up to + 1°C and the largest increase (by up to + 1.5 – + 2.5°C) was documented in the winter months.

Within the Western Dvina River Basin, annual precipitation ranges from 650 to 700 mm in the middle part, to 750–800 mm in the upper part of the Basin. About 70% of precipitation falls in liquid form during the warm part of the year. Snow accumulates in winter, with maximum ground snow cover occurring at the end of February. During the last decades (1989–2015), the moistening pattern in the River Basin has changed (**Figure 6**). Over the entire Basin, the annual precipitation totals increased by about 50 mm.

Recent Streamflow Pattern

Monthly Streamflow

Monthly and annual discharges in the Western Dvina River gradually increase with the river catchment growth (**Table 2**).

During the 1945–2015 period, several factors were responsible for changes of monthly and annual discharges of the River. The leading driver of streamflow changes in the study basin is precipitation. **Figure 7** represents the decadal changes of monthly discharges in the Western Dvina River near Velizh, Vitebsk and Polotsk gauging stations. The period of 1945–1964 is characterized by the variations of monthly and yearly discharges around the mean values for the 1945–2015 period. The smallest monthly discharges were observed in 1965–1984, except Velizh where the smallest monthly values were observed in 1963–1980. During these decades, the annual discharges were lower than the mean values and low streamflow was observed during all seasons. Discharges were less than the mean values by 3–56% near Velizh, 2–32% near Vitebsk, and 2–37% near Polotsk. The exception was in 1978, when streamflow was higher by 20–23% due to extremely high snowy conditions before the spring snowmelt and, consequently, large floods on many Belarusian rivers.

During the last decades (1985–2015), the discharges again varied around the long-term mean value at the Velizh gauging station, where positive and negative deviations reached up to 60% from the average. In the Belarusian part of the Western Dvina River Basin, the discharges were observed below the long-term mean only in 5 years during 1945–2015. The deviations varied by 2–62% near Vitebsk and 1–48% near Polotsk. The lowest discharge values were documented for 2014 and 2015 and were connected with an outstanding drought, which lasted for several

TABLE 2 | Hydrological characteristics of the Western Dvina River (within Russia and Belarus boundaries).

Gauging station	Catchment area, km^2	Distance from the mouth, km	Annual discharge, m^3 s^{-1}	Annual specific discharge, liter s^{-1} km^{-2}
Velizh	17600	710	80	4.55
Vitebsk	27000	622	230	8.51
Polotsk	41700	474	305	7.31

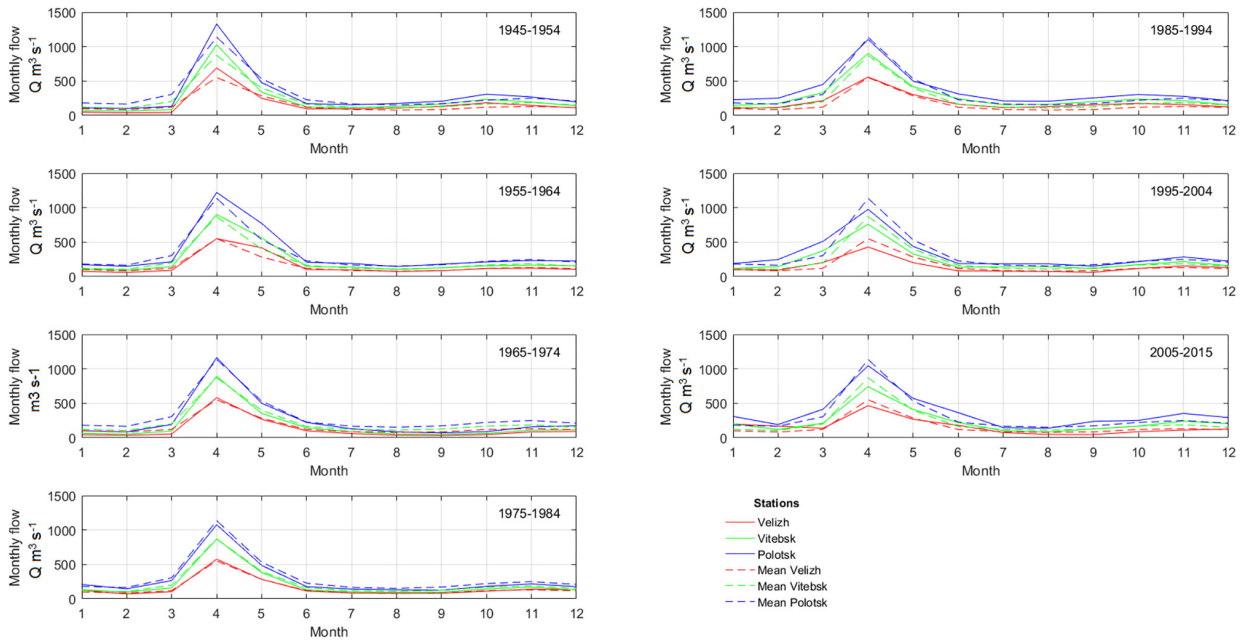

FIGURE 7 | Dynamics of monthly discharges (m^3 s^{-1}) in the Western Dvina River at the Velizh, Vitebsk and Polotsk gauging stations.

consequence months. The streamflow in 2014 was extremely low with discharge deviations comprised 60% near Velizh and Vitebsk and 46% near Polotsk. The historical extremes of warm low-water period were exceeded in 2014. However, during the 1985–2015 period in 25 years of 30, the annual discharges within the river length were higher than the mean values by 3–60%. The increase of annual discharges during the last decades is connected with the increase of winter streamflow due to frequent thaws and extra water supply in the winter season. At the same time, the spring runoff became lower due to a smaller amount of snowmelt water being available for spring floods.

Intra-Annual Distribution of Streamflow

The intra-annual distribution of streamflow in the Western Dvina River Basin is characterized by low streamflow in winter (December to February), when runoff rate constitutes about 15% of the annual total, spring (March to May) when snowmelt runoff corresponds to 50–55% of this total. During the summer (June to September), the rate of streamflow varied within 15–20% of the annual total and the same streamflow rate is in autumn (October to November). The differences in the rates of intra-annual distribution by the river length are small and varies within 1–3% (**Figure 8**).

During the last decades, when compared to the previous period, the intra-annual distribution has changed over the entire the Baltic Sea Basin (BACC Author Team, 2008, 2015). There is a large area with similar trends in the intra-annual distribution change in the eastern part of the Baltic Sea Basin, which is observed in the river basins of Western Dvina (Belarus and Russia), Velikaya, Luga, Narva, and Svir' (Russia). These changes connected with the growth in the frequency of winter floods and the increase of the values of minimum discharges during the winter low-water periods due to higher air temperatures and an additional inflow of melting water to the rivers (Partasenok et al., 2014; Zhuravlev et al., 2017). Low values or even the absence of snow and ice covers on the rivers and the ground and the low depth of seasonal ground freeze (Nekrasova, 2004) exhaust the water supply before the freshet onset and make conditions for large floods less probable. The differences in the intra-annual distribution at the major gauging stations were tested for significance by *t*-test, which showed the significant differences (at the significance level values, $\alpha = 0.05$) in winter and spring flows, while for summer-autumn periods no significant changes were found.

Extreme Characteristics During Spring Flood

The Western Dvina is a typical flat terrain river. The river is supplied mainly by the snow cover melt accumulated during the cold period. This is the reason for relatively high spring flood events observed every year. The flood season usually occurs

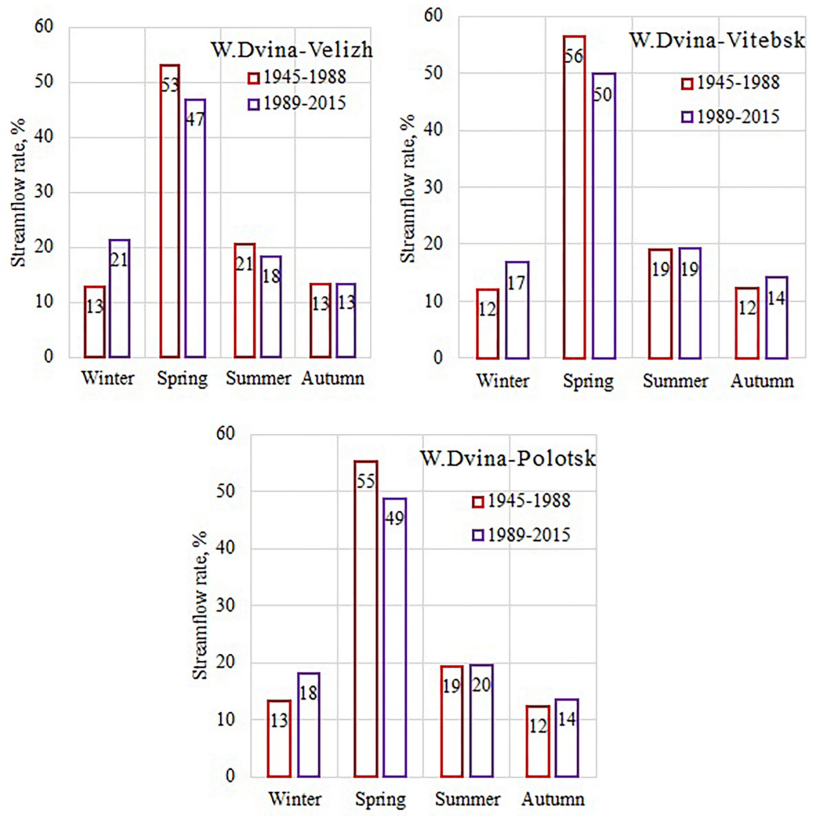

FIGURE 8 | The intra-annual streamflow distribution (percentage) on the Western Dvina River at the Velizh, Vitebsk, and Polotsk gauging stations.

within just two months: most often, it begins at the end of March (on the main river and in the middle of March on tributaries) and ends in early June when water declines. During the spring snowmelt time, the river level often rises sharply because of the jams.

During the period of remarkable climate change observed in the study region since 1989 up to date, the rise of winter air temperatures and frequent thaws were documented. That is the reason for the earlier flood season start that has shifted to the earlier dates by 4–12 days. At that period, the maximum flood levels in the Belarusian part of the Western Dvina River Basin decreased by 30 to 56 cm (Danilovich et al., 2017). The peaks of spring flood usually observed in the beginning or in the middle of April. The end of spring flood normally occurs in the middle or end of May.

The maximum discharges during spring flood changed during the last 70 years. During two decades, 1945–1954 and 1955–1964, the highest values of spring floods were documented (**Figure 6**). These decades are characterized by severe winter weather conditions and the formation of sufficient snow-water supply prior to the spring season. This caused an intensive inflow of snowmelt water into the River and its rapid water level rise. In the study river basin, a catastrophic inundation with a 1% probability of occurrence (with frequency once per 100 years) occurred in 1956. This was a highest spring flood in the Western Dvina River Basin and in many other rivers within neighboring regions of Russia and Belarus. The lowest values of maximum discharges during spring flood were observed during the last decades (1985–2015). This is connected with climate warming, which caused the intra-annual distribution change and decrease of the spring runoff rate.

The maximum SDs (a quantity of water which derived from a unit area in a drainage basin in the given time interval, SD) are noticed for small rivers. These rivers are often tributaries of the second order), which are usually located in the right bank of the river or upstream where relief has a higher amplitude of absolute heights and more water is accumulated in the relief depressions (**Figure 9**).

The maximum SDs were observed on the Western Dvina River near Velizh in 1958 and exceeded the average by 59% (82 liter s^{-1} km^{-2}). Vitebsk gauging station registered the highest discharge in 1931 (153 liter s^{-1} km^{-2}), while at Polotsk this extreme was reported in 1956 (97 liter s^{-1} km^{-2}). At that time, discharges exceeded twofold the average values. There were catastrophic floods in 1931 and 1956 with the 1% probability over large area of the eastern part of the Baltic Sea Basin.

Jams

The formation of jams is a quite frequent event in the Western Dvina River Basin. During the last few decades, the frequency of

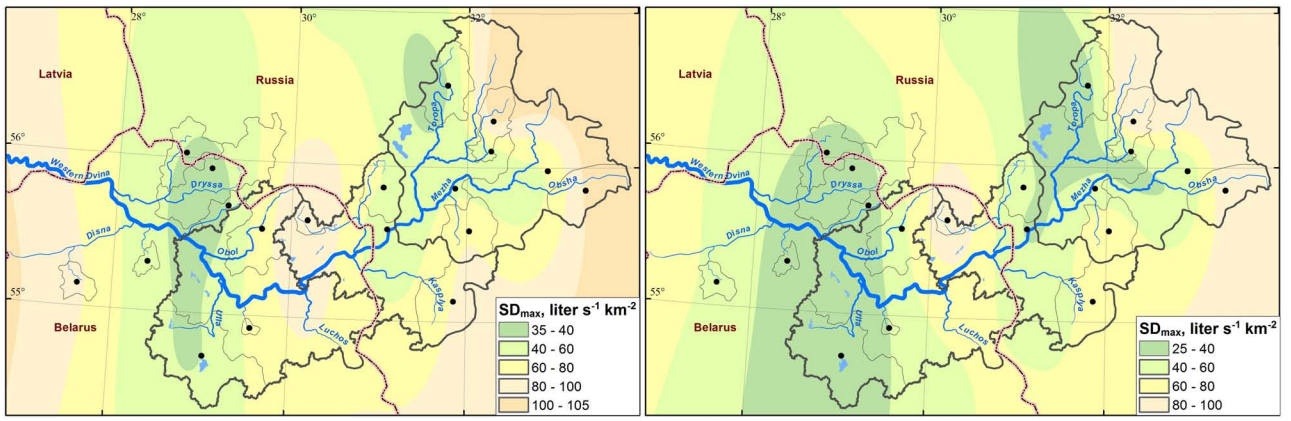

FIGURE 9 | Decadal variability of maximum specific discharges (liter s^{-1} km^{-2}) on the Western Dvina River and its tributaries.

jams in autumn and winter has increased. For example, according to the data from the Polotsk gauging station on the Western Dvina River, the frequency of jams in the cold season was one time per 17 years during the 1937–1970 period, and one time per 5 years during the 1971–2015 period. The rise of the jam frequencies is connected with a shift of freeze-up dates toward more late dates and with the processes of ice formation which occur inside the water and cause intensive formation of the studge ice and, as a consequence, the jam formation. The duration of jams has increased from 3 days on average during the 1937–1970 period to 20 days every year in the 1971–2015 period.

The spring jams occurrence on the Western Dvina River reduced during the last decades from one time per 2.5 years to one time per 3.5 years. Meanwhile, the highest jam levels during autumn-winter and spring periods has increased.

Low-Flow Periods

The hydrological regime of the Western Dvina River is characterized by low-flow periods in cold (winter) and warm (summer to autumn) seasons. The water supplying during the low-flow period comes from underground water storages. The cold season low-flow period starts with hydrological winter with the ice phenomena formation in November to December (in the last decades, often in January due to the winter temperature rise). This period ends when spring floods start in the end of March and beginning of April. Thereafter, intensive and rapid increases of the river level due to rainfalls occur often during the summer low-flow period.

The dynamic of minimum discharges of cold and warm periods is presented in **Figure 10**. The dynamic of streamflow in the Western Dvina River Basin in the warm period strongly depends on precipitation and varied about the norm during the study period. The lowest discharges were observed in 1964–1980, 1991–1995, and 2014–2015. The lowest minimum discharge of the cold season depends on precipitation and winter air temperature. The increase of the air temperature in winter and frequent thaws in the Western Dvina River Basin led to immediate snowmelt, extra water supplies into the rivers and formation of winter floods. That is the reason of rising of the minimum discharge during the cold season in the Western Dvina River and its tributaries. The low flow changes in cold period are significant for all rivers in Belarus and northwest of Russia, including the Western Dvina River Basin.

The smallest values of minimum discharge were registered in Velizh in 2002 and were equal to 15.1 m^3 s^{-1} in the warm period and in 1947 equal to 4.9 m^3 s^{-1} in the cold period. In Vitebsk, the smallest values of minimum discharge were registered in 1964 (equal to 27 m^3 s^{-1}) in the warm season and in 1952 (equal to 21.2 m^3 s^{-1}) in the cold season respectively. In Polotsk, lowest discharges were observed in 1952 and 2014 when they were equal to 39.5 m^3 s^{-1} in the warm period.

Usually the winter minimum discharge and level have the lowest values each year. During the last decades in the study area, the frequency of cases when annual minimum level became in the summer season increased strongly. It is connected with growth of winter streamflow rates in the hydrological cycle caused by climate warming and increase of drought frequency in the summer period. **Figure 11** represents the dynamics of the cases when summer minimum level exceeded the winter minimum level. The decrease of summer level is stronger in the upper stream of the Western Dvina River (cf., at the Velizh gauging station).

Trends

For the present study, we estimated trends of monthly and annual discharges, maximum discharge during the spring flood period, and minimum discharges during the winter and summer low-water periods.

The analysis of monthly runoff for the 1945–2015 period showed statistically significant trends (at the 0.05 significance level) for January through April at three gauging stations, and in December for Vitebsk and Polotsk stations (**Table 3**). The trend values are positive in winter months and March and become negative in April. The positive trends in December to March (during the hydrological winter) are related to a general increase of air temperature in the study region, frequent thaws, absence of ice cover and inflow of snowmelt water into the rivers. The negative trends in April might be explained by exhausted snow

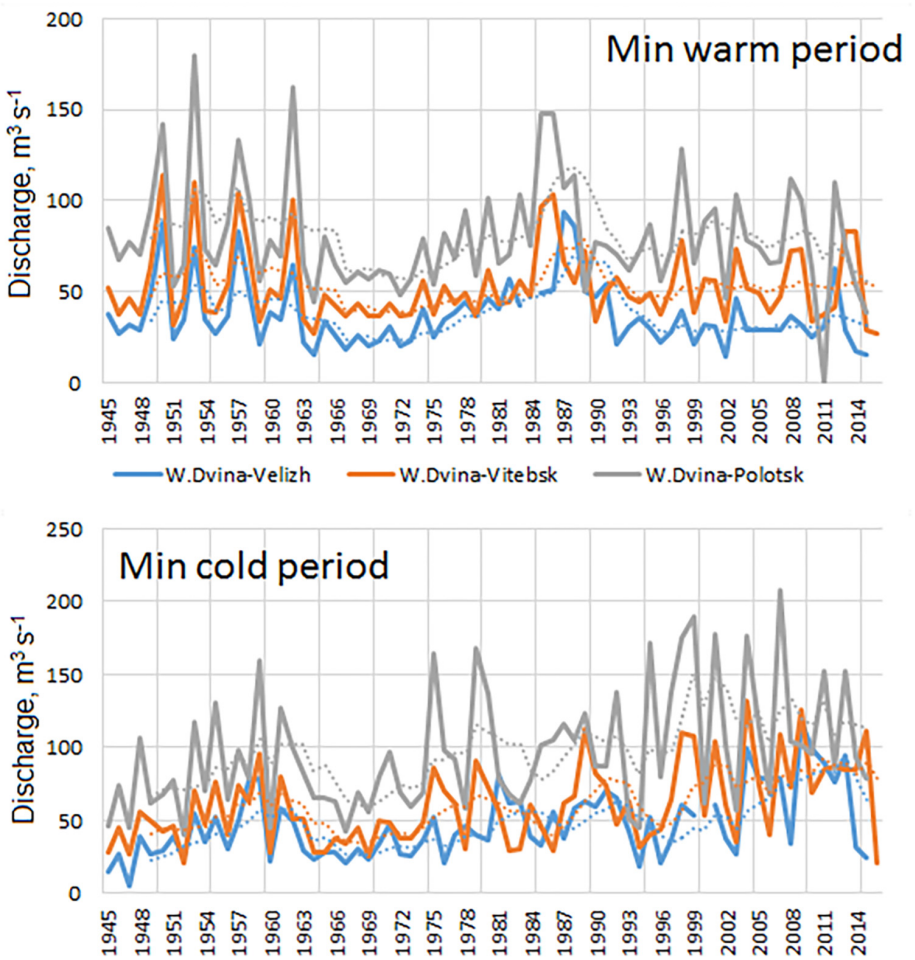

FIGURE 10 | The dynamics of low-flow annual discharges in the Western Dvina River in warm and cold seasons (solid lines) and smoothed by 5-year filter (dotted lines).

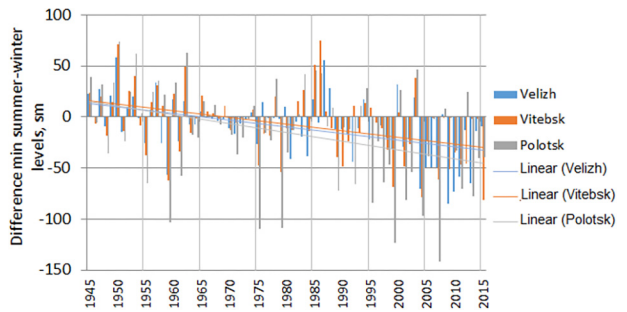

FIGURE 11 | The differences between minimum summer and minimum winter level and their linear trends.

storage after warm winters that supply rivers with the meltwater. There are no significant trends for other months.

The significant negative trends of the spring flood peak discharges were established for all three major Western Dvina gauging stations: Velizh, Vitebsk and Polotsk. The streamflow change estimates vary within 69–89 $m^3\ s^{-1}$ per decade with the largest values in the downstream of the study river basin and the smallest trend values in the upper stream of the Basin.

The minimum discharge trends during the winter low-water period are statistically significant and positive in Velizh, Vitebsk and Polotsk and vary within the 5.9–7.1 $m^3\ s^{-1}$ range. There are no significant changes the minimum discharges during the summer low-water period.

The annual discharges trends are significant only at the Polotsk gauging station, where largest changes of monthly and extreme values were observed.

Projected Climate Changes in the Study Region

According to model projections, the average annual mean values of air temperature will gradually increase in the study region. According to scenario RCP4.5 in 2021–2040, deviations of annual air temperature will fluctuate around + 1.4°C. Thereafter by 2060, the deviations will increase up to + 2.7°C. At the end of the 21st century, the greatest value of annual air temperature is

TABLE 3 | The monthly, annual, and extreme streamflow trends (m^3 s^{-1} per 10 years) and their significance (estimates that are significant at the significance levels from 0.001 to 0.05 are shown in bold).

Gauging station/month	Velizh	Vitebsk	Polotsk
January	**17.2**	**12.1**	**20.0**
February	**12.1**	**10.0**	**17.9**
March	**15.6**	**16.7**	**33.7**
April	**−33.0**	**−37.5**	**−52.6**
May	−9.35	−2.25	−8.00
June	3.28	3.92	6.21
July	0.93	2.07	3.04
August	−0.75	0.55	1.00
September	−2.41	−0.25	0.25
October	−1.66	1.09	1.00
November	0.48	7.53	9.27
December	5.71	**9.12**	**12.3**
Year	2.05	5.47	**9.55**
Maximum flood	**−69.1**	**−85.7**	**−88.8**
Minimum winter	**6.25**	**5.90**	**7.14**
Minimum summer	−0.48	1.08	0.60

expected to increase by 2.8°C. According to scenario RCP8.5, annual deviations of air temperature are expected to be + 1.5°C in the next decade (2021–2030). In the middle of the century (2051–2060), they will reach + 2.5°C, and by the end of the century (2091 to 2100), these deviations will increase up to + 4.7°C. It should be noted that the standard deviation of the air temperature projections remains within the 0.5–1.0°C range that testifies for the coherence of climatic models' calculations in ensemble.

Intra-seasonal distribution of air temperature deviations during the considered period is characterized by heterogeneity of changes in the cold and warm half of the year for all scenarios of radiative forcing. For scenario RCP4.5 during the winter season, deviations are expected to be positive in all decades, but a noticeable increase is predicted anomaly in the first two decades: up to + 1.5 – + 2.6°C. These anomalies will probably remain at this level up to the middle of the 21st century, and during the 2061–2070 period they will stabilize at 2.5°C. In the next two decades, deviations of annual air temperature will slightly increase by +3.3 to + 3.5°C and to the end of the century will again decrease to +2.8°C. According to scenario RCP8.5, temperature deviations during the winter season in the first half of the 21st century will be probably close to calculated values according to scenario RCP4.5 (+ 1.6 – + 2.5°C), and during several following decades they will be even slightly lower. However, since 2061, an intensive increase in air temperatures is expected in comparison to the previous decades, and these deviations are expected to be within + 4.5 – + 6.1°C.

The spring season is characterized by gradual increase in air temperature; however, the deviation values are expected to be less than in winter. At scenario RCP4.5, deviations of air temperature will probably increase slightly during the 21st century from + 1.0 to + 2.6°C. At scenario RCP8.5, the gradual growth of deviations is very likely occurred in the first half of the century within the 1.4–2.5°C range, and more intensive growth in the second half of century is expected to be within the 3.0–4.5°C range.

The summer season probably will be characterized by similar distribution of deviations by decades; however, their values will be lower than in spring. At scenario RCP4.5, deviations of air temperature will reach + 1.0 – + 2.0°C. At scenario RCP8.5, their values will gradually increase from + 0.8°C (2021 to 2030) to + 4.0°C by the last decade of the current century.

Autumn season are characterized by the smallest values of deviations for scenario RCP4.5. Their values are expected to be below 2.0°C in the first half of the century and then their decrease to + 0.9 – + 1.1°C is expected (2051 to 2091). Finally, for the last decade of the century, an increase up to + 2.2°C is expected.

According to climatic models' ensemble calculations, decadal future changes of precipitation within the Western Dvina River Basin are highly uncertain. Dynamics of annual precipitation totals under scenario RCP4.5 is also characterized by considerable uncertainty. Negative deviations of annual precipitation totals are noted for periods 2041–2050 and 2081–2090. In other decades, mostly positive deviations of annual precipitation are expected but all of them are small and, probably, range from five up to seven mm. These deviations are statistically insignificant at the 0.05 statistical significance level. Annual precipitation totals anomalies will fluctuate for the most of the 21st century within + 10 to + 15 mm without rapid deviations. The largest values of annual precipitation anomalies are expected to be within + 20 to + 25 mm.

For scenario RCP8.5, the deviations of the annual precipitation totals are more coherent within ensemble and varies from + 3 to + 16 mm by the 2091–2100 period. However, the majority of these precipitation deviations are insignificant at the 0.05 statistical significance level. Deviations of precipitation totals are expected to be within 10 to 30 mm, the greatest within 21–42 mm. At the same time, a gradual increase in precipitation deviation values during the 21st century is noted.

The seasonal distribution of precipitation deviations is characterized by the greatest values during the winter and spring seasons. During the winter season under scenario RCP4.5, precipitation deviations will probably vary within the + 20 to + 28 mm range during the 2031–2100 period. For scenario RCP8.5, seasonal sums of winter precipitation will grow by consecutive decades from 8 mm (2021–2030) to 50 mm at the end of the century. Spring deviations are expected to be practically within the same range. For scenario RCP4.5, precipitation totals will increase by about 15–31 mm and for scenario RCP8.5 precipitation deviations will grow from + 14 to + 50 mm (2081–2090).

Summer precipitation changes according to both scenarios of radiative forcing (RCP4.5 and RCP8.5) is reported with large uncertainties. According to model calculations, it is impossible to define further dynamics of deviations of seasonal summer precipitation. We can only assume that it will be within the variations of seasonal norms.

The autumn season does not express tendencies to increase or decrease. However, autumn precipitation deviations are positive in most cases and probably will be within + 5 to + 24 mm. The differences between deviations for two scenarios are small,

especially in the first half of century. The greatest autumn deviations are expected for scenario RCP8.5 for the periods 2041–2050, 2061–2080, and 2091–2100.

Projected Hydrological Changes

Assessments of expected runoff regime of the Western Dvina River were conducted for the 2021–2100 period. The following variables were analyzed: annual flow (Q_{mean}), yearly maximum (which usually corresponds to spring flood peaks, Q_{max}) and minimum discharges (which usually is observed during the winter or summer low-flow periods, Q_{min}).

It is projected that during 2021–2100, annual discharges will not change dramatically according to both scenarios – RCP4.5 and RCP8.5 (**Figure 12A**). There are no significant decadal trend estimates in annual discharges. Thus, the annual streamflow, as well as in the last decades, presumably will vary mostly near its present climatological values (i.e., near "norms"). According to scenario RCP4.5, the decadal streamflow changes will vary within a narrow range and will not exceeded ± 10–12% at the Velizh gauging station mainly with a negative anomaly sign (except the nearest decade, when decrease of annual streamflow up to 21% is expected). At the Vitebsk gauging station, no sizeable decadal changes are expected. However, some increase up to + 12% is expected in the 2071–2080 and 2091–2100 decades. The largest positive changes in projected streamflow were found for the Polotsk gauging station. Here, changes within + 6 to + 11% in the first half the current century and within + 21 to 36% since 2061 are projected up to the end of the study period. According to scenario RCP8.5, decadal streamflow changes at the Velizh gauging station will be less than historical norm by 11–22% with the largest changes projected for last two decades of the 21st century. At the Vitebsk station, decadal changes will not exceed ± 10%. At the Polotsk gauging station, the decadal changes will exceed the historical norm by + 11 to + 26% with maximum increase in the 2041–2070 period.

Projections of maximum streamflow show a general decrease of spring flood discharges (**Figure 12B**). However, according to RCP4.5 scenario in the nearest decade (2021–2030), the increase of maximum streamflow on 10 to 11% is projected for all three major gauging stations. At the Velizh station during the period of 2021–2100, the maximum streamflow will vary within the norm values without steady positive or negative deviations. At the Vitebsk station, the decadal changes of maximum streamflow will be mostly negative. It will vary within 8–24% with decrease by up to 20–24% in 2041–2050 and 2081–2090. At the Polotsk station, the decadal change will be more notable with decrease less than the historical norm by 11–26%. The smallest flood discharges in are anticipated during the 2031 to 2050 and 2081 to 2090 decades. According to RCP8.5 scenario, the decadal change in spring floods regime will be stronger. The deviations of maximum streamflow are expected to decrease by up to 5–42% for all three major gauging stations. The largest values of decrease will be in 2081–2090.

The minimum streamflow will be changed more remarkable (**Figure 12C**). The general increase of minimum discharges was projected for both scenarios at all gauging stations. The average increase of minimum discharges is expected to be 60–90%. In Velizh, it will be by 20–78%, in Vitebsk by 66–121%, and in Polotsk by 43–139%. The smallest increase is expected to be in the nearest decade (2021–2030) and the largest in the 2071–2090 decade.

SUMMARY

The current changes of monthly and extreme streamflow in the upper and middle part of the Western Dvina River Basin correspond to a general pattern of hydroclimatic changes in the Baltic Sea Basin occurred during recent decades.

The fluctuations of the streamflow during the period of 1945–2015 are characterized by regional peculiarities of the moistening regime. The smallest monthly discharges were observed in the 1960–1980s of the previous century. During the 1985–2015 period in most of the years, the discharges were higher than the average values by 3–60% along the entire River length. The increase of yearly discharges during the last decades is connected with an increase of winter streamflow due to frequent thaws and extra winter water supply into the River.

During the last decades, the intra-annual distribution in the upper and middle part of the Western Dvina River Basin has changed, the streamflow increased by 6–8% in winter and decreased by 5–6% in spring, in summer-autumn period the changes of streamflow vary within ±3%.

The following seasonal peculiarities have been noticed for the study river basin:

Winter. Presently, due to air temperature growth and frequent thaws, winter floods occurred more often. During the last decades, the frequency of jams in autumn and winter has increased by 17 days per year. Furthermore, the highest jam's levels during the autumn-winter and spring periods have increased.

Spring. During the period of 1945–1964, the highest values of spring flood were documented, while their smallest values were observed during the 1989–2015 period.

The largest values of maximum SDs are noticed for small rivers (often tributaries of the second order) which are usually located along the right bank of the main river or upstream, where relief has a higher amplitude of absolute heights and more water is accumulated in the relief depressions.

Summer. The lowest discharges were observed in 1964–1980, 1991–1995, and 2014–2015 decades; these are explained by the prevalence of the drought conditions in the Basin.

During the last decades, the frequency of years, when minimum annual discharge was observed in the summer season, significantly increased.

Trends. The analysis of monthly runoff for the 1945–2015 period showed significant positive trends for December through March monthly discharges and minimum winter's discharges; significant negative trends were found for April monthly discharges and maximum flood discharges. The trends slopes increase from the upper to middle part of the Basin, which can be explained by a closer location of the middle part of the Basin to the Atlantic Ocean and more significant influence here by climate warming.

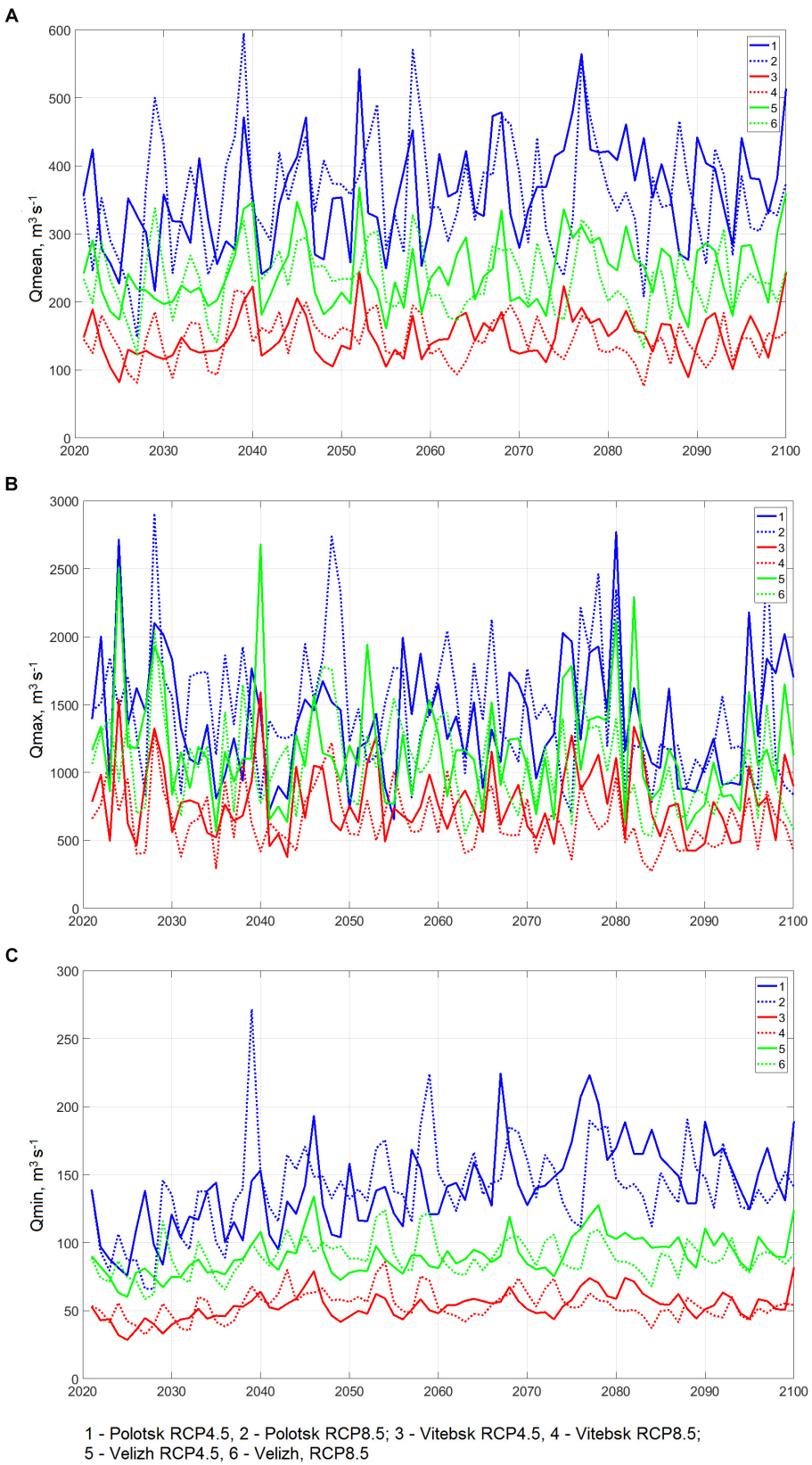

FIGURE 12 | Projected annual **(A)**, maximum **(B)**, and minimum **(C)** streamflow on the Western Dvina River during the 2021–2100 period.

Projected Changes in Climate. According to both scenarios of radiative forcing, the air temperature will increase gradually in the study region. According to the RCP 4.5 scenario, projected increases of annual air temperature will be by +1.4 to +2.8°C and under the RCP8.5 scenario they will be up to + 4.7°C. According to models' simulations for all scenarios of radiative forcing, the intra-seasonal distribution of air temperature deviations during the 21st century is characterized by heterogeneity for the cold and warm halves of the year. The largest increase of air temperature is expected in the cold season.

The dynamics of annual precipitation totals under the RCP4.5 scenario is characterized by considerable uncertainty. For scenario RCP8.5, the deviations of annual precipitation totals are more coherent across the model ensemble and vary from + 3 to + 16 mm for the 2091 to 2100 period. At the 0.05 statistical significance level, most of projected precipitation deviations are insignificant.

Projected Changes in Streamflow. Future hydrological regime within the Western Dvina River is expected to change. The projected hydrological changes are stronger for the climate projections under the RCP8.5 scenario. The annual streamflow is not expected to change, with its decadal changes being varied around the "norm" values (except the Polotsk gauging station, where n the second half of the current century an increase of annual streamflow by 21–36% is expected). The spatial pattern of the projections will be characterized by mostly negative runoff changes in the upper stream and positive runoff changes in the lower part of the study river basin. Projected maximum streamflow showed a general decrease with the largest changes in the lower part on the River Basin (Vitebsk and Polotsk; up to 25% of decrease). However, despite a general decrease of spring runoff, slight increases of maximum discharges (by up to + 10%) are projected for the nearest decade (2021–2030).

Projected minimum streamflow showed the largest changes. The minimum discharges are expected to be increased by 60–90% on average for the 2021–2100 period with largest changes being expected in the lower part of the study river basin.

AUTHOR CONTRIBUTIONS

SZ and ID designed the idea of the study. ID prepared the introduction and methodological part, provided the historical analysis, prepared the simulated climate data to force the hydrological model, and wrote the main part and conclusion. SZ set the hydrological model, prepared the historical hydrological data, calibrated and run the model, and generalized the simulated hydrological data. LK prepared the historical climate and hydrological data, provided the calculations, and prepared the graphs. PG improved the climate data generalization approach, corrected the statistical analyses throughout the manuscript, and edited the text.

FUNDING

The studies of ID were conducted under the subprogram 1 "The Nature Resources and Ecological Safety" of the State Research Program during 2016–2020 "The Nature Management and Ecology." The researches of SZ and LK were carried out with the financial support of the RGO-RFBR grant under Project No. 17-05-41118. The support for PG studies was provided by the ARCTIC-ERA Project within the Belmont Forum Initiative.

ACKNOWLEDGMENTS

We acknowledge the E-OBS dataset from the EU-FP6 project ENSEMBLES (http://ensembles-eu.metoffice.com) and the data providers in the ECA&D project (http://www.ecad.eu). We thank the reviewers and the editor for their valuable comments, which helped to improve the manuscript.

REFERENCES

Apsīte, E., Bakute, A., Elferts, D., Kurpniece, L., and Pallo, I. (2011). Climate change impacts on river runoff in Latvia. *Clim. Res.* 48, 57–71. doi: 10.3354/cr01004

Arheimer, B., and Lindström, G. (2015). Climate impact on floods: changes in high flows in Sweden in the past and the future (1911–2100). *Hydrol. Earth Syst. Sci.* 19, 771–784. doi: 10.5194/hess-19-771-2015

BACC Author Team, (2008). *Assessment of Climate Change for the Baltic Sea Basin*. Berlin: Springer-Verlag, 474.

BACC Author Team, (2015). *Second Assessment of Climate Change for the Baltic Sea Basin*. Cham: Springer International Publishing, 501.

Beldring, S., Engen-Skaugen, T., Førland, E. J., and Roald, L. A. (2008). Climate change impacts on hydrological processes in Norway based on two methods for transferring regional climate model results to meteorological station sites. *Tellus A Dyn. Meteorol. Oceanogr.* 60, 439–450. doi: 10.1111/j.1600-0870.2007.00306.x

Danilovich, I. S., Nahibina, M. E., Zhuravovich, L. N., and Kvach, E. G. (2017). The peculiarities of hydrological regime during last decades within the territory of Belarus. *Nat. Re.* 2, 5–12. [In Russian]

Döll, P., and Schmied, M. H. (2012). How is the impact of climate change on river flow regimes related to the impact on mean annual runoff? A global-scale analysis. *Environ. Res. Lett.* 7, 14037–14011. doi: 10.1088/1748-9326/7/1/014037

Donnelly, C., Greuell, W., Andersson, J., Gerten, D., Pisacane, G., Roudier, P., et al. (2017). Impacts of climate change on European hydrology at 1.5, 2 and 3 degrees mean global warming above preindustrial level. *Clim. Change* 143, 13–26. doi: 10.1007/s10584-017-1971-1977

Frolova, N. L., Agafonova, S. A., Kireeva, M. B., Povalishnikova, E. S., and Pakhomova, O. M. (2017). Recent changes of annual flow distribution of the Volga Basin Rivers. *Geogr. Environ. Sustain.* 10, 28–39. doi: 10.24057/2071-9388-2017-10-2-28-39

Gailiušis, B., Kriauèiûnienë, J., Jakimaviėius, D., and Šarauskienë, D. (2011). The variability of long-term runoff series in the Baltic Sea drainage basin. *Baltica* 24, 45–54.

Georgievskiy, V. Y., Grek, E. A., Grek, E. N., Lobanova, A. G., and Molchanova, T. G. (2018). Spatiotemporal changes in extreme runoff characteristics for the volga basin rivers. *Russ. Meteorol. Hydrol.* 43, 633–638. doi: 10.3103/s1068373918100011

Gupta, H. V., Sorooshian, S., and Yapo, P. O. (1999). Status of automatic calibration for hydrologic models: comparison with multilevel expert calibration. *J. Hydrol. Eng.* 4, 135–143. doi: 10.1061/(ASCE)1084-069919994:2(135)

Hansson, D., Eriksson, C., Omstedt, A., and Chen, D. (2011). Reconstruction of river runoff to the Baltic Sea, AD 1500–1995. *Int. J. Climatol.* 31, 696–703. doi: 10.1002/joc.2097

Haylock, M. R., Hofstra, N., Klein Tank, A. M. G., Klok, E. J., Jones, P. D., and New, M. (2008). A European daily high-resolution gridded dataset of

surface temperature and precipitation. *J. Geophys. Res.* 113:D20119. doi: 10.1029/2008JD010201

Hisdal, H., Holmqvist, E., Jonsdottir, J. F., Jonsson, P., Kuusisto, E., Lindstrom, G., et al. (2010). *Has Streamflow Changed in the Nordic Countries*? NVE Report No. 1. Oslo.

Jeppesen, E., Kronvang, B., Meerhoff, M., Sondergaard, M., Hansen, K. M., Andersen, H. E., et al. (2009). Climate change effects on runoff, catchment phosphorus loading and lake ecological state, and potential adaptations. *J. Environ. Qual.* 38, 1930–1941. doi: 10.2134/jeq2008.0113

Kendall, M. G. (1975). *Rank Correlation Methods*, 2nd Edn. New York, NY: Hafner.

Kıaviņš, M., and Rodinov, V. (2008). Long-term changes of river discharge regime in Latvia. *Nord. Hydrol.* 39, 133–141. doi: 10.1007/s10661-011-2315-0

Kıaviņš, M., Rodinov, V., Timukhin, A., and Kokorîte, I. (2008). Patterns of river discharge: long-term changes in Latvia and the Baltic region. *Baltica* 21, 41–49. doi: 10.1007/s10661-011-2315-0

Kriauciuniene, J., Meilutyte-Barauskiene, D., Reihan, A., Koltsova, T., Lizuma, L., and Sarauskiene, D. (2012). Variability in temperature, precipitation and river discharge in the Baltic states. *Boreal Environ. Res.* 17, 150–162.

Kriaučiūnienė, J., Meilutyte-Barauskiene, D., Rimkus, E., Kazys, J., and Vincevicius, A. (2008). Climate change impact on hydrological processes in Lithuanian Nemunas river basin. *Baltica* 21, 51–61.

Krylenko, I., Motovilov, Y., Antokhina, E., Zhuk, V., and Surkova, G. (2015). Physically-based distributed modelling of river runoff under changing climate conditions. *Proc. Int. Assoc. Hydrol. Sci.* 368, 156–161. doi: 10.5194/piahs-368-156-2015

Loginov, V., Volchek, A. A., and Volchek, An. A (2014). *Spring Floods on the Rivers of Belarus: Spatio-Temporal Fluctuations and Forecast*. Minsk: Belarusian Science.

Lopukh, P. S., and Partasenok, I. S. (2014). *Influence of Atmospheric Circulation on the Formation of the Hydrological Regime of the Rivers of Belarus*. Minsk: Belarus State University.

Makarieva, O. M. (2018). "Certificate of state registration of the computer program No. 2018619084," in *Complex Program of the Distributed Hydrological Model "Hydrograph"*, ed. O. M. Makarievacpesnm, (Rospatent: Moscow).

Mann, H. B. (1945). Nonparametric tests against trend. *Econometrica* 13, 245–259.

Meinshausen, M., Smith, S. J., Calvin, K., Daniel, J. S., Kainuma, M. L. T., Lamarque, J.-F. et al. (2011). The RCP greenhouse gas concentrations and their extensions from 1765 to 2300. *Clim. Change* 1, 213–241. doi: 10.1007/s10584-011-0156-z

Moriasi, D. N., Gitau, M. W., Pai, N., and Daggupati, P. (2015). Hydrologic and water quality models: performance measures and evaluation criteria. *Am. Soc. Agric. Biol. Eng.* 58, 1763–1785. doi: 10.13031/trans.58.10715

Nash, J. E., and Sutcliffe, J. V. (1970). River flow forecasting through conceptual model. Part 1-A discussion of principles. *J. Hydrol.* 10, 282–290. doi: 10.1016/0022-1694(70)90255-6

Nasonova, O. N., Gusev Ye, M., Volodin, E. M., and Kovalev, E. E. (2018). Application of the land surface model SWAP and global climate model INMCM4.0 for projecting runoff of northern russian rivers. 1. Historical simulations. *Water Resour.* 45(Suppl. 2):73. doi: 10.1134/S009780781806026X

Nekrasova, L. I. (2004). "Influence of climate warming on hydrological regime of rivers in Belarus during 1988-2002," in *Proceedings of XXIII Nordic Hydrological Conference: Fresh Water Resources Management*, Tallinn, 691.

Olsson, J., Yang, W., Graham, L. P., Rosberg, J., and Andreasson, J. (2011). Using an ensemble of climate projections for simulating recent and near-future hydrological change to lake Vanern in Sweden. *Tellus A* 63, 126–137. doi: 10.1111/j.1600-0870.2010.00476.x

Partasenok, I. S., Groisman, P Ya, Chekan, G. S., and Melnik, V. I. (2014). Winter cyclone frequency and following freshet streamflow formation on the rivers in Belarus. *Environ. Res. Lett.* 9:095005. doi: 10.1088/1748-9326/9/9/095005

Polishchuk, A. I., and Chekan, G. S. (eds) (2009). *Hydrological Monitoring of the Republic of Belarus*. Minsk: Knigazbor.

Reihan, A., Koltsova, T., Kriauèiûnienë, J., Lizuma, L., and Meilutytë-Barauskienë, D. (2007). Changes in water discharges of the Baltic States rivers in the 20th century and its relation to climate change. *Nord. Hydrol.* 38, 401–412. doi: 10.2166/nh.2007.020

Roudier, P. H., Andersson, J., Donnelly, C., Luc, F., Wouter, G., and Fulco, L. (2015). Projections of future floods and hydrological droughts in Europe under a +2°C global warming. *Clim. Change* 135, 341–355. doi: 10.1007/s10584-015-1570-1574

Sanchez, P. A., Ahamed, S., Carré, F., Hartemink, A. E., Hempe, J., Huising, J., et al. (2009). Digital soil map of the world. *Science* 325, 680–681. doi: 10.1126/science.1175084

Sen, P. K. (1968). Estimates of the regression coefficient based on Kendall's tau. *J. Am. Stat. Assoc.* 63, 1379–1389. doi: 10.1080/01621459.1968.10480934

Stahl, K., Hisdal, H., Hannaford, J., Tallaksen, L. M., van Lanen, H. A. J., Sauquet, E. et al. (2010). Streamflow trends in Europe: evidence from a dataset of near-natural catchments. *Hydrol. Earth. Syst. Sci.* 14, 2367–2382. doi: 10.5194/hess-14-2367-2010

Szwed, M., Karg, G., Pińskwar, I., Radziejewski, M., Graczyk, D., Kêdziora, A., et al. (2010). Climate change and its effect on agriculture, water resources and human health sectors in Poland. *Nat. Hazards Earth Syst. Sci.* 10, 1725–1737. doi: 10.5194/nhess-10-1725-2010

Thober, S., Kumar, R., Wanders, N., Marx, A., Pan, M., Rakovec, O., et al. (2018). Multi-model ensemble projections of European river floods and high flows at 1.5, 2, and 3 degrees global warming. *Environ. Res. Lett.* 13:014003. doi: 10.1088/1748-9326/aa9e35

Thodsen, H., Hasholt, B., and Kjarsgaard, J. H. (2008). The influence of climate change on suspended sediment transport in Danish rivers. *Hydrol. Process.* 22, 764–774. doi: 10.1002/hyp.6652

Veijalainen, N., Lotsari, E., Alho, P., Vehvilainen, B., and Kayhko, J. (2010). National scale assessment of climate change impacts on flooding in Finland. *J. Hydrol.* 391, 333–350. doi: 10.1016/j.jhydrol.2010.07.035

Vinogradov, Y. B., Semenova, O. M., and Vinogradova, T. A. (2011). An approach to the scalingproblem in hydrological modelling: the deterministic modelling hydrological system. *Hydrol. Process.* 25, 1055–1073. doi: 10.1002/hyp.7901

Volchek, A., Korneyev, V., Parfomuk, S., and Bulak, I. (2017). *Water Resources and Their Forecast According to the Climate Change in the Territory of Belarus*. Brest: Alternativa, 228.

Volchek, A. A., and Gryadinova, O. I. (2010). *Minimum River Flow in Belarus*. Brest: State University named after A.S. Pushkin.

Volchek, A. A., and Parfomuk, S. I. (2013). "Evaluation and forecast of natural water resources of Belarus," in *Modern Energy- and Resource-Saving, Environmentally Sustainable Technologies and Systems of Agricultural Production: Collection of Research Works by*, ed. N. V. Byshovacpesnm, (Ryazan: Brest State University of Technology), 434–440.

Volchek, A. A., and Shelest, T. A. (2012). Spatio-temporal fluctuations of rain floods on the rivers of Belarus. *News Russ. Acad. Sci.* 3, 76–83.

Wilson, D., Hisdal, H., and Lawrence, D. (2010). Has streamflow changed in the Nordic countries? Recent trends and comparisons to hydrological projections. *J. Hydrol.* 394, 334–346. doi: 10.1016/j.jhydrol.2010.09.010

Yang, W., Andréasson, J., Graham, L. P., Olsson, J., Rosberg, J., and Wetterhall, F. (2010). Distribution-based scaling to improve usability of regional climate model projections for hydrological climate change impacts studies. *Hydrol. Res.* 41, 211–229. doi: 10.2166/nh.2010.004

Zhmoydyak, R. A. (2009). *Atlas of Belarus Geography*. Minsk: Belarusian Science, 64.

Zhuravlev, S., Buzmakov, S., Kurochkina, L., and Shalashina, T. (2017). Spring flood variability and trends in northwest European Russia. *Russ. Meteorol. Hydrol.* 6, 99–108.

Conflict of Interest Statement: PG was employed by the company Hydrology Science and Services Corporation, Asheville, NC, United States.

The remaining authors declare that the research was conducted in the absence of any commercial or financial relationships that could be construed as a potential conflict of interest.

frontiers in Earth Science

ORIGINAL RESEARCH
published: 11 September 2019
doi: 10.3389/feart.2019.00232

Reconstruction of Large-Scale Sea Surface Temperature and Salinity Fields Using Sub-Regional EOF Patterns From Models

Jüri Elken[1], Mihhail Zujev[1], Jun She[2] and Priidik Lagemaa[1]*

[1] Department of Marine Systems, Tallinn University of Technology, Tallinn, Estonia, [2] Research and Development Department, Danish Meteorological Institute, Copenhagen, Denmark

A method for reconstruction of gridded fields of sea surface variables from time-dependent observations, using sub-regional EOF (Empirical Orthogonal Functions) patterns from models, is presented and tested. Covariance fields, calculated from the model results over long enough time span, are used to find EOF modes. The gravest "observational" amplitudes and their first temporal derivatives are determined from the least-square minimization of fitting errors in relation to the observed values. The field is reconstructed by superposition of continuous model-based mode patterns multiplied by observational amplitudes that meet adopted statistical limits. If the observational amplitude exceeds the limits, gridded fields for this and higher modes are not produced. We applied the method in the northeastern Baltic over the model time series 2010–2015. Daily averages of sea surface temperature (SST) and salinity (SSS) from the high-resolution (grid step 0.5 nautical miles) sub-regional HBM model were spatially averaged over bins of 5 × 5 nautical miles. Three first modes cover 99% of variance of temperature and 61.4% of salinity. As shown by experiments with pseudo-observations (model values at these points reconstructed to the model grid and then compared with the original model data), reconstruction performance depends on the configuration of the observation points in the model domain. Still, a few first modes usually produce acceptable results. When removing the SST seasonal cycle prior to EOF analysis, spatial patterns of leading modes remained practically unchanged, share of variance of the three first modes was reduced to 88.6% and reconstruction errors were reduced by about 25%. Sufficient spatial data coverage of the larger basin with ship-born observations usually takes quite long time – of the order of month; therefore, time correction of the amplitudes using the found temporal derivatives improves the accuracy of reconstruction. The method is compared with the Optimal Interpolation (OI) by using the pseudo-observations. Results show that, for SST reconstruction, the OI method is significantly worse than the EOF method. For SSS, OI is slightly better than EOF. The superiority of EOF is that the remote correlation patterns can be used in the reconstruction, which is important when the observations are sparse.

Keywords: sea surface observations, model-based patterns, EOF analysis, reconstruction of gap-free data, Baltic Sea

OPEN ACCESS

Edited by:
Marcus Reckermann, Helmholtz Centre for Materials and Coastal Research (HZG), Germany

Reviewed by:
Antonio Turiel, Spanish National Research Council (CSIC), Spain
Fabien Roquet, University of Gothenburg, Sweden

****Correspondence:***
Jüri Elken
juri.elken@taltech.ee

Specialty section:
This article was submitted to Interdisciplinary Climate Studies, a section of the journal Frontiers in Earth Science

Received: *14 January 2019*
Accepted: *22 August 2019*
Published: *11 September 2019*

Citation:
Elken J, Zujev M, She J and Lagemaa P (2019) Reconstruction of Large-Scale Sea Surface Temperature and Salinity Fields Using Sub-Regional EOF Patterns From Models. Front. Earth Sci. 7:232. doi: 10.3389/feart.2019.00232

INTRODUCTION

Many oceanographic tasks require appropriate reconstruction of gridded fields from different observational data: shipborne monitoring, coastal stations, offshore buoy stations, FerryBoxes, gliders and remote sensing. As a result, densely sampled sections may be neighbored with areas of rare or missing observational data.

Meteorology and oceanography share the same theoretical foundations of interpolation and data assimilation (Ghil and Malanotte-Rizzoli, 1991; Ide et al., 1997). Their practical implementation is, however, rather different (Ghil, 1989), owing to the nature of governing processes (landlocked basins, shallow areas and wind driving characterize oceans; atmosphere is unbounded, "deep" and self-driving by polar-tropical gradients), but also of techniques and amount/density of observations.

Many different methods have been applied for the data reconstruction, including both statistical [e.g., regression, optimal interpolation and Empirical Orthogonal Functions (EOFs)] and dynamic methods (e.g., data assimilation). Good reconstruction (in some statistical merit) should be based on the knowledge of multiscale spatial and temporal covariance. Atmospheric and ocean variability are similar (Woods, 1980; Cushman-Roisin and Beckers, 2011), if the lengths are scaled to the different values of baroclinic Rossby deformation radius (R_d). On the shorter scales, marginal seas and/or their sub-basins which have typical lateral dimensions less than 1000 km (typical R_d in the atmosphere), are forced by the same or neighboring weather patterns. This causes for example coherent upwelling/downwelling patterns (Lehmann et al., 2012) on the left-hand/right-hand coasts from the direction of weather-generated wind. Considering also faster heating or cooling of shallow coastal areas compared to the deeper offshore regions (Legrand et al., 2015), and freshwater spreading patterns due to the dynamics of river plumes (Soosaar et al., 2016), there could be significant covariance of sea surface temperature (SST) and sea surface salinity (SSS) in marginal seas over large distances, mainly stretched along the topography isolines and/or coasts (Fu et al., 2011).

Classical optimal interpolation (OI) (Gandin, 1963) assumes that covariance is represented by Gaussian, damped cosine or exponential decay of covariance with distance between the points. In case of open sea or dense observations (e.g., satellite SST), the OI is sufficiently good for the reconstruction (Høyer and She, 2007). However, when the observations are sparse or in the coastal waters where the covariance pattern is complicated, more comprehensive reconstruction method is needed.

Spatiotemporal variability of the ocean state can be regarded as an attractor of the dynamic ocean system in a linear phase space, in which any state can be presented as a linear summation of a complete set of orthogonal base functions. The EOFs (Davis, 1976) is one kind of such base functions, which is derived as eigenfunctions of the observed spatial covariance matrix. It projects the spatiotemporal variability of the system state onto correlation patterns of different scales, which are orthogonal. The time-space matrix of the field of interest is decomposed into the sum of space-dependent mode patterns multiplied by time-dependent amplitudes of each mode (eigenfunction). Eigenvalues present the variance of particular mode; the sum of all eigenvalues is equal to the variance of the initial field. Usually, a few most energetic modes present majority of the initial field variance. The method is not restricted to Gaussian or other similar decay over space lag.

One of the first developments of EOF interpolation in oceanography (Smith et al., 1996) considered SST on the global scale. During the period 1982–1993, when data coverage was good, SST data were gridded using traditional OI. Further, EOF modes were calculated from the gridded data. Subsequently, the EOF method was expanded to the globe in a longer period of 1950–1992. Compared to the traditional OI, the EOF produced enhanced large-scale patterns like ENSO. A number of studies (Kaplan et al., 1997; Kim, 1997; Menemenlis et al., 1997; Beckers and Rixen, 2003) have considered multivariate combined methods of interpolation: large-scale background field is approximated by the dominant EOFs; in the regions of dense sampling, the anomalies from large-scale fields are interpolated using OI or some of its modified method. There are also examples how iterated EOF method (DINEOF – Data Interpolating Empirical Orthogonal Functions) is used to reconstruct gap-free satellite images (Alvera-Azcárate et al., 2015; Jayaram et al., 2018).

The present paper has been initially motivated by the need of detailed examination of spatial covariance characteristics in a specific region – the northeastern Baltic, in relation to the data assimilation. Although using OI with Gaussian correlation function provided satisfactory results (Zujev and Elken, 2018), need for improved description of statistics deemed obvious. During different test options, we used also traditional EOF method. The covariance was determined from the model results since observational data were too irregular. The vast amount of available data was limited to the sea surface data, namely SST and SSS. Although SST is densely sampled by remote sensing, most demanding in terms of methodical aspects is using *in situ* data from a variety of platforms, e.g., research vessels, FerryBoxes and buoy stations. During the tests, we developed an easy algorithm, where "observational" amplitudes of leading base functions (EOF modes) can be evaluated by limited amount of instantaneous observational data using least-square minimization. Smith et al. (1996) have already developed this mathematics earlier, but they used the method in oceanic conditions where EOF behavior is quite different. Applying the method in the sub-region of the marginal sea, preliminary results were promising and they were presented in a recent conference paper by Elken et al. (2018).

The aim of the present paper is to develop and test the method for large-scale EOF analysis of sub-regional time-dependent SST and SSS data, based on the covariance estimates from the model results. In real oceanographic situations, spatial observations are spread over a certain time span (mapping of a sub-region by different countries/ships may take about month), therefore time correction of variables of reconstruction procedure would be useful. "Observational" EOF amplitudes and their temporal derivatives are calculated from the conditions of least-square minimization of EOF analysis error at observation points, compared to the observed values. After evaluating the covariance and EOF modes for 5-years test period, we analyze

the reconstruction accuracy using "pseudo-observations," i.e., extracting of model data at variable "observation" locations and comparing the reconstruction result with the original model result, using the EOF reconstruction but also OI. Further tests of the method include removal of SST seasonal cycle prior to reconstruction, partitioning of the study region into smaller sub-regions, comparison of reconstruction using time correction, and calculation of long sequences of gridded data using only ship-borne observations. The paper ends with discussion and conclusions.

METHODS AND DATA

Notations for Empirical Orthogonal Functions (EOF)

We follow the vector-matrix notation and consider the model results as $M \times N$ space-time matrix $\mathbf{X}$ containing deviations from space-dependent temporal mean values $\bar{\mathbf{x}}_m$. The columns $\mathbf{x}_i$ of matrix $\mathbf{X}$ are spatial time slices consisting of M points at time i, out of N time instances. Determine then the empirical orthogonal functions as $M \times M$ matrix $\mathbf{E}$, which columns are eigenvectors (normalized orthogonal spatial modes) $\mathbf{e}_k$. In the decomposition, the eigenvalues λ_k form the diagonal matrix $\mathbf{\Lambda}$ that has zeros outside the main diagonal. The eigenvalue of the specific mode presents the variance attributed to this mode; the sum of all eigenvalues is the variance of $\mathbf{X}$.

Time-dependent part of the decomposition is $M \times N$ matrix $\mathbf{A}$, which columns $\mathbf{a}_i$ are the values of time-dependent amplitude vectors (one amplitude time series value for each mode) at time i. As a result, we obtain

$$\mathbf{x}_i = \mathbf{E}\mathbf{\Lambda}\mathbf{a}_i \quad \text{or} \quad \mathbf{x}_i = \mathbf{E}\tilde{\mathbf{a}}_i \tag{1}$$

where $\tilde{\mathbf{a}}_i = \mathbf{\Lambda}\mathbf{a}_i$ is dimensional amplitude. For the whole data set $\mathbf{X} = \mathbf{E}\mathbf{\Lambda}\mathbf{A}$. Note the orthonormality as $\mathbf{e}_i\mathbf{e}_j = \delta_{i,j}$ and $\mathbf{a}_i\mathbf{a}_j = \delta_{i,j}$, where $\delta_{i,j}$is the Kronecker symbol. For the amplitudes, orthonormality usually is interpreted that amplitudes of different modes are uncorrelated in time.

The eigenvalue problem is

$$\mathbf{B}\mathbf{E} = \mathbf{\Lambda}\mathbf{E} \tag{2}$$

(equivalent to $|\mathbf{B} - \lambda\mathbf{I}| = 0$), where the covariance matrix averaged over N instances of time is

$$\mathbf{B} = \frac{1}{N-1}\mathbf{X}^{\mathrm{T}}\mathbf{X} \tag{3}$$

Matrix $\mathbf{E}$ can be found by a number of methods for solving linear system of equations. One favorite method is singular value decomposition (SVD). Due to the orthonormality $\mathbf{E}^{\mathrm{T}}\mathbf{E} = \mathbf{I}$. The dimensional amplitudes are determined by the relation

$$\tilde{\mathbf{a}}_i = \mathbf{\Lambda}\mathbf{a}_i = \mathbf{E}^{\mathrm{T}}\mathbf{x}_i \tag{4}$$

Reconstruction of Observed Fields Using EOF Modes

Consider now the case where observations at a specific time instance i are represented by vector $\mathbf{y}_i$ that has different set of K points than M points for $\mathbf{x}_i$. If observations include high-resolution data that contain multiple data points within the grid cell and time interval of model lattice, such oversampling has to be removed prior to further analysis, usually by averaging over the grid cell. Therefore $K \leq M$. Gridded data $\mathbf{x}_i$ are transformed to the observation points by matrix $\mathbf{H}_i$ (observation function) in a way that $\mathbf{H}_i\mathbf{x}_i$ has the same dimension as $\mathbf{y}_i$ and has to be directly compared with it. To be more specific, vector $\mathbf{y}_i$ presents the observed deviations from the temporal mean value $\mathbf{H}_i\bar{\mathbf{x}}_m$ whereas the observation function $\mathbf{H}_i$ depends on the configuration of observation points. Eigenvalue transformation takes the form $\mathbf{H}_i\hat{\mathbf{x}}_i = \mathbf{H}_i\mathbf{E}\,\hat{\mathbf{a}}_i$, where $\hat{\mathbf{a}}_i$is the "observational" amplitude, determined from observed values $\mathbf{y}_i$ at K observation points, using the full patterns of EOF modes $\mathbf{e}_k$ with M spatial points. For the least-squares minimization of $||\mathbf{y}_i - \mathbf{H}_i\mathbf{x}_i||^2 = ||\mathbf{y}_i - \mathbf{H}_i\mathbf{E}\hat{\mathbf{a}}_i||^2$, the system of equations is $\mathbf{H}^{\mathrm{T}}\mathbf{E}^{\mathrm{T}}\mathbf{H}\mathbf{E}\hat{\mathbf{a}}_i = \mathbf{H}^{\mathrm{T}}\mathbf{E}^{\mathrm{T}}\mathbf{y}_i$, where the amplitudes as $K \times 1$ vector and interpolated field $\hat{\mathbf{x}}_i$ are found from

$$\hat{\mathbf{a}}_i = (\mathbf{H}_i^{\mathrm{T}}\mathbf{E}^{\mathrm{T}}\mathbf{H}_i\mathbf{E})^{-1}\mathbf{H}_i^{\mathrm{T}}\mathbf{E}^{\mathrm{T}}\mathbf{y}_i, \quad \hat{\mathbf{x}}_i = \mathbf{E}\hat{\mathbf{a}}_i \tag{5}$$

Note, that we cannot here anymore use the condition that the mode patterns are orthonormal.

In the matrix of eigenvectors $\mathbf{E}$, where different modes are presented by column vectors, we take only L first vectors and the rest of the columns are truncated to zero. When using only L modes for reconstruction, contribution of truncated modes is added in the error variance.

For the clarity of the calculations, we spell out also the element-wise summation form without presenting the time index. Minimization is done for $Q = \sum_{k=1}^{K}\left(y_k - \sum_{l=1}^{L}\hat{a}_l\hat{e}_l^k\right)^2$, leading to the L conditions $\partial Q/\partial\hat{a}_l = 0$. It results in the $L \times L$ system of linear equations

$$\mathbf{D}\hat{\mathbf{a}} = \mathbf{h} \tag{6}$$

where the matrix and vector elements are

$$D_{mn} = \sum_{k=1}^{K}\hat{e}_m^k\,\hat{e}_n^k,\ h_m = \sum_{k=1}^{K}y_k\,\hat{e}_m^k \tag{7}$$

Here $\hat{e}_m^k$ is the m-th eigenvector mapped to the observation point k.

The original dimensional amplitudes $\tilde{\mathbf{a}}$ have some statistical regularities determined over a large number of samples. Such regularities contain e.g., standard deviation σ or variance σ^2, percentiles and covariance in relation to time lag etc. The observational amplitudes $\hat{\mathbf{a}}$ are determined from much less amount of information and are rather uncertain. There is a caution that with bad configuration of the observation points, observational EOF amplitudes of particular modes may get larger than limits determined from full statistics (details in section Covariance and EOF Characteristics). Therefore it is important to determine the maximum number of modes L by checking if determined $\hat{\mathbf{a}}$ values lie within the statistical limits of $\tilde{\mathbf{a}}$; if the limits are exceeded then this and higher modes are removed from the further analysis.

Extension of the EOF Reconstruction Method to Time-Dependent Data

Quite often in oceanographic practice, there are not enough observational data at a specific time instance i to perform reliable construction of observations. Shipborne surveys over larger sub-regions may take several days or even weeks. Usual procedure is to consider the observations $\mathbf{y}_p$ made within the time window $n_1 \ldots n_2$, $p \in n_1 \ldots n_2$ as instantaneous, and reference the (non-processed) result to the time instance i, when $n_1 \leq i \leq n_2$. Such procedure can introduce apparent distortions, when the observations are conducted during the increase or decrease period within the seasonal cycle. For example, when during the spring warming period the observations are first acquired in the southern part and later in the northern part, then higher temperatures presented in the northern part of the map compared to the southern part are just an artifact, due to missing treatment of time-dependence of the data.

Take now the P observed data $\mathbf{y}_p$ within window $p \in n_1 \ldots n_2$ and construct modified observation function $\hat{\mathbf{H}}_p$ that allows pointwise comparison of $\mathbf{y}_p$ at different times and $\hat{\mathbf{H}}_p\mathbf{x}$ based on gridded data at specified time i. Time difference of observation p and reference time i is determined $\Delta t_p = t_p - t_i$. Eigenvalue transformation is $\hat{\mathbf{H}}_p\hat{\mathbf{x}}_i = \hat{\mathbf{H}}_p\mathbf{E}\,\hat{\mathbf{b}}_p$, where modified amplitude, accounting for linear time dependence given by rate of change vector $\boldsymbol{\alpha}_i$, is $\hat{\mathbf{b}}_p = \hat{\mathbf{a}}_i + \boldsymbol{\alpha}_i \cdot \Delta t_p$. The function to be minimized is $Q = ||\mathbf{y}_p - \hat{\mathbf{H}}_p\mathbf{E}\hat{\mathbf{b}}_p||^2 = ||\mathbf{y}_p - \hat{\mathbf{H}}_p\mathbf{E}(\hat{\mathbf{a}}_i + \boldsymbol{\alpha}_i \cdot \Delta t_p)||^2$ regarding $\partial Q/\partial \hat{a}_l = 0$ and $\partial Q/\partial \alpha_l = 0$. Define the $2L$ unknown coefficients $\mathbf{z} = \{\hat{a}_1 \ldots \hat{a}_L,\ \alpha_1 \ldots \alpha_L\}$ and modified EOF mode values at observation points $\mathbf{f}_m^p = \{\hat{e}_1^p \ldots \hat{e}_L^p,\ \hat{e}_1^p \Delta t_p \ldots \hat{e}_L^p \Delta t_p\}$, we obtain $2L \times 2L$ system of linear equations

$$\mathbf{G}\mathbf{z} = \mathbf{w} \tag{8}$$

where the matrix and vector elements are

$$G_{mn} = \sum_{p=1}^{P} f_m^p f_n^p, \quad w_n = \sum_{p=1}^{P} y_p f_n^p \tag{9}$$

We note that when all observations have the same time stamp and $\Delta t_p = 0$, the system (8)-(9) is reduced to (6)-(7).

From the found vectors $\mathbf{z}$ we extract separately observational amplitudes $\hat{\mathbf{a}} = \{\hat{a}_1 \ldots \hat{a}_L\}$ and their temporal derivatives $\boldsymbol{\alpha} = \{\alpha_1 \ldots \alpha_L\}$, where they both are checked for the statistics of full data set, in order to determine the highest acceptable mode L.

Reference time i for observational amplitudes (and corresponding reconstructions) can be modified on the condition of acceptable accuracy. Finding these bounds is a subject of separate study. In principle, it is possible to perform centered referencing, including the data from past and future times (like it is done in processing of existing time series), but also backward referencing, including only the past data (like within data assimilation for on-line forecasts).

Estimation of Reconstruction Accuracy Using Pseudo-Observations

Accuracy of EOF reconstruction by a limited number of modes is performed by evaluating the reconstructed fields versus original fields over a sufficiently long span of time. In case of observational data, another key factor, besides the number of modes, is configuration (including the number) of observation points. Assuming that statistical features of observations are close to that of the model results, we introduce pseudo-observations as extract of model results in the predefined locations where usually observations are taken. Accuracy of reconstruction from the pseudo-observations was checked by a series of experiments containing the following steps: (i) Configuration of observation points was selected; (ii) model values were extracted at observation points (pseudo-observations were taken); (iii) reconstructed fields $\hat{\mathbf{x}}_i$ were calculated from pseudo-observations using (5)-(7); (iv) calculations were repeated for all time instances available, statistical characteristics like root-mean-square deviation (RMSD) between the reconstructed and original fields were evaluated.

The main experiments were made for the case of pseudo-observations on the variable grid. The factor N by which the grid step of observations were larger than the model grid was varied from 1 to 11. Additional experiments were performed with configurations typical to the FerryBox observation points and typical to the marine shipborne monitoring with reduced sampling network (Elken et al., 2018; not shown here).

In addition to the EOF reconstruction, OI was used for comparison purposes in two configurations: (i) interpolation of deviations from locally resolved mean (modeled) fields that includes high gradients in the coastal areas of river influence zones, (ii) interpolation of deviations from smooth climatological mean fields. Both configurations used Gaussian correlation function in the form $C(r) = \exp(-r^2/R^2)$ (e.g., Zujev and Elken, 2018), where r is the space lag and R is the correlation scale. The OI configurations used for smoothing purposes prescribed noise-to-signal ratio η^2.

Regional Setting of Experiments

We chose the area of our study in the northeastern Baltic (**Figure 1**) that contains two distinct geographical areas – Gulf of Finland and Gulf of Riga – and includes the northeastern part of the Baltic Proper. The Baltic Sea is a brackish estuarine-type multi-basin marginal sea (Elken and Matthäus, 2008; Leppäranta and Myrberg, 2009), where complex coastline and topography essentially guide the dynamics of SST and SSS. In the Gulf of Finland, EOF modes have profound structure (Elken et al., 2011). Thermal regime is dominated by the seasonal heat cycle, but it is also modified by differential heating/cooling above variable depths in the coastal and offshore areas. Ice cover occurs in the coastal areas every winter, while open parts of the sub-area are ice-covered during severe winters (Vihma and Haapala, 2009). SST is heavily modified by upwelling and downwelling patterns induced by the transient wind fields (e.g., Laanemets et al., 2011). Due to the fragmented coastline and multiple rivers entering the area, SSS has numerous high-gradient regions. Large scale SSS patterns are guided by unsteady circulation that depend on the climatic variations of atmospheric forcing; while earlier studies suggested cyclonic circulation patterns in both the Gulf of Finland and the Gulf of Riga and right-hand spreading of less saline waters from the large Neva and Daugava rivers, then recent

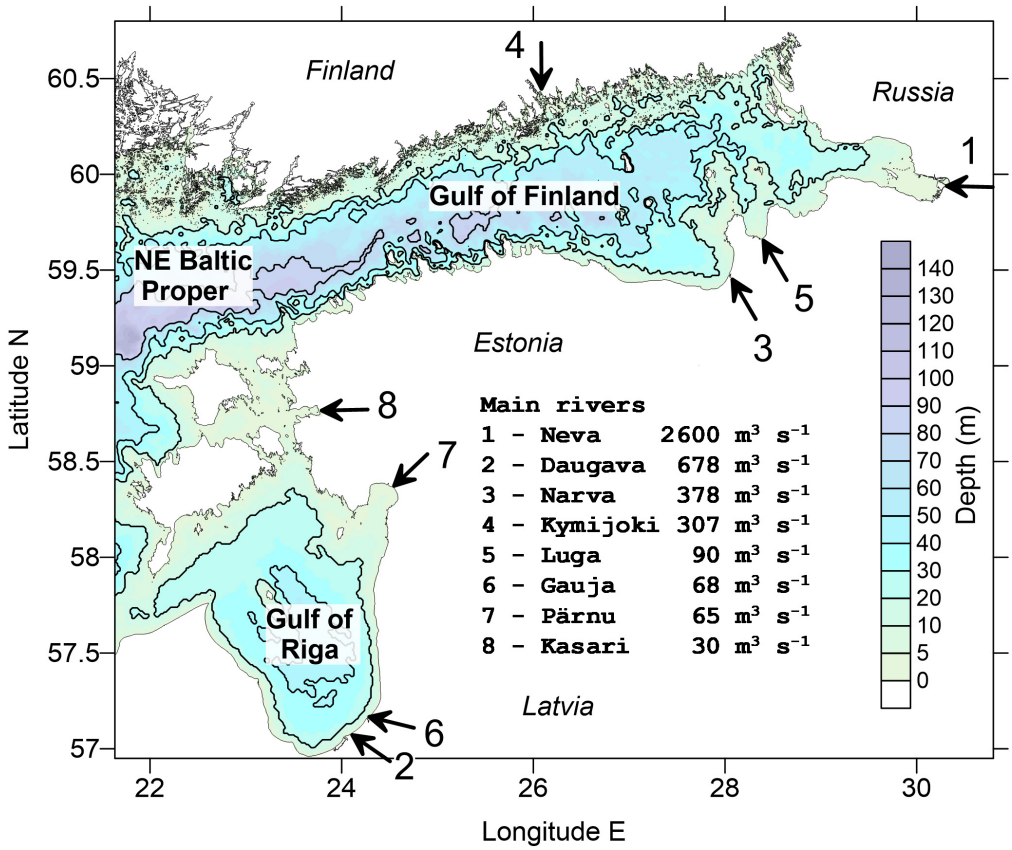

FIGURE 1 | A map of the study area in the northeastern Baltic. Shown are the main 8 rivers bringing into the sea mean freshwater discharge ($m^3\ s^{-1}$) as given in the legend.

studies frequently reveal also anticyclonic patterns (Soosaar et al., 2016). Mesoscale variability has rather short spatial scales; the R_d values are from a few km to about 7 km (Alenius et al., 2003).

We used the HBM model (Berg and Poulsen, 2012) with sub-regional 0.5 NM (nautical mile, 926 m) setup (Lagemaa, 2012; Zujev and Elken, 2018) in the geographical bounds shown in **Figure 1** to produce the SST and SSS data. This HBM-EST model domain contains 529 × 455 horizontal grid points. Forcing at the western open boundary is taken from the Baltic-wide HBM model, which operates routinely within the Copernicus Marine Environment Monitoring Service (CMEMS) with the resolution of 1 nautical mile. Forcing on the sea surface is obtained from the Estonian version of the HIRLAM model that is run by the national weather service for operational forecasts on 11-km grid.

HBM is a 3D oceanographic model for the North and Baltic Sea, which uses Arakawa C-grid and is forced by surface energy fluxes (mechanical, radiative, thermodynamic) using bulk parameterization formulae. The model includes sub-models for turbulence parameterization. A model for ice thermodynamics and ice mechanics is embedded into the model system. The HBM model has been upgraded within the CMEMS from earlier BSHCmod versions. The Baltic-wide HBM setup is extensively validated within CMEMS. The quality information document for physical variables can be found on the web http://cmems-resources.cls.fr/documents/QUID/CMEMS-BAL-QUID-003-006.pdf as accessed on 10 July 2019.

For the analysis we used daily model data of free run (without data assimilation) averaged over 10 × 10 grid points, resulting in 744 wet points with 5 NM (9.26 km) resolution on the coarse grid. Since the grid step of the averaged fields is larger than the Rossby deformation radius, mesoscale patterns were suppressed in the analysis results. The 5-year analysis period covered 1826 dates from July 1, 2010 to June 30, 2015.

In the observational data we focused on the *in situ* SST and SSS data and remotely sensed SST data were occasionally used for the comparison. Shipborne profile observations were acquired from HELCOM/ICES database, downloaded from https://ocean.ices.dk/helcom/ on 12 February 2018. After extraction of surface data within the study area, 2915 data records were retrieved within 2009-2014. Prior to using the data for the reconstruction, oversampling for each particular time instance was eliminated by taking averages on the coarse grid and selected time interval. CMEMS remote sensing SST Level 4 (L4) data were downloaded from the service portfolio http://marine.copernicus.eu/services-portfolio/access-to-products/ as the product SST_BAL_SST_L4_NRT_OBSERVATIONS_010_007_b. FerryBox data were obtained from the same portfolio as the product INSITU_BAL_NRT_OBSERVATIONS_013_032.

Climatological monthly temperature and salinity fields were adopted from the study made by Janssen et al. (1999), covering the period 1900–1996.

RESULTS

Mean and Standard Deviations of SST and SSS

The mean fields of surface temperature and salinity, shown in **Figures 2A,B**, were calculated as temporal mean values of individual grid points $\bar{\mathbf{x}}_m$ over the whole study period. Data assimilation was not performed; therefore, the presented maps may include some model bias. Primary purpose of the mean fields is to set the background for the variability study, i.e., investigate statistical properties of SST and SSS deviations from their fields.

The maps of mean SST and SSS are dependent on the average atmospheric conditions during the period summer 2010 – summer 2015. The period covered severe ice winter (2010/2011), and average (2011/2012, 2012/2013) and mild (2013/2014, 2014/2015) winters (FMI, 2018). The mean SST map reveals lower temperature along the Finnish coast; that occurs during dominating westerly winds favoring upwelling in that region. This is consistent with mean salinity distribution in the Gulf of Finland that exhibited pattern typical to the dominance of reversed estuarine circulation (Westerlund et al., 2019), where tongue of less saline water near the Finnish coast is not present. While our SSS map is close to the yearly climatological map (Janssen et al., 1999) then SST is in the Gulf of Finland higher by 1–1.5°C and in the Gulf of Riga by 0.5–1°C.

Based on all the model values for the period 2010–2015, we calculated total mean value and the corresponding standard

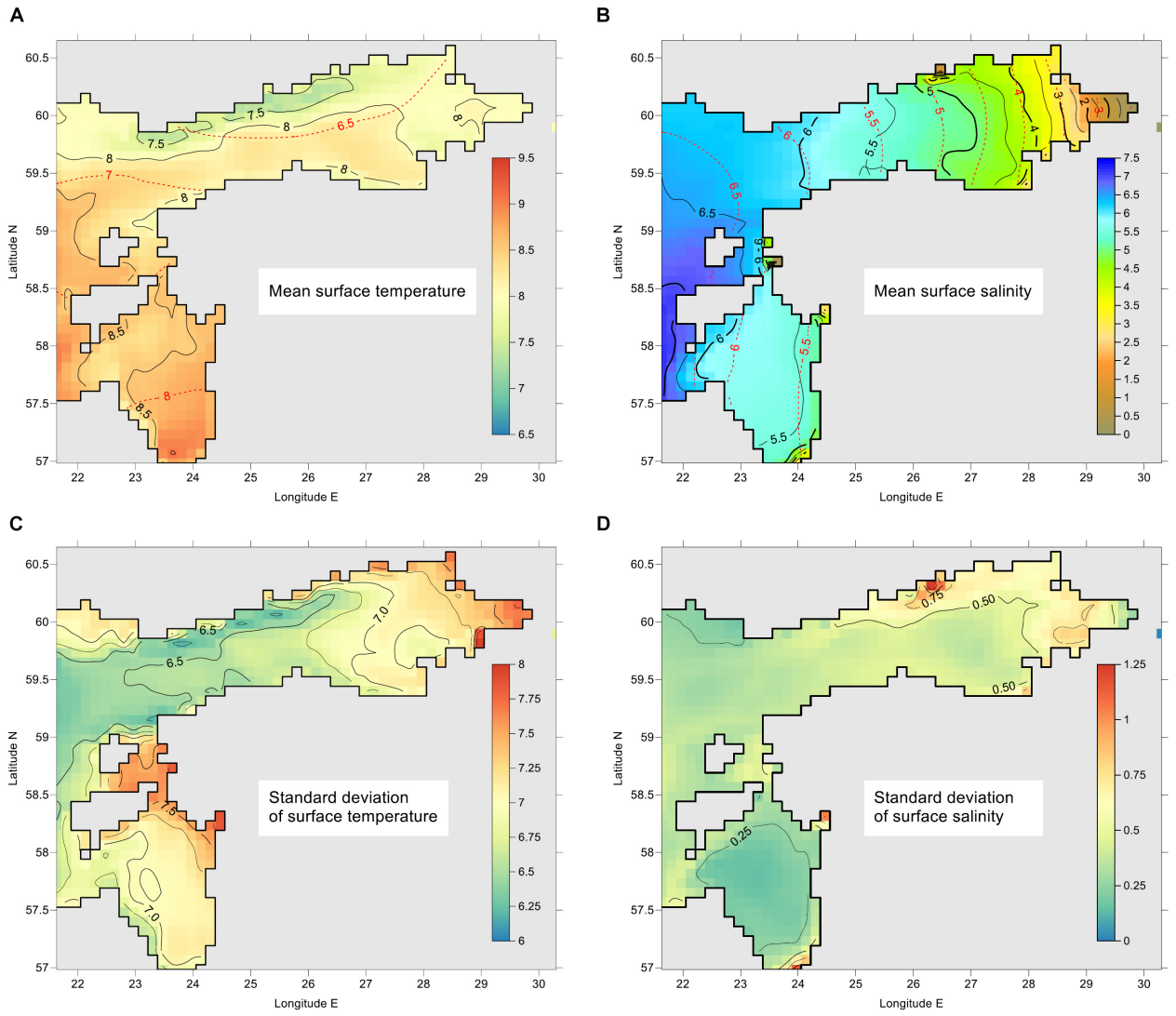

FIGURE 2 | Maps of mean values **(A,B)** and standard deviations **(C,D)** for SST **(A,C)** and SSS **(B,D)**. Model grid statistics is calculated from 1 July 1 2010 to 30 June 2015. Climatological mean values for the period 1900–1996 (Janssen et al., 1999) are shown in **(A,B)** by red isolines. The units are °C for SST and g kg^{-1} for SSS.

deviation σ for SST as 8.2 and 7.0°C, and for SSS as 5.45 and 1.3 g kg^{-1}. While variability of SST is strongly dominated by temporal changes, SSS variability reveals dominant spatial changes. Namely, mean temporal variance $\overline{\sigma_t^2(k)}^k$, calculated on the basis of all spatial points k, comprises 99% of total variance for SST but only 11% for SSS. The remaining percentage of variance is due to variability of spatial means. Alternatively, mean spatial variance $\overline{\sigma_x^2(i)}^i$, calculated on the basis of all temporal instances i, reveals 97% of total variance of SSS and only 3% of SST. During individual time instances, spatial standard deviation $\sigma_x(i)$ for SST was found from 0.08 (during winter) to 2.8°C; SSS values range from 0.95 to 1.5 g kg^{-1}.

Maps of temporal standard deviations $\sigma_t(k)$, calculated for each spatial point k, are presented in **Figures 2C,D**. These maps include seasonal cycle but also interannual and shorter period variations. Despite the small fraction of spatial variance of SST, some distinct spatial features over the area are evident. Higher temporal standard deviations of SST (above 7.2°C) are found in the shallow areas in the eastern part of the Gulf of Finland and in the Moonsund located between the large Estonian islands and the mainland. Spatial variations $\sigma_t(k)$ of SSS are in the range from 0.14 g kg^{-1} to 1.5 g kg^{-1} (**Figure 2D**), whereas higher values occur near the entrance of larger rivers. High spatial variations of standard deviation make difficult using spatial correlation functions, which calculation require normalizing covariance with variance.

Covariance and EOF Characteristics

We calculated SST and SSS covariance according to Equation (3). After EOF decomposition of **B** using Equation (2), we also calculated covariance of the sum of six most energetic modes and of the rest higher modes. Due to orthogonality, covariance is additive regarding the EOF modes, i.e., the full covariance is the sum of covariance of the component data sets (six most energetic modes, and the rest higher modes). In **Figure 3** SST and SSS covariance are presented as a function of space lag between the model points. We see significant spreading of individual values of covariance over pairs of points and conclude that calculated covariance is not homogeneous, which is usually assumed in implementation of OI.

In the bins of space lags, distribution (histogram) of covariance of original fields and of the sum of most energetic EOF modes (not shown) usually does not follow the normal distribution. Therefore, mean covariance values can be considered only as indicative, since they differ significantly from the median values. Still it is clear that big covariance values occur over large distances, especially for SST. Covariance of residual fields (sum of higher EOF modes) has a good normal distribution and it decays fast with increasing space lag. Correlation (not shown) goes below 0.2 at a distance of 30 km for both SST and SSS, justifying the use of OI for this part of the variability.

Spatial EOF mode patterns for 4 leading modes are given in **Figures 4**, **5** for SST and SSS, respectively. The one-dimensional vectors $\mathbf{e}_k$ of the SST and SSS modes are remapped back into the two-dimensional geographical framework.

Among the spatial patterns, large-scale physical interpretation can be easily found for four to six modes. The first, most energetic modes have nearly "flat" patterns without sign change; their amplitudes are dominated by a seasonal signal. Higher modes are considered random due to eddies and other mesoscale processes, therefore their correlation decays rapidly with increasing distance (see the earlier sub-chapter). In the SST patterns, the first mode dominates heavily (97.64% of variance explained) due to the seasonal cycle (**Table 1**). In the SSS patterns (**Table 2**), the share of different modes is more distributed and the first six modes explain 72.88% of the total variance.

Temporal variance of the mode amplitudes $\tilde{\mathbf{a}}$ equals to the eigenvalues of covariance matrix **B**. Based on the statistical features of the amplitudes, it is possible to set the "natural" limit F_k for each of the mode k. During EOF reconstruction, we use only the modes k where the estimated individual amplitude values at time i follow the condition $|\hat{a}_{i,k}| < F_k$. Since the absolute values depend on the number of grid point, configuration of the sea area and other factors, we do not present the numerical values of F_k. Excluding 10% of the higher and lower values of "natural" (calculated from full set of model results) amplitudes, a reasonable limit is $F_k = 2\,\sigma(\tilde{\mathbf{a}}_k)$.

We have presented in this paper the formulae (5)-(7) how to reconstruct gridded fields from observations made during one fixed time instance. Actual spatial observations are quite often not instantaneous in time. The weights of observations from past and future times depend on the temporal covariances (or correlations). Within the EOF decomposition, amplitudes of SST and SSS modes have different temporal correlation patterns, as shown in **Figure 6**. For the SST, the first and the second modes are nearly annually periodic with correlation $r > 0.9$ and shifted phases. Moderate semi-annual periodicity (r∼0.2–0.3) appears on the fifth mode. The first SSS mode has annual harmonic with $r \approx 0.4$. The second SSS mode has even stronger annual harmonic with $r \approx 0.6$. Based on long correlation times, we consider the method of EOF reconstruction of time-dependent observations, presented by formulae (8)-(9), justified for the time window up to 1–2 months.

Reconstruction Errors: Experiments With Pseudo-Observations

Dependence of accuracy of EOF reconstruction on the number and spacing of observation points was firstly studied by grid configuration of pseudo-observations (see section Estimation of Reconstruction Accuracy Using Pseudo-Observations) with variable grid step. At prescribed locations, model data were extracted on specific time instance; then the result of gridded reconstruction was compared with the original model data. Observational grid step Δ_o was taken as integer n times the model grid step Δ_m, $\Delta_o = n\,\Delta_m$. Observation grid step factor n was cycled from 1 (observations taken at all the model points) to 11 or more (leaving 2-6 observation points).

We made pointwise comparison of all the 744 spatial points during 1826 time instances, using 6 EOF modes for the reconstruction. Frequency histograms of deviations for SST and SSS are presented in **Figure 7** for two spacing options between

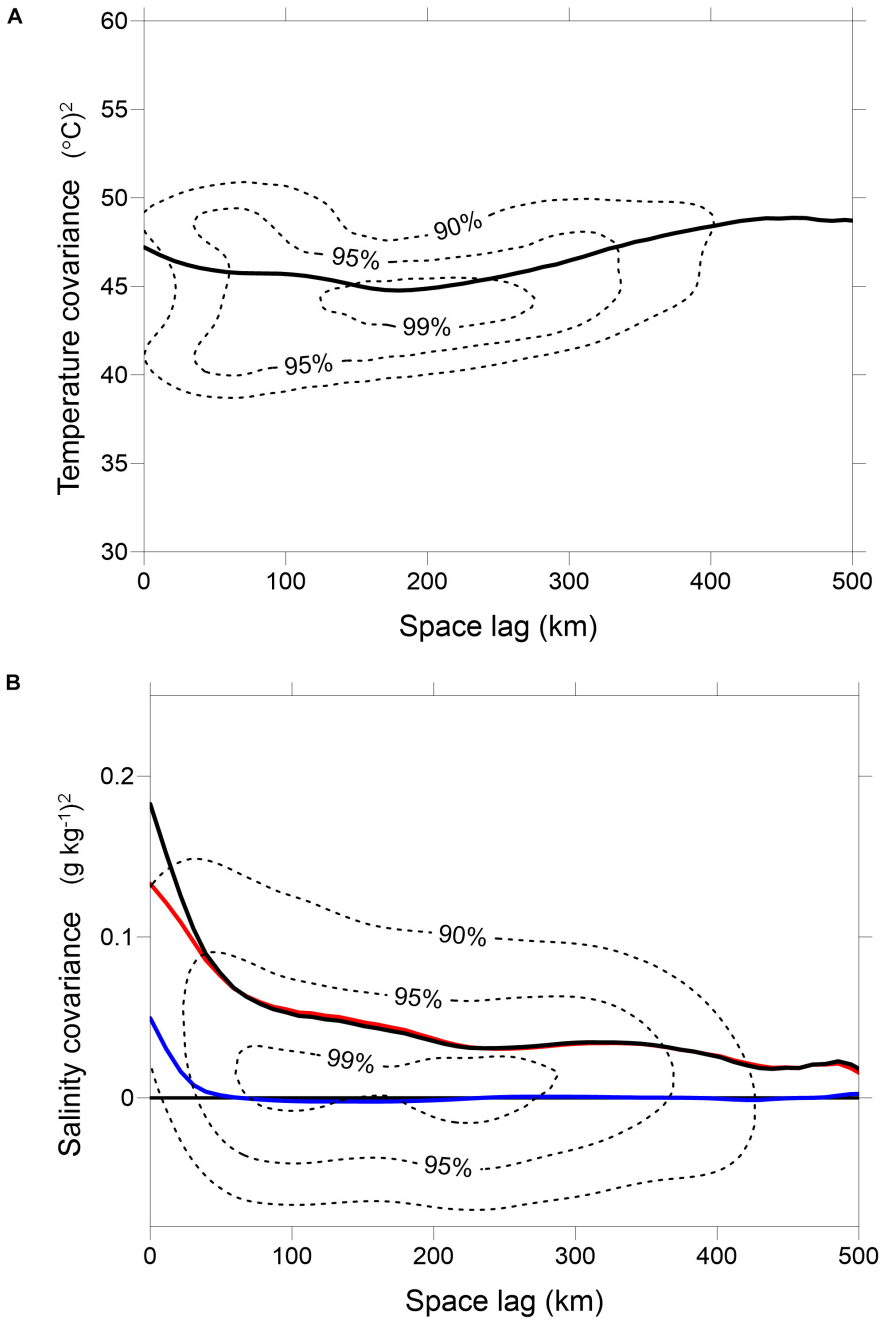

FIGURE 3 | Covariance of SST **(A)** and SSS **(B)** as a function of space lag between the model points. Shown are heavily smoothed two-dimensional relative histograms of the original data (dotted lines, percentiles 90, 95, and 99%) and mean covariance of original data (black line). For SSS are shown also covariance of the sum of six most energetic EOF modes (red line) and of higher EOF modes (blue line). For SST the latter curves are not distinguishable from mean covariance and zero, respectively.

the pseudo-observations. We reveal that error histograms are quite insensitive to the number of observations K, when it is larger than the number of significant modes L. However, at small observation amounts the number of larger errors (can be considered as outliers regarding normal distribution) increases. On the background of grid points of 37 km spacing, reconstructed SST and SSS maps are shown for one arbitrary date 19 June 2015 (**Figures 8C,D**) together with the original model data (**Figures 8A,B**).

With decreasing number of observations K, errors slightly increase when still $K > L$. For example, SSS absolute error is less than 0.3 g kg^{-1} for 88% of cases with K = 51 and 80% of cases with K = 10. Regarding SST, the errors are less than 0.6°C correspondingly for 90 and 82% cases. Regression of all

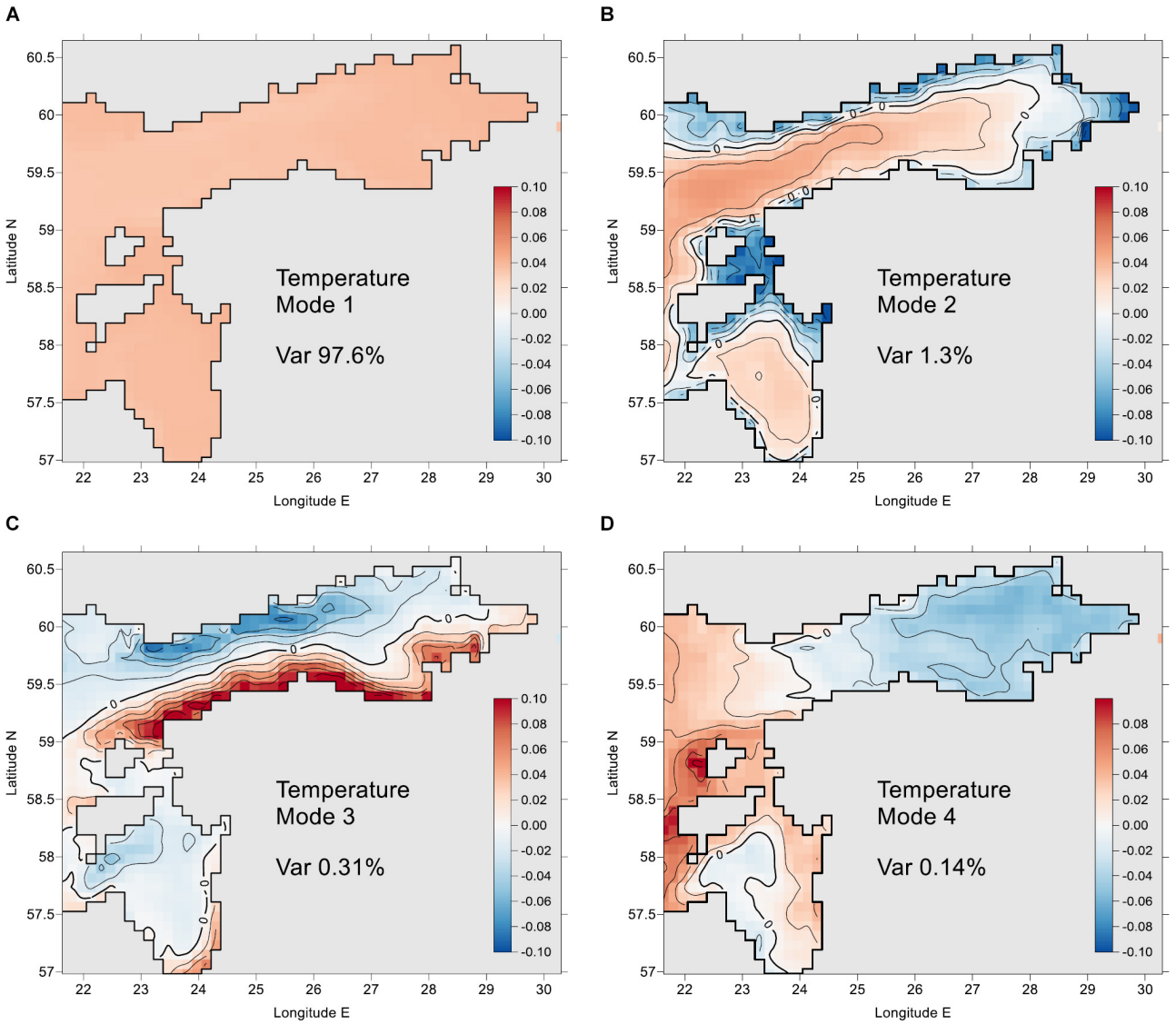

FIGURE 4 | EOF patterns for four first modes of SST. Shown are the number of mode (1 to 4 as **A** to **D**) and explained variance percentage of each mode. Contour interval for non-dimensional normalized modes (744 points) is 0.02.

the values of both SST and SSS yields tangent between initial and reconstructed data 0.99, their correlations follow $r > 0.95$. Relative errors of all the SST data, compared with horizontal standard deviation $\sigma_x(i)$ of each time instance, are from 6.7% (observation grid step 37 km) to 8.6% (93 km). Relative errors of SSS are somewhat larger, correspondingly 18 and 25%. For $K < L$ the errors increase abruptly and singularity errors may occur in Equations (5)–(7).

Reconstruction capability from realistic sampling schemes was evaluated for typical monitoring network (with smaller number of stations than usual) and for two routes of FerryBox along Tallinn-Helsinki and Tallinn–Stockholm (Petersen, 2014; Kikas and Lips, 2016). Pseudo-observations from the selected configurations were run through all the daily model maps. The error statistics did not differ much from that of the above-described observation grid experiments. Inspecting the reconstructed maps (not shown), even with small number of observations the reconstructed maps generally match well to the original maps. The monitoring type of stations has observations in all the three main areas: Gulf of Finland, Gulf of Riga and adjacent Baltic Proper. The SST and SSS maps reconstructed from the pseudo-observations (not shown) match well the original maps. FerryBox data set has no data in the eastern Gulf of Finland and in the Gulf of Riga (see an example by Elken et al., 2018), therefore larger deviations of reconstructed data from initial data occur in these regions. However, main large-scale SST and SSS features, present in the initial model data, can be identified in the reconstructed maps rather well.

For comparison of EOF reconstruction with OI, we set up an experiment where EOF statistics were calculated during 4 years

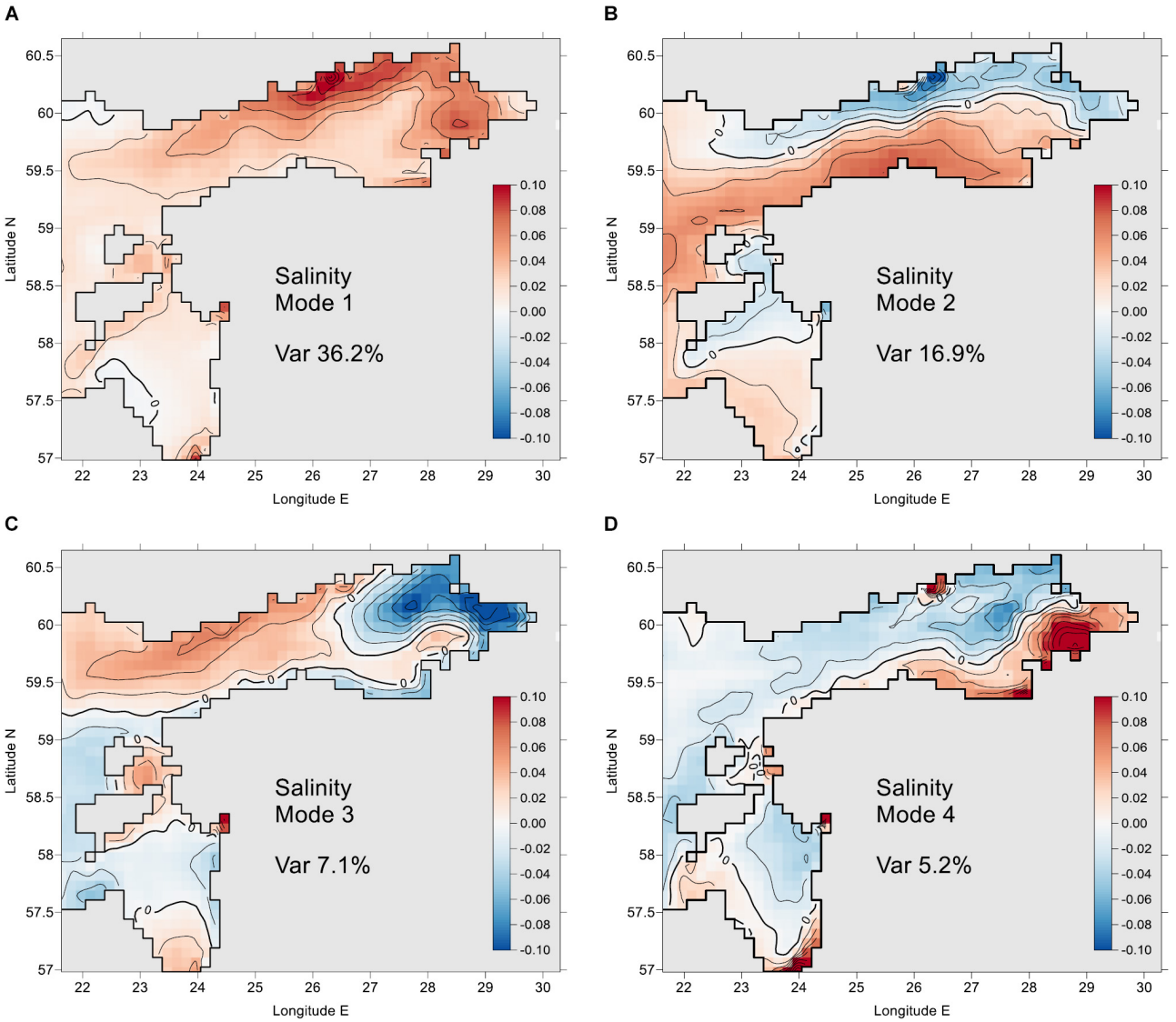

FIGURE 5 | EOF patterns for four first modes of SSS. Shown are the number of mode (1 to 4 as **A** to **D**) and explained variance percentage of each mode. Contour interval for non-dimensional normalized modes (744 points) is 0.02.

from 1 July 2010 to 30 June 2014, and the remaining 1 year period from 1 July 2014 to 30 June 2015 was dedicated for comparison. For each set of $\Delta_o = n\,\Delta_m$, we included all the possible shifts of observation grid into the comparison. For example, in case of $n = 8$ there are 64 options for grid shift. All those shift options produce different result of reconstruction, because of different resolution of topographic and coastline features and freshwater input areas. The points just neighboring the coast were excluded. The method of OI was used with correlation scale $R = 200$ km and noise-to-signal ratio $\eta^2 = 0.1$ (see section Estimation of Reconstruction Accuracy Using Pseudo-Observations).

Dependence of RMSD of reconstruction on the spacing for 3 compared methods – EOF, OI-M with modeled mean field, and OI-C with climatological mean fields – is presented in **Figure 9** as median values taken over all shift options.The spread

TABLE 1 | Characteristics of SST modes.

Mode nr	% variance	Description
1	97.6%	Nearly uniform over space increase or decrease of SST, represents seasonal heating and cooling.
2	1.3%	Faster heating (in spring) or cooling (in autumn) in the shallow coastal areas, compared with deeper offshore areas.
3	0.31%	Transverse colder or warmer anomaly stripes near northern or southern coasts, like upwelling and downwelling.
4	0.14%	Longitudinal colder or warmer anomalies appearing in east-west direction.
5	0.10%	Different heating or cooling of the SW Gulf of Riga and NW-N Gulf of Finland.
6	0.07%	Physics not clear.

TABLE 2 | Characteristics of SSS modes.

Mode nr	% variance	Description
1	36.2%	Increase or decrease of salinity over the whole study area (all changes have the same sign). Larger changes occur in the northeastern Gulf of Finland, near the discharge of the largest rivers in the region.
2	16.9%	Transverse anomalies of salinity near northern or southern coasts, like upwelling and downwelling.
3	7.1%	Salinity changes in the freshwater spreading pathway near the northern coast of the Gulf of Finland, reminds cyclonic circulation.
4	5.2%	Salinity changes near the southeastern coasts, characteristic to alteration of cyclonic and anticyclonic circulation.
5	4.1%	Physics not clear.
6	3.5%	Physics not clear.

of individual shift estimates increases from the spacing 46 km toward greater spacing and smaller number of pseudo-observations, especially for the EOF method. In case of SST, EOF methods produces on the average more accurate reconstruction than both of the OI methods using the values given above. Still, during individual time instances the reconstruction results may have similar difference pattern at large spacing of sampling (**Figures 10A,C**) since coastal features may remain unresolved. We had to choose large correlation scale and noise-to signal ratio in order to have reconstruction over the whole area even if the spacing of observations is large; then OI tends to make heavy smoothing that is reflected in **Figure 9A** by larger RMSD. SSS field is dominated by spatial variations; one control value of such domination is RMSD = 0.411 g kg^{-1} of "no observations" (at each grid point, mean value is taken instead of observed value) that lies in the range of RMSD variation (**Figure 9B**).

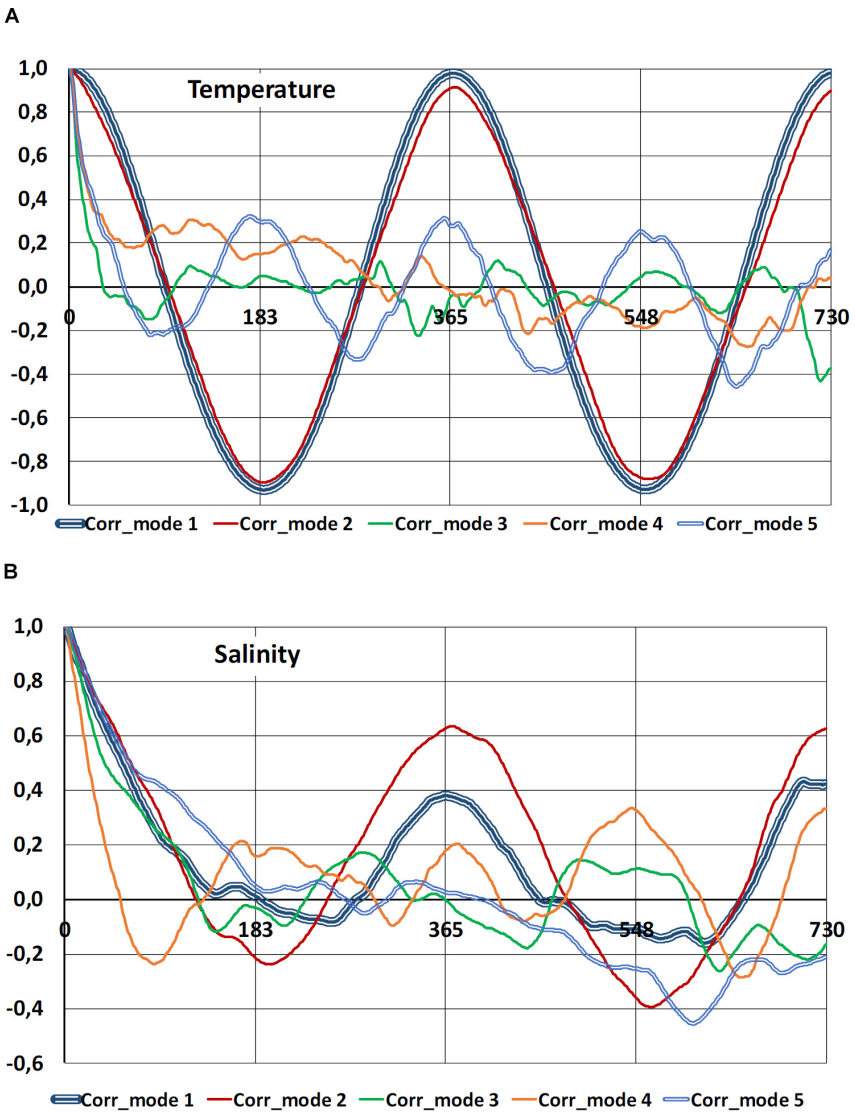

FIGURE 6 | Temporal correlation functions of first five EOF mode amplitudes given in the legend for SST **(A)** and SSS **(B)**. Horizontal axis shows time lag in days.

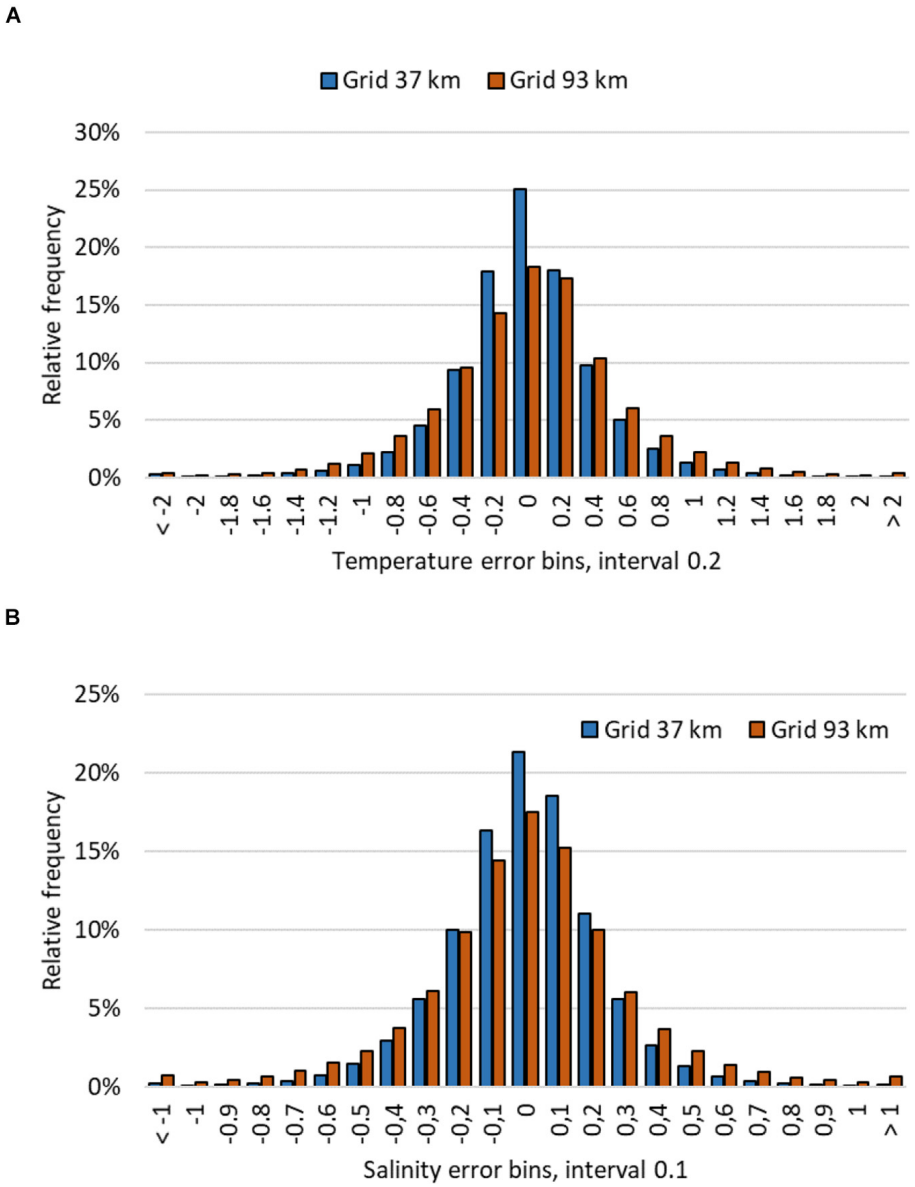

FIGURE 7 | Relative frequency of SST **(A)** and SSS **(B)** differences between reconstructed (sum of six EOF modes) and initial field. Shown are results with pseudo-observation data prescribed by 37 km grid step (51 observation points) and 93 km grid step (10 points). Compared are about million data pairs.

Evaluation reveals that EOF reconstruction has slightly larger error than OI relative to the modeled mean field. Commonly used OI with deviations from climatological mean reveals larger RMSD than EOF; it even exceeds the "no observations" already with spacing larger than 28 km. These features of RMSD appear due to the specific topographic and hydrographic features of the region: fragmented coastline and prevalence of low-salinity regions with surrounding higher spatial gradients and temporal standard deviations (**Figure 2**) near the entrances of larger rivers (**Figure 1**). If OI considers and interpolates the SSS deviations from highly variable spatial mean map (determined by the model that resolves local features), then such deviations follow normal distribution without significant outliers (not shown) and local features appear in the reconstruction product without remarkable distortion. Deviations from spatially smooth climatological mean values (**Figure 2B**) contain a high number of outliers to the normal distribution, that cause larger distortions of OI-C reconstruction in the river influence areas than EOF reconstruction (**Figures 10B,D**).

Seasonality Issues in EOF Reconstruction of SST

Among variety of physical processes, original SST data from model reveal significant seasonal variation in time. Annual cycle is evident in temporal correlation of the amplitudes of first and

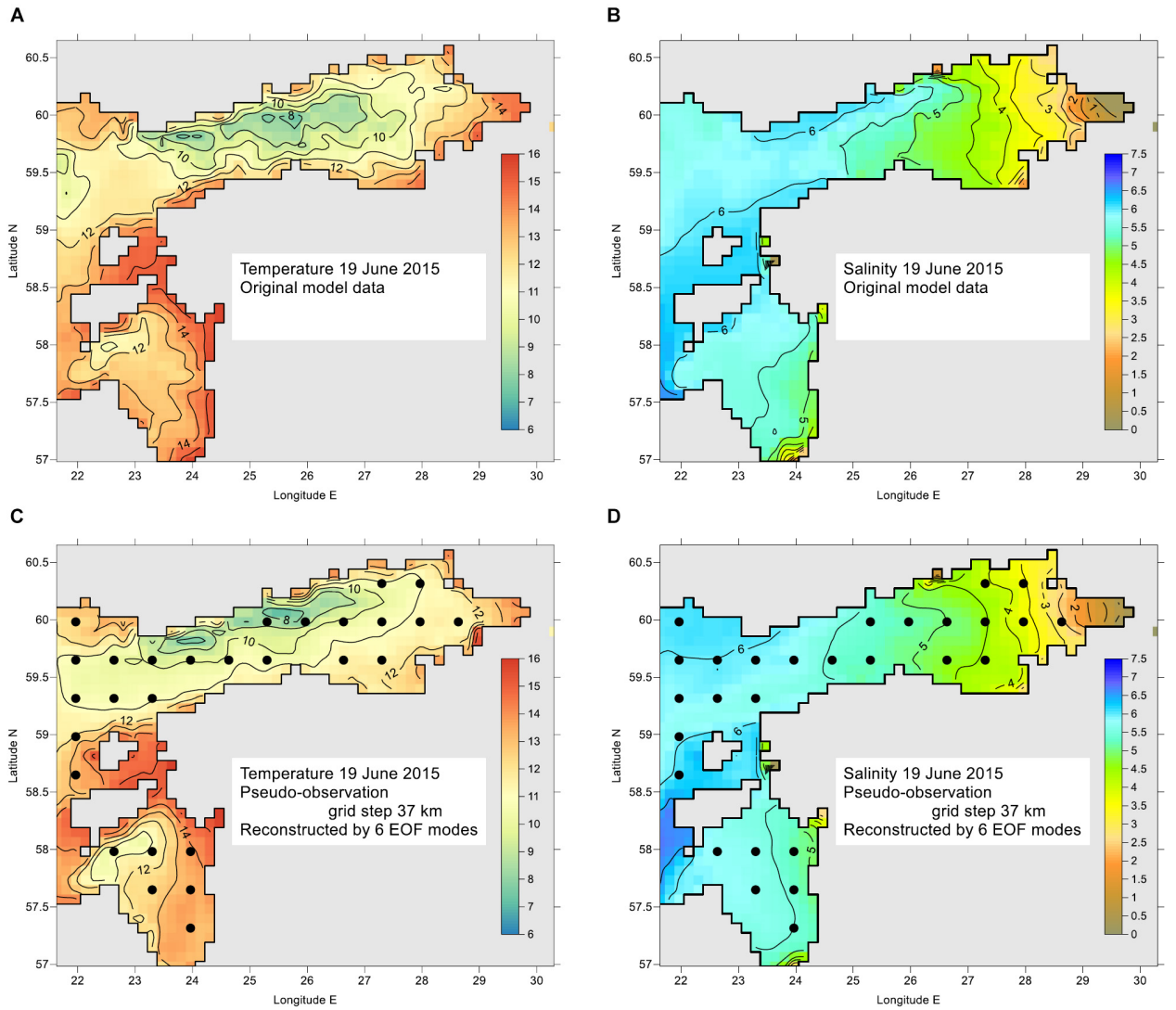

FIGURE 8 | Snapshot of original model data on 19 June 2015 for SST **(A)** and SSS **(B)** and corresponding reconstructed maps **(C,D)** using pseudo-observations from a grid with 37 km step shown by dots. Reconstruction was made by 6 gravest EOF modes. The units are °C for SST and g kg^{-1} for SSS.

second EOF mode (**Figure 6**) that cover 98.9% of total variance. This cycle is slightly variable in space, whereas highest spatial variations (not shown) occur during the spring heating period and smallest variations take place in the winter when SST is close to or equal to freezing temperature.

It is interesting to consider what will happen to the EOF reconstruction results when seasonal signal is removed from space-time matrix $\mathbf{X}$ prior to the procedures by Equations (1)–(7). Following Høyer and She (2007), we introduce a modified data set where time slices of spatial data with seasonality removed are defined at time index i as

$$\mathbf{x}_i^s = \mathbf{x}_i - \mathbf{s}_i, \tag{10}$$

where seasonal data $\mathbf{s}_i$ are evaluated in each model grid point k. Consider a time series vector $\mathbf{x}_k$ which values are available on times t_i counted as fractions of decimal year. Based on the total M data of $x_k\,(t_i)$, make an approximation of seasonal cycle by a biharmonic function

$$s_k\,(t) = C_{1,k}\sin 2\pi t + C_{2,k}\cos 2\pi t + C_{3,k}\sin 4\pi t + C_{4,k}\cos 4\pi t + C_{5,k}. \tag{11}$$

The coefficients from $C_{1,k}$ to $C_{5,k}$ are found to obtain best fit of $s_k\,(t_i)$ to the values $x_k\,(t_i)$in terms of minimizing their RMSD. The fitting coefficients and resulting seasonal cycle are spatially variable, whereas earlier and higher SST maxima generally appear in shallower coastal waters.

Overall variance of SST, determined in reference to the constant mean value, was 47.35 (°C)^2 whereas spatial variability due to temporally constant mean values in each grid point covered 0.3%. By introducing the seasonal cycle removal procedure by Equations (10)–(11), variance percentage of the

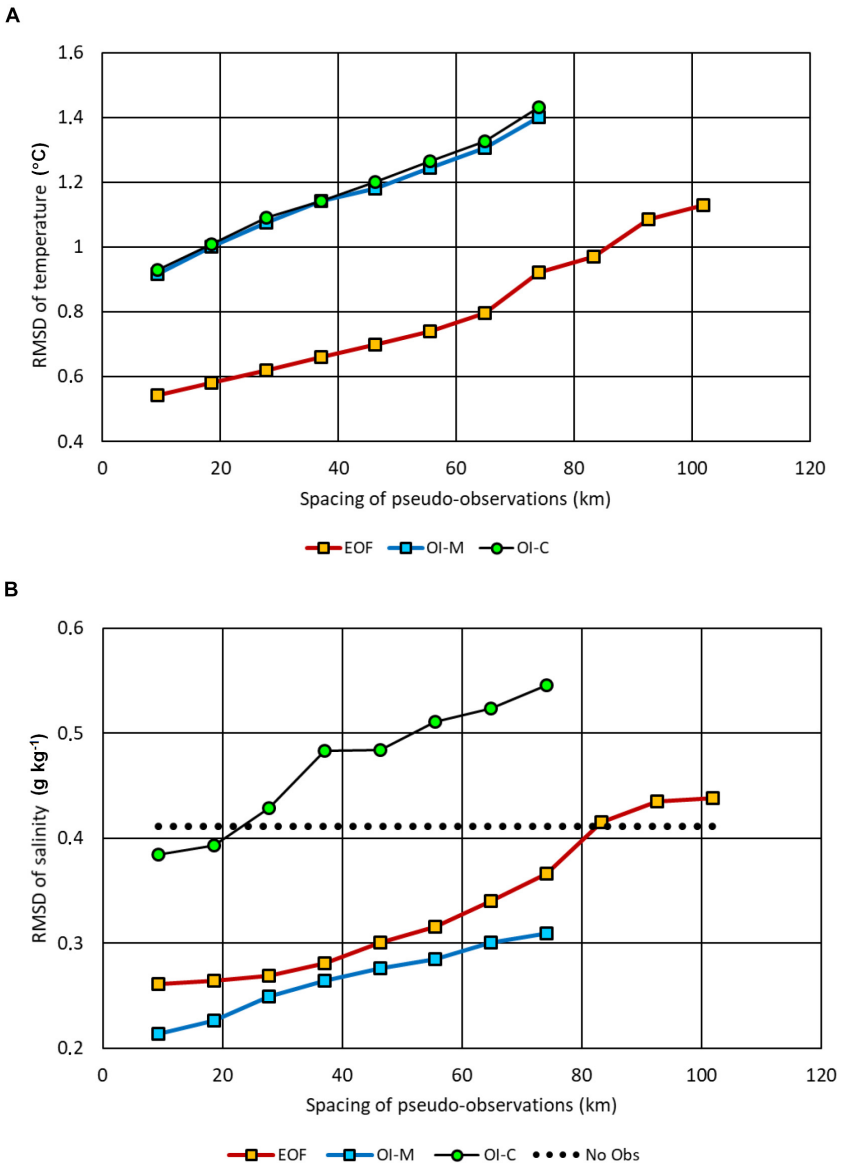

FIGURE 9 | Dependence of RMSD between reconstructed from pseudo-observations fields and original model output fields of SST **(A)** and SSS **(B)** for different methods: EOF, reconstruction by 6 gravest modes; OI-M, optimal interpolation with modeled mean field; OI-C, optimal interpolation with climatological mean field. The grid step of pseudo-observations cycled from 1 to 11 model grid steps, all possible shifted configurations of off-shore stations were taken into account. Median values of RMSD are presented. "No Obs" means the spatial standard deviation of temporal mean values.

input field for the EOF analysis was significantly reduced: from 99.7% for $\mathbf{x}_i$ to 6.1% for $\mathbf{x}_i^s$. The fitting biharmonic seasonal cycle contained 80.0% of total variance and the remaining 13.8% appeared in the covariance between $\mathbf{x}_i^s$ and $\mathbf{s}_i$.

Although variability of $\mathbf{x}_i^s$ was reduced as compared with $\mathbf{x}_i$, spatially mean deviation from the seasonal cycle was typically in the range from −2°C (mostly in autumn) to +4°C (in summer). Spatial standard deviations of $\mathbf{x}_i^s$ had maximum values during summer, amounting typically to 2.5°C. Wintertime minimum of spatial standard deviation, apparent in the initial $\mathbf{x}_i$ data, was not anymore apparent since biharmonic $s_k(t_i)$ had in winter problems to follow the constant level of freezing temperature.

Spatial covariance estimates of $\mathbf{x}_i^s$ (not shown) reveal significant similarity to the estimates based on the original data $\mathbf{x}_i$ (**Figure 3A**): covariance at distances of several hundreds of kilometers is close to the covariance at zero lag since significant part of SST variability is caused by weather events and interannual variations that occur nearly uniformly over smaller sub-regions like in our case. Based on the full covariance matrix, EOF analysis revealed highly similar patterns of leading modes of $\mathbf{x}_i^s$ to the modes of $\mathbf{x}_i$ which are shown in **Figure 4**. The share of "flat" first mode (**Figure 4A**) decreased from 97.6 to 80.5% after removal of biharmonic seasonal cycle. At the same time, the shares of higher modes 2–6 increased from 1.91 to 12.79%.

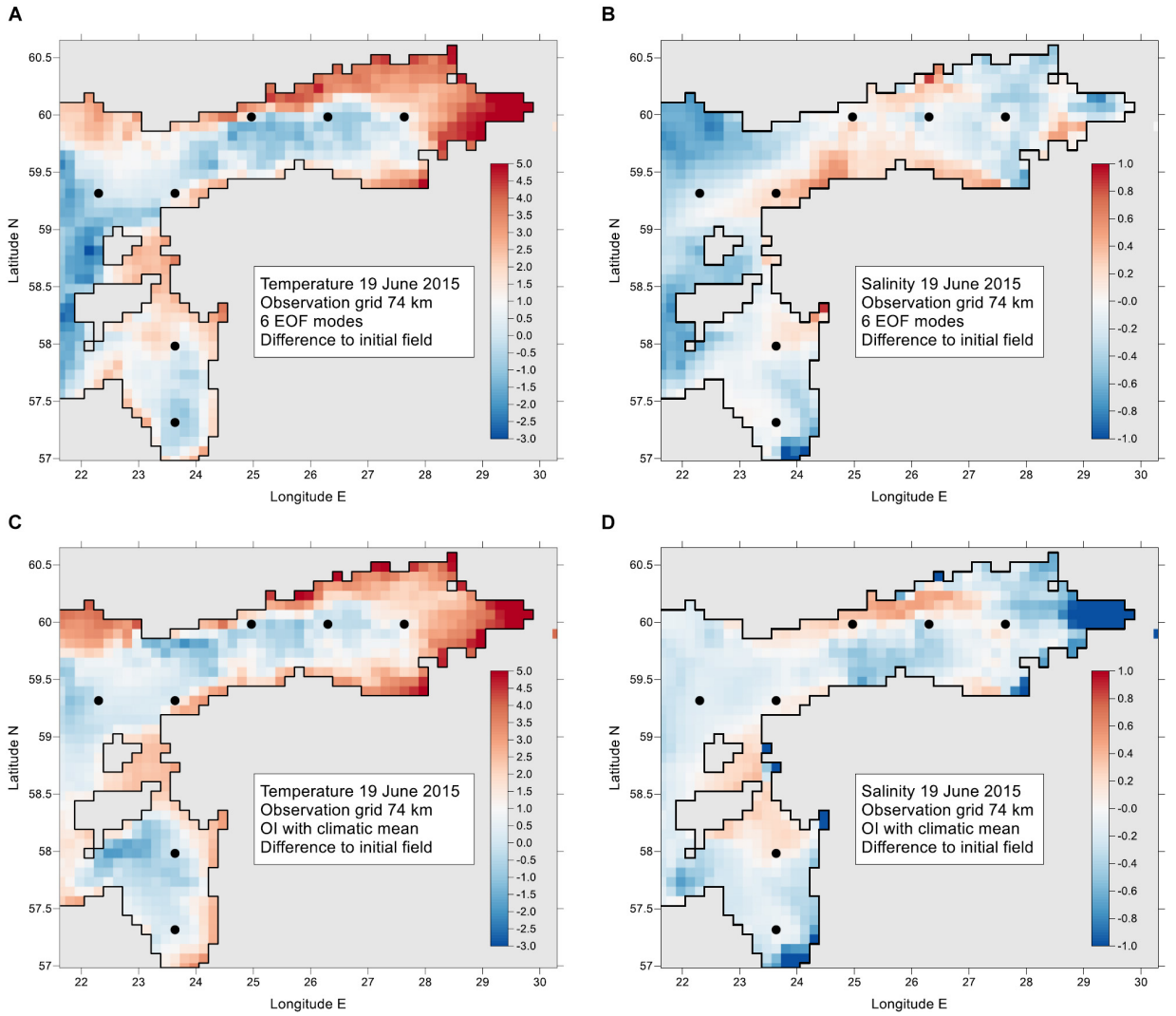

FIGURE 10 | Snapshot of differences between original model data and reconstructed data on 19 June 2015 for SST **(A,C)** and SSS **(B,D)**. Pseudo-observations were taken from a grid with 74 km step shown by dots. Reconstruction was made by 6 gravest EOF modes **(A,B)** and by OI using the deviations from climatological mean **(C,D)**. The units are °C for SST and g kg^{-1} for SSS.

In addition, the second and third mode changed their order and the "upwelling" mode (**Figure 4C** for $\mathbf{x}_i$) got a bit higher share of variance as the "differential heating" mode (**Figure 4B** for $\mathbf{x}_i$) since those variations were already partly included into the spatially variable seasonal cycle.

The original model field $\mathbf{X}$ can be approximated by leading EOF modes using equation (1), whereas the higher eigenvectors are truncated to zero. Using six leading modes both for $\mathbf{x}_i$ and $\mathbf{x}_i^s$ datasets, the decompositions seem highly similar. However, evaluation of RMSD allowed detecting of 4% reduction when seasonal cycle was removed prior to the EOF procedures.

When there are much less observations than the number of grid points, reconstruction accuracy can be estimated using the pseudo-observations method. Example of comparison of the two datasets is presented in **Figure 11**, based on the "observation" data that were extracted in seven locations shown in **Figure 10**. The reconstruction errors were correlated with $r = 0.71$, whereas the regression line was (errors of $\mathbf{x}_i^s$) = 0.965 (errors of $\mathbf{x}_i$). Both reconstructions had very high correlation with the initial model data $r > 0.99$ and the scatterplot graphs (not shown) created the impression that the data sets were nearly identical. Actually, already small variations in the correlation modify RMSD and in case of our example, there can be about 25% of RMSD reduction when seasonality is removed prior to the EOF analysis.

Splitting the Region Into Sub-Areas

In one of the experiments, the whole region presented in **Figure 1**, was split in three sub-regions: Gulf of Finland (GOF), Gulf of Riga (GOR), and NE Baltic Proper (NEBP). Individual EOF modes were calculated for each of the sub-area. Except for NEBP, the first two SST modes for GOF and GOR were similar to the patterns obtained for the whole area. Pairwise correlations of the SST

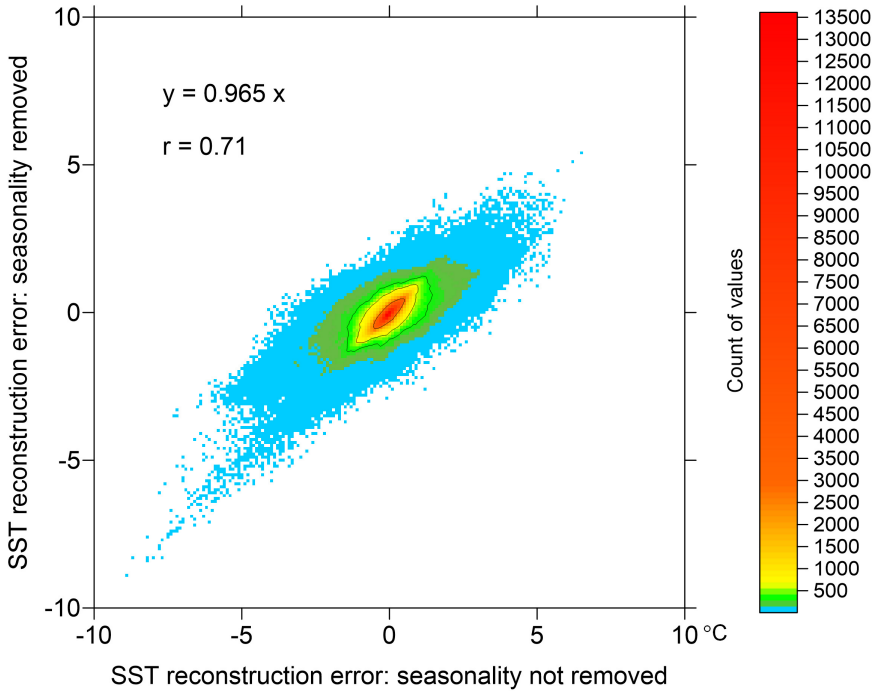

FIGURE 11 | Two-dimensional histogram of reconstruction errors within the experiment with pseudo-observations on the observation grid 74 km as shown in **Figure 10**. Compared are 678,528 values of reconstruction error in reference to original model data. Reconstruction was based on six EOF modes using the original approach where seasonality was not *a priori* removed (abscissa) and the modified approach where biharmonic seasonality was removed prior to EOF analysis (ordinate). Solid lines represent 90, 95, and 99% percentiles.

amplitudes were $r > 0.95$ between the GOF, GOR and the whole region. The whole region and GOR correlations for the first three SSS modes were $r > 0.9$ while the first mode of GOR correlated with GOF with $r > 0.72$ and with the whole region with $r > 0.78$. The first three modes of SSS of the whole region covered 61.4% of variance. The split regions had the mode coverage: GOF – 69.9%, GOR – 53.7%, NEBP – 72.8%. Although by splitting the region, mode convergence (share of variance of the lowest modes) increased slightly, we judged that EOFs of the whole region cover the regional dynamics in sufficient accuracy. Note, that region splitting may become important in other regions, where the mode convergence of the whole region might not be satisfactory.

Examples Using Actual Observations

Taking Into Account Time Dependence of Observations

It is usual practice, that spatial shipborne monitoring is carried out by different ships belonging to different institutes and countries. Covering the whole region may take quite long time. On an example, given in **Figure 12**, four ships with ICES codes 3499, 34AR, ESLV and LAVA made observations during 17 days from 18 May to 3 June 2009. During this spring heating period, SST generally increased from 7 to 15°C, but local SST variations were also evident. Over the time span, observations in the northern area were taken in the first part when water was not yet heated as much as by the end of the period. Considering the observations as instantaneous, reconstruction using Equations (5)–(7) provided rather cold waters there. In turn, warm waters were drawn in the coastal areas where observations were taken at the end of the period (**Figure 12A**). EOF reconstruction using the time dependence of observations based on Equations (8)–(9), setting the reference time in the middle of the period (**Figure 12B**), increased the temperature in the region of earlier observations and decreased in the region of later observations, reducing this way the artificial contrasts due to non-synchronous observations. Comparison with satellite based SST map from CMEMS L4 product (**Figure 12C**) reveals good similarity to the time-corrected map. Numerical differences are mostly less than 1°C, not exceeding the range of unresolved here diurnal oscillations (Karagali and Høyer, 2014). From the number of calculations we got the experience that reference time may be modified within the observational window without loosing the realism of reconstruction. However, extrapolation outside the window should be avoided like in the case of one-dimensional linear regression.

Automatic Reconstruction of Time Series of Maps

It is technically easy to set up procedures for automatic reconstruction of time series of maps, using the time dependence of observations based on Equations (8)–(9). We took the shipborne profile data from ICES database (see section Regional Setting of Experiments).

During the reconstruction procedure, EOF amplitudes for each map were checked against the $\left|\hat{a}_{i,k}\right| < F_k = 2\,\sigma\,(\tilde{\mathbf{a}}_k)$ criteria

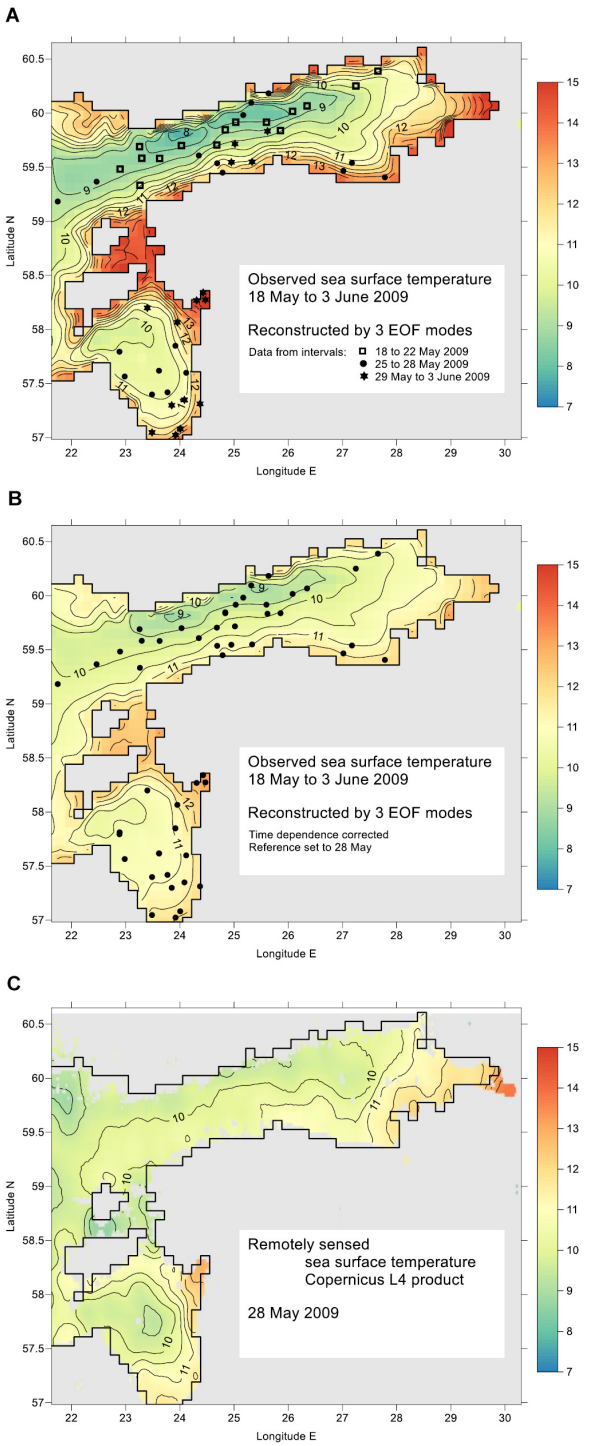

FIGURE 12 | Reconstruction of sea surface temperature (°C) using data from ship observations during the spring warming period from 18 May to 3 June 2009. Locations of the data from the ICES database are shown by symbols presented in the legends. Reconstruction is made using the three leading EOF modes: **(A)** considering all non-synchronous data as instantaneous (see three time intervals in the legend), **(B)** introducing correction for time dependence, with reference set to 28 May. For comparison, daily mean SST L4 map determined by remote sensing from satellites is presented for 28 May 2009 **(C)**.

(see section Covariance and EOF Characteristics) in order to determine the number of "good modes." Taking the time window for one map 1/12 year (about 1 month) and the limit of at least 8 non-duplicate observations within the time window (time average was taken over 2 days), we obtained 148 maps for SST and 137 maps for SSS, out of maximum 209 maps. Average number of data points is 25 and maximum amounts to 83 both for SST and SSS. We note that large number of observation points does not necessarily mean high number of good EOF modes. For example, the observations with highest amount 83 were fragmentarily located along the coasts as short-scale repeated maps; the number of good modes was only 3. Good six modes were in other configuration obtained already from 20 to 30 observation points.

From reconstructed maps, SST and SSS time series were extracted around monitoring stations LL12 (western Gulf of Finland, 59.4835 N, 22.8968 E), V15 (Moonsund, 58.8167 N, 23.2167 E), G1 (central Gulf of Riga, 57.6167 N, 23.6167 E), K21 (Pärnu Bay, 58.2167 N, 24.3083 E), F3 (central Gulf of Finland, 59.8383 N, 24.8383 E) and LL3A (northeastern Gulf of Finland, 60.0672 N, 26.3467 E). Such reconstructed time series can be easily extended to climate studies.

Individual maps, reconstructed by the automatic procedure (example is given in **Figure 13**), follow closely the observed values but also reveal realistic patterns compared to the published knowledge on Baltic Sea climatology and monthly and instantaneous distributions (e.g., Leppäranta and Myrberg, 2009).

DISCUSSION

There is a continued need for producing gap-free gridded oceanographic data using observations. Although new observation techniques became available, the problem of fragmentation remains in oceanographic data management. Reanalysis is a powerful, but costly method for production of gridded fields. Widespread statistically based methods like OI (optimal interpolation), DIVA (Data-Interpolating Variational Analysis, Troupin et al., 2010) etc. use mainly localized covariance patterns. Covariance estimates from models reveal large values over basin scales due to trends, seasonal signal and basin-wide dynamics (e.g., coherent upwelling-downwelling near opposite coasts). Such covariance estimates suggest using of methods that use full covariance fields. In this context, the classical EOF method is again gaining interest (e.g., Yang et al., 2017; Pilo et al., 2018), whereas the statistics of the studied field can be estimated from the model results. Amplitudes of EOF modes can be approximately estimated from the observational data set which dimension is much smaller than the number of model EOF mode grid points.

When using model data to create the EOF statistics, it is important to know how reliable the estimates of modes and amplitudes with respect to model uncertainties are. Thorough treatment of the above question cannot be found in the literature. However, on the sea surface, temperature and salinity results from different models are rather well validated by observations and the model-based covariance patterns can be considered trustful. As a common practice, modeled covariance have been

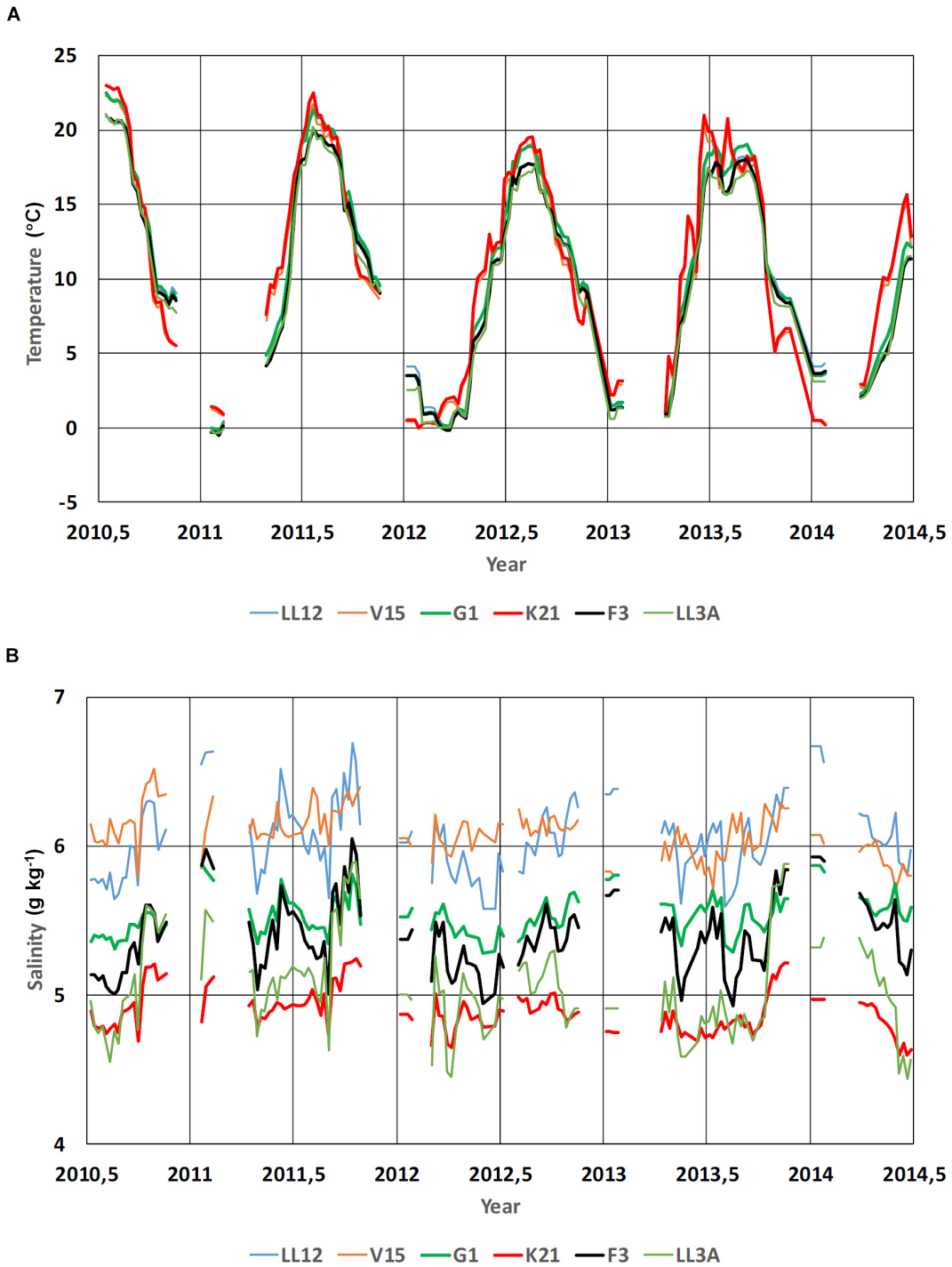

FIGURE 13 | Time series of sea surface temperature **(A)** and salinity **(B)** reconstructed from the shipborne data downloaded from the ICES database. Reconstruction is made for six locations (LL12, V15, G1, K21, F3 and LL3A, see the text for locations) for the times from 2010.5 to 2014.5 with 1/24 year (15.33 days) interval. Time window for including the observations and evaluating the EOF amplitude rate of change was taken 1/12 years. Presented are the periods when at least 8 points occur within the time window. Number of good modes was chosen three, but time instances when the highest good mode was two were also included.

used in data assimilation. Fu et al. (2011) compared covariance patterns from modeled SST and satellite SST, and found them agreeing well. CMEMS QUID report has presented validation of SSS against ferrybox data, showing that the SSS patterns were well simulated by the model. In deeper layers, however, there is usually larger spread between different model results.

While ocean data come from different platforms and observations are non-synchronous, taking into account the time dependence of observations is a challenge. Amplitudes of lowest EOF modes reveal distinct temporal correlation patterns, with time scale several months. This could be used to handle temporal gaps and/or non-synchronous data, if they lie within the temporal correlation scale. As a first step, we introduced linear correction to the EOF amplitude depending on the difference of observation time relative to reference time.

We have made comparison of the results from EOF reconstruction with the results from classical OI method. Our test region – NE Baltic – is characterized by fragmented coastline and highly variable topographic and hydrographic conditions. In such region the spatial changes of oceanographic variables may have quasi-permanent anomalies like low salinity near river influence areas or faster warming and cooling in shallow coastal areas, compared to the offshore SST variations. Therefore, EOF reconstruction has a potential to achieve comparable or better accuracy than OI method.

EOF modes and amplitudes depend on the selection of domain. We used a sub-region, containing two geographical regions and their transition area. It was found that some of the modes (mainly the first mode) do not change significantly when the domain is separated into smaller parts. If the convergence of leading EOF modes of large sea area is low (share of explained variance is small), refinement into smaller areas might be useful. In our example, the convergence improved only slightly when partition into three smaller areas was made. Workable criteria for the region selection is not yet established, although following geographical regions seems to be acceptable.

In case of data assimilation into the high-resolution model, it is reasonable to separate low-resolution component and make large-scale corrections into that, keeping high-resolution deviation patterns unchanged. The workable approach for correction and/or assimilation of the data on the basin scales is as follows: (1) to separate the coarse-grid part from the fine grid data by spatial averaging, (2) to perform corrections on the smaller dimension coarse grid, (3) to interpolate coarse grid data back to the fine grid and add fine grid deviations determined from the interpolation of the initial coarse grid. This is based on the assumption, that correction of basin-scale features does not influence the mesoscale patterns, apparent on the fine grid but filtered out on the coarse grid. The EOF approach allows additional assimilation of mesoscale patterns in the regions of high data coverage.

We have tested reconstruction of SST and SSS in one sub-region of the Baltic, based on the *in situ* observations. The method itself allows to be applied on different data sets (for example, including high-resolution remotely sensed SST) of different variables and their combinations (for example, joint data vector of temperature and salinity), on the condition that significant part of variability can be presented by a few leading modes. There could be obvious extensions of the approach to cover the whole water column. This could be especially important to properly match the consequences of large salt water inflows etc.

One straightforward application of the approach could be in marine ecology, where building the gap-free patterns of nutrients and biomass variables could allow more precisely estimate the total amounts and budgets of ecosystem variables, and to evaluate the values of environmental indicators that are important for environmental management.

CONCLUSION

We have developed statistically justified EOF reconstruction method to handle large-scale patterns of observed fields in the sub-regions. The method uses model-based EOF patterns to interpolate and extend the observational data over the full study region. In the smaller sea regions, which are affected by the same large-scale forcing patterns, the EOF patterns have obvious physical interpretations and their shape does not depend very much on the selection of boundaries. When removing the SST seasonal cycle prior to EOF analysis, spatial patterns of leading modes remained practically unchanged, share of variance of the three first modes was reduced from 99 to 88.6% and reconstruction errors were reduced by about 25%.

Since we use only the first most energetic EOF modes, we can cover with this method basin and sub-basin scales of variability. The relative interpolation errors, estimated over the full area, usually remain below 10% for SST and 20% for SSS, compared with multi-year standard deviation of all variability relative to their mean value over the basin. In comparing with OI, EOF is especially useful for reconstruction with very sparse observations. In the regions of denser sampling, EOF cannot exactly follow the observations. Mesoscale deviations from large-scale EOF patterns follow well-defined covariance decay with space lag; therefore, they could be treated by optimal interpolation or similar method.

AUTHOR CONTRIBUTIONS

All authors contributed in analysis and writing, with JE as lead author and JS making strong co-contribution. MZ made the EOF calculations while PL was in charge with the HBM model.

FUNDING

This study was supported by the Ph.D. program for MZ and the institutional research funding IUT 19-6 of the Estonian Ministry of Education and Research.

ACKNOWLEDGMENTS

A larger BAL MFC team within the EU projects MyOcean, MyOcean2, and MyOcean-FO did the development of HBM model. This cooperation is highly acknowledged.

REFERENCES

Alenius, P., Nekrasov, A., and Myrberg, K. (2003). Variability of the baroclinic Rossby radius in the Gulf of Finland. *Cont. Shelf Res.* 23, 563–573. doi: 10.1016/s0278-4343(03)00004-9

Alvera-Azcárate, A., Vanhellemont, Q., Ruddick, K., Barth, A., and Beckers, J. M. (2015). Analysis of high frequency geostationary ocean colour data using DINEOF. *Estuar. Coast. Shelf Sci.* 159, 28–36. doi: 10.1016/j.ecss.2015.03.026

Beckers, J. M., and Rixen, M. (2003). EOF calculations and data filling from incomplete oceanographic datasets. *J. Atmos. Ocean. Technol.* 20, 1839–1856. doi: 10.1175/1520-0426(2003)020<1839:ecadff>2.0.co;2

Berg, P., and Poulsen, J. W. (2012). *Implementation Details for HBM*. DMI Technical Report No. 12-11. Copenhagen.

Cushman-Roisin, B., and Beckers, J. M. (2011). *Introduction to Geophysical Fluid Dynamics: Physical and Numerical Aspects*. Cambridge, MA: Academic Press, 875.

Davis, R. E. (1976). Predictability of sea surface temperature and sea level pressure anomalies over the North Pacific Ocean. *J. Phys. Oceanogr.* 6, 249–266. doi: 10.1073/pnas.1610708114

Elken, J., and Matthäus, W. (2008). "Baltic Sea oceanography," in *Regional Climate Studies, Assessment of Climate Change for the Baltic Sea Basin Annex A*, eds H.-J. Bolle, M. Meneti, and I. Rasool, (Berlin: Springer), 379–385.

Elken, J., Nõmm, M., and Lagemaa, P. (2011). Circulation patterns in the Gulf of Finland derived from the EOF analysis of model results. *Boreal Environ. Res.* 16, 84–102.

Elken, J., Zujev, M., and Lagemaa, P. (2018). "Reconstructing sea surface temperature and salinity fields in the northeastern baltic from observational data, based on sub-regional Empirical Orthogonal Function (EOF) patterns from models," in *Proccedings of the IEEE/OES Baltic International Symposium (BALTIC)*, Klaipeda.

FMI, (2018). *Ice Winter in The Baltic Sea*. Helsinki: Finnish Meteorological Institute.

Fu, W., Høyer, J. L., and She, J. (2011). Assessment of the three dimensional temperature and salinity observational networks in the Baltic Sea and North Sea. *Ocean Sci.* 7, 75–90. doi: 10.5194/os-7-75-2011

Gandin, L. S. (1963). *Objective Analysis of Meteorological Fields*. Jerusalem: Israel program for scientific translations, 242.

Ghil, M. (1989). Meteorological data assimilation for oceanographers. Part I: description and theoretical framework. *Dyn. Atmos. Oceans* 13, 171–218. doi: 10.1016/0377-0265(89)90040-7

Ghil, M., and Malanotte-Rizzoli, P. (1991). Data assimilation in meteorology and oceanography. *Adv. Geophys.* 33, 141–266.

Høyer, J. L., and She, J. (2007). Optimal interpolation of sea surface temperature for the North Sea and Baltic Sea. *J. Mar. Syst.* 65, 176–189. doi: 10.1016/j.jmarsys.2005.03.008

Ide, K., Courtier, P., Ghil, M., and Lorenc, A. C. (1997). Unified notation for data assimilation: operational, sequential and variational. *J. Meteorol. Soc. Japan Ser. II* 75, 181–189. doi: 10.2151/jmsj1965.75.1b_181

Janssen, F., Schrum, C., and Backhaus, J. O. (1999). A climatological data set of temperature and salinity for the Baltic Sea and the North Sea. *Deutsche Hydrografische Zeitschrift* 51, 5–245. doi: 10.1007/bf02933676

Jayaram, C., Priyadarshi, N., Pavan Kumar, J., Udaya Bhaskar, T. V. S., Raju, D., and Kochuparampil, A. J. (2018). Analysis of gap-free chlorophyll-a data from MODIS in Arabian Sea, reconstructed using DINEOF. *Int. J. Remote Sens.* 39, 7506–7522. doi: 10.1080/01431161.2018.1471540

Kaplan, A., Kushnir, Y., Cane, M. A., and Blumenthal, M. B. (1997). Reduced space optimal analysis for historical data sets: 136 years of Atlantic sea surface temperatuures. *J. Geophys. Res. Oceans* 102, 27835–27860. doi: 10.1029/97jc01734

Karagali, I., and Høyer, J. L. (2014). Characterisation and quantification of regional diurnal SST cycles from SEVIRI. *Ocean Sci.* 10, 745–758. doi: 10.5194/os-10-745-2014

Kikas, V., and Lips, U. (2016). Upwelling characteristics in the Gulf of Finland (Baltic Sea) as revealed by Ferrybox measurements in 2007–2013. *Ocean Sci.* 12, 843–859. doi: 10.5194/os-12-843-2016

Kim, K. Y. (1997). Statistical interpolation using cyclostationary EOFs. *J. Clim.* 10, 2931–2942. doi: 10.1175/1520-0442(1997)010<2931:siuce>2.0.co;2

Laanemets, J., Väli, G., Zhurbas, V., Elken, J., Lips, I., and Lips, U. (2011). Simulation of mesoscale structures and nutrient transport during summer upwelling events in the Gulf of Finland in 2006. *Boreal Environ. Res.* 16, 15–26.

Lagemaa, P. (2012). Operational forecasting in Estonian marine waters. *TUT Press B* 128, 130.

Legrand, C., Fridolfsson, E., Bertos-Fortis, M., Lindehoff, E., Larsson, P., Pinhassi, J., et al. (2015). Interannual variability of phyto-bacterioplankton biomass and production in coastal and offshore waters of the Baltic Sea. *AMBIO* 44, 427–438. doi: 10.1007/s13280-015-0662-8

Lehmann, A., Myrberg, K., and Höflich, K. (2012). A statistical approach to coastal upwelling in the Baltic Sea based on the analysis of satellite data for 1990–2009. *Oceanologia* 54, 369–393. doi: 10.5697/oc.54-3.369

Leppäranta, M., and Myrberg, K. (2009). *Physical Oceanography of the Baltic Sea*. Berlin: Springer Science & Business Media, 378.

Menemenlis, D., Fieguth, P., Wunsch, C., and Willsky, A. (1997). Adaptation of a fast optimal interpolation algorithm to the mapping of oceanographic data. *J. Geophys. Res. Oceans* 102, 10573–10584. doi: 10.1029/97jc00697

Petersen, W. (2014). FerryBox systems: state-of-the-art in Europe and future development. *J. Mar. Syst.* 140, 4–12. doi: 10.1016/j.jmarsys.2014.07.003

Pilo, G. S., Oke, P. R., Coleman, R., Rykova, T., and Ridgway, K. (2018). Impact of data assimilation on vertical velocities in an eddy resolving ocean model. *Ocean Modell.* 131, 71–85. doi: 10.1016/j.ocemod.2018.09.003

Smith, T. M., Reynolds, R. W., Livezey, R. E., and Stokes, D. C. (1996). Reconstruction of historical sea surface temperatures using empirical orthogonal functions. *J. Clim.* 9, 1403–1420. doi: 10.1175/1520-0442(1996)009<1403:rohsst>2.0.co;2

Soosaar, E., Maljutenko, I., Uiboupin, R., Skudra, M., and Raudsepp, U. (2016). River bulge evolution and dynamics in a non-tidal sea–Daugava River plume in the Gulf of Riga. Baltic Sea. *Ocean Sci.* 12, 417–432. doi: 10.5194/os-12-417-2016

Troupin, C., Machin, F., Ouberdous, M., Sirjacobs, D., Barth, A., and Beckers, J. M. (2010). High-resolution climatology of the northeast atlantic using data-interpolating variational analysis (DIVA). *J. Geophys. Res. Oceans* 115: C08005.

Vihma, T., and Haapala, J. (2009). Geophysics of sea ice in the Baltic Sea: a review. *Prog. Oceanogr.* 80, 129–148. doi: 10.1016/j.pocean.2009.02.002

Westerlund, A., Tuomi, L., Alenius, P., Myrberg, K., Miettunen, E., Vankevich, R. E., et al. (2019). Circulation patterns in the Gulf of Finland from daily to seasonal time scales. *Tellus A Dyn. Meteorol. Oceanogr.* 1–24. doi: 10.1080/16000870.2019.1627149

Woods, J. D. (1980). Do waves limit turbulent diffusion in the ocean? *Nature* 288, 219–224. doi: 10.1038/288219a0

Yang, C., Masina, S., and Storto, A. (2017). Historical ocean reanalyses (1900–2010) using different data assimilation strategies. *Q. J. R. Meteorol. Soc.* 143, 479–493. doi: 10.1002/qj.2936

Zujev, M., and Elken, J. (2018). Testing marine data assimilation in the northeastern Baltic using satellite SST products from copernicus marine environment monitoring service. *Proc. Estonian Acad. Sci.* 67, 217–230.

Conflict of Interest Statement: The authors declare that the research was conducted in the absence of any commercial or financial relationships that could be construed as a potential conflict of interest.

frontiers in Earth Science

ORIGINAL RESEARCH
published: 18 September 2019
doi: 10.3389/feart.2019.00243

Sea Level Trends and Variability of the Baltic Sea From 2D Statistical Reconstruction and Altimetry

Kristine S. Madsen[1], Jacob L. Høyer[1], Ülo Suursaar[2], Jun She[1] and Per Knudsen[3]*

[1] Danish Meteorological Institute, Copenhagen, Denmark, [2] Estonian Marine Institute, University of Tartu, Tallinn, Estonia, [3] DTU Space, Lyngby, Denmark

2D sea level trend and variability fields of the Baltic Sea were reconstructed based on statistical modeling of monthly tide gauge observations, and model reanalysis as a reference. The reconstruction included both absolute and relative sea level (RSL) in 11 km resolution over the period 1900–2014. The reconstructed monthly sea level had an average correlation of 96% and root mean square error of 3.8 cm with 56 tide gauges independent of the statistical model. The statistical reconstruction of sea level was based on multiple linear regression and took land deformation information into account. An assessment of the quality of an open ocean altimetry product (ESA Sea Level CCI ECV, hereafter "the CCI") in this regional sea was performed by validating the variability against the reconstruction as an independent source of sea level information. The validation allowed us to determine how close to the coast the CCI can be considered reliable. The CCI matched reconstructed sea level variability with correlation above 90% and root-mean-square (RMS) difference below 6 cm in the southern and open part of the Baltic Proper. However, areas with seasonal sea ice and areas of high natural variability need special treatment. The reconstructed RSL change, which is important for coastal communities, was found to be dominated by isostatic land movements. This pattern was confirmed by independent observations and the values were provided along the entire coastline of the Baltic Sea. The area averaged absolute sea level change for the Baltic Sea was 1.3 ± 0.3 mm/yr for the 20th century, which was slightly below the global mean for the same period. Considering the relative shortness of the satellite era, natural variability made trend estimation sensitive to the selected data period, but the linear trends derived from the reconstruction (3.4 ± 0.7 mm/yr for 1993–2014) fitted with those of the CCI (4.0 ± 1.4 mm/yr for 1993–2015) and with global mean estimates within the limits of uncertainty.

Keywords: sea level change, sea level modeling, satellite altimetry, climate change, PSMSL, GIA

OPEN ACCESS

Edited by:
Marcus Reckermann, Helmholtz Centre for Materials and Coastal Research (HZG), Germany

Reviewed by:
Xiaoli Deng, The University of Newcastle, Australia
Marco Olivieri, National Institute of Geophysics and Volcanology (INGV), Italy

****Correspondence:***
Kristine S. Madsen
kma@dmi.dk

Specialty section:
This article was submitted to Interdisciplinary Climate Studies, a section of the journal Frontiers in Earth Science

Received: *04 December 2018*
Accepted: *02 September 2019*
Published: *18 September 2019*

Citation:
Madsen KS, Høyer JL, Suursaar Ü, She J and Knudsen P (2019) Sea Level Trends and Variability of the Baltic Sea From 2D Statistical Reconstruction and Altimetry. Front. Earth Sci. 7:243. doi: 10.3389/feart.2019.00243

INTRODUCTION

Considering ongoing climate change, adequate quantification of the global pattern of sea level change is of crucial importance to helping societies cope with its adverse impact on the future (IPCC, 2013). As the sea surface topography may dynamically vary in time and space in intricate patterns, the impact of climate change and of sea level change also occur differently in various areas

on Earth (Milne et al., 2009). This is particularly true for the semi-enclosed seas like the Baltic Sea (Hünicke et al., 2015; Suursaar and Kall, 2018).

Sea level measurement history in the Baltic Sea extends back to the 1770s, when tide gauge in Stockholm became operational (Ekman, 1996). Nevertheless, a problem in quantification of general sea level trends is that traditional, tide gauge-based estimation of relative sea level (RSL) change is dependent on local, spatially varying land surface movements (Santamaría-Gómez et al., 2017). Their removal, on the other hand, requires the use of a truly fixed (geocentric) reference network. Finally, tide gauges are mostly coastal-bound and unevenly spaced, and thus, not entirely representative for the whole sea area (e.g., Woodworth, 2006). Recent development in Global Isostatic Adjustment (GIA) modeling (e.g., Spada, 2017; Simon et al., 2018; Vestøl et al., 2019), use of satellite altimetry (e.g., Nerem et al., 2018) and sea surface reconstructions (Meier et al., 2004; Madsen et al., 2015) have contributed to overcoming the above-mentioned problems.

The Baltic Sea level varies on time scales from minutes and hours (e.g., waves and storm surges) to days, months and years, through preconditioning for storm surges, seasonal variability and variability related to e.g., North Atlantic Oscillation (the NAO; Hünicke et al., 2015). Observed RSL trends are dominated by the GIA, global sea level change and regional to local scale components (Johansson et al., 2004). The role of neotectonic and seismic movements is negligible in the area (e.g., Steffen and Wu, 2011). The GIA effect is relatively well described by the regional uplift models, such as the most recent NKG2016LU (Vestøl et al., 2019), and can thus be removed to obtain absolute sea level (ASL) change (Richter K. et al., 2012).

So far, two-dimensional reconstructions of the sea level of the Baltic Sea were limited to a simple interpolation study (Olivieri and Spada, 2016). The first attempts to use satellite altimetry data for sea level analysis were limited by the use of global altimetry products in this near-coastal region, which are degraded in quality close to the coast (Madsen, 2011; Stramska and Chudziak, 2013). Newer altimetry products such as the European Space Agency (ESA) sea level CCI ECV (Quartly et al., 2017; Legeais et al., 2018) contain data very close to the coast, and are used for assessment of coastal sea level change. For example, a Global and European sea level change indicator for northern Europe[1] has been made available by the European Environmental Agency and MyOcean (now Copernicus Marine Environmental Monitoring Service).

Several technical questions arise when dealing with past and present sea level change, among these: (i) There are many long tide gauge records for some coasts in the Baltic Sea, but also some coasts with none. Could past sea levels be reconstructed for all sections of the coast? (ii) Satellite altimetry is widely used to calculate sea level trends, but could these products be used in regions close to the coast? (iii) How do the trends from satellite altimetry compare with *in situ* measurements? In order to answer these questions, long-term records of sea level, both absolute and relative, are needed for the entire Baltic Sea.

This paper presents a reconstruction of past and present sea level, where hydrodynamic model reanalysis data (which have a good two-dimensional coverage but limited period of time, and which may lack information on sea level trends) and *in situ* observations (which have good time coverage but gapped spatial coverage) were integrated in a statistical model, providing the 2D pattern of past sea level trend and its long-term variability. Quite a similar methodology has been used e.g., in the Mediterranean Sea (Calafat and Jordà, 2011; Bonaduce et al., 2016), and partly by Madsen et al. (2015) in the Baltic Sea, but never to the same full extent.

The statistical model used in this study was independent of satellite altimetry and focused on monthly mean sea level. By carefully dealing with land uplift effects, both relative and absolute linear sea level trends and variability were deducted. The reconstructed sea level variability was then compared with satellite derived sea level variability to estimate in which areas of the Baltic Sea satellite-based global altimetry product can be used. In turn, the linear sea level trends of satellite altimetry time series, tide gauges, and statistical reconstructions were mutually compared.

MATERIALS AND METHODS

This section first introduces the tide gauge, reanalysis model and satellite data used, then the methods and data used for land movement correction, and finally the method used for the statistical sea level reconstruction (**Figure 1**).

Tide Gauge Data

Sea level measurements at tide gauges provided the empirical basis for the study. Many long records of tide gauge observations exist from the Baltic Sea, some (Stockholm, Saint Petersburg and Świnoujście) stretching back to the 1770s–1810s (Girjatowicz et al., 2016). However, older parts of the series are hardly usable due to gaps and uneven spatial coverage.

For this study, 56 tide gauges with unique records of at least 49 years of data after the year 1900 were identified from the PSMSL dataset (Holgate et al., 2013; Permanent Service for Mean Sea Level [PSMSL], 2016), and supplemented with 4 stations from the Estonian coast, made available from the Estonian Environmental Agency (**Figure 2**).

Although the oldest Estonian sea level measurements span back to 1842, they have not been yet included in the PSMSL. The main reason has been a poor link to reference systems with known geoid- or geocentric connections (Suursaar and Kall, 2018). The offsets between different height systems (as defined by the mean sea level) around the Baltic Sea may be up to 20 cm (Liibusk et al., 2014). Historically, the Estonian tide gauges have been connected to the Baltic Height System 1977 (BHS77), common in the former Soviet Union (Liibusk et al., 2014). Since 2018, Estonia has changed its height system to the European Vertical Reference System (EVRS), which is based on the level of

[1]http://www.eea.europa.eu/data-and-maps/indicators/sea-level-rise-2/assessment

the Normaal Amsterdams Peil (NAP), and thus, becoming more suitable for PSMSL (Suursaar and Kall, 2018).

The overall data coverage was good (**Figure 2**). However, the stations are not quite evenly distributed. On the south-eastern coastlines there is a lack of data, most notably before the 1950s. For some of the longest tide gauge records it was possible to partly fill gaps, using neighboring tide gauge records with a high correlation, to allow almost gap-free reconstruction and validation. We used data from Hanstholm to supplement Hirtshals series, Backevik data to supplement Smogen, Varberg to supplement Ringhals, Lemstrom to supplement Foglo/Degerby, Bjorn to supplement Forsmark, Lyokki to supplement Mantyluoto and Koserow to supplement Swinoujscie. Further, data from Landsort Norra was used to extend the Landsort series. The Danish stations Hirtshals, Hornbæk, Aarhus, Fredericia, Slipshavn, Korsør and Gedser only had data until 2012 in the PSMSL archive when this study was performed. Data from the Danish Meteorological Institutes data archives were used to extend the time series to 2014; however, a possible small decrease in the data quality for those last years can occur.

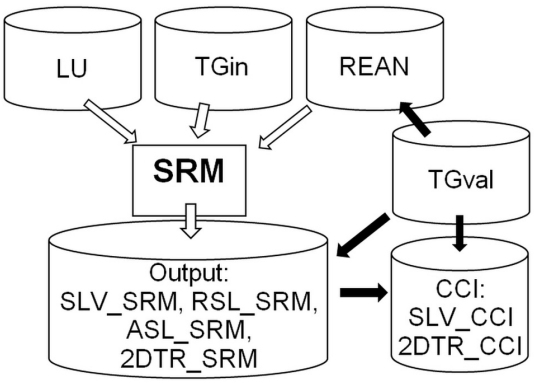

FIGURE 1 | Conceptual chart of model and data flows. SRM, statistical reconstruction model; REAN, reanalysis model data; CCI, CCI satellite altimetry product; LU, land uplift model data; TG, tide gauge data (for input and for validation); SLV, sea level variability; RSL, relative sea level; ASL, absolute sea level; 2DTR, 2D-trends; white arrows, data flow for the SRM; black arrows, validation.

Seven of the longest PSMSL records were used in 2D reconstruction (TGin, **Figure 1**), and the other records served for validation only (TGval). The seven selected tide gauges were: Hirtshals, Hornbæk, Warnemünde, Kungsholmsfort, Landsort, Ratan and Helsinki (**Figure 2**). They were selected based on record length, geographical distribution and by using the Akaike information criterion (AIC) method (Burnham and Anderson, 2002).

All linear trends in this paper were obtained as a least square fit of a line to the time series, where the trend is the slope of the line, and the trend uncertainty was set to be the fitting uncertainty.

Reanalysis Data

Available reanalysis products of the Baltic Sea include hydrodynamically modeled sea levels for 20–24 years. Reanalysis

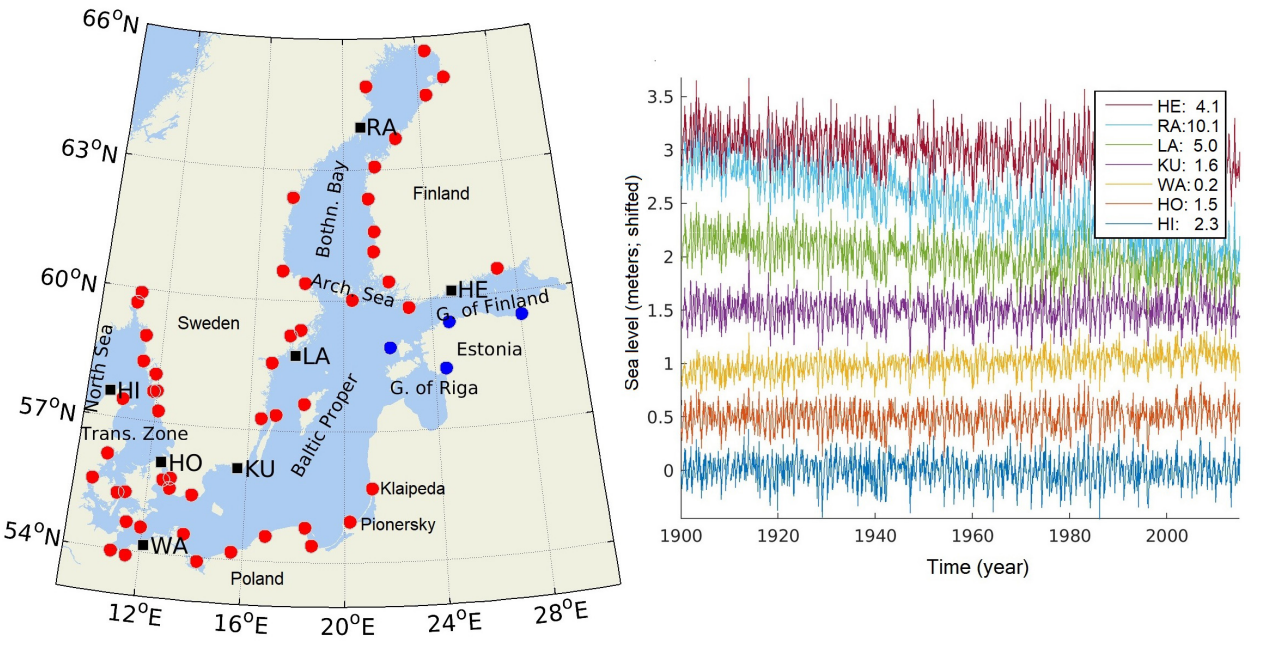

FIGURE 2 | Left: Study area and sea level stations used in the present study (red and black: PSMSL stations, blue: Estonian stations). The seven tide gauge records used for the sea level reconstruction (TGin, black squares) are: Helsinki (HE), Ratan (RA), Landsort (LA), Kungsholmsfort (KU), Warnemünde (WA), Hornbæk (HO), and Hirtshals (HI). All other stations were used for validation (TGval, red and blue circles). **Right:** Time series of monthly sea level (meters, zero-point shifted for each station) for TGin (1900–2014), showing the influence of land uplift. The value after the station code represents geocentric uplift rate at the location (Vestøl et al., 2019).

data from two hydrodynamic models, the High Resolution Oceanographic Model of the Baltic Sea (HIROMB; Axell and Liu, 2016) and the HIROMB-BOOS Model (HBM; Fu et al., 2012), were considered and compared for this study. These models have both been used for operational forecasting and are therefore calibrated both for normal conditions and extreme events. The HIROMB ocean-ice reanalysis is available in Copernicus Marine Environment Monitoring Service (CMEMS) with 5.5 km horizontal resolution for the period of 1989–2014, while the HBM-based reanalysis covers the years between 1990 and 2009 and is available from the Danish Meteorological Institute. It has a resolution of 6 nautical miles (approx. 11 km), but in the model calculations, a two way nesting in the North Sea – Baltic Sea transition zone with 6 times higher resolution is used. None of the simulations include effects of land uplift and long-term external sea level variability; neither do they assimilate any sea level data. Validation performed within this study showed that both model systems sufficiently reproduced the observed long term variability of the sea level with average RMS error around 6–7 cm and average correlation of 86–88% against tide gauges, and slightly better performance of HBM than HIROMB. For the further parts of this study, data from the HBM model reanalysis were therefore used, here denoted REAN.

Satellite Altimetry Product

Several different sea level change products based on satellite altimetry exist. Here, we focused on the ESA Sea Level CCI ECV v2.0 product[2] (Quartly et al., 2017; Legeais et al., 2018) for 1993–2014, hereafter denoted as CCI. The CCI record contains monthly fields of sea level variability and linear trend values, here denoted SLV_CCI and 2DTR_CCI, respectively. The two can be combined to form ASL, denoted ASL_CCI. It is developed based on open ocean altimetry data, and constitutes high quality monthly sea level variability and trend analysis for the open ocean.

Input data for the CCI record were corrected for tides, whereas the tidal signal is included in the tide gauge data and the reanalysis model. However, the difference was assumed to be negligible, since this study dealt with monthly mean sea level, and tides are small in the Baltic Sea (generally less than 10 cm, e.g., Samuelsson and Stigebrandt, 1996).

More importantly, the CCI by default includes a Dynamic Atmospheric Correction (DAC), which corrects the altimetry observations for the inverse barometer effect. This sea level signal is observed by the tide gauges, and also included in the ocean model. Therefore 6-hourly DAC fields were downloaded from the CCI-site, averaged to monthly values, and added back into the CCI data. While the trend of the DAC correction was almost zero, the variability on monthly time scales is significant and important for the comparison of sea level variability with tide gauge observations.

Reference Frames and Land Uplift

To assess the separate effects of sea level change and land uplift, accurate information on land deformations, especially from GIA (Steffen and Wu, 2011), is essential in the Baltic Sea region, as the deformations vary throughout the region. In this paper, we mapped both RSL, which is sea level relative to land, and ASL, which is measured in a fixed reference frame referring to the mass center of the Earth. The three data sources – tide gauge observations, satellite observations and reanalysis data based on a hydrodynamic model – all have different reference frames.

Tide gauges measure sea level changes relative to the land on which the tide gauges rest. By itself, a tide gauge cannot tell the difference between local vertical land motion and sea level changes. If a Global Navigation Satellite System (GNSS) station (which uses the satellite navigation signal to measure the position referring to the center of the Earth) is located in connection with the tide gauge, the ASL can be calculated directly (e.g., Nerem et al., 2018). If this kind of data is missing, the vertical land motion (especially GIA effects) can be removed using a land uplift model of the region (Vestøl et al., 2019). It must be taken into account that the corrections from both methods introduce some uncertainties. Since the collocated GNSS station approach is only possible for a limited number of stations in our study area, and includes some uncertainty due to the limited observational GNSS records, than the more general approach of using a land uplift model was used in this study.

The land uplift model used in this study is the NKG2016LU model by the Nordic Geodetic Commission (NKG), which is based on an empirical approach combining GNSS and leveling data in the Nordic region relative to the NKG2016GIA_prel0306 geophysical GIA model (Vestøl et al., 2019). The model was released in two versions: first, uplift relative to geocenter in ITRF2008 reference system (i.e., model version NKG2016LU_abs), and then, by applying a geoid change correction, uplift relative to geoid (NKG2016LU_lev). In this study, the geocentric version was used, and denoted LU (**Figure 1**). Their difference is not large (∼10%) and not considered important, since it is subtracted from the sea level data consistently over the whole study area. The coastal uncertainty of the NKG2016LU is 0.2 mm/yr (Vestøl et al., 2019), and this uncertainty was propagated into the uncertainty estimates of the ASL change in this study.

For the statistical modeling described below, the sea level variation of the tide gauge data was needed, but also, it had to be ensured that linear trends could be reconstructed. Therefore, RSL from TGin were first corrected for land uplift, giving the ASL. Then, the absolute, linear trend was calculated at each station, and the *overall mean* trend (MTR) was calculated as the average of the seven linear trend values over the full data period. MTR was assumed to represent the external sea level change signal. MTR was subtracted from the ASL records at the individual stations, resulting in tide gauge sea level variability records with only very small residual trends remaining, SLV_TGin.

Satellite altimetry observations are based on radar measurement of the distance from the satellite to the sea surface, in combination with precise location information of the satellite, in a reference frame referring to the mass

[2]www.esa-sealevel-cci.org/products/

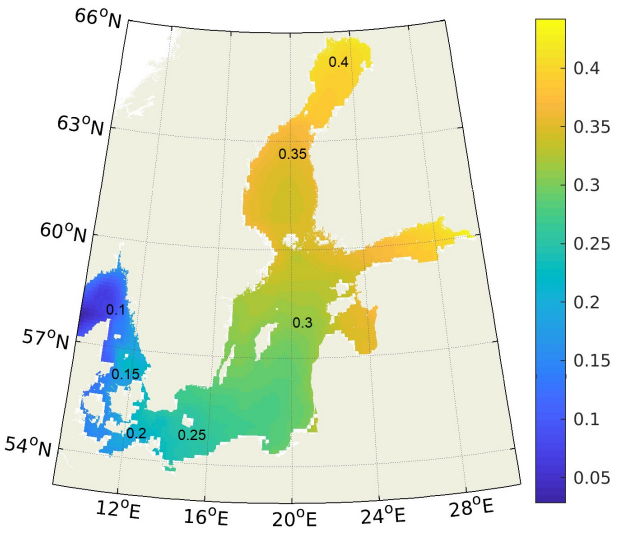

FIGURE 3 | Mean sea level (meters) in the Baltic Sea 1990–2009 from the HBM ocean model reanalysis.

center of the Earth. Thus, the satellite altimeter observation represents the ASL.

The reference frame for the reanalysis model is the model bathymetry, which typically refers to mean sea level (of various epochs). Furthermore, the reanalysis data used for this study has a free surface, which reflects surplus river runoff exiting to the Baltic Sea, steric effects generated inside the model area, and the wind setup of the general westerly wind patterns of the study area (Madsen, 2011). This results in a mean sea level setup in the model approximately reflecting the mean sea level setup relative to a geoid. The sea level difference due to a tilt from the Danish Straits toward NE part of the Baltic Sea can reach about 40 cm (**Figure 3**). The REAN data do not include external sea level change. In this study, only the detrended monthly variability fields of the REAN data were used, and therefore, the somewhat arbitrary reference level was assumed not to be important.

Statistical Model

For the statistical reconstruction of the sea level fields, a multiple linear regression was used, based on Madsen et al. (2007, 2015). With this method, the statistical model uses a training data set to calculate the optimal weights that each of the selected tide gauges should have in order to reconstruct the sea level with the lowest mean square differences. The optimal weights are calculated for each 2D grid point and the statistical model is thus able to reconstruct the 2D sea level field using only the tide gauge observations.

In the present study, SLV_TGin (7 single points, long time series), as well as a constant trend, were trained against the model reanalysis data (REAN, 2-dimensional, limited time period) (**Figure 1**). When calculating the statistical model coefficients, each point in the REAN 2D grid was treated individually, and the seven SLV_TGin records and the constant trend were linearly combined to fit the time series of REAN data in the point, in an optimal, damped least squares sense. A damping coefficient of 0.5 was selected to stabilize the model weights.

The result was a set of seven 2D fields of weights for the SLV_TGin records, and a 2D field of values for the overall mean trend, forming the statistical model, SRM. The RMS fitting error of the statistical model was 5 cm for tide gauges in most of the Baltic Sea, increasing to 7 cm for stations in the far northern and eastern parts. The weights of the overall mean trend were negative and small, with absolute values less than 0.06 mm/yr in all locations.

After derivation of the spatial regression patterns of this statistical model, the full monthly 2D sea level variability fields (SLV_SRM) were reconstructed. Then ASL change (ASL_SRM) was calculated by adding the *overall mean* sea level trend, MTR, back in, and finally, the effect of land uplift (LU) was taken into account to get the RSL change (RSL_SRM).

RESULTS

Reconstructed Sea Level

As described above, the monthly mean sea level in the approximately 11 × 11 km grid (same as for the REAN) was reconstructed for the entire Baltic Sea from 1900 to 2014, using SRM. Gaps were allowed, where observations from the seven tide gauges were missing (in total 41 months or 3%) with the biggest gaps in the 1980s and 1990s. The reconstruction allowed assessment of the monthly and annual sea level for all parts of the Baltic Sea, including those with limited tide gauge coverage, relative to the coast or absolute. It also allowed consistent assessment of the area-averaged sea level (**Figure 4**). The ASL rose over the last century (to be quantified further below), but with inter-annual variability of approximately the same magnitude. It is thus clear that a proper assessment of trends is sensitive to the period for which the trend is calculated.

The reconstructed datasets of 2D relative and absolute monthly mean sea level generated for this study, as well as the calculated linear trends (RSL_SRM, ASL_SRM and 2DTR_SRM), are available from Madsen et al. (2019).

Validation of Reconstruction Against Tide Gauges

SLV_SRM was validated using the 56 independent tide gauge records (TGval). For each record, the linear trend of the station was removed, forming SLV_TGval, and the closest water grid point of the SRM was found. The two time-series were used for the common time span. The average correlation was 96%, and the average RMS difference was 3.8 cm (**Figure 5**). Furthermore, few TGval stations with poor statistics stood out. Especially, Klaipeda had an RMS error of 7 cm, compared to 4 cm at the nearest station, Pionersky, and also showed a much lower correlation coefficient. We speculate that this was due to the influence of the nearby Curonian Lagoon on the Klaipeda tide gauge observations. The RMS difference was also higher in the northern Bothnian Bay (5–6 cm), probably related to the influence of seasonal sea ice. The correlation was 86–95% in the very dynamic North Sea – Baltic Sea (NS-BS) transition zone.

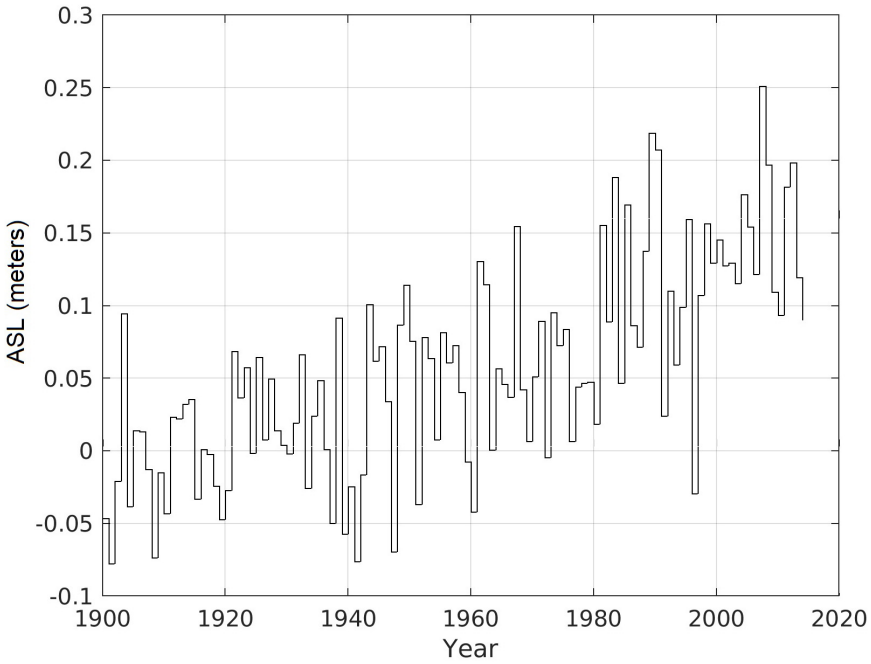

FIGURE 4 | Temporal variations in area averaged annual ASL_SRM in the Baltic Sea.

Even with these limitations, the statistical reconstruction (SRM) showed better validation results when compared to independent tide gauge observations (TGval) than the original reanalysis product (REAN, which has average correlation 88%, and RMS difference 6 cm for the same stations, but for 1990–2009).

Validation of Satellite Altimetry Variability and Area of High Quality Data

With the high correspondence between SLV_SRM and SLV_TGval, we determined that the statistical reconstruction was suitable for validation of the temporal and spatial variability of satellite products.

When comparing SLV_SRM with the CCI product (SLV_CCI), the correlation in the central Baltic Sea was generally high, with lower values in the NS-BS transition zone (**Figure 6**, right panel). There, the CCI was most likely affected by lack of data and interpolation over large scales. The RMS differences showed increased values of 7–12 cm in the northern Bothnian Bay, eastern Gulf of Finland, and south-eastern Gulf of Riga, (partly due to sea ice effects), as well as in parts of the NS-BS transition zone (**Figure 6**, left panel). Both correlation and RMS differences between SLV_TGval and SLV_CCI (nearest neighboring point) in all cases closely followed that of neighboring grid points of the statistical reconstruction, indicating that the main source of uncertainty is the CCI. The uncertainty is only slightly higher in the Archipelago Sea, indicating that the CCI was able to capture monthly sea level variations in this demanding area.

In order to find the areas with statistically reliable (hereafter "adequate") data quality, the CCI data was masked if the RMS difference between SLV_CCI and SLV_SRM was larger than 6 cm or the correlation was below 90%. These thresholds were selected to approximately match the quality level of the statistical reconstruction and the reanalysis product. The area with adequate data quality encompassed the Baltic Proper, the southern Gulf of Bothnia, the western Gulf of Finland and western Gulf of Riga (**Figure 7**, left).

Some relation was seen between the distance to the nearest coast and the amount of adequate data. In the zone 0–15 km from the shore, about 35% of the points in the Baltic Sea region were considered to be of degraded quality. The share decreased to about 10% in the 30–50 km offshore zone (**Figure 7**, right).

Sea Level Trends Derived From Satellite Altimetry

In order to make trustworthy assessments of the sea level trend, one must be able to reproduce the sea level variability. We considered that the areas where the SLV_CCI showed adequate quality were also suitable for trend estimation, considering that the CCI was designed for this task. The CCI linear sea level trend over the period 1993–2015 is shown in **Figure 8**, with dotted areas indicating areas of decreased quality of SLV_CCI. The CCI-based linear sea level trend was calculated as the overall average value over the area with adequate quality of SLV_CCI. It was 4.0 mm/yr for this period, with a standard deviation of 0.5 mm/yr. The error information provided with the CCI shows an error level of 1.0–1.3 mm/yr in this area (mean 1.2 mm/yr). The combined error (taking into account two sources) is therefore approximately $\sqrt{0.5^2 + 1.2^2} = 1.3$ mm/yr over the study period and for the area with trustworthy data.

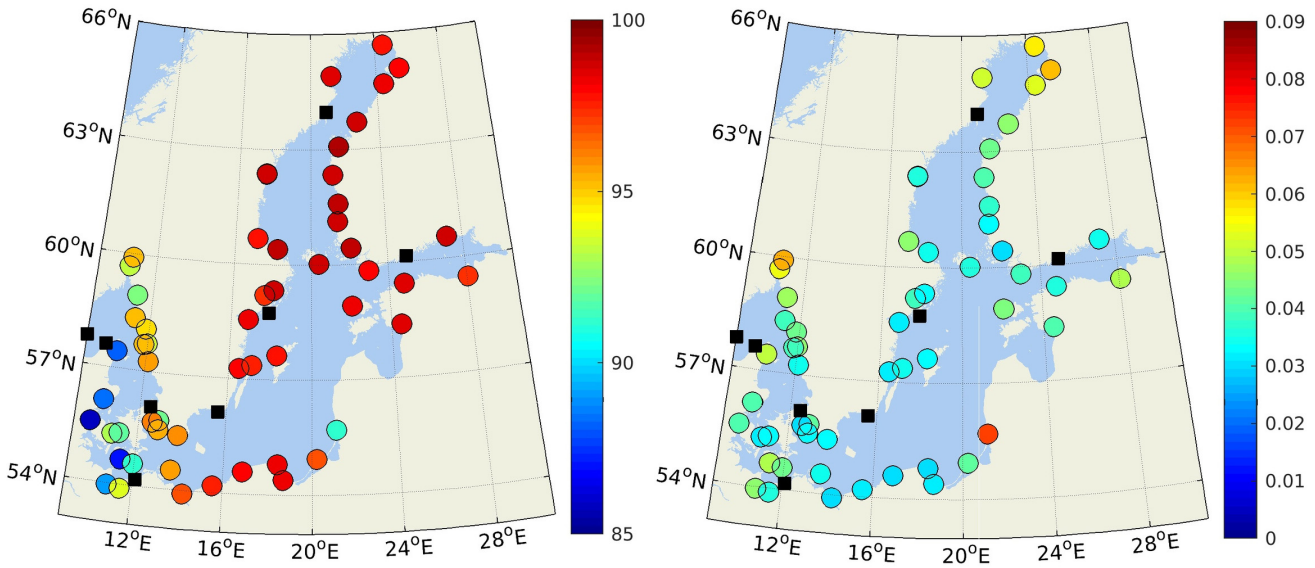

FIGURE 5 | Correlation (%, **left**) and RMS differences (meters, **right**) between SLV_TGval and the nearest neighboring point of SLV_SRM. Colored circles: validation stations. Black squares: TGin stations.

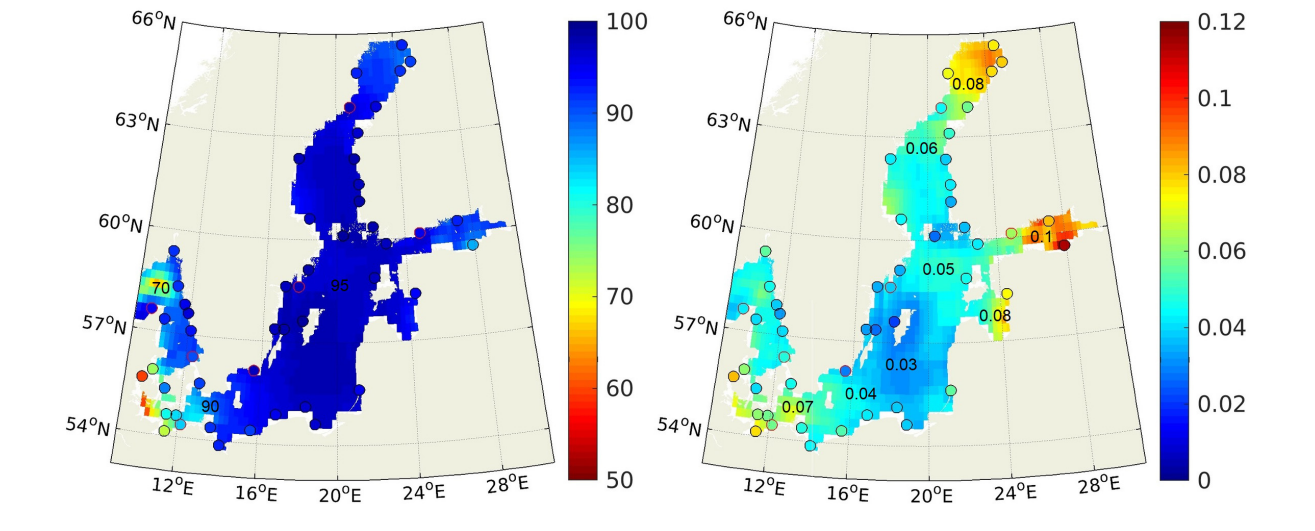

FIGURE 6 | Validation of monthly SLV_CCI against SLV_TGval (dots with black edges, nearest neighboring point), SLV_TGin (dots with red edges, nearest neighboring point) and reconstructed sea level (colored areas). **Left:** correlation (%), **Right:** RMS difference (meters).

The sea level trend error field from the CCI data did not reflect the assessment of areas with adequate data quality according to this study. Uncertainty sources from interpolation errors in the coastal areas and in the ice affected regions were not taken into account. Also, the provided uncertainty field had very low values in the North Sea – Baltic Sea transition zone (**Figure 8**, right).

Trends of the 20th Century Reconstruction

The hundred year's RSL_SRM trend from 1915 to 2014 was, as expected, dominated by the land uplift signal (**Figure 9**). Hence, decreasing sea level trends occurred in large parts of the Baltic Sea, reaching up to −9 mm/yr in the northern Bothnian Bay.

There was a close correspondence between the trends observed at the tide gauges and those at the neighboring grid cells of relative 2DTR_SRM. For the eastern Baltic Sea, which lacks very long observational records, the trend increased toward south-south-east, with coastal values increasing from −2 mm/yr on the north-western Estonian coast to +1 mm/yr at the Polish coast.

The ASL change of the same hundred years' time frame was much more uniform across the Baltic Sea. The observations (TGval) showed absolute linear trends of 1.2–2.5 mm/yr. Fitting

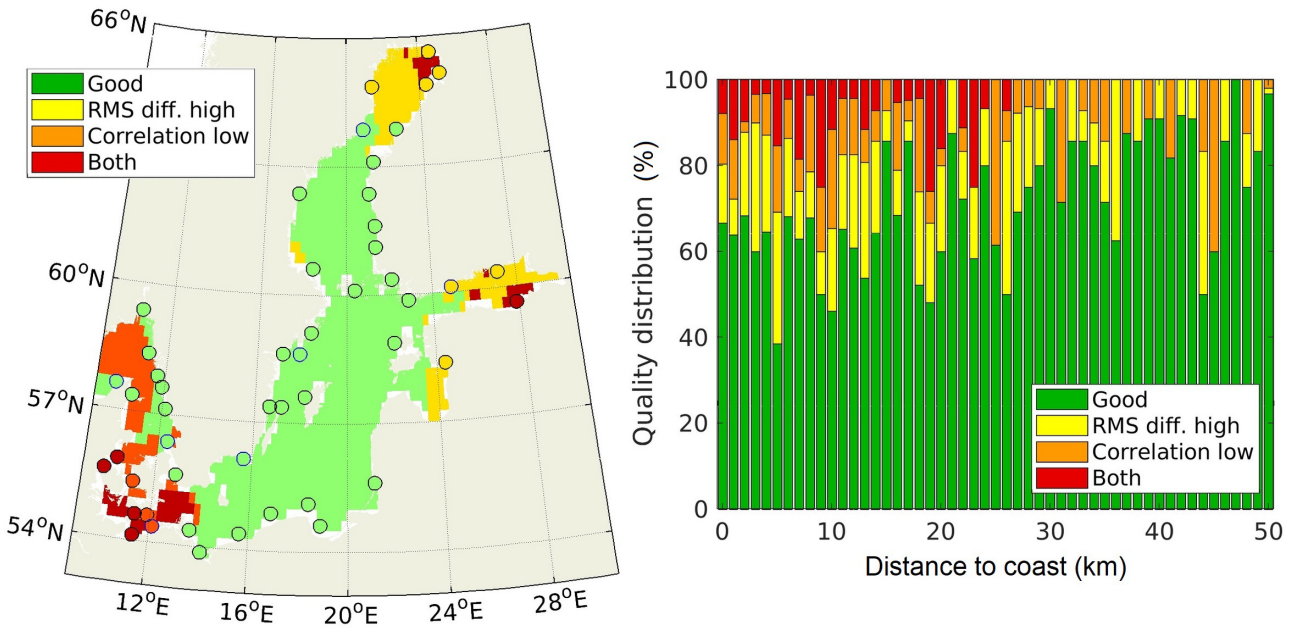

FIGURE 7 | Left: CCI data evaluation showing the areas with adequate data quality according to this study, and the areas with low correlation and/or high RMS difference to SLV_SRM (colored areas) and SLV_TG (circles). **Right:** percentage of areas with different quality classes versus distance to the coast.

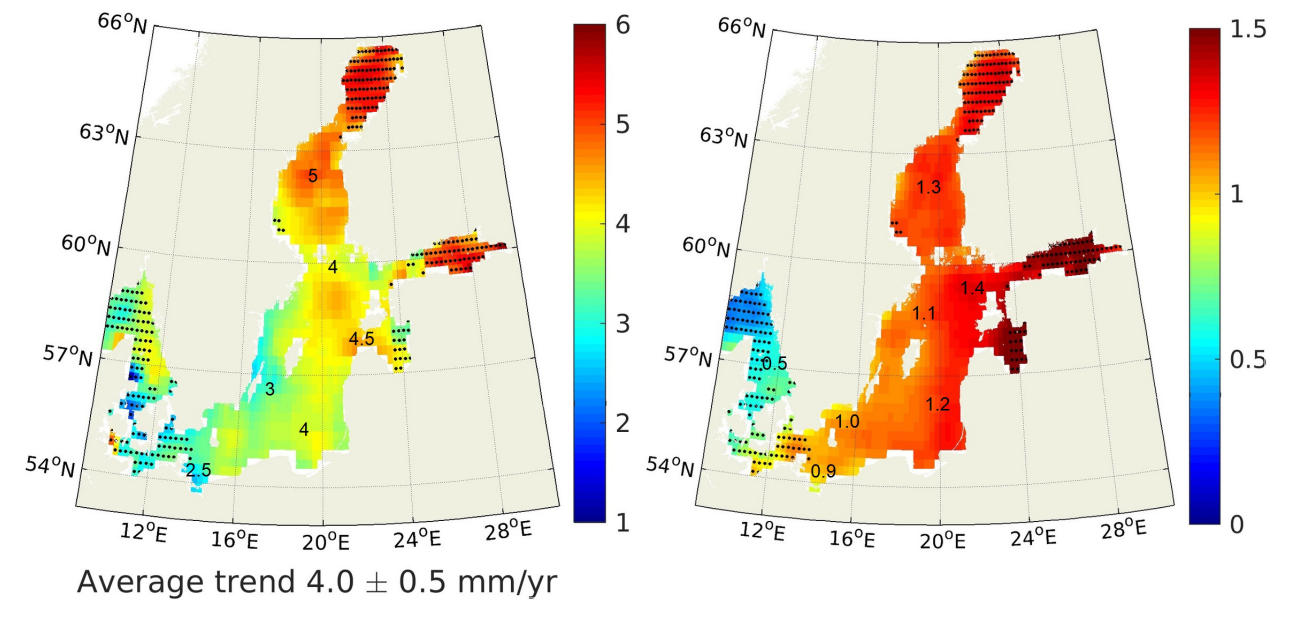

FIGURE 8 | Left: Spatial distribution of linear sea level trends in the Baltic Sea according to the CCI (1993–2015, mm/yr). **Right:** Corresponding trend error (mm/yr) fields as provided by the CCI. Black dotted areas denote the regions with decreased data quality of SLV_CCI according to this study.

uncertainties of the linear trends at the individual stations went up to 0.2 mm/yr with the highest values being located at individual stations in the northern Bothnian Bay as well as in the outer zone bordering with the North Sea. Similarly, the statistical model showed linear trends (absolute 2DTR_SRM for 1915–2014) of 1.2–2.1 mm/yr, but in a slightly different pattern. The highest values occurred in the stretch from Kattegat over the central Baltic Proper, and into the gulfs of Finland and Riga. These differences were within the uncertainty range. They could have occurred due to uncertainties in the statistical reconstruction, small-scale variations in land uplift field, or due to changes in wind setup. When comparing these absolute trends with absolute trends derived using other methods, the uncertainty of the uplift model must be taken

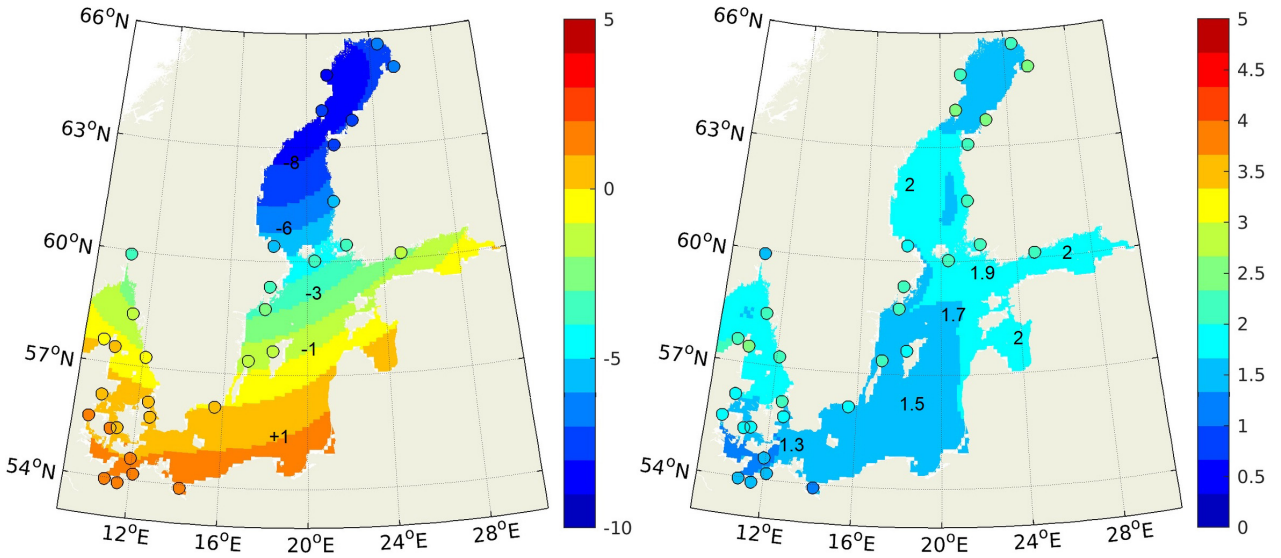

FIGURE 9 | Linear sea level trends (mm/yr) derived from SRM and from tide gauges, 1915–2014. **Left:** relative to land; **right:** absolute values. Note that only tide gauges with adequate record length have been included. Also note that the trends in tide gauges may exceed (up to 1 mm/yr) the trends in the offshore area.

into account, yielding a total uncertainty of approximately $\sqrt{0.2^2 + 0.2^2} = 0.3$ mm/yr.

Comparison in Satellite Era

For the satellite era, the overall averaged ASL change rates from the regression model (absolute 2DTR_SRM for 1993–2014) and satellite data (2DTR_CCI) are compared in **Table 1**. The fitting uncertainty is largely increased for this shorter time period. This uncertainty mainly occurs due to large interannual variability (see also section 3.1). Focusing on the satellite era, the ASL trend was higher in the latest decades than in the 100-year average values (1.2–2.5 mm/yr for 1915–2014). The reconstruction-derived trend was 3.4 ± 0.7 mm/yr for 1993–2014, and the highest trend estimate (4.0 ± 1.3 mm/yr over 1993–2015) was offered by CCI.

DISCUSSION

Reconstruction Versus Reanalysis

The reconstructed sea level (SRM) validated well against the tide gauge data (TGval) and provided good spatial data coverage. However, compared to the hydrodynamic model reanalysis (REAN), it had two main weaknesses. The SRM was sensitive to the data quality, coverage, and completeness, and it only provided information on the sea level, whereas a reanalysis can provide 3D fields of temperature, salinity and ocean currents to complement the sea level fields. The benefits of the statistical method are in its' good performance for the region and low computational costs. Also, this study demonstrated that a lot of information is available in the tide gauge records, which can be assimilated into model-based reanalyses in the future.

The SRM performed well in the open waters of the Baltic Sea, but it was challenged by the complex hydrodynamics in the North Sea – Baltic Sea transition zone. It mainly occurred due to shorter correlation scales in time and space, and less good representation in the input reanalysis model. This zone puts high demands on any ocean model, and also on the satellite altimetry products. However, the zone is densely covered by tide gauges and allows detailed validation. Future developments will require very high resolution modeling with high quality bathymetry and atmospheric forcing using e.g., UERRA (Ridal et al., 2017) reanalysis. Downscaling of ERA5 (within the Copernicus Climate Change initiative) is likely to provide even more detailed atmospheric forcing.

TABLE 1 | Mean linear ASL change rates in the Baltic Sea from SRM and CCI (mm/yr).

	Mean	Standard deviation	Average single point uncertainty	Maximum single point uncertainty	Total uncertainty estimate
Statistical model, 1900–1999	1.34	0.12	0.14	0.19	0.3
Statistical model, 1915–2014	1.64	0.11	0.14	0.19	0.3
Statistical model, 1993–2014	3.4	0.2	0.7	1.0	0.7
CCI data, 1993–2015	4.0	0.5	1.2	1.5	1.3

Standard deviations indicate variability of individual linear trends across the Baltic Sea. Since each trend has an uncertainty attached, which cannot be considered independent from point to point, the average and maximum uncertainty estimates at the individual points are shown. The average single point fitting uncertainty is further combined with other uncertainty sources (described in this paper) to yield an estimate for total uncertainty.

Land Uplift

Reconstruction of ASL trends relies on land uplift models, especially in the areas with a large land uplift signal, such as the Baltic Sea area. The newly developed land uplift model (Vestøl et al., 2019) helps to improve the determination of ASL change from tide gauges in the Baltic region. However, small errors could still occur e.g., due to un-modeled (local) land subsidence, that can introduce errors in the tide gauge records. An alternative approach would be to use collocated GNSS station data, as it was done by Richter A. et al. (2012). However, the uncertainties of that procedure are still relatively high, mainly due to the limited temporal coverage of the GNSS stations. In future situations, when the GNSS stations have the opportunity to continue their recordings for a longer period of time, the observed land uplift can be used instead of or in combination with a land uplift model. Finally, there may be small systematic errors in the connection of the geodetic height system to the international geodetic reference frame.

Satellite Altimetry in the Coastal Seas

The results presented in this paper demonstrate that the satellite altimetry observations can provide valuable information in the coastal sea for studying the long term linear sea level trends, and the two estimates of sea level trends (satellite versus reconstructed) agreed within the uncertainty limits. So far, the time series of the CCI is still relatively short considering the long-term variability in sea level and the observed global acceleration (Church and White, 2006; Sallenger et al., 2012). It is especially true in semi-enclosed areas like the Baltic Sea, where interannual sea level variability is higher than in the open ocean (Suursaar and Kall, 2018). It is also clear that the Baltic Sea is a challenging area for global satellite products due to lack of open sea spaces, complex coastlines, and presence of small islands. These features are demanding for both the along-track satellite processors and for the gridding and interpolation procedures (see e.g., Passaro et al., 2014; Ablain et al., 2015). A dedicated regional CCI would be beneficial to overcome these limitations and to extend the use of satellite observations at coast.

Yet another challenge for satellite products is the occurrence of seasonal sea ice e.g., in the Bothnian Bay and Gulf of Finland (e.g., Vihma and Haapala, 2009). The gaps due to missing data may last for several months in each year, which leads to a higher uncertainty in the linear sea level trends (**Figure 8**). In order to properly determine the sea level trends for the entire Baltic Sea, it is necessary to have an estimate of the sea level in ice covered areas, which would require a dedicated satellite product.

Sea Level Trends

The rates of ASL change found for the Baltic Sea (1.34 mm/yr in 1900–1999; 1.64 mm/yr in 1915–2014; **Table 1**) were similar to the global average of the same time period (1.7 mm/yr in 1900–2010; IPCC, 2013). For the 20th century, the area averaged ASL change for the entire Baltic Sea was 1.3 ± 0.3 mm/yr. For the satellite era (1993–2014), the linear trends derived from the reconstruction (3.4 ± 0.7 mm/yr) matched those of the CCI (4.0 ± 1.4 mm/yr for 1993–2015) within the uncertainty limits. While the century-long trend was quite stable, the trend of the satellite era is highly sensitive to interannual variability (**Figure 4**).

When discussing spatial variations in absolute trend reconstruction, the trend values were higher (by ∼0.5 mm/yr) in the ("lower quality") far ends of the elongated Baltic Sea: in the Bothnian Bay, Gulf of Finland and Gulf of Riga (**Figure 9**). They were higher also in the Kattegat, just before the narrowest parts of the Danish Straits, but less high in the south-western Baltic Sea. This was connected to the peculiarities of water exchange processes of the Baltic Sea in conditions of climatologically prevailing south-westerlies in that region (Suursaar and Kullas, 2006). Within the Baltic Sea, the sea level amplitudes (variability) of both external (i.e., long-term water surplus variations) and internal sea level oscillations (occurring as a half-wave-length oscillator) increase in the far ends of the sea, and decreases in the central, nodal part (Samuelsson and Stigebrandt, 1996). This has also been illustrated in several hydrodynamic modeling studies (e.g., Meier et al., 2004; Suursaar and Kullas, 2006). When comparing between datasets, the RMS difference is likely to increase when trends and sea level variability increase. On the other hand, neglecting those "lower quality" areas (with higher absolute trends) may lower the average Baltic Sea level trend estimates.

When comparing the obtained sea level change rates with the global ones, the focus should be on the ASL change. However, when assessing the impacts of ongoing climate change on the coast and coastal societies, the main focus should be on the RSL change. So far, the influence of global sea level change is largely canceled out by GIA effects in the central Baltic Sea area. However, with future global sea level change and its acceleration (IPCC, 2013), wider areas in the Baltic Sea will experience RSL change impacts as well.

CONCLUSION

This study on both ASL and RSL change in the entire Baltic Sea provides a basis to cope with anticipated climate-related sea level changes in the future. Using a statistical model, monthly mean sea level was reconstructed for the entire Baltic Sea in an 11 × 11 km grid from 1900 to 2014. The reconstructed monthly sea level variability was successfully validated using 56 tide gauge records and against satellite altimetry (CCI) products. The absolute and relative 2D sea level trend fields were calculated. It appeared that sea level data from satellite altimetry can be successfully used for assessing monthly sea level variability in the Baltic Sea, and that linear sea level trends from the 2D statistical reconstruction and satellite altimetry agreed with each other within the uncertainty range. It also appeared that coastal zones, especially in the areas with seasonal sea ice and the areas of high natural variability, need special treatment. However, the increased uncertainty in such areas was not reflected in the trend error field provided with the CCI. The RSL trend

(with values down to −9 mm/yr in the northern Bothnian Bay over 1915–2014) was dominated by postglacial uplift of that area. The area averaged ASL change for the entire Baltic Sea was 1.3 ± 0.3 mm/yr in the 20th century. For the satellite era (1993–2014), the linear trends derived from the reconstruction (3.4 ± 0.7 mm/yr) matched those of the CCI (4.0 ± 1.4 mm/yr for 1993–2015) within the uncertainty limits. Although shortness of the latter made trend estimation highly sensitive to the variability, the sea level change rates found in the study confirmed their acceleration over the last decades. Further refinement of the models and inclusion of new data hopefully enables more reliable results in the future.

AUTHOR CONTRIBUTIONS

KM was responsible for compiling the data, modeling, and writing the manuscript. JH, JS, and PK contributed to the data analysis, modeling, and writing. ÜS provided additional data and contributed to the writing.

FUNDING

The research leading to these results has received funding from the Baltic Sea Check Point project under contract number EASME/EMFF/2014/1,3,1,1/LOT 3/SI2.708189, Estonian Research Council grant PUT1439, and the Danish Government grant Klimaatlas.

ACKNOWLEDGMENTS

In situ observations have been obtained from PSMSL (http://www.psmsl.org/data/obtaining/), the Estonian Environment Agency and the Copernicus Marine Environment Monitoring Service, supplemented with data from the Danish Meteorological Institute. Satellite observations were obtained from the ESA Sea Level CCI, and the uplift data from the NKG (Vestøl et al., 2019). We thank the two reviewers for their suggestions that helped to improve and clarify the manuscript, as well as Beverly Bishop and April Bernhardsgrütter for their language advice.

REFERENCES

Ablain, M., Cazenave, A., Larnicol, G., Balmaseda, M., Cipollini, P., Faugère, Y., et al. (2015). Improved sea level record over the satellite altimetry era (1993–2010) from the climate change initiative project. *Ocean Sci.* 11, 67–82. doi: 10.5194/os-11-67-2015

Axell, L., and Liu, Y. (2016). Application of 3-D ensemble variational data assimilation to a Baltic Sea reanalysis 1989–2013. *Tellus* 68A:24220. doi: 10.3402/tellusa.v68.24220

Bonaduce, A., Pinardi, N., Oddo, P., Spada, G., and Larnicol, G. (2016). Sea-level variability in the mediterranean Sea from altimetry and tide gauges. *Clim. Dyn.* 47, 2851–2866. doi: 10.1007/s00382-016-3001-2

Burnham, K. P., and Anderson, D. R. (2002). *Model Selection and Multimodel Inference: A Practical Information-Theoretic Approach*, 2nd Edn. Berlin: Springer-Verlag.

Calafat, F. M., and Jordà, G. (2011). A Mediterranean sea level reconstruction (1950–2008) with error budget estimates. *Glob. Planet. Change* 79, 118–133. doi: 10.1016/j.gloplacha.2011.09.003

Church, J. A., and White, N. J. (2006). A 20th century acceleration in global sea-level rise. *Geophys. Res. Lett.* 33, 1–4. doi: 10.1029/2005GL024826

Ekman, M. (1996). A consistent map of the postglacial uplift of fennoscandia. *Terra Nova* 8, 158–165. doi: 10.1111/j.1365-3121.1996.tb00739.x

Fu, W., She, J., and Dobrynin, M. (2012). A 20-yr reanalysis Experiment in the Baltic Sea using three dimensional variational (3DVAR) method. *Ocean Sci.* 8, 827–844. doi: 10.5194/os-8-827-2012

Girjatowicz, J. P., Świątek, M., and Wolski, T. (2016). The influence of atmospheric circulation on the water level on the southern coast of the Baltic Sea. *Int. J. Climatol.* 36, 4534–4547. doi: 10.1002/joc.4650

Holgate, S. J., Matthews, A., Woodworth, P. L., Rickards, L. J., Tamisiea, M. E., Bradshaw, E., et al. (2013). New data systems and products at the permanent service for mean sea level. *J. Coast. Res.* 29, 493–504. doi: 10.2112/JCOASTRES-D-12-00175.1

Hünicke, B., Zorita, E., Soomere, T., Madsen, K. S., Johansson, M., and Suursaar, Ü (2015). "Recent change – sea level and wind waves," in *Second Assessment of Climate Change for the Baltic Sea Basin*, ed. BACC II Author Team, (Berlin: Springer), 155–186. doi: 10.1007/978-3-319-16006-1-9

IPCC (2013). "Fifth assessment report (AR5)," in *Climate Change 2013: The Physical Science Basis. Contribution of Working Group I to the Fifth Assessment Report of the Intergovernmental Panel on Climate Change*, eds T. F. Stocker, D. Qin, G. K. Plattner, M. Tignor, S. K. Allen, J. Boschung, et al. (Cambridge: Cambridge University Press).

Johansson, M., Kahma, K. K., Boman, H., and Launiainen, J. (2004). Scenarios for sea level on the finnish coast. *Boreal. Environ. Res.* 9, 153–166.

Legeais, J.-F., Ablain, M., Zawadzki, L., Zuo, H., Johannessen, J. A., Scharffenberg, M. G., et al. (2018). An improved and homogeneous altimeter sea level record from the ESA climate change Initiative. *Earth Syst. Sci. Data* 10, 281–301. doi: 10.5194/essd-10-281-2018

Liibusk, A., Kall, T., Ellmann, A., and Kõuts, T. (2014). "Correcting tide gauge series due to land uplift and differences between national height systems of the baltic sea countries," in *Proceedings of the 2014 IEEE/OES Baltic International Symposium (BALTIC)*, (Piscataway, NJ: IEEE), doi: 10.1109/BALTIC.2014.6887828

Madsen, K. S. (2011). *Recent and Future Climatic Changes of the North Sea and the Baltic Sea – Temperature, Salinity, and Sea Level*. Latvia: LAMBERT Academic Publishing.

Madsen, K. S., Høyer, J. L., Fu, W., and Donlon, C. (2015). Blending of satellite and tide gauge sea level observations and its assimilation in a storm surge model of the North Sea and Baltic Sea. *J. Geophys. Res.* 120, 6405–6418. doi: 10.1002/2015JC011070

Madsen, K. S., Høyer, J. L., Suursaar, Ü, She, J., and Knudsen, P. (2019). Reconstructed 2D relative and absolute monthly mean sea level of the Baltic Sea 1900-2014, and related linear trends. *Dataset*

Madsen, K. S., Høyer, J. L., and Tscherning, C. C. (2007). Near-coastal satellite altimetry: sea surface height variability in the North Sea–Baltic Sea area. *Geophys. Res. Lett.* 34:L14601. doi: 10.1029/2007GL029965

Meier, H. E. M., Broman, B., and Kjellström, E. (2004). Simulated sea level in past and future climates of the Baltic Sea. *Clim. Res.* 27, 59–75. doi: 10.3354/cr027059

Milne, G. A., Gehrels, W. R., Hughes, C. W., and Tamisiea, M. E. (2009). Identifying the causes of sea-level change. *Nat. Geosci.* 2, 471–478. doi: 10.1038/ngeo544

Nerem, R. S., Beckley, B. D., Fasullo, J. T., Hamlington, B. D., Masters, D., and Mitchum, G. T. (2018). Climate-change-driven accelerated sea-level rise detected in the altimeter era. *PNAS* 115, 2022–2025. doi: 10.1073/pnas.1717312115

Olivieri, M., and Spada, G. (2016). Spatial sea-level reconstruction in the Baltic Sea and in the pacific Ocean from tide gauges observations. *Ann. Geophys.* 59:0323.

Passaro, M., Cipollini, P., Vignudelli, S., Quartly, G. D., and Snaith, H. M. (2014). ALES: a multi-mission adaptive subwaveform retracker for coastal and open ocean altimetry. *Remote Sens. Environ.* 145, 173–189. doi: 10.1016/j.rse.2014.02.008

Permanent Service for Mean Sea Level [PSMSL], (2016). *Tide Gauge Data*. Available at: http://www.psmsl.org/data/obtaining/ (accessed January 7, 2016).

Quartly, G. D., Legeais, J.-F., Ablain, M., Zawadzki, L., Fernandes, M. J., Rudenko, S., et al. (2017). A new phase in the production of quality-controlled sea level data. *Earth Syst. Sci. Data* 9, 557–572. doi: 10.5194/essd-9-557-2017

Richter, A., Groh, A., and Dietrich, R. (2012). Geodetic observation of sea-level change and crustal deformation in the Baltic Sea region. *Phys. Chem. Earth* 53-54, 43–53. doi: 10.1016/j.pce.2011.04.011

Richter, K., Nilsen, J. E. Ø, and Drange, H. (2012). Contributions to sea level variability along the norwegian coast for 1960–2010. *J. Geophys. Res.* 117:C05038. doi: 10.1029/2011JC007826

Ridal, M., Olsson, E., Unden, P., Zimmermann, K., and Ohlsson, A. (2017). *HARMONIE Reanalysis Report of Results and Dataset. UERRA Deliverable D*2.7. Available at: http://www.uerra.eu/publications/deliverable-reports.html

Sallenger, A. H. Jr., Doran, K. S., and Howd, P. A. (2012). Hotspot of accelerated sea-level rise on the Atlantic coast of North America. *Nat. Clim. Change* 2:884. doi: 10.1038/nclimate1597

Samuelsson, M., and Stigebrandt, A. (1996). Main characteristics of the long-term sea level variability in the Baltic Sea. *Tellus* 48A, 672–683. doi: 10.3402/tellusa.v48i5.12165

Santamaría-Gómez, A., Gravelle, M., Dangendorf, S., Marcos, M., Spada, G., and Wöppelmann, G. (2017). Uncertainty of the 20th century sea-level rise due to vertical land motion errors. *Earth Planet. Sci. Lett.* 473, 24–32. doi: 10.1016/j.epsl.2017.05.038

Simon, K. M., Riva, R. E. M., Kleinherenbrink, M., and Frederikse, T. (2018). The glacial isostatic adjustment signal at present day in northern Europe and the British isles estimated from geodetic observations and geophysical models. *Solid Earth* 9, 777–795. doi: 10.5194/se-9-777-2018

Spada, G. (2017). Glacial isostatic adjustment and contemporary sea level rise: an overview. *Surv. Geophys.* 38, 153–185. doi: 10.1007/s10712-016-9379-x

Steffen, H., and Wu, P. (2011). Glacial isostatic adjustment in fennoscandia – a review of data and modeling. *J. Geodyn.* 52, 169–204. doi: 10.1016/j.jog.2011.03.002

Stramska, M., and Chudziak, N. (2013). Recent multiyear trends in the Baltic Sea level. *Oceanologia* 55, 319–337. doi: 10.5697/oc.55-2.319

Suursaar, Ü., and Kall, T. (2018). Decomposition of relative sea level variations at tide gauges using results from four estonian precise levelings and uplift models. *IEEE J. Sel. Top. Appl. Earth. Obs. Remote Sens.* 11, 1966–1974. doi: 10.1109/JSTARS.2018.2805833

Suursaar, Ü., and Kullas, T. (2006). Influence of wind climate changes on the mean sea level and current regime in the coastal waters of west estonia, Baltic Sea. *Oceanologia* 48, 361–383.

Vestøl, O., Ågren, J., Steffen, H., Kierulf, H., and Tarasov, L. (2019). NKG2016LU: a new land uplift model for fennoscandia and the baltic region. *J. Geod.* 93, 1–21. doi: 10.1007/s00190-019-01280-8

Vihma, T., and Haapala, J. (2009). Geophysics of sea ice in the Baltic Sea: a review. *Prog. Oceanogr.* 80, 129–148. doi: 10.1016/j.pocean.2009.02.002

Woodworth, P. L. (2006). Some important issues to do with long-term sea level change. *Philos. Trans. R. Soc. Lond. A.* 364, 787–803. doi: 10.1098/rsta.2006.1737

Conflict of Interest Statement: The authors declare that the research was conducted in the absence of any commercial or financial relationships that could be construed as a potential conflict of interest.

frontiers in Earth Science

ORIGINAL RESEARCH
published: 18 September 2019
doi: 10.3389/feart.2019.00241

Assessment of Water Balance for Russian Subcatchment of Western Dvina River Using SWAT Model

Pavel Terskii[1], Alexey Kuleshov[2], Sergey Chalov[1], Anna Terskaia[3], Pelagiya Belyakova[4], Daniel Karthe[5] and Thomas Pluntke[2]*

[1] Department of Land Hydrology, Lomonosov Moscow State University, Moscow, Russia, [2] Institute of Hydrology and Meteorology, Dresden University of Technology, Dresden, Germany, [3] Laboratory of Aerospace Methods, Lomonosov Moscow State University, Moscow, Russia, [4] Flood Hydrology Laboratory in Water Problems, Institute of Russian Academy of Sciences, Moscow, Russia, [5] Faculty of Engineering, German-Mongolian Institute for Resources and Technology, Nalaikh, Mongolia

The study provides a new assessment of the water balance components of the catchment (evapotranspiration, surface and lateral flow etc., and its spatial distribution and temporal variability) for the transboundary catchment of Western Dvina river within the poorly gaged Russian part of the catchment. The study focuses on modeling the inland flow generation processes using open source data and the SWAT (Soil Water Assessment Tool) hydrological model. The high interannual variability of river flow and impact of snowmelt processes were especially taken into account when setting up the model and processing the calibration. The database of daily meteorological data for the period 1981–2016 was prepared using global atmospheric reanalysis ERA-Interim data and observed station data from the GSOD NCDC/NOAA and ECA&D datasets. The considered datasets were tested on plausibility and regionalized. The catchment model was built on the basis of open land use/land cover (LULC) data sets, topography and soil, so that the entire transboundary catchment area could be easily implemented in the next step. For the daily model calibration, 19 sensitive parameters were chosen manually. The most sensitive are the parameters which consider snow melting processes and flow recession curve number. The area and distribution of wetlands have the highest impact on water balance components. Lakes strongly affect the evapotranspiration rate. The study provides further research with uncertainty analysis and recommendations for model improvement and model limitations. The developed modeling approach can be used to assess water resources, climate change impacts, and water quality issues in comparable regions.

Keywords: Western Dvina, SWAT, transboundary river, climatic data analysis, snowmelt runoff, calibration and validation, uncertainties, open source data

OPEN ACCESS

Edited by:
Markus Meier, Leibniz Institute for Baltic Sea Research (LG), Germany

Reviewed by:
Stefan Hagemann, Helmholtz Centre for Materials and Coastal Research (HZG), Germany
Paweł Wiśniewski, University of Gdańsk, Poland

****Correspondence:***
Pavel Terskii
pavel_tersky@mail.ru

Specialty section:
This article was submitted to Interdisciplinary Climate Studies, a section of the journal Frontiers in Earth Science

Received: *14 January 2019*
Accepted: *30 August 2019*
Published: *18 September 2019*

Citation:
Terskii P, Kuleshov A, Chalov S, Terskaia A, Belyakova P, Karthe D and Pluntke T (2019) Assessment of Water Balance for Russian Subcatchment of Western Dvina River Using SWAT Model. Front. Earth Sci. 7:241. doi: 10.3389/feart.2019.00241

INTRODUCTION

An exact knowledge of catchment-scale water balance is particularly important in international (transboundary) river basins, which cover two or more countries. Transboundary rivers form natural connections between riparian countries, no matter how good or bad their political relations are (Heininen, 2018). Collecting sufficient information on water-related hazards remains a crucial

task in international water management, environmental pollution control and the prevention of health problems. In transboundary basins, both water use and monitoring are often not fully coordinated between riparian states (Alekseevskii et al., 2015; Krengel et al., 2018). The consequences include data inconsistency and (sometimes critical) information gaps (Karthe et al., 2015). This can lead to inadequate scientific assessments or management strategies. These problems emphasize the need to develop new monitoring and modeling tools that take into account the specific challenges encountered in transboundary basins.

The availability and quality of water resources is the subject of constantly ongoing transnational negotiations between riparian states. The transboundary basins shared between the Russian Federation, the post-Soviet republics of Eastern Europe and EU countries constitutes one region where there are significant disparities regarding the monitoring and management of surface water resources (Krengel et al., 2018). One recent example for the development of water resources management in this region is the process of implementing EU water directives which has been started by the Ukrainian government. Currently, river basin management plans are being developed for nine major river catchments. Even though these changes lead to a harmonization at the EU's eastern border, they lead to more profound differences between Ukraine and the Russian Federation. This case study looks at the basin of the Western Dvina (or Daugava), which covers an area of about 86,000 km^2 with significant parts (roughly 1/3 each) located in Russia, Belarus and the EU (mostly in Latvia, a small part in Lithuania). Since 1990, many parts of Russia have experienced a rapid process of resettlement of citizens from rural areas to cities. This process is accompanied by the abandonment of previously cultivated land (pastures), which is different from the LULC development in many EU countries. European countries have at the same time experienced different socioeconomic changes (e.g., a decline of old industries but also partial re-industrialization, abandonment but also intensification of agricultural land use). These transitions have had strong impacts on the region's water usage (Krengel et al., 2018). In case of the Western Dvina, the downstream sections which are located within the territories of Latvia and Lithuania, fall under the jurisdiction of the European Union Water Framework Directive (directive 2000/60/EC). Contrastingly, the upper part of the catchment which is located within the Russian Federation and Belarus, has water resources monitoring and management regulated by laws which have evolved from Soviet legislation. This results in significant differences between the up- and downstream sections of the Western Dvina in terms of water resources monitoring and management (Krengel et al., 2018).

Water management in the Western Dvina basin faces the challenges of insufficient water quantity and quality monitoring which is based on a very limited number of gaging stations, particularly in Russian part of the catchment. To this date, hydrological assessments of the upper part of the catchment are based on limited data, whereas downstream areas have been intensively studied, e.g., based on Vitebsk and Polotsk gaging stations located in the Republic of Belarus (Parfomuk, 2006; Volchek and Lusha, 2006; Volchek and Shelest, 2012; Asadchaya and Kolmakova, 2014; Loginov et al., 2015). The recent construction of several dams in the Republic of Belarus necessitates further research regarding their hydrological impact, thus emphasizing the need for hydrological modeling tools to assess the water balance in this part of the catchment.

A conceptual approach for integrating monitoring and modeling efforts has been developed for the Western Dvina catchment under the Volkswagen Foundation project "Management of Transboundary Rivers between Ukraine, Russia and the EU – Identification of Science-Based Goals and Fostering Trilateral Dialogue and Cooperation (ManTra-Rivers)."

The main goal of this study was to set up a hydrological model for a Russian subcatchment of the transboundary Western Dvina watershed based on the open source data. This unified catchment-based model aims at filling gaps in hydrological measurements and more precisely assessing poorly understood water balance components. This is an important prerequisite for further research, such as simulating water quality, erosion processes and the hydrological consequences of future climatic change. In this study, particular emphasis was given to the simulation of snowmelt runoff which contributes about a half of the annual flow.

STUDY AREA

The study focuses on the Russian part of Western Dvina river catchment. The SRTM-derived catchment area is 17,250 km^2 (Krengel et al., 2018) with the outlet gaging station Velizh. This part of the catchment area contributes about 1% of the total Western Dvina runoff inflow to the Baltic Sea. The mean Western Dvina annual runoff at the Velizh gauge is 150 m^3/s (4.73 km^3/year), at the mouth (Riga) – about 500 m^3/s (15.8 km^3/year). Total Baltic Sea river inflow is estimated as 436 km^3/year (Mohrholz, 2018). The Western Dvina and its tributaries in the Russian part of the catchment are not regulated and poorly studied. Currently the monitoring consists of five meteorological stations and four hydrologic stations with daily discharge measurements.

The climate of the Western Dvina river basin is temperate and moderately continental. In the Russian part, the average temperature in January ranges from −6°C in the southwest to −10°C in the northeast. Monthly mean temperatures in July range between +17 and +19°C. Annual precipitation throughout the Russian subbasin totals about 650 mm. Along the Russian stretches of the Western Dvina, which total 325 km in length, maximum discharges are observed in spring due to snowmelt and spring rainfalls. The main soil classes are podzoluvisols (euthric, gleyic, and gelic), histosols (fabric), gleysols (dystric), and podzols (haplic, ferric) (Nachtergaele et al., 2008). The catchment is covered by 78% of forest (mostly mixed), 6% of wetlands, 2% of lakes (based on Globcover2009 dataset) (**Figure 1**). Land use mainly includes forestry and woodworking (Andreapol and Western Dvina towns) and agriculture (Western Dvina and Velizh towns).

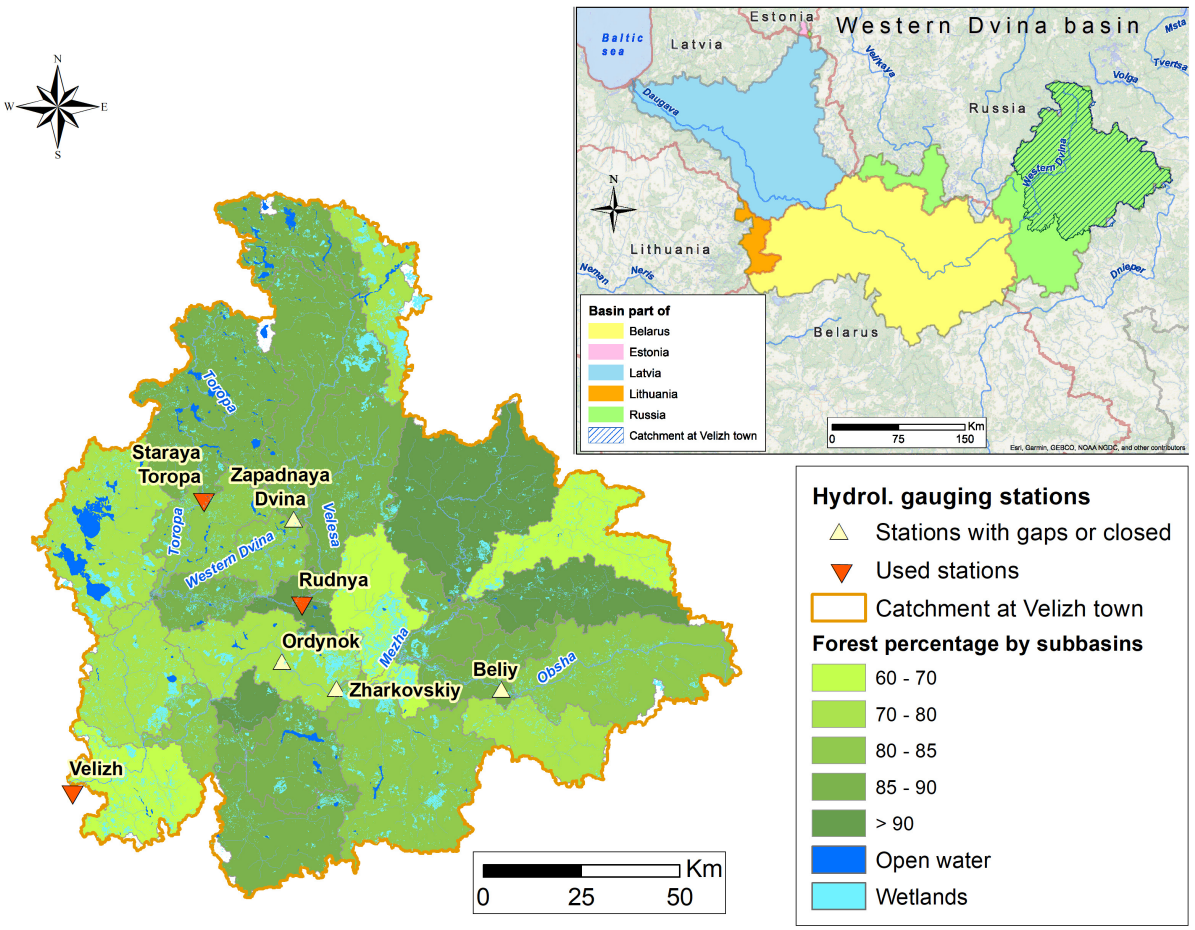

FIGURE 1 | Study area of the Western Dvina catchment (Russian part) with hydrological gaging stations used for model processing.

The Russian part of the Western Dvina river basin is home to approximately 1,70,000 people (8% of the total basin population), of which more than 8300 live in the subbasin's largest town, Western Dvina (Center for International Earth Science Information Network [CIESIN], 2014) 0.38, 51, and 2% of the total population live in the sub-basins located in Belarus, Latvia and Lithuania live, respectively, of the river basin.

METHODS AND DATA

The hydrological freely accessible model SWAT v.2012 was chosen (Arnold et al., 2012) as a tool to simulate the influence of topography, the influence of soil and LULC on the water balance. The advantages of the SWAT model are the availability of reliable and helpful documentation, the absence of limitations on the catchment area, compatibility with GIS software (ArcGIS, QGIS, MapWindow), the open source computer program for calibration of SWAT models –SWAT Calibration and Uncertainty Programs SWAT-CUP (Abbaspour et al., 2007), and a vast range of scientific publications on different aspects of the model and its practical application. The modeling process of different types of fluxes (water, dissolved and suspended matter) is based on calculations of the river discharge and its parametrization. Setting up a process-based model consisted of several steps: (a) preparation of the input data, including meteorological datasets and catchment layers, (b) optimization of the model (testing model sensitivity to different methods of stream delineation and determining hydrological response units), (c) parameter sensitivity analysis, (d) calibration and validation, and finally, and (e) water balance assessments (**Figure 2**).

Because of gaps in the time series of daily discharge, the period 1989–2004 was chosen for set-up, calibration and validation of the model (**Table 1**). This period contains years which are representative for relatively wet and dry conditions and can be used for both model calibration and validation. The analysis of data from the Velizh gaging stations revealed a negative runoff trend. Comparing the periods of 1992–2015 and 1976–1991, the average runoff in Velizh decreased (4.66 versus 5.68 km^3/year).

Climatic Data Analysis

The SWAT model calculates water balance components using daily minimum (TN) and maximum (TX) air temperatures,

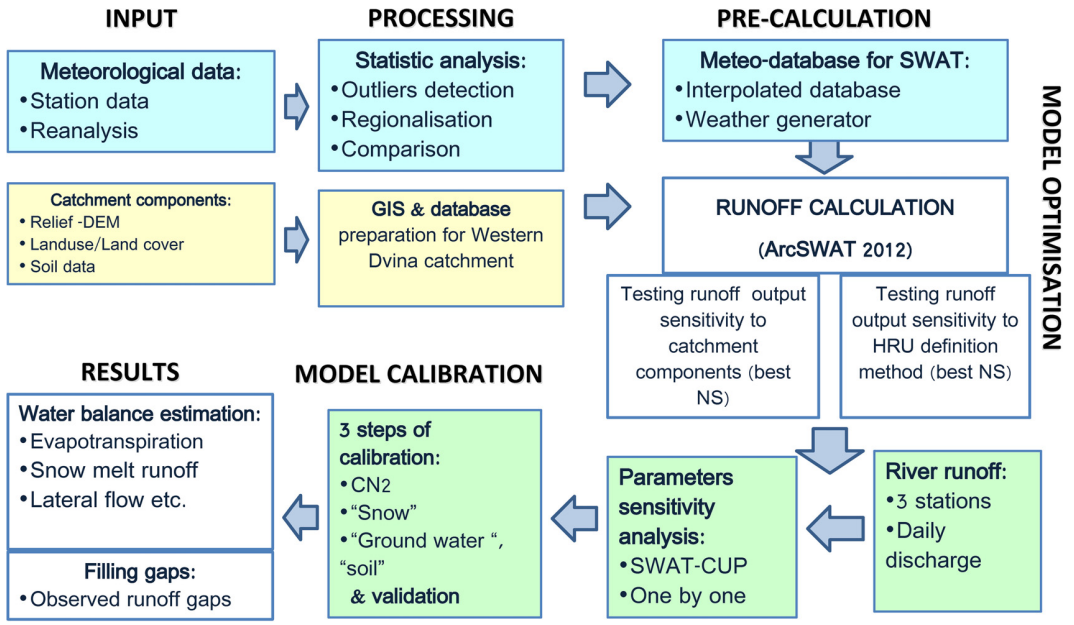

FIGURE 2 | The conceptual framework of the study: water balance model flow of Western Dvina catchment.

precipitations (RR), relative humidity (HU), wind speed (WND), and surface solar radiation downward (SSRD).

The question, which source of meteorological information is most suited for the model is considered in this section. There are several archives containing climate information, which can be divided into observational point and reanalysis data.

Reanalysis a systematic approach to produce global data sets of consistent spatial and temporal resolution. The essence of reanalysis is as follows: observation data are assimilated into a numerical climate model to obtain three-dimensional fields of various atmospheric variables as results. According to Serreze et al. (2005) and (Reichler and Kim, 2008), reanalysis does fairly well regarding temperatures but tends to be more error-prone regarding precipitation. In many reanalysis projects, observed precipitation is not assimilated. It is simulated by the model and shows henceforth more uncertainty. At the same time, the data from meteorological stations are not always accessible or complete, and often contain outliers which require further corrections (e.g., plausibility analyses). In this paper, two databases of the daily meteorological data for the period 1981–2016 were prepared. The first one bases on ECMWF ERA-Interim reanalysis data[1] at its highest resolution of 0.75° × 0.75°, which is equivalent to 84 × 84 km at the equator or 84 × 42 km at 60° north (Berezowski et al., 2016). The second one comprises two meteorological station data sources:

- European Climate Assessment & Data (ECA&D) (Internet Database ECA&D, 2013);
- Global Surface Summary of the Day from the National Climatic Data Center (GSOD NCDC/NOAA) (National Oceanic and Atmospheric Administration, 2019).

For the Russian part of the catchment area, the number of stations inside and outside the catchment area is the same for ECA&D and GSOD NCDC/NOAA databases and equals16. However, not all of these stations are the same. The list of stations considered in the region, with the series length corresponding to the precipitation measurement, is given in **Table 2**.

In the study area, solar radiation and sunshine duration are not measured; however, these solar characteristics are important for building a future model. Based on the recommendations of the ERA-Interim developers (Dee et al., 2011), the use of sunshine duration is not recommended. Therefore, in the present work, the reanalysis data of Solar Surface Radiation Downward (SSRD) without comparison with the interpolated station data is used.

The location of stations from **Table 2** is shown in **Figure 3**.

TABLE 1 | Discharge gaging stations situated in the catchment used for model setup, calibration and validation.

Roshydromet code	Gage name	River	Catchment area, km^2	Opened	Closed
73110	Velizh	Western Dvina	17,600	07.04.1878	Ongoing
73186	Staraya toropa	Toropa	1,480	12.09.1956	Ongoing
73182	Rudnya	Velesa	870	12.07.1930	2004

Plausibility Analysis

Before the data from the stations become publicly available, all values of the variables have already passed a first quality control (Berezowski et al., 2016). However, these first quality checks may

[1]http://apps.ecmwf.int/datasets/

TABLE 2 | Meteorological stations of the investigation area (Russian part of Western Dvina catchment).

Station	Lat., Lon.(deg.), Altitude (m.a.s.l.)	Variables	Series length
Belyj	55.9, 32.9, 214	RR, TN, TM, TX	D:1966–2001
	55.85, 32.95, 222	RR, TN, TX, TM, HU, WND	D:1948–2017
Bologoe	57.9, 34.1, 213	RR, TN, TM, TX	D:1966–2013
Demjansk	57.7, 32.5, 62	RR	D:1966–1996
	57.65, 32.47, 62	RR, TN, TX, TM, HU, WND	D:1959–2017
Gorki	54.3, 30.97, 200	RR	D:1881–2017
	54.3, 30.93, 205	RR, TN, TX, TM, HU, WND	D:1932–2017
Holm	57.2, 31.2, 71	RR, TN, TX	D:1936–1997
	57.15, 31.18, 71	RR, TN, TX, TM, HU, WND	D:1946–2017
Marevo	57.32, 32.04, 101	RR	D:1966–1987
Orsa	54.5, 30.4, 192	RR, TN, TM, TX	D:1952–2017
	54.5, 30.42, 185	RR, TN, TX, TM, HU, WND	D:1946–2017
Ostaskov	57.1, 33.1, 217	RR, TN, TM, TX	D:1950–2017
	57.13, 33.12, 218	RR, TN, TX, TM, HU, WND	D:1959–2017
Roslavl	53.97, 32.85, 219	RR, TN,TM, TX	D:1966–2005
	53.93, 32.83, 224	RR, TN, TX, TM, HU, WND	D:1946–2017
Rzhev	56.27, 34.32, 195	RR, TN, TM, TX	D:1936–1998
	56.27, 34.32, 196	RR, TN, TX, TM, HU, WND	D:1932–1999
Smolensk	54.75, 32.07, 239	RR, TN, TM, TX, HU	D:1944–2017
	54.75, 32.07, 239	RR, TN, TX, TM, HU, WND	D:1936–2017
S.-deminsk	54.4, 34, 238	RR	D:1936–1996
Velikie Luki	56.35, 30.62, 97	RR, TN, TM, TX, HU	D:1881–2017
	56.35, 30.62, 106	RR, TN, TX, TM, HU, WND	D:1932–2017
Vjazma	55.2, 34.4, 250	RR, TN, TM, TX	D:1984–2005
	55.12, 34.4, 251	RR, TN, TX, TM, HU, WND	D:1946–2017
V.volochek	57.57, 34.57, 167	RR	D:1893–1996
	57.55, 34.57, 169	RR, TN, TX, TM, HU, WND	D:1932–2017
Zhizdra	53.75, 34.72, 193	RR	D:1898–1996
Pochinok	54.42, 32.43, 201	RR, TN, TX, TM, HU, WND	D:1988–2017
Toropec	56.48, 31.63, 187	RR, TN, TX, TM, HU, WND	D:1963–2017
Velizh	55.62, 31.18, 166	RR, TN, TX, TM, HU, WND	D:1959–2017
Z. Dvina	56.27, 32.08, 197	RR, TN, TX, TM, HU, WND	D:1963–2003

The red color corresponds to the stations from the ECA&D database, green from NOAA.

not identify all problematic values. Therefore additional outlier tests should be applied.

In meteorology, it is difficult to accurately distinguish between outliers and extreme values. Special attention, especially for highly variable precipitation values is needed. The plausibility analysis consists of four steps: (a) visual inspection, (b) outlier tests, (c) calculation of reference values (RV), and (d) filling in data gaps and replacing suspicious values with RV.

Visual inspection allows determining some implausible values. For example, visualization of precipitation data sets in the GSCD NCDC/NOAA database showed that for most stations precipitation values of 74.9, 150.1, and 300 mm/day were frequently contained in the dataset. Since these values do not correspond to the values for the ECA&D database, these values do not have a logical explanation and seem to indicate a systematic error in the database. These numbers were excluded from further considerations.

Outlier tests of normally distributed values, such as temperature, can be based on three standard deviations method. However, for skewed data, such as precipitation, robust statistics methods such as Median Absolute Deviations (MAD) or Interquartile Range (IQR) should be used (Leys et al., 2013).

It was decided to use the MAD method, which, on the one hand, is sufficiently reliable, on the other hand very simple and universal (Formula 1).

$$\text{Outlier limits} = \underset{(\text{monthlydata})}{\text{med (monthly)}} \pm \text{MADfactor} \cdot \text{MAD} \quad (1)$$

Outlier limits detection is performed with monthly thresholds for precipitation, temperature, relative humidity; and with seasonal thresholds (3 month) for WND as this parameter is much less time-dependent.

Separate calculations for precipitation thresholds were conducted for stations located between altitudes of 0 to 100 m above mean sea level, and for 100 to 200 m, and 200 m and above.

For precipitation and WND, three MAD factors were selected: 2.5, 3, 3.5, and 4. For temperatures MAD factors were selected within the range 2.5–6.0. For the relative humidity, the limits were set within a range from 0% to 100%.

By comparing the median values of outlier limits depending on different MAD coefficients with actual meteorological data, the value of the MAD coefficient was chosen, according to which the final outlier limits were selected. Values outside the limits determined for each station, depending on the altitude above sea level, were marked as possible outliers.

For this purpose the normal ratio method (Young, 1992) was applied for the reference values (RVs) calculation to determine the set of correlation coefficients between the considered station datasets and each available surrounding station. Correlation coefficients between the 30 nearest meteorological stations were considered.

The following specific analyses were done for each meteorological variable. For precipitation, outliers are identified when the following criteria are fulfilled:

- The outlier test indicates an outlier,
- For small precipitation events (RF $<$ 2 mm): RR/RF $>$ 20,
- For winter precipitation events (RF $\geq$ 2 mm): RR/RF 8.

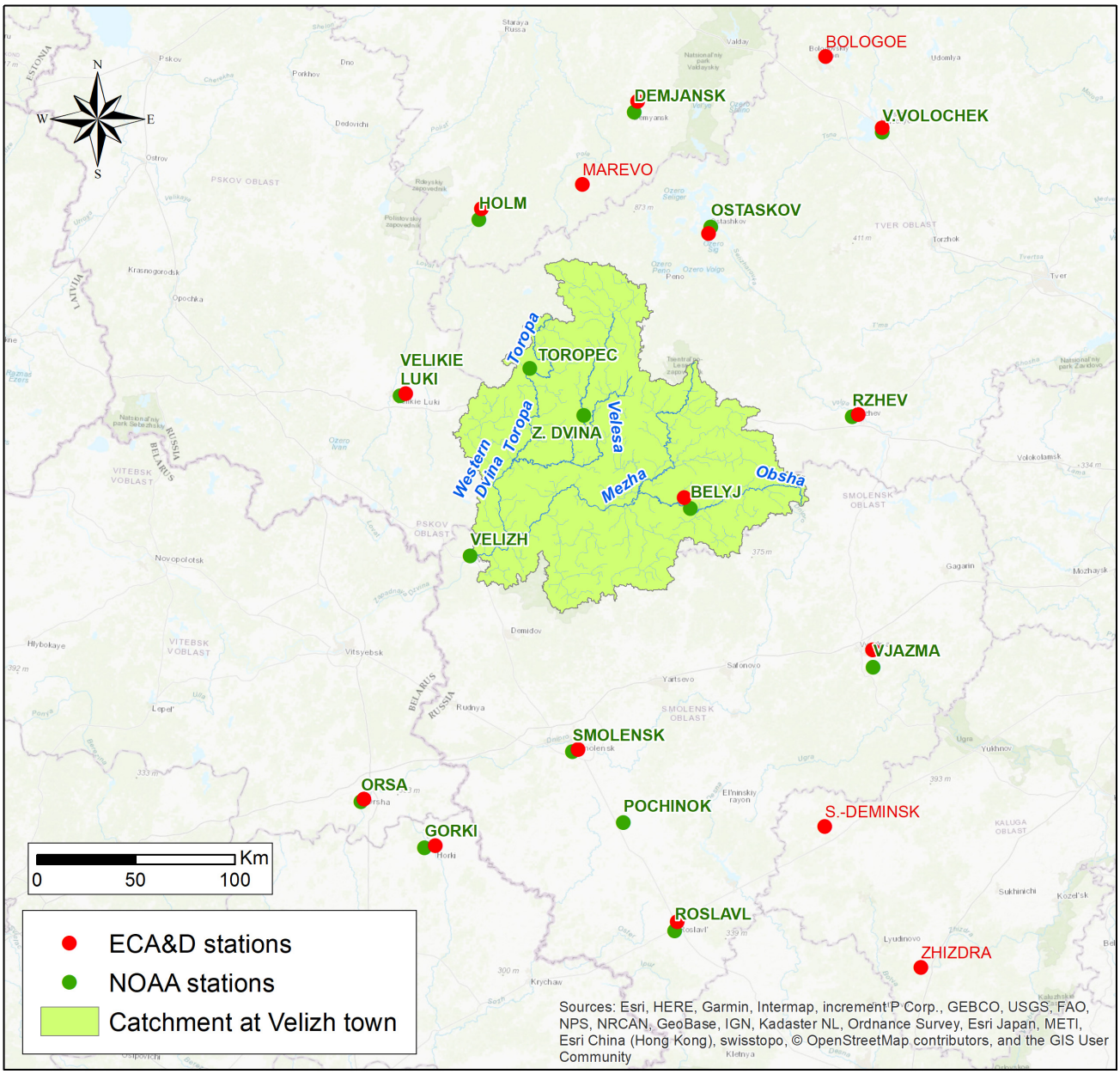

FIGURE 3 | Investigation area (Russian part of Western Dvina catchment). The red color corresponds to the stations from the ECA&D database, green from NOAA.

For temperature, mean and maximum values, are considered as an outlier if:

- The outlier test indicates an outlier,
- $|T - \text{Threshold}| \geqq 3°C$,
- $|T - RV| \geqq 4°C$.

For WND, outliers were identified on one of the following criteria:

- The statistical test described above defined it,
- $WND - RV > 7$ m/s.

The plausibility analysis ends with the replacement of the outlier values by RVs. Finally, the ECA&D and GSOD NCDC/NOAA databases were combined. If the station time series of both databases are highly correlated, the values were directly used to fill the gaps. If there are no values available in both databases, RVs were used.

Regionalization of the Station Data

The main problem when comparing reanalysis data and observed station data is their spatial inconsistency. Measurements at meteorological stations represent a point, while reanalysis data

represent average values of the applied spatial grid, which in our case has a spatial resolution of $0.75° \times 0.75°$.

There are two general approaches to compare station with gridded data: (1) to interpolate the gridded values to the observation points (area-to-point) and (2) to interpolate the point observations onto the reanalysis grid (point-to area). An evaluation of the methods is typically performed with statistical scores such as bias and RMSE.

It should be noted that both methods have considerable drawbacks (Tustison et al., 2001). The magnitude of the representativeness error in each method is significant, and the magnitude of the error in both cases is based primarily on the grid resolution.

Finally the point-to-area method was chosen, since it is widely used in climatological studies and well accepted (Maraun et al., 2010).

To improve the accuracy of the interpolation, the geostatistical spatial pattern analysis method (Christensen, 1991) was used. Many meteorological variables show elevation-dependent gradients. For instance, temperature is mostly decreasing and precipitation increasing with altitude. Therefore, a linear regression model is set up, which considers the dependence of measured values on the altitude of the stations. This model is applied for the whole grid, for which the altitude is known. In a second step, the residuals of each point observation from the linear model were determined. These residuals were interpolated with the inverse distance weighing (IDW) method onto the grid. The sum of the regression and IDW output gave the final value for each cell. Since the values at the boundaries of the considered region are not considered as reliable, it was decided to delete all the values obtained for the boundary beyond the catchment area.

Performance Measures

For comparison of the reanalysis with interpolated station data, a set of performance measures were calculated: root-mean-square error (RMSE), ratio of standard deviations (rSD), index of agreement (d), Pearson correlation coefficient (r), and the bias (BIAS) (Formulas 2 – 6).

The index of agreement is one of the most reliable measures of prediction error (Willmott et al., 2012). This index varies between zero and one (whereby one indicates an ideal agreement). The index of agreement can detect additive and proportional differences in compared pairs in datasets.

Modeling Approach and Spatial Data Description

The catchment model was built with the ArcSWAT2012 GIS-interface. The modeling process of different types of fluxes (water, dissolved and suspended matter) is based on the calculations of river discharge and its parameterization. Modeling with SWAT comprises the following steps: catchment model building (relief data is based on Advanced Land Observing Satelite [ALOS], 2017) including initial soil and plant data (GlobalLand30, 2014) (because no detailed information was available for this study, default parameters were chosen based on global LULC and soil parameters), preparation of the meteorological data, calibration of parameters, validation and then implementation.

The following input data were used (**Table 3**). Periods of model calibration (1992–1998) and validation (1999–2004) are chosen according to continuous hydrological observations inside the catchment.

It must be noted that for the soils of the catchment HWSD (Harmonized world soil database) (Nachtergaele et al., 2008) contains the characteristics only for two upper soil layers. For this reason, the third and further soil layers were not taken into account in the model.

For the evapotranspiration the Pennman–Monteith approach was chosen, and for the channel routing the Muskingum approach. A period of 3 years was chosen as a spin-up period. To model the rainfall-runoff-routing processes, in this study the Daily rain/CN/daily route method was selected (where CN is a rainfall-runoff curve number) as a default option used by SWAT model (another option is the sub-daily scale). These options are described in Neitsch et al. (2005). The model performance is evaluated with Nash-Sutcliff Efficiency (NS), as main objective function, and Kling-Gupta Efficiency (KGE), square correlation (R2) and PBIAS as additional model performance criteria (Nash and Sutcliffe, 1970; Gupta et al., 1999).

Basins in which a significant part of the runoff is formed by snowmelt tend to be challenging for hydrological models. Freezing and thawing processes modify the flow paths for water and its availability for evaporation (Woo et al., 2000; Hülsmann et al., 2015). In SWAT, hydrological processes including snowmelt are realized at the "hydrological response units" (HRU) level. The watershed is automatically subdivided into a number of subbasins based on provided river network layer and elevation data. In our case, two subbasins were delineated based on manually positioned outlets at discharge gaging sites to include these subbasins into calibration procedure using measured time series. The last subbasin is terminates at the outlet of whole catchment at the gaging station Velizh. Portions of a subbasin that possess unique land use/management/soil attributes are grouped together and defined as one HRU (Neitsch et al., 2005).

TABLE 3 | The datasets used to set up and operate the model.

Dataset	Source name	Scale	Resolution	Description/link
Relief (DEM)	ALOS DEM	Global	12.5 m	https://www.asf.alaska.edu
	Globallandcover	Global	30 m	http://www.globallandcover.com
Soil	HWSD	Global	Approx 1:3 mln	http://www.fao.org
Climatic data	Roshydromet	Russia	–	www.meteo.ru
	ECA&D	Europe	–	www.ecad.eu
	NOAA	Global	–	https://data.nodc.noaa.gov
	ERA interim	Global	–	https://www.ecmwf.int
Hydrological data	Roshydromet	Russia	–	Daily discharge data for three stations (1992–2004)

Depending on Data Availability and modeling accuracy, one subbasin may have one or several HRUs defined.

Preliminary results of the discharge model allowed us to identify the best method for determining HRUs. For the delineation of the "hydrological response units" (HRU) threshold values of 20/10/20 percent for land cover, soil and slope areas were chosen, respectively, because this percentage brings the best NS value for preliminary modeling results without calibration procedure. NS was also chosen as the objective function for model calibration.

Parameter sensitivity analysis was performed manually using the software SWAT-CUP (one by one to determine the effect of each parameter on the result. Nineteen sensitive parameters were found to be sensitive. They were divided into genetically homogeneous groups: CN2 parameter (runoff curve number), "snow" parameters, "soil and groundwater" parameters, other parameters.

When the mean daily air temperature is less than the snowfall temperature, the precipitation within an HRU is classified as snow and the liquid water equivalent of the snow precipitation is added to the snowpack. The snowpack increases with additional snowfall, but decreases with snowmelt or sublimation. The SWAT model has eight "snow" parameters directly related to snow water equivalent calculations and freezing-melting processes: SFTMP (snow fall temperature), SMTMP (snow melt base temperature), SMFMX (maximum melt rate), SMFMN (minimum melt rate), SNOCOVMX (snow water equivalent before melting), SNO50COV (fraction of snow cover), TIMP (snow pack temperature lag time) and CN_FROZ (parameter for frozen soil adjustment). Main "soil and groundwater" parameters include SOL_AWC (available water capacity), ALPHA_BF (base flow factor), GW_DELAY (groundwater delay), RCHRG_DP (Deep aquifer percolation fraction), ESCO (evaporation compensation factor) and others (Neitsch et al., 2005).

Calibration and Validation

It is recommended that the calibration and validation periods should include a comparable number of dry, medium, and wet years (Arnold et al., 2012). Based on the analysis of the residual mass curve of annual runoff, the period 1989–2004 (including 3 years of "spin-up") is considered as the average period. Both series – calibration and validation contain dry (1997, 2002) and wet (1995, 1999) years. The model was calibrated and validated using daily discharge time series for three gaging stations inside the basin all together by adjusting the best objective function value for each gauge.

As the first step, "snow" parameters were calibrated inside the physically based range with automatic procedure (SWAT-CUP) separately from the other groups of parameters. Values for snow water equivalent before melting (SNOCOVMX) and initial temperature of snow fall and snowmelt (SFTMP, SMTMP) with very small parameters range were defined for fine tuning during the further calibration procedure. To put the SNOCOVMX in realistic range, nearest station data was used. For the stations Velikie Luki and Velizh maximum decadal snow water equivalent falls in range 60–110 mm. In a second step, CN2 parameter was set for forested and non-forested land cover types and calibrated as a distributed parameter together with "snow" parameters small range. This small range was defined on the previous step and this range has not been changed during the whole calibration procedure.

In a third step, genetically homogeneous parameters (ground water and soil routine parameters) and other sensitive parameters (e.g., evapotranspiration rate and channel routing) were calibrated within physically based ranges with the autocalibration procedure SUFI-2, which is provided by the SWAT-CUP software.

RESULTS

Climatic Components Analysis

The meteorological station data were processed for elimination of outliers and interpolated into the selected grid, taking into account the altitude of each cell above sea level. Furthermore, these two data sets (reanalysis and interpolated station data) were compared with each other using the methods of descriptive statistics. The demonstrated difference between the datasets shows that the reanalysis and interpolated stations data results are very similar to each other. This is evidenced by similar seasonal and climate change trends and significant spatial correlation coefficients between datasets. The results are summarized in **Table 4**.

The correlation coefficients are significant everywhere ($r > 0.72$). The values of temperatures correlate very well with each other. Despite the high correlation coefficient ($r > 0.86$) the WND time series do not agree well with each other ($d = 0.74$), due to some difference in the amplitude of the values (difference of 1.38 m/s or 33%). One of the possible reasons for this is an underestimation of the surface roughness for the particular region in the reanalysis.

Meteorological variables have a pronounced seasonal distribution. The interpolated stations data and reanalysis graphs repeat each other quite well throughout the year (**Figure 4**), with the exception of WND.

The annual precipitation for the interpolated station data and the reanalysis is 723 and 725 mm, respectively. According to Timm et al. (2009), the average annual precipitation for the entire Western Dvina catchment area ranges from 600 to 800 mm, which corresponds to the data obtained.

TABLE 4 | Descriptive statistical analysis for the meteorological variables comparing reanalysis and interpolated station data: precipitation (RR), mean temperature (TM), wind speed (WND), and relative humidity (HU).

Statistic*	RR	TN	TM	TX	WND	HU
RMSE	2.43	1.68	0.65	1.35	1.65	4.04
rSD	0.98	1.00	>0.99	0.96	1.39	0.94
R	0.72	0.98	>0.99	0.99	0.86	0.95
D	0.84	0.99	>0.99	>0.99	0.74	0.97

** – root-mean-square error (RMSE), ratio of standard deviations (rSD), index of agreement (d), and Pearson correlation coefficient (r).*

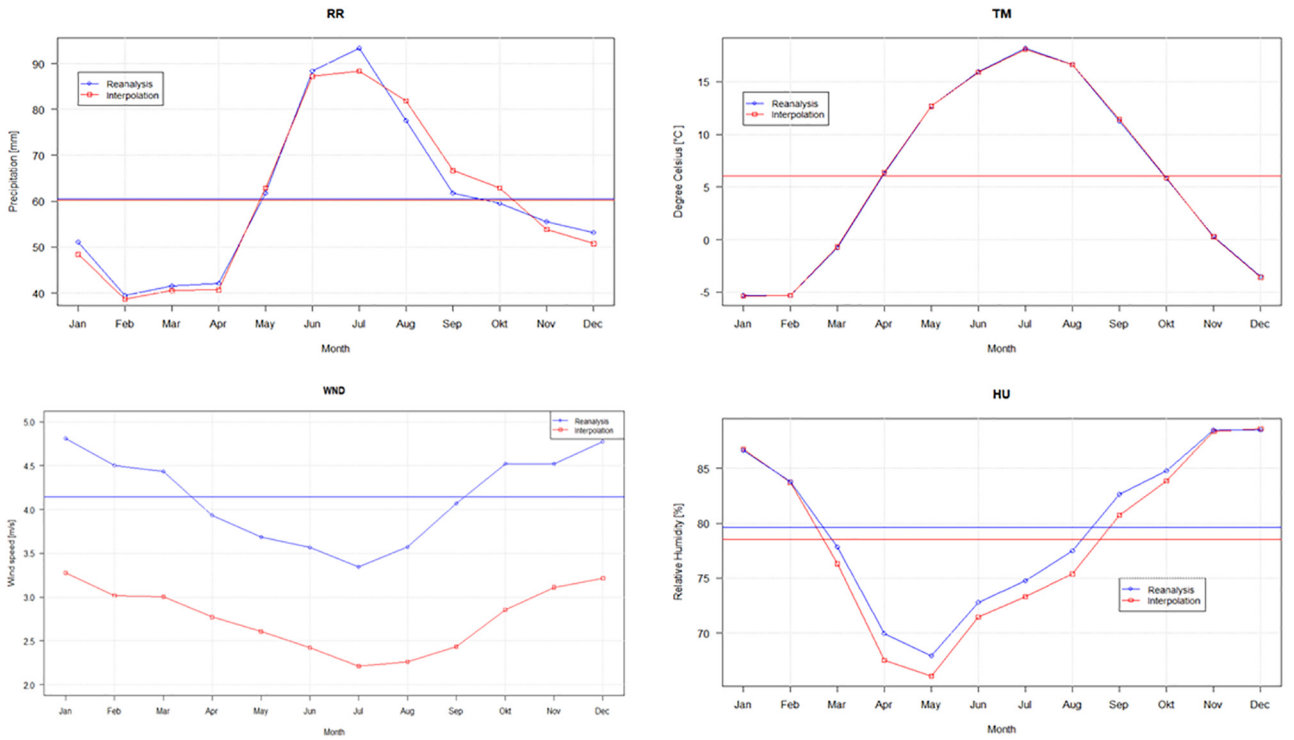

FIGURE 4 | Seasonal cycles of interpolated stations and reanalysis ECMWF ERA-Interim data for precipitation (RR), mean temperature (TM), wind speed (WND), and relative humidity (HU).

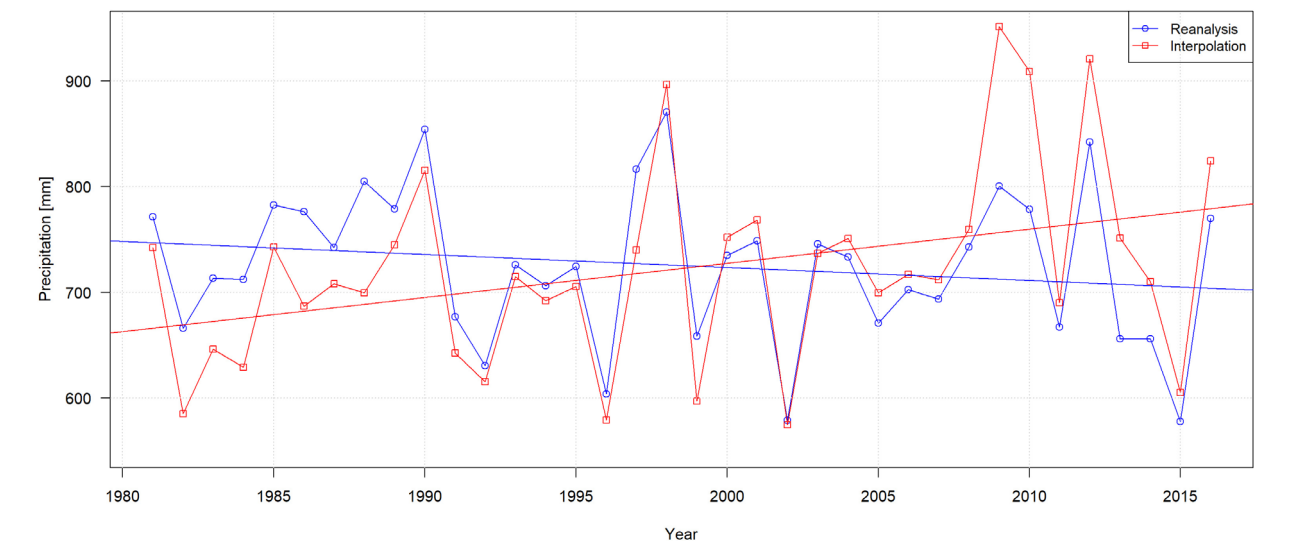

FIGURE 5 | Comparison of annual mean precipitation (RR) obtained by interpolation of station data and reanalysis ECMWF ERA-Interim.

The reanalysis and interpolated stations data curves of the mean temperatures are very similar. Interestingly, the maximum temperatures of reanalysis show lower and the minimum temperatures show higher values than interpolated station data. This means that temperature regime of the reanalysis is smoothened.

Long-term reanalysis and interpolated stations data curves have the same shape. Gradual increasing trends of temperatures and surface solar radiation are indicators of warming over the past few decades. Trends are very similar for temperature and WND, but differ for precipitation (**Figure 5**).

The use of interpolated station data with SSRD from reanalysis is the preferable solution for meteorological input for Western Dvina catchment model. Thus, for the runoff modeling authors have prepared and used the meteorological database filled with the interpolated station data and SSRD component from ECMWF ERA-Interim reanalysis. We have used the five nearest and most reliable meteorological stations – Velizh, Belyi, Toropetz, Velikiye Luki, and Smolensk. These stations have the most complete sets of measured data on all weather parameters. SWAT input datasets were completed by filling gaps with interpolated NOAA/ECA&D station data and with SSRD interpolated from ERA-Interim gridded data into station locations.

TABLE 5 | Parameters calibration results for the model.

Parameter name	Parameter description Neitsch et al., 2005	Method for parameter adjustment	Parameter mean value (range)
CN2_FRST	SCS runoff curve number for forested lands	R	44
CN2_RNGE	SCS runoff curve number for lands without forest	R	56–64
SFTMP	Snowfall temperature (°C)	V	3.55
SMTMP	Snow melt base temperature (°C)	V	1.97
SMFMX	Maximum melt rate for snow during year [mm H_2O/(°C·day)]	V	4.32
SMFMN	Minimum melt rate for snow during year [mm H_2O/(°C day)]	V	3.12
SNOCOVMX	Minimum snow water content that corresponds to 100% snow cover (mm)	V	120
SNO50COV	Fraction of snow volume represented by SNOCOVMX that corresponds to 50% snow cover (mm)	V	0.17
SOL_AWC	Available water capacity (mm H_2O/mm of soil)	V	0.17
GWQMN	Threshold depth of water in the shallow aquifer required for return flow to occur (mm)	V	484
GW_DELAY	Groundwater delay (days)	V	18.9
RCHRG_DP	Deep aquifer percolation fraction	A	0.35
GW_REVAP	Groundwater "revap" coefficient	A	0.05
ALPHA_BF	Baseflow alpha factor (days)	A	0.19
TIMP	Snow pack temperature lag factor	A	0.42
ESCO	Soil evaporation compensation factor	R	0.87
REVAPMN	Threshold depth of water in the shallow aquifer for "revap" to occur (mm)	R	903
CN_FROZ	Parameter for frozen soil adjustment infiltration/runoff	V	0.29
MSK_X	Weighting factor that controls the relative importance of inflow and outflow in determining the storage in the reach	V	0.33

V, parameter certain value is set from given range or replaced with certain value (good for lumped parameters); R, relative change of the parameter by multiplying the default value by (1 + R) (good for distributed parameters); A, adds a given value or range to the existing default parameter value (good for distributed parameters with close values).

SWAT Model Calibration and Validation Results

Initial SWAT-based water balance component calculations (without calibration) for Western Dvina catchment for the period 1992–2004 gave adequate values. Simulated annual runoff is 278 mm (observed is 275 mm), evapotranspiration is 379 mm (395 mm estimated by MODIS – MOD16 Global).

Sensitivity analysis made with one-by-one method (SWAT-CUP) allowed to identify 19 sensitive parameters. Results of parameter calibration are shown in **Table 5**. According to Moriasi et al. (2007) model efficiency is satisfactory (**Table 6**).

The model simulates well the beginning of floods, but peaks are underestimated especially for highest peaks (**Figure 6**). The recession of the flood curve is simulated too slow.

At the same time it is obvious that small rain floods are often simulated with insufficient accuracy. We consider two reasons. Because of sparse station density, spatial distribution of rainfall is insufficiently captured. Furthermore, the insufficient reproduction of the soil distribution and its parameters can course an erroneous simulation of water flows.

Water Balance Components Calculation

For the period 1992–2016, water balance components were calculated based on simulated annual means. Annual snowmelt water amount is about 20–30% of annual precipitation sum. Mean annual water discharge is overestimated and also minimum and maximum values (**Table 7**).

Precipitation has the increasing trend, snowmelt does not have trend, runoff and evapotranspiration have also increasing trend (not statistically significant). Snowmelt occurs at the end of the winter and the maximum amount of melted water coincides mostly with maximal runoff (**Figure 7**).

Spatial distribution of all simulated water balance components represents the structure of flow generation drivers inside the catchment. It strongly depends on land cover. The highest ET is linked to subbasins with lakes predomination in the western part of the catchment – correlation between open water fraction of each subbasin and ET of each subbasin is 0.78 and it is the highest for certain subbasin which contain largest lakes.

TABLE 6 | Model efficiency evaluation for daily runoff calculation.

Criteria	Calibration	Validation
R^2	0.77	0.78
NS	0.76	0.76
PBIAS%	−11.7	−16.5
KGE	0.80	0.75
Model performance in general Moriasi et al., 2007	Good	Satisfactory

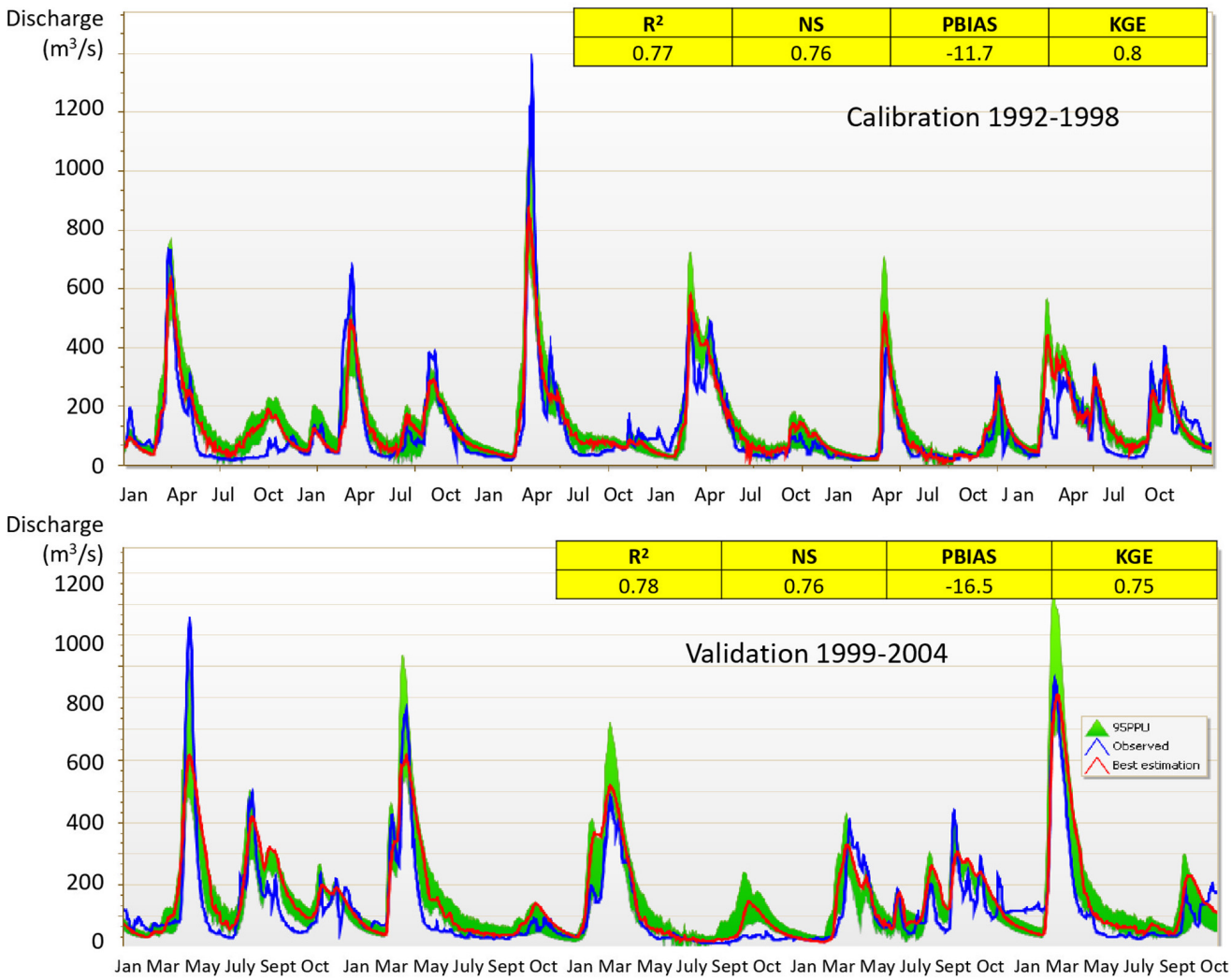

FIGURE 6 | Model calibration and validation. Western Dvina river at Velizh town, blue line represents measured runoff, red line – simulated runoff in cubic meters per second (Q, m^3/s), green area – 95 percent prediction uncertainty range (95 PPU).

The wetlands fraction varies between 0 and 33% of subbasin area and has the strongest impact on flow generation variability among other main land cover types, with correlations reaching 0.72 and 0.51 for surface runoff and soil water. However, percolation and ground water flow are negatively correlated to the wetlands fraction of the subbasin area (correlation for both is −0.69). Wetlands significantly increase surface runoff by decreasing percolation and ground water yield. Forest coverage in the subbasins ranges between 62% and complete forest cover (100%). It does not have strong affect on water balance fluctuations between subbasins (correlation varies from −0.23 to 0.12).

Higher snowmelt is linked to higher precipitation in the eastern part. In general higher soil water and lower lateral and groundwater flow are linked to gleic soils and histosols widespread in wetlands (**Figure 8**).

DISCUSSION

The analysis of climate data from different sources was performed to identify the best input for the hydrological model SWAT. Station data of the ECA&D and the GSOD NCDC/NOAA databases were compared with the reanalysis ECMWF ERA-Interim. The average annual precipitation is almost the same in the two cases under consideration (723 and 725 mm for interpolated station data and reanalysis, respectively). There is a discrepancy between precipitation trends in the period 1981–2016. Reanalysis data show a downward trend whereas interpolated station data does not. Interpolated station data have lower values than reanalysis at the beginning and higher values at the end of the period. The reason for this discrepancy may be the decreasing number of station data over time. One of the trends in the region under consideration is the closure of stations recording comparatively low precipitation

TABLE 7 | Simulated annual water balance components for the period 1992–2016 (values of annual sums in mm) and the fraction of the annual sum of precipitation (%).

Component	Code	Mean annual value	Fraction of the precipitation (%)	Minimum	Maximum
Precipitation (average station data)	PRECIP	731	–	544	1015
Snow melt in the watershed (simulated)	SNOWMELT	133	18.2	68	199
Potential evapotranspiration (simulated)	PET	468	64.0	377	550
Actual evapotranspiration (simulated)	ET	364	49.8	312	443
Soil water content (simulated)	SW	188	25.7	175	206
Percolation (simulated)	PERC	311	42.5	177	519
Surface runoff (simulated)	SURQ	51.8	7.1	21.6	91.4
Groundwater flow (simulated)	GW_Q	239	32.7	130	411
Lateral subsurface flow (simulated)	LAT_Q	4.66	0.6	3.36	6.91
Water yield (simulated)	WYLD	296	40.5	155	509
Measured discharge (direct gaging station data)	Qmeas	265	36.3	114	418

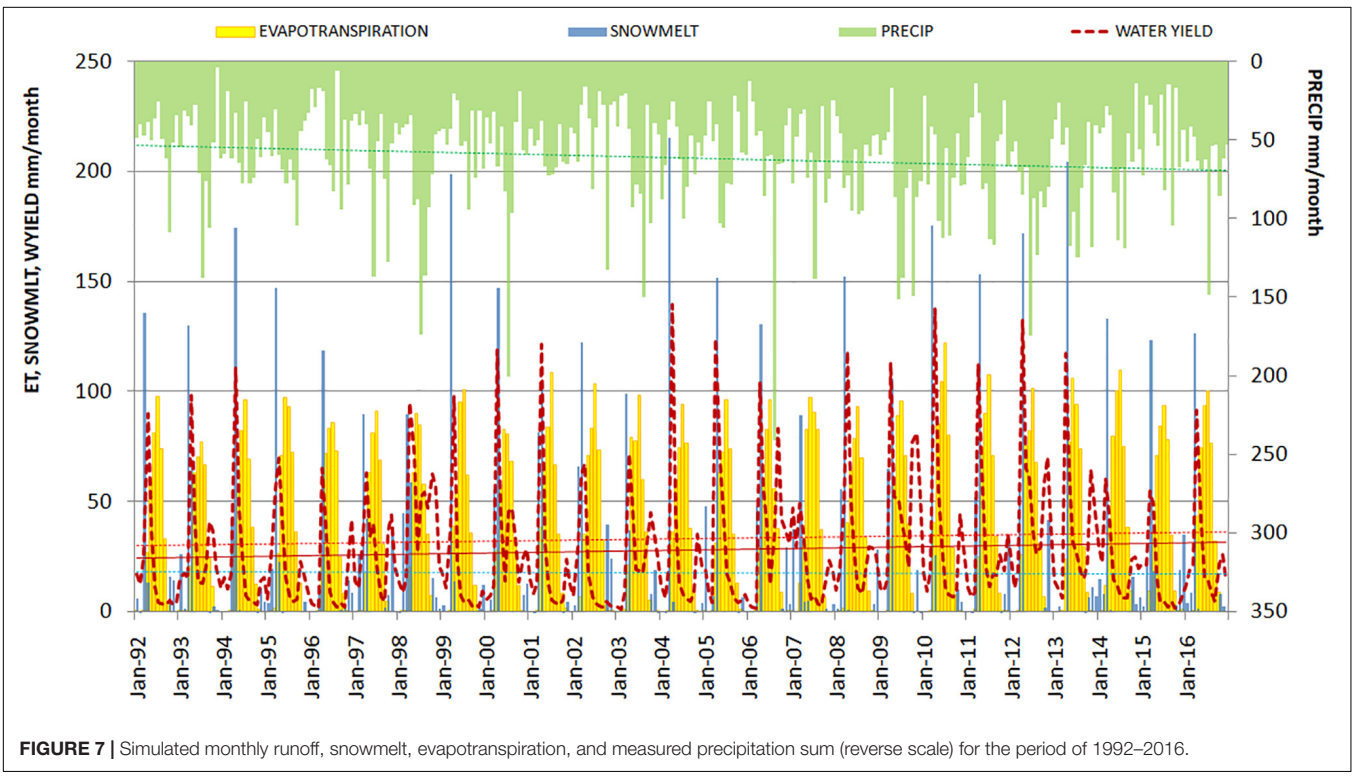

FIGURE 7 | Simulated monthly runoff, snowmelt, evapotranspiration, and measured precipitation sum (reverse scale) for the period of 1992–2016.

sums. Mean temperature values coincide very well, but daily minimum and maximum temperatures are underestimated by the reanalysis.

The relative humidity values of the reanalysis are slightly higher than interpolated station data. The WND values are about 33% (or 1.38 m/s) higher for reanalysis in comparison to interpolated station data.

As there are no observations from the solar energy component at the stations, and since sunshine duration is not recommended to use from reanalysis, the SSRD from reanalysis was the only reasonable choice.

Because of mentioned uncertainties of reanalysis data, it was decided to use station data for precipitation, temperature, humidity and WND.

In general the model shows a "good" performance for river runoff simulation based on rough open source data. But mean runoff is overestimated. One of the reasons is an overestimated (comparing to naturally considered) SNOCOVMX parameter which was obtained by the calibration procedure and provided best representation of hydrograph.

The model overestimates mostly the low flow which can be explained by the general error in evapotranspiration calculation

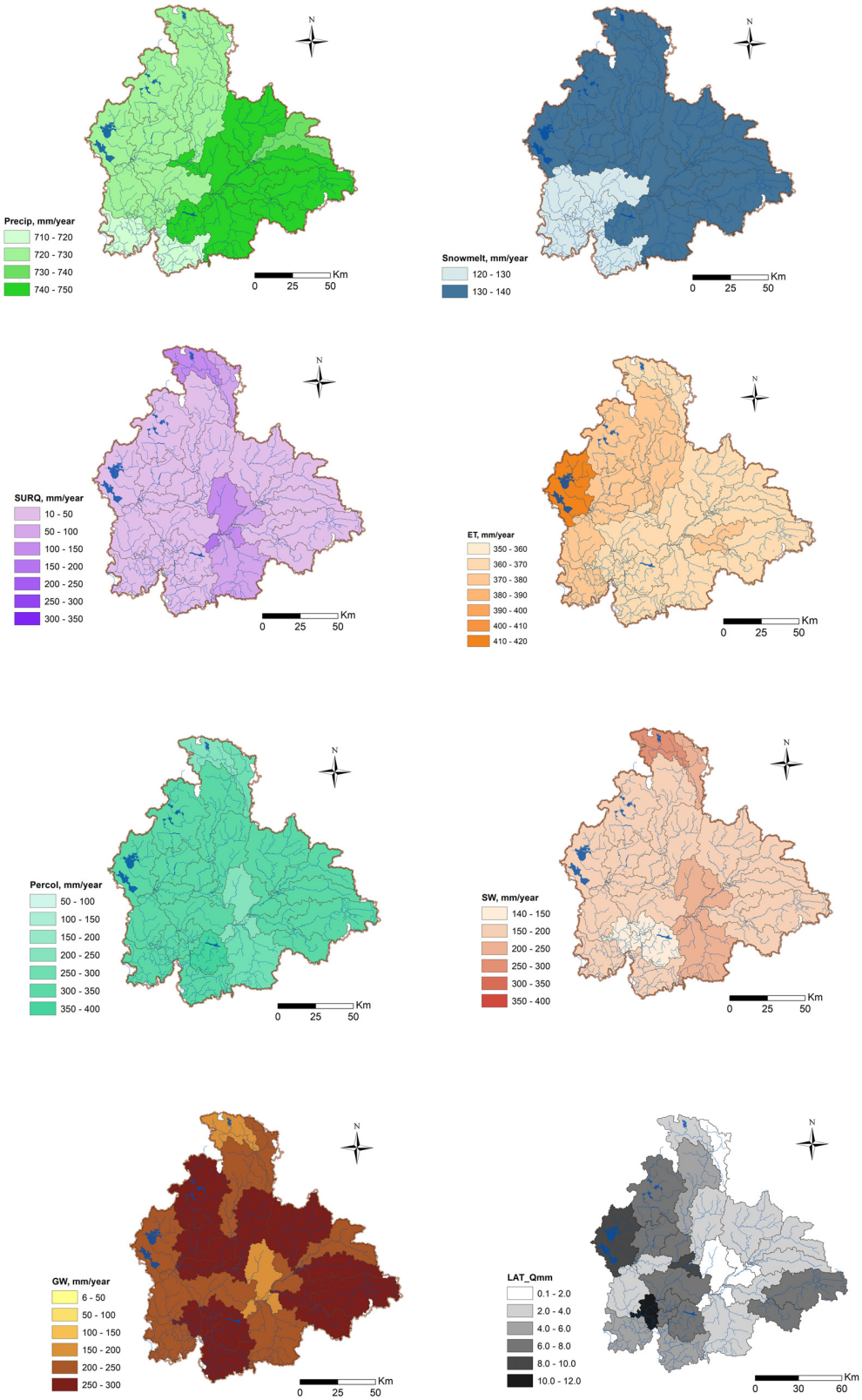

FIGURE 8 | Annual calculated mean water balance components distribution on the Western Dvina catchment area (Precipitation, snowmelt, surface Q, actual ET, percolation, soil water, ground water, and lateral Q).

(based on methods without sufficient taking into account the transpiration processes) and insufficient consideration of surface water and ground water interactions, because these two processes are the most important for the summer base flow assessment.

The most sensitive are the "snow" and "groundwater" parameters, and also the distributed CN2 parameter. The calibration of the "snow" parameters should be done separately from others. Moreover, it should be considered that the open source soil database, which was used, included only the two uppermost soil levels.

In general model uncertainties may have several reasons. In Russian Federation gaging network is sparse and has many gaps in data. Global spatial data used for land cover and soil databases does not consider local features – e.g., temporal variability of wetlands conditions, local soil distribution (for example, alluvial soils in river valleys, peat soils).

Also two features of the SWAT model may cause some more uncertainties for this region. First, freezing and thawing of soil water are not considered by the SWAT model. Second – it has lumped snow parameters, which could not be distributed for such flattened catchment and could not be calibrated separately for different land cover types.

Inside the Russian part of Western Dvina catchment the absence of runoff measurement in huge wetlands, which were drained with abandoned drainage channels, creates a strong data deficit for runoff modeling. All possible data sources and field investigations should be taken into account for model improvement, particularly data on soil profile characteristics and snow cover dynamics during the winter and adjacent seasons. Ideally, the soil database should be more detailed.

In comparison to other water balance research papers (e.g., Pluntke et al., 2014; Rouholahnejad Freund et al., 2017; Osypov et al., 2018) it should be noted that SWAT based surface and lateral flow are rather low in most cases. Daily runoff models often are based on specialized local soil maps and LULC databases which may provide adequate ground and lateral flow parameters and their distribution. In most cases SFTMP and SMTMP are close to 0 degrees, but in the spring highly forested lands may store coldness longer than open areas where stations are often situated. In reality, the lumped snowmelt temperature may be higher than suggested by station temperatures of 0°C; for example, it is known that forested area temperatures are about 2 degrees lower for some Russian Far East river basins as compared to station temperatures (Bugaets et al., 2018).

The calibrated model can be implemented to estimate some water balance components in case of climate change in the future. With the input climatic projections data the assessment of the annual distribution dynamics of the evapotranspiration, snow melt, surface, lateral and ground flow can be done for Western Dvina catchment.

Semi-distributed water runoff models can be used as an important part of water resources monitoring strategies and can play a significant role in transboundary water resources management (see Alekseevskii et al., 2015). Moreover, well calibrated models are an important tool for various applications in water management, such as the estimation of water resources availability and balances, water quality and sediment transport modeling etc.

AUTHOR CONTRIBUTIONS

PT made the proposal, performed the calculations with SWAT model and drafted the manuscript. AK made the climatic analysis, prepared the meteorological database, and wrote parts of the manuscript text. SC is a leader of the Russian team of MANTRA-Rivers project and wrote parts of the manuscript text. AT provided the GIS support and made the editorial work. DK is one of the MANTRA-Rivers project scientists, proofread and improved the manuscript. PB is one of the MANTRA-Rivers project scientists, prepared and processed the input data. TP is the leader of MANTRA-Rivers project from German side and suggested conclusions for the manuscript.

FUNDING

This study was supported by the Volkswagen Foundation within the project "Management of Transboundary Rivers between Ukraine, Russia and the EU – Identification of Science-Based Goals and Fostering Trilateral Dialogue and Cooperation (ManTra-Rivers)" (Grant No: Az.: 90 426).

ACKNOWLEDGMENTS

The authors would like to thank the Volkswagen Foundation for the funding provided for the project "Management of Transboundary Rivers between Ukraine, Russia and the EU – Identification of Science-Based Goals and Fostering Trilateral Dialogue and Cooperation (ManTra-Rivers)". GIS analyses are done within the framework of Russian Scientific Foundation project (18-17-00086). The authors are grateful to all who helped to organize the collaboration: Yu. Nabivanets and N. Osadcha (Hydrometeorological Institute, Ukraine), and C. Bernhofer and B. Helm (Technical University of Dresden, Germany).

REFERENCES

Abbaspour, K. C., Vejdani, M., and Haghighat, S. (2007). "SWAT-CUP calibration and uncertainty programs for SWAT," in *Proceedings of the MODSIM 2007 International Congress on Modelling and Simulation*, eds L. Oxley and D. Kulasiri (Canberra, ACT: Modelling and Simulation Society of Australia and New Zealand), 1603–1609.

Advanced Land Observing Satelite [ALOS] (2017). *Dataset: JAXA/METI ALOS-1 PALSAR RTC*. Available at: http://www.eorc.jaxa.jp/ALOS/en/obs/palsar_strat.htm (accessed August 15, 2017).

Alekseevskii, N., Zavadskii, A., Krivushin, M., and Chalov, S. (2015). Hydrological monitoring at international rivers and basin. *Water Resour.* 42, 747–757. doi: 10.1134/s0097807815060020

Arnold, J. G., Moriasi, D. N., Gassman, P. W., Abbaspour, K. C., White, M. J., Srinivasan, R., et al. (2012). SWAT: model use, calibration, and validation. *Trans. ASABE* 55, 1491–1508. doi: 10.13031/2013.42256

Asadchaya, M., and Kolmakova, Y. (2014). Tendencies of changes of Belarusian rivers water flow in years of minimum and maximum water availability in climate warming conditions. *Bull. Belarusian State Univ. Ser.* 2, 84–88.

Berezowski, T., Szczesniak, M., Kardel, I., Michalowski, R., Okruszko, T., Mezghani, P., et al. (2016). High-resolution gridded daily precipitation and temperature data set for two largest Polish river basins. *Earth. Syst. Sci. Data* 8, 127–139. doi: 10.5194/essd-8-127-2016

Bugaets, A. N., Gartsman, B. I., Tereshkina, A. A., Gonchukov, L. V., Bugaets, N. D., Sidorenko, N., et al. (2018). Using the SWAT model for studying the hydrological regime of a small river basin (the Komarovka River, Primorsky Krai). *Russian Meteorol. Hydrol.* 43, 323–331. doi: 10.3103/s1068373918050060

Center for International Earth Science Information Network [CIESIN] (2014). *Columbia University.Gridded Population of the World, Version 4 (GPWv4) 2014*. Palisades, NY: Columbia University.

Christensen, R. (1991). *Linear Models for Multivariate, TimeSeries, and SpatialData*. New York, NY: Springer.

Dee, D., Uppala, S., Simmons, A., Berrisford, P., Poli, P., Kobayashibi, S., et al. (2011). The ERA-Interim reanalysis: configuration and performance of the data assimilation system. *Q. J. R. Meteor. Soc.* 137, 553–597.

GlobalLand30 (2014). *Open source data "30-meter GlobalLand Cover Data Product", 2014*. Available at: http://www.globallandcover.com/ (accessed November 19, 2017).

Gupta, H. V., Sorooshian, S., and Yapo, P. O. (1999). Status of automatic calibration for hydrologic models: comparison with multilevel expert calibration. *J.Hydrolog. Eng.* 4, 135–143. doi: 10.1061/(ASCE)1084-069919994:2(135)

Heininen, L. (2018). Arctic geopolitics from classical to critical approach – importance of immaterial factors. *Geography. Environ. Sustain.* 11, 171–186. doi: 10.24057/2071-9388-2018-11-1-171-186

Hülsmann, L., Geyer, T., Schweitzer, C., Priess, J., and Karthe, D. (2015). The effect of subarctic conditions on water resources: initialresults and limitations of the SWAT model applied to the KharaaRiver Basin in Northern Mongolia. *Environ. Earth Sci.* 73, 581–592. doi: 10.1007/s12665-014-3173-1

Internet Database ECA&D (2013). *European Climate Support Network of EUMETNET Report 2008*. Available at: www.ecad.eu/

Karthe, D., Chalov, S., and Borchardt, D. (2015). Water resources and their management in central asia in the early 21st century: status, challenges and future prospects. *Environ. Earth Sci.* 73, 487–499. doi: 10.1007/s12665-014-3789-1

Krengel, F., Bernhofer, C., Chalov, S., Efimov, V., Efimova, L., Gorbachova, L., et al. (2018). Challenges for transboundary river management in Eastern Europe–three case studies. *J. Geogr. Soc. Berlin* 149, 157–172.

Leys, C., Ley, C., Klein, O., Bernard, P., and Licata, L. (2013). Detecting outliers: do not use standard deviation around the mean, use absolute deviation around the median. *J. Exp. Soc. Psychol.* 49, 764–766. doi: 10.1016/j.jesp.2013.03.013

Loginov, V., Volchek, A., and Shelest, T. (2015). Analysis and modeling of hydrographs of rain floods on Belarusian rivers. *Water Resour.* 42, 292–301. doi: 10.1134/s0097807815030069

Maraun, D., Wetterhall, F., Ireson, A. M., Chandler, R. E., Kendon, E. J., Widmann, M., et al. (2010). Precipitation downscaling under climate change: recent developments to bridge the gap between dynamical models and the end user. *Rev. Geophys.* 48, 1–34.

Mohrholz, V. (2018). Major baltic inflow statistics – revised. *Front. Mar. Sci.* 5:384. doi: 10.3389/fmars.2018.00384

Moriasi, D. N., Arnold, J. G., Van Liew, M. W., Bingner, R. L., Harme, R. D., and Veith, T. L. (2007). Model evaluation guidelines for systematic quantification of accuracy in watershed simulations. *Am. Soc. Agric. Biol. Eng.* 50, 885–900. doi: 10.13031/2013.23153

Nachtergaele, F., Van Velthuizen, H., Verelst, L., Batjes, N., Dijkshoorn, K., Van Engelen, V., et al. (2008). *Harmonized World Soil Database*. Rome: Food and Agriculture Organization.

Nash, J. E., and Sutcliffe, J. V. (1970). River flow forecasting through conceptual models I. A discussion of principles. *J. Hydrol.* 10, 282–290. doi: 10.1016/0022-1694(70)90255-6

National Oceanic and Atmospheric Administration (2019). *Global Surface Summary of the Day – GSOD*. Available at: https://data.nodc.noaa.gov/cgi-bin/iso?id=gov.noaa.ncdc:C00516 (accessed June 12, 2019).

Neitsch, S. L., Arnold, J. G., Kiniry, J. R., and Williams, J. R. (2005). *Soil and Water Assessment Tool.Theoretical Documentation. Version* 2005. Berlin: Springer.

Osypov, V., Osadcha, N., Hlotka, D., Osadchyi, V., Nabyvanets, J. (2018). The desna river daily multi-site streamflow modeling using SWAT with detail snowmelt adjustment. *J. Geogr. Geol.* 10, 92–110.

Parfomuk, S. (2006). Analysis of perennial fluctuations in the annual water flow of the Western Dvina River. *Bull. Polotsk State Univ. Ser. B Appl. Sci.* 3, 178–182.

Pluntke, T., Pavlik, D., and Bernhofer, C. (2014). Reducing uncertainty in hydrological modelling in a data sparse region. *Environ. Earth Sci.* 72, 4801–4816. doi: 10.1007/s12665-014-3252-3

Reichler, T., and Kim, J. (2008). Uncertainties in the climate mean state of global observations, reanalyses, and the GFDL climate model. *J. Geophys. Res.* 113:D05106. doi: 10.1029/2007JD009278

Rouholahnejad Freund, E., Abbaspour, K. C., and Lehmann, A. (2017). Water resources of the Black Sea catchment under future climate and landuse change projections. *Water* 9:598. doi: 10.3390/w9080598

Serreze, M., Barrett, A., and Lo, F. (2005). Northern high-latitude precipitation as depicted by atmospheric reanalyses and satellite retrievals. *Mon. Weather Rev.* 133, 3407–3430. doi: 10.1175/mwr3047.1

Volchek, A., and Lusha, V. (2006). Cyclicity of the annual flow of the Western Dvina. *Bull. Polotsk State Univ.* 3, 172–177.

Volchek, A., and Shelest, T. (2012). *Winter floods forming on Belarusian rivers*. Saint-Petersburg: Uchenye zapiski Rossiyskogo gosudarstvennogo gidrometeorologicheskogo universiteta, 5–19.

Timm, H., Olsauskyte, V., and Druvietis, I. (2009). "Rivers of Europe," in *Baltic and Eastern Continental Rivers*, eds K. U. Tockner and C. T. Uehlinger (London: Academic Press), 607–642.

Tustison, B., Harris, D., and Foufoula-Georgiou, E. (2001). Scale issues in verification of precipitation forecasts. *J.Geophys. Res. Atmos.* 106, 11775–11784. doi: 10.1029/2001jd900066

Willmott, C. J., Robeson, S. M., and Matsuura, K. (2012). A refined index of model performance. *Int. J. Climatol.* 32, 2088–2094. doi: 10.1002/joc.2419

Woo, M. K., Marsh, P., and Pomeroy, J. W. (2000). Snow, frozen soils and permafrost hydrology in Canada, 1995–1998. *Hydrol. Process.* 14, 1591–1611. doi: 10.1002/1099-1085(20000630)14:9<1591::aid-hyp78>3.3.co;2-n

Young, K. (1992). Three-way Model for interpolating for monthly precipitation values. *Am. Meteorol. Soc.* 120, 2561–2569. doi: 10.1175/1520-0493(1992)120<2561:atwmfi>2.0.co;2

Conflict of Interest Statement: The authors declare that the research was conducted in the absence of any commercial or financial relationships that could be construed as a potential conflict of interest.

frontiers in Earth Science

ORIGINAL RESEARCH
published: 01 November 2019
doi: 10.3389/feart.2019.00284

Low-Frequency Baltic Sea Level Spectrum

Igor Medvedev[1,2]* *and Evgueni Kulikov*[1]

[1] Shirshov Institute of Oceanology, Russian Academy of Sciences, Moscow, Russia, [2] Fedorov Institute of Applied Geophysics, Moscow, Russia

This study examines the Baltic Sea level spectrum in the interval of periods from a few months to decades. Effective statistical methods of time series analysis have been applied to the long-term data from 36 tide gauges in the Baltic Sea (BS), the Danish straits (DS), and southeastern part of the North Sea (NS) to examine the character of low-frequency sea level variability. Using the spectral and wavelet analyses, we obtained estimates of the magnitudes of the main long period components of the sea level oscillations with periods of 8.4, 7.76, 6.16, 2.5, 1.7, 1.2 year and discussed their possible origin. The peak with a period of 255 days is revealed in both the sea level spectra of the BS and in the spectra of atmospheric processes. It is more pronounced in the air pressure variations from atmospheric reanalyses, especially ERA-Interim and National Centers for Environmental Prediction/Climate Forecast System Reanalysis (NCEP/CFSR). Wavelet analysis revealed high coherence between the sea level oscillations at different stations and also with the zonal wind component. The result of the study shows that the low-frequency sea level variability in the BS is highly correlated with the zonal wind variations over the extensive shallow-water areas of the sea.

Keywords: sea level, Baltic Sea, North Sea, zonal wind, spectral analysis, wavelet analysis, pole tide, 255-day oscillation

OPEN ACCESS

Edited by:
Markus Meier,
Leibniz Institute for Baltic Sea Research (LG), Germany

Reviewed by:
Ralf Weisse,
Helmholtz Centre for Materials and Coastal Research (HZG), Germany
Inga Dailidienė Dailidienė,
Klaipėda University, Lithuania

***Correspondence:**
Igor Medvedev
patamates@gmail.com;
medvedev@ocean.ru

Specialty section:
This article was submitted to Interdisciplinary Climate Studies, a section of the journal Frontiers in Earth Science

Received: *14 December 2018*
Accepted: *17 October 2019*
Published: *01 November 2019*

Citation:
Medvedev I and Kulikov E (2019) Low-Frequency Baltic Sea Level Spectrum. Front. Earth Sci. 7:284. doi: 10.3389/feart.2019.00284

INTRODUCTION

The mean sea level (MSL) variation is one of the most representative indicators of the global climate change. The sea level variability in each specific region is influenced by various factors: atmospheric processes, such as variations in atmospheric pressure and wind fields, ocean temperature changes, tidal forces, geodynamic processes, etc. Depending on the predominance of one or another factor, the sea level variations exhibit different properties in different parts of the World Ocean.

The region of the present study is the North Sea (NS) – BS system. The NS is a marginal sea of the Atlantic Ocean while the BS is a semi-enclosed inland sea, which is connected to the NS through the narrow and shallow Danish straits (DS) (the Great Belt, the Little Belt, and the Oresund), the Skagerrak and the Kattegat. The water exchange through these straits is the basic factor in the formation of the low-frequency Baltic Sea level variability. The limited throughput of the DS plays the role of a natural low-pass filter for the sea level oscillations: high-frequency sea level variations from the NS are effectively damped, while the low-frequency signal can pass into the BS almost undisturbed (Carlsson, 1997; Kulikov et al., 2015b).

The overall change in the MSL at the BS coast is the combined result of the large-scale and regional factors. The main large-scale factors are the thermal expansion of the sea water with rising

ocean temperatures and the melting of the land ice (glaciers and the polar ice sheets). These factors cause the global MSL (GMSL) to rise over the 20th century by 1.7 ± 0.2 mm/year (Church and White, 2011). For 1993–2009 the rate is 3.2 ± 0.4 mm/year from the satellite altimeter data and 2.8 ± 0.8 mm/year from the *in situ* data (Church and White, 2011). The changes in the MSL in the BS are formed by the influence of the GMSL, but sea level variations within the BS can noticeably deviate from those of the World Ocean and of the NS. According to Hünicke et al. (2015), the average rate of the MSL rise in the BS corrected for the vertical land movements during the 20th century was 1.5 mm/year. Wahl et al. (2013) show that MSL trend for the NS region for the 1900–2009 period was determined to be 1.54 ± 0.11 mm/year and for the 1993–2009 period was determined to be 4.00 ± 1.53 mm/year.

The main regional factor, which determines the long-term MSL changes in the BS, is the glacial isostatic adjustment (GIA) (Peltier, 2004). It causes the uplift of the Earth's crust in the north part of the sea with its maximum in the Gulf of Bothnia being about 10 mm/year (Hammarklint, 2009) and subsidence in parts of the southern BS coast of about 1 mm/year (Richter et al., 2011). Land uplift leads to decreased and even negative trends in the MSL. These features of the GIA in the BS region are described in detail in Ekman (2009).

The sea level in the semi-enclosed BS is modulated by meteorological factors, especially by the wind forcing, as persistent winds from the south-west or north-east transport water into the BS or out of it, respectively, thereby raising or lowering the BS level as a whole (Hünicke et al., 2015). Wind forcing redistributes the water within the BS, producing high or low sea levels at the ends of the basin depending on the wind direction (Ekman, 2007).

The sea level variations in the BS from interannual to decadal timescales are strongly influenced by the strength of the westerly winds, closely related to the North Atlantic Oscillation (NAO), which represents the large-scale atmospheric circulation over the north-west Atlantic (Hünicke et al., 2015). A positive NAO index (strong Azores High and Icelandic Low) is associated with strong westerly winds in the BS area, which causes its sea level to rise. A negative NAO index (weak Azores High and Icelandic Low) causes the sea level decreasing. The correlation between NAO and the BS level is especially strong in winter (Andersson, 2002; Hünicke et al., 2015).

Some components of the long-period sea level oscillations in the BS are well known: the seasonal component (Lisitzin, 1974; Samuelsson and Stigebrandt, 1996; Medvedev, 2014), the pole tide (Lisitzin, 1974; Vermeer et al., 1988; Ekman and Stigebrandt, 1990; Medvedev et al., 2014, 2017), and the nodal tide (Lisitzin, 1974; Wróblewski, 2001). We used the spectral analysis to detect the main components of the long-period sea level oscillations. Spectral analysis of tide gauge sea level data in the NS and the BS was made by Currie (1976) and by Trupin and Wahr (1990). Their analyses detected interesting properties of the long-period sea level variability components. Currie (1976) used a maximum entropy spectral analysis of tide-gauge records spanning the late 19th and 20th centuries. They detected the 18.6-year lunar nodal tide, a solar-cycle signal with a period of 10.9 year and an unknown origin signal with a period of 6.3 year. Trupin and Wahr (1990) used the procedure of stacking the tide gauge sea level data from around the globe and detected in the sea level spectrum the 18.6-year lunar nodal tide and the 14-month pole tide. They also found that for periods greater than 2 months, the response of the sea level to atmospheric pressure is according to the inverted barometer. Trupin and Wahr (1990) also found a large coherence at 437 days between the pressure and sea level data in the NS, BS and especially in the Gulf of Bothnia. These results support the hypothesis that the pole tide in this region has a meteorological origin.

In present study, we examined the sea level variability in the BS in time scale range from months to decades and it is the links to potential forcing factors. The use of the long-term datasets and modern methods of spectral and wavelet analyses allowed us to better explain the nature of the already known components of variability in the BS level, and to highlight a number of new and interesting properties of these variations.

DATA AND METHODS

In the present study, the monthly MSL data from 36 tide gauges have been collected from the database of the Permanent Service for Mean Sea Level (PSMSL, Holgate et al., 2013) and Unified State System of Information for World Ocean Conditions, Russia (ESIMO). These tide gauges are located around the BS coastline (14 tide gauges), in the DS (13 tide gauges) and on the southeast coastline of the NS (9 tide gauges). Their location is shown in **Figure 1** and their characteristics are given in **Table 1**. In this study, we used long-term sea level records (>110 year) with total gaps of less than 3%. The series of observations were carefully checked; the short gaps were interpolated. Such long-term sea level records in the BS have a significant trend, which is caused by the postglacial land uplift and/or the MSL rise. It was deducted from all datasets.

Hourly data sets of the air pressure at the sea level were obtained from the National Centers for Environmental Prediction Climate Forecast System Reanalysis (NCEP CFSR) from 1979 to 2010, with a spatial resolution at 0.5° × 0.5°. Monthly data sets of wind at 10 m and air pressure at the sea level were obtained from the 20th Century Reanalysis from 1871 to 2012. Monthly data sets of the air pressure at the sea level were obtained from the NCEP/NCAR Reanalysis (the National Centers for Environmental Prediction and the National Center for Atmospheric Research), from 1948 to 2015 and from the ERA-Interim reanalysis from 1979 to 2015. The Scandinavia pattern (SCAND) index was taken from the NOAA Climate Prediction Center from 1950 to 2015. The Scandinavian pattern consists of a primary circulation center over Scandinavia, with weaker centers of the opposite sign over Western Europe and eastern Russia/western Mongolia (Bueh and Nakamura, 2007). The Scandinavian (SCA) pattern was originally identified by Barnston and Livezey (1987) and previously referred to the Eurasia-1 pattern. The positive phase of this pattern is associated with positive height anomalies, sometimes reflecting major blocking anticyclones, over Scandinavia and western Russia, while the negative phase of the pattern is associated with

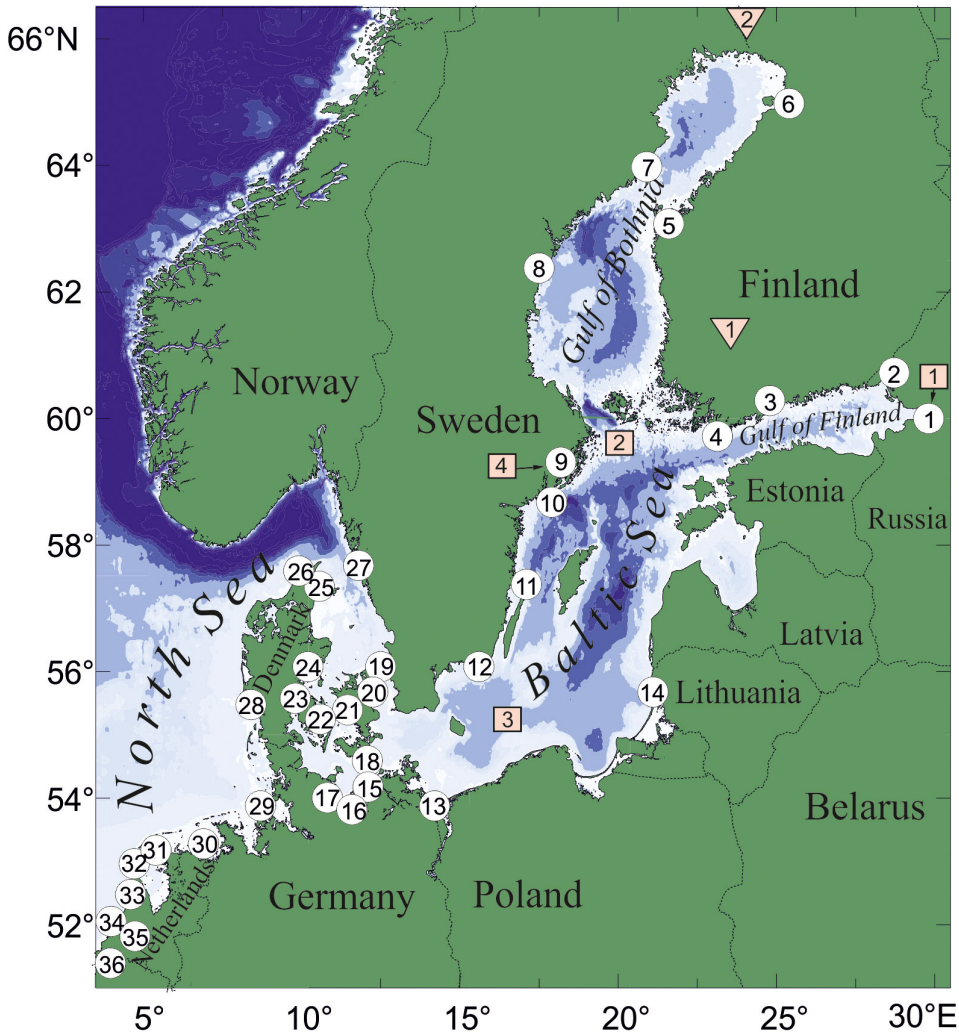

FIGURE 1 | Locations of the tide gauge stations (white circles); the names of the stations are given in **Table 1**. The red squares indicate reanalysis grid point locations which were used to analyze (1) the air pressure from the NCEP/NCAR, (2) the air pressure from the ERA-Interim, (3) the air pressure and wind data from the 20th Century Reanalysis, and (4) the air pressure from the NCEP/CFSR. The red triangles show the location of the weather stations: (1) Pirkkala Tampere-Pirkkalan Lentoasema and (2) Pello Kk Museotie.

negative height anomalies in these regions. The positive phase of the Scandinavian pattern is associated with below-average temperatures across central Russia and over western Europe. It is also associated with above-average precipitation across central and southern Europe and below-average precipitation across Scandinavia[1].

In this study, we used mean daily sea level pressure (SLP) from the weather stations of the European Climate Assessment (ECA) dataset (Klein Tank et al., 2002). Data and metadata are available at http://www.ecad.eu. Also, we used daily non-homogenous SLP observation data from the Stockholm Old Astronomical Observatory (59.35°N, 18.05°E) 1756–2012 (Moberg et al., 2002). These data were reduced to 0°C, normal gravity and MSL (Moberg et al., 2002).

To examine the periodical component in the sea level records we used the spectral analysis based on the fast Fourier transform (FFT). To obtain a better spectral resolution and the shortest confidence interval we stack the tide gauge data for three areas: the BS, the DS, and the NS. The procedure of stacking multistation data to enhance small signals has been used by seismologists to improve their estimates of the Earth's free oscillation eigen frequencies (Gilbert and Dziewonski, 1975), and to search for short-period oceanic normal modes in the Pacific (Luther, 1982). Stacking is particularly useful in cases where the spatial dependence of the signal is known beforehand (Trupin and Wahr, 1990). For this procedure, we used rectangular spectral window. The window length N was 2048 months. The final sea level spectrum was calculated by averaging the periodograms counted for individual tide gauges without overlapping. The spectral resolution Δf was 0.0059

[1]https://www.cpc.ncep.noaa.gov/data/teledoc/scand.shtml

TABLE 1 | The monthly MSL records in the Baltic Sea and the Southeast North Sea.

No.	Tide gauge	Coordinates		Country	Observation period (years)	Length (years)	Available data (%)
		Longitude (°E)	Latitude (°N)				
Baltic Sea							
1	Kronstadt	29.8	60.0	Russia	1835–2013	179	100
2	Vyborg	28.7	60.7	Russia	1889–2013	125	95
3	Helsinki	25.0	60.2	Finland	1879–2012	134	100
4	Hanko	23.0	58.8	Finland	1887–2012	126	95
5	Vaasa	21.6	63.1	Finland	1883–2012	130	95
6	Oulu	25.4	65.0	Finland	1889–2012	124	95
7	Ratan	20.9	64.0	Sweden	1892–2013	122	100
8	Draghällan/Spikarna	17.5	62.4	Sweden	1898–2013	116	100
9	Stockholm	18.1	59.3	Sweden	1801–2013	213	100
10	Landsort	17.9	58.7	Sweden	1887–2005	119	100
11	Ölands Norra Udde	17.1	57.4	Sweden	1887–2013	127	100
12	Kungsholmsfort	15.6	56.1	Sweden	1887–2013	127	100
13	Świnoujście	14.2	53.9	Poland	1811–1999	189	96
14	Klaipeda	21.1	55.7	Lithuania	1898–2011	114	92
Danish straits							
15	Warnemünde	12.1	54.2	Germany	1855–2010	158	100
16	Wismar	11.5	53.9	Germany	1848–2012	165	100
17	Travemünde	10.9	54.0	Germany	1856–2012	157	95
18	Gedser	11.9	54.6	Denmark	1892–2012	121	99
19	Hornbaek	12.5	56.1	Denmark	1891–2012	122	98
20	København	12.6	55.7	Denmark	1889–2012	124	98
21	Korsør	11.1	55.3	Denmark	1897–2012	116	98
22	Slipshavn	10.8	55.3	Denmark	1896–2012	117	96
23	Fredericia	9.8	55.6	Denmark	1889–2012	124	99
24	Aarhus	10.2	56.1	Denmark	1888–2012	125	97
25	Frederikshavn	10.5	57.4	Denmark	1894–2012	119	96
26	Hirtshals	10.0	57.6	Denmark	1892–2012	121	96
27	Göteborg	11.8	57.7	Sweden	1887–2013	127	100
North Sea							
28	Esbjerg	8.4	55.5	Denmark	1889–2012	124	98
29	Cuxhaven	8.7	53.9	Germany	1843–2010	168	100
30	Delfzijl	6.9	53.3	Netherlands	1865–2013	149	100
31	Harlingen	5.4	53.2	Netherlands	1865–2013	149	100
32	Den Helder	4.8	53.0	Netherlands	1865–2013	149	100
33	IJmuiden	4.6	52.5	Netherlands	1871–2013	143	100
34	Hoek van Holland	4.1	52.0	Netherlands	1864–2013	150	100
35	Maassluis	4.3	51.9	Netherlands	1848–2013	166	100
36	Vlissingen	3.6	51.4	Netherlands	1862–2013	152	100

*Station numbers in column 1 correspond to those in **Figure 1**.*

cycles per year (cpy). The Nyquist frequency was 6 cpy. The number of degrees of freedom was 28 for the BS, 26 for the DS, and 18 for the NS.

Spectral analyses of stochastic processes are commonly used in order to estimate the distribution of the sea level variance (energy) over the frequency. The spectrum can have a continuous character of the energy distribution (continuum) or the form of sharp delta-like peaks (discrete spectrum). It depends on the nature of the oscillations. For instance, tidal oscillations appear in the spectrum in the form of sharp peaks at the major tidal harmonic frequencies (K_1, O_1, M_2, S_2, etc., see Medvedev et al., 2013). The changes in sea level caused by the influence of alternating atmospheric pressure and wind fields at the sea surface are basically random in nature and have a noise spectrum as a continuous function of frequency.

To investigate temporal variations of low-frequency sea level oscillations the wavelet method was used. It was applied as in Torrence and Compo (1998), decomposing the time series into time-frequency space, in order to determine all dominant modes of the variability and the way these modes change in time. We used the continuous wavelet transform (Morlet wavelet). To analyze direct links between the sea level in different parts of these

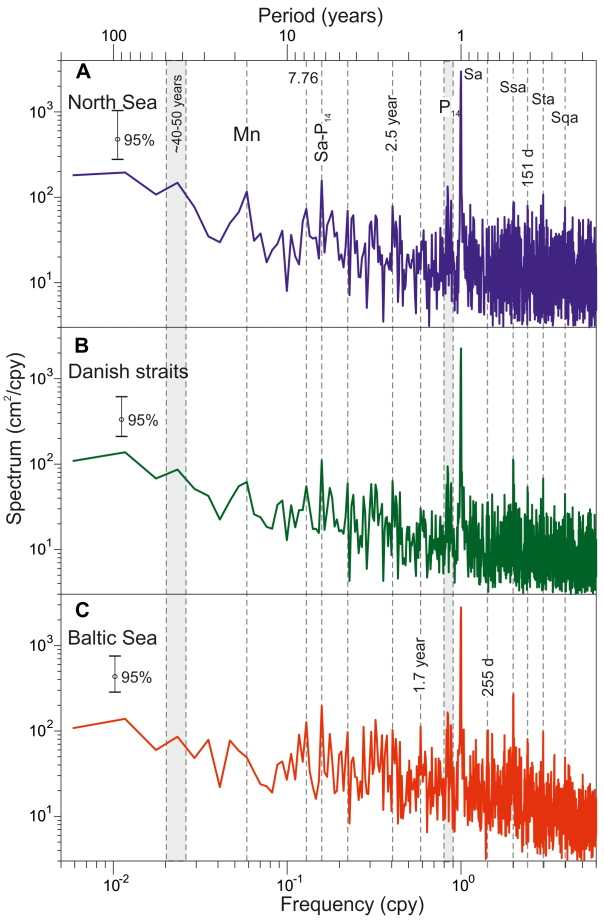

FIGURE 2 | The low-frequency sea level spectra estimated from mean monthly sea level records in **(A)** the North Sea, **(B)** the Danish straits, and **(C)** the Baltic Sea. Labels "Mn," "Sa," "Ssa," "Sta," "Sqa," and "P_{14}" mark nodal, annual, semiannual, terannual, quartoannual, and 14-month spectral peaks, respectively.

two seas and wind variations the wavelet coherence method was used (Grinsted et al., 2004; Jevrejeva et al., 2005).

SPECTRAL ANALYSIS

Figure 2 shows the spectra of sea level for three areas: the BS, the DS, and the NS. The major peak at all spectra corresponds to the annual cycle (Sa). The seasonal oscillations are the dominant feature of the long-period sea-level variability in most of the World Ocean. They are formed by the following components: air pressure and wind stress; seasonal variability of the water balance components, such as evaporation, precipitation, river runoff, water exchange with adjacent water bodies; steric effects (water temperature and salinity fluctuations); and long-period gravitational (astronomical) tides.

Higher seasonal components (semiannual – Ssa, terannual – Sta, quartoannual – Sqa) are caused by the asymmetry of the annual oscillations. In the NS, the amplitudes of higher seasonal harmonics are small and it is difficult to detect them in the background noise at the NS-spectrum (**Figure 2A**). To the contrary, in the BS these harmonics have significant amplitudes. The semiannual oscillations' amplitudes for some years are about 25–30 cm (Medvedev, 2014). The maximum long-term amplitude (average climatic) of Ssa is 5 cm and is observed in the Åland Sea (Medvedev, 2014). The maximum of Sta harmonic is observed in the Åland Sea also (∼1.5 cm). The quartoannual harmonic is the highest in the Gulf of Finland, 2.7 cm (Medvedev, 2014). The spectral seasonal peaks Ssa, Sta and Sqa are well distinguished at BS-spectrum (**Figure 2C**). In the DS, the peaks Ssa, Sta, and Sqa are weaker than in the Baltic. According to the equilibrium theory of tides, the amplitude of the annual and semiannual gravitational constituents is ∼0.15 and 0.95 cm, in the BS (Lisitzin, 1974).

In the intra-annual frequency band, two stable spectral peaks with periods of 151 and 255 days can be identified in addition to the seasonal components (Sa, Ssa, Sta, Sqa). The first peak is localized in the DS and in the BS basin (**Figures 2B,C**). The second one is identified only on the sea level spectra within the BS (**Figure 2C**). The important feature of these spectral peaks is their sharp character, which corresponds to the deterministic processes.

The unknown origin wide peak with a period of 40–50 year and the nodal tide Mn peak with a period 18.61-year are distinguished in the low-frequency band. According to Wróblewski (2001), the amplitude of Mn in the BS is about 0.6–0.9 cm. It is close to the value of the static tide (Lisitzin, 1974). The nodal spectral peak is most pronounced at the NS-spectrum. In the BS, the nodal peak is not detected at the spectra.

It is possible to detect a frequency peak of about 0.84 cpy (14-month period) in all spectra of sea level oscillations (**Figure 2**). This harmonic corresponds to the Chandler frequency [Chandler wobble (CW)], which is the frequency of a free nutation of the Earth axis. It is considered, that the CWs cause weak tidal sea level oscillations in the World Ocean with a period of about 14 months. George Darwin called this oscillation the "pole tide" (Darwin, 1898).

The nutation of the Earth axis (the polar motion) affects not only the CW but also the annual component (with a frequency of 1 cpy). The annual polar component in the sea level oscillations hard to be detected, because seasonal oscillations of hydrometeorological origin are much stronger than this component. The influence of the sea level polar motion becomes apparent at lower frequencies. Thus, the sea level spectra for all three regions have a pronounced spectral peak with a 6.16-year period. Currie (1976), Trupin and Wahr (1990), and Hilmi et al. (2002) have also singled out this peak in the spectra. In their studies, the authors have not been able to determine the origin of this stable peak. It is likely that this peak is the result of interference of seasonal oscillations and the pole tide in the atmosphere, and has the frequency equal to the difference between the annual frequency and the Chandler frequency: $f(\mathrm{Sa}) - f(\mathrm{CW}) = 1\ \mathrm{cpy} - 0.84\ \mathrm{cpy} = 0.16\ \mathrm{cpy}$ (6.16 year).

In the period band from 2 to 8 year, there is also a peak with a period of 7.76 year. In the interannual (intradecadal) frequency band, except for the already mentioned peaks, we can distinguish

spectral peaks with periods of 2.5 and 1.7 year. The spectral peak with a period of 2.5 year is well pronounced at the NS spectra (**Figure 2A**) and the spectral peak with a period of 1.7 year is well pronounced at the BS spectra (**Figure 2C**). The oscillations in the 2.2–7.8-year band in individual sea level records have been associated with large-scale atmospheric circulation signals (Unal and Ghil, 1995; Jevrejeva et al., 2005). They generate sea level response through a number of processes: the direct influence of changes in atmospheric pressure, changes in wind stresses, and changes in atmosphere-ocean fluxes as well as storm surges (Jevrejeva et al., 2006). A peak with a period of 8.47 year can be identified in the spectrum of the BS level variability (**Figure 2C**). Its origin is explained by the lunar perigee.

WAVELET ANALYSIS

To isolate different timescales of variability and analyze temporal changes of the sea level variance and periods, their behavior in time-frequency space have been examined using the Morlet wavelet analysis. **Figure 3** shows the wavelet power spectrum for four sea level time series, displayed as a function of cycle period and time. The left axis is the Fourier period; the bottom axis shows time in years. We selected four tide gauges with long series of observations in different parts of the study region: IJmuiden (the NS), Gedser (the area of the DS), Stockholm (central part of the BS), and Kronstadt (the head of the Gulf of Finland). In general, the results of wavelet analysis confirm the results of spectral analysis of the prevalence of annual oscillations in the spectrum of low-frequency sea-level variability. The strong non-stationary behavior of the spectra is evident. The magnitude of the annual signal in the BS is much more variable from year to year compared with the NS. The period of the annual component demonstrates a significant change from year to year too. If the central period of this signal is strictly equal to 1 year for the NS, while the annual signal period in the BS experiences some changes from year to year. It must be caused by the influence of variations water exchange through DS and changes in the month of annual maximum river discharge (flood). Water exchange through straits causes large volume changes of the BS (Lehmann and Post, 2015) with the duration is about 40 days (Lehmann et al., 2012). These events cause the sea level rise by several dozens of centimeters (Soomere and Pindsoo, 2016) and may cause the variations of near-annual period. In some years (1910, 1990–2000), the magnitude of the annual signal does not exceed the background noise level. In 1990–2000 years the annual signal is absent in the wavelet spectra in the BS (Gedser, Stockholm, Kronstadt). The sea level variance in this decade cross to the 2–4-year band and semiannual oscillations. In wavelet power spectra of sea level variability, a semiannual component is higher in the BS but is difficult to detect in background noise in the NS. This is in good agreement with the results of the spectral analysis (**Figure 2**).

The Chandler component of the sea level oscillations is not detected on these wavelet spectra due to the proximity of its period to the annual period. Perhaps variations of the annual component period shown in **Figures 3B–D** are caused by the influence of the pole tide, thereby increasing the period of the annual sea level component. To separate the annual and Chandler components, some other time-frequency analysis methods should be used, for example, multiple-filter technique (MFT) (Kulikov et al., 2004; Thomson and Emery, 2014). In Medvedev et al. (2017), the use of MFT with increasing frequency and decreasing time resolution allowed us to separate these two signals.

In all wavelet power spectra, especially in the BS, an increase in the variance of the oscillations with periods of about a 6–8 year has been detected since 1930. In the wavelet spectrum of the NS (**Figure 3A**), we can also distinguish an increase in sea level oscillations with a period of 16−20 year. It can be interpreted as a nodal tidal component (18.6 year) which was detected by the sea level spectrum in the NS (**Figure 2A**) and which was absent on the sea level spectra in the BS (**Figure 2C**). At Kronstadt, the wavelet power spectrum demonstrated an increase of the sea level variance in the 20−40-year band (**Figure 3D**).

CROSS-WAVELET ANALYSIS

To identify frequency bands within which time series of sea level in different sea parts are covarying, the wavelet coherence method was used (Grinsted et al., 2004; Jevrejeva et al., 2005, 2006). Synchronous time series of the monthly MSL for IJmuiden, Gedser, Stockholm, and Kronstadt were analyzed. **Figure 4** shows wavelet coherence diagrams for four pairs of the sea level time series: (A) IJmuiden–Gedser, (B) IJmuiden–Stockholm, (C) Gedser–Stockholm, (D) Stockholm–Kronstadt. High coherence (>0.9) between IJmuiden–Gedser, and IJmuiden–Stockholm was revealed at the seasonal frequency and in the 2–8-year band in the second half of the 20th century. In general, the wavelet coherence for IJmuiden–Stockholm is higher than for IJmuiden–Gedser. It is caused by topographical features of the DS and the whole Baltic. The large basin in combination with topographic flow resistance in the connecting sounds act as a low-pass filter and lead to a reduction of amplitude (Andersson, 2002). The BS behavior is then that of a quarter-wave oscillation with a node at the entrance (Samuelsson and Stigebrandt, 1996), and the variance of the oscillations increases from the BS mouth toward the north because of the internal forcing (variations in local wind, air pressure, and density). Minimum amplitudes of the main long-period sea level components are observed in the DS: seasonal oscillations, pole tide as well as the total variance of the interannual sea level variability of the BS (Ekman, 1996; Medvedev, 2014, Medvedev et al., 2017). Weak coherence between the sea level oscillations in the North and BS s is detected for periods of more than 20 year.

Very high coherence is observed between the sea level oscillations at different stations inside the BS over a wide range of periods. For Gedser–Stockholm, local coherence decreases in the 0.5–8-year band in single years and a general coherence decreases over periods of more than 10 year, but very high coherence (>0.8–0.9) was observed for Stockholm–Kronstadt in all of the studied frequency-time domain. Some local low coherence is found in the 0.16–0.5-year band. Permanently high

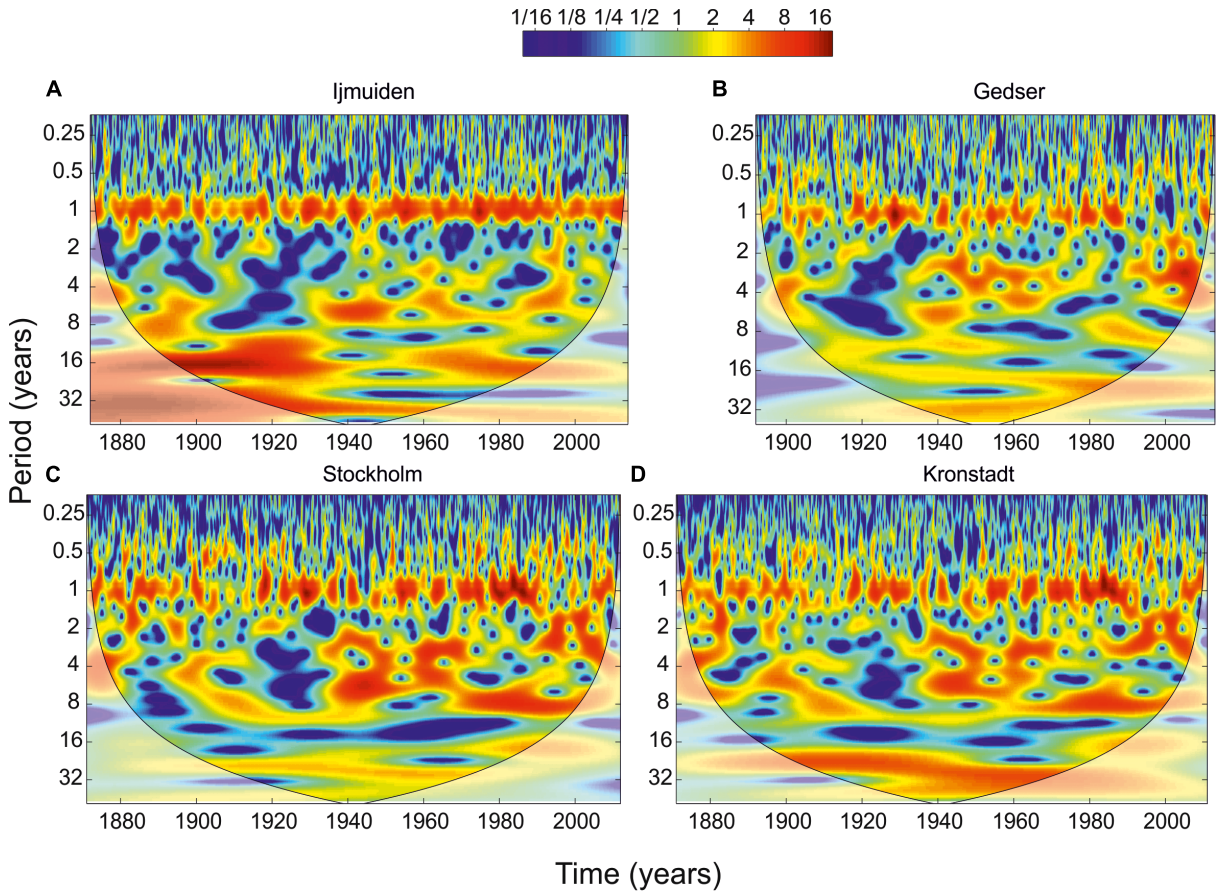

FIGURE 3 | Wavelet power spectrum (Morlet) of the MSL for the **(A)** IJmuiden (NS), **(B)** Gedser (DS), **(C)** Stockholm, and **(D)** Kronstadt (BS). The contours are in variance units. The color bar represents normalized variances. In all panels, the black thin line is the cone of influence where edge effects might distort the picture, shown in a lighter shade.

coherence and close to zero phase difference are observed for periods of more than 0.5 year. It means that the sea level oscillations occur synchronously throughout the entire BS in a wide frequency range.

Because of the permanently high coherence in a wide frequency range, we should pay attention to the local coherence minima, which were found in the 3–4-year band during the 1910–1930 time period and for a 16-year signal during 1870–1930. The last wavelet peak in **Figure 4** is of particular interest. The coherence in the 16-year oscillation of sea level between Stockholm and Kronstadt was weak from 1870 to the early 20th century, while from the 1940s the coherence for the 16-year oscillation increased substantially, exceeding 0.8 in the second half of the 20th century.

Mean sea level variations in the BS are closely related to the large-scale atmospheric circulation. Kauker and Meier (2003) showed that the variations of the NAO index describe up to 50% of the SLP variance over Northern Scandinavia, but only 10–30% of the variance over the BS. The SLP pattern shows a strong meridional gradient over the BS, causing strong zonal geostrophic winds, which influence sea level variations along the Baltic coast (Jevrejeva et al., 2005). In the present study, we examined the relationship between the sea level oscillations in the BS and wind variations. The wavelet spectrum of U-wind (zonal) component (**Figure 5A**) has the same structure as the wavelet spectra in Kronstadt and Stockholm: (1) an increase in the variance of the oscillations with periods of about a 6–8-year band has been detected since 1930; (2) the annual signal is absent in 1990–2000; and (3) the variance in 1990–2000 cross to the 2–4-year band and semiannual oscillations. The wavelet spectrum of the meridional (V) wind component (**Figure 5B**) has a significantly different structure than those of sea level (**Figure 3**).

Figures 5C–F shows the wavelet coherence diagrams for time series of the monthly average zonal and meridional components of wind speed from the 20th Century Reanalysis (Compo et al., 2011) and the sea level oscillations in Stockholm and Kronstadt. The wavelet coherence diagrams in the 0.2–8-year band demonstrate a possible link between the zonal wind and the sea level variability at both tide gauge stations (coherence is 0.8–0.9). Both at Kronstadt and Stockholm the coherence decreases in the 4–8-year band in the late 19th – early 20th centuries and a permanently low coherence in the 14–20-year band. The cause

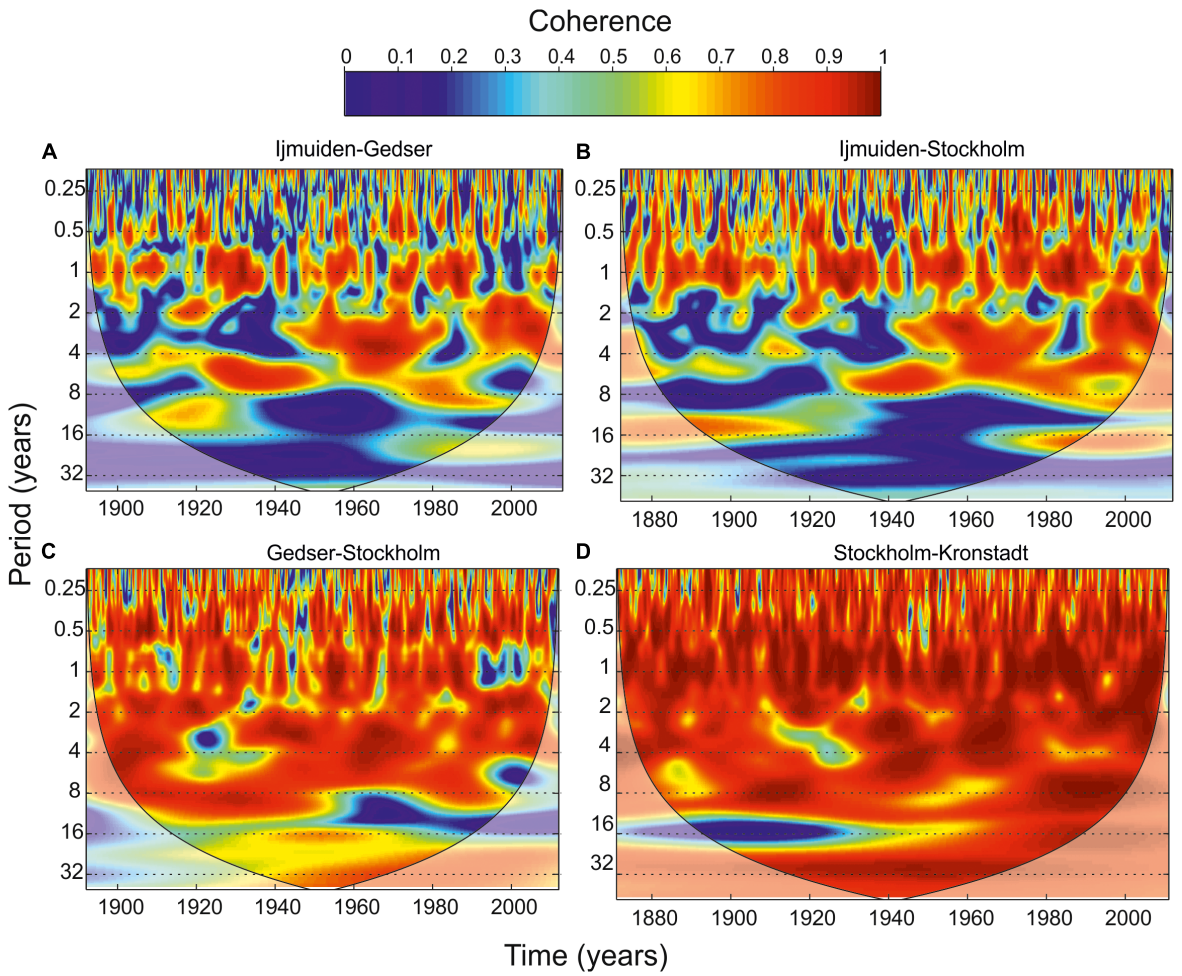

FIGURE 4 | Wavelet coherence between **(A)** IJmuiden–Gedser, **(B)** IJmuiden–Stockholm, **(C)** Gedser–Stockholm, **(D)** Stockholm–Kronstadt. In all panels, the black thin line is the cone of influence where edge effects might distort the picture, shown in a lighter shade.

of the first minimum is not clear, while the second coherence minimum appears to be caused by the astronomical origin of sea level oscillations with a well-defined nodal period of 18.6 year. The locally high coherence between meridional wind and sea level is observed for the annual component and in the 24–32-year period band.

OSCILLATION WITH A PERIOD OF 255 DAYS

In this study, we would like the particular attention to a vague spectral peak with a period of about 255 days. This spectral peak was also detected in the sea level spectra in different parts of the sea. **Figure 6** shows the sea level spectra for four tide gauges: Kemi, Oulu, and Mäntyluoto in the Gulf of Bothnia, and Helsinki in the Gulf of Finland. These spectra were calculated without smoothing. Length of segments were 1116 months for Kemi, 1488 months for Oulu, 1228 months for Mäntyluoto, and 1608 months for Helsinki. The 95% significance levels were calculated according to the Chi-squared distribution of the variance of background noise. The peak with a period of 255 days at these spectra has their sharp character, which corresponds to the deterministic processes, and exceeds the 95% significance level.

This peak was initially detected in spectral analysis of the results of numerical modeling of the sea level oscillations in the BS from 1979 to 2010 (Kulikov et al., 2015a). The numerical modeling of sea level variability in Kulikov et al. (2015a) was carried out using the closed basin approximation (closed DS), while the driving force in the model was due to the variations in atmospheric pressure and surface wind fields. The cause of the formation of this spectral component is therefore in the forcing. The atmospheric data for that model were taken from the NCEP/CFSR reanalysis (Saha et al., 2010).

We analyzed the spectral structure of the air pressure variations from different reanalyses. We used data at nodes near the Stockholm for ERA-Interim and NCEP/CFSR, near Kronstadt from NCEP/NCAR, and in the Bornholm Basin from 20th Century Reanalysis (see **Figure 1**). Spectra were calculated

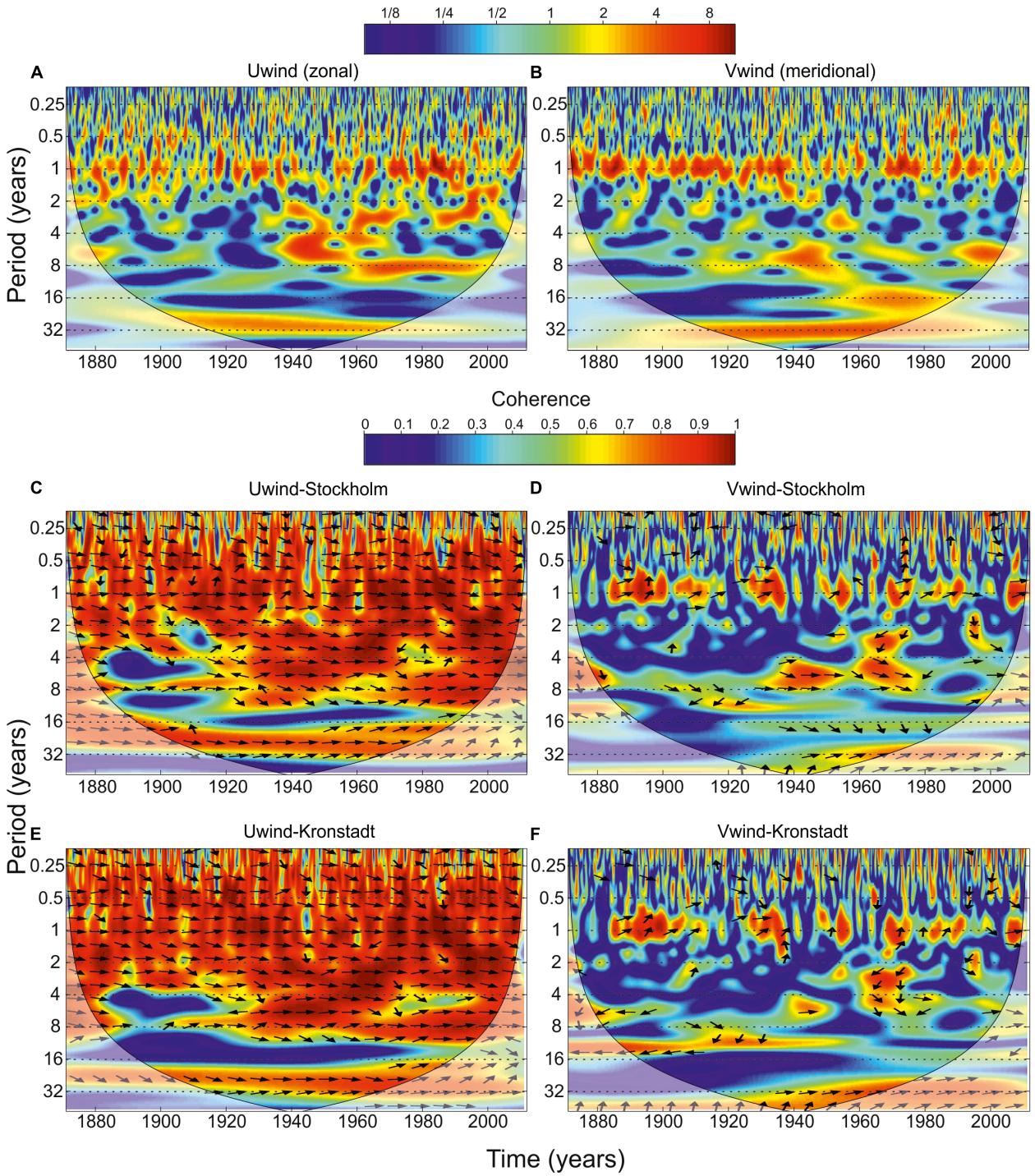

FIGURE 5 | Wavelet power spectrum (Morlet) of mean monthly values of **(A)** zonal and **(B)** meridional components of wind speed from the 20th Century Reanalysis. Contours are in variance units. The color bar represents normalized variances. Wavelet coherence and the phase difference between **(C)** zonal wind – Stockholm, **(D)** meridional wind – Stockholm, **(E)** zonal wind – Kronstadt, and **(F)** meridional wind – Kronstadt. Contours are wavelet squared coherencies. The vectors indicate the phase difference. In all panels, the black thin line is the cone of influence where edge effects might distort the picture is shown as a lighter shade.

without smoothing. Length of segments were 418 months for ERA-Interim, 792 for NCEP/NCAR, 245448 h (∼336 months) for NCEP/CFSR, and 1376 months for 20th Century Reanalysis. The 95% significance levels were calculated according to the Chi-squared distribution of the variance of background noise. **Figure 7D** illustrates the spectra of fluctuations in atmospheric

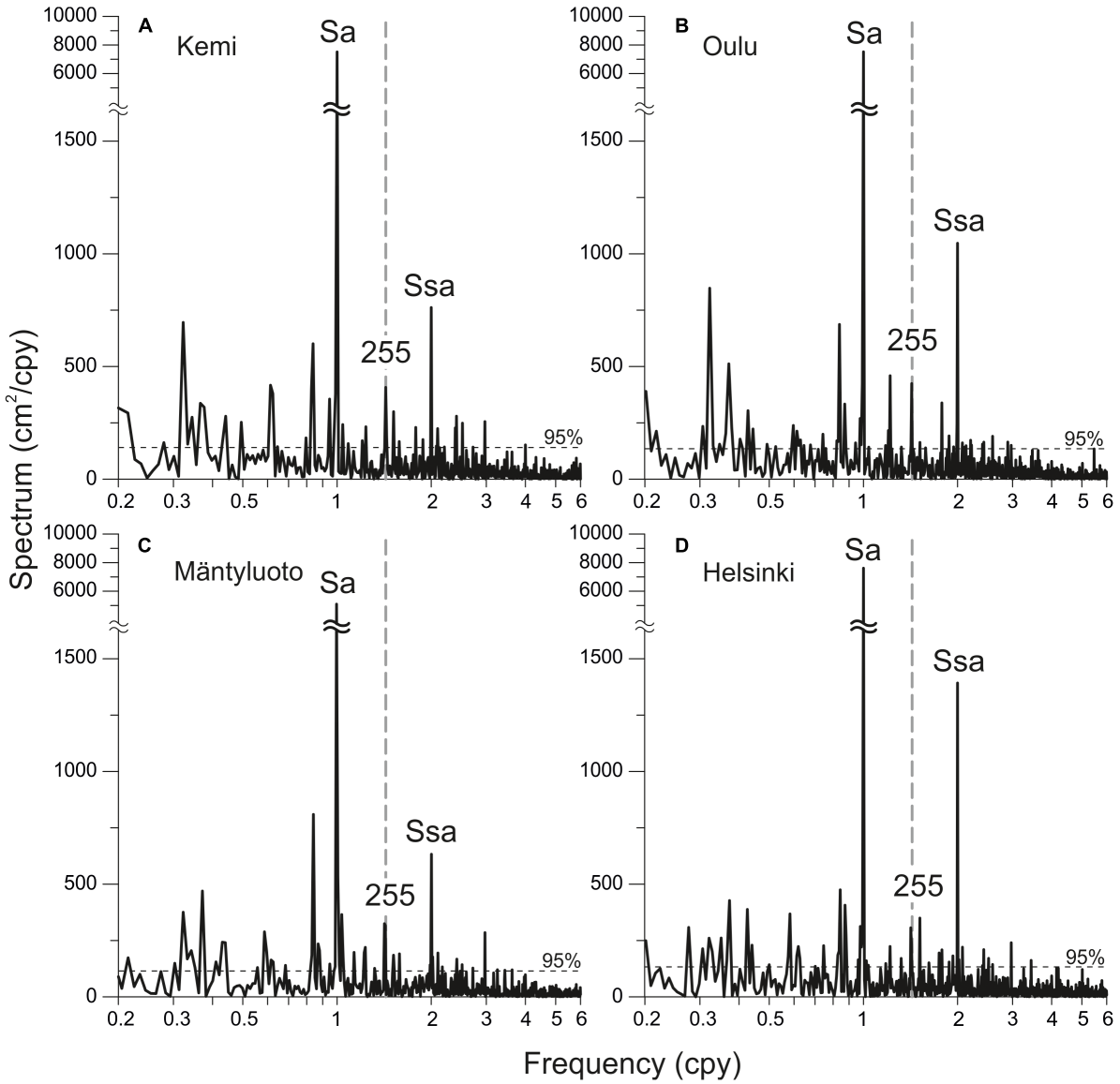

FIGURE 6 | The sea level spectra estimated from mean monthly sea level records at **(A)** Kemi, **(B)** Oulu, **(C)** Mantyluoto, and **(D)** Helsinki. Labels "Sa," "Ssa," and "255" mark annual, semiannual, and 255-daily spectral peaks, respectively. Thin dashed lines show 95% significance level calculated according to Chi-squared distribution.

pressure at the NCEP/CFSR reanalysis node near Stockholm. On these spectra, the peak with a period of 255 days dominates significantly all other peaks, including the annual peak. The air pressure data from other reanalyses (NCEP/NCAR, 20th Century Reanalysis, ERA-Interim) were tested as well and a peak with a period of 255 days was also detected (**Figures 7A–C**). While in NCEP/NCAR, ERA-Interim reanalyses it is revealed better, than in 20th Century Reanalysis. However, it is presented at all the considered spectra and significantly exceeds the background noise level.

As a next step, we have analyzed the air pressure observations from weather stations. We used daily observations of SLP from the Stockholm Old Astronomical Observatory during 1756–2012 (Moberg et al., 2002), and daily MSL pressure at weather stations from the ECA dataset (Klein Tank et al., 2002). **Figure 7E** shows air pressure spectrum for Stockholm. It was calculated by 93,868-month record without smoothing. The peak with a period of 255 days exceeds the background noise level. However, the main long-period components (annual, semiannual, and terannual) are larger. We have also checked air pressure spectra of observations at different weather stations in Europe. The peak with a period of 255 days was detected at weather stations of the Scandinavian region. **Figures 7G,H** show the air pressure spectra at Finnish weather stations Pirkkala Tampere-Pirkkalan Lentoasema (length of the record is 418 months) and Pello Kk Museotie (length of the record is 536 months), respectively. Spectra At the first

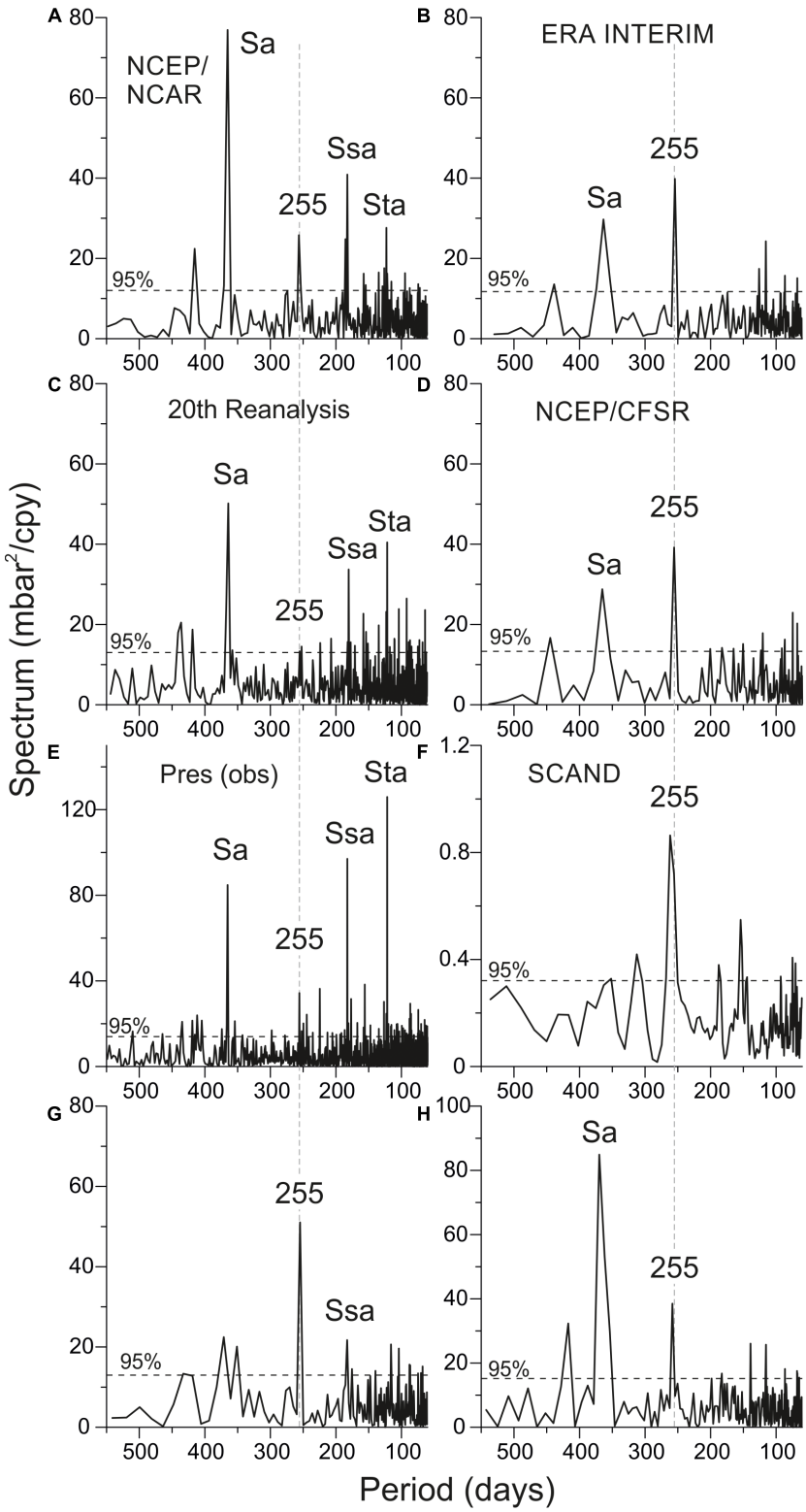

FIGURE 7 | The air pressure spectra estimated from **(A)** NCEP/NCAR, **(B)** ERA-Interim, **(C)** 20th Century Reanalysis, **(D)** NCEP/CFSR reanalysis, air pressure observations at **(E)** Stockholm, **(G)** Pirkkala Tampere-Pirkkalan Lentoasema, **(H)** Pello Kk Museotie weather stations, and **(F)** Scandinavian index time series. Labels "Sa," "Ssa," "Sta," and "255" mark annual, semiannual, terannual, and 255-daily spectral peaks, respectively. Thin dashed lines show 95% significance level calculated according to Chi-squared distribution.

station, the peak with a period of 255 days is significantly larger than all other peaks, including the annual peak. At Pello Kk Museotie, the peak with a period of 255 days is larger than other peaks, except for the annual peak, and significantly exceeds the background noise level.

At the conclusion of the study, we analyzed the Scandinavian pattern (SCAND index). We used the Kaiser-Bessel spectral window with a length of segment 370 months with half window overlaps and 6 degrees of freedom. The 95% significance levels were calculated according to the Chi-squared distribution of the variance of background noise. The peak with a period of 255 days is the main component of the spectrum of SCAND index (**Figure 7F**). One of its main features is its high quality (Q) factor, characteristic of deterministic geophysical processes, such as the tide. However, there are no frequencies in the expansion of the tidal potential that are close to 255 days. Consequently, the question of the nature of this peak remains open and requires further research.

DISCUSSION

In the present study, we detected several peaks in the long-period sea level spectra in the NS and in the BS. In addition to the dominant annual and semiannual oscillations in the spectrum of long-period sea level variations, other peaks were also identified. In the period band less than 1 year, we detected the spectral peak with a period with 255 days. Our analyses revealed this peak in both the sea level spectra of the BS and in the spectra of the atmospheric processes. Vermeer et al. (1988) singled out the peak of the close period (242 days) at the sea level spectra of several tide gauges on the Finish coast of the BS. But Vermeer et al. (1988) did not give any explanation about the possible nature of this peak. O'Connor et al. (2000) reveled the peak with close period at the spectrum of the velocity of the zonal wind in the NS region, spatially averaged from NCEP/NCAR. But O'Connor et al. (2000) focused on the study of the pole tide and did not pay attention to the peak with a period of 255 days.

The pole tide peak with a period 14 months is one of the main distinguishing features of the sea level spectra of the BS and the NS. Typically, the pole tide has an equilibrium amplitude of about 0.5–0.7 cm. However, the pole tide amplitude estimated from the long tide gauge records in the North and Baltic Seas is 6–8 times higher than the equilibrium amplitude of the pole tide. The highest pole tide amplitude is in the Gulf of Finland is up to 6.5 cm (Medvedev et al., 2017). The pole tide does not have an exact fixed frequency, as the astronomical tide, and had significant temporal fluctuations in amplitudes and periods during the 19th and 20th centuries. If we use short sea level records for spectral analysis (30–40 year), we have a wide peak with a central frequency of 1/434 cpd in this band (Medvedev et al., 2014, 2017). If we apply spectral analysis to long records (>100 year), the spectral peak of the pole tide splits into a few separate components (Medvedev et al., 2014, 2017). The main pole tide peak has a period of ∼434 days (**Figure 2**). Also, we can distinguish pole tide peaks with periods of 417 and 443 days. The variations in the pole tide periods cause some spectral peaks in the pole tide frequency band. According to Munk and MacDonald (1960), the CW period varies in the interval by ±4%.

The spectral peak with a 6.16-year period is one of the strongest and most stable components of long-period sea level spectra for the BS and the NS in the period band from 1 year to a few decades. Currie (1976) and Trupin and Wahr (1990) have also singled out this peak in the spectra of the BS and the NS too. Vermeer et al. (1988) distinguished this peak at the sea level spectra of several tide gauges on the Finish coast of the BS. A similar signal with a period of 6–7 years was observed by Hilmi et al. (2002) in the sea level data in the Gulf of Saint Lawrence.

The nodal spectral peak Mn with a period 18.6-year is most pronounced at the sea level spectra in the NS (**Figures 2A**, **3A**) and is not detected at the Baltic spectra (**Figures 2C**, **3C,D**) and in the wavelet power spectra of the zonal wind (**Figure 5A**). The wavelet coherence between zonal wind and sea level in the BS is very low in these period band. It means that the nodal tide has the astronomical origin and has not the meteorological origin unlike the pole tide. Currie (1976) revealed a nodal peak in the sea level variations at tide gauges in the NS and DS region with amplitude up to 1.0–1.5 cm. At the Baltic stations, Currie (1976) did not find this peak. Only at Oulu, he found a similar peak, but the period of it was 20 year. Trupin and Wahr (1990) identified that the BS is the region where long-period noise seriously masks the 18.61-year signal. Currie (1976) also found the spectral peak with a solar-cycle period (10.5–11.5 year) in the low-frequency spectra in the NS and in the BS. However, in our results (**Figure 2**), this peak was not distinguished in each spectrum.

The sea level component with an 8.47-year period is probably linked to the lunar perigee. Munk and Cartwright (1966) showed evidence of the lunar perigee in influencing long-term water level variations. Hilmi et al. (2002) distinguished this peak at the sea level spectra of several tide gauges in the Gulf of Saint Lawrence.

Sea level oscillations with 12–30-year periods are probably linked to the propagation of the Atlantic water masses through the DS and decadal variability in the freshwater budget (Meier and Kauker, 2003; Jevrejeva et al., 2005). The oscillations in the 2.2–7.8-year band in sea level records have been associated with large-scale atmospheric circulation signals (Unal and Ghil, 1995; Jevrejeva et al., 2005). Changes in the atmospheric circulation would generate sea level response through a number of processes: the direct influence of changes in atmospheric pressure, changes in wind stresses, and changes in atmosphere-ocean fluxes as well as storm surges (Jevrejeva et al., 2005). The variations of these components could influence on the sea level variability.

As numerous studies (Andersson, 2002; Hünicke et al., 2015; Johansson and Kahma, 2016) shown the main factor of the Baltic long-period sea level formation is zonal wind. In this study, we describe the increase in the variance of sea level oscillations themselves and increased coherence between these oscillations and wind fluctuations in the BS since 1940s. Thus, high coherences have been detected between sea level variability in the North and Baltic Seas at the annual frequency and in the 2–8-year period band. The coherence between the 16-year sea level oscillations at Stockholm and Kronstadt was weak from 1870 to early 1900s, but increased substantially since the 1940s. Jevrejeva et al. (2005, 2006) have found a similar increase in various parts

of the World Ocean. It was noted by Jevrejeva et al. (2006) that the amplitude of 3.5–13.9-year oscillations significantly increased since the 1940s in the Northeast and Northwest Atlantic, and in the East Pacific Jevrejeva et al. (2006) also showed that the noticeable increase of the influence (coherence) of the Arctic Oscillation on the sea level variability in the North Atlantic after 1940 is associated with the 2.2–13.9-year periodicity.

CONCLUSION

This research was primarily conceived to study the Baltic Sea level spectrum in the interval of periods from a few months to decades. Effective statistical methods of time series analysis have been applied to the long-term data from 36 tide gauges in the BS, the DS, and southeastern part of the NS, to examine the character of low-frequency sea level variability. The high spatial and temporal resolution of data allowed us to consider the features of the sea level spectrum in detail, to validate earlier conclusions and results of other investigators and to reveal some additional features which were previously unknown.

Our analysis supports the preliminary assumption that the sea level of the BS is governed mainly by changes in the zonal wind over this sea, which is one of the shallowest marginal seas. Extensive shallow-water areas provide favorable conditions for effective generation of intense wind-driven motions and creation of destructive storm surges in the Gulf of Finland and other shallow-water regions of the sea (e.g., Kulikov and Medvedev, 2013). The same effect appears to be responsible for the unusually high 14-month Chandler oscillations, wind-driven seasonal variations, and other long-period sea level variability (Medvedev et al., 2017). The presented analysis has enabled us to determine the nature of the low-frequency sea level variations as a response to the variable zonal winds in a very shallow sea.

In addition, our research has new findings. The cross-wavelet analysis shows that very high coherence ($>$0.8–0.9) over a wide range of periods from 2 months to 8–10 year is observed between the sea level oscillations inside the BS. It means that the sea level oscillations occur almost synchronously throughout the entire BS in a wide frequency range. However, there are some local coherence minima: in the 3–4-year band from 1910 to 1930 and for a 14–20-year band from 1870 to 1930. The wavelet spectrum of zonal wind component has the same structure as the wavelet spectra in Kronstadt and Stockholm: (1) an increase in the variance of the oscillations with periods of about a 6–8 year has been detected since 1930; (2) the annual signal is absent in 1990–2000 years; and (3) the variance in 1990–2000 years cross to the 2–4-year band and semiannual oscillations. The wavelet coherence diagrams demonstrate the strong relations of the zonal wind on the sea level variability at both tide gauge stations in the 0.2–8-year band. For example, the results for Kronstadt show a permanently low coherence in the 14–20-year band, which may be due to the astronomical origin of the sea level oscillations with the nodal period (18.6 year). Local high coherence between meridional wind and sea level variability are observed for the annual component and in the 24–32 year band.

The new and important result of this research is that we have identified in the BS separate periodic components, especially the peaks with the periods of 6.16 year and 255 days. Currie (1976), Trupin and Wahr (1990), and Hilmi et al. (2002) have also detected the 6.16-year sea level oscillation, but its origin was not explained. We propose that this peak is the result of interference between the seasonal oscillations and the pole tide in the atmosphere and has the frequency equal to the difference between the annual and the Chandler frequencies. This 255-day oscillation is the most intriguing result of this study. Our analyses revealed this peak in both the sea level spectra of the BS and in the spectra of the atmospheric processes. It is more pronounced in the air pressure variations from atmospheric reanalysis, especially in the ERA-Interim and NCEP/CFSR. This means that the reanalysis models reproduce this oscillation well enough. However, the origin of this 255-day oscillation is still unclear.

AUTHOR CONTRIBUTIONS

IM coordinated the work on the manuscript, wrote the initial version of the manuscript, and prepared the figures. EK coordinated the work on the manuscript, and revised the text and figures substantially. IM and EK actively contributed to the development of the manuscript idea, writing, and preparation of figures.

FUNDING

This research was supported by the Russian Foundation for Basic Research, project 18-05-60250 (processing of reanalysis data) and the state assignment of IO RAS, theme 0149-2019-0005 (processing of tide gauge data).

REFERENCES

Andersson, H. C. (2002). Influence of long-term regional and large-scale atmospheric calculation on the Baltic sea level. *Tellus A* 54, 76–88. doi: 10.3402/tellusa.v54i1.12125

Barnston, A. G., and Livezey, R. E. (1987). Classification, seasonality and persistence of low-frequency atmospheric circulation patterns. *Mon. Weather Rev.* 115, 1083–1126. doi: 10.1175/1520-0493(1987)115%3C1083:CSAPOL%3E2.0.CO;2

Bueh, C., and Nakamura, H. (2007). Scandinavian pattern and its climatic impact. *Q. J. R. Meteorol. Soc.* 133, 2117–2131. doi: 10.1196/annals.1446.014

Carlsson, M. (1997). *Sea Level and Salinity Variations in the Baltic Sea – an Oceanographic Study Using Historical Data*. Gothenburg: Göteborg University. Ph. D. thesis.

Church, J. A., and White, N. J. (2011). Sea level rise from the late 19th to the early 21st century. *Surv. Geophys.* 32, 585–602. doi: 10.1007/978-94-007-2063-3_17

Compo, G. P., Whitaker, J. S., Sardeshmukh, P. D., Matsui, N., Allan, R. J., Yin, X., et al. (2011). The twentieth century reanalysis project. *Q. J. R. Meteorol. Soc.* 137, 1–28.

Currie, R. G. (1976). The spectrum of sea level from 4 to 40 years. *Geophys. J. R. Astron. Soc.* 46, 513–520. doi: 10.1111/j.1365-246x.1976.tb01245.x

Darwin, G. H. (1898). *The Tides and Kindred Phenomena in the solar System*. New York, NY: Houghton Mifflin and company.

Ekman, M. (1996). A common pattern for interannual and periodical sea level variations in the Baltic Sea and adjacent waters. *Geophysica* 32, 261–272.

Ekman, M. (2007). *A Secular Change in Storm Activity Over the Baltic Sea Detected Through Analysis of Sea Level Data. Small Publ Hist Geophys*. Åland Islands: Summer Institute for Historical Geophysics.

Ekman, M. (2009). *The Changing Level of the Baltic Sea During 300 Years: a Clue to Understanding the Earth*. Åland Islands: Summer Institute for Historical Geophysics.

Ekman, M., and Stigebrandt, A. (1990). Secular change of the seasonal variation in sea level and of the pole tide in the Baltic Sea. *J. Geophys. Res.* 95, 5379–5383.

Gilbert, F., and Dziewonski, A. M. (1975). An application of normal mode theory to the retrieval of structural parameters and source mechanisms from seismic spectra. *Philos. Trans. R. Soc. Lon. A* 278, 187–269. doi: 10.1098/rsta.1975.0025

Grinsted, A., Moore, J. C., and Jevrejeva, S. (2004). Application of the cross wavelet transform and wavelet coherence to geophysical time series. *Nonlinear Process. Geophys.* 11, 561–566. doi: 10.5194/npg-11-561-2004

Hammarklint, T. (2009). *Swedish Sea Level Series – A Climate Indicator*. Norrköping: . Swedish Meteorological and Hydrological Institute.

Hilmi, K., Murty, T., El Sabh, M. I., and Chanut, J.-P. (2002). Long-Term and short-term variations of sea level in Eastern Canada: a review. *Mar. Geodesy* 25, 61–78. doi: 10.1080/014904102753516732

Holgate, S. J., Matthews, A., Woodworth, P. L., Rickards, L. J., Tamisiea, M. E., Bradshaw, E., et al. (2013). New data systems and products at the permanent service for mean Sea level. *J. Coast. Res.* 29, 493–504.

Hünicke, B., Zorita, E., Soomere, T., Madsen, K. S., Johansson, M., and Suursaar, Ü (2015). *Recent Change–Sea Level and Wind Waves. In Second Assessment of Climate Change for the Baltic Sea Basin*. Cham: Springer, 155–185.

Jevrejeva, S., Grinsted, A., Moore, J. C., and Holgate, S. (2006). Nonlinear trends and multiyear cycles in sea level records. *J. Geophys. Res.* 111:C09012.

Jevrejeva, S., Moore, J. C., Woodworth, P. L., and Grinsted, A. (2005). Influence of large scale atmospheric circulation on the European sea level: results based on the wavelet transform method. *Tellus A* 57, 129–149.

Johansson, M., and Kahma, K. K. (2016). On the statistical relationship between the geostrophic wind and sea level variations in the Baltic Sea. *Coast. Res.* 21, 25–43.

Kauker, F., and Meier, H. E. M. (2003). Modeling decadal variability of the Baltic Sea: 1. Reconstructing atmospheric surface data for the period 1902–1998. *J. Geophys. Res.* 108:3267. doi: 10.1029/2003JC001797

Klein Tank, A. M. G., Wijngaard, J. B., Können, G. P., Böhm, R., Demarée, G., Gocheva, A., et al. (2002). Daily dataset of 20th-century surface air temperature and precipitation series for the European Climate Assessment. *Int. J. of Climatol.* 22, 1441–1453. doi: 10.1002/joc.773

Kulikov, E. A., and Medvedev, I. P. (2013). Variability of the baltic sea level and floods in the gulf of finland. *Oceanology* 53, 145–151. doi: 10.1134/s0001437013020094

Kulikov, E. A., Fain, I. V., and Medvedev, I. P. (2015a). Numerical modeling of anemobaric fluctuations of the Baltic Sea level. *Russ. Meteorol. Hydrol.* 40, 100–108. doi: 10.3103/s1068373915020053

Kulikov, E. A., Medvedev, I. P., and Koltermann, K. P. (2015b). Baltic sea level low-frequency variability. *Tellus A* 67:25642. doi: 10.3402/tellusa.v67.25642

Kulikov, E. A., Rabinovich, A. B., and Carmack, E. C. (2004). Barotropic and baroclinic tidal currents on the Mackenzie shelf break in the southeastern Beaufort Sea. *J. Geophys. Res.* 109:C05020. doi: 10.1029/2003JC001986

Lehmann, A., Myrberg, K., and Höflich, K. (2012). A statistical approach to coastal upwelling in the Baltic Sea based on the analysis of satellite data for 1990–2009. *Oceanologia* 54, 369–393. doi: 10.5697/oc.54-3.369

Lehmann, A., and Post, P. (2015). Variability of atmospheric circulation patterns associated with large volume changes of the Baltic Sea. *Adv.Sci.Res.* 12, 219–225. doi: 10.5194/asr-12-219-2015

Lisitzin, E. (1974). *Sea Level Changes*. Amsterdam: Elsevier.

Luther, D. S. (1982). Evidence of a 4–6 day barotropic, planetary oscillation of the Pacific Ocean. *J. Phys. Oceanogr.* 12, 644–657. doi: 10.1175/1520-0485(1982)012<0644:eoadbp>2.0.co;2

Medvedev, I. P. (2014). Seasonal fluctuations of the Baltic sea level. *Russ. Meteorol. Hydrol.* 39, 814–822. doi: 10.3103/s106837391412005x

Medvedev, I. P., Rabinovich, A. B., and Kulikov, E. A. (2013). Tidal oscillations in the Baltic Sea. *Oceanology* 53, 526–538. doi: 10.1134/s0001437013050123

Medvedev, I. P., Rabinovich, A. B., and Kulikov, E. A. (2014). Pole tide in the Baltic Sea. *Oceanology* 54, 121–131. doi: 10.1134/s0001437014020179

Medvedev, I. P., Rabinovich, A. B., and Kulikov, E. A. (2017). The pole tide/14-month oscillations in the Baltic Sea during the 19th and 20th centuries: spatial and temporal variations. *Cont. Shelf Res.* 137, 117–130. doi: 10.1016/j.csr.2017.02.001

Meier, H. E. M., and Kauker, F. (2003). Modeling decadal variability of the Baltic Sea: 2. Role of freshwater inflow and large-scale atmospheric circulation for salinity. *J. Geophys. Res.* 108:3368. doi: 10.1029/2003JC001799

Moberg, A., Bergström, H., Ruiz Krigsman, J., and Svanered, O. (2002). Daily air temperature and pressure series for Stockholm (1756-1998). *Clim. Change* 53, 171–212. doi: 10.1007/978-94-010-0371-1_7

Munk, W. H., and Cartwright, D. E. (1966). Tidal spectroscopy and prediction. *Phil. Trans. Roy. Soc. London. Ser. A* 259, 533–581.

Munk, W. H., and MacDonald, G. J. F. (1960). *The Rotation of the Earth*. New York: Cambridge University Press.

O'Connor, W. P., Chao, B. F., Zheng, D., and Au, A. Y. (2000). Wind stress forcing of the North Sea 'Pole Tide'. *Geophys. J. Int.* 142, 620–630. doi: 10.1046/j.1365-246x.2000.00184.x

Peltier, W. R. (2004). Global glacial isostasy and the surface of the ice-age Earth: the ICE-5G (VM2) model and GRACE. *Annu. Rev. Earth Planet. Sci.* 32, 111–149. doi: 10.1146/annurev.earth.32.082503.144359

Richter, A., Groh, A., and Dietrich, R. (2011). Geodetic observation of sea level change and crustal deformation in the Baltic Sea region. *Phys. Chem. Earth* 5, 43–53. doi: 10.1016/j.pce.2011.04.011

Saha, S., Moorthi, S., Pan, H.-L., Wu, X., Wang, J., Nadiga, S., et al. (2010). The NCEP climate forecast system reanalysis. *Bull. Am. Meteorol. Soc.* 91, 1015–1057.

Samuelsson, M., and Stigebrandt, A. (1996). Main characteristics of the long-term sea level variability in the Baltic Sea. *Tellus A* 48, 672–683. doi: 10.1034/j.1600-0870.1996.t01-4-00006.x

Soomere, T., and Pindsoo, K. (2016). Spatial variability in the trends in extreme storm surges and weekly-scale high water levels in the eastern Baltic Sea. *Cont. Shelf Res.* 115, 53–64. doi: 10.1016/j.csr.2015.12.016

Thomson, R. E., and Emery, W. J. (2014). *Data Analysis Methods in Physical Oceanography*, Third and revised edition. New York, NY: Elsevier.

Torrence, C., and Compo, G. P. (1998). A practical guide to wavelet analysis. *Bull. Am. Meteorol. Soc.*79, 61–78.

Trupin, A., and Wahr, J. (1990). Spectroscopic analysis of global tide gauge sea level data. *Geophys. J. Int.* 100, 441–453. doi: 10.1111/j.1365-246x.1990.tb00697.x

Unal, Y. S., and Ghil, M. (1995). Interannual an interdecadal oscillation patterns in sea level. *Clim. Dyn.* 11, 255–278. doi: 10.1007/bf00211679

Vermeer, M., Kakkuri, J., Mälkki, P., Boman, H., Kahma, K. K., and Leppäranta, M. (1988). Land uplift and sea level variability spectrum using fully measured monthly means of tide gauge readings. *Finn. Mar. Res.* 256, 1–75.

Wahl, T., Haigh, I. D., Woodworth, P. L., Albrecht, F., Dillingh, D., Jensen, J., et al. (2013). Observed mean sea level changes around the North Sea coastline from 1800 to present. *Earth Sci. Rev.* 124, 51–67. doi: 10.1016/j.earscirev.2013.05.003

Wróblewski, A. (2001). Lunar nodal tide in the Baltic Sea. *Oceanologia* 43, 99–112.

Conflict of Interest: The authors declare that the research was conducted in the absence of any commercial or financial relationships that could be construed as a potential conflict of interest.

frontiers in Earth Science

REVIEW
published: 05 February 2020
doi: 10.3389/feart.2020.00007

Baltic Sea Operational Oceanography—A Stimulant for Regional Earth System Research

Jun She[1], H. E. Markus Meier[2,3], Miroslaw Darecki[4], Patrick Gorringe[3], Vibeke Huess[1], Tarmo Kouts[5], Jan Hinrich Reissmann[6] and Laura Tuomi[7]*

[1] Department of Research and Development, Danish Meteorological Institute, Copenhagen, Denmark, [2] Leibniz Institute for Baltic Sea Research Warnemünde, Rostock, Germany, [3] Swedish Meteorological and Hydrological Institute, Norrköping, Sweden, [4] Institute of Oceanology Polish Academy of Sciences (IOPAN), Sopot, Poland, [5] Department of Marine Systems, Tallinn University of Technology, Tallinn, Estonia, [6] Marine Sciences, Federal Maritime and Hydrographic Agency, Hamburg, Germany, [7] Marine Research Unit, Finnish Meteorological Institute, Helsinki, Finland

OPEN ACCESS

Edited by:
Klaus D. Joehnk, Commonwealth Scientific and Industrial Research Organisation (CSIRO), Australia

Reviewed by:
Anna Rutgersson, Uppsala University, Sweden
Beata Szymczycha, Institute of Oceanology (PAN), Poland

***Correspondence:**
Jun She
js@dmi.dk

Specialty section:
This article was submitted to Interdisciplinary Climate Studies, a section of the journal Frontiers in Earth Science

Received: *14 January 2019*
Accepted: *16 January 2020*
Published: *05 February 2020*

Citation:
She J, Meier HEM, Darecki M, Gorringe P, Huess V, Kouts T, Reissmann JH and Tuomi L (2020) Baltic Sea Operational Oceanography—A Stimulant for Regional Earth System Research. Front. Earth Sci. 8:7. doi: 10.3389/feart.2020.00007

Two important communities related to oceanography in the Baltic Sea are those working on operational oceanography and Earth system science, with focusing on the same water body but different temporal scales. They have been coordinated through two organizations/programs: the Baltic Sea Operational Oceanographic System (BOOS) and the Baltic Sea Experiment (BALTEX) and its successor, the Baltic Earth Program (Earth system science for the Baltic Sea region), respectively. Although the two communities have archived significant progresses in their own fields since early 1990s, there were few interactions between the communities. Rapid advancements of operational oceanography on ocean monitoring, data sharing, modeling, and historical ocean state reconstruction in the last decade have provided a wide range of data, products and modeling tools which may be used in Earth system and climate change research. This is especially true when operational oceanography in the Baltic Sea is in a transition to a seamless service, i.e., from basin to local scales, from synoptic to climate scales and from physical to biogeochemical and biological systems. On the other hand, the Baltic Sea Earth system research can help to improve operational oceanography by contributing research observations and transferring their research achievements to the operational system. Based on a review of state-of-the-art of BOOS monitoring and modeling capabilities and on-going BOOS research, this paper will highlight topics and areas which are related to the Baltic Earth Grand Challenges, i.e., salinity dynamics, land-sea biogeochemical linkages, natural hazards and extreme events, sea level dynamics, coastal morphology and erosion, regional variability of water and energy exchanges, and multi-drivers of regional Earth system changes. Potential win-win cooperation and interaction between the BOOS and the Baltic Earth communities are also proposed and discussed.

Keywords: operational oceanography, Baltic Sea, BOOS, observational networks, seamless modeling, earth system study, Baltic Earth

INTRODUCTION

Oceanographic monitoring and research has a long history in the Baltic Sea. The earliest sea level observations started from 1770s (Ekman, 2009). After early German and Swedish expeditions in 1871 ("Pommerania" from Kiel) and 1877 (Swedish expedition by G. Ekman and O. Petterson), the Baltic Sea countries Denmark, Finland, Germany, Russia and Sweden signed in 1892 a resolution on international cooperation in Baltic Sea monitoring and in 1898 an agreement on simultaneous investigations on a regular basis at a few selected deep stations in the Baltic Sea. With the start of the International Council of the Exploration of the Sea (ICES) in 1902 a systematic monitoring of the Baltic Sea was established. In the past two decades, community coordination of the Baltic Sea oceanography has been organized mainly in three areas: marine environment monitoring and protection—coordinated by The Baltic Marine Environment Protection Commission (HELCOM) since 1992, operational oceanography—coordinated by the Baltic Sea Operational Oceanographic System (BOOS) since 1998 and oceanography research related to climate variability and Baltic Sea system science—coordinated by the Baltic Earth program (Earth system science for the Baltic Sea region), the successor program of the Baltic Sea Experiment (BALTEX) since 1993. In addition, fishery monitoring and data management has been coordinated by ICES and DG MARE in the Baltic-North Sea and European scale, respectively. Due to their different mandates, HELCOM members are mainly conducting offline, physical-biogeochemical and biological monitoring for environment assessment, protection, and ecosystem-based management (HELCOM, 2013); BOOS members are mainly responsible for online, physical-biogeochemical monitoring for operational oceanographic services, e.g., forecast, nowcast and hindcast (Buch and Dahlin, 2000; Buch et al., 2006); ICES members mainly carry out offline monitoring ranging from hydrographic to biological parameters for fishery management; ICOS (Integrated Carbon Observation System) is a European research infrastructure to quantify and understand the greenhouse gas balance of the European continent and of adjacent regions and is built up as a collaboration of nationally operated measurement stations in 12 European countries. Most of the monitoring activities in the above categories are regular.

BALTEX/Baltic Earth has a much wider focus. BALTEX was founded in 1993 as a network of operational weather services, climate centers, and universities with the aim to exchange both operational and climate data of the atmosphere, ocean, and land surface and to analyze water, energy and matter cycles in the Baltic Sea region (Raschke et al., 2001; Omstedt et al., 2004, 2014; Reckermann et al., 2011). BALTEX/Baltic Earth is a Regional Hydroclimate Project (RHP) within the Global Energy and Water Cycle Exchanges Project (GEWEX) of the World Climate Research Programme (WRCP). Baltic Earth research aims to fill knowledge gaps of the entire regional Earth system (Meier et al., 2014). However, in this review we limit the discussion mainly to the oceanographic component of Baltic Earth following Omstedt et al. (2004, 2014).

Since their establishments, both BALTEX/Baltic Earth and BOOS have reached significant achievements in their own fields. For operational oceanography, advanced monitoring, and forecasting capacities have been developed at local, sub-basin, and sea basin scales. Observations and forecasts are shared in real or near real time. With sustained observing, the ocean state is identified and new phenomena and related knowledge are discovered and transferred to the operational hindcast and forecast modeling platforms for optimizing existing models; by assimilating observations into the operational models, the capacity on reconstructing historical and forecasting future ocean states is improved. The products generated have been used in marine service for blue economy, ocean health, and climate change adaptation and mitigation (She, 2018a). Currently the BOOS monitoring network provides a significant amount of real time observations from e.g., tide gauge stations, FerryBox lines, mooring buoys, fixed stations, Argo profilers and research vessels (She, 2018b; Siiriä et al., 2018). The quality of operational ocean-ice-wave-biogeochemical models has been significantly improved. Based on the models developed, operational forecasting service has been made both in national and regional levels (She and Murawski, 2018; Tuomi et al., 2018). Data assimilation has been developed to ingrate modeling and observations to derive a better initial field for the forecasting models and reanalysis for reconstructing the history of the Baltic Sea (Zhuang et al., 2011; Fu et al., 2012; Axell, 2013; Liu et al., 2017). Major sources for the development of the operational oceanography in the Baltic Sea have been the Member States. In the past decades, programs from European commission, e.g., Operational Oceanography Cluster in the Framework Programs 5 and 6 (Cieślikiewicz et al., 2007), MyOcean (Bahurel et al., 2010) and following Copernicus Marine Environment Monitoring Service (CMEMS) Program have strongly supported the integration of Baltic Sea operational oceanography in advancing the operational service at the sea basin scale.

Baltic Earth is an independent and open research network with the following vision: "Baltic Earth strives to achieve an improved Earth System understanding of the Baltic Sea region as the basis for science-based management in the face of climatic, environmental, and human impact in the region. Baltic Earth brings together a broad international research community around core scientific issues identified as fundamental to informing societal efforts to achieve sustainability in the region. These "Grand Challenges (GC)" are tackled through joint research efforts, workshops, conferences, and capacity building events accompanied by a continuous process of synthesis of the current state of knowledge. Communication with stakeholders and research funders aims to ensure impact and relevance of the research. Baltic Earth targets the atmosphere, land, and marine environment of the Baltic Sea, its drainage basin and nearby areas with relevance for the Baltic Sea region." (Baltic Earth Science Plan Writing Team, 2017). Following this vision, Baltic Earth fosters interdisciplinary and international collaboration on processes in the atmosphere, on land and in the sea and also in the anthroposphere by organizing conferences, workshops, seminars, dedicated sessions at conferences, etc.

Dedicated working groups (WGs) identify at Baltic Earth conferences and by using assessments of existing research new GCs. Currently, the Baltic Earth community has identified six GCs for the Baltic Earth system research: (GC1) salinity dynamics, (GC2) land-sea biogeochemical linkages, (GC3) natural hazards and extreme events, (GC4) sea level dynamics, coastal morphology and erosion, (GC5) regional variability of water and energy exchanges, and (GC6) multi-drivers of regional Earth system changes. For each of the GCs, WGs were installed. In addition, WGs on outreach and communication, education, and regional climate system modeling are active. A new WG on climate and environmental ocean observing systems such as the Boknis Eck Time-Series Station is in the planning.

Another important aspect of Baltic Earth are thematic assessments that provide an overview over knowledge gaps which need to be filled, e.g., by funded projects. Two assessments of climate change of the Baltic Sea region, which are research community efforts such as the regular assessments of the Intergovernmental Panel on Climate Change (IPCC) of past, present and future climate, have been performed, and a third one is on the way (BACC Author Team, 2008; BACC II Author Team, 2015). Further assessments focussed on Baltic Sea models (Eilola et al., 2011; Placke et al., 2018) and ensembles of scenario simulations with coupled physical-biogeochemical models (Meier et al., 2018a, 2019), both in past and future climates (Meier et al., 2012). Recently, a more comprehensive Baltic Sea Model Inter-comparison Project (BMIP) including also process-based assessments has started.

For the closure of knowledge gaps identified by Baltic Earth assessments, several projects funded by national and European Union (EU) programs have been carried out under the umbrella of Baltic Earth. Selected examples are the BONUS projects AMBER, BALTIC-C, ECOSUPPORT, INTEGRAL, BalticAPP, and SHEBA (see http://baltic.earth). Baltic Earth is coordinated by the International Baltic Earth Secretariat at Helmholtz Zentrum Geesthacht, the Baltic Earth Science Steering Group and the Baltic Earth Advisory Board.

However, the BOOS and BALTEX/Baltic Earth communities had few interactions in the past two decades. Now it is time to enhance cooperation and integration between operational oceanography and Earth system science communities. This is in line with the recent trend of development in several international initiatives such as seamless prediction of the Earth system from the World Meteorological Organization (WMO, 2015) where observing and modeling development at the synoptic scale will be integrated with the climate scale. In the Global Ocean Observing System (GOOS), ocean observing has been extended from mainly for operational service to cover also climate change and ocean health. It is expected that GOOS Regional Alliances (GRAs, e.g., EuroGOOS) and Regional Ocean Observing Systems (ROOSs) will follow this vision to further integrate the ocean observing in operational oceanography, climate change and ocean health fields, as indicated by recent development of a sustained European Ocean Observing System (EOOS, http://www.eoos-ocean.eu). For the assessment and services in climate change adaptation and mitigation, long-term change of extreme events are more and more emphasized which needs calibrated high quality models to perform trustworthy simulations of climate projections.

In addition, the European Commission has asked for "responsive research and innovation" in its research policy in the FPs (Rodriguez et al., 2013; von Schomberg, 2013). Integration and interactions between the operational oceanography community and research community will certainly enhance the responsiveness of our research.

The purpose of this paper is to introduce the state-of-the-art of operational oceanography in the Baltic Sea, set up the scene and identify potential areas of collaboration between the operational oceanography community and the Baltic Earth community. The paper is organized as follows: section Operational oceanography in the Baltic Sea reviews the state-of-the-art of operational oceanography in the Baltic Sea, including operational observing and modeling. Section BALTEX/Baltic Earth marine research reviews the state-of-the-art of Baltic Earth system science while section Operational oceanography and Baltic Earth research—interactions identifies potential collaboration areas between the two communities. Section Discussions and recommendations gives recommendations for future BOOS—Baltic Earth cooperation. Acronyms used in this study are explained in **Table 1**.

OPERATIONAL OCEANOGRAPHY IN THE BALTIC SEA

Operational Observing—Current Status and Major Challenges

Ocean observing value chain includes three components: observing, data management, and data usage. The observing aims at generating cost-effective and fit-for-purpose observations; the data management is responsible for providing user friendly data access while the data usage component will transfer data into information products for user applications, in many cases through integrating satellite and *in-situ* observations with models. The Baltic Sea has been monitored with comprehensive, self-coordinated monitoring programs: operational monitoring is coordinated by BOOS, environmental monitoring by HELCOM and fishery monitoring by ICES. The research monitoring activities are not coordinated but the regional and EU research programs (e.g., BONUS and Horizon 2020) have their own data policies.

Operational Monitoring

The operational observing system in the Baltic Sea provides real time (RT) and near real time (NRT) observations by BOOS members to fit for the purpose of model validation and data assimilation for the improvement of the operational forecasting and reanalysis. The observations include sea level, temperature/salinity (T/S), currents, waves, dissolved oxygen (DO), and chlorophyll a, etc. The station locations and types of platforms are illustrated in **Figure 1**. High resolution data are generated by tide gauges (sea level, in 1–60 min sampling interval), FerryBox (spatial continuous sampling of

TABLE 1 | List of frequently used acronyms, their explanation, and references (in alphabetical order, assessed on 2019-01-13).

Acronym	Explanation	Comment	References
BACC	BALTEX/Baltic Earth Assessment of Climate Change for the Baltic Sea Basin	Regional assessments	https://www.baltic.earth/BACC2/index.html
BALTEX	Baltic Sea Experiment	Research network	http://www.baltex-research.eu
Baltic Earth	Earth System Science for the Baltic Sea Basin	Research network, successor of BALTEX	http://baltic.earth
BAL MFC	Baltic Sea Monitoring and Forecasting Center	Providing free and open Baltic Sea forecast and reanalysis	http://marine.copernicus.eu
BEAR	Baltic Earth Assessment Reports	Ongoing project focussing on assessments of the Baltic Earth Grand Challenges	http://baltic.earth
BED	Baltic Environmental Database	Marine observational data from the Baltic Sea monitoring programs	http://nest.su.se/bed/
BMIP	Baltic Sea Model Intercomparison Project	Baltic Earth working group project	https://www.baltic.earth/organisation/bewg_BMIP/index.html
BMP	BOOS Modeling Program	Joint BOOS modeling research	http://www.boos.org
BONUS	Science for a better future of the Baltic Sea region	Joint Baltic Sea research and development programme for the years 2010–2017	https://www.bonusportal.org/
BOOS	Baltic Operational Oceanographic System	Coordinated operational oceanography research and services in the Baltic	http://www.boos.org
BSAP	Baltic Sea Action Plan	Nutrient load abatement strategy for the Baltic Sea	http://www.helcom.fi/baltic-sea-action-plan
CLAIM	Cleaning marine Litter by developing and Applying Innovative Methods	Monitoring, modeling and cleaning marine plastics in the Baltic and Mediterranean Seas	http://www.claim-h2020project.eu/
CMEMS	Copernicus Marine Environment Monitoring Service	European marine service in global and regional seas	http://marine.copernicus.eu
EMODnet	European Marine Observation Data Network	Centralized data portals for marine physics, habitat, bathymetry, geology, chemistry, biology and human activity	http://www.emodnet.eu/
EOOS	European Ocean Observing System	A coordination framework of European ocean observing	http://www.eoos-ocean.eu
EuroGOOS	European Global Ocean Observing System	Coordinated operational oceanography research and services in Europe	http://eurogoos.eu/
EuroSEA	European Contribution to the Future of the Seas and Oceans Flagship Initiative	Horizon 2020 project	N/A
FP	Framework Program of the European Commission	EU space research is supported through framework programmes	https://ec.europa.eu/growth/sectors/space/research/
GEWEX	Global Energy and Water Cycle Exchanges Project	WCRP project that coordinates science activities to facilitate research into the global water cycle and interactions between the land and the atmosphere	https://www.gewex.org/
GOOS	Global Ocean Observing System	Global ocean observing for operational, climate and ocean health applicaitons	http://www.goosocean.org/
HELCOM	Baltic Marine Environment Protection Commission—Helsinki Commission	Governing body of the Convention on the Protection of the Marine Environment of the Baltic Sea Area, known as the Helsinki Convention	http://www.helcom.fi
Horizon 2020	Framework Program of the European Commission	Financial instrument implementing the Innovation Union, a Europe 2020 flagship initiative aimed at securing Europe's global competitiveness	https://ec.europa.eu/growth/sectors/space/research/horizon-2020_en
ICES	International Council of the Exploration of the Sea	Global network of scientists that develops science and advice to support the sustainable use of the oceans	http://www.ices.dk
ICOS	Integrated Carbon Observation System	European Research Infrastructure for high quality and high precision greenhouse gas monitoring	https://www.icos-cp.eu/
IOW	Leibniz Institute for Baltic Sea Research Warnemunde	German research institute	http://io-warnemuende.de

(Continued)

TABLE 1 | Continued

Acronym	Explanation	Comment	References
IOWDB	Leibniz Institute for Baltic Sea Research Warnemünde Database	Oceanographic Database research with Interactive Navigation (Odin 2)	https://odin2.io-warnemuende.de/
IOWMETA	Leibniz Institute for Baltic Sea Research Warnemünde Data Portal	Marine observational data from the German monitoring program	http://iowmeta.io-warnemuende.de
IPCC	Intergovernmental Panel of Climate Change	Performed assessment reports of past and future changes in 1990, 1995, 2001, 2008, and 2013	http://www.ipcc.ch
MARNET	Marine environmental monitoring network	Monitoring of the marine environment	https://www.bsh.de/EN/DATA/Marine_environment_monitoring_network/marine_environment_monitoring_network_node.html
SHARK	Swedish Ocean Archive	Marine observational data from the Swedish monitoring program	http://sharkweb.smhi.se
SMHI	Swedish Meteorological and Hydrological Institute	Swedish center for weather forecasts and climate scenarios	http://www.smhi.se
ROOS	Regional Ocean Observing System	Coordinated operational oceanography research and services in	http://eurogoos.eu/regional-operational-oceanographic-systems/
UERRA	Uncertainties in Ensembles of Regional Reanalyses	Atmospheric reanalysis data used *inter alia* as atmospheric forcing for ocean models	http://www.uerra.eu/
WCRP	World Climate Research Program	Analysis and prediction of Earth system change	https://www.wcrp-climate.org/
WMO	World Meteorological Organization	Intergovernmental organization with a membership of 191 Member States and Territories	https://www.wmo.int/

surface temperature, salinity, DO and fluorescence etc. in 1–7 day sampling interval), moorings (hourly sampling of met-ocean variables, T/S, currents, turbidity, DO and chlorophyll fluorescence) and shallow water Argo profilers (T/S, DO and chlorophyll fluorescence in 1–7 day sampling interval). Low frequency (mostly monthly or less frequent) observations are made by research vessels. Most of the operational observations cover the coastal water, only a few moorings, Argo profiler and ship stations cover the open Baltic Sea. In recent years, the shallow water Argo profiler has been demonstrated as an efficient tool for monitoring hydrographic conditions in operational mode (Haavisto et al., 2018). There is also a potential to derive the currents from the shallow water Argo profilers (Roiha et al., 2018).

A recent survey on the observational infrastructure to BOOS members showed that the member institutes (not including Russian) own or have access to 211 tide gauges, 7 shallow water Argo floats, 29 buoys, 22 Research Vessels (R/Vs), 6 Remotely Operated Vehicles (ROVs, e.g., gliders), 22 Acoustic Doppler Current Profilers (ADCPs), 25 other fixed stations and 23 FerryBoxes. Not all of them are used for operational observing. Most of the R/Vs are used for research and/or regular basin wide environmental monitoring, coordinated by HELCOM.

Data Management

BOOS partners share their observations through a ftp-network. This forms a basis for Baltic Sea *in-situ* Thematic Assembling Center (BAL INS-TAC) in CMEMS and EMODnet (European Marine Observation Data Network) Physics, which provide open and free operational data access to users.

Major Challenges

The final goal for Baltic Sea observing is to build up a sustainable, integrated, and cost-effective observing system, which can fit for multi-purpose for operational, climate, commercial, and ecological applications. BOOS observing will be an important subsystem. Major gaps in the existing BOOS observational network for operational oceanography are lack of current measurements and profile observations (especially for biogeochemical variables) in the open Baltic Sea (She, 2018b; Le Traon et al., 2019). Key questions have to be answered: how observations from other sectors can be used to fill the gaps; if new observations are needed, which sampling schemes and technologies should be applied and how to be combined to generate a cost-effective gap-filling solution.

Operational Modeling—Current Status and Major Challenges

The operational modeling activities in the Baltic Sea is coordinated by BOOS Modeling Program (BMP) and CMEMS BAL MFC (Baltic Sea Monitoring and Forecasting Center), including joint research on operational model system development, data assimilation, model calibration and validation (cal/val), multi-model ensemble forecast, products generation, and services.

Model Development

Operational modeling has a long history in the Baltic Sea. The ocean wave forecast model (WAM) was developed in Europe in the 1980s (WAMDI, 1988). Operational wave forecasts were implemented in the late 1990s in Denmark and Finland (She and

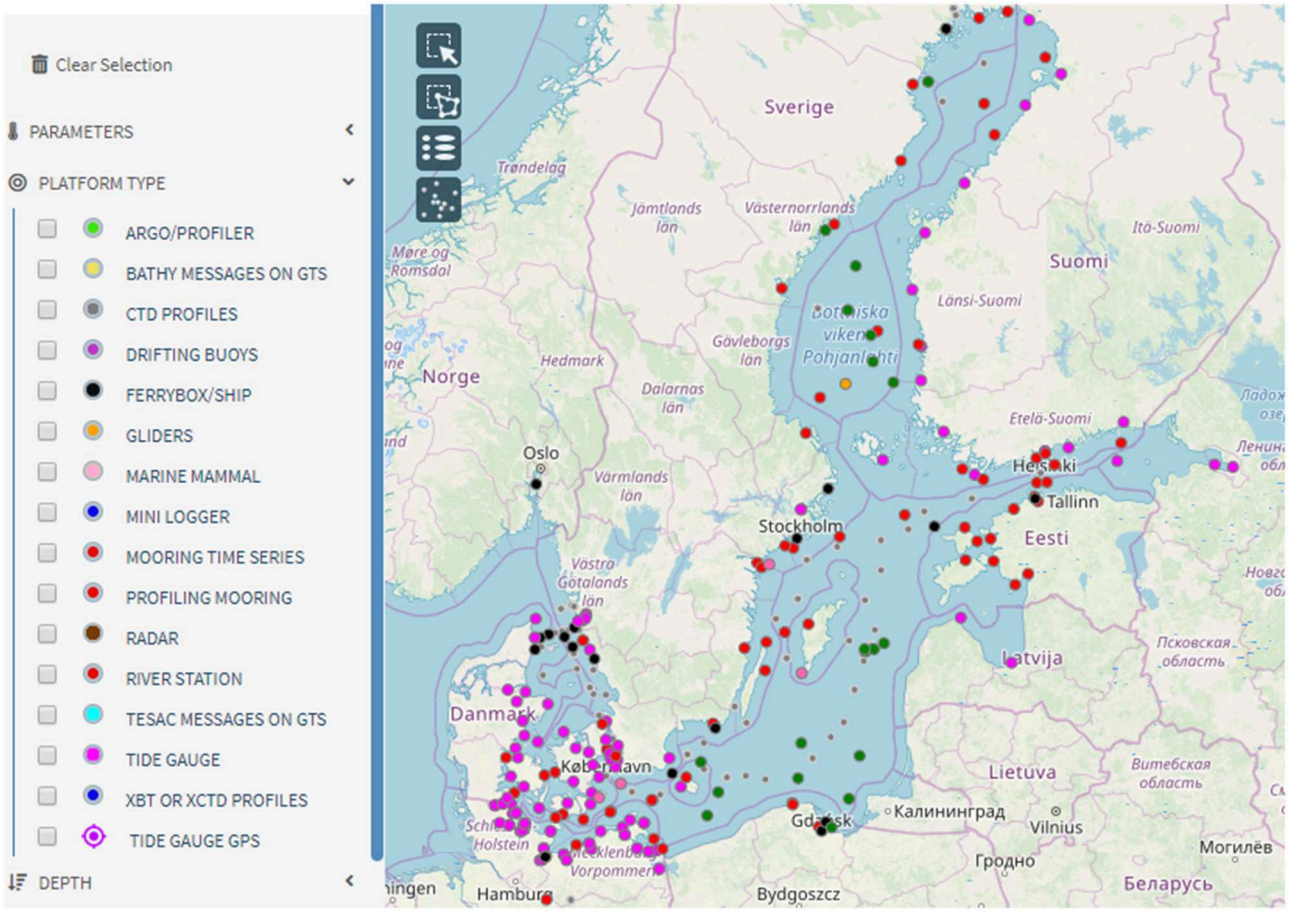

FIGURE 1 | Station distribution of operational observations in the Baltic Sea.

Nielsen, 1999; Tuomi et al., 1999) based on the WAM model. Ocean, ice and oil drift forecast models BSH-Cmod, BSH-Dmod, HIROMB, and HELMI had been developed and operationalized in the early and mid-1990s (Haapala and Leppäranta, 1996; Dick et al., 2001; Wilhelmsson, 2002; Funkquist and Kleine, 2007). They are currently updated by more advanced coupled ocean-ice forecasting systems HBM (HIROMB-BOOS Model, Berg and Poulsen, 2012), NEMO-Nordic (Hordoir et al., 2018), and GETM (General Estuarine Transport Model, Burchard and Bolding, 2002; Büchmann and Söderkvist, 2016). HBM is a dynamically two-way nested model with excellent hybrid parallel computing performance (Poulsen et al., 2014). NEMO is the European operational model with the largest user community. GETM has advantages in resolving the coastal-estuary continuum with specific advances in turbulence closure schemes and reduced diapycnal mixing due to the usage of vertically adaptive coordinates (Burchard et al., 2009). Biogeochemical models such as ERGOM (Neumann, 2000; Maar et al., 2011) and SCOBI (Swedish Coastal and Ocean BIogeochemical model, Eilola et al., 2009) have been developed in this century for setting up operational ecological service. The former has been used to provide basin-scale biogeochemical forecasts for CMEMS since 2009 (Tuomi et al., 2018) while the latter was used for producing biogeochemical reanalysis (Liu et al., 2017). The above operational model systems have been applied for basin-scale forecasts in 0.5–1 nautical mile (nm) resolution and a up to 60 m resolution for local scale forecasts (She and Murawski, 2018). Coupled model development, especially wave related coupling processes, e.g., ocean-wave, atmosphere-wave, and wave-ice interaction, is an on-going activity by BOOS partners. In the Phase II of CMEMS BAL MFC (2018–2021), a fully coupled ocean-wave-ice-biogeochemical model system NEMO-LIM-WAM-ERGOM together with PDAF (Parallel Data Assimilation Framework) assimilation is under development.

Data Assimilation

Significant data assimilation capacity has also been developed in the operational community, ranging from a simplified Kalman Filter for sea surface temperature (SST) assimilation in BSH-Cmod (Larsen et al., 2007), pre-operational 3DVAR (3D Variational method), and EnOI (Ensemble OI) for T/S assimilation and reanalysis production in HBM (Zhuang et al., 2011; Fu et al., 2012) to the ensemble variational method and PDAF simplified Karman filter for physical-biogeochemical

reanalysis production in RCO-SCOBI and NEMO-SCOBI (Axell and Liu, 2016; Liu et al., 2017). Currently the Baltic Sea data assimilation collaboration in CMEMS focuses on developing physical and biogeochemical assimilation systems by using the PDAF both for operational NRT forecast and also for reanalyses. Assimilation schemes for SST, T/S, sea ice and nutrients are relatively mature. New schemes are developed for assimilating sea level and satellite ocean-color data (Tuomi et al., 2018).

Model Quality and Validation

Before 2009, the operational model validation and quality assessment were mainly done at national level with different methods and quality standards. Common cal/val methodology had been developed and applied in the MyOcean projects (2009–2015), including cal/val metrics definition and error statistics calculation and presentation for new model version, NRT validation and reanalysis quality assessment. The cal/val has been part of the BAL MFC operational activities since 2015. Before release of each new BAL MFC model version—both forecasting and reanalysis systems, a correspondent QUID (Quality Information Document) report has to be released to demonstrate the quality of the new version products (e.g., Golbeck et al., 2017). The NRT validation for the BAL MFC forecast products (ocean-ice-wave-biogeochemical parameters) is shown online at the BOOS website. The cal/val method and toolbox developed in the BAL MFC is now further extended to a BOOS model quality and validation cooperation.

Multi-Model Ensemble (MME) Forecasting

Based on NRT exchange of both model and observational data via the BOOS ftp network, a MME forecast system has been developed for sea level, SST, sea surface salinity (SSS), T/S and currents (Golbeck et al., 2015). By weighting the individual forecast related to its forecasting error, a weighted MME method is used to generate the MME forecast. The results, shown online at the BOOS website, demonstrate superior quality of the MME forecast to the individual ones. The MME is a joint achievement of ROOSs and MFCs in the Baltic and North Sea. Currently the BOOS MME Working Group aims at extending the current MME system for national forecasting use.

Major Challenges

Future direction of the operational modeling in the Baltic Sea is seamless modeling in spatial, temporal, and state variable dimensions (WMO, 2015; She and Murawski, 2018). In spatial scales, the modeling capacity will be extended from basin scale to local coastal-estuary scale and from mesoscale to sub-mesoscale. In temporal scales, the synoptic and climate scales will be resolved by the same operational modeling framework. For state variables, future operational modeling capacity (including forecast, reanalysis, and scenario-based projections) will be extended to cover sedimentation, movements of pollutants (either as particles or Eulerian tracers) and biological parameters. In this dimension, operational ecological modeling will be developed, different modeling sectors will be coupled, e.g., hydrological-ocean coupling, wave-ocean and wave-ice coupling, and ocean-optical coupling.

There still exist many knowledge gaps toward the establishment of the seamless operational service. Monitoring and accurate modeling of water and biogeochemical mass transport caused by coastal-estuary interaction, inter-sub-basin exchange and meso- and submeso-scale eddies is still a challenge. Capacities for precisely predicting currents, upwelling, extreme sea level and waves in icing waters, skin temperature, algae bloom, and oxygen depletion are yet to be improved.

BALTEX/BALTIC EARTH MARINE RESEARCH

In the following, a few selected research highlights from BALTEX/Baltic Earth are presented, documenting the progress in physical oceanography of the Baltic Sea during 2003–2014 (Omstedt et al., 2004, 2014; see also BACC Author Team, 2008; BACC II Author Team, 2015) and after. One of the main motivations for the foundation of BALTEX in the 1990s was the exchange of data between eastern and western Baltic Sea countries. Due to the Iron Curtain after World War II, the exchange of scientific information was limited. Hence, after the rise of the Iron Curtain in the 1990s BALTEX aimed to enhance international collaboration between the Baltic Sea countries and to increase the exchange of especially observational data.

Process Understanding

With the help of project-oriented research data and process modeling, our knowledge about oceanographic processes and the interactions of the ocean with the other components of the Earth system such as atmosphere, land surface and sediments has considerably increased since the start of BALTEX (Omstedt et al., 2004, 2014). For instance, the importance of surface waves in air–sea interaction of heat, momentum, and matter is better understood, and Stokes drift and Langmuir circulation have been identified as likely playing an important role in surface water mixing explaining the underestimation of mixed layer depth in many Baltic Sea models (Reissmann et al., 2009).

Research on water exchange between the Baltic Sea and North Sea and saltwater inflows into the Baltic has a long tradition. Today we know that, on average, half of the total amount of salt imported into the Baltic is supplied by barotropic inflows of highly saline water (Mohrholz, 2018). In particular, the well-observed, exceptionally strong Major Baltic Inflow (MBI) of 2014 (Mohrholz et al., 2015) enabled unprecedented, detailed studies of the dynamics of saltwater inflow events and of their implications for the ecosystem (e.g., Gräwe et al., 2015; Schmale et al., 2016; Holtermann et al., 2017; Bergen et al., 2018). In a long-term average MBIs contribute 20 to 25% to the total salt import into the Baltic (Mohrholz, 2018), beside this they are the solely mechanism for deep water ventilation of the central Baltic (Meier et al., 2006). Despite the decrease of nutrient supply after the 1980s, recently observed oxygen consumption rates are higher than ever observed (Meier et al., 2018b). According to model results, oxygen consumption in the water column

has increased relatively more than oxygen consumption in the sediment. Subsequently, natural ventilation has become less effective representing a positive feedback for hypoxia (Meier et al., 2018b).

Observations from field campaigns from the northern Baltic Sea suggested that the flow regimes are intermittent and that hydraulic control occurs in only about 55% of the cases, i.e., less frequently than anticipated (Green et al., 2006). Further, in wider gravitational flows, transverse Ekman circulation was identified to be an important process for the generation of mixing (Umlauf and Arneborg, 2009a,b).

Recently, there has been increased research into the Baltic Sea coastal zone, particularly into upwelling, nutrient retention and the coastal filter capacity of nutrients (e.g., Edman et al., 2018). Estimates suggest that the coastal filter of the entire Baltic Sea removes 16% of nitrogen and 53% of phosphorus inputs from land (Asmala et al., 2017). Simulated long-term nutrient retention was found to be associated with the physical characteristics of a water body, such as the surface area, depth and residence time of the water.

Progress was also made in understanding the large-scale circulation, water mass transformations, and mixing processes in the Baltic Sea using high-resolution ocean circulation models that were running for many decades together with Eulerian concentration and age tracers (e.g., Meier, 2005, 2007). The model results illustrate possible pathways and ages of either inflowing saline water from the North Sea or freshwater originating from the various rivers. Freshwater is found to be subject to an efficient recirculation in the Baltic (e.g., Rodhe and Winsor, 2002). These simulations are complementary to an interesting tracer release experiment in the deep water of the central Gotland Basin showing a considerable increase in vertical mixing rates after the tracer reached the lateral boundaries of the basin (Holtermann and Umlauf, 2012; Holtermann et al., 2012). Hence, boundary mixing is perhaps the key process of basin-scale vertical mixing. For further details, the reader is referred to the review article by Omstedt et al. (2014) and the original literature cited therein.

Climate and Environmental Observations and Reanalyses

Nowadays, meteorological databases (both station data and high-resolution gridded datasets) are freely available with high quality to force ocean models on decadal and even centennial time scales. For instance, the regional reanalysis project Uncertainties in Ensembles of Regional ReAnalyses (UERRA, http://www.uerra.eu) delivers homogenous atmospheric surface fields for the period 1961 until today. In addition, oceanographic data became more easily accessible and new important measurement platforms, such as the MARNET stations (https://www.io-warnemuende.de/marnet-en.html), long-term moorings, e.g., in the Gotland Deep region, FerryBoxes, and satellites, have provided temporally and spatially better resolved observations. River runoff data are crucial for the understanding of the Baltic Sea dynamics and new catchment-wide high-resolution datasets based on process-based hydrological modeling calibrated to available station data are now available. However, a homogeneous hydrological dataset that covers the entire period from the 1960s to the present day comparable to atmospheric reanalysis data is still missing. Further, available nutrient load and other environmental data are nowadays collected and stored in publicly available databases.

A big step forward to understand climate variability in the Baltic Sea region was the development of historical reconstructions of atmospheric, hydrological and oceanic datasets since around 1850. With the help of Baltic Sea models, the impact of increasing nutrient loads and climate change on the marine ecosystem was detected and attributed to the various drivers of the system. We have now a better understanding of the natural variability in the Baltic Sea region and how large-scale atmospheric circulation affects the Baltic Sea climate variability (e.g., Börgel et al., 2018). During recent decades, changes in large-scale atmospheric circulation have caused a north-eastward shift in low-pressure tracks consistent with a more zonal circulation over the Baltic Sea basin (e.g., Trenberth et al., 2007). The decadal and multi-decadal regional variability of the past climate is partly explained by the North Atlantic Oscillation (NAO, mainly during winter) and the Atlantic Multi-decadal Oscillation (AMO). Despite the pronounced internal variability, trends were detected that could probably be attributed to anthropogenic climate change on centennial time scale (e.g., Kniebusch et al., 2019a,b). A highlight was the revision of the empirically derived barotropic saltwater inflow statistics for 1887 until present that shows no statistically significant trend but the same multi-decadal variability as in precipitation data (Mohrholz, 2018). Further, based upon model results it was concluded that stagnation periods such as the one between 1983 and 1992 are part of the natural variability of the system and occur once per 100 years on average (Schimanke and Meier, 2016).

While atmospheric reanalysis data have long been used to force ocean models, long-term reanalyses for the ocean on multi-decadal time scales became only recently available including both physical and biogeochemical variables (e.g., Liu et al., 2017). Ocean reanalysis data play an important role for the development and evaluation of ocean models (Placke et al., 2018).

Climate and Environmental Modeling

Within BALTEX, the first coupled atmosphere-ice-ocean regional models were developed about 20 years ago (Gustafsson et al., 1998; Hagedorn et al., 2000; Döscher et al., 2002; Schrum et al., 2003). Nowadays several coupled models for the Baltic Sea—North Sea system are under development (e.g., Gröger et al., 2013; Tian et al., 2013, 2016; Van Pham et al., 2014; Wang et al., 2015; Ho-Hagemann et al., 2017). Regional climate models contributed to a better quantitative understanding of the energy and water cycles of the Baltic Sea basin. However, especially processes important for the regional water cycle are still not well-understood causing, *inter alia,* precipitation and runoff biases over the catchment area in long-term atmosphere climate simulations with considerable impact on the quality of ocean climate simulations (Meier et al., 2019).

These models will be the future tools to investigate the dynamics of regional Earth systems. Within Baltic Earth a

dedicated WG on regional climate system models (RCSMs) is planning and performing coordinated experiments of an ensemble of RCSMs with the aim to improve coupled models, to exchange expertise and to investigate the added value of RCSMs. Based upon the dynamical downscaling approach using RCSMs with lateral boundary data from global climate models, paleo-climate simulations of the past 1,000 years (e.g., Schimanke et al., 2012) and projections of the twenty-first century were performed (e.g., Meier et al., 2018a; Dieterich et al., 2019; Gröger et al., 2019). As the sizes of the ensembles were relatively large, they allowed to estimate uncertainty ranges and to identify the sources of uncertainties. For further details, the reader is referred to the review article by Meier et al. (2019) and the original literature cited therein.

Ongoing Activities

Following the original idea of identifying knowledge gaps (Baltic Earth Science Plan Writing Team, 2017), currently a series of extensive Baltic Earth Assessment Reports (BEAR) is in preparation. For each of the GCs, a team of experts from the Baltic Earth network has started to collect information from scientific publications to summarize the current state of knowledge in the respective research fields and to identify knowledge gaps. In addition, one of these assessments will be the BACC III report, an update of the knowledge recently gained after the publication of the comprehensive BACC I and II reports (BACC Author Team, 2008; BACC II Author Team, 2015). As for the previous two BACC reports, a close collaboration between Baltic Earth and HELCOM is envisaged. For the update of the Baltic Sea Action Plan (BSAP), climate change will be considered. Moreover, Baltic Earth scientists participate in the HELCOM—Baltic Earth Expert Network on Climate Change (EN CLIME) that will produce a Climate Change Fact Sheet for policy makers and the public based upon BACC results. Assessments of our knowledge on the regional Earth system (including aspects of processes, climate, and environment) are an integral part of Baltic Earth.

OPERATIONAL OCEANOGRAPHY AND BALTIC EARTH RESEARCH—INTERACTIONS

Use of Operational Observing for Baltic Earth Research

Due to the operational feature of the observation production, quality control and open and free dissemination, the operational data are useful to all kinds of users, ranging from research, ecosystem-based management, climate change adaptation, and mitigation to blue economy information service. For the Baltic Earth research, the BOOS observations are especially valuable due to three reasons: (i) long history: operational monitoring of temperature, salinity, sea level, currents and ice started 100 years ago; (ii) the high resolution observations provide rich information on hydrographical and biogeochemical processes, and (iii) NRT delivery of data ensures timely access. The historical operational observations are the major data source of the climate data archive in the sea. However, a significant part of them has not been digitized, e.g., Finnish ice charts (since 1915) and Danish sea level, T/S, currents and ice measurements before 1930. High-resolution SST and sea ice products in the past 100 years are essential in the reconstruction of accurate atmosphere-ocean states. The high-frequency sea level observations can be used for studying important ocean processes in scales of hours to a few weeks, e.g., storm surges, coastal waves, basin-scale sea level dynamics (GCs 1, 3, and 4). FerryBox and shallow water Argo floats data can be used for investigating processes of sub-mesoscale and mesoscale eddies, river plumes and coastal-estuary interaction, inter-subbasin water exchange, upwelling, ocean heat content anomaly, algae bloom and oxygen depletion etc. Mooring observations, with hourly measurements and more parameters, in addition to the above usages, are also suitable for studying the diurnal variation of SST, chl-a and trophic layer optical features.

Considering the free and 24/7 (all time) availability of the BOOS data, any research field campaign should use them as background observations, for the design of the campaign sampling schemes whenever necessary. The research observing program can also consider joint observing activities by mobilizing the observing infrastructure from the BOOS members.

Use of Operational Modeling for Baltic Earth Research

The operational modeling platforms, products (both short- and long-term) and data assimilation and cal/val tools, as described in section BALTEX/Baltic Earth marine research, can be used for the Baltic Earth research, for example,

1. Reconstruction of past hydrodynamic and biogeochemical state: decadal ocean-ice-wave-biogeochemical reanalysis and reprocessed satellite and *in-situ* observation products from CMEMS provide ready to use data for the GCs 1, 3, 4, and 5.
2. The operational cal/val toolbox developed in the BAL MFC can be applied and further developed for evaluating climate models
3. Downscaled operational models are capable of predicting small-scale variability in up to tens-of-meter resolution. Some of them are computationally so efficient that they can be applied in climate simulations with very high resolution (GCs 2, 5, and 6)
4. The short-term operational products, e.g., forecast, interim reanalysis, can be used for studying the natural hazards and extreme events (GC3)
5. End-to-end modeling: the solid operational products can provide robust inputs (ocean-ice-wave-biogeochemical variables) to end-to-end modeling (GC6)

Potential Contribution From Baltic Earth Community to Operational Oceanography

Operational Observing

Research observations from the Baltic Earth community, if they can be adapted to meet operational requirements, will be very useful for filling the gaps of the BOOS observational network. ICES database collects ship observations from the HELCOM

monitoring program, fishery monitoring and some research projects, which has a much better coverage then the BOOS network in the open Baltic Sea. Most of the research observations are not in real or near real time. The research observing program can be made to fit for the operational application through open data policy and NRT data delivery, which will fill the observational data gaps. For example, research data from classical observations like CTD can be made available in NRT before the final processing for (climate) research. Vice versa, good quality operational observations can be used for (climate) research after appropriate quality control and exposing it to appropriate processing in delayed mode.

Operational Modeling

The research on the six GCs by the Baltic Earth community is highly relevant to improve the operational modeling capacity. By revealing important factors controlling the salinity and sea level dynamics, results from the GCs 1, 4, and 5 can be used to improve the long-term performance of operational ocean models. The GC2 research can be used to improve the downscaled models for resolving coastal-estuary continuum. The GC3 may find new features and knowledge regarding to the extreme events, which are always challenge cases in the operational modeling. The GC6 and GC2 research may benefit emerging areas of operational modeling, e.g., operational ecological modeling, coupled ocean-hydrological modeling and sediment transport modeling etc.

In order to benefit the operational modeling, there should be a platform to transform the Baltic Earth research results into the operational models. This is similar to the "Service Evolution" element in the CMEMS where dedicated, short-term mini-R&D projects are funded to transfer the best practice in modeling and observing research into CMEMS system.

DISCUSSIONS AND RECOMMENDATIONS

The Baltic operational oceanography community and the BALTEX/Baltic Earth community have co-existed in the past two/three decades. However, only very preliminary interactions have been carried out because differing objectives of both communities hampered an intensive collaboration as outlined below.

Through analysis of the state-of-the-art of operational oceanography and regional Earth system research, it was found that the operational observations, modeling platforms, and products can significantly benefit the Baltic Earth research, e.g., in the areas of the six grand challenges, while the Baltic Earth research can also benefit operational oceanography. Most of the research databases such as the Baltic Environmental Database (BED, http://nest.su.se/bed) at Stockholm University, the Swedish Ocean Archive (SHARK, http://sharkweb.smhi.se) and all other environmental databases operated by the Swedish Meteorological and Hydrological Institute (SMHI) and the German Baltic Sea monitoring data archive (IOWDB, http://iowmeta.io-warnemuende.de and https://odin2.io-warnemuende.de/) operated by the Leibniz Institute for Baltic Sea Research Warnemünde (IOW) are already open access. In the future, a common database including both operational and research data may be established. In Europe, EMODnet has integrated marine observations, both online and offline data, in the entire parameter domain ranging from physical, biogeochemical, biological to human activities. In future, it may play a more important and active role for linking research observations and operational oceanography. However, for the research of, for instance, detecting ocean changes high accuracy of measurements is needed which is today not assured by all operational data products. The calibration of measurement devices is time consuming and expensive. Quality control is also the reason why not all research data of IOWDB and other databases can be provided in real or near real time.

Research observations can be an important complementary in emerging observations for developing operational ecology, predicting the fate of visible, and invisible marine plastics in the Baltic Sea, modeling and forecasting sediment transport, underwater noise etc. For these areas, operational observing capacity has not been established yet. They will need to heavily rely on data from research projects.

As mentioned above, reanalysis data sets are useful for climate analysis and for the evaluation of climate models used within Baltic Earth. However, current reanalysis data sets are usually not based on first principles, i.e., the conservation of mass, energy and momentum. Hence, many data assimilation schemes may cause problems, for instance, for budget and flux calculations of nutrients (Liu et al., 2017). This may lead to problems when using reanalysis for trend and long-term variability analyses. Hence, reanalysis products should be improved for the climate research purpose by using more mass and energy conserved assimilation method, e.g., 4D variational assimilation.

Research observing infrastructure should be made more usable for various applications. Examples of observing systems that fulfill such a criterion are the Australian IMOS (Integrated Marine Observing System, Hill et al., 2009) system, the German COSYNA (Coastal Observing System for the Northern and Arctic Seas, Baschek et al., 2017) and the IOW long-term monitoring program outside the German territorial waters. Although funded as a research infrastructure, the programs provide openly accessible observations, which can be used for many other purposes. These systems have been operated for more than 10 years.

The new knowledge made from the Baltic Earth research, both on the processes and model system development, can be transferred to the operational models, which will fill the knowledge and technological gaps in the operational modeling. The two communities should have regular joint meetings to identify topics with common interests and make the technology transfer from regional Earth system research to operational oceanography. For such a working group Baltic Earth would provide an ideal discussion platform. Unfortunately, state-of-the-art climate and operational ocean model versions usually differ although some institutes aim to have only one version for both applications. However, in reality two model versions are still needed because not all processes are well-enough understood such that their parameterizations fulfill the requirements of both applications on short and long time scales. An example is diapycnical mixing. Climate models require that long-term

simulations do not artificially drift whereas data assimilation can always compensate shortcomings in operational mode. The development of operational oceanography in the last two decades, by integrating field monitoring, research (knowledge generation), operation and service, has demonstrated successfully the value chain of ocean research. In the Baltic Sea region, the future research is moving to an Earth system scale and be more responsive, the operational and adaptive level of the services for marine, climate, environment, and fishery are evolving. The value chain practiced by the operational oceanography is similar to other areas, e.g., Earth system research and environment protection. Seamless monitoring, modeling, and service provides a unified platform for integrating the research and services.

Next generation operational service system needs capacities on reconstructing, forecasting and projecting the states of marine ecosystems in basin and coastal waters. Significant new knowledge is needed for understanding and forecasting ocean processes such as inter-basin and sub-basin transport, sub-mesoscale eddies, coast-estuary interaction, sediment transport, algae bloom, oxygen depletion, and marine litter transportation. An idea solution is to carry out monitoring-modeling integrated and targeted research programs in the Baltic Sea scale (She et al., 2016). Joint force from BOOS and Baltic Earth community is a great advantage for responsive and collaborative research on the development of seamless service capacities, from synoptic to climate scales, from open sea to local waters, from physical to biological subsystems. During the procedure, scientific issues e.g., Baltic Earth GCs and interactions and coupling between different subsystems, will be addressed. Well-designed research programs should cover not only dedicated field experiment and new knowledge generation but also knowledge transfer into seamless operational model system and product service.

Naturally BOOS and Baltic Earth will consider to engage other important Baltic networks such as HELCOM, ICOS, and ICES in their cooperation as Baltic Earth and BOOS already collaborate with them. Within EN CLIME Baltic Earth and HELCOM are working together to produce a climate fact sheet and HELCOM and ICES representatives are members of the Baltic Earth Advisory Board. In the upcoming EuroSea project, BOOS and HELCOM partners will work together on improving fast delivery of HELCOM data to BOOS and a delivery of a better reanalysis to HELCOM by BOOS to assimilating HELCOM data. HELCOM is also an important stakeholder for both BOOS and Baltic Earth communities. Many projects carried out by BOOS and Baltic Earth partners, such as Baltic Sea Check Point, CLAIM, ECOSUPPORT, address HELCOM goals. HELCOM monitoring is an important source of biogeochemical and biological (lower trophic level) observations for both research and operational services. Carbon observations from ICOS and biological observations collected by ICES are important to BOOS future priority on operational ecology and Baltic Earth System studies.

Recommendations

BOOS and Baltic Earth communities share similar basic research instruments, i.e., monitoring and modeling. Their human resources are also overlapping to a certain degree: most of BOOS partners are also Baltic Earth partners. Collaboration between BOOS and Baltic Earth can help in understanding the climate change influence on the Baltic Sea region in many aspects. For example, adaptation of well-calibrated, high resolution operational models (both local and basin scales) to climate scales can help to reach the last mile to the end users in climate applications. High resolution BOOS observations, e.g., from moorings, ferrybox and shallow water Argo profilers, can benefit for Baltic Earth system process studies, especially for extreme events e.g., salty water inflow, storm surge, marine heat wave, oxygen depletion and algae bloom. The CMEMS ocean reanalysis, with an operational update to months, can provide comprehensive data for most recent changes of climate signals especially statistics of extreme events, although trend analysis from the reanalysis products are problematic because the number of observations changes with time.

Hence, under the background of WMO seamless prediction of Earth systems, GOOS and EuroGOOS focus on provision of information not only for operational services but also for climate change and ocean health and for the UN Decade of Ocean Science, the two communities are motivated to have joint forces in the following two areas:

1. Harmonization and integration of existing research and infrastructure:
   - Between synoptic and climate scales:
     - Harmonizing model calibration and validation methods for operational and climate scales: Most of the operational models running by BOOS partners have regular calibration and validation. In BAL MFC, such procedure has been standardized based on a continuous effort since 2004 for developing Copernicus Marine Service. This includes models both for near real time forecast and long-term reanalysis. Also the Baltic Earth community has organized several multi-model inter-comparisons and validation studies, mainly for climate scales. The most recent Baltic Earth project is BMIP. The two task forces should harmonize the efforts and aim to reach a more general, standardized calibration and validation procedure for both operational and climate models.
     - Adapting calibrated operational models for climate study: Although many institutes still use different models for operational forecast and climate study, there is a trend that more and more models are developed for both forecast and climate modeling. However, there still exist technical challenges when using an operational model for climate purpose. Some adaptations of the operational models to climate modeling are still needed.
     - Extending the operational forecast range from synoptic to climate scales (seasonal and decadal predictions): The Baltic Sea is dominated by many slow processes such as seasonal stratification and sea ice, saltwater inflows, water stagnation, and ventilation. Hence, the predictability of seasonal to decadal variability should be investigated in an Earth system framework and forecasting capability

should be developed for the corresponding scales with high predictability.

- From physical ocean to ocean system and Earth system:
  - End-to-end Earth system modeling: BOOS and Baltic Earth partners from weather and climate, environmental and fishery institutes should work together to jointly develop end-to-end Baltic Earth system modeling framework, including human pressure models, atmospheric models, physical and biogeochemical ocean models, higher trophic level food-web models and socioeconomic models. Such modeling framework can be used both at basin and national levels to support ecosystem-based management and climate change adaptation.
  - Data integration: Multi-disciplinary observations, ranging from air, water, seabed and human activity, should be collected and disseminated centrally to serve multiple operational and research purposes. Currently, BOOS and Baltic Earth are working independently for their own purposes in this area. Hence, it is recommended that a common data infrastructure for both research and operational observations should be established.
  - Extending forecast from physical ocean to marine ecosystem and to the entire Earth system: operational (coupled) Earth system model should be developed for the Baltic Sea, considering the interactions between atmosphere-ocean-wave-sea ice-marine biogeochemistry-land surface systems.
- Between local and basin scales:
  - Stakeholders concern in many cases local applications in relation to climate change, e.g., in the coastal-estuary-catchment continuum. Basin-scale model systems are too coarse for these applications. BOOS partners have developed very high resolution operational models to address local challenges such as storm surges, coastal flooding and eutrophication. However, these local model systems are mainly applied for short time scales. Hence, also for climate applications high-resolution coastal zone models two-way nested into basin-wide Earth system models should be developed.

2. Optimizing research instruments and products:
   - Monitoring network: The Baltic Sea monitoring network, including operational, environmental, fishery, and research should be harmonized and optimized through fit-for-purpose assessment, breaking institutional barriers and cost-effective sampling design. Especially, requirements and current gaps for observations for operational Earth system prediction and long-term Earth system study should be identified.
   - Modeling platforms: Standards for the next generation of Baltic Earth system models should be defined; common technical challenges for both operational, and climate models should be identified. Joint forces can be made for improving especially high performance computational efficiency, grid flexibility, and model coupling interfaces for targeted model systems.

AUTHOR CONTRIBUTIONS

All authors contributed in writing, with JS as lead author and main author on operational oceanography, HM as main author on Baltic Earth and VH as main author on BAL MFC.

FUNDING

Funds for supporting this publication is from Danish Meteorological Institute.

REFERENCES

Asmala, E., Carstensen, J., Conley, D. J., Slomp, C. P., Stadmark, J., and Voss, M. (2017). Efficiency of the coastal filter: nitrogen and phosphorus removal in the Baltic Sea. *Limnol. Oceanogr.* 62, S222–S238. doi: 10.1002/lno.10644

Axell, L. (2013). *BSRA-15: A Baltic Sea Reanalysis 1990-2004*. Reports Oceanography, 45. Swedish Meteorological and Hydrological Institute, Norrköping, Sweden.

Axell, L., and Liu, Y. (2016). Application of 3-D ensemble variational data assimilation to a Baltic Sea reanalysis 1989–2013. *Tellus A* 68:1. doi: 10.3402/tellusa.v68.24220

BACC Author Team (2008). *Assessment of Climate Change for the Baltic Sea Basin*. Regional Climate Studies. Berlin; Heidelberg: Springer-Verlag.

BACC II Author Team (2015). *Second Assessment of Climate Change for the Baltic Sea Basin.* Cham: Springer.

Bahurel, P., Adragna, F., Bell, M. J., Jacq, F., Johannessen, J. A., Le Traon, P.-Y., et al. (2010). "Ocean Monitoring and Forecasting Core Services, the European MyOcean Example," in *Proceedings of OceanObs'09: Sustained Ocean Observations and Information for Society*, eds J. Hall, D. E. Harrison, and D. Stammer (Venice: ESA Publication WPP-306). doi: 10.5270/OceanObs09.pp.02

Baltic Earth Science Plan Writing Team (2017). *Baltic Earth Science Plan 2017*. International Baltic Earth Secretariat Publication No. 11, February 2017.

Baschek, B., Schroeder, F., Brix, H., Riethmüller, R., Badewien, T. H., Breitbach, et al. (2017). The coastal observing system for northern and arctic seas (COSYNA). *Ocean Sci.* 13, 379–410. doi: 10.5194/os-13-379-2017

Berg, P., and Poulsen, J. W. (2012). *Implementation Details for HBM*. DMI Technical Report No. 12–11 (Copenhagen), 149. Available online at: www.dmi.dk/fileadmin/Rapporter/TR/tr12-11.pdf.

Bergen, B., Naumann, M., Herlemann, D. P. R., Gräwe, U., Labrenz, M., and Jürgens, K. (2018). Impact of a Major inflow event on the composition and distribution of bacterioplankton communities in the Baltic Sea. *Front. Mar. Sci.* 5:383. doi: 10.3389/fmars.2018.00383

Börgel, F., Frauen, C., Neumann, T., Schimanke, S., and Meier, H. E. M. (2018). Impact of the Atlantic Multidecadal Oscillation on Baltic Sea Variability. *Geophys. Res. Lett.* 45, 9880–9888. doi: 10.1029/2018GL078943

Buch, E., and Dahlin, H. (2000). *BOOS Plan. Baltic Operational Oceanographic System 1999–2003*. EuroGOOS Publications nr, *14*.

Buch, E., Elken, J., Gajewski, J., Haakansson, B., Kahma, K., and Soetje, K. (2006). "Baltic Operational Oceanographic System BOOS," in *2006 IEEE US/EU Baltic International Symposium on Integrated Ocean Observation*

Syst. for Managing Global & Regional Ecosys. Marine Resch, 1–5. doi: 10.1109/BALTIC.2006.7266162

Büchmann, B., and Söderkvist, J. (2016). Internal variability of a 3-D ocean model. *Tellus A* 68. doi: 10.3402/tellusa.v68.30417

Burchard, H., and Bolding, K. (2002). *GETM A General Estuarine Transport Model. Scientific Documentation.* Technical Report EUR 20253 EN. Ispra: European Commission. Available online at: https://getm.eu/

Burchard, H. F., Janssen, K., Bolding, L., and Rennau, H. (2009). Model simulations of dense bottom currents in the Western Baltic Sea. *Continental Shelf Res.* 29, 205–220. doi: 10.1016/j.csr.2007.09.010

Cieślikiewicz, W., Connolly, N., Ollier, G., and O'Sullivan, G. (editors.) (2007). *Proceedings of the EurOCEAN 2004 European Conference on Marine Science & Ocean Technology*. Published by European Commission, 420.

Dick, S., Kleine, E., and Müller-Navarra, S. (2001). *The Operational Circulation Model of BSH (BSH cmod).* Model description and validation. Berichte des Bundesamtes für Seeschifffahrt und Hydrographie 29/2001, 48.

Dieterich, C., Wang, S., Schimanke, S., Gröger, M., Klein, B., Hordoir, R., et al. (2019). Surface heat budget over the north sea in climate change simulations. *Atmosphere* 10:272. doi: 10.3390/atmos10050272

Döscher, R., Willén, U., Jones, C., Rutgersson, A., Meier, H. E. M., Hansson, U., et al. (2002). The development of the regional coupled ocean-atmosphere model RCAO. *Boreal Environ. Res.* 7, 183–192.

Edman, M., Eilola, K., Almroth-Rosell, E., Meier, H. E. M., Wåhlström, I., and Arneborg, L. (2018). Nutrient retention along the Swedish coastline. *Front. Marine Sci.* 5:415. doi: 10.3389/fmars.2018.00415

Eilola, K., Gustafson, B. G., Kuznetsov, I., Meier, H. E. M., Neumann, T., Savchuk, O. P. (2011). Evaluation of biogeochemical cycles in an ensemble of three state-of-the-art numerical models of the Baltic Sea during 1970-2005. *J. Marine Systems* 88, 267–284, doi: 10.1016/j.jmarsys.2011.05.004

Eilola, K., Meier, H. E. M., and Almroth, E. (2009). On the dynamics of oxygen, phosphorus and cyanobacteria in the Baltic Sea; a model study. *J. Marine Syst.* 75, 163–184. doi: 10.1016/j.jmarsys.2008.08.009

Ekman, M. (2009). *The Changing Level of the Baltic Sea during 300 Years: A Clue to Understanding the Earth.* Published by the Summer Institute for Historical Geophysics.

Fu, W., She, J., and Dobrynin, M. (2012). A 20-year reanalysis experiment in the Baltic Sea using three-dimensional variational (3DVAR) method. *Ocean Sci.* 8, 827–844. doi: 10.5194/os-8-827-2012

Funkquist, L., and Kleine, E. (2007). *HIROMB: An Introduction to HIROMB, an Operational Baroclinic Model for the Baltic Sea*. Report Oceanography, 37. Swedish Meteorological and Hydrological Institute, Norrkoping, Sweden.

Golbeck, I., Izotova, J., Jandt, S., Janssen, F., Lagemaa, P., Brüning, T., et al. (2017). *Quality Information Document (QUID) Baltic Sea Physical Analysis and Forecasting Product BALTICSEA_ANALYSIS_FORECAST_PHY_003_006: Issue 4.0*. Available online at: http://marine.copernicus.eu/documents/QUID/CMEMS-BAL-QUID-003-006.pdf

Golbeck, I., Li, X., Janssen, F., Brüning, T., and Nielsen, J. W. (2015). Uncertainty estimation for operational ocean forecast products – a multi-model ensemble for the North Sea and the Baltic Sea. *Ocean Dynam.* 65, 1603–1631. doi: 10.1007/s10236-015-0897-8

Gräwe, U., Naumann, M., Mohrholz, V., and Burchard, H. (2015). Anatomizing one of the largest saltwater inflows into the B altic S ea in D ecember 2014. *J. Geophys. Res.* 120, 7676–7697. doi: 10.1002/2015JC011269

Green, J. M., Liljebladh, B., and Omstedt, A. (2006). Physical oceanography and water exchange in the Northern Kvark Strait. *Continental Shelf Res.* 26, 721–732. doi: 10.1016/j.csr.2006.01.012

Gröger, M., Arneborg, L., Dieterich, C., Höglund, A., and Meier, H. E. M. (2019). Hydrographic changes in the North Sea and Baltic Sea projected in an ensemble of climate scenarios downscaled with a coupled regional ocean-sea ice-atmosphere model. *Climate Dynam.* 53, 5945–5966. doi: 10.1007/s00382-019-04908-9

Gröger, M., Maier-Reimer, E., Mikolajewicz, U., Moll, A., and Sein, D. (2013). NW European shelf under climate warming: implications for open ocean-shelf exchange, primary production, and carbon absorption. *Biogeosciences* 10, 3767–3792. doi: 10.5194/bg-10-3767-2013

Gustafsson, N., Nyberg, L., and Omstedt, A. (1998). Coupling of a high-resolution Atmospheric Model and an Ocean Model for the Baltic Sea. *Monthly Weather Rev.* 126, 2822–2846. doi: 10.1175/1520-0493(1998)126<2822:COAHRA>2.0.CO;2

Haapala, J., and Leppäranta, M. (1996). Simulating the Baltic Sea ice season with a coupled ice-ocean model. *Tellus A* 48, 622–643. doi: 10.1034/j.1600-0870.1996.t01-4-00003.x

Haavisto, N., Tuomi, L., Roiha, P., Siiriä, S.-M., Alenius, P., and Purokoski, T. (2018). Argo floats as a novel part of the monitoring the hydrography of the Bothnian Sea. *Front. Mar. Sci.* 5:324. doi: 10.3389/fmars.2018.00324

Hagedorn, R., Lehmann, A., and Jacob, D. (2000). A coupled high resolution atmosphere-ocean model for the BALTEX region. *Meteorol. Zeitschr.* 9, 7–20. doi: 10.1127/metz/9/2000/7

HELCOM (2013). *HELCOM Monitoring and Assessment Strategy*, 37. Available online at: http://www.helcom.fi/Documents/Action%20areas/Monitoring%20and%20assessment/Monitoring%20and%20assessment%20strategy/Monitoring%20and%20assessment%20strategy.pdf

Hill, K. L., Moltmann, T., Proctor, R., and Allen, S. (2009). Australia's integrated marine observing system. *Meteorol. Technol. Int.* 1, 114–120.

Ho-Hagemann, H. T. M., Gröger, M., Rockel, B., Geyer, B., Zahn, M., and Meier, H. E. M. (2017). Effects of air-sea coupling over the North Sea and the Baltic Sea on simulated summer precipitation over Central Europe. *Climate Dynam.* 49, 3851–3876. doi: 10.1007/s00382-017-3546-8

Holtermann, P. L., Prien, R., Naumann, M., Mohrholz, V., and Umlauf, L. (2017). Deepwater dynamics and mixing processes during a major inflow event in the central Baltic Sea. *J. Geophys. Res.* 122, 6648–6667. doi: 10.1002/2017JC013050

Holtermann, P. L., Umlauf, L. (2012). The Baltic Sea tracer release experiment: 2. Mixing processes. *J. Geophys. Res.* 117:C01022. doi: 10.1029/2011JC007445

Holtermann, P. L., Umlauf, L., Tanhua, T., Schmale, O., Rehder, G., Waniek, J. J. (2012). The Baltic Sea tracer release experiment: 1. Mixing rates. *J. Geophys. Res.* 117:C01021. doi: 10.1029/2011JC007439

Hordoir, R., Axell, L., Höglund, A., Dieterich, C., Fransner, F., Andersson, M. (2018). Nemo-Nordic 1.0: a NEMO based ocean model for Baltic & North Seas, research and operational applications. *Geosci. Model Dev. Discuss.* 11, 2353–2371. doi: 10.5194/gmd-2018-2

Kniebusch, M., Meier, H. E. M., and Neumann, T. (2019a). Temperature variability of the Baltic Sea since 1850 in model simulations and observations and attribution to atmospheric forcing. *J. Geophys. Res.* 124, 4168–4187. doi: 10.1029/2018JC013948

Kniebusch, M., Meier, H. E. M., and Radtke, H. (2019b). Changing salinity gradients in the Baltic Sea as a consequence of altered freshwater budgets. *Geophys. Res. Lett.* 46, 9739–9747. doi: 10.1029/2019GL083902

Larsen, J., Høyer, J. L., and She, J. (2007). Validation of a hybrid optimal interpolation and Kalman filter scheme for sea surface temperature assimilation. *J. Mar. Sys.* 65, 122–133. doi: 10.1016/j.jmarsys.2005.09.013

Le Traon, P.-Y., Reppucci, A., Fanjul, E. A., Aouf, L., Behrens, A., Belmonte, M., et al. (2019). From observation to information and users: the Copernicus Marine Service perspective. *Front. Mar. Sci.* 6:234. doi: 10.3389/fmars.2019.00234

Liu, Y., Meier, H. E. M., and Eilola, K. (2017). Nutrient transports in the Baltic Sea – results from a 30-year physical–biogeochemical reanalysis. *Biogeosciences* 14, 2113–2131. doi: 10.5194/bg-14-2113-2017

Maar, M., Møller, E. F., Larsen, J., Madsen, K. S., Wan, Z., She, J., et al. (2011). Ecosystem modelling across a salinity gradient from the North Sea to the Baltic Sea. *Ecol. Model.* 10:1696–1711. doi: 10.1016/j.ecolmodel.2011.03.006

Meier, H. E. M. (2005). Modeling the age of Baltic Seawater masses: quantification and steady state sensitivity experiments. *J. Geophys. Res.* 110:C02006, doi: 10.1029/2004JC002607

Meier, H. E. M. (2007). Modeling the pathways and ages of inflowing salt- and freshwater in the Baltic Sea. *Estuarine Coastal Shelf Sci.* 744, 717–734. doi: 10.1016/j.ecss.2007.05.019

Meier, H. E. M., Andersson, H. C., Arheimer, B., Blenckner, T., Chubarenko, B., Donnelly, C., et al. (2012). Comparing reconstructed past variations and future projections of the Baltic Sea ecosystem - first results from multi-model ensemble simulations. *Environ. Res. Lett.* 7:034005. doi: 10.1088/1748-9326/7/3/034005

Meier, H. E. M., Edman, M., Eilola, K., Placke, M., Neumann, T., Andersson, H., et al. (2018a). Assessment of eutrophication abatement scenarios for

the Baltic Sea by multi-model ensemble simulations. *Front. Mar. Sci.* 5:440. doi: 10.3389/fmars.2018.00440

Meier, H. E. M., Edman, M., Eilola, K., Placke, M., Neumann, T., and Savchuk, H. (2019). Assessment of uncertainties in scenario simulations of biogeochemical cycles in the Baltic Sea. *Front. Mar. Sci.* 6:46. doi: 10.3389/fmars.2019.00046

Meier, H. E. M., Feistel, R., Piechura, J., Arneborg, L., Burchard, H., Fiekas, V., et al. (2006). Ventilation of the Baltic Sea deep water: a brief review of present knowledge from observations and models. *Oceanologia* 48, 133–164.

Meier, H. E. M., Rutgersson, A., and Reckermann, M. (2014). Baltic Earth - a new earth system science program for the Baltic Sea Region. *EOS Trans. AGU* 95, 109–110. doi: 10.1002/2014EO130001

Meier, H. E. M., Väli, G., Naumann, M., Eilola, K., and Frauen, C. (2018b). Recently accelerated oxygen consumption rates amplify deoxygenation in the Baltic Sea. *J. Geophys. Res.* 123, 3227–3240. doi: 10.1029/2017JC013686

Mohrholz, V. (2018). Major Baltic Inflow Statistics – Revised. *Front. Marine Sci.* 5:384. doi: 10.3389/fmars.2018.00384

Mohrholz, V., Naumann, M., Nausch, G., Krüger, S., and Gräwe, U. (2015). Fresh oxygen for the Baltic Sea—An exceptional saline inflow after a decade of stagnation. *J. Marine Syst.* 148, 152–166. doi: 10.1016/j.jmarsys.2015.03.005

Neumann, T. (2000). Towards a 3d-ecosystem model of the Baltic Sea. *J. Mar. Sys.* 25, 405–419. doi: 10.1016/S0924-7963(00)00030-0

Omstedt, A., Elken, J., Lehmann, A., Leppäranta, M., Meier, H. E. M., Myrberg, K., et al. (2014). Progress in physical oceanography of the Baltic Sea during the 2003–2014 period. *Progress Oceanogr.* 128, 139–171. doi: 10.1016/j.pocean.2014.08.010

Omstedt, A., Elken, J., Lehmann, A., and Piechura, J. (2004). Knowledge of the Baltic Sea physics gained during the BALTEX and related programmes. *Progress Oceanogr.* 63, 1–28. doi: 10.1016/j.pocean.2004.09.001

Placke, M., Meier, H. E. M., Gräwe, U., Neumann, T., and Liu, Y. (2018). Long-term mean circulation of the Baltic Sea as represented by various ocean circulation models. *Front. Mar. Sci.* 5:287. doi: 10.3389/fmars.2018.00287

Poulsen, J. W., Berg, P., and Raman, K. (2014). "Chapter 3 - Better concurrency and SIMD on HBM," in *High Performance Parallelism Pearls: Multicore and Many-core Programming Approaches,* eds J. Jeffers and J. Reinders (Morgan Kaufmann Publishing), 43–67. doi: 10.1016/B978-0-12-802118-7.00003-0

Raschke, E., Meywerk, J., Warrach, K., Andrea, U., Bergström, S., Beyrich, F., et al. (2001). The Baltic Sea Experiment (BALTEX) a European contribution to the investigation of the energy and water cycle over a large drainage basin. *Bull. Am. Meteorol. Soc.* 82, 2389–2413. doi: 10.1175/1520-0477(2001)082<2389:TBSEBA>2.3.CO;2

Reckermann, M., Langner, J., Omstedt, A., von Storch, H., Keevallik, S., and Hünicke, B. (2011). BALTEX - An interdisciplinary research network for the Baltic Sea region. *Environ. Res. Lett.* 6:045205. doi: 10.1088/1748-9326/6/4/045205

Reissmann, J. H., Burchard, H., Feistel, R., Hagen, E., Lass, H. U., Mohrholz, V., et al. (2009). Vertical mixing in the Baltic Sea and consequences for eutrophication–A review. *Progress Oceanogr.* 82, 47–80. doi: 10.1016/j.pocean.2007.10.004

Rodhe, J., and Winsor, P. (2002). On the influence of the freshwater supply on the Baltic Sea mean salinity. *Tellus A* 54, 175–186. doi: 10.3402/tellusa.v54i2.12134

Rodriguez, H., Fisher, E., and Schuurbiers, D. (2013). Integrating science and society in European Framework Programmes: trends in project-level solicitations. *Res. Policy* 42, 1126–1137. doi: 10.1016/j.respol.2013.02.006

Roiha, P., Siiriä S.-M., Haavisto, N., Alenius, P., Westerlund, A., and Purokoski, T. (2018). Estimating currents from argo trajectories in the bothnian Sea, Baltic Sea. *Front. Mar. Sci.* 5:308. doi: 10.3389/fmars.2018.00308

Schimanke, S., and Meier, H. E. M. (2016). Decadal-to-centennial variability of salinity in the Baltic Sea. *J. Climate* 29, 7173–7188. doi: 10.1175/JCLI-D-15-0443.1

Schimanke, S., Meier, H. E. M., Kjellström, E., Strandberg, G., and Hordoir, R. (2012). The climate in the Baltic Sea region during the last millennium simulated with a regional climate model. *Climate Past* 8, 1419–1433. doi: 10.5194/cp-8-1419-2012

Schmale, O., Krause, S., Holtermann, P., Power Guerra, N. C., and Umlauf, L. (2016). Dense bottom gravity currents and their impact on pelagic methanotrophy at oxic/anoxic transition zones. *Geophys. Res. Lett.* 43, 5225–5232. doi: 10.1002/2016GL069032

Schrum, C., Hübner, U., Jacob, D., and Podzun, R. (2003). A coupled atmosphere/ice/ocean model for the North Sea and the Baltic Sea. *Climate Dynam.* 21, 131–151. doi: 10.1007/s00382-003-0322-8

She, J. (2018a). "Emerging needs on operational oceanography to serve sustainable development in Baltic-North Sea," in *Proceedings of the Eight EuroGOOS International Conference*, eds E. Buch, V. Fernández, D. Eparkhina, P. Gorringe, and G. Nolan (Belgium : EuroGOOS), 463–472.

She, J. (2018b). "Assessment of Baltic Sea observations for operational oceanography," in *Proceedings of the Eight EuroGOOS International Conference*, eds E. Buch, V. Fernández, D. Eparkhina, P. Gorringe and G. Nolan (Brussels: EuroGOOS), 79–87.

She, J., Allen, I., Buch, E., Crise, A., Johannessen, J. A., Le Traon, P.-Y., et al. (2016). Developing European operational oceanography for Blue Growth, climate change adaptation and mitigation, and ecosystem-based management. *Ocean Sci.* 12, 953–976. doi: 10.5194/os-12-953-2016

She, J., and Murawski, J. (2018). "Towards seamless modelling for the Baltic Sea. Operational Oceanography serving Sustainable Marine Development," in *Proceedings of the Eight EuroGOOS International Conference*, eds E. Buch, V. Fernández, D. Eparkhina, P. Gorringe, and G. Nolan (Belgium: EuroGOOS), 233–241.

She, J., and Nielsen, J. W. (1999). *Operational Wave Forecasts Over Baltic and North Sea.* Scientific Report 99-7, Danish Meteorological Institute, Copenhagen, Denmark.

Siiriä, S., Roiha, P., Tuomi, L., Purokoski, T., Haavisto, N., and Alenius, P. (2018). Applying area-locked, shallow Argo floats in the Baltic Sea monitoring. *J. Operat. Oceanogr.* 12, 58–72. doi: 10.1080/1755876X.2018.1544783

Tian, T., Boberg, F., Christensen, O. B., Christensen, J. H., She, J., and Vihma, T. (2013). Resolved complex coastlines and land–sea contrasts in a high-resolution regional climate model: a comparative study using prescribed and modelled SSTs. *Tellus A* 65:19951. doi: 10.3402/tellusa.v65i0.19951

Tian, T., Su, T., Boberg, F., Yang, S., and Schmith, T. (2016). Estimating uncertainty caused by ocean heat transport to the North Sea: experiments downscaling EC-Earth. *Climate Dynam.* 46, 99–110. doi: 10.1007/s00382-015-2571-8

Trenberth, K. E., Jones, P. D., Ambenje, P., Bojariu, R., Easterling, D., Klein Tank, A., et al. (2007). "Observations: surface and atmospheric climate change," in *Climate Change 2007: The Physical Science Basis. Contribution of Working Group I to the Fourth Assessment Report of the Intergovernmental Panel on Climate Change,* eds S. Solomon, D. Qin, M. Manning, Z. Chen, M. Marquis, K. B. Averyt, M. Tignor, and H. L. Miller (Cambridge: Cambridge University Press). 235–336.

Tuomi, L., Pettersson, H., and Kahma, K. (1999). *Preliminary Results From the WAM Wave Model Forced by the Mesoscale EUR-HIRLAM Atmospheric Model.* MERI – Report series of the Finnish Institute of Marine Research 40, 19–23.

Tuomi, L., She, J., Lorkowski, I., Axell, L., Lagemaa, P., Schwichtenberg, F., et al. (2018). "Overview of CMEMS BAL MFC Service and Developments," in *Proceedings of the Eigth EuroGOOS International Conference,* eds E. Buch, V. Fernández, D. Eparkhina, P. Gorringe, and G. Nolan (Brussels; Belgium: EuroGOOS), 261–268.

Umlauf, L., and Arneborg, L. (2009a). Dynamics of rotating shallow gravity currents passing through a channel. Part I: observation of transverse structure. *J. Phys. Oceanogr.* 39, 2385–2401. doi: 10.1175/2009JPO4159.1

Umlauf, L., and Arneborg, L. (2009b). Dynamics of rotating shallow gravity currents passing through a channel. Part II: analysis. *J. Phys. Oceanogr.* 39, 2402–2416. doi: 10.1175/2009JPO4164.1

Van Pham, T., Brauch, J., Dieterich, C., Frueh, B., and Ahrens, B. (2014). New coupled atmosphere-ocean-ice system COSMO-CLM/NEMO: assessing air temperature sensitivity over the North and Baltic Seas. *Oceanologia* 56, 167–189. doi: 10.5697/oc.56-2.167

von Schomberg, R. (2013). "A vision of responsible research and innovation," in *Responsible Innovation*, eds R. Owen, J. Bessant, and M. Heintz (London: John Wiley), 51–74. doi: 10.1002/9781118551424.ch3

WAMDI (1988). The WAM model - A third generation ocean wave prediction model. *J. Phys. Oceanogr.* 18, 1775–1810. doi: 10.1175/1520-0485(1988)018<1775:TWMTGO>2.0.CO;2

Wang, S., Dieterich, C., Döscher, R., Höglund, A., Hordoir, R., Meier, H. E. M., et al. (2015). Development and evaluation of a new regional coupled

atmosphere–ocean model in the North Sea and Baltic Sea. *Tellus A* 67:24284. doi: 10.3402/tellusa.v67.24284

Wilhelmsson, T. (2002). *Parallellization of the HIROMB Ocean Model*. Licentiate Thesis. Royal Institute of Technology, Department of Numerical and Computer Science, Stockholm, Sweden.

WMO (2015). World Meteorological Organisation. *Seamless Prediction of the Earth System: From Minutes to Months*. Available online at: https://library.wmo.int/opac/doc_num.php?explnum_id=3546

Zhuang, S., Fu, W., and She, J. (2011). A pre-operational 3-D variational data assimilation system in the North/Baltic Sea. *Ocean Sci. Discuss.* 7, 771–781. doi: 10.5194/os-7-771-2011

Conflict of Interest: The authors declare that the research was conducted in the absence of any commercial or financial relationships that could be construed as a potential conflict of interest.

frontiers in Earth Science

ORIGINAL RESEARCH
published: 13 February 2020
doi: 10.3389/feart.2020.00012

High Resolution Discharge Simulations Over Europe and the Baltic Sea Catchment

Stefan Hagemann[1], Tobias Stacke[1,2] and Ha T. M. Ho-Hagemann[1]*

[1] Institute of Coastal Research, Helmholtz-Zentrum Geesthacht, Geesthacht, Germany, [2] Max Planck Institute for Meteorology, Hamburg, Germany

Regional coupled system models require a high-resolution discharge component to couple their atmosphere/land components to the ocean component and to adequately resolve smaller catchments and the day-to-day variability of discharge. As the currently coupled discharge models usually do not fulfill this requirement, we improved a well-established discharge model, the Hydrological Discharge (HD) model, to be globally applicable at 5 Min. resolution. As the first coupled high-resolution discharge simulations are planned over Europe and the Baltic Sea catchment, we focus on the respective regions in the present study. As no river specific parameter adjustments were conducted and since the HD model parameters depend on globally available gridded characteristics, the model is, in principle, applicable for climate change studies and over ungauged catchments. For the validation of the 5 Min. HD (HD5) model, we force it with prescribed fields of surface and subsurface runoff. As no large-scale observations of these variables exist, they need to be calculated by a land surface scheme or hydrology model using observed or re-analyzed meteorological data. In order to pay regard to uncertainties introduced by these calculations, three different methods and datasets were used to derive the required fields of surface and subsurface runoff for the forcing of the HD5 model. However, the evaluation of the model performance itself is hampered by biases in these fields as they impose an upper limit on the accuracy of simulated discharge. 10-years simulations (2000–2009) show that for many European rivers, where daily discharge observations were available for comparison, the HD5 model captures the main discharge characteristics reasonably well. Deficiencies of the simulated discharge could often be traced back to deficits in the various forcing datasets. As direct anthropogenic impact on the discharge, such as by regulation or dams, is not regarded in the HD model, those effects can generally not be simulated. Thus, discharges for many heavily regulated rivers in Scandinavia or for the rivers Volga and Don are not well represented by the model. The comparison of the three sets of simulated discharges indicates that the HD5 model is suitable to evaluate the terrestrial hydrological cycle of climate models or land surface models, especially with regard to the separation of throughfall (rain or snow melt) into surface and subsurface runoff.

Keywords: discharge modeling, large-scale river routing, daily runoff, high resolution, Europe

OPEN ACCESS

Edited by:
Martin Stendel, Danish Meteorological Institute (DMI), Denmark

Reviewed by:
Deniz Bozkurt, University of Chile, Chile
Xander Wang, University of Prince Edward Island, Canada

****Correspondence:***
Stefan Hagemann
stefan.hagemann@hzg.de

Specialty section:
This article was submitted to Interdisciplinary Climate Studies, a section of the journal Frontiers in Earth Science

Received: *17 October 2018*
Accepted: *20 January 2020*
Published: *13 February 2020*

Citation:
Hagemann S, Stacke T and Ho-Hagemann HTM (2020) High Resolution Discharge Simulations Over Europe and the Baltic Sea Catchment. Front. Earth Sci. 8:12. doi: 10.3389/feart.2020.00012

INTRODUCTION

The hydrological cycle is crucially important to life on Earth since water is essential nourishment for all organisms. Consequently, the importance of the hydrological cycle is highlighted by the Global Energy and Water Cycle Experiment (GEWEX; e.g., Sorooshian et al., 2005), which is now in its third phase (2013–2022[1]). The implications of changes in the hydrological cycle induced by climate change may affect the society more than any other changes, e.g., with regard to flood risks, water availability and water quality. For example, large irrigation activities in many parts of Middle Asia led to man-made climate change in the Aral Sea region that were caused by the lake's catastrophic desiccation within the last five decades (Breckle and Geldyeva, 2012). This had severe consequences for the societies living in this area. Another example is the prominent drought period in the Sahel that began at the end of the 1960s and ended in the mid-1980s (Anyamba and Tucker, 2005). This caused a noticeable decline of per capita food production and food self-sufficiency ratios in the Sahel (Epule et al., 2014).

Discharge (or river runoff) is an important component of the global water cycle and comprises about one third of the precipitation over land areas. It closes the water cycle between land and ocean. On the one hand, the freshwater inflow affects the thermohaline circulation, especially in regions where deep convection occurs (Hordoir et al., 2008). For example, an increased freshwater anomaly may cause a weakening of the meridional overturning in the Northern Atlantic (Marzeion et al., 2007). An important source of stratification in the North−Western European Shelf is the outflow from the Baltic Sea (Hordoir and Meier, 2010) that is mainly induced by river runoff into and net precipitation over the Baltic Sea. Decadal variations in Baltic Sea salinity are caused largely by the accumulated runoff to the Baltic Sea (Väli et al., 2013). In addition, the thermohaline circulation of the Baltic Sea is also influenced by inflows of highly saline water from the North Sea that itself may be strongly impacted by uncertainties in precipitation and/or river runoff (Lehmann and Hinrichsen, 2000).

On the other hand, river discharge and the associated nutrient loads are important factors that influence the functioning of the marine ecosystem. Lateral inflows from land, carrying fresh, nutrient-rich water determine coastal physical conditions and nutrient concentration and, hence, dominantly influence primary production in the system. Since this forms the basis of the trophic food web, it impacts the variability of the whole ecosystem (Daewel and Schrum, 2017). This becomes even more relevant in systems like the Baltic Sea, which is almost decoupled from the open ocean and land-borne nutrients play a major role for determining ecosystem productivity (Thurow, 1997; Österblom et al., 2007). With respect to global biogeochemical cycles, a proper description of the transport of, e.g., nitrogen, phosphorus, carbon, and silicon, into the ocean requires a very detailed representation of stream characteristics (such as flow paths, lakes, ponds, reservoirs, wetlands, and floodplains) because the smallest water bodies may exhibit large parts of the retention on land (Bouwman et al., 2013).

In climate change studies, runoff is generated differently in hydrological and climate modeling communities. In hydrology, global hydrology models (GHMs) or local/regional hydrological models (HMs) are used that are forced with climate model input. This method has two major advantages. First, the GHMS and HMs are specific impact models focusing on hydrology, and, hence, hydrology is not just one of many processes such as it is in a climate model where the main purpose is to simulate the climate. Second, it is well known that general circulation models (GCMs) and regional climate models (RCMs) suffer from substantial biases, especially with regard to precipitation and the hydrological cycle (Flato et al., 2013; Kotlarski et al., 2014). When using GHMs or HMs, climate model input can still be bias-corrected before these data are fed into the hydrology model. Local and regional HMs are often calibrated. On the one hand, this leads to more accurate discharge simulations for current climate. On the other hand, the calibration may obscure deficiencies in process representations that may lead to erroneous behavior in ungauged catchments or different climates under global warming conditions. On the downside of the HM application is that no feedbacks to the atmosphere are considered, and the simulated hydrology may be inconsistent with climate model forcing. Using different models changes the uncertainty of the results (Hagemann et al., 2013). This is especially important when using a model chain comprising bias corrected GCM data fed into GHMs as being applied within the European Union (EU) project WATer and global Change (WATCH[2]; see, e.g., Harding et al., 2011) and the Inter-Sectoral Impact Model Intercomparison Project (ISIMIP; Warszawski et al., 2014).

In climate modeling, runoff is generated within the land surface schemes of global or regional climate models. Thus, the simulated runoff and other hydrological variables are consistent with the climate variables and hydrology – atmosphere feedbacks are regarded. A disadvantage is that potentially large biases exists due to climate model biases, especially in precipitation (see above). This approach is used for coupled system model studies, where interactions between the different compartments of the Earth system shall be considered. In a coupled Earth system model, the discharge is the interface between the land surface hydrology and the ocean, and thus an integral part of the coupled system.

For global applications of a discharge model within a fully coupled GCM or an Earth System Model (ESM), a grid resolution of 0.5° is usually sufficient. The same applies for regional applications of coupled system models where the main objective is an adequate representation of the mean monthly discharge of large rivers. If research and applications focus on the representation of daily discharge, consider smaller catchments or investigate the transport of biogeochemical compounds on the regional scale, higher resolutions are required for the appropriate simulation of discharge. Zhao et al. (2017) demonstrated the importance of the routing scheme (i.e., the discharge model) to simulate peak discharges. Their routing model did not only

[1] www.gewex.org

[2] www.eu-watch.org

account for floodplain storage and backwater effects that are not represented in most GHMs, but also was using a higher resolution (0.25°) than the nine GHMs (0.5°) from which the forcing data were taken. While most of the GHMs use a 0.5° resolution, some of them are available at higher resolutions, e.g., LISFLOOD at 0.1° (Van Der Knijff et al., 2010), PCR-GLOBWB at 0.08° (López López et al., 2016) and WaterGap3 at 5 Min. (Flörke et al., 2013). Moreover, several large-scale regional HMs exist, such as E-Hype with a median catchment size of 215 km^2 (Donnelly et al., 2016; Lindström et al., 2010), LISFLOOD at 5 km and mHM at 1–24 km (Samaniego et al., 2010) for Europe, and MODCOU at 1–8 km over France (Decharme et al., 2013). Bierkens et al. (2015) summarized ongoing and planned activities in large-scale high-resolution hydrological modeling.

In addition to traditional RCMs, regional coupled system models (RCSM) have been recently developed to conduct climate change studies at high spatial and temporal resolutions. These models require a high-resolution discharge component to couple their atmosphere/land components to the ocean component and to adequately resolve smaller catchments and the day-to-day variability of discharge. The current discharge models applied in coupled (or Earth system) models for global or regional climate simulations usually do not fulfill this requirement. In ESMs, discharge (or routing) models are frequently part of the coupled system (often as part of the land surface scheme) but their spatial resolution is usually 0.5° (Roeckner et al., 2003; Guimberteau et al., 2012) or coarser (Best et al., 2011; Lawrence et al., 2011; Milly et al., 2014). For RCSMs, a few setups exists where a discharge model is included, but its resolution is rarely higher than 0.5°. Examples comprise the HD model (Hagemann and Dümenil, 1998) at 0.5° (Elizalde, 2011; Sein et al., 2015; Sitz et al., 2017), TRIP (Oki and Sud, 1998) at 0.5° (Dell'Aquila et al., 2012; Sevault et al., 2014) and LARSIM (Bremicker, 2000) at 1/6° over Northern Europe (Lorenz and Jacob, 2014). Several studies exists where a RCM was coupled to a very-high resolution regional HM but currently these studies cover only short periods or relatively small catchments/areas (e.g., Mauser and Bach, 2009; Larsen et al., 2014; Shrestha et al., 2014; Senatore et al., 2015). Over Korea, the discharge model TRIP has been coupled to a RCM at 0.5°, 0.25°, and 0.125° in preparation of future RCMS studies (Lee et al., 2015). To our knowledge, none of the HMs used in the studies listed above has been used in a fully coupled RCSM setup that can be applied for climate time scales and large-scale areas.

At the Helmholtz-Zentrum Geesthacht, RCSM simulations are planned with GCOAST (Geesthacht Coupled cOAstal model SysTem) over Europe and the Baltic Sea (Ho-Hagemann et al., submitted). Consequently, to prepare high-resolution discharge simulations over these regions within GCOAST, we further developed a well-established discharge model, the Hydrological Discharge (HD) model (Hagemann and Dümenil, 1998), to be globally applicable at 5 Min. resolution. Here, we chose to follow the climate modeling approach (see above) to calculate discharge, as the simulated discharge should be consistent with the climate model forcing. For the planned application within a RCSM, we aim at simulating river discharge with a realistic daily variability and capturing the timing and magnitude of the main peaks and low flow periods on the daily time scale. The representation of minor short-term daily fluctuations is not required, as this is neither expected to be obtained from RCSM simulations nor from using coarse resolution forcing datasets as utilized for the evaluation of the model results in the present study. This study shows first results in comparison with available observations over Europe and the Baltic Sea catchment. The HD model, data and evaluation metrics are described in section "Data and Methods." In section "Results," the forcing data and the discharge simulations are evaluated and discussed, followed by section "Summary and Conclusion" where a summary and conclusions are provided.

DATA AND METHODS

With regard to the lateral flow of water at the land surface, the term runoff is often used, which commonly leads to some communication problems. Sometimes it refers to the water from rain and snowmelt that is not infiltrated into the soil (surface runoff), to the whole amount of water that may be transported laterally at a certain location (total runoff), or to the amount of water that is already laterally transported as discharge by rivers (river runoff). In the long-term annual mean, total runoff equals discharge within a catchment, and in this case, runoff is equivalent to precipitation minus evaporation averaged over the catchment. To avoid these communication problems the clear specification of the term runoff is generally recommended and subsequently used in the present study. Here, runoff refers to the total runoff and comprises surface runoff and drainage from the soil (or subsurface runoff). The first represents water amounts that may flow laterally off at the surface or the near-surface layers of the soil, while the latter designates the respective water amounts in the deeper layers of the soil.

The HD Model

The HD model (Hagemann and Dümenil, 1998; Hagemann and Dümenil Gates, 2001) is used in this study for the calculation of river runoff. The HD model has already been used for many years in the global ESM of the Max Planck Institute for Meteorology (MPI-M), MPI-ESM (Giorgetta et al., 2013), and its predecessor ECHAM5/MPIOM (Roeckner et al., 2003; Jungclaus et al., 2006). Recently, it was also included in the regional ESMs ROM (Sein et al., 2015) and RegCM-ES (Sitz et al., 2017) as well as the regional climate model REMO-MPIOM (Elizalde, 2011). Furthermore, the HD model is currently implemented into the RCSM GCOAST of the Helmholtz-Zentrum Geesthacht. The HD model was designed to run on a fixed global regular grid of 0.5° horizontal resolution, and it uses a pre-computed river channel network to simulate the horizontal transport of water within model watersheds. Originally, the HD model used a daily time step, but some refinements made during the MPI-ESM development allow sub-daily time steps, e.g., hourly.

Figure 1 shows the structure of the HD model. It separates the lateral water flow into the three flow processes of overland flow, baseflow, and riverflow. Overland flow and baseflow represent the fast and slow lateral flow processes within a grid box, while riverflow represents the lateral flow between grid boxes. Overland

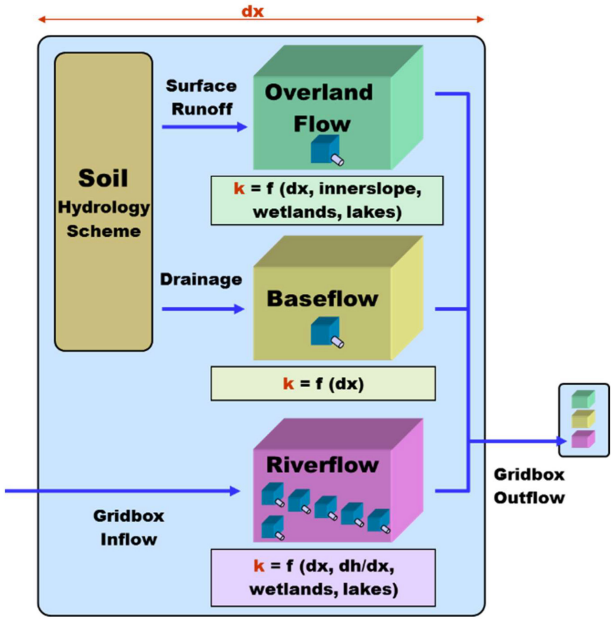

FIGURE 1 | The HD model structure. The figure was designed by S. Kotlarski (pers. comm. 2006).

flow and baseflow are both computed using a single linear reservoir. The first uses surface runoff as input, while the latter is fed by drainage from the soil. Riverflow receives the inflow from other grid boxes as input and it is simulated by a cascade of five equal linear reservoirs. The sum of the three flow processes is equal to the total outflow from a grid box. The model parameters are functions of the topography gradient between grid boxes, the slope within a grid box, the grid box length, the lake area, and the wetland fraction of a particular grid box. The model input fields of surface runoff and drainage resulting from the various climate or land surface model resolutions are interpolated to the HD grid before being fed into the HD model.

Model Improvements

The HD model has been adapted to run on a regular grid of 5 Min. horizontal resolution, which corresponds to an average grid box size of 8–9 km. It can be forced with daily or sub-daily time series of surface runoff and drainage using a time step that equals the forcing time step. In the present study, the model time step was set to the respective forcing time step (see section "Forcing Data and Experimental Setup"). However, as the minimum travel time through a grid box is limited by the time step chosen, an internal time step of 0.5 h is used for riverflow. For the initial development and application of the 5 Min. HD version (HD5), a regional domain over Europe was chosen that covers the land areas between −1°W to 69°E and 27°N to 72°N. The domain is shown in **Figure 2** together with the catchments areas for selected rivers that are specifically mentioned in the manuscript. River directions and digital elevation data were provided by Bernhard Lehner (pers. comm., 2014) and were derived from the HydroSHEDS (Lehner et al., 2006) database and from the Hydro1K dataset for areas north of 60°N[3]. We compared the HD5 catchment areas with literature values for the whole catchment and with station values for the station-related catchments. In general, we found a good agreement with the observed areas. Larger deviations between gridded and observed areas occur only for a few rivers that are mainly located north of 60°N, i.e., in the Hydro1K part of the HD5 grid. Lake fractions are taken from the European Space Agency (ESA) Land Cover Climate Change Initiative (LC_CCI) for epoch 2010 (version 2.0.7; available at[4]) and wetland fractions from the LSP2 (Land Surface Parameter vs. 2) dataset (Hagemann, 2002). To adapt the HD model parameters used at 0.5° resolution to the higher resolution, global scaling factors were applied to the reservoir retention coefficients of overland flow and base flow. These two factors are global constants and were applied in every HD model grid box. Thus, as for the operational HD model at 0.5° resolution, no river specific parameter adjustments were conducted. Since the HD model parameters depend on globally available grid box characteristics, it is, in principle, applicable for climate change studies and over ungauged catchments, i.e., river basins where no daily discharges are available at a downstream station. Here, we imply that if the HD5 model yields satisfactory simulated discharges for many rivers without river and time period specific calibration, then we can be confident that the model is likely to also provide reasonable discharge in climate change studies and over ungauged catchments where an evaluation is not possible.

Forcing Data and Experimental Setup

As mentioned in section "Introduction," it is well known that climate models suffer from substantial biases, especially with regard to precipitation and the hydrological cycle. In order to avoid uncertainties introduced by model biases of the atmospheric component of a RCSM, the HD5 model was driven by pre-generated fields of surface and subsurface runoff. As no large-scale observations of these variables exist, they need to be calculated by a land surface scheme or hydrology model using observed or re-analyzed meteorological data. **Figure 3** summarizes the main steps of generating simulated discharges with HD model in stand-alone mode and conducting their evaluation. These steps comprise three parts:

1. Preparation of HD model forcing: Choose an atmospheric forcing dataset and use a land surface (or hydrology) model to generate the forcing for the HD model,
2. Run the HD model: Interpolate the forcing data of surface runoff and drainage to the HD model grid and simulate daily discharges with the HD model,
3. Evaluation of results: Compare simulated and observed discharges at station location and calculate various evaluation metrics.

Note that in coupled HD model applications, part 1 is replaced by direct input from the respective RCM or GCM. In order to

[3]https://www.usgs.gov/centers/eros/science/usgs-eros-archive-digital-elevation-hydro1k

[4]http://maps.elie.ucl.ac.be/CCI/viewer/

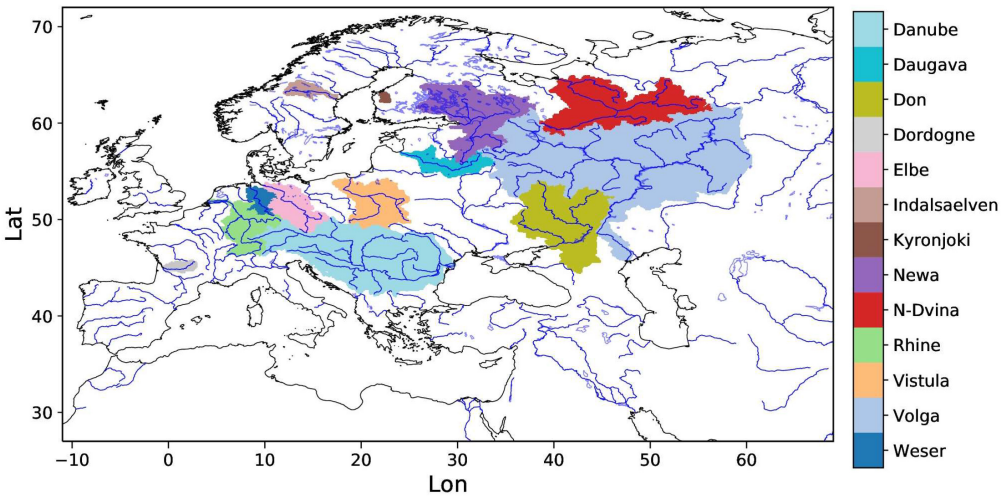

FIGURE 2 | European HD5 domain and catchment areas for selected rivers.

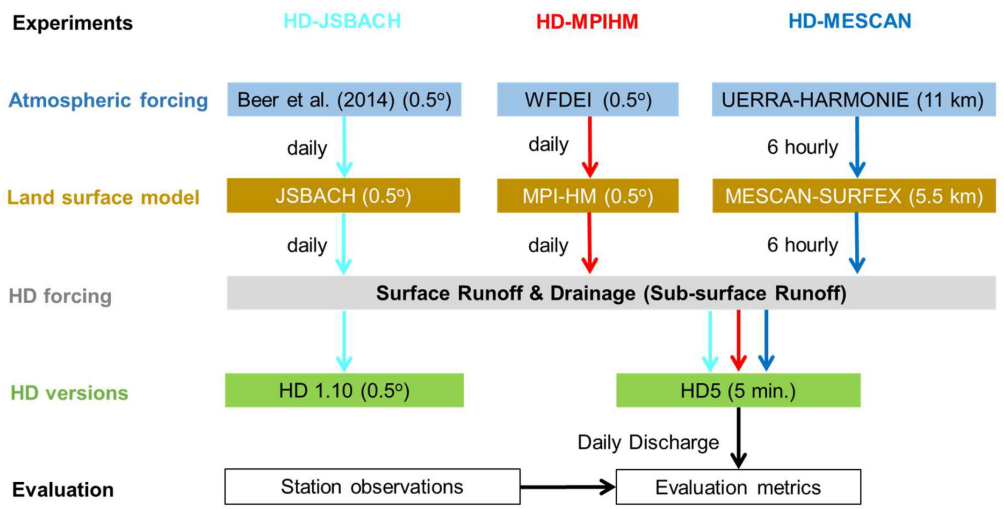

FIGURE 3 | Flowchart showing the main steps of generating simulated discharges with the HD model and conducting their evaluation in the present study.

pay regard to uncertainties introduced by the inputs generated in part 1, three different methods and datasets were used to derive the required fields of surface and subsurface runoff for the forcing of the HD5 model. **Table 1** provides an overview on these three forcing datasets and their characteristics.

HD5-JSBACH

In order to generate daily input fields of surface runoff and drainage, the land surface scheme JSBACH (vs. 3 + frozen soil physics; Ekici et al., 2014) was forced globally at 0.5° with daily atmospheric forcing data based on the Interim Re-Analysis of the European Center for Medium-Range Weather Forecast (ERA-Interim; Dee et al., 2011). These forcing data are bias-corrected (see Beer et al., 2014) toward the so-called WATCH forcing data (WFD; Weedon et al., 2011) that have been generated in the EU project WATCH. For our study, we spatially interpolated the surface runoff and drainage data to the European 5-Min. domain using conservative remapping and fed into the HD5 model. The simulation period is 1979–2009. This forcing was also used for an analogous simulation with the HD model at 0.5° resolution. This 0.5° simulation is denoted with HD 1.10 in the following.

HD5-MPIHM

The MPI-M hydrology model MPI-HM (Stacke and Hagemann, 2012) was driven by daily WATCH forcing data based on ERA-Interim (WFDEI; Weedon et al., 2014) from 1979–2009 to generate daily input fields of surface runoff and drainage. MPI-HM is a GHM operating at a spatial resolution of 0.5°. It has contributed to the WATCH Water Model Intercomparison Project (WaterMIP; Haddeland et al., 2011) and ISIMIP (Warszawski et al., 2014).

TABLE 1 | Model experiments and their forcing data.

Experiment	Atmospheric forcing	Land surface model	Resolution: Atmosphere/Land	Simulation period
HD5-JSBACH	Beer et al. (2014)	JSBACH	0.5°	1979–2009
HD5-MPIHM	WFDEI	MPI-HM	0.5°	1979–2009
HD5-MESCAN	UERRA-HARMONIE	MESCAN-SURFEX	11 km/5.5 km	2000–2009

HD5-MESCAN

Six hourly data of surface runoff and drainage (variable name: percolation) were retrieved from the MESCAN-SURFEX regional surface reanalysis (Bazile et al., 2017) created in the EU project UERRA (Uncertainties in Ensembles of Regional ReAnalysis[5]). SURFEX (Masson et al., 2013) is a land surface platform that was driven by atmospheric forcing at 5.5 km. The forcing comprises 24 h-precipitation, near-surface temperature and relative humidity analyzed by the MESCAN surface analysis system as well as radiative fluxes and wind downscaled at 5.5 km from the 3DVar re-analysis conducted with the HARMONIE system at 11 km (Ridal et al., 2017). The latter has been generated using 6-hourly fields of the ERA-Interim reanalysis as boundary conditions and covers a domain comprising Europe and parts of the Atlantic, which is similar to the European domain of the Coordinated Downscaling Experiment (CORDEX) at 11 km.

Observed Discharge Data

Given the resolution of the HD5 model, an adequate simulation of discharge is not expected for small catchments. Therefore, we only considered rivers with catchment areas around 3000 km^2 or larger. Most of the daily discharge data used in this study were provided by the GRDC (Global Runoff Data Center, 56068 Koblenz, Germany). Further data were obtained from various sources such as: Banque Hydro (France), Bundesanstalt für Gewässerkunde Koblenz (Germany), Office of Public Works (Ireland), Norwegian Water and Energy Directorate, Institute of Meteorology and Water Management (Poland), Sistema Nacional de Informação (Portugal), R-ArctivNET (Onega river), Sistema Integrado de Información del Agua (Spain), National River Flow Archive (United Kingdom), and various regional hydrological offices in Italy (Abruzzo, Emilia Romagna, Latio, Puglia, Toscana, Veneto). For each river, the most downstream river gauge was considered for which daily discharge data were available, i.e., from that measurement station, which is closest to the river mouth.

Evaluation Metrics

The discharge evaluation of the HD5 simulations was conducted for those grid boxes that correspond to the station locations within the river network of the respective discharge observations. All evaluation metrics were calculated using simulated and observed time series of daily discharge for the period 2000–2009.

[5]www.uerra.eu

Standard Deviation

The standard deviation σ_x of a time series x_i with n values and the arithmetic mean μ_x is defined as

$$\sigma_x = \sqrt{\frac{1}{n-1} \cdot \sum_{i=1}^{n} (x_i - \mu_x)^2}$$

Note that we use the standard deviation of a sample (division by *n-1*), and not the one for the population (division by *n*).

Coefficient of Variation

The coefficient of variation CV_x is defined as the ratio of the standard deviation σ_x to the mean μ_x of a time series x_i. It shows the extent of variability in relation to the temporal mean.

Pearson Correlation Coefficient

The correlation of two time series x_i and y_i is expressed by the correlation coefficient r_{cor} of the Pearson product-moment correlation. Alternative names of r_{cor} are Bravais-Pearson correlation, Pearson correlation or just correlation coefficient.

$$r_{cor} = \frac{1}{n-1} \frac{\sum_{i=1}^{n} (x_i - \mu_x) \cdot (y_i - \mu_y)}{\sigma_x \cdot \sigma_y}$$

Kling Gupta Efficiency

The Kling Gupta efficiency (KGE) developed by Gupta et al. (2009) is used to measure the agreement between simulated and observed discharge. It provides diagnostically interesting insights into the model performance due to its decomposition of the mean squared model error into correlation, variability and bias terms. This facilitates the analysis of the relative importance of these different components, which is frequently used to evaluate hydrological simulations. Here, we used a revised version of this index (Kling et al., 2012) to ensure that the bias and the variability ratio are not cross-correlated:

$$KGE = 1 - \sqrt{c_1^2 + c_2^2 + c_3^2}$$

with $c_1 = r_{cor} - 1$, $c_2 = \frac{CV_{sim}}{CV_{obs}} - 1$, $c_3 = \frac{\mu_{sim}}{\mu_{obs}} - 1$

The computation of KGE comprises three main components:

1. The Pearson correlation coefficient r_{cor}, with an ideal value of one.
2. The variability ratio that is computed by using the coefficients of variation (Kling et al., 2012) of simulated and observed data, with an ideal value of one. Note that in the original method, the ratio of the standard deviations was used (Gupta et al., 2009).

3. The ratio between the means of the simulated values μ_{sim} and the observed values μ_{obs}, with an ideal value of one. Note that c_3 corresponds to the bias of the simulated values.

The Kling-Gupta efficiencies range from negative infinity to one. Essentially, the closer to one, the more accurate the model is. For a full discussion of the KGE-statistic and its advantages over the Nash–Sutcliffe efficiency (Nash and Sutcliffe, 1970) or the mean squared error, see Gupta et al. (2009).

Lag

The lag between two time series describes the temporal discrepancy between the centers of gravity between both time series. The cross correlation or lag correlation coefficient r_τ of two time series, which are shifted to each other by τ time steps, is defined as:

$$r_\tau = \frac{1}{n-1} \frac{\sum_{i=1}^{n-\tau} (x_i - \mu_x) \cdot (y_{i+\tau} - \mu_y)}{\sigma_x \cdot \sigma_y}$$

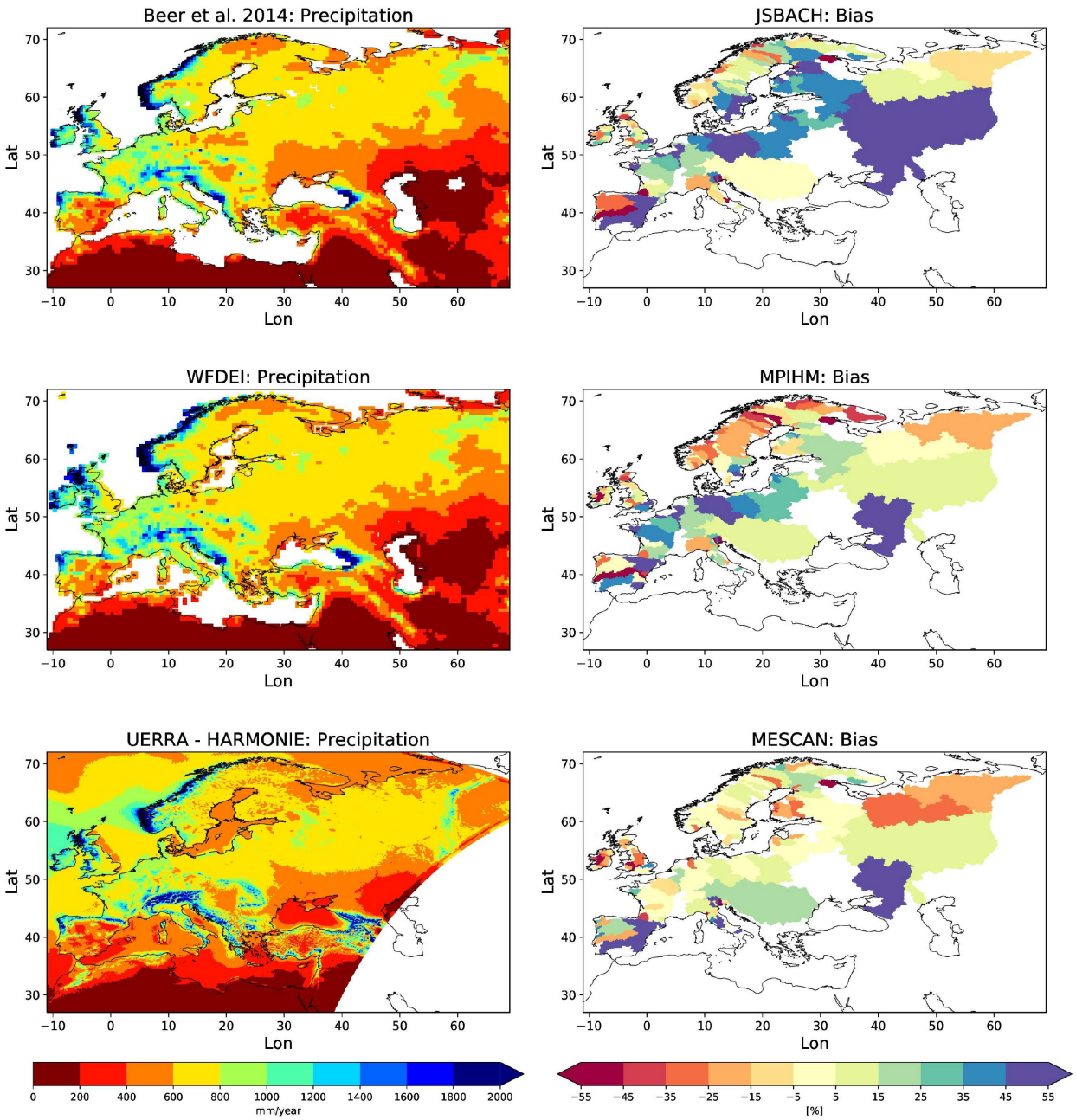

FIGURE 4 | Mean precipitation [mm/a] **(left column)** and bias in total runoff **(right column)** of the forcing data for Beer et al. (2014) and JSBACH (1st row), WFDEI and MPI-HM (2nd row), and UERRA-HARMONIE and MESCAN (3rd row), respectively.

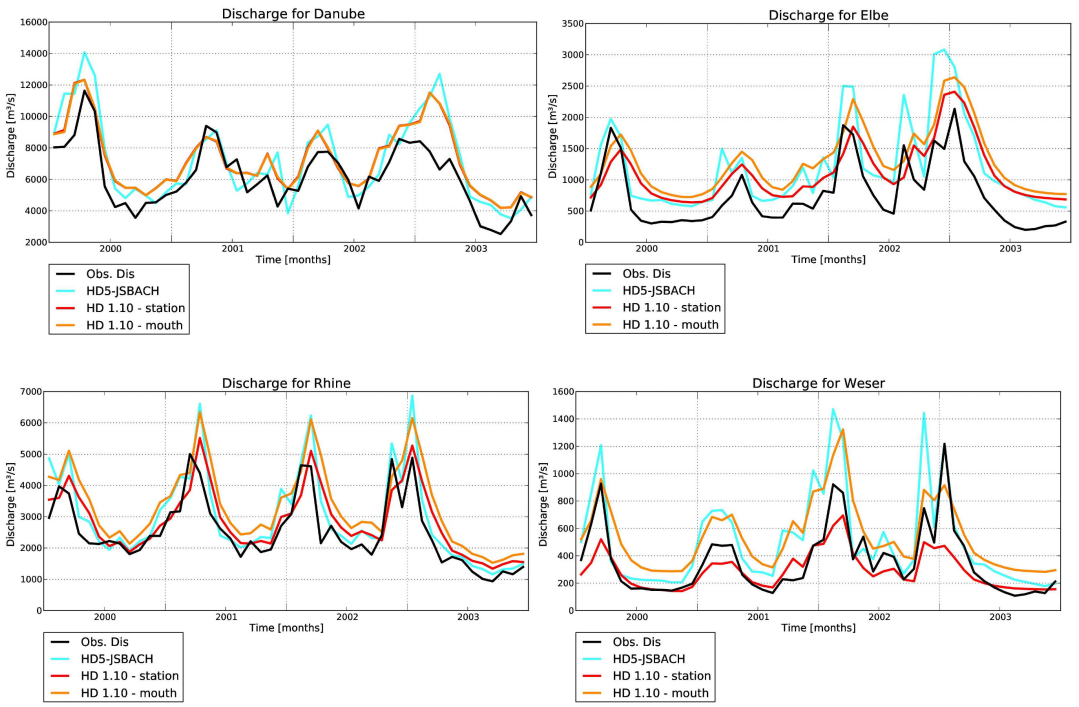

FIGURE 5 | Simulated and observed monthly discharges for selected rivers from 2000–2003. Simulated discharges comprise HD5-JSBACH and HD 1.10 simulations at 0.5° whereat for the latter, discharges close to the discharge gauge and the river mouth are provided. Note that for the Danube, the station is close to the river mouth so that the related discharges are almost identical.

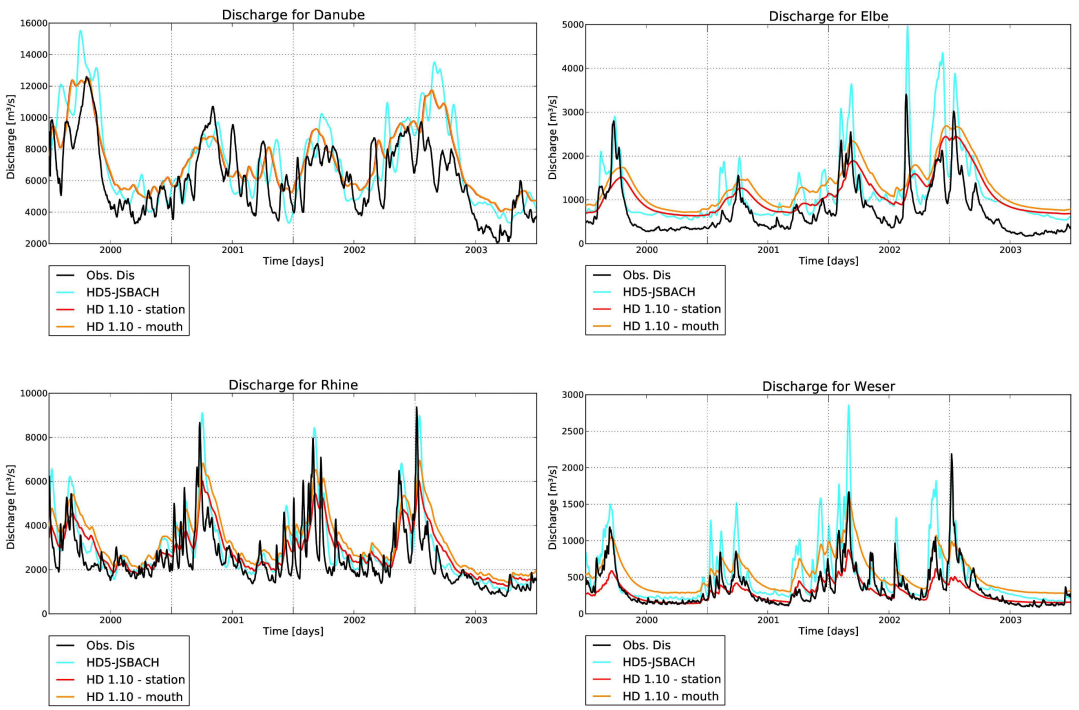

FIGURE 6 | Simulated and observed daily discharges for selected rivers from 2000–2003. Simulated discharges comprise HD5-JSBACH and HD 1.10 simulations at 0.5° whereat for the latter, discharges close to the discharge gauge and the river mouth are provided. Note that for the Danube, the station is close to the river mouth so that the related discharges are almost identical.

The lag L between these two time series is the value of τ where r_τ reaches its maximum. For $\tau = 0$ the cross correlation coefficient corresponds to the Pearson correlation coefficient.

Root-Mean-Square-Error (RSME)

The root-mean-square error (RMSE) is a common measure of the differences between simulated (x_i) and observed (y_i) time series. It is defined as

$$RMSE = \sqrt{\frac{\sum_{i=1}^{n}(x_i - y_i)^2}{n}}$$

In the present study, we used the normalized RMSE that facilitates the comparison between datasets or models with different scales, where the RMSE is divided by the range (defined as the maximum value minus the minimum value) of the observed data.

RESULTS

First, a short evaluation of the forcing datasets is provided in this section, and then the impact of a higher spatial resolution on the simulated discharge is addressed. The results of the 5 Min. simulations are evaluated in section "Evaluation of 5 Min. Simulations," which is followed by a discussion of the results. Note that since we do not have perfect forcing data of surface and subsurface runoff, the evaluation of simulated discharge is not straight forward, as deficiencies may be caused by shortcomings in the HD5 model or by deficits of the forcing data. Hence, if deficiencies in the simulated discharge for a specific river can be largely attributed to deficits of the forcing data, this would suggest that the HD5 model likely performs reasonably well for this river as HD5 is just transferring these deficits into the simulated discharge. In addition, if a certain metric shows a good agreement for those experimental setups with no noteworthy biases in the respective forcing, this would point to a good performance of HD5 for the considered river.

Evaluation of Forcing Datasets

Figure 4 (left column) compares the annual mean precipitation for 2000–2009 that was used to generate the forcing data of surface and subsurface runoff. To allow for an easier comparison, the precipitation was interpolated to the HD5 model grid using conservative remapping. While the general pattern agree between the three datasets, the HARMONIE precipitation provides a more detailed precipitation distribution than the

TABLE 2 | Evaluation metrics (2000–2009) for all experiments and those rivers shown in **Figures 4–6**: Discharge *bias*, Kling-Gupta Efficiency (KGE), Pearson correlation r_{cor}, normalized RMSE, variability ratio and lag.

River	Exp.	*Bias*	*KGE*	r_{cor}	RMSE	Var. rat.	Lag [d]
Danube	HD5-JSBACH	8.1%	0.69	0.71	15.3%	94.5%	4
	HD5-MPIHM	7.3%	0.66	0.68	17.3%	107.6%	34
	HD5-MESCAN	22.7%	0.35	0.50	20.9%	65.7%	42
	HD 1.10	10.1%	0.62	0.78	12.7%	70.2%	4
Dordogne	HD5-JSBACH	−6.5%	0.76	0.82	8.7%	115.2%	2
	HD5-MPIHM	3.7%	0.80	0.86	7.0%	85.8%	2
	HD5-MESCAN	−12.1%	0.33	0.72	11.0%	40.0%	2
	HD 1.10	−9.5%	0.59	0.72	9.7%	72.1%	3
Elbe	HD5-JSBACH	51.2%	0.45	0.81	15.5%	91.1%	2
	HD5-MPIHM	50.3%	0.49	0.91	15.0%	104.6%	3
	HD5-MESCAN	11.9%	0.50	0.78	9.5%	56.8%	5
	HD 1.10	47.6%	0.29	0.76	13.3%	53.8%	12
Kyrönjoki	HD5-JSBACH	36.7%	0.39	0.55	14.7%	82.7%	−5
	HD5-MPIHM	3.4%	0.64	0.69	12.5%	119.1%	−1
	HD5-MESCAN	−28.5%	0.35	0.70	11.4%	50.2%	1
	HD 1.10	–	–	–	–	–	–
N. Dvina	HD5-JSBACH	8.7%	0.79	0.87	10.5%	85.4%	−1
	HD5-MPIHM	−2.6%	0.85	0.85	11.2%	100.8%	7
	HD5-MESCAN	−35.3%	0.37	0.81	16.0%	51.6%	2
	HD 1.10	6.9%	0.53	0.85	11.6%	56.5%	−7
Rhine	HD5-JSBACH	19.8%	0.68	0.75	11.2%	98.5%	7
	HD5-MPIHM	18.9%	0.70	0.77	10.7%	99.0%	7
	HD5-MESCAN	5.8%	0.40	0.56	10.5%	59.6%	9
	HD 1.10	16.2%	0.57	0.72	9.8%	71.5%	7
Weser	HD5-JSBACH	47.6%	0.49	0.83	12.9%	107.9%	1
	HD5-MPIHM	45.6%	0.53	0.91	10.9%	104.6%	1
	HD5-MESCAN	0.5%	0.50	0.81	7.2%	54.1%	3
	HD 1.10	−12.6%	0.58	0.82	7.4%	64.5%	1

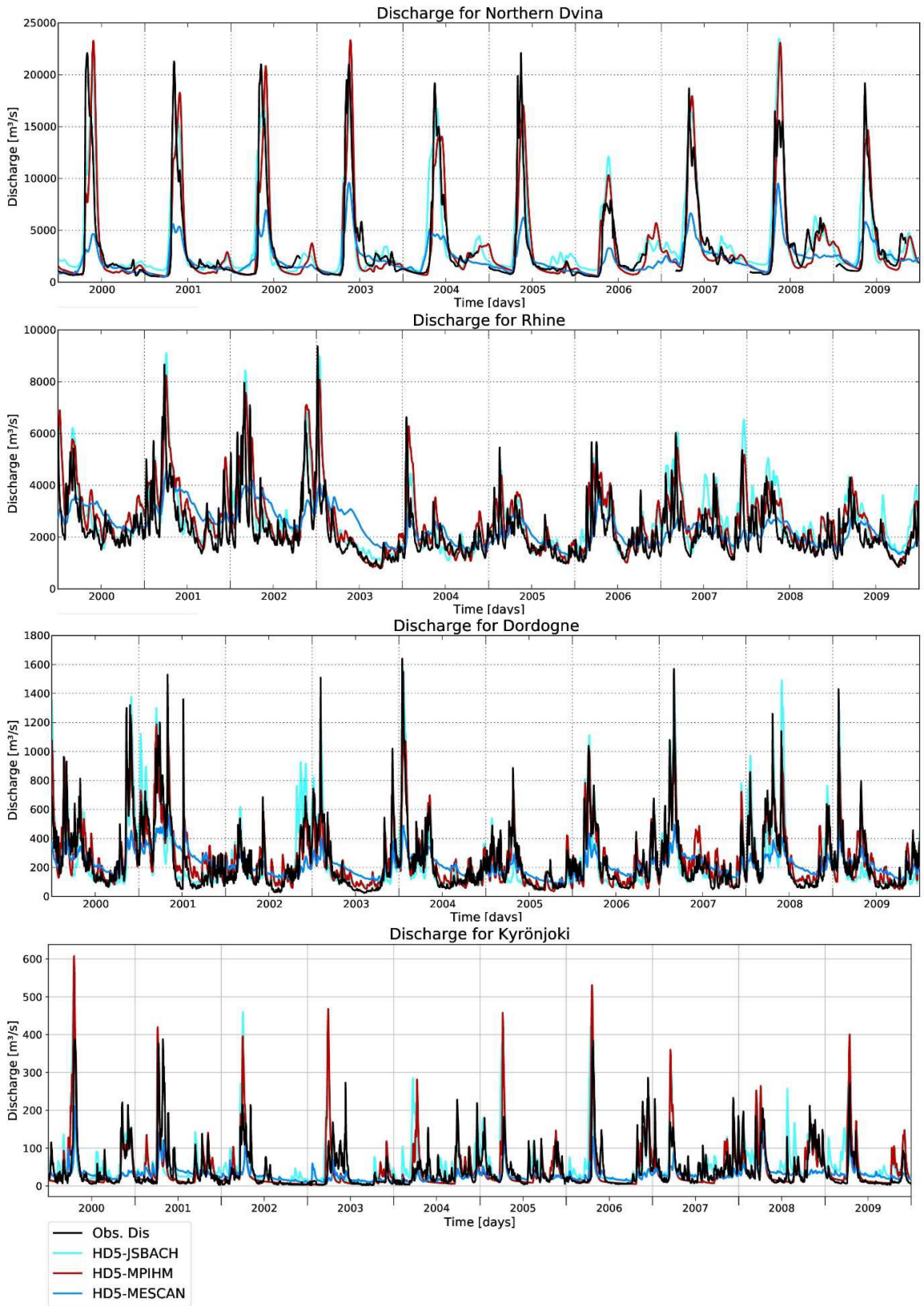

FIGURE 7 | Simulated and observed discharges from 2000–2009 for Northern Dvina (384000 km^2), Rhine (160800 km^2), Dordogne (14925 km^2) and Kyrönjoki (4833 km^2). The maximum KGE values are yielded by HD5-MPIHM and are 0.85, 0.70, 0.80, and 0.64, respectively.

other two datasets due to its higher resolution. Beer et al. (2014) and WFDEI precipitation are very similar as the monthly means of both datasets are based on two different versions of precipitation data from the Global Precipitation Climatology Centre (GPCC) using the same method of undercatch correction (cf. Weedon et al., 2011, 2014).

The biases of total runoff are shown for the three forcing datasets in **Figure 4** (right column), whereat for each river, the bias is allocated to the respective catchment area. The JSBACH runoff tends to be overestimated for many catchments, especially in the Baltic area, the Volga River, central Europe and northern France. The MPI-HM runoff is often lower than the JSBACH data, showing similar positive biases only over Central Europe and France, and reduced biases over the southern Baltic area. However, in the Barents Sea area, northern and central Scandinavia, the runoff is underestimated for many rivers instead. The MESCAN data generally show the lowest runoff biases, having noticeable negative biases especially over Northern Russia and the British Isles. Note that the runoff of the Don River is largely overestimated by all forcing datasets, which is related to

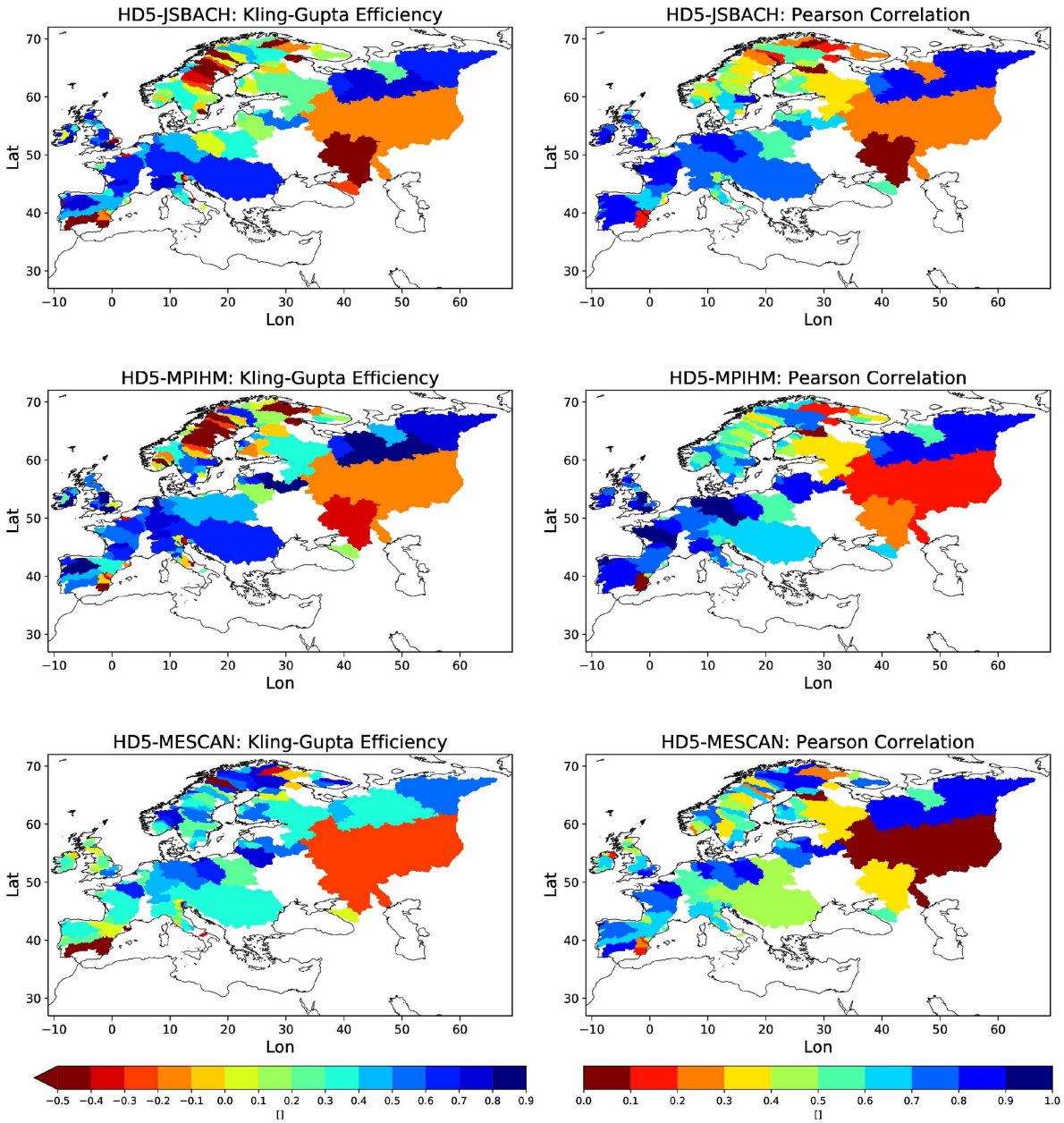

FIGURE 8 | Kling Gupta efficiencies **(left column)** and Pearson correlations **(right column)** with the observed daily discharges for HD5-JSBACH (1st row), HD5-MPIHM (2nd row), and HD5-MESCAN (3rd row).

the large human water withdrawals that comprise more than 50% of the perennial discharge (Khublaryan, 2009). The same seems to be the case for several rivers in southern and eastern Spain where larger amounts of water are withdrawn for irrigation purposes (see, e.g., Merchán et al., 2013; Expósito, 2018).

The runoff biases shown in **Figure 4** impose an upper limit on the accuracy of simulated discharge. Except for rivers with large abstractions of water, biases in total runoff and discharge agree in long-term averages. Therefore, if the KGE of a specific river with a runoff bias c_3 is considered, the maximum KGE that can be yielded after simulating the discharge is 1-c_3.

Impact of Resolution

First, we consider whether it is beneficial to simulate the discharge at 5 Min. resolution compared to the HD standard resolution of 0.5°. While the answer is trivial for smaller catchments where using the coarse resolution model is not appropriate, this is not obvious for larger rivers.

In **Figure 5**, monthly discharges of HD5-JSBACH are compared to the 0.5° discharges of HD 1.10 for a few selected rivers. Note that for HD 1.10, we consider not only the grid boxes close to the location of the discharge observations, but also the simulated discharge at the river mouth. The reason is

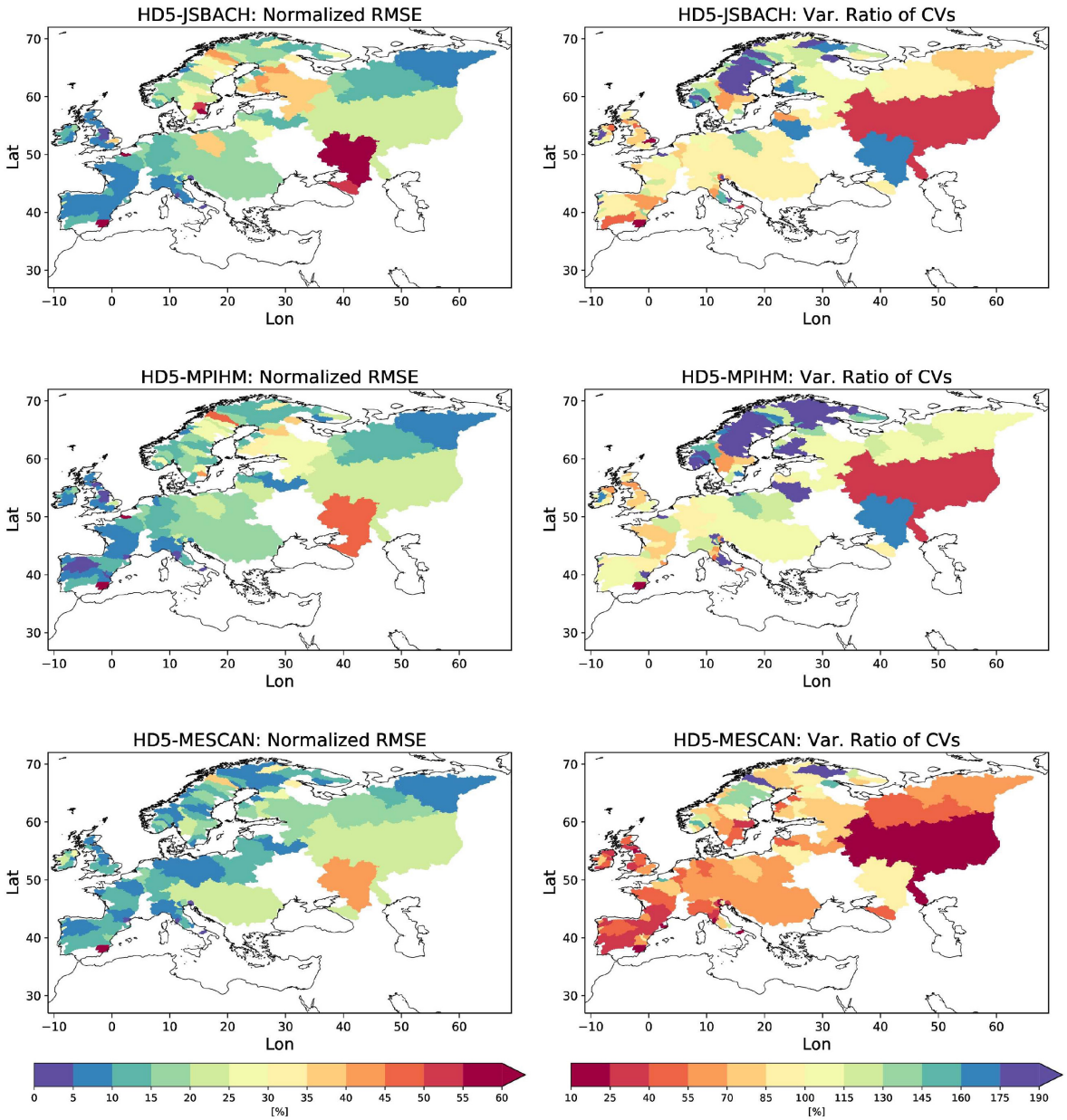

FIGURE 9 | Normalized RSME **(left column)** and variability ratio of the coefficients of variation **(right column)** for HD5-JSBACH (1st row), HD5-MPIHM (2nd row), and HD5-MESCAN (3rd row).

that flow directions at 0.5° were only adjusted for main river paths and at the catchment boundaries, but not for every grid box (Hagemann and Dümenil, 1998). Hence, in some cases, the 0.5° model catchment at a station location may deviate from the actual catchment. **Figure 5** shows that it is difficult to judge whether the 5 Min. resolution leads to better discharges or the 0.5° resolution. Despite of some biases, the HD model is able to capture the monthly discharge reasonably well with both resolutions. Only for the Weser, the standard HD model is clearly worse if the grid box near the river gauge is considered. However, this clear discrepancy vanishes if the 0.5° discharge simulated at the river mouth is considered for the reasons mentioned above. Here, the 0.5° model catchment at the station location deviates from the actual catchment within the Weser basin.

The situation is different when daily discharges are considered as clear improvements are caused by using the higher resolution (**Figure 6**). With the higher resolution, the variations of many discharge peaks are much better captured than by using the 0.5° resolution. This is also reflected by the increase in the variability ratio that is much closer to the observations with HD5-JSBACH than for HD 1.10 (**Table 2**). The improved simulation of daily discharges is especially obvious for the Elbe and Weser rivers, but also applies to the Rhine and the Danube. Note that positive runoff biases (see **Figure 4**) in the JSBACH forcing data limit the overall performance of simulated discharge (cf. discharge bias in **Table 2**) over the Elbe (runoff bias: 46.1%), Rhine (15.7%), and Weser (43.7%).

Evaluation of 5 Min. Simulations

Figure 7 shows simulated and observed discharges for several rivers across a range of different catchment sizes (shown in brackets with regard to the discharge gauge), ranging from large scale catchments such as the Northern Dvina to small catchments as the Kyrönjoki. The corresponding evaluation metrics are provided in **Table 2** for all experiments. As for the rivers shown in **Figure 6**, the timing of the main peaks is often captured by HD5 for many rivers across Europe, especially by HD5-JSBACH and HD5-MPIHM. In order to evaluate the simulated discharges in a more comprehensive way, various metrics (cf. section "Evaluation Metrics") were calculated for the different rivers where observed discharge was available within the period of 2000–2009. For the graphical representation, these metrics were allocated to the respective catchment areas.

Figure 8 (left column) shows the spatial distribution of Kling-Gupta efficiencies (KGEs) across the European catchments for the three experiments. Over northern Russia, Central and Western Europe and Northern Iberia, HD5-JSBACH and HD5-MPIHM yield relatively high KGEs (>0.4, bluish colors). In addition, several rivers flowing into the Baltic Sea show some acceptable performance (>0.3), especially in the southern part. In the contrary, the discharge of many Scandinavian, south Russian and east Spanish rivers is not well represented. HD5-MESCAN shows less good, but still acceptable performance (>0.3) over northern Russia, Central and Western Europe, but an improved simulation of discharge over Scandinavia.

As KGE comprises contributions from correlation, bias and variability terms, correlation r_{cor}, RMSE and the variability ratio of the coefficients of variation are considered in **Figure 8** (right column) and **Figure 9**, left and right column, respectively. Over western Iberia, Central and Western Europe, correlation pattern are similar to the KGE distributions, with HD5-JSBACH and HD5-MPIHM having higher correlations (>0.6) than HD5-MESCAN (>0.4), while all experiments show high correlations (>0.7) over northern Russia. Acceptable correlations (>0.4) are also yielded for many Baltic rivers except for the Newa and

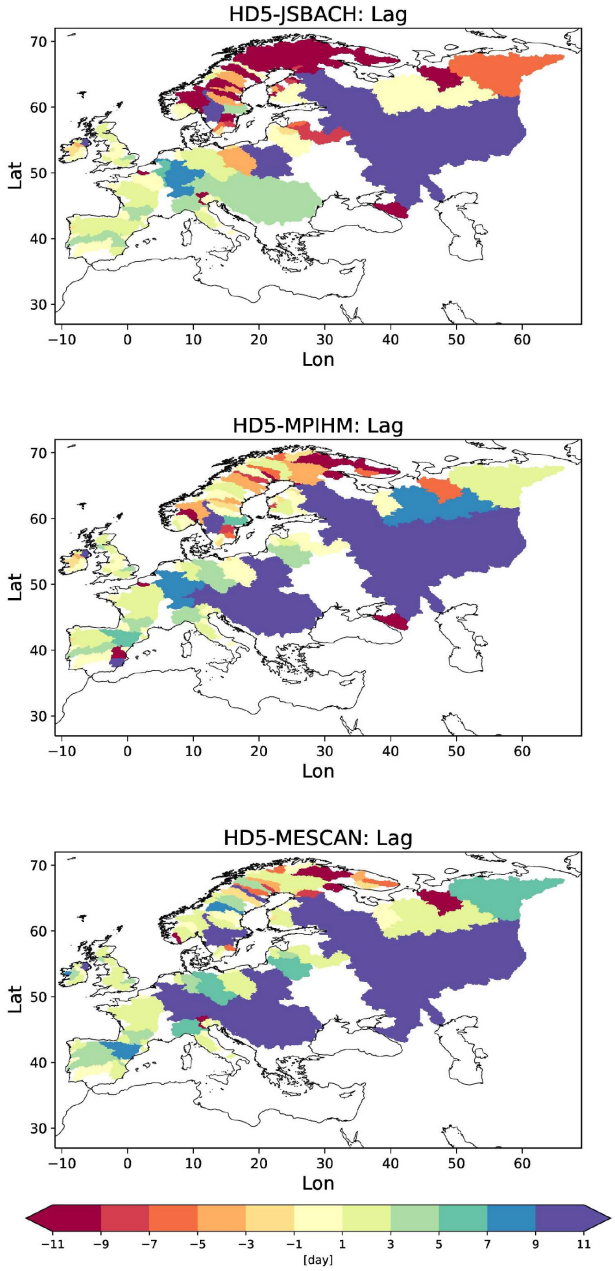

FIGURE 10 | Lags to the observed daily discharges for HD5-JSBACH **(upper panel)**, HD5-MPIHM **(middle panel),** and HD5-MESCAN **(lower panel)**. A positive lag indicates that the simulated discharge is delayed compared to the observed one.

some Scandinavian rivers, with HD5-MPIHM being somewhat better than the other two experiments. For the normalized RMSE, HD5-MESCAN tends to have lower values than the other two experiments and has values below 25% for most of the rivers. The other two experiments yield rather high values over some Baltic rivers, but also stay below 25% for many rivers. Again, all experiments have lowest RSME values over northern Russia, western Iberia, Central and Western Europe. A somewhat different picture is obtained for the variability ratios. Here, JSBACH and HD5-MPIHM yield rather good ratios close to one (deviations smaller than 15%) for most rivers in northern Russia, eastern Baltic, western Iberia, Central and Western Europe, but largely overestimate the variability for most Scandinavian rivers and the Don. HD5-MESCAN generally underestimates the variability across all European rivers, except for some Baltic rivers and the Don. Hence, this lower variability induces the main KGE differences to the other two experiments.

To consider the temporal behavior of simulated discharge, the lags compared to the observations are considered in **Figure 10**. All experiments have low lags (<3 days) for Western Europe and tend to simulate late discharges over Central and especially over Eastern Europe. The HD5-JSBACH discharge generally arrives too early over Northern Europe, while HD5-MESCAN tends to be late across all considered rivers, with some exceptions over Northern Europe. HD5-MPIHM shows much lower lags over Northern Europe, even though it also tends to be too early in this region.

Discussion of Results

In Scandinavia, especially in Sweden, many rivers are regulated. As this regulation is not regarded in the HD model, its effects can generally not be simulated. A typical example is given for the Indalsaelven (**Figure 11**). On the one hand, apparent snowmelt induced discharge peaks in spring are simulated, but only weak indications of such peaks occur in the observed time series. On the other hand, there is only little variation in the observed low flow periods, while there is more variability and generally lower discharge in the simulations. This can be interpreted as extractions of water during the snowmelt season and supply of the stored water during low flow periods. It can be noted that rainfall induced discharge peaks outside the

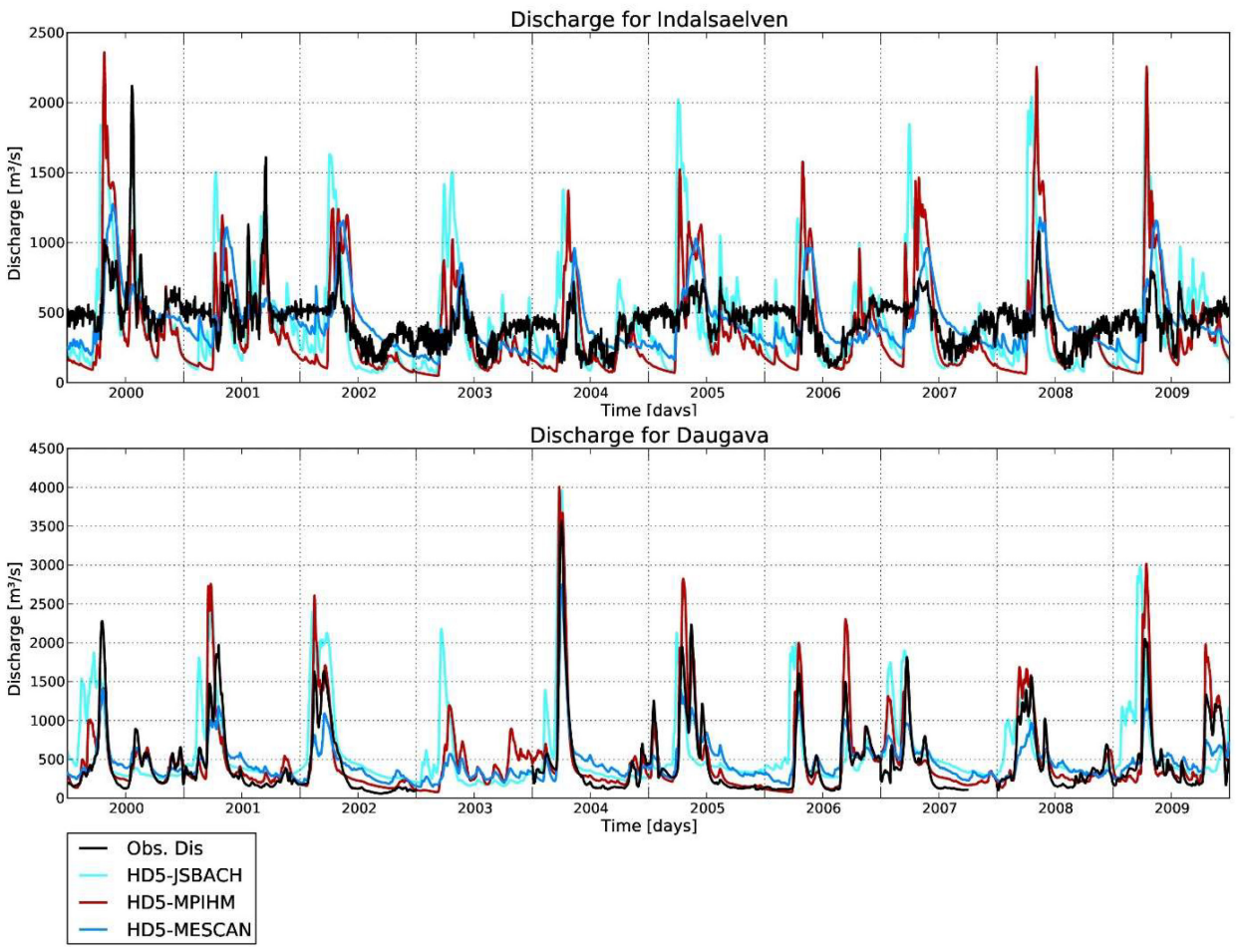

FIGURE 11 | Simulated and observed discharges from 2000–2009 for Indalsälven (25761 km^2), and Daugava (64500 km^2).

snowmelt season are rather well captured by the HD model, e.g., in the second halves of the years 2001, 2004, and 2005 for HD5-JSBACH and HD5-MPIHM.

In general, HD5-MESCAN simulates much lower discharge peaks and higher amounts of low flows than the other two experiments. This leads to a worse simulation of daily discharge for many rivers. This is demonstrated for the rivers Rhine and Dordogne (**Figure 7**) where the discharge peak values are poorly represented by HD5-MESCAN, while the low flows and especially the receding discharge curves after many peaks are strongly overestimated. This erroneous behavior is induced by a different separation of the lateral flow into surface and subsurface runoff in the MESCAN-SURFEX model (**Figure 12**). This behavior points to deficiencies in its land surface scheme that tends to produce largely under- and overestimated amounts of surface and subsurface runoff, respectively. The biased separation of the lateral flow toward subsurface runoff leads to a general smoothing of the simulated discharge curves. On the one hand, this smoothing leads to a lower variability (**Figure 9**) than in the observations and the two other experiments. On the other hand, the too strong contribution of slow flow components (subsurface runoff) compared to the fast flow component (surface runoff) leads to a delayed total flow as indicated by the generally larger lags in **Figure 10**. In a way, the general smoothing is a similar effect as caused by human river regulation. As the erroneous smoothing partially compensates for the missing river regulation process (see above), the simulated discharges are improved for many anthropogenically influenced rivers compared to the other two experiments, especially over Scandinavia. This is also indicated by larger KGE (**Figure 8**) and lower RSME (**Figure 9**) than in the other two experiments.

For many rivers where the discharge curve is characterized by a snowmelt induced discharge peak in spring, HD5-JSBACH tends to simulate earlier peaks than the other two experiments. This simulated peak often occurs also earlier than in the observations, such as can be seen for the Daugava (**Figure 11**). As this is not the case for the other two experiments, this points to a deficiency in the JSBACH land surface scheme in simulating a too early snowmelt. As the snowmelt peak in the spring is the dominant characteristic of the discharge curve for these rivers, this deficiency becomes also visible in the lag of the whole discharge time series considered in **Figure 10** before.

Since the MESCAN data have a higher spatial resolution compared to other two experiments, it was originally expected that this would yield better-simulated discharge than for the two experiments using 0.5° forcing, particularly over smaller-scale basins with relatively complex terrain like in Scandinavia. With regard to the total bias (**Figure 4**) and RMSE (**Figure 9**), this expectation partially holds as HD5-MESCAN shows the lowest error for many rivers. But due to the too low surface runoff ratio, the high resolution advantage is often more than compensated if other metrics are considered (KGE and Pearson correlation in **Figure 8**, variability ratio of the coefficients of variation in **Figure 9**), where HD5-MESCAN performs less well than the other two experiments for many rivers, except for Scandinavia (see above).

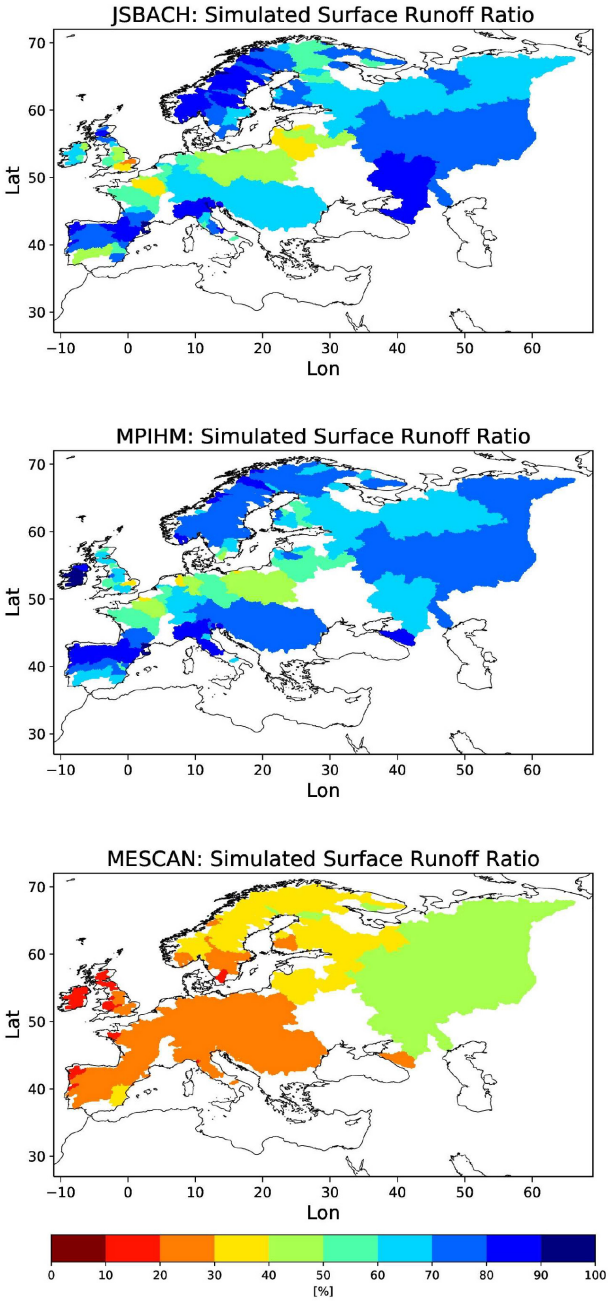

FIGURE 12 | Simulated surface runoff ratio (catchment averaged surface runoff divided by total runoff) for JSBACH **(upper panel)**, MPIHM **(middle panel)** and MESCAN **(lower panel)**.

SUMMARY AND CONCLUSION

In the present study, a well-established discharge model, the HD model, was further developed to be globally applicable at 5 Min. resolution. The improved HD5 model is one of the very first gridded discharge models that is (a) developed for applications in RCSMs, and (b) features a noticeably higher resolution than utilized in previous RCSMs. As the HD5 model

shall be applied in climate change studies and over ungauged catchments, no river specific parameter adjustments, e.g., by calibration, were conducted. In order to prepare high-resolution discharge simulations over Europe and the Baltic Sea catchment within a RCSM setup, its initialdevelopment and evaluation wereconducted for a European domain. Note that the HD5 model has already been successfully coupled within the GCOAST-AHOI setup over this domain (Ho-Hagemann et al., submitted). For the validation of the HD5 model, three different methods and datasets were used to derive the required fields of surface and subsurface runoff for the forcing of the HD5 model. Biases in these fields impose an upper limit on the accuracy of simulated discharge that has to be regarded in the evaluation of the HD5 performance. Results from the three respective simulations show that the HD5 model is able to capture the general behavior of discharge for many European rivers, especially in northern Russia, northern Iberia, Western and Central Europe. Several biases could be traced back to deficits in the forcing data, especially with regard to the total amount of runoff, the early snowmelt in JSBACH and the too low surface runoff ratio in MESCAN. For many catchments affected by the deficits of a specific forcing, the corresponding biases are low in those simulations where the respective deficits are not present in the forcing. This indicates that the HD5 model is representing the discharge behavior well for these rivers. Larger deviations of the simulated from the observed discharges occur for rivers that are strongly affected by human impacts such as water abstractions, e.g., for irrigation, and regulation, e.g., by dams. Consequently, for the hydrological modeling of rivers and watersheds that are highly influenced by human activities, related processes need to be implemented into the HD5 model. This includes the implementation of dams and reservoirs (based on available global databases), their management of river flow regulations as well as modules to simulate water withdrawals, e.g., for irrigation.

Apart from lags induced by deficits in the forcing data and the missing representation of human river regulations and water abstractions, some lags may also be introduced if HD5 does not adequately capture the flow regime of a river. This can be caused by the impacts of lakes and wetlands on the river flow, which is currently only simply parameterized (Hagemann and Dümenil, 1998). Here, the Newa is an example whose discharge curve is largely determined by the outflow from the Lake Ladoga. Also a strong meandering, which slows down the flow, or human stream straightening, which accelerates the flow, are not specifically regarded by the model. To overcome such lags, Alwardt (2015) suggested adjusting the flow velocities of the main river flow path

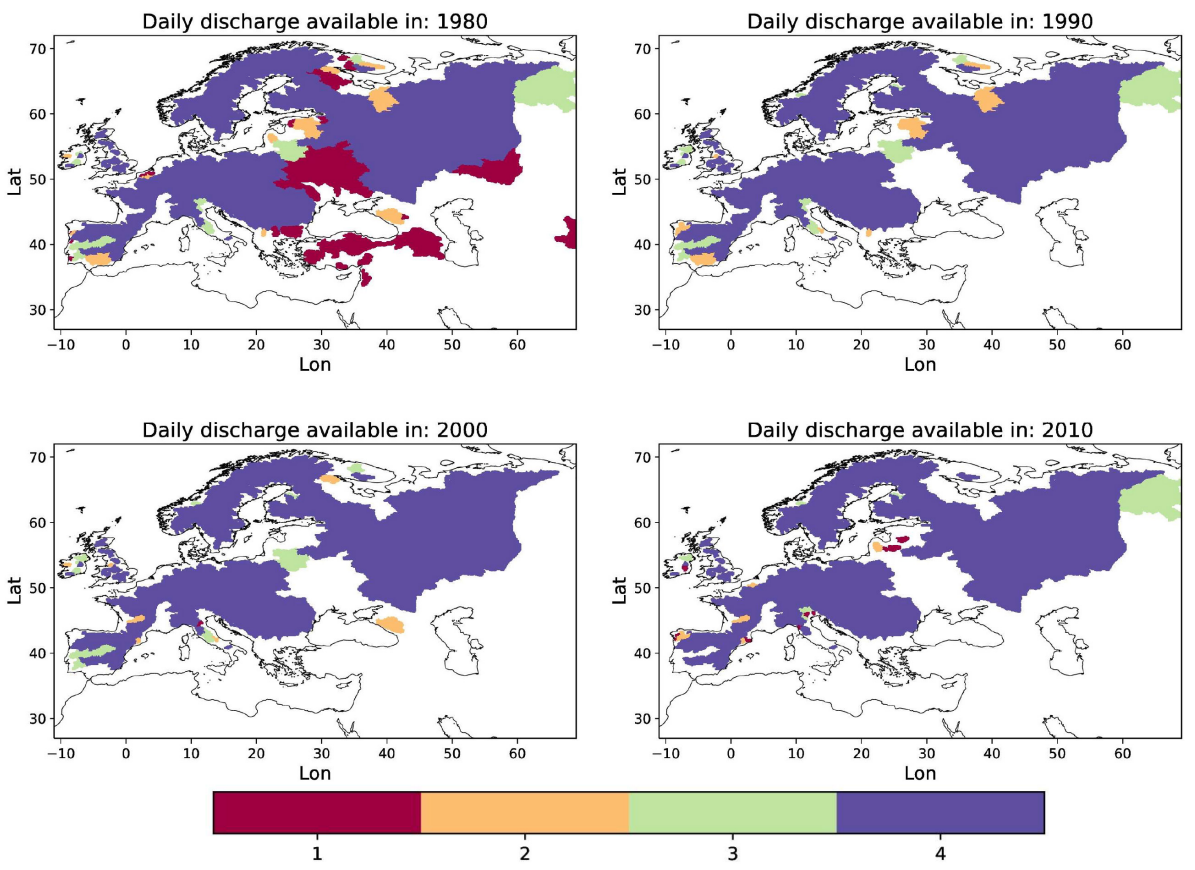

FIGURE 13 | Catchments with daily discharge observations available at a downstream station for more than 90% of days in the years 1980, 1990, 2000, and 2010. Colors indicate the number of years within these 4 years, when discharge data are available.

of the respective rivers. However, such a correction is not straight forward as it has to be ensured that the lag is caused neither by deficits in the forcing nor by the missing human impact. If a lag were caused by the latter, an adjustment of the flow velocity in the main river flow path would improve the current discharge simulation but may spoil later attempts to include human impacts into the HD model. Potentially, this may be done for rivers where the lag more or less agrees in discharge simulations with different forcings. Using the three forcings of the present study, such a correction may be feasible for the Rhine (lags of 7–9 days) and the Vistula (lags of 15–19 days), but not for the heavy regulated Volga and Don and the lake outflow dominated Newa.

The insufficient availability of daily discharge observations prevents an evaluation of HD5 over all larger European catchments. **Figure 13** shows catchments where daily discharge observations were available to us at a downstream station for selected years across the recent decades. Note that we only considered rivers with catchment areas around 3000 km^2 or larger. While the situation is rather good in Northern, Western and central Europe, almost no daily data are available for Southern Europe (except for Iberia and northern Italy) and some Eastern European rivers. The spatial coverage of daily data is largest in 1980 and decreases in later decades. Reasons for the data gaps are manifold. Either there are no available downstream stations, the data are not accessible or the available time series are rather short. Often data exists at National authorities, but they were neither making the data freely available nor via GRDC.

Such lack of data is not only a south European problem as large-scale international archives of water data are insufficiently equipped in several areas of the world (Hannah et al., 2011). Dixon et al. (2013) pointed out that "globally, funding constraints and changing governmental priorities have resulted in a decline in some river gauging station networks, while concerns about misuse of data, commercial drivers, political sensitivities about transboundary resources and an overarching lack of understanding about the value of river flow information limit the exchange of the hydrological data that is collected." They further noted that "freshwater environments, their drivers, controls and impacts are not constrained by national boundaries and, hence, international cooperation is vital to provide the information needed to further our understanding of hydrological systems." Thus, future data policies in Europe should support the open access of discharge data, e.g., via public national data portals or via GRDC.

Despite some recommended developments with regard to human impacts on rivers, our results show that the HD5 model is already well suited for the application within a RCSM. In this respect, an interface to the OASIS coupler (Valcke, 2013) has already been developed which makes the HD model more flexible for coupling purposes. Hence, it may not only be coupled within the GCOAST system (see section "The HD Model"), but also to any other RCM and ocean model via the OASIS coupler. In addition, the comparison of the simulated discharges from the three experiments indicates that the HD5 model is also suitable to evaluate the terrestrial hydrological cycle of climate models or land surface models, especially with regard to the separation of throughfall (rain or snow melt) into surface and subsurface runoff. Currently, such evaluation attempts must be limited to rivers that are not highly influenced by human activities.

AUTHOR CONTRIBUTIONS

SH carried out the HD model improvements, discharge simulations, analysis of results, and wrote the manuscript. HH-H initiated the study and helped with model adaptations suitable for the coupling within a RCSM. TS generated the MPIHM forcing data. TS and HH-H helped with the analysis and revised the manuscript.

ACKNOWLEDGMENTS

We are very grateful to Bernhard Lehner (World Wide Fund For Nature) who prepared the used river directions and digital elevation data at 5 Min. for us. We thank the Global Runoff Data Centre for providing most of the discharge observations used in this study. We also thank Sonja van Leuwen (Royal Netherlands Institute for Sea Research) for providing us with some further discharge data from various sources.

REFERENCES

Alwardt, C. (2015). *Entwicklung eines Aggregierten Modellsystems zur Szenariobasierten Simulation der Wasserhaushalte von Flusseinzugsgebieten, unter Berücksichtigung klimatischer und sozioökonomischer Einflüsse*. Ph.D. Thesis, Universität Hamburg, Hamburg.

Anyamba, A., and Tucker, C. J. (2005). Analysis of Sahelian vegetation dynamics using NOAA-AVHRR NDVI data from 19812003. *J. Arid. Environ.* 63, 596–614. doi: 10.1016/j.jaridenv.2005.03.007

Bazile, E., Abida, R., Szczypta, C., Verelle, A., Soci, C., and Moigne, P. L. (2017). *Deliverable D2.9: Ensemble Surface Reanalysis Report*. Technical Report No. 607193. Golden, CO: UERRA.

Beer, C., Weber, U., Tomelleri, E., Carvalhais, N., Mahecha, M., and Reichstein, M. (2014). Harmonized European long-term climate data for assessing the effect of changing temporal variability on land-atmosphere CO2 fluxes*. *J. Climate* 27, 4815–4834. doi: 10.1175/jcli-d-13-00543.1

Best, M. J., Pryor, M., Clark, D. B., Rooney, G. G., Essery, R. L. H., Ménard, C. B., et al. (2011). The Joint UK Land Environment Simulator (JULES), model description - Part 1: energy and water fluxes. *Geosci. Model Dev.* 4, 677–699. doi: 10.5194/gmd-4-677-2011

Bierkens, M. F. P., Bell, V. A., Burek, P., Chaney, N., Condon, L. E., David, C. H., et al. (2015). Hyper-resolution global hydrological modelling: what is next? *Hydrol. Process.* 29, 310–320. doi: 10.1002/hyp.10391

Bouwman, A. F., Bierkens, M. F. P., Griffioen, J., Hefting, M. M., Middelburg, J. J., Middelkoop, H., et al. (2013). Nutrient dynamics, transfer and retention along the aquatic continuum from land to ocean: towards integration of ecological and biogeochemical models. *Biogeosciences* 10, 1–22. doi: 10.5194/bg-10-1-2013

Breckle, S.-W., and Geldyeva, G. V. (2012). "Dynamics of the Aral Sea in geological and historical times," in *Ecological Studies 218, Aralkum - a Man-Made Desert: The Desiccated Floor of the Aral Sea (Central Asia)*, eds S.-W. Breckle, et al. (Berlin: Springer-Verlag), 13–35. doi: 10.1007/978-3-642-21117-1_2

Bremicker, M. (2000). *Das Wasserhaushaltsmodell LARSIM - Modellgrundlagen und Anwendungsbeispiele. Freiburger Schriften zur Hydrologie 11*. Freiburg im Breisgau: University of Freiburg im Breisgau.

Daewel, U., and Schrum, C. (2017). Low-frequency variability in North Sea and Baltic Sea identified through simulations with the 3-D coupled physical–biogeochemical model ECOSMO. *Earth Syst. Dyn.* 8:801. doi: 10.5194/esd-8-801-2017

Decharme, B., Martin, E., and Faroux, S. (2013). Reconciling soil thermal and hydrological lower boundary conditions in land surface models. *J. Geophys. Res. Atmos.* 118, 7819–7834. doi: 10.1002/jgrd.50631

Dee, D. P., Uppala, S. M., Simmons, A. J., Berrisford, P., Poli, P., Kobayashi, S., et al. (2011). The ERA-interim reanalysis: configuration and performance of the data assimilation system. *Quart. J. Roy. Meteor. Soc.* 137, 553–597. doi: 10.1002/qj.828

Dell'Aquila, A., Calmanti, S., Ruti, P., Struglia, M., Pisacane, G., Carillo, A., et al. (2012). Effects of seasonal cycle fluctuations in an a1b scenario over the euro-mediterranean region. *Clim. Res.* 52, 135–157. doi: 10.3354/cr01037

Dixon, H., Rodda, J., Jenkins, A., Demuth, S., and Looser, U. (2013). "Sharing water observations: turning local data into global information," in *Free Flow - Reaching Water Security Through Cooperation*, eds J. Griffiths, and R. Lambert (France: UNESCO).

Donnelly, C., Andersson, J. C. M., and Arheimer, B. (2016). Using flow signatures and catchment similarities to evaluate the e-hype multi-basin model across europe. *Hydrol. Sci. J.* 61, 255–273. doi: 10.1080/02626667.2015.1027710

Ekici, A., Beer, C., Hagemann, S., Boike, J., Langer, M., and Hauck, C. (2014). Simulating high-latitude permafrost regions by the JSBACH terrestrial ecosystem model. *Geosci. Model Dev.* 7, 631–647. doi: 10.5194/gmd-7-631-2014

Elizalde, A. (2011). *The Water Cycle in the Mediterranean Region and the Impacts of Climate Change*. Ph.D. Thesis. MPI for Meteorology, Hamburg, doi: 10.17617/2.1216556

Epule, E. T., Peng, C., Lepage, L., and Chen, Z. (2014). The causes, effects and challenges of Sahelian droughts: a critical review. *Reg. Environ. Change* 14, 145–156. doi: 10.1007/s10113-013-0473-z

Expósito, A. (2018). Irrigated agriculture and the cost recovery principle of water services: assessment and discussion of the case of the Guadalquivir river basin (Spain). *Water* 10:1338. doi: 10.3390/w10101338

Flato, G., Marotzke, J., Abiodun, B., Braconnot, P., Chou, S., Collins, W., et al. (2013). "Evaluation of climate models," in *Climate Change 2013: The Physical Science Basis. Contribution of Working Group I to the Fifth Assessment Report of the Intergovernmental Panel on Climate Change*, eds T. Stocker, D. Qin, G.-K. Plattner, M. Tignor, S. Allen, J. Boschung, et al. (Cambridge: Cambridge University Press), 741–866.

Flörke, M., Kynast, E., Barlund, I., Eisner, S., Wimmer, F., and Alcamo, J. (2013). Domestic and industrial water uses of the past 60 years as a mirror of socio-economic development: a global simulation study. *Glob. Environ. Change* 23, 144–156. doi: 10.1016/j.gloenvcha.2012.10.018

Giorgetta, M. A., Jungclaus, J., Reick, C. H., Legutke, S., Bader, J., Böttinger, M., et al. (2013). Climate and carbon cycle changes from 1850 to 2100 in MPI-ESM simulations for the Coupled Model Intercomparison Project phase 5. *J. Adv. Model. Earth Syst.* 5, 572–597. doi: 10.1002/jame.20038

Guimberteau, M., Drapeau, G., Ronchail, J., Sultan, B., Polcher, J., Martinez, J.-M., et al. (2012). Discharge simulation in the sub-basins of the amazon using ORCHIDEE forced by new datasets. *Hydrol. Earth Syst. Sci.* 16, 911–935. doi: 10.5194/hess-16-911-2012

Gupta, H. V., Kling, H., Yilmaz, K. K., and Martinez, G. F. (2009). Decomposition of the mean squared error and NSE performance criteria: implications for improving hydrological modelling. *J. Hydrol.* 377, 80–91. doi: 10.1016/j.jhydrol.2009.08.003

Haddeland, I., Clark, D. B., Franssen, W., Ludwig, F., Voß, F., Arnell, N. W., et al. (2011). Multimodel estimate of the global terrestrial water balance: setup and first results. *J. Hydrometeorol.* 12, 869–884. doi: 10.1175/2011jhm1324.1

Hagemann, S. (2002). *An Improved Land Surface Parameter Dataset for Global and Regional Climate Models*. Max Planck Institute for Meteorology Report No. 336. Hamburg: MPI for Meteorology.

Hagemann, S., Chen, C., Clark, D. B., Folwell, S., Gosling, S. N., Haddeland, I., et al. (2013). Climate change impact on available water resources obtained using multiple global climate and hydrology models. *Earth Syst. Dyn.* 4, 129–144. doi: 10.5194/esd-4-129-2013

Hagemann, S., and Dümenil, L. (1998). A parametrization of the lateral waterflow for the global scale. *Climate Dyn.* 14, 17–31. doi: 10.1007/s003820050205

Hagemann, S., and Dümenil Gates, L. (2001). Validation of the hydrological cycle of ECMWF and NCEP reanalyses using the MPI hydrological discharge model. *J. Geophys. Res. D* 106, 1503–1510. doi: 10.1029/2000JD900568

Hannah, D. M., Demuth, S., van Lanen, H. A. J., Looser, U., Prudhomme, C., Rees, G., et al. (2011). Large-scale river flow archives: importance, current status and future needs. *Hydrol. Process.* 25, 1191–1200. doi: 10.1002/hyp.7794

Harding, R., Best, M., Blyth, E., Hagemann, S., Kabat, P., Tallaksen, L. M., et al. (2011). WATCH: current knowledge of the terrestrial global water cycle. *J. Hydrometeorol.* 12, 1149–1156. doi: 10.1175/jhm-d-11-024.1

Hordoir, R., and Meier, H. E. M. (2010). Freshwater fluxes in the Baltic Sea: a model study. *J. Geophys. Res.* 115:C08028. doi: 10.1029/2009jc005604

Hordoir, R., Polcher, J., Brun-Cottan, J.-C., and Madec, G. (2008). Towards a parametrization of river discharges into ocean general circulation models: a closure through energy conservation. *Climate Dyn.* 31, 891–908. doi: 10.1007/s00382-008-0416-4

Jungclaus, J. H., Keenlyside, N., Botzet, M., Haak, H., Luo, J.-J., Latif, M., et al. (2006). Ocean circulation and tropical variability in the coupled model ECHAM5/MPI-OM. *J. Climate* 19:3952. doi: 10.1175/jcli3827.1

Khublaryan, M. G. (2009). "Water resources for sustainable development, with particular reference to Russia," in *Area Studies (Regional Sustainable Development Review): Russia*, Vol. I, ed. N. P. Laverov (Oxford: Eolss Publishers Co. Ltd), 81–94.

Kling, H., Fuchs, M., and Paulin, M. (2012). Runoff conditions in the upper Danube basin under an ensemble of climate change scenarios. *J. Hydrol.* 42, 264–277. doi: 10.1016/j.jhydrol.2012.01.011

Kotlarski, S., Keuler, K., Christensen, O. B., Colette, A., Déqué, M., Gobiet, A., et al. (2014). Regional climate modeling on European scales: a joint standard evaluation of the EURO-CORDEX RCM ensemble. *Geosci. Model Dev.* 7, 1297–1333. doi: 10.5194/gmd-7-1297-2014

Larsen, M. A. D., Refsgaard, J. C., Drews, M., Butts, M. B., Jensen, K. H., Christensen, J. H., et al. (2014). Results from a full coupling of the HIRHAM regional climate model and the MIKE SHE hydrological model for a danish catchment. *Hydrol. Earth Syst. Sci.* 18, 4733–4749. doi: 10.5194/hess-18-4733-2014

Lawrence, D. M., Oleson, K. W., Flanner, M. G., Thornton, P. E., Swenson, S. C., Lawrence, P. J., et al. (2011). Parameterization improvements and functional and structural advances in version 4 of the community land model. *J. Adv. Model. Earth Syst.* 3:M03001. doi: 10.1029/2011MS00045

Lee, J.-W., Hong, S.-Y., Kim, J.-E. E., Yoshimura, K., Ham, S., and Joh, M. (2015). Development and implementation of river-routing process module in a regional climate model and its evaluation in korean river basins. *J. Geophys. Res. Atmos.* 120, 4613–4629. doi: 10.1002/2014JD022698

Lehmann, A., and Hinrichsen, H.-H. (2000). On the thermohaline variability of the baltic sea. *J. Mar. Syst.* 25, 333–357. doi: 10.1016/s0924-7963(00)00026-9

Lehner, B., Verdin, K., and Jarvis, A. (2006). *HydroSHEDS Technical Documentation*. Washington, DC: World Wildlife Fund US.

Lindström, G., Pers, C., Rosberg, J., Strömqvist, J., and Arheimer, B. (2010). Development and testing of the HYPE (Hydrological Predictions for the Environment) water quality model for different spatial scales. *Hydrol. Res.* 41, 295–319. doi: 10.2166/nh.2010.007

López López, P., Wanders, N., Schellekens, J., Renzullo, L. J., Sutanudjaja, E. H., and Bierkens, M. F. P. (2016). Improved large-scale hydrological modelling through the assimilation of streamflow and downscaled satellite soil moisture observations. *Hydrol. Earth Syst. Sci.* 20, 3059–3076. doi: 10.5194/hess-20-3059-2016

Lorenz, P., and Jacob, D. (2014). BALTIMOS — a coupled modelling system for the Baltic Sea and its drainage basin. *Theor. Appl. Climatol.* 118:715. doi: 10.1007/s00704-014-1276-y

Marzeion, B., Levermann, A., and Mignot, J. (2007). The role of stratification-dependent mixing for the stability of the Atlantic overturning in a global climate model. *J. Phys. Oceanogr.* 37, 2672–2681. doi: 10.1175/2007jpo3641.1

Masson, V., Moigne, P. L., Martin, E., Faroux, S., Alias, A., Alkama, R., et al. (2013). The SURFEXv7.2 land and ocean surface platform for coupled or offline simulation of earth surface variables and fluxes. *Geosci. Model Dev.* 6, 929–960. doi: 10.5194/gmd-6-929-2013

Mauser, W., and Bach, H. (2009). PROMET - Large scale distributed hydrological modelling to study the impact of climate change on the water flows of mountain watersheds. *J. Hydrol.* 376, 362–377. doi: 10.1016/j.jhydrol.2009.07.046

Merchán, D., Causapé, J., and Abrahao, R. (2013). Impact of irrigation implementation on hydrology and water quality in a small agricultural basin in Spain. *Hydrol. Sci. J.* 58, 1400–1413. doi: 10.1080/02626667.2013.829576

Milly, P. C. D., Malyshev, S. L., Shevliakova, E., Dunne, K. A., Findell, K. L., Gleeson, T., et al. (2014). An enhanced model of land water and energy for global hydrologic and earth-system studies. *J. Hydrometeorol.* 15, 1739–1761. doi: 10.1175/jhm-d-13-0162.1

Nash, J., and Sutcliffe, J. (1970). River flow forecasting through conceptual models part I - A discussion of principles. *J. Hydrol.* 10, 282–290. doi: 10.1016/0022-1694(70)90255-6

Oki, T., and Sud, Y. C. (1998). *Earth Interact.* 2, 1–37. doi: 10.1175/1087-35621998002<0001:dotrip<2.3.co;2

Österblom, H., Hansson, S., Larsson, U., Hjerne, O., Wulff, F., Elmgren, R., et al. (2007). Human-induced trophic cascades and ecological regime shifts in the Baltic Sea. *Ecosystems* 10, 877–889. doi: 10.1007/s10021-007-9069-0

Ridal, M., Olsson, E., Unden, P., Zimmermann, K., and Ohlsson, A. (2017). *Deliverable D2.7: HARMONIE Reanalysis Report of Results and Dataset*. Research Report No. 607193 Golden, CO: UERRA.

Roeckner, E., Bäuml, G., Bonaventura, L., Brokopf, R., Esch, M., Giorgetta, M., et al. (2003). *The Atmospheric General Circulation Model ECHAM 5. PART I: Model Description. Max Planck Institute for Meteor*. Report No. 349, MPI for Meteorology, Hamburg.

Samaniego, L., Kumar, R., and Attinger, S. (2010). Multiscale parameter regionalization of a grid-based hydrologic model at the mesoscale. *Water Resour. Res.* 46:W05523. doi: 10.1029/2008WR007327

Sein, D. V., Mikolajewicz, U., Gröger, M., Fast, I., Cabos, W., Pinto, J. G., et al. (2015). Regionally coupled atmosphere-ocean-sea ice-marine biogeochemistry model ROM: 1. description and validation. *J. Adv. Model. Earth Syst.* 7, 268–304. doi: 10.1002/2014ms000357

Senatore, A., Mendicino, G., Gochis, D. J., Yu, W., Yates, D. N., and Kunstmann, H. (2015). Fully coupled atmosphere-hydrology simulations for the central mediterranean: impact of enhanced hydrological parameterization for short and long time scales. *J. Adv. Model. Earth Syst.* 7, 1693–1715. doi: 10.1002/2015ms000510

Sevault, F., Somot, S., Alias, A., Dubois, C., Lebeaupin-Brossier, C., Nabat, P., et al. (2014). A fully coupled mediterranean regional climate system model: design and evaluation of the ocean component for the 1980-2012 period. *Tellus A* 66:23967. doi: 10.3402/tellusa.v66.23967

Shrestha, P., Sulis, M., Masbou, M., Kollet, S., and Simmer, C. (2014). A scale-consistent terrestrial systems modeling platform based on COSMO. CLM, and ParFlow. *Mon. Weather Rev.* 142, 3466–3483. doi: 10.1175/mwr-d-14-00029.1

Sitz, L. E., Sante, F. D., Farneti, R., Fuentes-Franco, R., Coppola, E., Mariotti, L., et al. (2017). Description and evaluation of the earth system regional climate model (Reg CM-ES). *J. Adv. Model. Earth Syst.* 9, 1863–1886. doi: 10.1002/2017ms000933

Sorooshian, S., Lawford, R., Try, P., Rossow, W., Roads, J., Polcher, J., et al. (2005). Water and energy cycles: investigating the links. *WMO Bull.* 54, 58–64. doi: 10.3389/fmicb.2016.00214

Stacke, T., and Hagemann, S. (2012). Development and evaluation of a global dynamical wetlands extent scheme. *Hydrol. Earth Syst. Sci.* 16, 2915–2933. doi: 10.5194/hess-16-2915-2012

Thurow, F. (1997). Estimation of the total fish biomass in the Baltic Sea during the 20th century. *ICES J. Mar. Sci.* 54, 444–461. doi: 10.1006/jmsc.1996.0195

Valcke, S. (2013). The OASIS3 coupler: a european climate modelling community software. *Geosci. Model Dev.* 6, 373–388. doi: 10.5194/gmd-6-373-2013

Väli, G., Meier, H. E. M., and Elken, J. (2013). Simulated halocline variability in the Baltic Sea and its impact on hypoxia during 1961-2007. *J. Geophys. Res. Oceans* 118, 6982–7000. doi: 10.1002/2013jc009192

Van Der Knijff, J. M., Younis, J., and Roo, A. P. J. D. (2010). LISFLOOD: a GIS-based distributed model for river basin scale water balance and flood simulation. *Int. J. Geogr. Inf. Sci.* 24, 189–212. doi: 10.1080/13658810802549154

Warszawski, L., Frieler, K., Huber, V., Piontek, F., Serdeczny, O., and Schewe, J. (2014). The inter-sectoral impact model intercomparison project (ISIMIP): project framework. *Proc. Natl. Acad. Sci. U.S.A.* 111, 3228–3232. doi: 10.1073/pnas.1312330110

Weedon, G. P., Balsamo, G., Bellouin, N., Gomes, S., Best, M. J., and Viterbo, P. (2014). The WFDEI meteorological forcing data set: WATCH Forcing Data methodology applied to ERA-Interim reanalysis data. *Water Resour. Res.* 50, 7505–7514. doi: 10.1002/2014WR015638

Weedon, G. P., Gomes, S., Viterbo, P., Shuttleworth, W. J., Blyth, E., Österle, H., et al. (2011). Creation of the WATCH Forcing Data and its use to assess global and regional reference crop evaporation over land during the twentieth century. *J. Hydrometeorol.* 12, 823–848. doi: 10.1175/2011JHM1369.1

Zhao, F., Veldkamp, T. I. E., Frieler, K., Schewe, J., Ostberg, S., Willner, S., et al. (2017). The critical role of the routing scheme in simulating peak river discharge in global hydrological models. *Environ. Res. Lett.* 12:075003. doi: 10.1088/1748-9326/aa7250

Conflict of Interest: The authors declare that the research was conducted in the absence of any commercial or financial relationships that could be construed as a potential conflict of interest.

frontiers in Earth Science

ORIGINAL RESEARCH
published: 28 April 2020
doi: 10.3389/feart.2020.00069

Synoptic Conditions of Droughts and Dry Winds in the Black Sea Steppe Province Under Recent Decades

Inna Semenova and Mariia Slizhe*

Odessa State Environmental University, Odessa, Ukraine

The features of regional atmosphere circulation, which are accompanied simultaneously by two high impact hydrometeorological phenomena (such as droughts and dry winds) in the Black Sea Steppe zone of Ukraine were considered. Dry wind as a complex phenomenon is widespread throughout Ukraine during the warm season of the year. Dry winds often accompany a drought, but they appear as peripheral processes in contrast to the droughts, which are usually formed in the central parts of anticyclones. The number of days with dry winds at the Steppe stations varies on average from 10 to 20 cases to 40–50 cases per warm season, while in the coastal zone the number of days decreases sharply due to a common increase of air atmospheric relative humidity. Analysis of the interannual dynamics of dry winds showed that the number of days with dry winds increases significantly in seasons characterized by a high aridity, according to values of the drought index used. Two time intervals with high and low frequency of seasonal droughts and dry winds were detected during the considered period: 1995–2015. These phenomena have become more intense after 2004, compared to the previous decade. Backward trajectories of air particles showed that the most cases of dry winds originate in air masses, which form up to 5 days previously at the surface level to the east or north-east outside of the territory of Ukraine and then pass into the study area within 5 days.

Keywords: dry wind, drought, drought index, anticyclone, air mass trajectory

OPEN ACCESS

Edited by:
Hayley Jane Fowler, Newcastle University, United Kingdom

Reviewed by:
Xander Wang, University of Prince Edward Island, Canada
Martin Stendel, Danish Meteorological Institute (DMI), Denmark

****Correspondence:***
Inna Semenova
innas.od@gmail.com

Specialty section:
This article was submitted to Interdisciplinary Climate Studies, a section of the journal Frontiers in Earth Science

Received: *15 August 2018*
Accepted: *26 February 2020*
Published: *28 April 2020*

Citation:
Semenova I and Slizhe M (2020) Synoptic Conditions of Droughts and Dry Winds in the Black Sea Steppe Province Under Recent Decades. Front. Earth Sci. 8:69. doi: 10.3389/feart.2020.00069

INTRODUCTION

The territory of Ukraine is exposed to droughts of different intensities and durations almost every year. Meteorological (or agroclimatic) seasonal droughts are widespread. The Ukrainian Steppe encompasses most of the western segment of the Eurasian Steppe, known as the Black Sea Steppe province or Pontic (**Figure 1**). The border between the Forest-Steppe and the Steppe is not distinct. The Steppe occupies about 40% of the territory of Ukraine and belongs to the driest areas of the country (Kubiiovych and Husar Struk, 1993).

The Steppe stores the greatest heat resources in Ukraine and has the longest growing season, but receives the least precipitation and often suffers from drought. The relatively moderate climate and growing season that lasts between 210 and 245 days allows for the cultivation of heat-loving crops, and even doubles cropping. But the annual precipitation decreases southward from 450 mm along the forest-steppe margin to 300 mm at the coastal plain. The moisture deficit, generated by an average annual evaporation of 900–1,000 mm, is in part compensated by a summer precipitation maximum, just when the plants need more water.

The climate in the Black Sea Steppe province has undergone significant changes over a relatively short period, from the end of the 20th century through to the beginning of the 21st century (Semenova, 2015). At the end of the 20th century the winter temperatures were close to climate conditions. But in the first decade of the 21st century positive temperature anomalies (+0.2, +0.4°C) were observed. The end of the 20th century showed small negative anomalies of summer temperatures. In the first decade of the 21st century strong positive temperature anomalies (up to +1.5°C) are observed. This means that winters and, especially, summers have become warmer. On the other hand, summer precipitation in the Black Sea Steppe province was close to climatic average at the end of the 20th century. But in the first decade of the 21st century there was a strong decline in precipitation, especially in the Western Steppe. So, the current climate is characterized by hot and dry summer conditions, which often lead to drought.

As is well known, drought is a normal, recurring feature of climate. It occurs in high and low rainfall areas and in virtually all climatic regimes. Generally, a natural drought is defined as a negative deviation of hydrometeorological parameters (e.g., precipitation, soil moisture, river flow, groundwater level etc.) from the climatic mean condition. A shortage of weather-related water supply is usually caused by a deviation of precipitation, soil moisture and river discharge that constitute meteorological, agricultural and hydrological droughts, respectively. Socio-economic drought is defined as a lack of weather-related water supply needed to meet the normal water demands for human activities.

There is still no universal method to describe all drought-related processes due to the complexity drought phenomena. The main approach to drought assessment is to use different drought indices such as hydrometeorological non-standardized drought indices [e.g., Hydro-thermal Coefficient of Selyaninov (HTC), Palmer Drought Severity Index (PDSI)] and more flexible and all-applicable standardized indices [e.g., Standardized Precipitation Index (SPI), Standardized Precipitation Evapotranspiration Index (SPEI)] as well as satellite-based indices [e.g., Vegetation Condition Index (VCI), Vegetation Health Index (VHI)] (Svoboda and Fuchs, 2016).

In some cases, drought may be accompanied by dry and hot winds, locally named "Sukhovei," that cause additional damage (Buchinskij, 1976; Schubert et al., 2014). Suchovey is associated with high impact weather conditions, causing strong winds under high air temperatures and low relative humidity that causes vegetation stress. Sukhovey, or the same type of wind in the steppes and semi-desert areas of Eurasia, emanate from the deserts of Africa, Asia Minor, southern Kazakhstan, or Central Asia.

Under dry winds, the main factor determining the level of damage to plants is the state of the water balance of the leaves, dependent on inflows-outflows of water in the leaves. In the field, at an air temperature of 35–37°C, in most plants the stomatal apparatus stops normally regulating the evaporation, which greatly accelerates the drying process in leaves during dry winds. Damage from dry winds occurs due to partial or complete drying of leaves, appearance of brown spots on them, and early yellowing and falling from the trees (Zolotokrylin, 2010). One to two days of dry winds can cause desiccation of flowers and sterilization of pollen, which is especially dangerous for cereals in the stages of ear emergence and flowering. At the later growing stages, dry winds lead to early ripening and desiccation of not fully ripened grain. Under insufficient soil moisture content (below 30%), the impact of dry winds during the milk development stage can cause a decrease in the crop of 13–18% and during the ear stage on 20–25% (Buchinskij, 1976).

Early studies of Zuberbiller E.A. and Romushkevich V.I., developed by Buchinskij (1970) showed that dry winds in the former Soviet republics occur under certain synoptic conditions, which move air masses from the northern regions southward with their subsequent transformation. In any case, the processes of dry wind formation are associated with the evolution of anticyclones in the region.

The relationship of dry winds in the Ukraine with Azores baric ridges, which spread to the east, was established in the 1970s (Volevakha and Romushkevych, 1972). Other cases of dry winds occur on the western periphery of the anticyclone, with its center located to the east outside the country, as well as on the south periphery of an anticyclone with Arctic origin. In the steppe area, dry winds may also form under the influence of summer thermal depression as a result of local air mass transformation. Dry winds, which originate under propagation of western ridges, are prevalent in Ukraine.

In Ukraine the anticyclone type of weather can last for a year. There are some types of the anticyclone trajectories, such as Scandinavian types, which most commonly occur in the west and north-west (Kivganov and Goloshchak, 1998). In the warm period, anticyclones are often related to the Azores high, which produces western and south-western trajectories of anticyclones. As shown by Martazinova and Sologub (2000) and Martazinova and Sverdlik (1998), in the last decades due to some eastward shifting of location of the Azores high (in relation to the climatic norm of 1950–1974) there are more frequent western ridges over the territory of Ukraine, where the anticyclone usually becomes stationary. According to this, three types of synoptic processes were identified, which lead to the propagating of warm dry air over the territory of Eastern Europe. The first type is related to the air masses which move from the west and connect to the Azores high. The second type is related to the meridional structure of the baric field and is characterized by air flow from the south. The third type is characterized by penetration of the territory of Ukraine by warm continental air on the southern periphery of an anticyclone located over the Urals. All types of these synoptic processes can be an origin of hot and dry winds.

The latest published study contains data on dry wind frequencies in Ukraine for 1991–2000 (Tatarchuk and Barabash, 2007). The set of weather stations presented in this paper differs from our study. For most stations, comparison is possible only with climatic data, e.g., the monograph of Buchinskij (1976), where the periods of 1936–1964 and 1945–1964 are available. Also, a difficulty in comparing studies of dry winds for different periods and in different countries is the absence of a unified concept and criteria for this phenomenon. In the meteorology of the former Soviet Union, the geophysical criterion of the dry

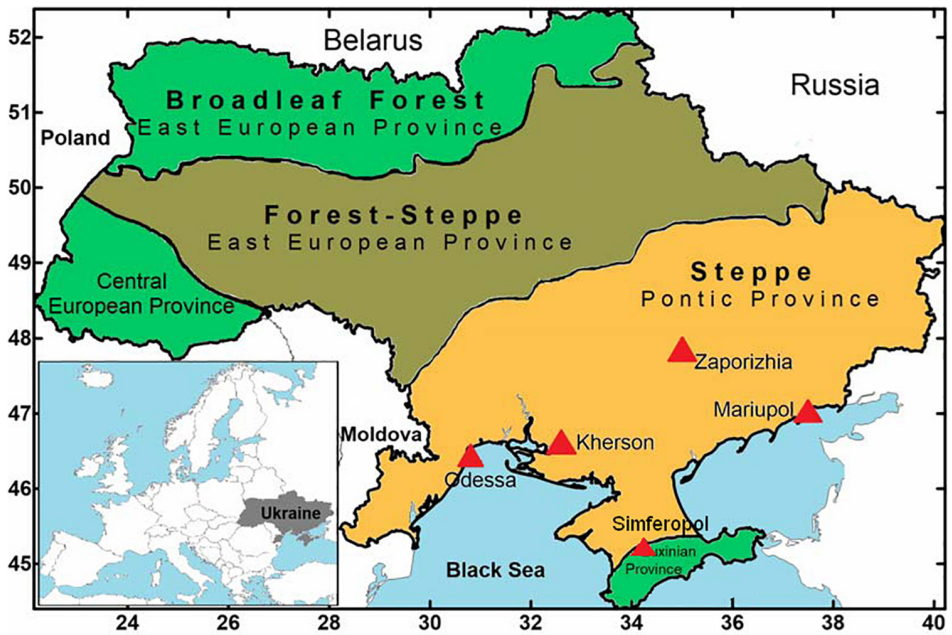

FIGURE 1 | The map of Ukraine with the location of meteorological stations (red triangles) in the Black Sea Steppe province, and schematic location the territory of Ukraine on the map of Europe. Frontiers Media SA remains neutral with regard to jurisdictional claims in published maps and institutional affiliations.

wind as a complex phenomenon combined the simultaneous action of three factors: temperature, humidity and wind. This criterion is in contrast to biophysical ones, evaluates only the atmospheric conditions, and does not include the effect on plants (Lipinskiy et al., 2003). In agroclimatic references of Ukraine, the biophysical criterion of Zuberbiller (1959) is used, because it indirectly takes into account the reaction of plants to the influence of sukhovey.

Lydolph (1964) wrote about the complexity of understanding the Russian term "Suchovey" noting that is a phenomenon that differs in origin and in nature from local winds such as a foehn or sirocco. "So significant are they that outstanding occurrences have been tagged with specific names, and in many instances these occurrences are so classic in form that the Russian descriptive terms have been accepted the world over. Such a term is "sukhovey." The word itself means dry or drought. "Zasukha" is the Russian word that is directly analogous to the English word "drought"... "Sukhovey" refers to individual spells of hot dry flows of air which have immediate and profound effects on vegetation... It is rapid wilting of vegetation that best identifies the sukhovey."

The sukhovey is typically defined as prolonged periods of dry weather when dry, hot air circulates around the periphery (often to the south) of a high-pressure system. However, as shown by Volevakha and Romushkevych (1972), in Ukraine- especially in the steppe regions- the occurrence of a dry, hot wind is possible both in the warm sector of cyclones and in conditions of summer thermal depressions. Such winds are usually short-term but can be intense and destructive for vegetation. As shown by Buchinskij (1976) the dry winds usually last for 2–4 days, but the extreme events span 2–3 weeks. According to the author's studies (Slizhe and Semenova, 2017a,b), in 1995–2015 at Ukrainian weather stations in April–May, 1-day sukhovei occurred in more than 90% of cases. In the summer months, 1-day sukhovei were observed on average in 60% of cases; dry winds of a duration of 2–4 days were found in 30–35% of cases. Sukhovei of longer durations were observed in less than 10% of cases.

The indicated features of the sukhovey phenomenon define the main task of this study as an update of information on the spatiotemporal distribution of dry, hot winds and the synoptic conditions of their formation in southern areas of Ukraine in the last few decades.

MATERIALS AND METHODS

This study evaluates the dynamics of droughts during April-August of 1995–2015. The assessment is based on the Standardized Precipitation Evapotranspiration Index (SPEI), whose time series were obtained from the Global 0.5° gridded SPEI database (Global SPEI database, 2018). The SPEI was introduced by Vicente-Serrano et al. (2010) and is based on monthly precipitation data and potential evapotranspiration data, which depends on air temperature. Air temperature is especially important in the warm season and under global warming, when evapotranspiration increases.

The SPEI may be defined for various time intervals. Short time intervals (from one to a few months) shows short- and medium-range conditions of moistening and provide a seasonal assessment of precipitation; therefore, these scales are widely used for detecting meteorological and agroclimatic droughts. A drought event for a selected time scale is defined as a period

in which the SPEI is continuously negative. Drought intensity is defined for values of the SPEI with the following categories: values from 0 to −0.99 correspond to mild drought; from −1.00 to −1.49 correspond to moderate drought; from −1.50 to −1.99 correspond to severe drought; values less than −2.00 characterize an extreme drought.

In our study, a 6 month period was applied to detect growing period drought (from April to August). According to criteria from the Hydrometeorological service of Ukraine, the dry wind is identified if, in at least one observation, values of the meteorological parameters simultaneously are: air temperature 25°C and higher, wind speed at 10 m height is 5 m/s or more, and relative air humidity is 30% or lower (Lipinskiy et al., 2003). In such conditions, water quickly evaporates from the soil, causing damage to crops and grains.

An assessment of the spatiotemporal distribution of dry winds was done using station observations for air temperature, humidity, and wind at the five meteorological stations of Ukraine, located in the coastal zone of the Black Sea and Sea of Azov, from April to August of 1995–2015 using the Climate data Online [CDO], 2018.

For determination of the sea level pressure (SLP) patterns for periods with dry winds in the southern areas of Ukraine, we selected days in which this phenomenon was observed. The composite pressure fields were built using the NCEP/NCAR reanalysis using the NOAA Earth System Research Laboratory (NOAA/ESRL, 2018).

To study the regions in which the dry winds originate, the HYSPLIT modeling system of Air Resources Laboratory NOAA (Stein et al., 2015; READY. NOAA Air Resources Laboratory, 2018) was used to build backward trajectories of air particles at the sea level pressure surface and at the levels of 1,500 and 3,000 m for the period of 120 h (5 days). For this purpose we selected periods in which dry winds were maximally widespread over the study area that is, in which the sukhovey was observed at the largest number of stations simultaneously.

RESULTS AND DISCUSSION

During 1995–2015, warm season droughts in the Black Sea Steppe province were observed during more than one half of the period. Mild drought occurred 11 times, moderate drought was observed 3 times, and severe drought appeared once. Extreme drought covered the Steppe zone in the growing season of 2007 (**Figure 2**). The time series of SPEI values show that drought prevailed in the Ukrainian Steppe every year after 2007, which correspond to the observed negative anomalies of precipitation and positive anomalies of temperature at this period as shown earlier.

Studies of drought frequency have shown a prominent decrease in long drought events (≥6 months) in Ukraine for 1951–2012 (Spinoni et al., 2016). Also, drought severity and duration tended to decrease in Ukraine, but along the Black Sea coast these parameters have shown an increase. So, the considered period from 2007 may be the beginning of a change in drought characteristics, which tend to strengthen in the southern region of Ukraine.

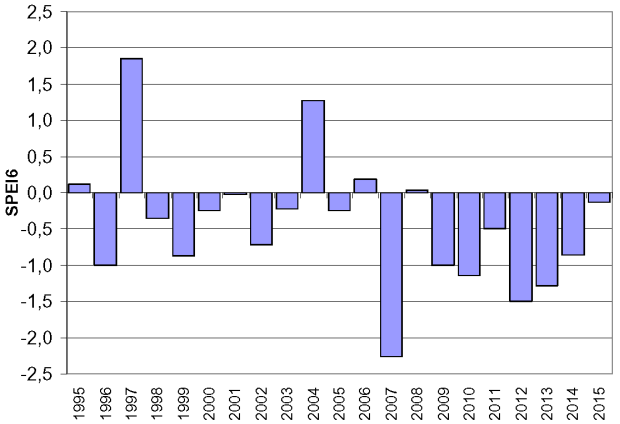

FIGURE 2 | Time series of the SPEI at 6-months time scale (April–August) during 1995–2015.

Analysis of dry wind frequencies showed an increase of the number of days with dry winds in 1996, 2000–2003, 2007, and 2012–2013 (**Figure 3A**). As seen, in these years the largest negative values of the index SPEI were noted (compare with **Figure 1**). In these years, as shown by Cherenkova et al. (2015), over the East European Plain during the vegetation period an anticyclonic pressure field was dominant, accompanied by blocking processes, which led to the formation of extensive droughts. In 1997 and 2004, all stations observed the lowest number of days with dry winds, while at the same time the index SPEI reached its highest positive values.

In general, we can see two periods with different patterns of dry winds: 1995–2004 with low frequencies and 2005–2015 with high frequencies. The average number of days with dry winds in the second period is two times higher than for the first at almost all stations except Kherson. Analysis of the linear trends of number of days with dry winds using an F-test statistic showed that this increase is significant at the 95% confidence level for four stations, excluding Kherson where the interannual variability is small during the study period.

Analysis of the frequency of dry winds by month showed that the sum of days increases from April to August (**Figure 3B**), when the dry winds appear most frequently (excluding Kherson, where the maximum is observed in July). The total sum of days with dry winds in August varies from 107 days in Mariupol to 215 days in Simferopol.

Most frequently dry wind durations of 1 day and 2–4 days are observed. During the study period, the total number of 1-day dry winds ranged from 69 days in Mariupol to 132 days in Odessa. The number of episodes with 2–4-day dry winds varied from 30 cases in Kherson to 84 cases in Zaporizhzhia. At other stations, the number of cases with dry winds with a duration of 5–7-days ranged from 9 cases in Odessa to 19 cases in Simferopol. Dry winds with a duration of 8–10 days or more are rare; their number at stations was 2–6 cases for the entire period. Prolonged episodes of dry winds from 5 days or more were not observed at Kherson.

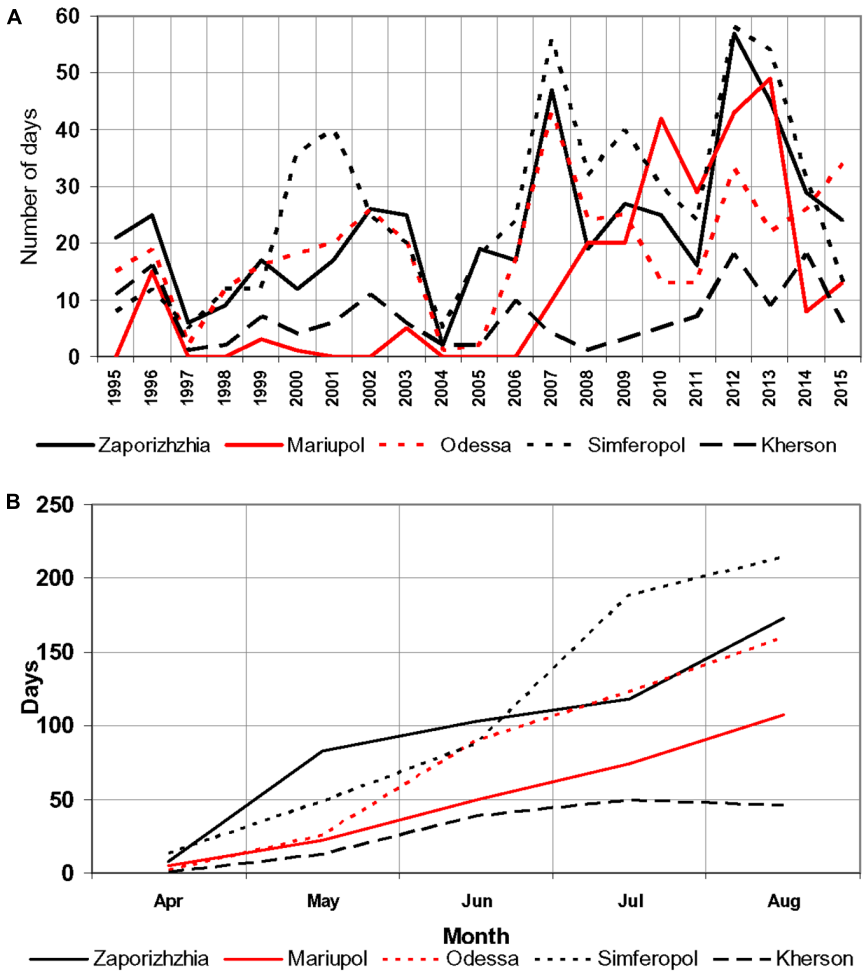

FIGURE 3 | Dynamics of the total number of days with dry wind **(A)**, and the total sum of days with dry wind **(B)** by months of growing season (April–August) of 1995–2015 at the stations located in the Black Sea Steppe province.

In some cases meteorological parameters during the dry wind phenomenon can reach extreme values. Thus, the maximum air temperature of 40.0°Ñ was observed on August 8 and 10, 2010 in Zaporizhzhia and on July 23, 2007 in Odessa. The maximum wind speed of 15 m/s was observed on August 29, 2011 in Simferopol. The relative air humidity during the dry wind in Odessa in five cases fell to 4%.

As seen, a complex criterion used to define sukhovey at the weather stations contains meteorological parameters that are very sensitive to local conditions, even within the same synoptic situation. Therefore, the frequency of the dry wind events at stations located in the steppe zone will be determined by their location in relation to water basins and the prevailing wind direction. The greatest number of cases of dry winds, as can be seen in **Figure 3**, is observed in Zaporizhia and Simferopol, which are located at a distance from the sea (see **Figure 1**). The minimum number of days with a dry wind is observed in Kherson, which is located close to the Black Sea coast and the delta of Dnieper River, which ensures high humidity in the area and reduces the risk of a dry wind. At stations located in the coastal zone, during the summer period, the increase in humidity and decrease in air temperature is significantly affected by the development of sea breezes that could also lead to reductions in the number of days with sukhovey. It should be noted that the study presents the results for Odessa-airport, which is located at a distance of 6 km from the coast, which increases the probability of suchovey. In Mariupol in summer, the breezes develop weakly due to the warm sea surface of the Sea of Azov and the shallow Taganrog Bay. Therefore, the seasonal advection of dry and hot air masses from the continental surface with north-eastern winds prevails in this region, which can provide a high frequency of days with dry winds.

The analysis of the SLP fields composited on days with dry wind showed some interesting features. In April and May, dry winds appear in Ukraine, when the territory of central Europe is under a stationary cyclone, which is especially deep in April (**Figures 4A,B**). Thus the territory of Ukraine is located on the peripheral area, with dry and warm air flow from the south and south-east between a westerly cyclone and ridges to the south-east and north of the Russian Plain.

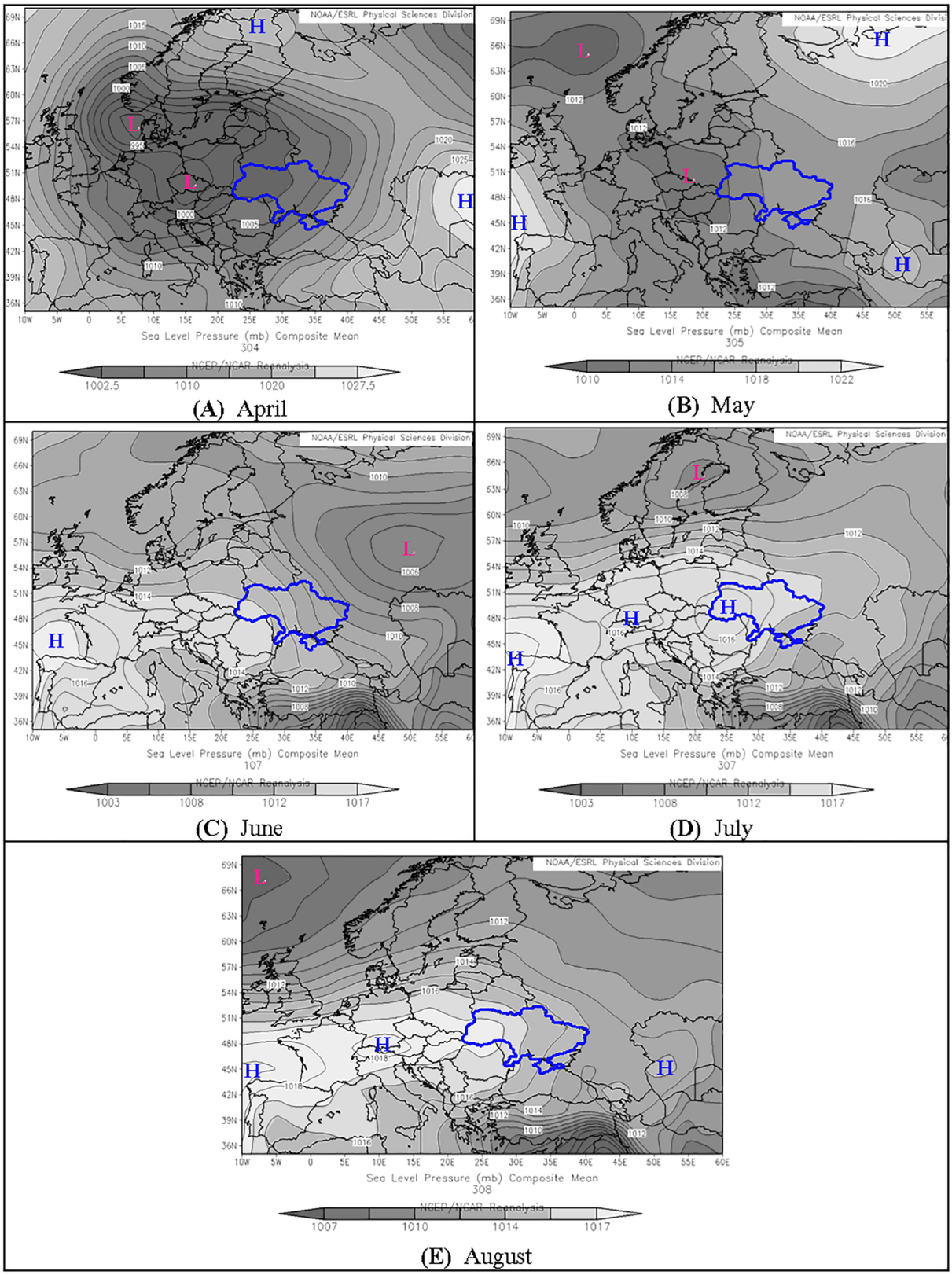

FIGURE 4 | Sea level pressure fields averaged for days with dry winds in the Black Sea Steppe province for the months of warm season (territory of Ukraine is marked). **(A)** April; **(B)** May; **(C)** June; **(D)** July; **(E)** August.

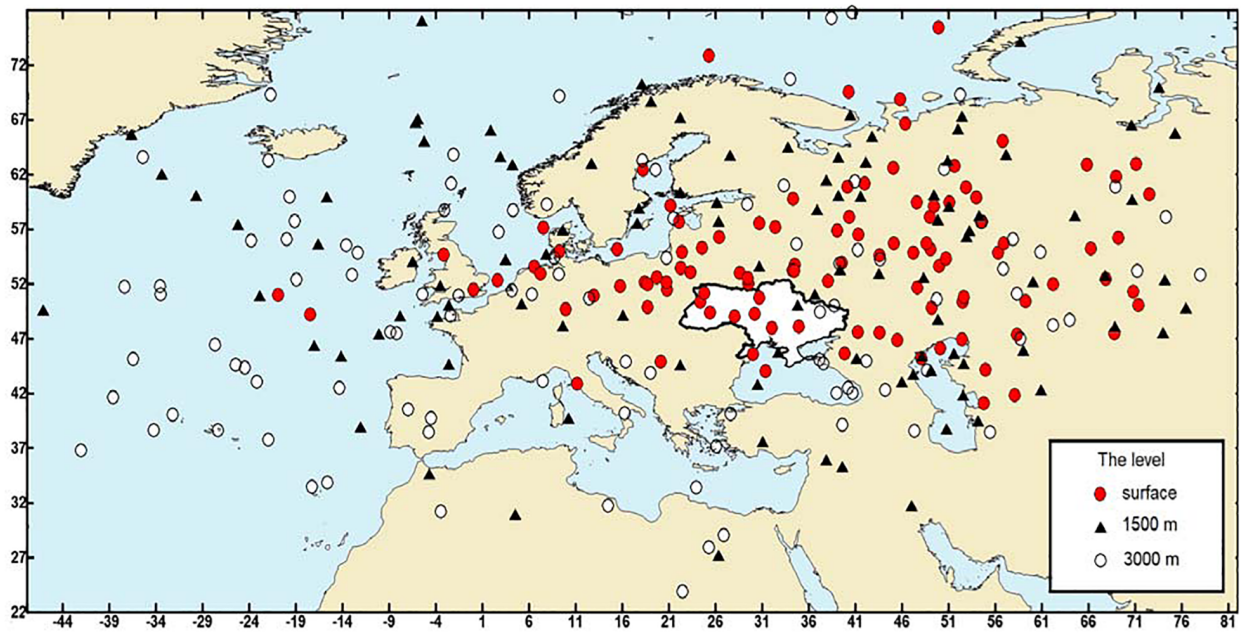

FIGURE 5 | Initial points of 5-day backward trajectories of air masses particles for periods with dry winds at the meteorological stations located in the Black Sea Steppe province.

In June the pressure fields transform to the summer type of circulation, characterized by propagation eastward toward the ridges of the Azores high, which reach up to the territory of Ukraine quite often (**Figure 4C**). Dry north-western and north winds in the Steppe are formed in the transitional area, with high gradients between the Azores ridge and the low-pressure field over the Russian Plane.

In July and August, the SLP patterns are similar, therefore in both months in southern areas of Ukraine dry winds are formed on the eastern periphery of anticyclones over central and Eastern Europe connected with the Azores ridges (**Figures 4D,E**). Dry winds in the Steppe have mainly a north-east direction.

On the whole, the obtained SLP patterns for the last few decades show correspondence to those considered in early studies of the synoptic processes accompanied by dry winds in the steppe regions of Ukraine. Therefore, we were interested in the geographic localization of the regions of air mass formation, which come to the Black Sea Steppe province and transform into dry winds while moving. In early research (Volevakha and Romushkevych, 1972), it was shown that about 55% of the trajectories of air mass particles coming as dry winds originate in the lower troposphere of the Arctic basin and come to the Caspian lowland or to the Lower Volga region and then pass to the Ukraine. About 20% of the trajectories pass from the Atlantic coast directly to the territory of Ukraine along the northern periphery of well-developed anticyclones eastward toward the Azores. Some trajectories (12%) begin in the south or south-east of Central Asia or Iran. Other cases of dry winds are related to stationary anticyclones located over the center of the Russian Plain.

In synoptic meteorology a well-known method for constructing the backward trajectories of air particles is used to determine the regions of formation of air masses and their temperature and humidity characteristics (David et al., 2010). In our study, 5-day backward trajectories of air particles were analyzed using the HYSPLIT model at three levels for the four above-mentioned stations located in the Black Sea Steppe province. In total, we built 318 trajectories for the days with dry winds.

Figure 5 shows the initial points of trajectories relative to the territory of Ukraine, which correspond to the regions of origin of air masses from which dry winds appear. At the surface level the trajectories are most frequent, which start in the north-east (27%) or to the east (18%) outside the territory of Ukraine. From the west and the north, air masses come in 16% of cases. A significant number of trajectories (14%) begin within the territory of the country. There were no cases of air particles moving at the surface level from the south and south-west for our dataset of dry wind days.

At the 1,500 m level (corresponding to an isobaric surface of 850 hPa) air masses with dry winds most often originate in the west (25%) outside of Ukraine. Also, air particles often travel from the north-east (18%) or from the north-west (16%), traveling more rarely from the north (11%). In the other directions there are only single cases of trajectories.

At the 3,000 m level (corresponding to an isobaric surface of 700 hPa) more than half of the trajectories of air particles begin in the west (45%) and northwest (13%) outside the territory of Ukraine. The frequency of other directions, from where air particles come, is almost the same and is 7–9% of cases. Several cases of the initial points of trajectories within the territory of Ukraine, as well as to the south-west of it, are noted.

Although this analysis refers to all cases of dry winds over the entire warm period, a comparison with the mean pressure fields in the future will allow for more details of monthly and seasonal features of the air masses trajectories to be established.

As mentioned above, the question of the relationship between drought and dry winds was raised in some earlier studies. It should be noted that these phenomena occur on different time scales, wherein the dry wind, by definition, does not depend on precipitation as a drought. However, it is obvious that the transformation of the moving air mass, which leads to a sharp decrease in the air relative humidity, must occur quickly.

According to our preliminary studies of the three-dimensional structure of the air mass movement, in most cases air particles moving at different levels at the same time move downward, therefore the adiabatic descent of the air mass is occurring. In addition, analysis of the initial points of air particles in **Figure 5** shows that at the surface level for 5 days, air particles usually move several hundred kilometers, and at high atmospheric levels move thousands of kilometers before reaching the steppe regions of Ukraine. In this case, additional drying and warming of the air mass will occur if it moves over dry areas and soils, which are already affected by drought.

The reverse interaction of dry winds and droughts was also found. An increase of wind speed at high air temperatures enhances evapotranspiration, which accelerates the process of drying the soil. If the precipitation deficit continues at the same time, this process will lead to agricultural drought and reduce the crop as a result. But formal verification of the sukhovey occurrence for months with drought, or months without drought, showed that 15–35% cases of dry winds occurred non-concurrently with drought (Semenova and Slizhe, 2019). Drought events were determined using SPEI index on a 1-month time-scale for each weather station. This result emphasizes the fact that a sukhovey can be considered as a separate phenomenon that occurs independently of drought but which does not exclude the interaction of both phenomena. The process of interaction between drought and dry winds resembles a phenomenon described as a "flash drought," which is characterized by a rapid rate of intensification (according to Otkin et al., 2018). It seems that dry winds can act as a trigger mechanism in the rapid development of drought, when the drought severity index falls to a critical value during a short time period. Examining this however, would require the adaptation of drought indicators and dry wind criteria to identical time scales that enable these phenomena to be correctly compared.

CONCLUSION

As the territory of Ukraine is one of the most important agricultural areas in eastern Europe, spring-summer droughts and dry winds can considerably worsen productivity of grain crops or even completely damage them. The increasing aridity of the current climate requires the timely estimates of risks of developing seasonal droughts, by considering the trends of arid phenomena.

The results obtained in this study clearly demonstrate that during the two most recent decades the Black Sea steppe province has been characterized by a significant increasing frequency of droughts and dry winds. The frequency of drought in the growing season especially increased after 2007, since when extreme drought has prevailed over the Black Sea Steppe province. The interannual dynamics of dry wind frequencies demonstrates the opposite tendency to SPEI values, that is, with a decrease in the values of the index, the number of days with dry winds increases as would be expected.

The structure of pressure fields in the lower troposphere plays a decisive role for both droughts and dry winds, with the main elements being persistent cyclones and anticyclones, as well as their peripheral areas with high pressure gradients where dry winds are observed. Analysis of the SLP fields for days with dry winds showed that in the spring months in the Black Sea steppe province southerly and south-easterly dry winds are observed on the eastern periphery of stationary cyclones located over central Europe. In the summer months, the main SLP pattern providing dry winds in the Steppe is the intense development and propagation of the ridge of the Azores high toward central-eastern Europe. In this case, northerly and north-easterly winds appear on the eastern periphery of these ridges.

Detailing the air particles trajectories shows that dry winds appear in air masses which, at the surface level, form mainly from the east or north-east outside the territory of Ukraine, but at higher atmospheric levels the western component of the flow prevails. Planned further studies of the three-dimensional temperature-humidity structure of flow in the lower troposphere will make it possible to establish a mechanism for transformation of the air mass that leads to formation of dry wind phenomenon.

DATA AVAILABILITY STATEMENT

The datasets of station data for this study can be found in the Climate data online (CDO), NOAA-NCDC, https://www.ncdc.noaa.gov/cdo-web. The datasets of the SPEI index for this study can be found in the Global SPEI database, http://spei.csic.es/database.html. The datasets of the NCEP/NCAR reanalysis for this study can be found in the NOAA/ESRL. Physical Sciences Division, https://www.esrl.noaa.gov/psd/data/reanalysis/reanalysis.shtml.

AUTHOR CONTRIBUTIONS

The tasks for IS are as follows: setting of the research problem; definition of the algorithm and research methods; review of the relevant publications; analysis of time series of the drought index; comparative analysis of the frequency of droughts and dry winds; analysis of the mean pressure fields; writing the abstract and body of the manuscript. The tasks for MS are as follows: creation of the dataset for dry winds using meteorological criteria for selected stations; analysis of the frequency of dry winds at the stations; construction and analysis of the mean pressure fields; construction the trajectories of air particles and analysis of the regions of formation the air masses.

REFERENCES

Buchinskij, I. E. (1970). *Droughts, Dry Winds and Dust Storms In Ukraine and The Fight Against Them*. Kiev: Urozhaj.

Buchinskij, I. E. (1976). *Droughts and Dry Winds*. St. Petersburg: Gidrometeoizdat.

Cherenkova, E. A., Semenova, I. G., Kononova, N. K., and Titkova, T. B. (2015). Droughts and dynamics of synoptic processes in the south of the East European Plain at the beginning of the twenty first century. *Arid Ecosyst.* 5, 45–56. doi: 10.1134/s2079096115020055

Climate data Online [CDO] (2018). *NOAA-NCDC*. Available at: https://www.ncdc.noaa.gov/cdo-web (accessed August 10, 2016).

David, M. H., Luke, S., Robert, E. D., David, B. K., Stephen, D. G., Michael, L. D., et al. (2010). A back-trajectory and airmass climatology for the Northern Shenandoah Valley, USA. *Int. J. Climatol.* 30, 569–581.

Global SPEI database (2018). Available at: http://spei.csic.es/database.html (accessed February 2, 2018).

Kivganov, A. F., and Goloshchak, O. P. (1998). Anticyclones of the Eastern Europe. *Meteorol. Climatol. Hydrol.* 35, 81–90.

Kubiiovych, V., and Husar Struk, D. (1993). *Encyclopedia of Ukraine*. Toronto: University of Toronto Press.

Lipinskiy, V. M., Djachuk, V. A., and Babichenko, V. M. (eds) (2003). *Climate of Ukraine*. Kiev: Raevskyy Publishing House.

Lydolph, P. E. (1964). The russian sukhovey. *Ann. Assoc. Am. Geograph.* 3, 291–309.

Martazinova, V. F., and Sologub, T. A. (2000). Atmospheric circulation, which forms drought conditions on the territory of Ukraine at the end of the 20th century. *Sci. Proc. UkrGMI* 248, 36–47.

Martazinova, V. F., and Sverdlik, T. A. (1998). Large-scale atmospheric circulation of the 20th century, its change and its present state. *Sci. Proc. UkrGMI* 246, 21–27.

NOAA/ESRL (2018). *Physical Sciences Division (PSD)*. Available at: https://www.esrl.noaa.gov/psd/data/reanalysis/reanalysis.shtml (accessed November 22, 2017).

Otkin, J. A., Svoboda, M., Hunt, E. D., Ford, T. W., Anderson, M. C., Hain, C., et al. (2018). Flash droughts: A review and assessment of the challenges imposed by rapid-onset droughts in the United States. *Bull. Amer. Meteor. Soc.* 99, 911–919. doi: 10.1175/BAMS-D-17-0149.1

READY. NOAA Air Resources Laboratory (2018). Available at: https://ready.arl.noaa.gov/HYSPLIT_traj.php (accessed July 17, 2017).

Schubert, S. D., Wang, H., Koster, R. D., Suarez, M. J., and Groisman, P. (2014). Northern Eurasian heat waves and droughts. *J. Clim.* 27, 3169–3207. doi: 10.1175/jcli-d-13-00360.1

Semenova, I. G. (2015). "Climate conditions and droughts in the black sea steppe province under the modern period and the near future," in *Poster at the Program Book: XIX INQUA Congress: Quaternary Perspectives on Climate Change, Natural Hazards and Civilization. 112-112. (Poster No. P06-P01)*. Available at: http://inqua2015.jp/program/INQUA2015program.pdf

Semenova, I., and Slizhe, M. (2019). *Distribution of Dry And Hot Conditions In Ukraine At The Present Time And Near Future. The Workshop On Correlated Extreme Events*. New York, NY: Columbia University.

Slizhe, M. O., and Semenova, I. G. (2017a). Spatiotemporal distribution and meteorological characteristics of hot dry winds in Ukraine at the end of XX - beginning of the XXI century. *Bull. Odessa State Environ. Univer.* 22, 21–29.

Slizhe, M. O., and Semenova, I. G. (2017b). Hot dry winds of different length in Ukraine in the early ÕÕI century. Sakharov Readings 2017: Environmental Problems of the 21st Century: materials of the 17th int. scientific conf. may 18-19, 2017, minsk, republic of belarus. *Sci. Conf.* 2, 179–180.

Spinoni, J., Naumann, G., Vogt, J., and Barbosa, P. (2016). *Meteorological Droughts in Europe: Events and Impacts – Past Trends and Future Projections*. Luxembourg: Publications Office of the European Union.

Stein, A. F., Draxler, R. R., Rolph, G. D., Stunder, B. J. B., Cohen, M. D., and Ngan, F. (2015). NOAA's HYSPLIT atmospheric transport and dispersion modeling system. *Bull. Amer. Meteor. Soc.* 96, 2059–2077. doi: 10.1175/BAMS-D-14-00110.1

Svoboda, M., and Fuchs, B. A. (eds) (2016). *Handbook of Drought Indicators And Indices. Integrated Drought Management Programme*. Geneva: World Meteorological Organization and Global Water Partnership.

Tatarchuk, O. G., and Barabash, M. B. (2007). Study of the spatiotemporal distribution of dry winds in the territory of Ukraine under modern climate conditions. *UkrHMI Sci. Pap.* 256, 140–154.

Vicente-Serrano, S. M., Beguería, S., and López-Moreno, J. I. (2010). A Multiscalar drought index sensitive to global warming: the standardized precipitation evapotranspiration index – SPEI. *J. Clim.* 23, 1696–1718. doi: 10.1175/2009jcli2909.1

Volevakha, V. O., and Romushkevych, V. I. (1972). *Dry Winds in Ukraine*. Kiev: University of Kiev.

Zolotokrylin, A. N. (2010). "Dry winds, dust storms and prevention of damage to agricultural land," in *Natural Disasters*, ed. V. M. Kotlyakov (Singapore: EOLSS/UNESCO), 1–18.

Zuberbiller, E. A. (1959). *Agrometeorological Characteristics Of Dry Winds Leningrad*. St. Petersburg: Gidrometeoizdat.

Conflict of Interest: The authors declare that the research was conducted in the absence of any commercial or financial relationships that could be construed as a potential conflict of interest.

frontiers in Earth Science

ORIGINAL RESEARCH
published: 05 May 2020
doi: 10.3389/feart.2020.00106

Changes of Nutrient Concentrations in the Western Baltic Sea in the Transition Between Inner Coastal Waters and the Central Basins: Time Series From 1995 to 2016 With Source Analysis

Joachim Kuss[1], Günther Nausch[1], Clemens Engelke[2]*, Mario von Weber[2], Hannah Lutterbeck[3], Michael Naumann[4], Joanna J. Waniek[1] and Detlef E. Schulz-Bull[1]*

[1] Department of Marine Chemistry, Leibniz Institute for Baltic Sea Research Warnemünde (IOW), Rostock, Germany, [2] Department of Geology, Water and Soil, State Agency for Environment, Nature Conservation and Geology Mecklenburg-Vorpommern (LUNG), Güstrow, Germany, [3] Department of Water, State Agency for Agriculture, Environment and Rural Areas Schleswig-Holstein (LLUR), Flintbek, Germany, [4] Department of Physical Oceanography and Instrumentation, Leibniz Institute for Baltic Sea Research Warnemünde (IOW), Rostock, Germany

OPEN ACCESS

Edited by:
Hayley Jane Fowler, Newcastle University, United Kingdom

Reviewed by:
Justus Van Beusekom, Helmholtz Centre for Materials and Coastal Research (HZG), Germany
Marcus Reckermann, Helmholtz Centre for Materials and Coastal Research (HZG), Germany

***Correspondence:**
Joachim Kuss
joachim.kuss@io-warnemuende.de
Clemens Engelke
Clemens.Engelke@lung.mv-regierung.de

Specialty section:
This article was submitted to Interdisciplinary Climate Studies, a section of the journal Frontiers in Earth Science

Received: *03 December 2018*
Accepted: *24 March 2020*
Published: *05 May 2020*

Citation:
Kuss J, Nausch G, Engelke C, Weber M, Lutterbeck H, Naumann M, Waniek JJ and Schulz-Bull DE (2020) Changes of Nutrient Concentrations in the Western Baltic Sea in the Transition Between Inner Coastal Waters and the Central Basins: Time Series From 1995 to 2016 With Source Analysis. Front. Earth Sci. 8:106. doi: 10.3389/feart.2020.00106

Anthropogenic nitrogen input to the western Baltic Sea has continued to decline by about 30% since 1995, whereas phosphorus input, after a strong decrease of 25% from 1995 to 2000, remained almost on the same level. Despite this development, the Arkona Sea and Belt Sea apparently show no strong changes of nutrient concentrations in the last two decades. In this study, we investigate the concentrations of nitrate, nitrite, ammonium, dissolved inorganic nitrogen (DIN), dissolved inorganic phosphorus (DIP), total nitrogen (TN), and total phosphorus (TP), as the substances of major concern in respect to the eutrophication of the Baltic Sea. To link open-sea nutrient concentrations with nutrient supply by freshwater drain, we used nutrient vs. salinity linear fits, including data from coastal waters obtained during regular German monitoring campaigns. Therefore, the data set was grouped according to differently sized areas to identify regional differences and was subsequently analyzed for four time intervals: 1995–1999, 2000–2004, 2005–2009, and 2010–2016. By extrapolation to a salinity of "zero," we obtained hypothetical freshwater end-members of the different N and P parameters. Most of these end-members indicated a decline during the four time intervals, supporting a reduction of freshwater-borne N and P supply to the western Baltic Sea. For the period 1995–1999, the freshwater end-members of TN were determined between 200 and 400 μM. This improved to a TN range between 150 and about 300 μM in 2010–2016. TP ranged from about 2.3 to 5.4 μM in 2010–2016, with previous values of slightly above 4 μM and up to almost 15 μM in the period 1995–1999. The end-members determined by our method would fulfill limnic–marine target values of the EU Water Framework Directive of TN = 186 μM and river-type-specific target values

of TP between 3 and 5 μM for some areas of the western Baltic Sea in recent years, because the method includes removal processes in the transition zone. Finally, the end-member values were compared with area-specific averages of measured values at the limnic–marine transition point.

Keywords: nutrients, eutrophication, salinity gradient, coastal waters, freshwater end-member, limnic–marine transition, western Baltic Sea, coastal filter

INTRODUCTION

The western Baltic Sea is subjected to various anthropogenic stressors caused by agriculture, shipping, fishing, aquaculture, tourism and water sports, exploitation of natural resources (e.g., sand), and off-shore installations (Newton et al., 2014). Effluents from land contribute to hypertrophication of the coastal waters of the western Baltic Sea, although modern wastewater treatment plants were shown to have reduced the burdens (Nausch et al., 2011). Large inputs of N and P with additionally unbalanced N/P ratio still cause growth of opportunistic green algae (Korpinen et al., 2007), development of strong algae blooms that appear more or less harmful (Majaneva et al., 2012), loss of seagrass, and the formation of hypoxic and anoxic bottom waters (Conley et al., 2011), leading to decreased diversities of benthos organisms, fish, and birds (Newton et al., 2014). Thus, there is a strong and far-reaching impact of excess nutrient supply to western Baltic Sea coastal waters.

The Baltic Sea is a semi-enclosed sea with a limited water exchange with the North Sea via shallow and narrow straits (Lass et al., 2005). The freshwater is drained from a catchment area in the humid part of Europe that is more than four times larger than the Baltic Sea itself. The brackish water system is characterized by a net outflow and episodic inflows of haline North Sea waters. Brackish water leaves the Baltic Sea through the Danish Straits after an average residence time of 30 years (Reissmann et al., 2009) and modifications. The nutrient concentration of the surface water is determined by locally added nutrients, supplied by rivers, direct discharges (e.g., mariculture), shipping, and atmospheric deposition superimposed on internal nutrient recycling and removal processes.

Atmospheric deposition contributes to nutrient supply in addition to direct and diffuse sources from land mainly carried by rivers. According to the sixth pollution load compilation (PLC-6) (HELCOM, 2018), the annual nitrogen input to the western Baltic Sea (Danish Straits/Belt Sea, and Arkona Sea) has declined from 130,000 Mg in 1995 to 90,000 Mg in 2014, whereas phosphorus dropped from 3,900 Mg in 1995 to 2,900 Mg in 2000 and remained relatively stable thereafter. This corresponded to a reduction of nitrogen by 30% and of phosphorus by 25% over the whole time span.

The concentrations of inorganic nitrogen and phosphorus compounds in Baltic Sea surface waters are characterized by a pronounced seasonality. High concentrations are observed in winter, with low primary production as well as deep winter mixing, although these concentrations decrease to extremely low values in the period of high primary productivity and a shallow mixed layer between spring and midsummer (Nausch et al., 2008).

The coastal ecosystem partially utilizes, removes, and transforms the supplied nutrients and can thus contribute to reductions in nutrient concentrations by various mechanisms (Asmala et al., 2017). Nutrient uptake by high biomass and low nutrient turnover plants (e.g., seagrass) could lead to a long-term fixation of nutrients, showing a "good coastal filter functioning," whereas unattached ephemeral algae with low biomass and high nutrient turnover rates reflect a marginal ecosystem service in this sense (McGlathery et al., 2007). The western Baltic Sea shows different ecosystem types, comprising open coast, embayment, estuary, and lagoon. Embayments and especially estuaries are regions of elevated sedimentations, whereas lagoons are prone to denitrification and sedimentation, and the open coast provides no important coastal filtering function (Asmala et al., 2017).

The aim of the study is to elucidate long-term changes of nutrient concentrations and the N/P ratio in western Baltic Sea waters in the salinity gradient during the last 20 years. The data set consists of the parameters nitrate, nitrite, phosphate [dissolved inorganic phosphorus (DIP)], dissolved inorganic nitrogen (DIN: the sum of nitrate, nitrite, and ammonium), total nitrogen (TN), total phosphorus (TP), the ratios TN/TP, and DIN/DIP combined with position, time of sampling, and sampling depth and of course salinity and temperature. The hypothesis is that a reduction in nutrient supply by freshwater should be visible in corresponding decrease of the *y*-axis intercepts of the significant regression lines of the nutrient parameters versus salinity. The *y*-axis intercept reflects a hypothetical freshwater end-member, which is compared between four time periods in the last two decades to show temporal changes. In addition, we investigate two different salinity ranges: one more focused on the low salinity range and one going up to the median of the respective subset of the data. The comparison of the same region/parameter combination between a reduced and a wider salinity range revealed deviations from conservative mixing (Officer, 1979). In this way, removal or supply processes during mixing of the less haline water with seawater from the central basins were indicated. Finally, the theoretical freshwater end-member values were compared with measured values for the so-called limnic–marine transition (LMT) point, at the border between river water and brackish seawater.

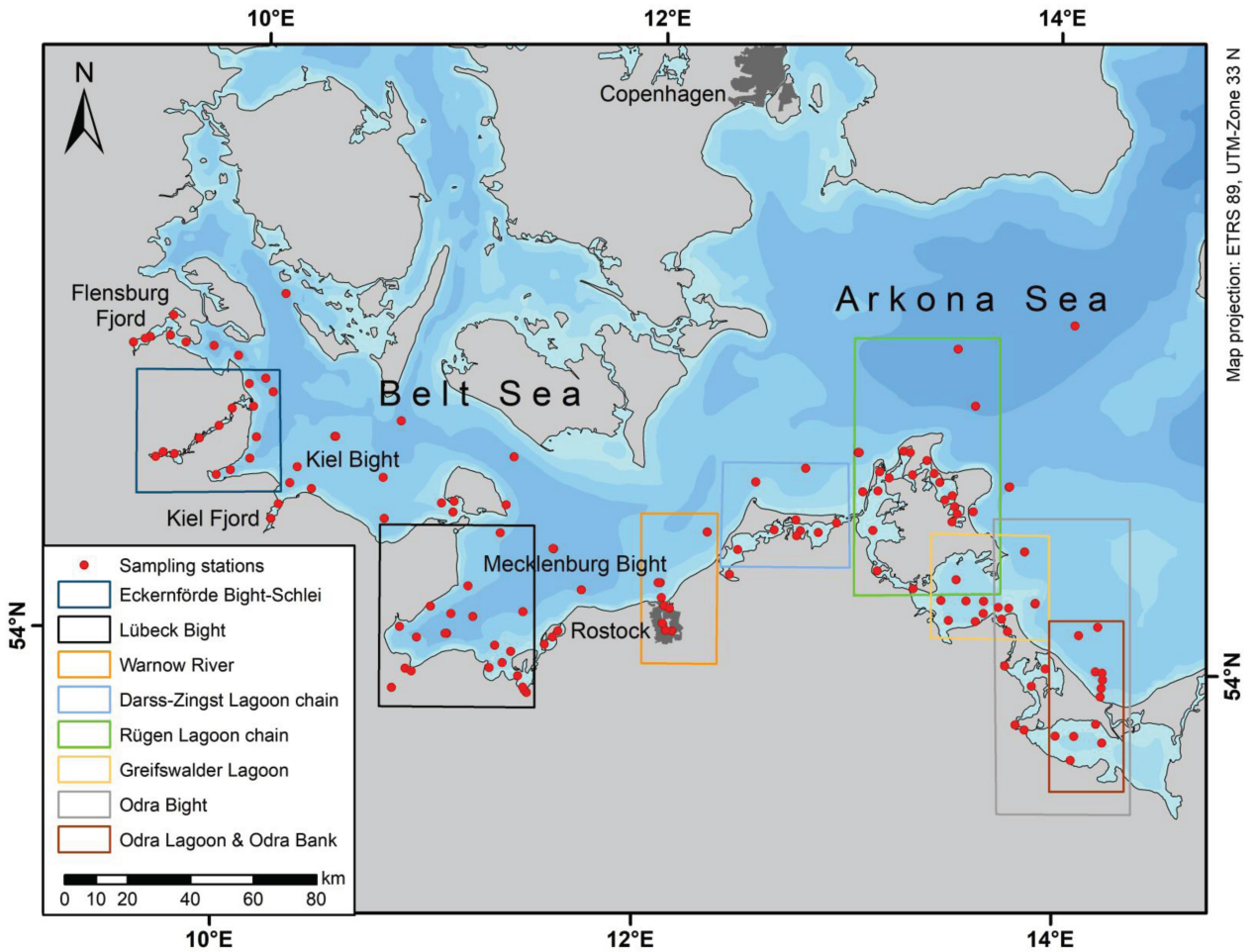

FIGURE 1 | Map of the study area with stations monitored by the LLUR, IOW, and LUNG used in the study; the analyzed regions are indicated in the map by frames or by names.

MATERIALS AND METHODS

Study Area

The study was carried out using data obtained from German territorial waters of the western Baltic Sea including river estuaries, lagoons, and bordering open-sea areas during regular monitoring activities (**Figure 1**). The German part of the drainage area sums up to 28,600 km^2, of which 18,200 km^2 drains in the Baltic Proper and 10,400 km^2 into the Belt Sea (BLANO, 2014). Coastal and inner coastal waters were monitored by the State Agency for Environment, Nature Conservation and Geology Mecklenburg-Vorpommern (LUNG), and the State Agency for Agriculture, Environment and Rural Areas Schleswig-Holstein (LLUR) in their particular water bodies. The data sets (Leibniz Institute for Baltic Sea Research Warnemünde, 2014; German Environment Agency, 2018) were combined for the time period of January 1995 to December 2016 from monthly monitoring of coastal waters (LUNG and LLUR) and of open-sea waters (Leibniz Institute for Baltic Sea Research Warnemünde, IOW). The open sea was mainly studied by the IOW during five campaigns each year in February, March, May, July/August, and October/November. We investigated the southwestern Belt Sea, the southern Arkona Sea, and the Odra Lagoon including the Odra Bank area. The latter represents the southeastern part of the study area, already part of the Bornholm Sea. The study comprises coastal waters: oligohaline ($0.5 \leq S \leq 5$) and mesohaline ($5 \leq S \leq 18$) inner as well as open coastal waters, meso-polyhaline ($10 \leq S \leq 30$) open coastal waters with seasonal stratification, and the open-sea waters comprising the exclusive economic zones of Germany, Denmark, and Sweden.

The western Baltic Sea reflects the transition zone between the brackish Baltic Proper and the North Sea, which shows almost oceanic salinity of >34. The area is characterized in the western part by narrow straits between German and Danish islands and the mainland of Denmark, Sweden, and Germany and by relative shallow basins in the east. Only relatively small rivers supply freshwater into the German coastal waters, for example, the Füsinger and Loiter Meadows via the Schlei Fjord, Schwentine, Trave, Warnow, Recknitz, Barthe, Ryck, Peene, and Uecker Rivers; however, a major contributor is the Odra River with a

fraction of 4.7% drained from German territory, and the other part comes from Poland 89.9% and the Czech Republic 5.4%. It is estimated that about 15% Odra River outflow is directly released to German coastal waters at the southeastern part of the study area (BLANO, 2014). At the southern coast, lagoons form large freshwater–seawater transition regions, whereas in the western part, the coast is structured by fjords and bights with an almost direct river input to the sea. An exception reflects the Schlei Fjord in the northwestern part of the Belt Sea (**Figure 1**) that stretches along 40 km with a salinity range from a few to above 20 until the open Kiel Bight is reached (Rieper, 1976). It should be mentioned that also groundwater discharge in the nearby Eckernförde Bight supplies freshwater to the sea, and because of the negligible surface runoff by rivers, this reflects a significant pathway within the hydrological cycle of this coastal region (Schlüter et al., 2004). The lagoons and semi-enclosed bays of the southern coast of the Baltic Sea were formed during glacial times by denudation by pleistocenic inland ice and by flooding after the melting of the ice cover and the sea level rise. Subsequent transformation by bay bars and spits by sediment relocation in easterly direction led to the current shape of the coast (Lampe, 1994). The chains of linked lagoons show a freshwater inlet at the western or central part and the outlet being often at the eastern end of the lagoon chain. Thus, the lagoons function as a cascade of filters with the river load subjected to chemical, physical, and biological transformation processes and sedimentation (Lampe, 1994).

Chemical Analyses

Nitrate, Nitrite, and Phosphate (Dissolved Inorganic Phosphorus): Water samples were analyzed by manual or automated air-segmented continuous-flow spectrophotometry. The respective nutrient compounds were converted by wet-chemical treatment into colored compounds with high molar absorptivity (Hansen and Koroleff, 1999) that enabled low detection limits of the substances of interest.

Nitrite was analyzed as a red azo dye that is formed with sulfanilamide and a naphthylamine derivate. Nitrate was measured as the sum of nitrate and nitrite after reduction by using a column filled with a copper-coated cadmium as the same azo dye. Subsequently, nitrate was determined by subtraction of nitrite from the sum of nitrate and nitrite.

Phosphate was quantified with ammonium molybdate at pH < 1 by reduction of the formed heteropolymolybdate phosphoric acid to molybdenum blue.

Ammonium: For quantification, ammonium is transformed with hypochlorite and phenol to the indophenol blue dye and determined by photometric measurements, taking care to avoid contamination by airborne ammonia and ammonium compounds.

DIN was calculated from the sum of nitrate, nitrite, and ammonium concentrations, only if all three parameters were available. LLUR also measured nutrients from unfiltered samples, and if no DIN from filtered sample was available, DIN determination on unfiltered water was used.

Total Nitrogen and Total Phosphorus: For analyses of TN as nitrate and TP as phosphate, the compounds of the unfiltered samples were digested by peroxodisulfate in pressure vessels, heated by using either a microwave oven (IOW and LUNG) or an autoclave with a high-temperature thermostat (LLUR). Final analysis was then done by spectrophotometry as described for nitrate and phosphate.

There is a long tradition of strict quality assurance in nutrient analysis (Grasshoff, 1976) for monitoring purposes that has meanwhile been accredited according to the ISO/IEC 17025.

Data Synthesis and Analysis

For data analysis, Microsoft Excel 2016 functions as well as the MATLAB Release 2014a statistical tools were used. We selected suitable nutrient parameters that indicate eutrophication, nitrate (μM), DIN (μM), phosphate (DIP, μM), TN (μM), and TP (μM). Ammonium and nitrite contributed to the sum-parameter DIN but appeared to be less informative in terms of eutrophication of coastal surface waters. Moreover, the ratios TN/TP (mol/mol) and DIN/DIP mol/mol were considered. A low ratio of the latter indicates phosphate excess situations that could foster blooms of diazotrophic cyanobacteria.

First, we looked at open-sea data for the 20-year time period from IOW only. Thereby, the time series of surface and bottom water nutrient concentrations were investigated for each season separately. Second, nutrient–salinity relations of surface waters of the upper 10 m were subsequently deduced by including near-coastal, inner coastal, and river water data from LLUR and LUNG. Especially, the extrapolated *y*-axis intercepts that represent hypothetical freshwater end-members of the respective nutrient concentration were aimed for further interpretations. In contrast to direct measurements of freshwater, this method accounts for the contributions of diffuse and direct sources as well as for water column processes and sediment interaction. We compared nutrient–salinity relations of the 5-year periods 1995–1999, 2000–2004, and 2005–2009 as well as the 7-year period 2010–2016. Therefore, the data set was restricted to the months October to May excluding summer values, because it was found that the occurrence of low nutrient concentrations in surface waters over a broad salinity range during summer clearly negatively impacted the regression analysis. A change in the freshwater source concentrations is thus assumed to be revealed by the change of the regression lines and the corresponding end-members during different phases of the two decades. To emphasize the weight of the low salinity range, the median salinity of the respective subset of data was calculated and used as an upper limit for the correlation. Subsequently, measured nutrient concentrations at the LMT point were used in the *Discussion* section for comparison with the end-member values. Therefore, the measured values were averaged according to the discharges of the respective rivers or meadows of the investigated areas to obtain comparable weighted averages. For consistency, also summer values were excluded from the averaging process.

To address potential enrichment or removal processes during transport to the open sea, also, a further restricted salinity range was investigated for the end-member calculation. An *F*-test on homogeneity of variance revealed for five areas with up to four parameters and almost all time intervals a significant difference ($>99\%$) for the two salinity ranges. This was certainly supported

by the usually large number of data used for the correlations (n = 114–1104) that somehow balances the natural scatter of data. However, in two cases, for the Warnow river area (n = 28–51) and the Odra Bight, a significance level of only 95% was fulfilled, and in the Mecklenburg Bight, a parameter was not significantly different for the two salinity ranges in a certain time period.

The data set was geographically split into subsets according to specified regions (**Figure 1**) to investigate the contribution of each subregions to certain open-sea areas or the open Western Baltic Sea. First, the study area was separated at the Darss Sill into the main sea areas, the Belt Sea, and the Arkona Sea with respective coastal zones. Second, the next group of larger areas represented the combined Eckernförde Bight–Schlei region, the Kiel Bight, the Mecklenburg Bight, the Darss-Zingst region ("Darss-Zingst Lagoon chain") with the Saaler and Barther Lagoons. The area comprises the Island of Rügen with surrounding waters. The Kubitz Lagoon, Great Jasmund Lagoon, Strelasund, and Greifswald Lagoon are summarized here as the Rügen Lagoon chain. Further southeast is the Odra Bight region. Third, a few smaller subregions were selected: Flensburg Fjord, Schlei, Eckernförde Bight, Kiel Fjord, Lübeck Bight, Warnow River, Greifswald Lagoon, and Odra Lagoon with Odra Bank (**Figure 1**). As far as possible, a clear land–sea gradient was realized by the selection of stations, which means that nearby off-shore stations were included. Hence, the large data set was split into data subsets by simply defined boxes, which are not chosen to precisely follow defined geographical areas. We think that this simplification does not bias the analysis significantly. However, an important criterion was that the obtained regression lines were significant. We used a t-test with a significance level of >99%.

RESULTS

Time Series of the Open-Sea Surface and Bottom Waters From 1995 to 2016

The decline of the anthropogenic nutrient input to the western Baltic Sea was assessed by various Pollution Load Compilations for the last decades (HELCOM, 2004, 2011, 2018). The question addressed here is how the changes are reflected in the nutrient concentrations found in the open western Baltic Sea waters. It is expected that surface water as well as deep water reflects the highest variability on the regional and temporal scales. The surface water data are restricted here to the upper 8-m depth, showing the influence of river water supply. The bottom water data were taken from the lowest 3 m of the water column, reflecting the impact of sedimented material.

The IOW nutrient data of February, March, May, July/August, and October/November of 1995 to 2016 were plotted according to the particular seasons of sampling versus the year. Especially, the TP and TN data allow a good overview about temporal nutrient changes, because all kinds of phosphorus and nitrogen compounds are included (**Figure 2**). The concentration of TP was usually below 2 μM. Only summer and autumn of the first decade of the study period TP showed elevated values. Mainly in bottom waters, the TP concentration reached up to 4 μM (**Figures 2C,D**). In summer, increased values were found in 1997, 2000, 2001, 2010, and 2014 of above ∼ 2 μM and in autumn 1995, 1997, and 2002 of few single values of about TP = 3 μM. The highest concentrations of TN were found in spring in surface waters in the first half of the investigated time span (1995–2004). The concentration of TN scatters around 25 μM in winter, of ∼40 μM of TN in spring until 2005, and of about 25 μM of TN thereafter, with higher values in surface waters. In summer and autumn, TN was slightly lower at about 20 μM. Also, a weak sinuous pattern is recorded during the two decades with minima in 1998 and 2007, which is best seen in autumn (**Figure 2H**). In summary, the monitoring of nutrients showed a relatively stable annual variability with no clear trend since 1995, neither in the surface water nor in the bottom water. In order to determine if a temporal trend could be shown, we investigate the nutrient–salinity relationships between 1995 and 2016.

Nutrient–Salinity Regression Analysis and the Interpretation of the *y*-Axis Intercepts

The nutrient–salinity data set of the surface waters was subsequently grouped according to the selected regions. The regression analysis was then done on data obtained from samples with a salinity equal to or below the median for the four time periods separately. Here, we show TN and TP for the Rügen Lagoon chain as an example (**Figure 3**). The scatter of the data is obvious and caused by the spatial heterogeneity of the regions in combination with temporal variability during spring, autumn, and winter of several years. For the correlation, a linear fit was applied; and the slopes, the y-axis intercepts, and the confidence intervals were calculated (**Table 1**). The slopes were always negative in the sense that we observed increasing nutrient concentrations with decreasing salinities, hence, in the direction of the freshwater source. Thereby, the slopes were mainly determined by nutrient values at low salinity, because the open-sea nutrient concentrations ranged at clearly lower levels.

To investigate the trend, only significant regression lines for all four time periods were used. This reduced the amount of correlations (15 regions, 7 parameters) to 35. The determined freshwater end-members were subsequently plotted for the respective nutrient parameters versus the time periods for a better overview (**Figure 4**). The different regions were grouped from larger to small size and according to the geographical localization from the northwest to the southeast of the study area. The regions that show significant correlations versus salinity are given for nitrate in **Figures 4A,B**; phosphate in **Figure 4C**; DIN in **Figures 4D,F**; TN in **Figures 4G–I**; and TP in **Figures 4J–L**. It turned out that the end-members mostly decreased from 1995–1999 to 2010–2016. Only in two cases concerning the Warnow River was an increase determined. Thereby, we obtained different patterns, an almost continuous decline, a plateau from the second to third interval, or even an intermittent increase from the first to second or from the second to third period. Also, a strong decline from the first to second time period and no significant change thereafter were found.

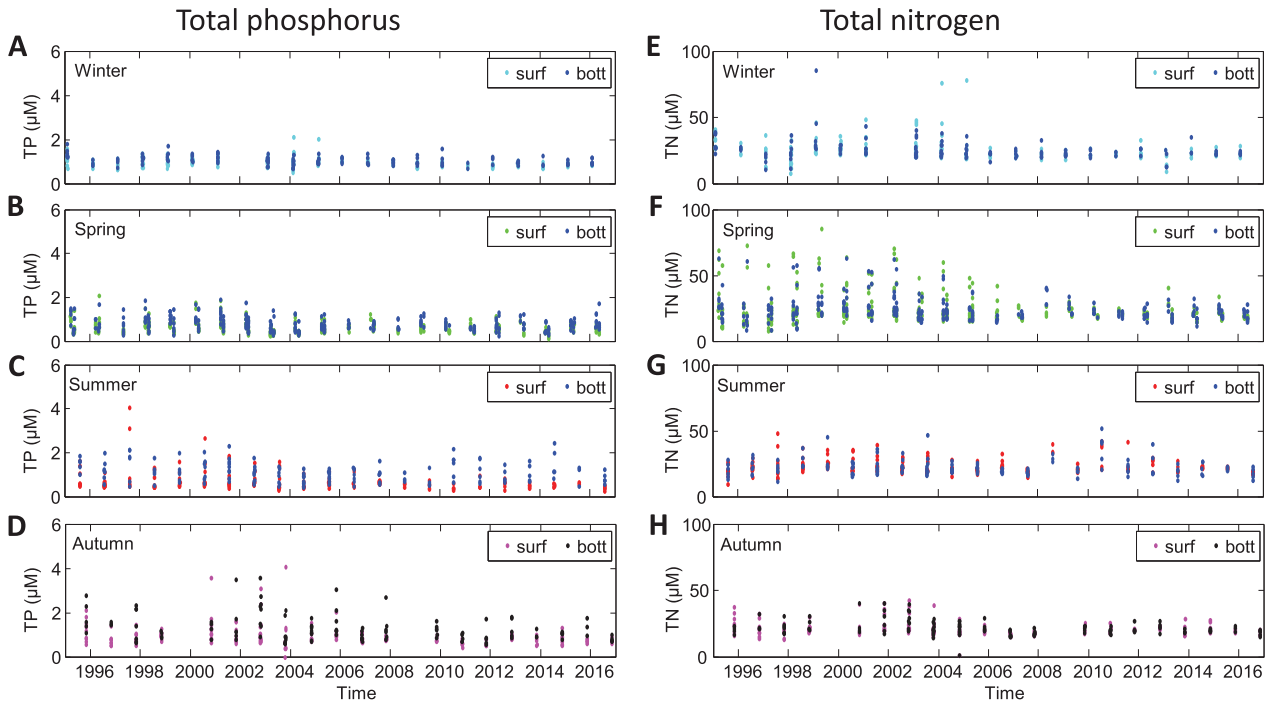

FIGURE 2 | Time series of surface and bottom water concentration of total nitrogen and total phosphorus in open-sea waters of the western Baltic Sea according tothe seasons winter **(A,E)**, spring **(B,F)**, summer **(C,G)**, and autumn **(D,H)**.

Remarkable changes during two decades were determined for nitrate and DIN with an overall strong decrease in the Eckernförde Bight–Schlei (**Figures 4A,D**) and an increase of nitrate by 20% and DIN by 10% (**Figures 4A,E**, **Table 1**) in the Warnow River. However, both show a plateau between the second 2000–2004 and the third 2005–2009 period. In the Rügen Lagoon chain, the DIN end-member reflected an intermittent maximum for 2005–2009 (**Figure 4F**). The decline of nitrate and DIN end-members determined for the Belt Sea (**Figures 4A,D**), the Arkona Sea (**Figures 4B,F**), and the Greifswald Lagoon (**Figures 4B,F**) basically happened from the first to second period (1995–1999 to 2000–2004), and there were no significant changes thereafter.

Also, TN decreased during the two decades, in the Belt Sea (**Figure 4G**), the Rügen Lagoon chain (**Figure 4H**), and the Greifswald Lagoon (**Figure 4I**) but showed stable end-member concentrations between the second 2000–2004 and third 2005–2009 periods. The overall decrease in the Mecklenburg Bight (**Figure 4G**) and in the Darss-Zingst Lagoon chain (**Figure 4H**) is interrupted by intermittent TN maxima in the 2005–2009, whereas TN in the Arkona Sea showed an almost continuous decline by ∼20% (**Figure 4I**). The TN end-member development in the Warnow River during the whole time period with the maximum in the 2000–2004 period followed by a minimum in 2005–2009 (**Figure 4G**) as well as for the Odra Bight with a minimum in 2000–2004 and a maximum in 2005–2009 (**Figure 4I**) just reflects variability, which is supported by the broad confidence ranges.

Phosphate remained relatively stable between the first and third periods and declined subsequently to 2010–2016 by about 40% in the Arkona Sea area (**Figure 4C**), which represented the eastern half of the study area.

The Warnow River area showed a TP end-member decline by ∼40% from 1995–1999 to 2010–2016 with relative stable values between the second and third periods (**Figure 4J**, **Table 1**). In the Darss-Zingst Lagoon chain, TP declined overall by more than 50% but also showed a strong maximum in 2005–2009 (**Figure 4K**). In the Rügen Lagoon chain, an almost continuous decline down to one-third (**Figure 4K**) was determined. A decrease of TP is documented in the Arkona Sea, the Greifswald Lagoon, and the Odra Lagoon with Odra Bank (**Figure 4L**), especially after the maximum in the 2000–2004 period.

The end-members of the DIN/DIP and TN/TP ratios generally seem to decrease in the last two decades (**Table 1**). However, a clear maximum in the second period from 2000–2004 is documented for TN/TP in the Belt Sea and the Mecklenburg Bight as well as in the Greifswald Lagoon. A relative nitrogen deficit compared with phosphorus cannot be deduced, because the DIN/DIP end-members of about a few hundred mole per mole (**Table 1**) are far beyond the Redfield ratio (Redfield et al., 1963). Thus, cyanobacteria growth seems not to be supported by the freshwater source in these regions.

It could be highlighted that in the period 2010–2016, the freshwater end-members of nitrate differed between 20 µM in the Rügen Lagoon chain and 245 µM for the Warnow River area

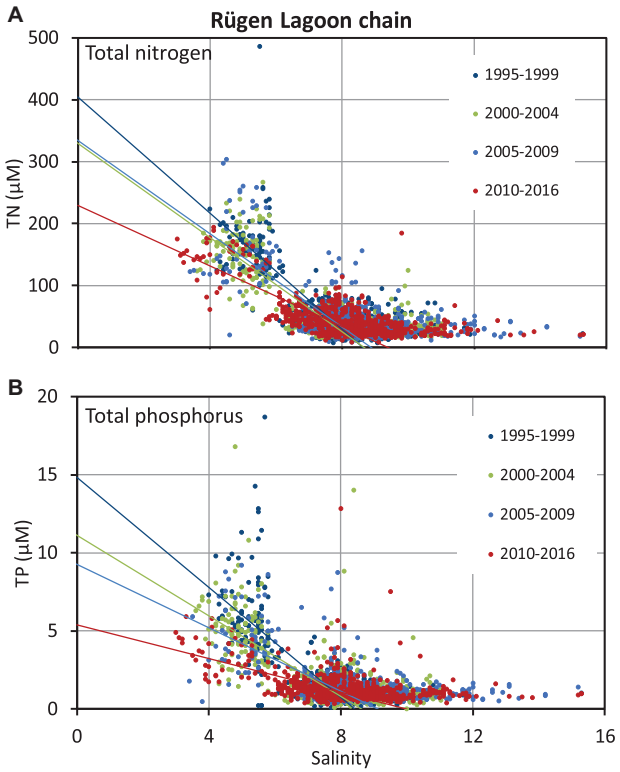

FIGURE 3 | Evaluation of the regression lines for the selected time periods for the area of the Rügen Lagoon chain for total nitrogen **(A)** and total phosphorus **(B)** for theupper 10 m of the water column; the fits were done in this case for a salinity range equal to or below 8.

Time period	TN	TP
1995–1999	$TN = -46.95S + 404.45$, $R^2 = 0.57$	$TP = -1.76S + 14.84$, $R^2 = 0.53$
2000–2004	$TN = -38.03S + 329.38$, $R^2 = 0.68$	$TP = -1.29S + 11.09$, $R^2 = 0.56$
2005–2009	$TN = -37.70S + 334.58$, $R^2 = 0.53$	$TP = -1.01S + 9.25$, $R^2 = 0.38$
2010–2016	$TN = -24.42S + 229.24$, $R^2 = 0.27$	$TP = -0.54S + 5.40$, $R^2 = 0.26$

(**Table 1**). Accordingly, DIN was clearly below about 100 µM in the Rügen Lagoon chain, the Greifswald Lagoon, and for the whole Arkona Sea area, whereas in the Belt Sea area, with the Eckernförde Bight–Schlei, Mecklenburg Bight, and Warnow River, the DIN end-member concentrations ranged between 125 and above 250 µM in that period. Similarly, for these regions, the TN end-members were determined from below 150 to more than 300 µM in the recent period (2010–2016). TP ranged from about 2.3 µM in the Warnow River to 5.4 µM in the Rügen Lagoon chain in this time interval, with corresponding values of slightly above 4 µM in the Warnow River and almost 15 µM in the Rügen Lagoon chain in the 1995–1999 period. Phosphate showed significant correlations only for the Arkona Sea with a decline from 1.76 to 0.64 µM within 20 years. For comparison, weighted averages of the nutrient concentrations at the river mouths, so-called LMT points for assessments, were given for the respective regions in **Table 1**. Potential differences of these values with the extrapolated end-member nutrient concentrations could indicate changes during mixing and transportation of the water ingredients on the way to the open sea. Overall, 17 German meadows and rivers were included for the Belt Sea and 7 rivers for the Arkona Sea to obtain weighted averages of the measured nutrient concentration for all investigated areas.

Changes of the End-Member Values by Considering Different Salinity Ranges for the Regression Analysis

Another interesting point was a potential deviation of the slope of the nutrient concentrations versus salinity from linearity. Just conservative mixing of the freshwater with seawater would cause a linear relationship, but removal and supply processes lead to deviations from the strict linear relation. A slope below the straight line would indicate removal processes, whereas a positive aberration would indicate a supply process. However, the scatter of the data failed to support curve-shaped slopes in comparison with linear relationships. We therefore follow the alternative approach, to further restrict the salinity range to investigate if the end-members change. Subsequently, we limit the salinity to a maximum of 0.75 times the median of the data subset (restricted

TABLE 1 | Freshwater end-members (*y*-axis intercepts) from regression lines of parameter–region pairs for all four investigated time periods with >99% significance, the range (±) of the 95% confidence interval, and average measured values for the limnic–marine transition (LMT) given for comparison.

	1995–1999		2000–2004		2005–2009		2010–2016	
Region	**End-member**	**LMT**	**End-member**	**LMT**	**End-member**	**LMT**	**End-member**	**LMT**
			Nitrate (μM)					
Belt Sea	166.0 ± 16.8	253.2	145.3 ± 12.3	237.8	148.6 ± 16.1	258.0	143.4 ± 13.8	233.1
Eck. B.-Schlei	257.8 ± 59.8	439.9	192.3 ± 41.6	424.9	190.6 ± 45.6	443.8	116.8 ± 29.3	350.4
Meckl. B.	158.4 ± 19.6	258.0	140.9 ± 15.2	242.7	141.9 ± 21.1	264.7	151.8 ± 18.7	241.9
Warn. Riv.	209.2 ± 34.0	170.6	236.7 ± 30.2	154.5	228.5 ± 38.8	156.2	244.8 ± 39.8	141.3
Arkona S.	116.4 ± 8.1	191.5	76.2 ± 6.3	190.7	83.1 ± 7.5	190.8	72.3 ± 5.3	185.3
Rüg. Lagoon	25.1 ± 7.9	415.7	16.7 ± 4.7	404.8	19.7 ± 8.1	404.4	20.0 ± 5.5	356.2
Greif. Lagoon	103.1 ± 17.0	316.2	54.9 ± 11.2	379.0	67.8 ± 10.3	334.0	59.2 ± 7.4	339.1
			DIN (μM)					
Belt Sea	188.2 ± 17.7	275.3	156.4 ± 12.9	250.4	163.6 ± 17.3	269.1	153.9 ± 14.5	243.9
Eck. B.-Schlei	273.6 ± 63.2	468.3	198.4 ± 43.2	441.4	197.3 ± 47.4	458.5	125 ± 30.8	363.2
Meckl. B.	182.2 ± 20.7	280.6	152 ± 16.0	254.7	158.7 ± 22.9	275.3	163.4 ± 19.6	252.5
Warn. Riv.	223.6 ± 36.1	203.3	248.2 ± 31.8	167.8	236.0 ± 41.2	166.1	254.4 ± 41.7	149.7
Arkona S.	126.7 ± 8.5	228.3	84.7 ± 6.3	207.5	87.3 ± 8.0	205.6	80.1 ± 5.7	200.5
Rüg. Lagoon	62.8 ± 14.3	466.3	30.2 ± 6.4	423.6	54.5 ± 12.8	424.9	35.3 ± 7.9	374.2
Greif. Lagoon	109.4 ± 17.1	371.5	58.0 ± 11.5	408.2	72.6 ± 10.5	356.2	64.4 ± 7.5	362.4
			TN (μM)					
Belt Sea	322 ± 19.4	342.0	289.3 ± 13.7	321.4	290.9 ± 17.3	334.9	262.3 ± 14.1	289.6
Eck. B.-Schlei	390.9 ± 62.2	524.9	294.7 ± 51.0	499.6	279.4 ± 49.1	516.8	204.3 ± 30.8	388.6
Meckl. B.	325.5 ± 22.2	348.8	297.4 ± 15.9	327.4	306.9 ± 21.9	342.8	286.4 ± 18.3	299.8
Warn. Riv.	295.6 ± 40.2	269.1	339.6 ± 34.6	237.5	291.9 ± 42.6	238.0	314.8 ± 39.5	206.1
Arkona S.	199.8 ± 11.3	279.7	177.6 ± 8.1	279.7	171.5 ± 9.2	295.1	162.5 ± 7.0	269.4
Darss-Zingst	388.2 ± 72.9	295.9	275.5 ± 43.7	302.7	317.4 ± 50.5	300.8	279 ± 33.0	280.9
Rüg. Lagoon	404.4 ± 32.7	522.2	329.4 ± 19.4	503.6	334.6 ± 32.0	529.1	229.2 ± 29.5	431.8
Greif. Lagoon	195.4 ± 17.3	416.4	157.7 ± 13.5	478.4	156.5 ± 14.0	468.4	143.6 ± 8.3	441.0
Odra Bight	199.2 ± 22.7	272.2	170.5 ± 19.8	269.5	191.2 ± 20.4	288.5	180.6 ± 14.4	262.1
			Phosphate (μM)					
Arkona S.	1.76 ± 0.27	1.51	1.75 ± 0.14	1.57	1.61 ± 0.17	1.65	0.64 ± 0.08	1.99
			TP (μM)					
Belt Sea	5.4 ± 0.44	4.55	4.41 ± 0.29	3.49	4.80 ± 0.39	4.01	3.87 ± 0.32	3.89
Meckl. B.	5.8 ± 0.38	4.45	4.65 ± 0.33	3.37	5.51 ± 0.48	4.01	3.95 ± 0.39	3.95
Warn. Riv.	4.03 ± 0.48	4.34	3.07 ± 0.56	2.76	3.00 ± 0.60	3.10	2.31 ± 0.46	2.85
Arkona S.	5.00 ± 0.46	4.06	6.12 ± 0.32	3.33	5.14 ± 0.36	3.82	3.62 ± 0.15	3.61
Darss-Zingst	10.94 ± 4.54	3.76	5.27 ± 0.98	3.39	8.15 ± 2.45	3.73	4.78 ± 0.40	3.77
Rüg. Lagoon	14.84 ± 1.31	8.33	11.09 ± 0.85	6.01	9.25 ± 1.16	6.95	5.4 ± 0.66	7.35
Greif. Lagoon	3.41 ± 0.37	4.19	4.2 ± 0.57	2.33	3.64 ± 0.49	2.72	2.82 ± 0.24	3.21
Odra L. & B.	4.93 ± 0.40	4.09	6.62 ± 0.75	3.33	5.92 ± 1.06	3.85	4.37 ± 0.57	3.58
			DIN/DIP (mol/mol)					
Belt Sea	419 ± 153	356	270 ± 96	379	395 ± 127	208	230 ± 48	169
Eck. B.-Schlei	2, 997 ± 969	239	1, 714 ± 553	287	1, 777 ± 630	282	557 ± 228	247
			TN/TP (mol/mol)					
Belt Sea	795 ± 84	83	1, 276 ± 166	96	653 ± 142	90	515 ± 86	81
Meckl. B.	942 ± 113	83	1, 533 ± 221	99	773 ± 204	91	655 ± 123	82
Warn. Riv.	1, 000 ± 186	62	1, 013 ± 250	86	581 ± 121	77	574 ± 111	72
Greif. Lagoon	582 ± 112	99	1, 072 ± 366	205	596 ± 171	172	521 ± 86	137

S range in **Table 2**). This still revealed 14 area–parameter pairs with significant correlation for the four time intervals (**Table 2**): Belt Sea (nitrate, DIN, TN, TP, and TN/TP), Mecklenburg Bight (nitrate, DIN, TN, TP, and TN/TP), Warnow River (TN), Arkona Sea (nitrate and DIN), and the Odra Bight (TN).

Subsequently, the end-members of the same area–parameter pairs of the original salinity range were compared with the ones of the salinity range restricted closer to the freshwater side. The comparison revealed that the latter end-members were in general significantly higher, indicating an increased steepness

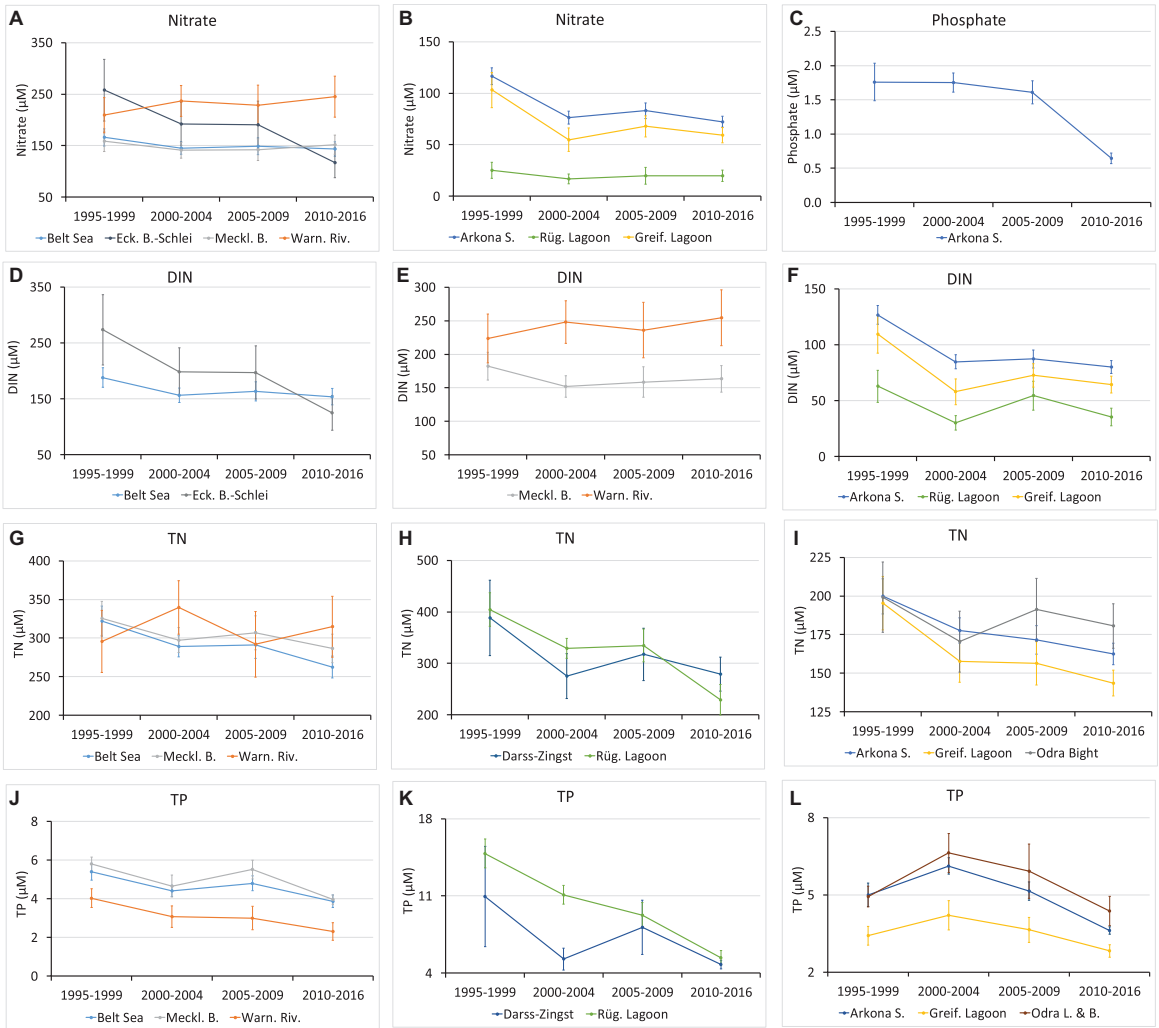

FIGURE 4 | Freshwater end-member concentrations of the investigated nutrients, nitrate **(A,B)**, phosphate **(C)**, DIN **(D–F)**, TN **(G–I)**, and TP **(J–L)** versus the time periods from significant regression lines (>99%); the upper andlower boundaries of the 95% confidence interval are given as error bars (see **Table 1**).

of the nutrient–salinity relations to lower salinity (**Figure 5**). This in turn supported the hypothesis that removal processes are operating during mixing and transport between river and open sea for certain compounds and regions. The differences were in the range of mostly a few percent up to 24% (**Table 2**). A significant reduction of nitrogen compounds during transport to the open sea was thus deduced for the Belt Sea (**Figures 5A–C**). For the narrower salinity range, it showed a 9% higher hypothetical end-member for nitrate and of 10% for DIN in 2010–2016, as well as of 13% in 2005–2009 and 16% 2010–2016 for TN. In agreement with this observation, the subregion Mecklenburg Bight showed a 10% higher TN end-member for the narrower salinity range in the last two time periods (**Figure 5G**). For DIN and nitrate, the changes varied and partly changed sign in the Mecklenburg Bight (**Figures 5E,F**). The TN differences in the Warnow River area since 2000–2004 (**Figure 5I**) show considerable differences of 7%, 9%, and 7% but were less significant (>95%) in the 2000–2004 interval. For the Arkona Sea area as whole (**Figures 5J,K**), changes are notified for nitrate of 3%, 4%, 2%, and 5% for the time intervals between 1995 and 2016, and for DIN, only weak changes were determined with changing sign. It should be mentioned that also for the Odra Bight area, TN end-members differed by 15% in the 2005–2009 and 7% in 2010–2016 periods (**Figure 5L**).

For the TP end-members, the changes between the two salinity ranges were 7% (1995–1999), 11% (2000–2004), 24% (2005–2009), and 13% (2010–2016) for the Belt Sea area (**Figure 5D**), as well as 19% (2005–2009) and 15% (2010–2016) in the Mecklenburg Bight (**Figure 5H**) in the last decade of the study. This indicated strong removal processes for 2005–2009 in the Belt Sea and the Mecklenburg Bight transition zones, but in 2010–2016, the difference was less significant (>95%) for the Mecklenburg Bight. Also, the TP differences in the Mecklenburg Bight (**Figure 5H**) show difference of 19% for 2005–2009 and 15% for 2010–2016 for the two salinity ranges. The latter was however significant on the 95% level only.

TABLE 2 | Calculated differences of the nutrient concentration end-members (>99% significance) of the restricted salinity (*S*) range* and the salinity range until the median; the change is given in% in brackets (see text for further information).

Area	Restricted *S* range*	*S* range**	1995–1999	2000–2004	2005–2009	2010–2016
				ΔNitrate (μM)		
Belt Sea	$S \leq 10$	$S \leq 13.3$	10.7 (6%)	2.3 (2%)	−1.6 (− 1%)	14.8 (9%)
Meckl. B.	$S \leq 9.2$	$S \leq 12.3$	0.3 (0%)	6.2 (4%)	−8.3 (− 6%)	−0.7 (0%)
Arkona S.	$S \leq 5.3$	$S \leq 7.0$	4.1 (3%)	3.0 (4%)	1.4 (2%)	4.0 (5%)
				ΔDIN (μM)		
Belt Sea	$S \leq 10$	$S \leq 13.3$	13.6 (7%)	2.2 (1%)	3.4 (2%)	17.5 (10%)
Meckl. B.	$S \leq 9.2$	$S \leq 12.3$	2.2 (1%)	6.4 (4%)	−4.8 (− 3%)	1.3 (1%)
Arkona S.	$S \leq 5.3$	$S \leq 7.0$	2.9 (2%)	2.8 (3%)	−3.4 (− 4%)	1.0 (1%)
				ΔTN (μM)		
Belt Sea	$S \leq 10$	$S \leq 13.3$	29.0 (8%)	25.3 (8%)	45.0 (13%)	49.1 (16%)
Meckl. B.	$S \leq 9.2$	$S \leq 12.3$	14.6 (4%)	22.2 (7%)	32.8 (10%)	32.5 (10%)
Warn. Riv.	$S \leq 8.3$	$S \leq 11.0$	−16.3 (− 6%)	24.1 (7%)	27.2 (9%)	22.8 (7%)
Odra Bight	$S \leq 2.6$	$S \leq 3.5$	7.7 (4%)	5.6 (3%)	33.6 (15%)	13.3 (7%)
				ΔTP (μM)		
Belt Sea	$S \leq 10$	$S \leq 13.3$	0.4 (7%)	0.5 (11%)	1.5 (24%)	0.6 (13%)
Meckl. B.	$S \leq 9.2$	$S \leq 12.3$	0.3 (4%)	0.4 (7%)	1.3 (19%)	0.7 (15%)
				ΔTN/TP (mol/mol)		
Belt Sea	$S \leq 10$	$S \leq 13.3$	171 (18%)	375 (23%)	224 (26%)	148 (22%)
Meckl. B.	$S \leq 9.2$	$S \leq 12.3$	120 (11%)	281 (15%)	251 (25%)	129 (16%)

Regression analysis for data restricted to or below 0.75 times the median of the data subset. **Regression analysis for data at or below the median of the data subset (as in **Table 1).*

DISCUSSION

The central hypothesis of the study is that changes of nutrient supply by rivers and groundwater discharges to the sea should be visible in temporal changes of the nutrient–salinity relationships. Moreover, depending on the selected salinity range, removal or supply sources from river mouths to the open sea could be revealed.

The temporal evolution of the nutrient concentrations in open waters generally appears stable between 1995 and 2016 (**Figure 2**) with regard to the efforts undertaken to reduce nutrient supply to the Baltic Sea. However, using the nutrient–salinity relationships, a view from the open sea in direction to the freshwater source provides additional information.

The principal hydrographical difference between the southern coast, which is characterized by lagoons, and the western coast, showing bays and fjords seem to influence the outcome of the analysis. In bays and fjords, the transition area between freshwater and seawater is restricted to a relative small distance, whereas at the coast of Mecklenburg-Vorpommern, the transport occurs over a long distance (Lampe, 1994). The latter certainly enabled processes additional to conservative mixing compared with the more or less direct discharge at the western coast. This makes statistically robust nutrient–salinity correlations for the latter region less probable. Moreover, the freshwater supply by rivers is less important in the Kiel Bight compared with the Mecklenburg Bight because the Warnow and Trave Rivers account for more than 50% of the freshwater supply from the German drainage basin to the Belt Sea, whereas only about 12% is supplied to the Kiel Bight (BLANO, 2014). Likely, this is the reason that the Flensburg Fjord, the Eckernförde Bight, the Kiel Fjord and the Kiel Bight, and the Lübeck Bight did not show correlation that could be analyzed and interpreted between 1995 and 2016. An exception was the Schlei where the mixing of freshwater supplied by the Füsinger and Loiter Meadows with seawater also stretches along a few tens of kilometers. However, several areas have been identified, providing some insight into changes during the about 20 years' time period of this study.

The end-member method revealed the hypothetical freshwater concentration but did not provide information about the load. The impact of nutrient end-member concentrations of certain regions could be seen by comparison with the next larger and a neighboring region and finally with the corresponding basin, Arkona Sea or Belt Sea. In some cases, the pattern of the end-member versus the time periods showed clear similarity for certain geographical regions and subregions, for example, for nitrate and DIN in the Greifswald Lagoon and the Arkona Sea (**Figures 4B,F**) and for TP in the Warnow River, the Mecklenburg Bight, and the Belt Sea (**Figure 4J**). The same is true for TP in the Greifswald Lagoon, the Odra Lagoon with Odra Bank area, and the Arkona Sea (**Figure 4L**). This finding indicates that these rivers and potential processes of the mixing zone have a dominant impact.

With caution, this end-member values could be compared with the target nutrient concentrations defined at the LMT point of 186 μM (2.6 mg/L) of TN (BLANO, 2014; LUNG, 2015) and river-type-specific targets of 3–5 μM (0.1–0.15 mg/L) of TP (BLANO, 2014). In the Arkona Sea, the Greifswald Lagoon, and the Odra Bight, hypothetical end-members were below the target values for the LMT since 2000, with the period 2005–2009 TN = 191 μM in the Odra Bight being slightly above the

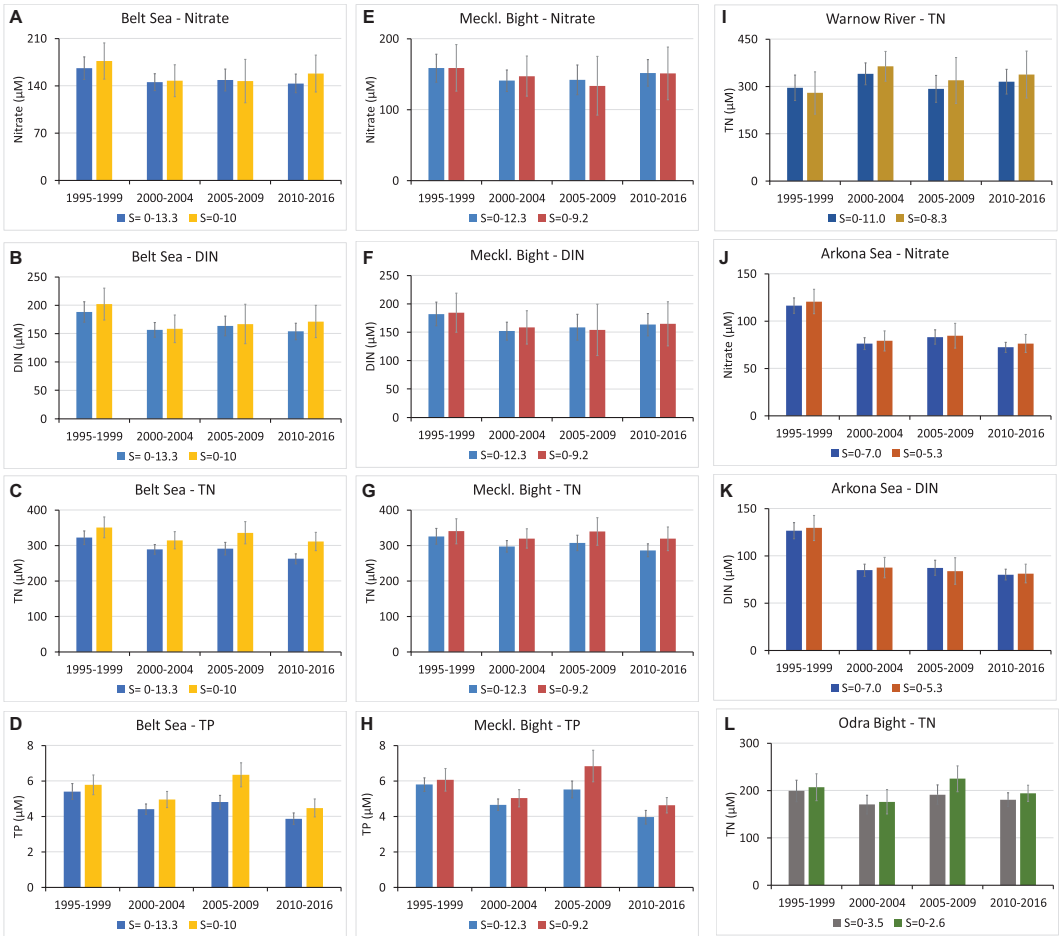

FIGURE 5 | Comparison of the freshwater end-members of **Figure 4** (left bars) for the Belt Sea: nitrate **(A)**, DIN **(B)**, TN **(C)**, and TP **(D)**, for the Mecklenburg Bight: nitrate **(E)**, DIN **(F)**, TN **(G)**, and TP **(H)**, for Warnow River TN **(I)**, for Arkona Sea nitrate **(J)**, and DIN **(K)**, and for Odra Bight TN **(L)** with the results for the restricted salinity ranges (right bars, significant, >99%) as anindicator of changes of the respective parameter during transport to the open sea (see **Table 2**); the 95% confidence intervals are given as error bars.

value (**Table 1**). Most areas showed end-member values equal or lower for the selected time periods, if we compare the TP end-members to TP = 5 µM as threshold value: Belt Sea (since 2000–2004), Mecklenburg Bight (in 2000–2004 and 2010–2016), Warnow River (since 1995–1999), Arkona Sea (in 1995–1999 and 2010–2016), Darss-Zingst Lagoon chain (2010–2016), Greifswald Lagoon (since 1995–1999), and Odra Lagoon with Odra Bight (in 1995–1999 and 2010–2016). The TP end-member values of the Warnow River (since 2005–2009) and the Greifswald Lagoon (since 2010–2016) would meet or were below the TP target value of 3 µM. This shows that the filter function in coastal zone is operating and indicates a sink for nitrogen compounds, likely by denitrification under the precondition of low oxygen. For phosphorous compounds, it can be assumed that removal means accumulation in sediments, piling up a legacy stock. However, these values are still clearly different to the pristine conditions of the rivers of the German Baltic Sea catchment that were estimated to be below ∼70 µM (∼1,000 µg/L) of TN and 1.6 µM (∼50 µg/L) of TP (Hirt et al., 2014).

Measured Nutrient Concentrations at the Limnic–Marine Transition Compared With the End-Members

The comparison (**Table 1**) of calculated end-member values with the measured values at the LMT for the respective nutrient parameter and areas could indicate a potential filter function of the coastal areas or possibly a source in the respective regions. So for most regions and nutrient parameters, the LMT values are about (40 ± 30)% higher. This already would suggest important nutrient removal processes. However, especially Rügen Lagoon chain and the slightly less strong Greifswald Lagoon chain reflect factors of 17 to 24, and 3 to 7, respectively, which are higher LMT values for nitrate and similarly for DIN compared with the end-member values. This indeed indicates a strong filter function for inorganic nitrogen compounds in those areas. In comparison with DIN, TN values obtained from the end-member approach were in reasonable agreement with LMT values. So for TN, the ratio LMT/end-member scatters around 1 (0.7–1.9) with the

exception of the Greifswald Lagoon showing an average of 2.8, indicating a stronger removal process here.

For the Arkona Sea area, phosphate shows similar LMT and end-member values of ∼ 1.6 μM. Only for the last time interval 2010–2016 was an end-member found to be considerably lower, potentially indicating exceptional removal of phosphate during that time in the Arkona Sea area that, however, remains unexplained. For TP, the ratio LMT/end-member scatters around 1 (0.3–1.4) with an average of 0.8 (0.3 represents an exception), showing some agreement between the two methods. Moreover, 0.8 likely indicates slight TP contribution during passage of the coastal area from diffusive sources or sediments. The DIN/DIP ratio of the end-member approach and the LMT measurements is in reasonable agreement for the Belt Sea (0.5–1.4) as a whole. For the subregion Eckernförde Bight–Schlei, the end-member DIN/DIP ratio is up to one order of magnitude higher than the LMT value. This shows a shift to higher nitrogen/lower phosphorus values during transition to the open sea. The TN/TP ratio is about a magnitude higher for the end-member values compared with the LMT values for the Belt Sea region, the Mecklenburg Bight, and the Warnow River and a factor of 4 to 6 for the Greifswald Lagoon, indicating a strong shift to higher nitrogen and/or lower phosphorus values during mixing. This might be explained by a faster remineralization/redissolution of phosphorus from particulate material compared with nitrogen and subsequent removal to the sediment. Thereby, usually, no clear temporal change during the two decades is indicated, except for the Eckernförde Bight–Schlei area where the LMT values decrease slower than the end-member values for nitrate and DIN, showing an increasing importance of nitrogen removal processes there. A more drastic exception reflects the Warnow River. The measured values at LMT decline from about 80%, 90% (1995–1999) to 60%, 65% (2010–2016) for nitrate and DIN, respectively, of the end-member values indicate additional contributions of nitrogen compounds during mixing. Likely, this originates from diffusive fluxes or from sediments with an increasing tendency in the last 20 years.

An explicit judgment of the end-member values is difficult, because the end-members of the nutrient concentrations depend on the underlying salinity range. From **Table 2**, it is clear that the end-members increased at least by several percent and often more than 10% above the values of **Table 1**. The end-members likely would proceed to increase by further restriction of the salinity range but could not be analyzed because of a lack of significance. However, an increase of the end-member values from the broader to the narrower salinity interval indicates a significant loss during mixing and passage through the coastal zone. The loss could be permanent, as in the case of removal by, for example, denitrification or by sedimentation with subsequent burial. A retention or temporary loss is caused during uptake by algae or seagrass, which is followed by remineralization of matter (Asmala et al., 2017). An efficient long-term reduction would indicate a clear ecosystem service and might prove its relative health. However, the latter is certainly not the case during denitrification, which is accompanied by a strong oxygen deficiency. From the comparison of the end-members for the narrower and the wider salinity range, in some cases, also the opposite is seen, indicating a supply process during transport to the open sea. Potential mechanisms could be groundwater discharge or contact and remobilization with sediments or bottom waters, potentially enriched by legacy deposits. Nitrate and TN gain during mixing in the Warnow River between 1995–1999 and Mecklenburg Bight 2005–2009 may indicate re-dissolution from sediments or supply from other discharge sites in combination with a probably stressed ecosystem.

CONCLUSION

The Baltic Sea is naturally burdened by its special hydrography that seems to amplify disturbances. However, a responsible governance by HELCOM and the European Union (EU) led to an overall improvement in the ecosystem status of the Baltic Sea (Reusch et al., 2018), which is for the first time indicated on the basis of seawater nutrient concentrations in the western Baltic Sea. Thereby, the end-member approach does integrate the freshwater concentrations on the one hand, but on the other hand, it accounts for processes in the river/sea transition zone. However, it requires precise definition of the salinity range and the time intervals that are subjected to analysis to secure comparability. It appears that the extrapolated concentrations are mostly lower than measured freshwater values.

A strategy to further reduce anthropogenic nutrient supply requires atmospheric emission reduction of, for example, nitrogen oxides and ammonium compounds and a decline of the nutrient load from drainage areas. A principal approach to manage diffuse phosphorus sources emphasized low cost measures at the source for phosphorus reduction, conservation, and mitigation of losses (Macintosh et al., 2018). Otherwise, removing phosphorus from aquatic sinks and finally recovery of diffuse phosphorus would require increased expenses. Besides innovative technologies and food waste reduction, circular economy sustainability solutions include supporting local food supply chains with less waste, closing nutrient loops, pricing the true cost of resource consumption and losses in natural capital, and creating policy mechanisms to promote recovery and reduce loss of critical raw materials in particular (Jurgilevich et al., 2016). A compilation of measures from the German government include "Agricultural cooperation project on reducing direct inputs into coastal waters via drainage systems"; "Strengthening the assimilative capacity of estuaries, using the example of the River Ems," "Promotion measures to reduce NOx inputs from shipping"; and "Supporting the designation of a Nitrogen Emission Control Area (NECA) in the North and Baltic Seas" (BMUB, 2016).

AUTHOR CONTRIBUTIONS

The study was initiated by DS-B. Preliminary results were presented by JK, GN, MN, and DS-B at the 2nd Baltic Earth Conference in Helsingør, Denmark "Variability of nutrient concentrations in the western Baltic Sea between 1995 and 2017." Data synthesis and analysis were done by JK, JW, GN, HL, and MW.

JK wrote the draft version and synoptically implemented the revisions by CE, JW, MW, HL, GN, MN, JW, and DS-B. MN and JK prepared the graphics.

ACKNOWLEDGMENTS

We especially thank our colleagues at the nutrient labs of IOW (in the last years run by Birgit Sadkowiak and Lars Kreuzer) and the LLUR (by Gerda Rünger, Claudia Roschinski, Petra Schramm, and George Borchert) for their skillful and high-quality work. We also thank the staff involved in the sampling campaigns, as well as the people that maintain the long-term database of IOW and the MUDAB. We acknowledge the organization effort of chief scientists and the cooperation of the captain and the crews of many research vessels that have been involved in multiple monitoring campaigns. We are grateful to the Federal Maritime and Hydrographic Agency of Germany for funding of the HELCOM monitoring carried out by IOW.

REFERENCES

Asmala, E., Carstensen, J., Conley, D. J., Slomp, C. P., Stadmark, J., and Voss, M. (2017). Efficiency of the coastal filter: Nitrogen and phosphorus removal in the Baltic Sea. *Limnol. Oceanogr.* 62, S222–S238. doi: 10.1002/lno.10644

BLANO (2014). *Harmonisierte Hintergrund- und Orientierungswerte für Nährstoffe und Chlorophyll-a in den deutschen Küstengewässern der Ostsee sowie Zielfrachten und Zielkonzentrationen für die Einträge über die Gewässer*. Bonn: Bund/Länder-Ausschuss Nord- und Ostsee (BLANO).

BMUB (2016). *English Summary - MSFD Programme of Measures for Marine Protection in the German Parts of the North Sea and the Baltic Sea - Report pursuant to Article 45h(1) of the Federal Water Act*. Bonn: Federal Ministry of the Environment, Nature Conservation, Construction and Nuclear Safety of Germany (BMUB).

Conley, D. J., Carstensen, J., Aigars, J., Axe, P., Bonsdorff, E., Eremina, T., et al. (2011). Hypoxia is increasing in the coastal zone of the Baltic Sea. *Environ. Sci. Tech.* 45, 6777–6783. doi: 10.1021/es201212r

German Environment Agency (2018). *Meeresumwelt Datenbank - MUDAB (Data Base of the Marine Environment*. Koblenz: The German Federal Institute of Hydrology - BfG.

Grasshoff, K. (1976). *Methods of seawater analysis*. Weinheim: Verlag-Chemie.

Hansen, H. P., and Koroleff, F. (1999). "Determination of nutrients," in *Methods of Seawater Analysis*, 3rd Edn, eds K. Grasshoff, K. Kremling, and M. Ehrhardt (Weinheim: Wiley-VCH), 159–228.

HELCOM (2004). "The fourth Baltic Sea pollution load compilation (PLC-4)," in *Proceedings of the Baltic Sea Environment proceedings*, (Helsinki: HELCOM).

HELCOM (2011). "The fifth Baltic Sea pollution load compilation (PLC-5)," in *Baltic Proceedings of the Sea Environment proceedings*, (Helsinki: HELCOM).

HELCOM (2018). *Sources and pathways of nutrients to the Baltic Sea - HELCOM PLC-6*. Helsinki: HELCOM.

Hirt, U., Mahnkopf, J., Gadegast, M., Czudowski, L., Mischke, U., Heidecke, C., et al. (2014). Reference conditions for rivers of the German Baltic Sea catchment: reconstructing nutrient regimes using the model MONERIS. *Reg. Environ. Chang.* 14, 1123–1138. doi: 10.1007/s10113-013-0559-7

Jurgilevich, A., Birge, T., Kentala-Lehtonen, J., Korhonen-Kurki, K., Pietikäinen, J., Saikku, L., et al. (2016). Transition towards circular economy in the food system. *Sustainability* 8:69. doi: 10.3390/su8010069

Korpinen, S., Honkanen, T., Vesakoski, O., Hemmi, A., Koivikko, R., Loponen, J., et al. (2007). Macroalgal communities face the challenge of changing biotic interactions: review with focus on the Baltic Sea. *AMBIO* 36, 203–211. doi: 10.1579/0044-7447(2007)36[203:mcftco]2.0.co;2

Lampe, R. (1994). Die vorpommerschen Boddengewässer - Hydrographie, Bodenablagerungen und Küstendynamik. *Die Küste* 56, 25–49.

Lass, H. U., Mohrholz, V., and Seifert, T. (2005). On pathways and residence time of saltwater plumes in the Arkona sea. *J. Geophys. Res.* 110, 1–24. doi: 10.1029/2004JC002848

Leibniz Institute for Baltic Sea Research Warnemünde (2014). *IOWDB - the oceanographic data base of IOW*. Warnemünde: Leibniz Institute for Baltic Sea Research Warnemünde.

LUNG (2015). *Aktualisierung des Maßnahmenprogramms nach §82 WHG bzw. Artikel 11 der Richtlinie 2000/60/EG für die Flussgebietseinheit Warnow/Peene für den Zeitraum von 2016 bis 2021*. Güstrow: Landesamt für Umwelt, Naturschutz und Geologie Mecklenburg-Vorpommern.

Macintosh, K. A., Mayer, B. K., McDowell, R. W., Powers, S. M., Baker, L. A., Boyer, T. H., et al. (2018). Managing diffuse phosphorus at the source versus at the sink. *Environ. Sci. Tech.* 52, 11995–12009. doi: 10.1021/acs.est.8b01143

Majaneva, M., Rintala, J.-M., Hajdu, S., Hällfors, S., Hällfors, G., Skjevik, A.-T., et al. (2012). The extensive bloom of alternate-stage Prymnesium polylepis (Haptophyta) in the Baltic Sea during autumn–spring 2007–2008. *Eur. J. Phycol.* 47, 310–320. doi: 10.1080/09670262.2012.713997

McGlathery, K. J., Sundbäck, K., and Anderson, I. C. (2007). Eutrophication in shallow coastal bays and lagoons: the role of plants in the coastal filter. *Mar. Ecol. Prog. Ser.* 348, 1–18. doi: 10.3354/meps07132

Nausch, G., Bachor, A., Petenati, T., Voss, J., and Weber, M. (2011). Nährstoffe in den deutschen Küstengewässern der Ostsee und angrenzenden Seegebieten. *Meeresumwelt Aktuell Nord- und Ostsee* 1, 1–16.

Nausch, G., Nehring, D., and Nagel, K. (2008). "Nutrient concentrations, trends and their relation to eutrophication," in *State and Evolution of the Baltic Sea, 1952-2005*, eds R. Feistel, G. Nausch, and N. Wasmund (Hoboken, NJ: John Wiley & Sons, Inc), 337–366.

Newton, A., Icely, J., Cristina, S., Brito, A., Cardoso, A. C., Colijn, F., et al. (2014). An overview of ecological status, vulnerability and future perspectives of European large shallow, semi-enclosed coastal systems, lagoons and transitional waters. *Estuar. Coast. Shelf Sci.* 140, 95–122. doi: 10.1016/j.ecss.2013.05.023

Officer, C. B. (1979). Discussion of the behaviour of nonconservative dissolved constituents in estuaries. *Estuar. Coast. Mar. Sci.* 9, 91–94. doi: 10.1016/0302-3524(79)90009-4

Redfield, A. C., Ketchum, B. H., and Richards, F. A. (1963). "The influence of organisms on the composition of sea water," in *The Sea*, ed. M. N. Hill (New York, NY: J. Wiley), 26–77.

Reissmann, J. H., Burchard, H., Feistel, R., Hagen, E., Lass, H. U., Mohrholz, V., et al. (2009). Vertical mixing in the Baltic Sea and consequences for eutrophication – A review. *Prog. Oceanogr.* 82, 47–80. doi: 10.1016/j.pocean.2007.10.004

Reusch, T. B. H., Dierking, J., Andersson, H. C., Bonsdorff, E., Carstensen, J., Casini, M., et al. (2018). The Baltic Sea as a time machine for the future coastal ocean. *Sci. Adv.* 4:eaar8195. doi: 10.1126/sciadv.aar8195

Rieper, M. (1976). Investigations on the relationships between algal blooms and bacterial populations in the Schlei Fjord (western Baltic Sea). *Helgoländer Wissenschaftliche Meeresuntersuchungen* 28, 1–18. doi: 10.1007/BF01610792

Schlüter, M., Sauter, E. J., Andersen, C. E., Dahlgaard, H., and Dando, P. R. (2004). Spatial distribution and budget for submarine groundwater discharge in Eckernförde Bay (Western Baltic Sea). *Limnol. Oceanogr.* 49, 157–167. doi: 10.4319/lo.2004.49.1.0157

Conflict of Interest: The authors declare that the research was conducted in the absence of any commercial or financial relationships that could be construed as a potential conflict of interest.

frontiers in Earth Science

ORIGINAL RESEARCH
published: 16 June 2020
doi: 10.3389/feart.2020.00184

Spatial Distribution of Energy of Subinertial Baroclinic Motions in the Baltic Sea

Andrey Kurkin[1]*, *Artem Rybin*[1], *Tarmo Soomere*[2,3], *Oxana Kurkina*[1] and *Ekaterina Rouvinskaya*[1]

[1] Laboratory of Modeling of Natural and Anthropogenic Disasters, Nizhny Novgorod State Technical University n.a. R. E. Alekseev, Nizhny Novgorod, Russia, [2] Department of Cybernetics, School of Science, Tallinn University of Technology, Tallinn, Estonia, [3] Estonian Academy of Sciences, Tallinn, Estonia

We explore the basic properties of the "climate" of the field of subinertial motions with periods of 2–12 days in the Baltic Sea. The calculations are performed using the output of the Rossby Center Ocean Model RCO with a spatial resolution of 2 nautical miles for 1961–2005. The field of such motions in the Baltic Sea is strongly asymmetric, with much more energy present in the eastern regions of the sea. Spatial distributions of 5-yr average amplitudes of fluctuations of the main and seasonal pycnocline, near-bottom velocity and kinetic and potential energy reflect this asymmetry and also exhibit extensive variability on scales of a few tens of kilometers. The majority of potential energy of such motions is concentrated in a narrow nearshore strip of the sea with a typical width of <20 km. The largest values of kinetic energy occur along the gently sloping seabed at intermediate depths. The areas of maximum of absolute nearbed velocities only partially match similar areas hosting very large kinetic energy or strong fluctuations of the location of the pycnocline. Both the major properties and spatial details of the discussed distributions exhibit almost no difference for the years 1961–1965 and 2000–2005, except for the maximum seabed velocities that are somewhat larger in 2000–2005 apparently because of exceptional storms in 2001 and 2005.

Keywords: baroclinic waves, internal seiches, pycnocline variations, near-bed velocity, Baltic Sea

OPEN ACCESS

Edited by:
Hayley Jane Fowler, Newcastle University, United Kingdom

Reviewed by:
Tatyana V. Belonenko, Saint Petersburg State University, Russia
Markus Meier, Leibniz Institute for Baltic Sea Research (LG), Germany

***Correspondence:**
Andrey Kurkin
aakurkin@gmail.com

Specialty section:
This article was submitted to Interdisciplinary Climate Studies, a section of the journal Frontiers in Earth Science

Received: *13 January 2019*
Accepted: *08 May 2020*
Published: *16 June 2020*

Citation:
Kurkin A, Rybin A, Soomere T, Kurkina O and Rouvinskaya E (2020) Spatial Distribution of Energy of Subinertial Baroclinic Motions in the Baltic Sea. Front. Earth Sci. 8:184. doi: 10.3389/feart.2020.00184

INTRODUCTION

The well-being of the Baltic Sea ecosystem (e.g., in terms of eutrophication, Reissmann et al., 2009) and many details of the functioning of the entire sea (Leppäranta and Myrberg, 2009) substantially rely on the mechanisms that support strong vertical stratification in this water body. It is therefore natural that internal waves play a major role in the functioning of the entire sea. Their role is particularly large in the driving of mixing processes (Axell, 1998; Meier, 2001) and the formation of the vertical structure of its water masses (Axell, 2002; Lass et al., 2003), especially near the bottom slopes (Ozmidov, 1994). The importance of the impact of internal waves in this water body extends far beyond the classic dynamics and kinematics of motions in the sea and extends toward governing many major biochemical processes such as the formation and maintaining the anoxic zones or denitrification of the water column (Dalsgaard et al., 2013).

While the interplay of turbulence and internal waves is a generic issue in the coastal ocean (Burchard et al., 2008), the related aspects are particularly important in the Baltic Sea where steep vertical gradients often occur near the bottom. For example, about 30% of the energy needed for

deep water mixing below the halocline in the Baltic Sea may be provided by the breaking of internal waves (Meier et al., 2006). The impact of internal waves is apparently significant for diapycnal mixing in the deep water of the Baltic Sea (Nohr and Gustafsson, 2009). It is also substantial in relatively sheltered but comparatively deep-water sub-basins such as the Gulf of Finland (Lilover and Stips, 2008, 2011).

The vertical structure of water masses of the Baltic Sea expresses the interplay of fresh water influx from the drainage area and water and salt exchange through the Danish straits. It leads to the presence of a strong relatively deeply located halocline and a relatively shallow seasonal thermocline in most parts of the sea (Leppäranta and Myrberg, 2009). The main density jump layer (pycnocline) is present permanently and usually lies at depths of about 60–80 m in the central part of sea called Baltic (Sea) proper. It is *inter alia* the most important waveguide for different scale baroclinic waves, including short-period internal waves, and a core channel of wave energy transfer between different parts of the sea. Its position indirectly affects the functioning of water masses in the medium-range depths of the sea through changing the kinematic and non-linear baroclinic wave properties (Talipova et al., 1998), supporting the generation, turning, and breaking of internal waves and associated intense mixing (Reissmann et al., 2009), and possible resuspension of bottom sediment (Friedrichs and Wright, 1995).

The main pycnocline and other jump layers are often located fairly close to the sea bottom of the Baltic Sea (Leppäranta and Myrberg, 2009) and in a number of locations even touch the seabed. Therefore, changes in the pycnocline depth may substantially relocate the typical areas of internal-wave-generated hydrodynamic loads and thus locations of intense resuspension of bottom sediment (e.g., Lundhansen and Skyum, 1992; Friedrichs and Wright, 1995; Bentley and Nittrouer, 1999). These changes also impact the associated conditions of sediment non-deposition favorable for the formation of ferromanganese concretions (Glasby et al., 1996) and indirectly affect large-scale infrastructure at the bottom. Even in areas that host large-scale quasi-stationary bottom gravity currents, relatively low-frequency motions with periods up to 30 min (that are possibly related to internal waves) strongly contribute to the bottom stress (Umlauf and Arneborg, 2009).

The related consequences are particularly extensive for the Baltic Sea (Massel, 2015). The usually existing three-layer structure supports specific types of non-linear internal waves (Kurkina et al., 2011a,b) in this basin. Moreover, changes to the properties of bottom mixed layers (Turnewitsch and Graf, 2003) or to the near-bottom hydrodynamic loads may adversely affect, e.g., chemical munitions dumped there after World War II (Beldowski et al., 2016) or govern the fate of new environmental agents such as plastic fibers with very low resuspension threshold (Bagaev et al., 2017).

The major properties of the most energetic (usually resonant) standing wave motions, their spatio-temporal distribution and frequency spectra in (semi-)enclosed basins are governed by the geometry, bathymetry and hydrology of the particular water body (Vlasenko et al., 2005). The basin-scale energy budget of the micro-tidal Baltic Sea is largely governed by two kinds of motions: inertial oscillations and low-mode near- and sub-inertial wave motions that are generated near the lateral slopes of the basin (van der Lee and Umlauf, 2011; Lappe and Umlauf, 2016). The properties of these motions are further modified by spatial inhomogeneities of stratification and water depth (Massel, 2015, 2016), reflections from the seabed, non-linear steepening, disintegration and breaking at the seabed and the nearshore, and various kinds of transformations (Rouvinskaya et al., 2015; Pelinovsky et al., 2018). The resulting motions are often extremely complicated and contain a multitude of different modes and types of motions. Resonance effects frequently play the core role in such processes (Friedrichs and Wright, 1995). They may amplify certain (long-wave) components of fluctuations or create energy cascade between different spectral components. The resulting resonant standing baroclinic waves can be a direct source of short-period internal waves, as well as affect the generation of internal waves by the wind (Whalen et al., 2018).

The properties of long barotropic and baroclinic wave phenomena and their signatures at sea surface are well-known for the Baltic Sea (Wübber and Krauss, 1979; Metzner et al., 2000; Kulikov et al., 2015). The predominant surface self-oscillations of the Baltic proper have periods around 27–29 hours. Their spatial structure and interrelations with seiches in other sub-basins of the Baltic Sea have been analyzed in detail in Jonsson et al. (2008). Less known are properties of large-scale baroclinic oscillations. Their approximate periods for the two lowest horizontal basin-scale modes for the Baltic Sea and its sub-basins lie in the range of 2–12 days. This time interval clearly exceeds the inertial period and is several times larger than the typical time scale of surface seiches in this water body (Leppäranta and Myrberg, 2009; Massel, 2015). The motions with these periods are usually not free waves. Zakharchuk and Tikhonova (2013) demonstrate that low-frequency motions have wave nature at a few locations at the margin of the deep-water Gotland Basin. Such motions still serve as effective means of (wave) energy exchange between different regions and eventually drive a multitude of processes on the shelves of medium-size water bodies such as the Baltic Sea or the Aral Sea (Roget et al., 2017). The associated waveguides are co-located with the main and seasonal pycnoclines. This kind of energy flux has been attributed, for example, to the development of sediment waves (Ribó et al., 2016), pockmarks (León et al., 2014) and large subaqueous sand dunes (Reeder et al., 2011) in other seas such as the Mediterranean Sea.

As baroclinic and internal waves propagate at much lower speeds than long surface waves (Massel, 2015), "internal wave storms" arrive remote areas much later than surface waves or oscillations of sea level. Moreover, their impact is often hidden and/or acts in a certain range of depths that is dictated by the specific combination of the local vertical stratification and the arriving internal wave field. Similarly to the surface wave climate, the field of such motions is a strong source of remote impact in the sense that the location of the largest hydrodynamic loads is separated from the typical generation area of such oscillations.

In this paper we analyze the main properties of long-period subinertial baroclinic motions in the Baltic Sea. The focus is on phenomena with periods in the range of 2–12 days. The analysis

relies on numerically simulated properties of water masses in this water body in 1961–2005. The structure of the paper is as follows. Section Data and Methods shortly describes the circulation model, its output data set and the method for the calculations of the spectral properties of the field of subinertial baroclinic motions. Section Results focuses on the analysis of spectral properties of fluctuations of the main and seasonal pycnocline and spatial distributions of near-bottom velocities and kinetic and potential energy of the motions in this range of periods. Section Conclusions and Discussion reiterates the main conclusions and makes an attempt to put the results into the wider context of the entire Baltic Sea.

DATA AND METHODS

Numerically Simulated Hydrographic Data

The analysis relies on time series of hydrological properties of the entire Baltic Sea produced by the Swedish Meteorological and Hydrological Institute (SMHI) using the Rossby Center Ocean Model RCO (Meier et al., 2003; Meier and Höglund, 2013) for May 1961–May 2005 and provided in the framework of BONUS BalticWay cooperation (Soomere et al., 2014). This 3D circulation model has been designed for simulations with moderate spatial resolution over long time intervals for studies of climate changes. The underlying equations (see detailed implementation, e.g., in Meier et al., 2003; Meier, 2007; Meier and Höglund, 2013) are solved on a regular rectangular grid (2×2 nautical miles) in the horizontal plane and using up to 41 vertical levels with thicknesses of 3–12 m in z-coordinates. Subgrid mixing is parameterized using the k–ε turbulence closure (Meier, 2001). The transport scheme embeds a flux-corrected, monotonicity-preserving routine with no explicit horizontal diffusion. A splitting scheme uses 150 s for the baroclinic and 15 s for the barotropic timestep. The output is stored once in 6 h.

The RCO model takes into account inflow of fresh water from the major rivers and water exchange through the Danish straits. The model uses wind properties at the height of 10 m above sea level, air temperature and specific humidity at a height of 2 m, precipitation, total cloudiness and sea level pressure. The meteorological forcing used to drive the particular model run was derived from the ERA-40 re-analysis (Uppala et al., 2005) using a regional atmospheric model with a horizontal resolution of 25 km (Samuelsson et al., 2011). Winter conditions are replicated using a Hibler-type sea ice model (Hibler, 1979).

The skill of the model in terms of replication of various features with different spatial and temporal scales has been thoroughly studied. A detailed assessment of the replicated vertical profiles and time series against representative monitoring stations and observations from the Baltic Environmental Database (BED) is performed in Placke et al. (2018). The RCO model provides better quality of replication of temperature and salinity profiles than, e.g., the GETM (General Estuarine Transport Model) or MOM (Modular Ocean Model) (Placke et al., 2018). The seasonal cycle and variability of temperature and salinity are simulated close to observations. Simulated current velocities lie mainly within the standard deviation of the measurements at the two monitoring stations (10 years of Acoustic Doppler Current Profiler (ADCP) measurements in the Arkona basin and 5 years of mooring observations in the Gotland basin, Placke et al., 2018).

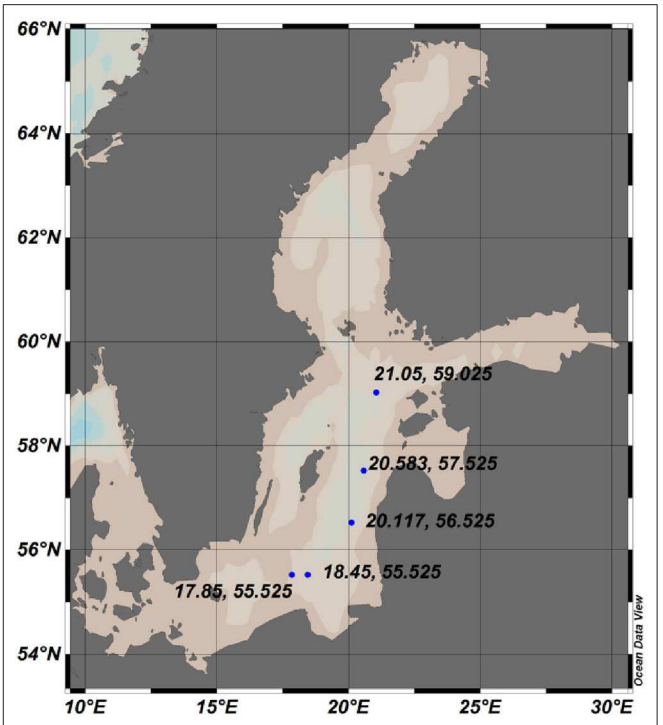

FIGURE 1 | Locations of data points from the World Ocean Database used for comparison with the output ot the RCO model.

To further illustrate the accuracy of the RCO model, we also compared the output of this model with data from the World Ocean Database (WOD). We present here the comparison of the modeled and measured vertical profiles of temperature, salinity and density at selected 5 locations (**Figure 1**) and at different time instants. Since the data sources have different vertical resolution, we performed a linear interpolation of the data to calculate the correlation coefficients and an estimate of the dissimilarity between the modeled and measured data in term of the relative error

$$\varepsilon_{rel} = \frac{|RCO_{value} - WOD_{value}|}{WOD_{value}} \cdot 100\%. \quad (1)$$

An example of the match of the measured and modeled profiles at 20.583°E, 57.525°N on August 28, 1994 is presented in **Figure 2**. The modeled profiles follow well the measured one. The relevant correlation coefficients are 0.98 for temperature, 0.974 for salinity and 0.986 for density. The relative error is usually below 15% (<10% for density) and exceeds 30% only for temperature and salinity in a narrow range of depths at or near jump layers. For our purposes the most important feature is the match of modeled and measured profiles of density as this parameter is decisive for the properties of the medium in which internal waves propagate. The relevant values mostly differ by <5% (**Figure 2**). The largest difference (up to 15–20%) occurs at the lower margins of pycnoclines; however, the vertical structure of density and

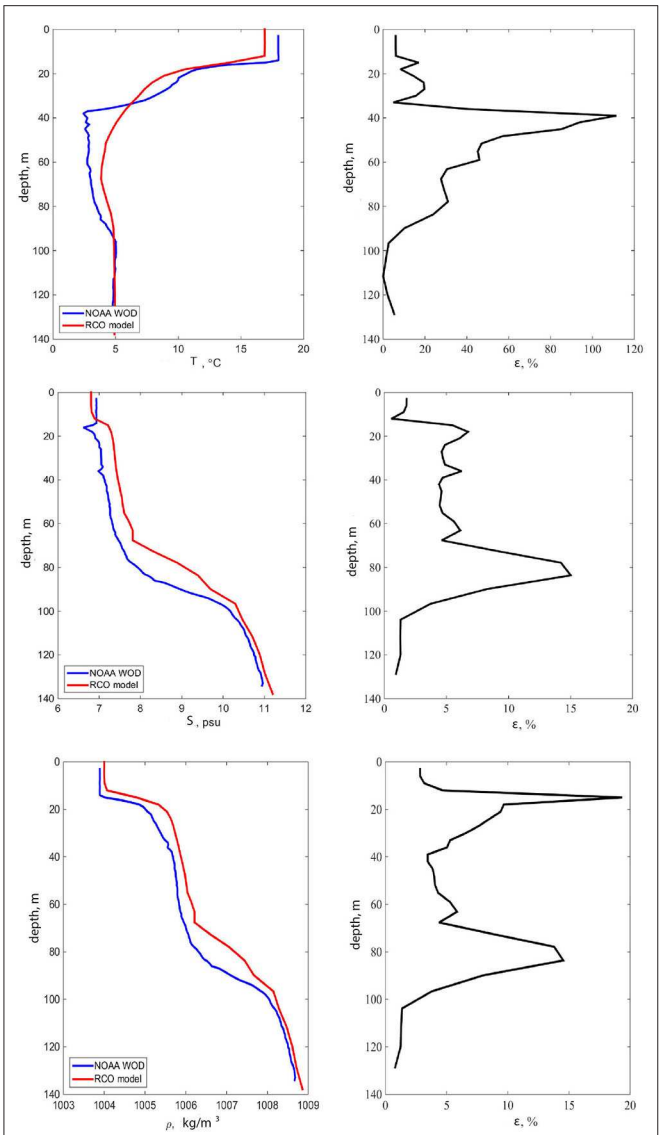

FIGURE 2 | Temperature (T), salinity (S) and density (ρ) profiles from the World Ocean Database and from the RCO model, and the associated relative error (ε) at the location with coordinates 20.583°E, 57.525°N on August 28, 1994.

the depth, magnitude and thickness of the jump layers are fairly well represented.

The largest shortages of the model are a too shallow halocline (Meier, 2007), problematic mixing during salt water inflows (Meier et al., 2003), and numerical noise affecting the sea surface temperature (Löptien and Meier, 2011). The mean circulation differs considerably between the models and due to the lack of current measurements only the baroclinic velocities can be compared with measured data (Placke et al., 2018). These problems insignificantly affect the results of our study.

The performance of the model to replicate processes with a time scale from hours up to few days has been evaluated in terms of water level. The time series and extremes of sea surface heights generally follow the measured values in the eastern Baltic Sea (except for a few locations that are affected by strong wave set-up, Eelsalu et al., 2014). This feature suggests that the model is suitable for the replication of processes with time scales of a few days. The trends in extreme water levels are also reproduced adequately for these measurement locations in the eastern Baltic Sea that well-represent offshore water level (Soomere and Pindsoo, 2016). Only storm surges in the western Baltic Sea are not always correctly replicated (Meier et al., 2004). The model resolves the major properties of mesoscale motions in the Baltic proper as well as the core changes in the vertical structure of water masses (Väli et al., 2013). It is therefore safe to say that the output of the model is suitable for the purposes of our study.

As mentioned above, a specific feature of water masses of the Baltic Sea is the presence of two density jump layers with comparable magnitudes. The spatial structure and temporal course of these layers are clearly resolved by the RCO model. The uppermost mostly mixed layer naturally exists in the entire sea. Its salinity is almost zero in the northernmost Gulf of Bothnia and easternmost Gulf of Finland, and has typical values of 7–8 g/kg in large parts of the sea. The temperature of this layer varies from almost zero to >20°C.

Near-bottom water masses (and thus the main pycnocline) spread only over deeper parts of the sea and have typical salinity 10–21 g/kg and temperature in the range of 4–12°C. The intermediate layer has usually temperatures of 2–6°C (occasionally also below zero, Mohrholz et al., 2006) and salinity of 8–10 g/kg. It is formed via a long-term process of mixing of surface and near-bottom waters. Relatively intense mixing acts at times from the sea surface down to depths of 50–60 m where the main pycno/halocline prevents its further impact.

Variations in the Location of the Pycnoclines

We evaluated first the variations in the depth of the main pycnocline following similar calculations in Väli et al. (2013). A location scheme of points in the Baltic Sea selected for the analysis below is presented in **Figure 3** (including location of a Swedish/HELCOM monitoring station BY31 at the deepest place in the Baltic Sea). The sea water density in the water column was calculated using the standard equation of state (Fofonoff and Millard, 1983) from the modeled temperature, salinity and the vertical location of the water parcels. The location of the main pycnocline was evaluated as the depth of the largest density gradient at depths ≥30 m. The evaluation was performed four times a day for locations where the total sea depth exceeded 60 m.

The seasonal pycnocline in the upper layer of the sea (in which the local gradients may be even stronger than in the main pycnocline) was determined in a similar way but assumed to be not deeper than 30 m. The procedure resulted in discrete values of these two depths (corresponding to the relevant vertical levels in the RCO model) that varied all the way from surface to about 30 m depth level for the seasonal pycnocline and from 30 m depth level to the near-bottom layers for the main pycnocline. For the locations where the total depth was <60 m, the location of only the seasonal pycnocline was evaluated.

The largest variations in the location of the pycnoclines (**Figure 4**) reflect the seasonal course in the hydrological properties of water masses. The depth of the seasonal thermocline

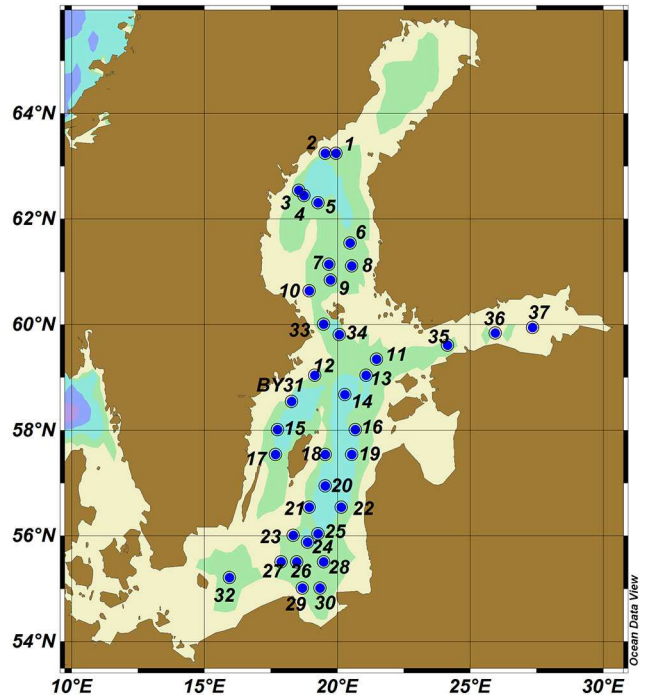

FIGURE 3 | Location scheme of points in the Baltic Sea selected for the analysis.

fluctuates considerably. It occasionally moves closer to the sea surface or even disappears owing to enhanced mixing during the windy (autumn and winter) season. Its location is much more stable and it deepens gradually during the relatively calm spring and summer seasons. These properties match the well-known features of the Baltic Sea stratification (Leppäranta and Myrberg, 2009). An exception was the year 2003 when the seasonal thermocline was located close to the sea surface during entire spring and most of summer.

The main pycnocline behaves in counter-phase with respect to the seasonal one. It moves deeper in spring and is relocated closer to the sea surface in autumn so that in some years the main and seasonal pycnoclines eventually coalesced. However, the two clearly defined jump layers exist during most of the time and the water masses normally possess clear three-layer vertical structure in all parts of the sea where the main pycnocline exists. In particular, during the summer season the intermediate layer is quite thick. Consequently, the "symmetric" situation (with equal thicknesses of the uppermost and lowermost layers and the intermediate layer with a thickness twice as large as the other layers; Kurkina et al., 2011a) may persist in several locations of the sea for longer time intervals.

Vertically Integrated Kinetic and Potential Energy

We perform the analysis of spatial distribution of energy of baroclinic motions in terms of the relevant vertically integrated quantities. The core measures are (i) the fluctuations of vertical locations of the pycnoclines, (ii) near-bottom speed U and (iii) potential and (iv) kinetic energy in the entire water column per unit of sea surface. While vertical motions of the pycnocline to a large extent reflect the amplitude of internal waves and baroclinic motions, the other quantities involve also the impact of other motions of water masses. However, high near-bottom speeds are often associated with intense internal waves or other baroclinic motions. We employ the classic expressions for the kinetic (E_k) and potential (E_p) energy in this study:

$$E_p\left(x,y,t\right) = g\int_0^H \rho\left(x,y,z,t\right)\left(H-z\right)dz, \tag{2}$$

$$E_k\left(x,y,t\right) = \frac{1}{2}\int_0^H \rho\left(x,y,z,t\right)\left[u^2\left(x,y,z,t\right)+v^2\left(x,y,z,t\right)\right]dz. \tag{3}$$

Here x, y are horizontal coordinates, z is the vertical coordinate, $z = 0$ corresponds to the undisturbed sea surface, H is the total water depth, t is time, ρ is the density of sea water and (u, v) are horizontal velocity components of water parcels.

The location of the main pycnocline correlates well (with a large negative correlation coefficient) with the near-bottom speed (**Figure 5**). This kind of correlation may reflect the seasonal intensification of the baroclinic motions. Also, it may mirror the impact of changes in the vertical structure of water masses on local properties of baroclinic motions and associated velocity fields. For example, it is expected that shallower near-bottom layers host to higher near-bottom speeds even if the energy of internal waves is the same.

Spectral Properties

We use spectral analysis to identify the spatial patterns and maxima and minima of the energy of motions in the range of periods of 2–12 days. The choice of the lower limit is dictated by the temporal resolution of the data set (6 h). The use of this sampling interval does not allow for an analysis of oscillations with periods shorter than 12 h. It is also desirable to implicitly exclude inertial motions and the signal of tides but still keep motions that correspond to relatively large energy in subbasins of the Baltic Sea (e.g., a secondary maximum at 8 h in the Gulf of Finland, see Sukhachev et al., 2014). Such an analysis is often used as a powerful tool to extract the predominant (resonant) modes or (eigen)oscillations of the basin. However, well-defined peaks of resonant modes are relatively infrequent and natural basins are more commonly characterized by wide peaks or gently sloping spectra. This is the situation also with slow motions in the Baltic Sea (**Figure 5C**). For this reason we address the entire field of motions in the discussed range of periods. The upper limit of 12 days, on the one hand, supports the propagation of wave energy over the entire Baltic Sea basin. On the other hand, it excludes the impact of certain specific basin-scale motions (e.g., major changes in the entire water volume of the Baltic Sea, see Lehmann et al., 2004; Lehmann and Post, 2015) on the outcome of the analysis.

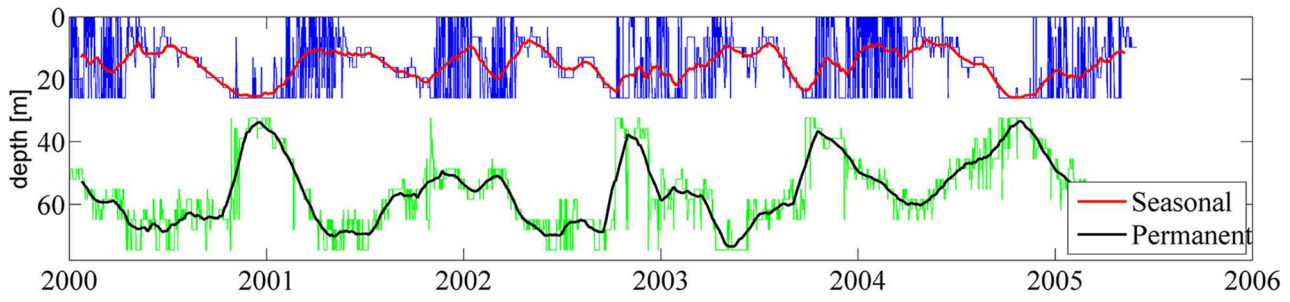

FIGURE 4 | Vertical location of the seasonal (upper line) and main (permanent) pycnocline (lower line) 18.35°E, 58.01°N (point 23 in **Figure 3**) in 2000–2005. Thin lines represent the locations of the jump layer with a resolution of 6 h whereas the bold lines present the monthly moving average. Note that the restriction for the main pycnocline (below 30 m) and for the seasonal pycnocline to be located above this level may lead to an artificial separation of the two jump layers during certain time intervals (e.g., December 2001 or November 2005).

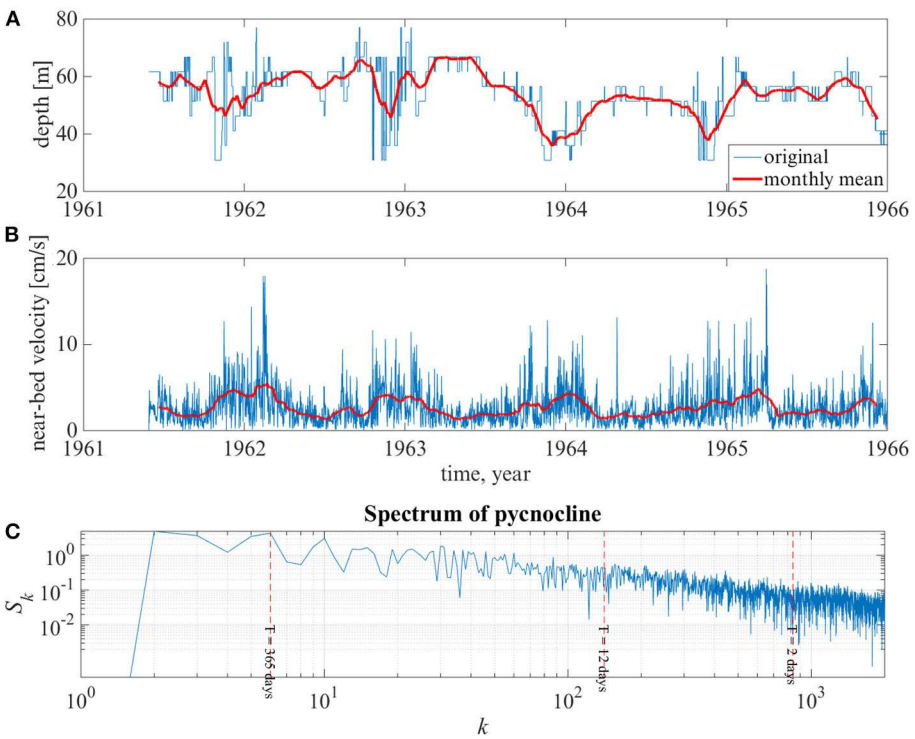

FIGURE 5 | Temporal course of the location of the main pycnocline **(A)**, near-bottom speed **(B)** and wavenumber spectra of fluctuations of the vertical location of the main pycnocline **(C)** at 18.25°E, 58.56°N (point BY31 in **Figure 3**). Thin lines in **(A,B)** panels show the course each 6 h. Bold lines represent moving average over 1 month.

The results of spectral analysis are presented below in terms of time-averaged spectral amplitudes A:

$$A = T \int_{f_l}^{f_u} S(f)\, df. \tag{4}$$

Here f_l and f_u are the minimum and maximum frequencies of the chosen range of periods (2–12 days), the factor T corresponds to its length (10 days), and $S(f)$ presents the discrete spectral amplitude for the discrete time series s_j of any quantity mentioned above:

$$S_k = S(f_k) = \frac{|\hat{S}_k|}{N}, \quad \hat{S}_k = \sum_{j=1}^{N} s_j \exp\left[-\frac{2\pi i}{N}(j-1)(k-1)\right], \tag{5}$$

N is the number of single values in the time series of s_j, $f_k = \frac{kF_s}{N}$ are the discrete frequencies, $F_s = \frac{1}{T_s}$ is the step in frequency space and T_s is the associated time interval, equal to the time step of the modeled hydrophysical data (6 h). As all quantities in Equation (4) are discrete, integration was performed using

the simple trapezoidal rule. As we use the modeled values over almost half century but all existing measurements cover much shorter time periods, the calculated spectral amplitudes are not directly comparable with the ones extracted from measurements. However, given the demonstrated quality of the output of the RCO model (see the relevant references above), it is likely that the established qualitative patterns and areas that host high and low levels of different quantities are reliable.

RESULTS

Fluctuations of the Main and Seasonal Pycnocline

We use spectral amplitudes of fluctuations of the seasonal pycnocline as a proxy of the intensity of the baroclinic motions. These amplitudes are the largest along a narrow strip along the eastern Baltic Sea coast from the Bay of Gdańsk until the entrance to the Gulf of Finland (in locations approximately 50 km from the shore), in the middle of the southern Baltic proper between Hel Peninsula and the island of Öland, along the eastern coast of the Sea of Bothnia and in the offshore of the southern part of this water body (**Figure 6**). The lowest levels of spectral amplitudes in question are found in the archipelago areas in the nearshore of Finland and western Estonia and, somewhat surprisingly, in the Arkona basin, Belt Sea and the Kattegat. The pattern is thus substantially anisotropic and reveals notable eastern intensification. The areas with large amplitudes of motions of the seasonal pycnocline are predominantly in the eastern nearshore of the entire Baltic Sea and the Sea of Bothnia.

Interestingly, the described pattern has almost no changes from the 1960s until 2000s (**Figure 6**). Even though the overall storminess in the Baltic Sea basin has not significantly altered since the 1880s (Hünicke et al., 2015), a substantial increase has occurred in the mean winter (December–January) wind speed in the entire Baltic Sea basin 1970–1995 (see, for example, Figure 4.10 of Rutgersson et al., 2015). Therefore, the overall stability of the established pattern is deeply non-trivial.

The calculations are performed in terms of spectral amplitudes of motions. The results thus characterize the average magnitude of motions over many years and, strictly speaking, cannot be directly associated with any particular phenomena. It is still likely that the revealed pattern to some extent reflects a regularly repeating configuration of baroclinic motions in the Baltic Sea. It qualitatively matches a typical picture of the amplitude distribution of standing oscillations of the lower basin-wide baroclinic mode with antinodes (amplitude maxima) in relatively shallow areas of the basin and nodal regions (with amplitudes close to zero) in central deeper parts of the sea. This pattern becomes evident not only in the Baltic proper but also in the Gulf of Finland, Sea of Bothnia, and Gulf of Bothnia. The relative amplitudes of the pycnocline fluctuations are much smaller in the subbasins than in the Baltic proper even though stratification in these subbasins is much weaker (Leppäranta and Myrberg, 2009).

Similar spectral amplitudes of fluctuations of the depth of the main pycnocline (**Figure 7**) represent only relatively deep areas where this jump layer is present during most of the time. Differently from the above, western intensification is observed. Namely, the areas with the most intense fluctuations (and thus with the largest baroclinic wave activity) are predominantly located near the western shores of the Baltic proper and the Sea of Bothnia, and in the Åland Sea. Only very small areas with comparable spectral amplitudes are found near the entrance of the Gulf of Finland (in an area to the north-west of the Western Estonian archipelago). If this pattern is interpreted as above (reflecting regularly repeating configuration of baroclinic waves or internal seiches), it may reflect frequently occurring baroclinic internal seiches with antinodes in the nearshore. This pattern in the Baltic proper seems to be strongly modified by the island of Gotland. Its presence seems to give rise to two separate structures whereas the nodal areas are more clearly localized.

A combined spatial distribution of spectral amplitudes (**Figure 8**) reveals that the energy of baroclinic motions is inhomogeneously distributed along the nearshore of the Baltic Sea. The eastern and north-western coasts of the Baltic proper and most of the nearshore and offshore of the Sea of Bothnia host substantial activity of this sort of motions. As above, this pattern signals that these basins may have frequent internal (standing) oscillations with antinodes in these locations. The western coast of the Western Gotland Basin, the entire south-western part of the sea and smaller sub-basins (Gulf of Riga, Gulf of Finland and Bay of Bothnia) have much lower levels of spectral amplitudes of pycnocline fluctuations. This feature may interpreted as an indication of the frequent presence of nodes of such oscillations. This pattern is also basically the same for the 1960s and the 2000s.

Near-Bottom Velocities

The distributions of maximum near-bottom velocities and their spectral amplitudes (**Figures 9**, **10**) substantially differ from the above-discussed ones. The basin-wide pattern of high velocities resembles the pattern of large spectral amplitudes of vertical fluctuations of the main pycnocline. In both occasions high velocities systematically occur along the eastern nearshore of the Baltic proper and the Sea of Bothnia. The areas of high velocities are closer to the shore. This feature indicates a significant contribution to water velocities from surface waves (e.g., via wave-driven nearshore currents during long wave storms or relaxation of wave set-up events), wind-driven local currents and offshore circulation patterns.

The spatial distributions of velocities also have several considerably different features from those for fluctuations of pycnocline. The largest near-bottom velocities occur in specific spots located along sloping seabed. Large near-bed velocities may also occur in the Archipelago Sea between the Åland Islands and the Finnish mainland. It is likely that internal waves may be often generated in this area owing to shear flow through the deep channel between the Åland Islands and the Swedish mainland similarly to processes in the Gibraltar Strait (Vlasenko et al., 2009). The pattern of large near-bottom velocities only partially matches the spatial distribution of spectral amplitudes of near-bottom velocities (**Figure 10**). Both distributions suggest that the intensity of nearbed processes driven by baroclinic motions and internal waves is relatively low in the Gulf of Riga, Gulf of Finland

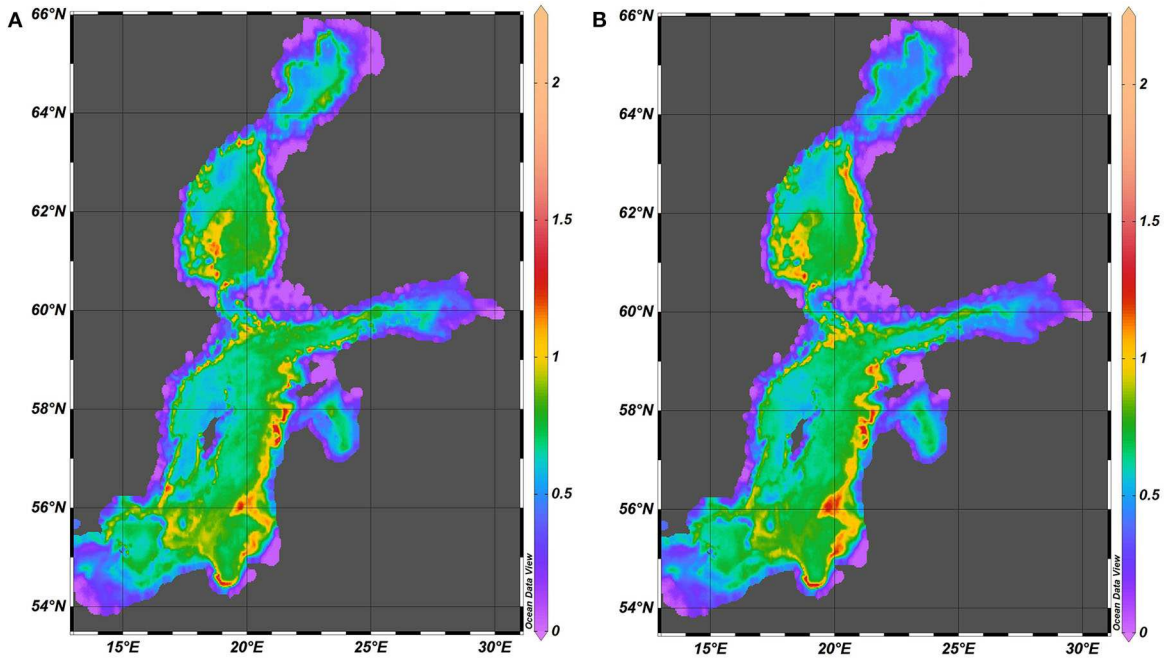

FIGURE 6 | Spatial distribution of the spectral amplitude (Equation 4) of vertical fluctuations of the seasonal pycnocline (m) in 1961–1965 **(A)** and 2000–2005 **(B)**.

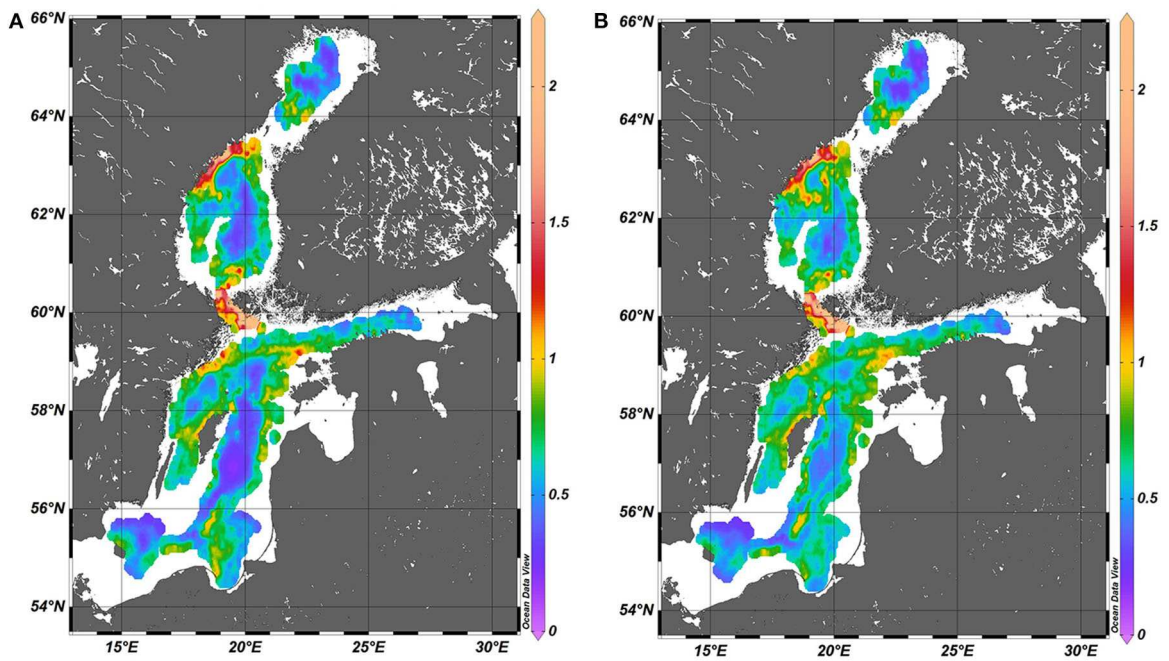

FIGURE 7 | Spatial distribution of the spectral amplitude (Equation 4) of vertical fluctuations of the main pycnocline (m) in 1961–1965 **(A)** and 2000–2005 **(B)**. The maximum value is 4.5 but for better readability the scale is limited to 2.25.

and Bay of Bothnia compared to the open Baltic proper and the vicinity of Danish straits.

Even though some details and particular maximum values of nearbed velocities in 2000–2005 (**Figure 9**) are slightly different from those in 1961–1965, the spatial patterns of maximum velocities for these two time intervals almost exactly match each other. The single maxima in 2000–2005 are somewhat larger apparently because of a few unusually strong storms in 2001

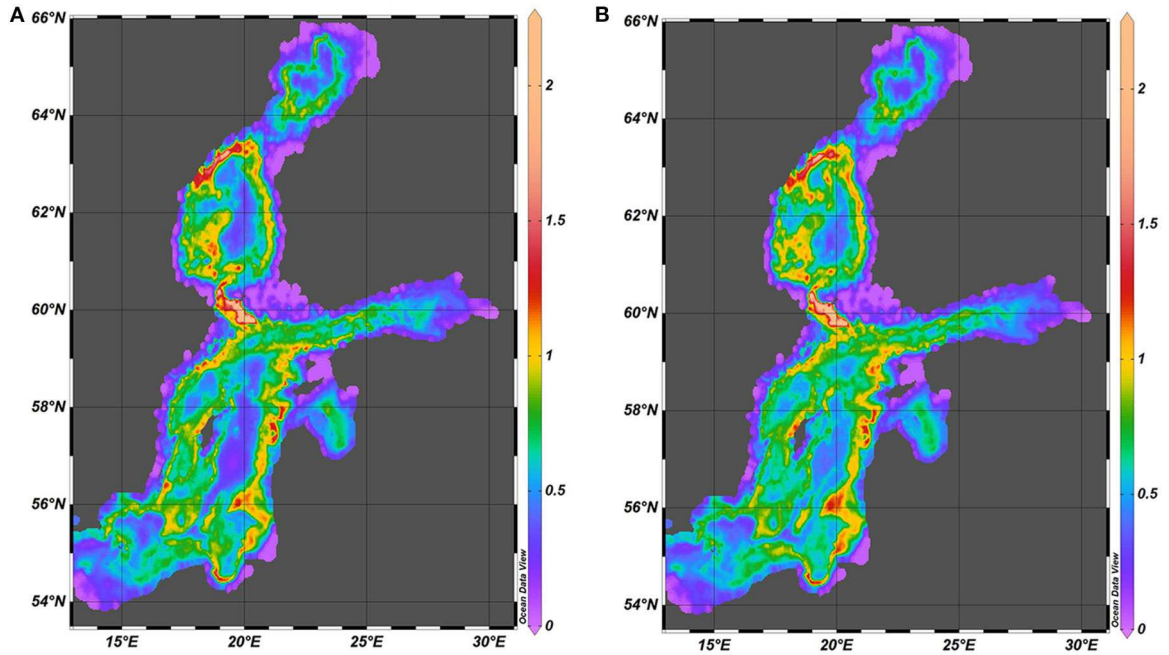

FIGURE 8 | Spatial distribution of the combined spectral amplitude (Equation 4) of vertical fluctuations of pycnocline (m) in 1961–1965 **(A)** and 2000–2005 **(B)**. The diagrams show this quantity for the main pycnocline in regions where it exists and the spectral amplitude for the seasonal pycnocline in the rest of the sea. The maximum value is 4.5 but for better readability the scale is limited to 2.25.

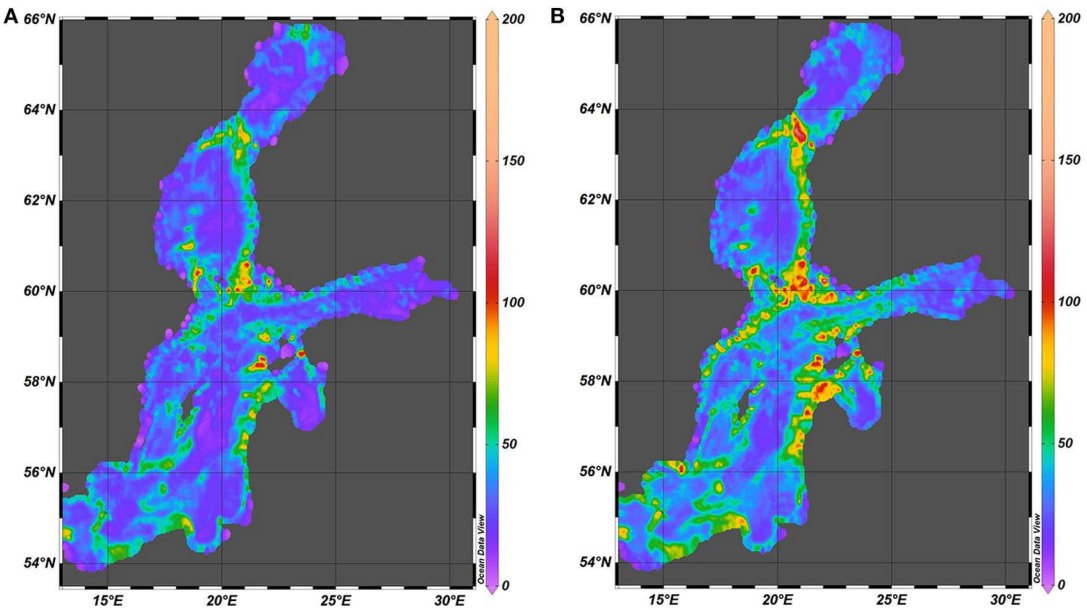

FIGURE 9 | Spatial distribution of the maximum nearbed speed (cm/s) in 1961–1965 **(A)** and in 2000–2005 **(B)**.

and 2005. These storms created exceptionally large water levels in many sections of the eastern Baltic Sea coast (Suursaar et al., 2006). A substantial level of baroclinic motions and/or internal wave activity evidently was created during the relaxation phase of these events. The match of the relevant distributions for the two time intervals suggests that the locations where the internal waves and/or other baroclinic motions exert the strongest impact on the seabed in terms of high water velocities are governed by certain long-term combinations of the vertical structure of water masses and the appearance of seabed bathymetry.

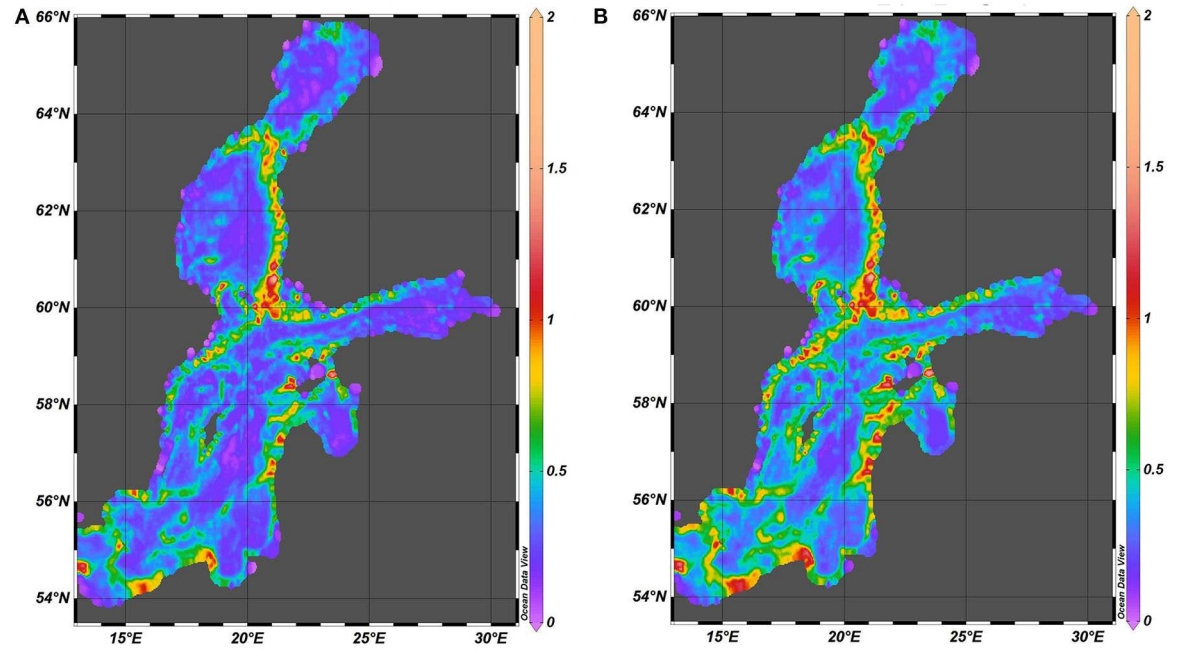

FIGURE 10 | Spatial distribution of the spectral amplitude of nearbed speed (cm/s) in 1961–1965 **(A)** and in 2000–2005 **(B)**.

Spatial Distributions of Potential and Kinetic Energy

Spatial distributions of spectral amplitude of potential energy normalized by the squared total depth (**Figure 11**) involve to some extent variations in the entire water level that may be largely driven by baroclinic perturbations (Zakharchuk et al., 2017). The spectral amplitudes in question thus provide another proxy of the intensity and frequency of baroclinic motions in this water body. Their distributions are substantially different from all distributions considered so far. Similarly to the above, these distributions for 1961–1965 and 2000–2005 almost exactly match each other. They are different from those discussed above first of all by a strong concentration of the majority of normalized potential energy of in a narrow nearshore strip of the sea with a typical width of $<$20 km. All deeper parts of the sea have much lower levels of normalized potential energy. These amplitudes (equivalently, the level of potential energy of the motions in question) substantially vary along the shoreline. The nearshore sections with the largest spectral amplitudes differ from similar locations for surface waves (e.g., Soomere and Räämet, 2011). This feature is not particularly surprising because refraction and transformation properties of baroclinic motions and internal waves greatly differ from similar (refraction and shoaling) properties of surface waves.

The kinetic energy of motions in Equation (3) also involves the energy of currents. It is therefore not surprising that it is distributed in a considerably different manner compared with the potential energy. The maxima of kinetic energy are located along sloping sections of the seabed around the deep areas in all basins of this water body (**Figure 12**). Very little kinetic energy is found in the deepest parts of the Baltic proper. The distribution has certain asymmetry: there is more kinetic energy in the eastern parts of the sea compared to the western parts. However, there is a visible correlation with the spatial distribution of the combined spectral amplitude of vertical fluctuations of the pycnocline (**Figure 8**).

The levels of kinetic energy are much smaller in the Gulf of Riga and Gulf of Finland than in the Baltic proper or in the Sea of Bothnia. This feature is expected for the Gulf of Riga (that is separated from the Baltic proper by a sill) but somewhat surprising for the Gulf of Finland (that is widely open to the Baltic proper).

A comparison of the magnitudes of spectral amplitudes of kinetic energy and near-bottom velocities (**Figure 13**) indicates a strong dependence of the impact of water motions possibly driven by different phenomena on the seabed on a particular location. For relatively small depths (below 50 m), there is a significant scatter of kinetic energy relative to the near-bottom velocities. For larger depths these two quantities exhibit a power-law-like dependence of the form $E_k \sim U^a$, $a < 1$.

CONCLUSIONS AND DISCUSSION

The presented estimates of spatial distributions of the main parameters that characterize the long-term statistics of baroclinic motions in the period range of 2–12 days in 1961–2005 first of all suggest that the relevant field of motions in the Baltic Sea is highly inhomogeneous and strongly asymmetric. Interplay of the complicated geometry of the basin with its spatially and temporally varying stratification gives rise to extensive

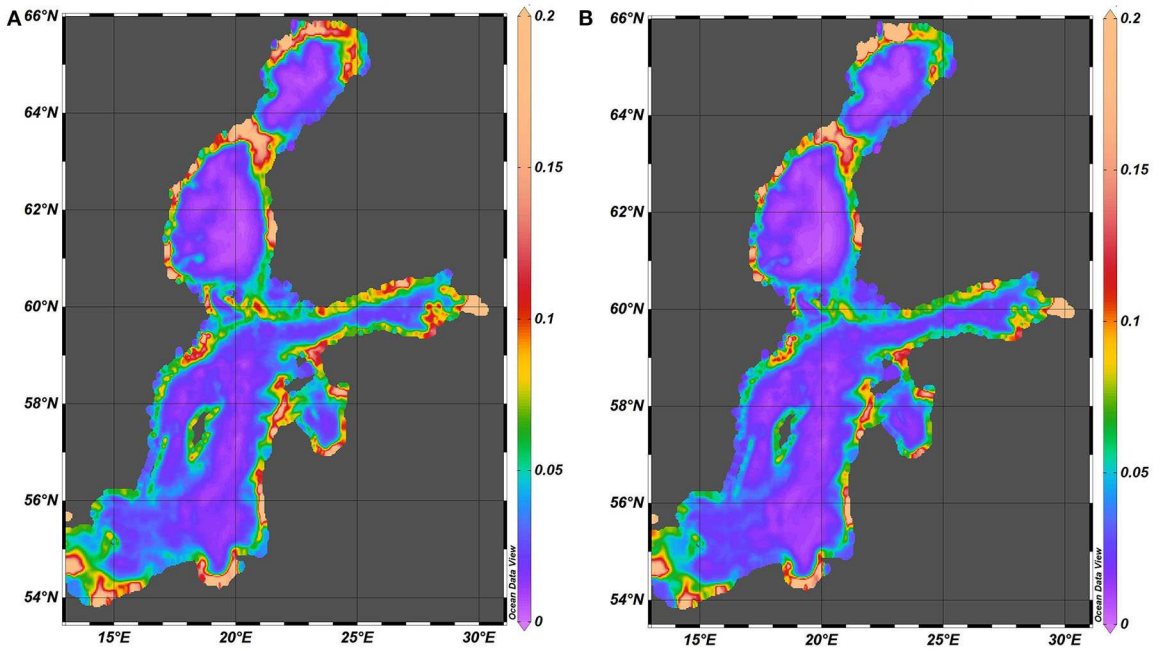

FIGURE 11 | Spatial distribution of the normalized ($1/H^2$) potential energy spectral amplitude (kg·s^{-2}·m^{-2}) in 1961–1965 **(A)** and 2000–2005 **(B)**.

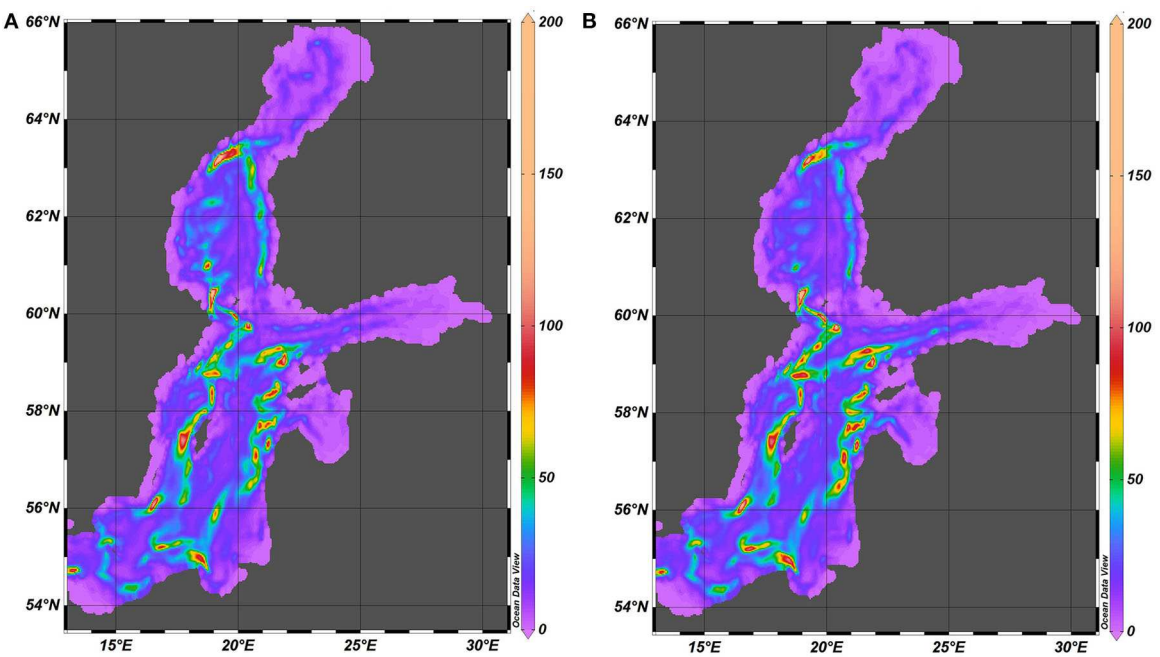

FIGURE 12 | Spatial distribution of kinetic energy (kg·s^{-2}) of internal waves in 1961–1965 **(A)** and 2000–2005 **(B)**. The maximum value is 400 kg·s^{-2} but for better readability the scale is limited to 200 kg·s^{-2}.

spatial variability of the associated quantities such as the typical amplitudes of fluctuations of the main and seasonal pycnocline, near-bottom velocity, and kinetic and potential energy. The variability extends from the basin scale down to scales on the order of about 10 km. This pattern matches well the perception that non-linear internal waves may change their appearance and kinematic properties along their usual pathways of propagation (Rouvinskaya et al., 2015) or that the internal wave dynamics

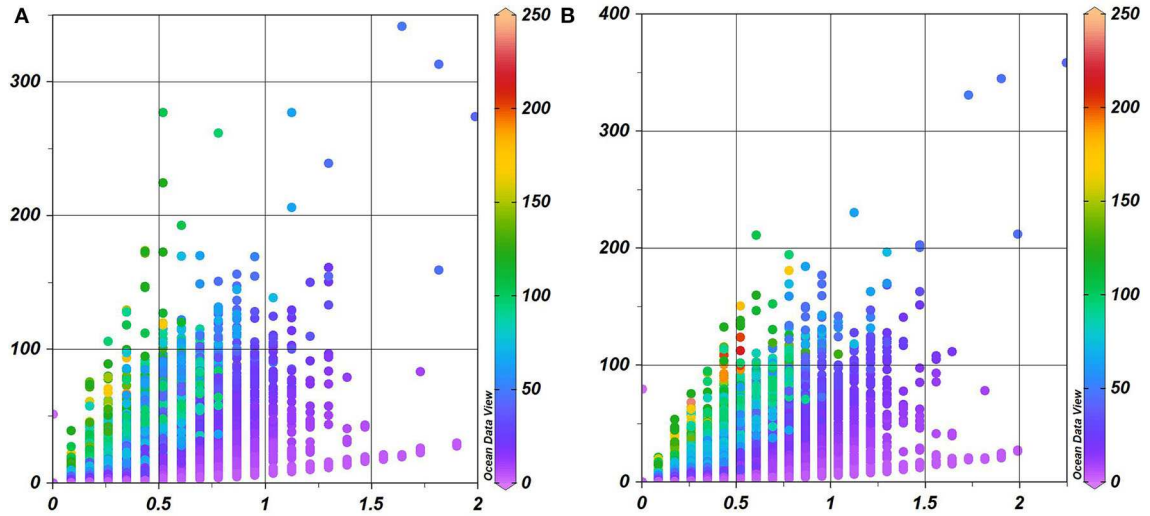

FIGURE 13 | Scatterplots of spectral amplitudes of kinetic energy (vertical axis) and nearbed velocities (horizontal axis) in 1961–1965 **(A)** and 2000–2005 **(B)**. Color scale indicates the water depth.

on both sides of several sills (e.g., Slupsk Sill, Massel, 2016) may be different due to the different vertical density stratification in these areas.

Even though the results are presented in terms of certain statistical quantities (spectral amplitudes of motions over many years) and do not resolve single events, some of the established patters may reflect the systematic presence of certain motions. In particular, the spatial distributions of fluctuations of both pycnoclines resemble the similar distribution of standing oscillations with antinodes in relatively shallow areas and nodal regions in central parts of the sea. This pattern exists for the Baltic proper, Gulf of Finland, Sea of Bothnia, and Gulf of Bothnia.

Most of the normalized potential energy of motions in question is concentrated in a narrow nearshore strip of the sea with a typical width of <20 km. All deeper parts of the sea have much lower levels of this quantity. This result is not unexpected as the amplitude of baroclinic and internal waves that are generated in deeper waters generally increases when the water depth decreases. It is not surprising that the average amplitude of this quantity greatly varies along the shoreline. However, it is interesting that this variation does not follow the similar variation of wave heights (Soomere and Räämet, 2011) or onshore wave energy flux of surface waves (Soomere and Eelsalu, 2014).

The majority of kinetic energy is concentrated in a different region of the sea and thus apparently may be associated with other kinds of motions than baroclinic or internal waves. Namely, the eastern parts of the Baltic Sea along the gently sloping seabed at depths of about 20–40 m apparently are impacted by mesoscale and basin-scale currents that persist for a few days. Owing to strong non-linearity of such motions, these regions can serve as the main zones of generation of short-period internal waves (on the possible wave regimes, see: Kurkina et al., 2014). The areas of maximum nearbed velocities only partially match similar areas of very large kinetic energy or areas with the largest fluctuations of the pycnocline depth. This also not unexpected as the motions excited by baroclinic motions of the kind addressed in this paper are mostly concentrated in the vicinity of jump layers and only drive large near-bottom velocities if the bottom layer is thin or the wave is breaking. Therefore, it is necessary to take into account the particular appearance of the motion, its detailed characteristics and the local vertical structure of water masses for reliable estimates of its impact on the seabed.

The presence of several hot spots of hydrodynamic activity driven by baroclinic motions and quantified here in terms of near-bottom velocity (**Figures 9**, **10**) is a principally new feature of the dynamics of the Baltic Sea. Such spots in regions with rocky bottom (mostly around the Åland Islands) may greatly contribute into the limitations and forcing factors of the local ecosystem but apparently do not strongly affect the dynamics of bottom sediment. Similar spots along the nearshore of Latvia (where the seabed predominantly consists of finer sediment) may change the current understanding of the stability and integrity of seabed in this area. It is commonly thought that the sediment properties and motions in the areas much deeper than the closure depth (about 6–7 m for this coastal stretch, Soomere et al., 2017) are basically determined by the properties of near-bottom motions driven by large-scale circulation and mesoscale features. Our results suggest that in several locations specifically the baroclinic and/or internal wave activity may be the main factor controlling the deposition and resuspension and affecting and shaping the features of the seabed.

Both the major properties and spatial details of the discussed distributions exhibit almost no difference for the years 1961–1965 and 2000–2005. Only the maximum seabed velocities are somewhat larger in 2000–2005 apparently because of exceptional storms in 2001 and 2005. This stability suggests that the clear changes in the external forcing

(e.g., Soomere et al., 2015), including a substantial increase in the mean winter (December–January) wind speed in the entire Baltic Sea basin 1970–1995 (Rutgersson et al., 2015), and variations in the vertical structure of water masses (Väli et al., 2013) over the second half of the twentieth century have almost not influenced the discussed features of "climate" of baroclinic motions in the Baltic Sea.

Finally, we emphasize that the described features stem exclusively from model simulations. Even though the model itself has been extensively validated against hydrophysical data (Meier et al., 2004; Placke et al., 2018) and the quality of forcing fields has been estimated in detail (Placke et al., 2018), the level of uncertainty of the presented results remains an open question.

DATA AVAILABILITY STATEMENT

The data analyzed in this study was obtained from the Swedish Meteorological and Hydrological Institute in the framework of the BONUS BalticWay initiative. The data are free for academic research purposes. Requests to access these datasets should be directed to Prof. H. E. Markus Meier (meier@io-warnemuende.de).

AUTHOR CONTRIBUTIONS

AK, TS, and OK designed the study, supervised the entire process, developed the method for the analysis, provided the first interpretation of results, created test images, and drafted the body parts of the paper. AR extracted the necessary data from the RCO output data set and wrote most of the scripts for the analysis. TS drafted the introduction and discussion sections and wrote the description of the RCO model. AR and ER performed the analysis, created the images, and contributed to the drafting of the Results section. All authors participated in the final polishing of the manuscript and have accepted the submitted version of the manuscript.

FUNDING

This study was initiated in the framework of grants of the President of the Russian Federation (NSh-2485.2020.5 and SP-1225.2019.5), institutional block grant IUT33-3 of the Estonian Ministry of Education and Research, and the Flag-ERA project Large scale experiments and simulations for the second generation of FuturICT (FuturICT 2.0), Estonian Research Council grant 4-8/17/1.

REFERENCES

Axell, L. B. (1998). On the variability of Baltic Sea deepwater mixing. *J. Geophys. Res.-Oceans* 103, 21667–21682. doi: 10.1029/98JC01714

Axell, L. B. (2002). Wind-driven internal waves and Langmuir circulations in a numerical ocean model of the southern Baltic Sea. *J. Geophys. Res.-Oceans* 107:922. doi: 10.1029/2001JC000922

Bagaev, A., Mizyuk, A., Khatmullina, L., Isachenko, I., Chubarenko, I. (2017). Anthropogenic fibres in the Baltic Sea water column: field data, laboratory and numerical testing of their motion. *Sci. Total. Environ.* 599, 560–571. doi: 10.1016/j.scitotenv.2017.04.185

Beldowski, J., Klusek, Z., Szubska, M., Turja, R., Bulczak, A. I., Rak, D., et al. (2016). Chemical munitions search and assessment-an evaluation of the dumped munitions problem in the Baltic Sea. *Deep Sea Res. II* 128, 85–95. doi: 10.1016/j.dsr2.2015.01.017

Bentley, S. J., and Nittrouer, C. A. (1999). Physical and biological influences on the formation of sedimentary fabric in an oxygen-restricted depositional environment: Eckernförde Bay, southwestern Baltic Sea. *Palaios* 14, 585–600. doi: 10.2307/3515315

Burchard, H., Craig, P. D., Gemmrich, J. R., van Haren, H., Mathieu, P.-P., Meier, H. E. M., et al. (2008). Observational and numerical modeling methods for quantifying coastal ocean turbulence and mixing. *Progr. Oceanogr.* 76, 399–442. doi: 10.1016/j.pocean.2007.09.005

Dalsgaard, T., De Brabandere, L., and Hall, P. O. J. (2013). Denitrification in the water column of the central Baltic Sea. *Geochim. Cosmochim. Acta* 106, 247–260. doi: 10.1016/j.gca.2012.12.038

Eelsalu, M., Soomere, T., Pindsoo, K., and Lagemaa, P. (2014). Ensemble approach for projections of return periods of extreme water levels in Estonian waters. *Cont. Shelf Res.* 91, 201–210. doi: 10.1016/j.csr.2014.09.012

Fofonoff, N., and Millard, R. Jr. (1983). Algorithms for computation of fundamental properties of seawater. *UNESCO Tech. Paper Mar. Sci.* 44, 15–25.

Friedrichs, C. T., and Wright, L. D. (1995). Resonant internal waves and their role in transport and accumulation of fine sediment in Eckernförde Bay, Baltic Sea. *Cont. Shelf Res.* 15, 1697–1709. doi: 10.1016/0278-4343(95)00035-Y

Glasby, G. P., Uscinowicz, S., and Sochan, J. A. (1996). Marine ferromanganese concretions from the polish exclusive economic zone: influence of major inflows of North Sea water. *Mar. Geores. Geotechnol.* 14, 335–352. doi: 10.1080/10641199609388321

Hibler, W. D. (1979). A dynamic thermodynamic sea ice model. *J. Phys. Oceanogr.* 9, 815–846. doi: 10.1175/1520-0485(1979)009<0815:ADTSIM>2.0.CO2

Hünicke, B., Zorita, E., Soomere, T., Madsen, K. S., Johansson, M., and Suursaar, Ü. (2015). "Recent change - sea level and wind waves," in *Second Assessment of Climate Change for the Baltic Sea Basin*, The BACC II author team (Cham: Springer), 155–185. doi: 10.1007/978-3-319-16006-1_9

Jonsson, B., Döös, K., Nycander, J., and Lundberg, P. (2008). Standing waves in the gulf of Finland and their relationship to the basin-wide Baltic seiches. *J. Geophys. Res.-Oceans* 113:C03004. doi: 10.1029/2006JC003862

Kulikov, E. A., Fain, I. V., and Medvedev, I. P. (2015). Numerical modeling of anemobaric fluctuations of the Baltic Sea level. *Russian Meteorol. Hydrol.* 40, 100–108. doi: 10.3103/S1068373915020053

Kurkina, O., Kurkin, A., Soomere, T., Rybin, A., and Tyugin, D. (2014). "Pycnocline variations in the Baltic Sea affect background conditions for internal waves," in *The 6th IEEE/OES Baltic Symposium Measuring and Modeling of Multi-Scale Interactions in the Marine Environment, May 26–29, Tallinn Estonia* (IEEE Conference Publication). doi: 10.1109/BALTIC.2014.6887879

Kurkina, O., Pelinovsky, E., Talipova, T., and Soomere, T. (2011b). Mapping the internal wave field in the Baltic Sea in the context of sediment transport in shallow water. *J. Coast. Res.* Special Issue 64, 2042–2047.

Kurkina, O. E., Kurkin, A. A., Soomere, T., Pelinovsky, E. N., and Ruvinskaya, E. A. (2011a). Higher-order (2+4) Korteweg-de Vries-like equation for interfacial waves in a symmetric three-layer fluid. *Phys. Fluids* 23:116602. doi: 10.1063/1.3657816

Lappe, C., and Umlauf, L. (2016). Efficient boundary mixing due to near-inertial waves in a nontidal basin: observations from the Baltic Sea. *J. Geophys. Res.-Oceans* 121, 8287–8304. doi: 10.1002/2016JC011985

Lass, H. U., Prandke, H., and Liljebladh, B. (2003). Dissipation in the Baltic proper during winter stratification. *J. Geophys. Res. Oceans* 108(C6):3187. doi: 10.1029/2002JC001401

Lehmann, A., Lorenz, P., and Jacob, D. (2004). Modelling the exceptional Baltic Sea inflow events in 2002–2003. *Geophys. Res. Lett*. 31:L21308. doi: 10.1029/2004GL020830

Lehmann, A., and Post, P. (2015). Variability of atmospheric circulation patterns associated with large volume changes of the Baltic Sea. *Adv. Sci. Res*. 12, 219–225. doi: 10.5194/asr-12-219-2015

León, R., Somoza, L., Medialdea, T., González, F. J., Gimenez-Moreno, C. J., and Pérez-López, R. (2014). Pockmarks on either side of the Strait of Gibraltar: formation from overpressured shallow contourite gas reservoirs and internal wave action during the last glacial sea-level lowstand? *Geo Mar. Lett*. 34, 131–151. doi: 10.1007/s00367-014-0358-2

Leppäranta, M., and Myrberg, K. (2009). *Physical Oceanography of the Baltic Sea*. Berlin: Springer. doi: 10.1007/978-3-540-79703-6

Lilover, M.-J., and Stips, A. (2008). "Observation, parameterization and simulation of turbulent mixing in the Gulf of Finland, the Baltic Sea," in *2008 IEEE/OES US/EU-Baltic International Symposium* (IEEE), 253–259. doi: 10.1109/BALTIC.2008.4625524

Lilover, M.-J., and Stips, A. K. (2011). An alternative parameterization of eddy diffusivity in the Gulf of Finland based on the kinetic energy of high frequency internal wave band. *Boreal Environ. Res*. 16(Suppl. A), 103–116.

Löptien, U., and Meier, H. E. M. (2011). The influence of increasing water turbidity on the sea surface temperature in the Baltic Sea: a model sensitivity study. *J. Mar. Syst*. 88, 323–331. doi: 10.1016/j.jmarsys.2011.06.001

Lundhansen, L. C., and Skyum, P. (1992). Changes in hydrography and suspended particulate matter during a barotropic forced inflow. *Oceanol. Acta* 15, 339–346.

Massel, S. R. (2015). *Internal Gravity Waves in the Shallow Seas.* Cham: Springer. doi: 10.1007/978-3-319-18908-6_7

Massel, S. R. (2016). On the nonlinear internal waves propagating in an inhomogeneous shallow sea. *Oceanologia* 58, 59–70. doi: 10.1016/j.oceano.2016.01.005

Meier, H. E. M. (2001). On the parameterization of mixing in three-dimensional Baltic Sea models. *J. Geophys. Res.-Oceans* 106, 30997–31016. doi: 10.1029/2000JC000631

Meier, H. E. M. (2007). Modeling the pathways and ages of inflowing salt- and freshwater in the Baltic Sea. *Estuar. Coast. Shelf Sci*. 74, 610–627. doi: 10.1016/j.ecss.2007.05.019

Meier, H. E. M., Broman, B., and Kjellström, E. (2004). Simulated sea level in past and future climates of the Baltic Sea. *Clim. Res*. 27, 59–75. doi: 10.3354/cr027059

Meier, H. E. M., Döscher, R., and Faxén, T. (2003). A multiprocessor coupled ice-ocean model for the Baltic Sea: application to salt inflow. *J. Geophys. Res.-Oceans* 108, 32–73. doi: 10.1029/2000JC000521

Meier, H. E. M., Feistel, R., Piechura, J., Arneborg, L., Burchard, H., Fiekas, V., et al. (2006). Ventilation of the Baltic Sea deep water: a brief review of present knowledge from observations and models. *Oceanologia* 48, 133–164.

Meier, H. E. M., and Höglund, A. (2013). "Studying the Baltic Sea circulation with eulerian tracers," in *Preventive Methods for Coastal Protection*, eds T. Soomere and E. Quak (Cham: Springer), 101–130. doi: 10.1007/978-3-319-00440-2_4

Metzner, M., Gade, M., Hennings, I., and Rabinovich, A. B. (2000). The observation of seiches in the Baltic Sea using a multi data set of water levels. *J. Mar Syst*. 24, 67–84. doi: 10.1016/S0924-7963(99)00079-2

Mohrholz, V., Dutz, J., and Kraus, G. (2006). The impact of exceptionally warm summer inflow events on the environmental conditions in the Bornholm Basin. *J. Mar. Syst*. 60, 285–301., doi: 10.1016/j.jmarsys.2005.10.002

Nohr, C., and Gustafsson, B. G. (2009). Computation of energy for diapycnal mixing in the Baltic Sea due to internal wave drag acting on wind-driven barotropic currents. *Oceanologia* 51, 461–494. doi: 10.5697/oc.51-4.461

Ozmidov, R. V. (1994). The significance of the seaboard effects on the deep-water exchange in the Baltic Sea. *Okeanologiya* 34, 490–495.

Pelinovsky, E. N., Talipova, T. G., Soomere, T., Kurkina, O. E., Kurkin, A. A., Tyugin, D., et al. (2018). Modelling of internal waves in the Baltic Sea. *Fund. Appl. Hydrophys*. 11, 8–20. doi: 10.7868/S2073667318020016

Placke, M., Meier, H. E. M., Gräwe, U., Neumann, T., Frauen, C., and Liu, Y. (2018). Long-term mean circulation of the Baltic Sea as represented by various ocean circulation models. *Front. Mar. Sci*. 5:287. doi: 10.3389/fmars.2018.00287

Reeder, D. B., Ma, B. B., and Yang, Y. J. (2011). Very large subaqueous sand dunes on the upper continental slope in the South China Sea generated by episodic, shoaling deep-water internal solitary waves. *Mar. Geol*. 279, 12–18. doi: 10.1016/j.margeo.2010.10.009

Reissmann, J. H., Burchard, H., Feistel, R., Hagen, E., Lass, H. U., Mohrholz, V., et al. (2009). Vertical mixing in the Baltic Sea and consequences for eutrophication - a review. *Progr. Oceanogr*. 82, 47–80. doi: 10.1016/j.pocean.2007.10.004

Ribó, M., Puig, P., Muñoz, A., Lo Iacono, C., Masqué, P., Palanques, A., et al. (2016). Morphobathymetric analysis of the large fine-grained sediment waves over the Gulf of Valencia continental slope (NW Mediterranean). *Geomorphology* 253, 22–37. doi: 10.1016/j.geomorph.2015.09.027

Roget, E., Khimchenko, E., Forcat, F., and Zavialov, P. (2017). The internal seiche field in the changing south aral sea (2006-2013). *Hydrol. Earth Syst. Sci*. 21, 1093–1105. doi: 10.5194/hess-21-1093-2017

Rouvinskaya, E., Talipova, T., Kurkina, O., Soomere, T., and Tyugin, D. (2015). Transformation of internal breathers in the idealised shelf sea conditions. *Cont. Shelf Res*. 110, 60–71. doi: 10.1016/j.csr.2015.09.017

Rutgersson, A., Jaagus, J., Schenk, F., Stendel, M., Bärring, L., Briede, A., et al. (2015). "Recent change-Atmosphere," in *Second Assessment of Climate Change for the Baltic Sea Basin*, The BACC II Author Team (Cham: Springer), 69–97. doi: 10.1007/978-3-319-16006-1_4

Samuelsson, P., Jones, C. G., Willén, U., Ullerstig, A., Gollvik, S., Hansson, U., et al. (2011). The Rossby Centre regional climate model RCA3: model description and performance. *Tellus A* 63, 4–23. doi: 10.1111/j.1600-0870.2010.00478.x

Soomere, T., Bishop, S. R., Viška, M., and Räämet, A. (2015). An abrupt change in winds that may radically affect the coasts and deep sections of the Baltic Sea. *Clim. Res*. 62, 163–171. doi: 10.3354/cr01269

Soomere, T., Döös, K., Lehmann, A., Meier, H. E. M., Murawski, J., Myrberg, K., et al. (2014). The potential of current- and wind-driven transport for environmental management of the Baltic Sea. *Ambio* 43, 94–104. doi: 10.1007/s13280-013-0486-3

Soomere, T., and Eelsalu, M. (2014). On the wave energy potential along the eastern Baltic Sea coast. *Renew. Energy* 71, 221–233. doi: 10.1016/j.renene.2014.05.025

Soomere, T., Männikus, R., Pindsoo, K., Kudryavtseva, N., and Eelsalu, M. (2017). Modification of closure depths by synchronisation of severe seas and high water levels. *Geo Mar. Lett*. 37, 35–46. doi: 10.1007/s00367-016-0471-5

Soomere, T., and Pindsoo, K. (2016). Spatial variability in the trends in extreme storm surges and weekly-scale high water levels in the eastern Baltic Sea. *Cont. Shelf Res*. 115, 53–64. doi: 10.1016/j.csr.2015.12.016

Soomere, T., and Räämet, A. (2011). Spatial patterns of the wave climate in the Baltic proper and the Gulf of Finland. *Oceanologia* 53, 335–371. doi: 10.5697/oc.53-1-TI.335

Sukhachev, V. N., Zakharchuk, E., Klevantsov, Yu. P., and Tikhonova, N. A. (2014). Variability of hydrological properties in the eastern part of the Gulf of Finland based on measurements in automated seabed station SPO GOIN (Изменчивость гидрологических характеристик в восточной части Финского залива по данным измерений на автоматической донной станции СПО ГОИ). *Problems Arctic Antarctic* (Проблемы Арктики и Антарктики) 3, 97–108. (in Russian).

Suursaar, Ü., Kullas, T., Otsmann, M., Saaremäe, I., Kuik, J., and Merilain, M. (2006). Cyclone Gudrun in January 2005 and modelling its hydrodynamic consequences in the Estonian coastal waters. *Boreal. Environ. Res*. 11, 143–159.

Talipova, T. G., Pelinovsky, E. N., and Kõuts, T. (1998). Kinematic characteristics of internal wave field in the Gotland Deep of the Baltic Sea. *Okeanologiya* 38, 37–46.

Turnewitsch, R., and Graf, G. (2003). Variability of particulate seawater properties related to bottom mixed layer-associated internal waves in shallow water on a time scale of hours. *Limnol. Oceanogr*. 48, 1254–1264. doi: 10.4319/lo.2003.48.3.1254

Umlauf, L., and Arneborg, L. (2009). Dynamics of rotating shallow gravity currents passing through a channel. Part I: observation of transverse structure. *J. Phys. Oceanogr*. 39, 2385–2401. doi: 10.1175/2009JPO4159.1

Uppala, S. M., Kållberg, P. W., Simmons, A. J., Andrae, U., da Costa, B. V., Fiorino, M., et al. (2005). The ERA-40 re-analysis. *Q. J. R. Meteorol. Soc*. 131, 2961–3012. doi: 10.1256/qj.04.176

Väli, G., Meier, H. E. M., and Elken, J. (2013). Simulated halocline variability in the Baltic Sea and its impact on hypoxia during 1961-2007. *J. Geophys. Res. Oceans* 118, 6982–7000. doi: 10.1002/2013JC009192

van der Lee, E. M., and Umlauf, L. (2011). Internal wave mixing in the Baltic Sea: near-inertial waves in the absence of tides. *J. Geophys. Res. Oceans*, 116:C10016. doi: 10.1029/2011JC007072

Vlasenko, V., Sanchez Garrido, J. C., Stashchuk, N., Lafuente, J. G., and Losada, M. (2009). Three-dimensional evolution of large-amplitude internal waves in the Strait of Gibraltar. *J. Phys. Oceanogr*. 39, 2230–2246. doi: 10.1175/2009JPO4007.1

Vlasenko, V., Stashchuk, N., and Hutter, K. (2005). *Baroclinic Tides: Theoretical Modeling and Observational Evidence*. Cambridge: Cambridge University *Press*. doi: 10.1017/CBO9780511535932

Whalen, C. B., MacKinnon, J. A., and Talley, L. D. (2018). Large-scale impacts of the mesoscale environment on mixing from wind-driven internal waves. *Nat. Geosci*. 11, 842–847. doi: 10.1038/s41561-018-0213-6

Wübber, C., and Krauss, W. (1979). The two-dimensional seiches of the Baltic Sea. *Oceanol. Acta* 2, 435–446.

Zakharchuk, E., Tikhonova, N., Gusev, A., and Diansky, N. (2017). "Influence of baroclinicity on sea level oscillations in the Baltic Sea," in *Conference on Physical and Mathematical Modeling of Earth and Environment Processes*, 380. doi: 10.1007/978-3-319-77788-7_38

Zakharchuk, E. A., and Tikhonova, N. A. (2013). Synoptic variability of the currents in the Gotland basin of the Baltic Sea. *Oceanology* 53, 385–400. doi: 10.1134/S0001437013030119

Conflict of Interest: The authors declare that the research was conducted in the absence of any commercial or financial relationships that could be construed as a potential conflict of interest.

Advantages of publishing in Frontiers

OPEN ACCESS
Articles are free to read for greatest visibility and readership

FAST PUBLICATION
Around 90 days from submission to decision

HIGH QUALITY PEER-REVIEW
Rigorous, collaborative, and constructive peer-review

TRANSPARENT PEER-REVIEW
Editors and reviewers acknowledged by name on published articles

Frontiers
Avenue du Tribunal-Fédéral 34
1005 Lausanne | Switzerland

Visit us: www.frontiersin.org
Contact us: frontiersin.org/about/contact

REPRODUCIBILITY OF RESEARCH
Support open data and methods to enhance research reproducibility

DIGITAL PUBLISHING
Articles designed for optimal readership across devices

FOLLOW US
@frontiersin

IMPACT METRICS
Advanced article metrics track visibility across digital media

EXTENSIVE PROMOTION
Marketing and promotion of impactful research

LOOP RESEARCH NETWORK
Our network increases your article's readership